THIS WEEK

EDITORIALS



WORLD VIEW UN wants to ride the rising tide of international hydro-diplomacy **p.6**

SOCIAL SELECTION If you build a crowd on social media, the money for your research will come **go.nature.com/t5ytxr**

Time for the social sciences

Governments that want the natural sciences to deliver more for society need to show greater commitment towards the social sciences and humanities.

Physics, chemistry, biology and the environmental sciences can deliver wonderful solutions to some of the challenges facing individuals and societies, but whether those solutions will gain traction depends on factors beyond their discoverers' ken. That is sometimes true even when the researchers are aiming directly at the challenge. If social, economic and/or cultural factors are not included in the framing of the questions, a great deal of creativity can be wasted.

This message is not new. Yet it gets painfully learned over and over again, as funders and researchers hoping to make a difference to humanity watch projects fail to do so. This applies as much to business as to philanthropy (ask manufacturers of innovative crops).

All credit, therefore, to those who establish multidisciplinary projects — for example, towards enhancing access to food and water, in adaptation to climate change, or in tackling illness — and who integrate natural sciences, social sciences and humanities from the outset. The mutual framing of challenges is the surest way to overcome the conceptual diversities and gulfs that can make such collaborations a challenge.

All credit, too, to leading figures in policy who demonstrate their commitment to this multidimensional agenda. And all the more reason for concern when governments show none of the same comprehension.

Such is the case in the United Kingdom. Research-wise, the country is in a state that deserves a bit of attention from others and certainly merits some concern from its own citizens. Its university funders last month announced the results of a unique exercise in nationwide research assessment — the Research Excellence Framework (REF), which will have a major impact on the direction of university funding. Almost simultaneously, its government released a strategy document: 'Our plan for growth: science and innovation'. And in November, its government's chief science adviser published a wide-ranging annual report that reflects the spirit of inclusiveness mentioned above. Unfortunately, the government's strategy does not.

THE IMPORTANCE OF INCLUSIVITY

Whatever the discipline, a sensible research-assessment policy puts a high explicit value both on outstanding discovery and scholarship, and on making a positive impact beyond academia. In that spirit, the REF (www.ref.ac.uk) aggregated three discretely documented aspects of the research of each university department: the quality and importance of the department's academic output, given a 65% weighting in the overall grade; the quality of the research environment (15%); and the reach and significance of its impact beyond academia (20%).

The influences of the data and panel processes that went into the REF results will not be analysed publicly until March. The signs are that the impacts component of assessment has allowed some universities to rise higher up the rankings than they would otherwise. But the full benefits and perverse incentives of the system will take deeper analysis to resolve.

A remarkable and contentious aspect of UK science policy is the extent to which the REF rankings will determine funding. The trend has been for such exercises to concentrate funding sharply towards the upper tiers of the rankings.

Most important in the current context is whether an over-dependence on funding formulae will undermine the nation's abilities to meet its future needs. A preliminary analysis by a policy magazine, *Research Fortnight*, reaches a pessimistic conclusion for those who believe that the social sciences are strategically important: given the REF results, the social sciences will gain a smaller slice of the pie than the size of the community might have suggested. If that reflects underperformance in social science at a national scale, and given the strategic importance of these disciplines, a national ambition in, for example, sociology, anthropology and psychology that reaches beyond the funding formula needs to be energized.

"If you want science to deliver for society, you need to support a capacity to understand that society."

A reader of the government's science and innovation strategy (go.nature.com/u5xbnx) might reach the same conclusion. Its fundamental message is to be welcomed: understandably focusing on enhancing economic growth, it highlights the need for support of fundamental research, open information, strategic technologies and stimuli for business engagement and investment. But there is just one sentence that deals with the social sciences and humanities: a passing mention in the introduction that they are included whenever the word 'science' is used.

Credit to both chief science adviser Mark Walport and his predecessor, John Beddington, for their explicit and proactive engagement with the social sciences. This year's report, 'Innovation: managing risk, not avoiding it' (see go.nature.com/lwf1o7), demonstrates a commitment to inclusivity: it is a compendium of opinion and reflection from experts in psychology, behavioural science, statistics, risk, sociology, law, communication and public engagement, as well as natural sciences.

An example of the report's inclusive merits can be found in the sections on uncertainty, communication, conversations and language, in which heavyweight academics highlight key considerations in dealing with contentious and risk-laden areas of innovation. Case studies relating to nuclear submarines, fracking and flood planning are supplied by professionals and advocates directly involved in the debates. This is complemented by discussions of the human element in estimating risk from the government's behavioural insights team, as well as discussions of how the contexts of risk-laden decisions play a part. Anyone who has a stake in science or technology that is in the slightest bit publicly contentious will find these sections salutary.

The report's key message should be salutary for policy-makers worldwide. If you want science to deliver for society, through commerce, government or philanthropy, you need to support a capacity to understand that society that is as deep as your capacity to understand the science. And your policy statements need to show that you believe in that necessity. ■

© 2014 Macmillan Publishers Limited. All rights reserved



MARK GARTEN/UN PHOTO

The rising pressure of global water shortages

Water is becoming more scarce as populations increase, potentially leading to conflict. The age of hydro-diplomacy is upon us, says **Jan Eliasson**.

The world is experiencing a surge of water-related crises. The eastern basin of the Aral Sea dried up completely in August, for the first time in 600 years. California has experienced an unprecedented three-year drought. Demographic changes and unsustainable economic practices are affecting the quantity and quality of the water at our disposal. Rapid urbanization is creating huge pressure on water use and infrastructure, with lasting consequences on human health and urban environments. These changes make water an increasingly scarce and expensive resource — especially for the poor, the marginalized and the vulnerable.

Demand for water is projected to grow by more than 40% by 2050. By 2025, an estimated 1.8 billion people will live in countries or regions in which water is scarce, and two-thirds of the world's population could be living in conditions in which the supply of clean water does not meet the demand.

The picture is not entirely dark. Thanks to global mobilization behind the Millennium Development Goals, 2 billion people have benefited from access to improved water sources.

Still, let us remember that 750 million people do not have access to safe drinking water. Roughly 80% of wastewater is discharged untreated into oceans, rivers and lakes. Nearly 2 million children under the age of 5 die every year for want of clean water and decent sanitation. One billion people in 22 countries still defecate in the open. Two and a half billion people do not have adequate sewage disposal.

That is why I launched the 2013 Call to Action on Sanitation on behalf of the United Nations Secretary-General. We want to break the silence and taboo surrounding toilets and open defecation. These words must be natural elements of the diplomatic discourse on development.

In today's world, we see how the lack of access to water can fuel conflict and even threaten peace and stability. That is why in the coming year I would like to see more attention on what I call hydro-diplomacy.

Degraded access to water increases the risk of social tensions, political instability and intensified refugee flows. Even more disturbing is when we see this resource used as a weapon of war.

I witnessed this first-hand during the Darfur conflict in Sudan. On one trip in 2007 to a village in north Darfur, we were met by a group of women chanting: "Water, water, water." The enemy militia had poisoned their well, they said, forcing them to move to the overcrowded camps for internally displaced people.

In Iraq, ISIL has exploited access to water to expand its control over territory and to subjugate the population. This extremist group has cut off water to villages that resist its advance. It has deliberately flooded substantial areas of land, displacing thousands of civilians. In recent months, it has directed its operations to Iraqi hydroelectric dams — in particular, the Mosul dam. All of Mosul and 500,000 people in Baghdad would be in grave peril if the dam were to burst — a chilling prospect.

We have also seen tensions related to large hydroelectric projects, such as the Rogun Dam in Tajikistan and the Grand Ethiopian Renaissance Dam. Neighbouring countries have expressed deep concerns, and energy and agricultural interests are clashing.

Still, it would be a mistake to get caught up in 'water-war' rhetoric. Certainly, as freshwater shortages become increasingly acute, the threat of violence over water is a real one. But we must not lose sight of the opportunities that water offers as a source of cooperation. Tensions over water resources have historically led to more collaboration than conflict. Shared water has brought states together; the 1960 Indus Water Treaty between India and Pakistan survived three wars and remains in force today.

LACK OF **ACCESS TO WATER** CAN FUEL CONFLICT AND EVEN THREATEN **PEACE AND STABILITY.**

In other words, water can and should drive cooperation and conflict resolution. More than 90% of the world's population lives in countries that share river and lake basins, and 148 countries share at least one transboundary river basin. Almost 450 agreements on international waters were signed between 1820 and 2007. The Water Convention that was forged under the auspices of the United Nations Economic Commission for Europe in 1992 is one such notable agreement.

Moreover, shared water access can create space for inter-state dialogue on points of contention that, if left unattended, may threaten regional or international peace and security. One recent example of such cooperation is among countries of the Lake Chad Basin. Chad, Cameroon, Niger and Nigeria established the Basin Commission in 1964 to manage the declining waters of Lake Chad equitably. They were later joined by other concerned states, including Libya and the Central African Republic. This year, the mandate of the commission was expanded to cover regional security challenges such as terrorism, the arms trade and cross-border insurgencies.

All this to say that hydro-diplomacy is a reality. The potential for shared management of water as a means to achieve regional cooperation and conflict prevention is vital. In 2015 and beyond, through efforts in diplomacy, economics and scientific research, we need to focus on water as a source of cooperation, rather than as a source of conflict. ■

➲ NATURE.COM
Discuss this article online at:
go.nature.com/wxrhzk

Jan Eliasson *is deputy secretary-general of the United Nations.*
e-mail: valdrep@un.org

© 2015 Macmillan Publishers Limited. All rights reserved

NATURE | **NEWS**

Nicaragua defies canal protests

Scientists call for independent environmental assessment.

Lucas Laursen

27 December 2014

MANAGUA



Esteban Felix/AP

Lake Nicaragua is to be dredged along a 105-kilometre channel for the Grand Canal project.

Print

Nicaragua has great expectations for the Grand Canal, a US$50-billion, 5-year project to link its Caribbean and Pacific coasts with a 280-kilometre waterway. President Daniel Ortega and other supporters of the canal, who celebrated the start of construction on 22 December, say that it will generate much-needed income for residents of the second-poorest country in the Western Hemisphere.

But the plan has attracted protests from residents along the proposed route and from scientists around the world (A. Meyer and J. A. Huete-Peréz *Nature* **506,** 287–289; 2014), who charge that the Nicaraguan government and the Chinese company overseeing the project have sidestepped the environmental review process. With the release of a social and environmental impact assessment delayed from November 2014 until April, an informal group of researchers has banded together to produce what it says the government has failed to deliver: an independent evaluation of the project's potential impact.

Normally, before a major infrastructure project begins in Nicaragua, an independent commission would generate an environmental impact report and the environment ministry would take 6–8 months to review it and make recommendations, says engineer Víctor Campos, director of the Alexander von Humboldt Centre, an environmental non-profit

Top picks
from nature news

- Human sperm and egg precursors made from stem cells
- NASA's carbon mapper overcomes design flaw
- Physicists take a stand against multiverse

organization in Managua. But those rules do not apply to the canal: a law passed in 2013 exempts the project from standard environmental review.

speculations

HKND, the Hong Kong-based company that is building the canal, has commissioned its own assessment. The company says that a draft will be available for public review this month, with a final report in March or April. In November 2014, the company delivered an eight-hour presentation in Managua that critics say largely played down potential environmental impacts. A government spokesman did not reply to requests for information about the review process.

Scientists have therefore assembled an ad hoc review process of their own. An assessment completed in September by the Humboldt centre concluded that the canal would cause “very significant environmental impacts”, and probably would not have been approved under Nicaragua’s usual rules. And in November, participants at a scientific workshop in Managua hosted by the Nicaraguan Academy of Sciences came up with a list of environmental concerns about the canal project. “We can’t offer any advice, but we can pose the important questions that anyone should answer before embarking on a project this big,” says water-conservation researcher Luís Zambrano of the Autonomous University of Mexico in Mexico City, who was one of the 13 international scientists invited to the workshop.

Related stories

- Conservation: Nicaragua Canal could wreak environmental ruin
- Species mix across Panama Canal
- The Economic Effects of Ship Canals

More related stories

Topping the list of concerns are potential impacts on Lake Nicaragua, the largest lake in central America, which will be dredged to a depth of 30 metres along a 105-kilometre channel. By churning up bottom sediments, the dredging and subsequent maintenance of the channel is expected to make lake waters more turbid and decrease their oxygen levels. Projected consequences include fish die-offs and blooms of blue-green algae that could make the water undrinkable.

Invasive inlet

The construction plan also calls for creation of a 400-square-kilometre artificial lake near the canal’s Caribbean terminus. Researchers have expressed concern that this lake would open up the nation’s waterways to invasive species, as has happened in other such development projects (see ‘Suez expansion’).

Suez expansion

Juli Berwald

Nicaragua’s is not the only canal project moving forward faster than its environmental effects can be assessed. In August, Egypt announced a project to add a second lane to the Suez canal for 72 kilometres of its 162-kilometre length. By next summer, the canal is expected to ferry twice as much ship traffic between the Red Sea and the Mediterranean than it does at present.

The concern among marine scientists is that invasive species may find the expanded canal similarly convenient. Because it has no locks or other barriers, the canal’s currents, which mostly flow from the Red Sea to the Mediterranean, offer marine organisms a free ride — and an expanded canal means that more sea life can ride those currents. But as in Nicaragua, no environmental review was conducted before the project began.

In early December, 225 scientists from 25 countries signed a letter urging environmental oversight. “There are means available to limit the introduction of non indigenous species which can be carried out at the early stages of a project but which become increasingly expensive as the project progresses. The ecological and economic cost of inaction may be substantial,” the letter said. Three United Nations treaties have jurisdiction over activities that affect the health of the Mediterranean, but none has been enforced.

Of the nearly 700 invasive species already in the Mediterranean, more than half arrived through the Suez (B. S. Galil *et al. Ethol. Ecol. Evol.* **26,** 152–171; 2014). Fish hauls off Turkey are up to 80% non-native species by weight, especially in shallow waters (M. Goren *et al. Rapp. Comm. Int. Mer. Médit.* **39,** 535; 2010). “We don’t know where the tipping point is, but it will be reached soon,” says marine biologist Bella Galil at the National Institute of Oceanography in Haifa, Israel. Without environmental oversight, she adds, there is no predicting what the system will tip to, either. But native communities are already eroding.

Near Turkey, for example, two species of shell-forming plankton (*Amphistegina lobifera* and *Amphisorus hemprichi*) now grow regularly. When they die, their remains accumulate in sandy layers that can be 50 centimetres thick (M. B. Yokes *et al. Mar. Biodivers. Rec.* **7,** e52; 2014), smothering natural rocky-bottom ecosystems. Two species of Red Sea rabbitfish (*Siganus luridus* and *Siganus rivulatus*) have razed swathes hundreds of metres long in rich seaweed meadows in the eastern Mediterranean, demolishing habitat for many natives. And just as in terrestrial ecosystems, says Enric Sala, a marine ecologist and explorer-in-residence at the National Geographic Society in Washington DC who has studied the rabbitfish,“when you remove the forest, all the birds are gone”.

At the same time, the canal could pose a barrier to native terrestrial animals. At its eastern end, it will cut through the Cerro Silva Natural Reserve, 286,000 hectares of protected forest. It could have a significant impact on wildlife migration corridors, says Roberto Salom-Pérez, regional coordinator of the Mesoamerica Jaguar Program for Panthera, a conservation charity in Costa Rica. But he says that animals can co-exist with infrastructure if it is well planned. “We know that jaguars and other big mammals can cross the Panama Canal,” he says. “But this is only possible because the well-protected Barro Colorado Island works as a stepping-stone for these species, and because protected areas surround the canal.”

About 2% of Nicaragua’s people live along the Grand Canal’s proposed route. The Humboldt centre estimates that the canal zone will pass through or near 282 communities, including a large tract of indigenous communal land. The canal concession gives HKND the right to seize this and other land, and Nicaraguans far from the canal route have reported visits to their land by Chinese surveyors accompanied by Nicaraguan military escorts. In mid-December, people marched in Managua to protest against the canal project.

In 2007, Ortega promised citizens that he would not risk the waters of Lake Nicaragua for all the gold in the world. This October, he said that he had come around to the idea of the canal because it would be the country’s fastest route to economic development. The nation’s public sector stands to benefit from the deal: HKND will pay the government $10 million annually for the first 10 years of the canal's operation, and hand ownership of the canal to the government gradually at a rate of roughly 10% per decade to a maximum of 99%.

Nature **517,** 7–8 (01 January 2015) doi:10.1038/517007a

Related stories and links

From nature.com

- **Conservation: Nicaragua Canal could wreak environmental ruin**
 19 February 2014
- **Species mix across Panama Canal**
 18 August 2004
- **The Economic Effects of Ship Canals**
 15 December 1898
- **The Nicaragua Canal**

11 June 1896

From elsewhere

- **HKND Group**
- **Nicaragua Academy of Sciences**
- **Suez Canal Authority**

For the best commenting experience, please login or register as a user and agree to our Community Guidelines. You will be re-directed back to this page where you will see comments updating in real-time and have the ability to recommend comments to other users.

1 comment

Subscribe to comments



Matt Chew • 2014-12-30 06:01 PM

Mentions of a "free ride" through canals perpetuate an unjustifiable impression that organisms want to be swept away when they literally have no ability to conceive of such a thing.

See other News & Comment articles from *Nature*

Nature ISSN 0028-0836 EISSN 1476-4687

© 2014 Nature Publishing Group, a division of Macmillan Publishers Limited. All Rights Reserved.
partner of AGORA, HINARI, OARE, INASP, CrossRef and COUNTER

NATURE | NEWS

Ebola raises profile of blood-based therapy

Convalescent plasma therapy is trialled to fight Ebola, but could also be used for new and emerging pathogens.

Declan Butler

23 December 2014



Michel du Cille/The Washington Post via Getty Images

Survivors of Ebola carry antibodies that might be used to save the lives of those infected with the virus.

With no drugs available to treat Ebola, eyes are turning to a therapy that had largely been relegated to the history books: transfusing patients with blood plasma donated by survivors, which contains antibodies against the virus.

Clinical trials of convalescent plasma therapy (CPT) have started in the past few weeks in Liberia, and are due to begin soon in Guinea and Sierra Leone. If the therapy saves lives, the approach could quickly be scaled up.

Success would also raise awareness of CPT's potential to treat other new and emerging infectious diseases for which there are no readily available effective drugs or vaccines, such as SARS, avian influenza and Middle East

Top picks
from nature news

- Human sperm and egg precursors made from stem cells

respiratory syndrome (MERS). “Clinical trials of convalescent plasma should be considered in other emerging infections,” says David Heymann, an infectious-disease researcher at the London School of Hygiene and Tropical Medicine, and chair of Public Health England.

- NASA's carbon mapper overcomes design flaw
- Physicists take a stand against multiverse speculations

Many scientists have long argued that CPT has been wrongly neglected, both as a therapy for emerging diseases and in preparation for future unknown threats. Today, the approach is gaining ground. Trials of convalescent plasma are beginning for the treatment of patients with MERS, which has infected 938 people and killed 343 of them since it was discovered in 2012. And an international protocol aimed at removing hurdles to quickly rolling out trials of convalescent plasma has recently been drafted.

Convalescent plasma was found to effectively treat diphtheria and tetanus at the end of the nineteenth century, and was widely used in the first half of the twentieth century to treat diseases such as measles, mumps and pneumonia. But it fell off the radar after the development of antibiotics, antiviral drugs and vaccines. (An exception was the adoption of CPT in Argentina for Argentine haemorrhagic fever after a successful controlled trial in the 1970s.)

When available, drugs and vaccines are usually a better option. They are easier to mass-produce and administer, and their quality and dosing can be better controlled. CPT is more complicated — it requires collecting survivors’ blood, screening it for pathogens and then organizing patient transfusion. And standardizing batches of plasma is difficult, because antibody levels in donated blood can vary widely.



***Nature* special:** Ebola outbreak in West Africa

But an epidemic or pandemic of a new pathogen turns that logic on its head. As in the case of the Ebola epidemic, there are typically no drugs or vaccines available, and developing these usually takes years. By contrast, “convalescent plasma is one of the few things you can get up and running quickly”, says Calum Semple, a paediatrician and clinical virologist at the University of Liverpool, UK, who is involved in the Guinea Ebola trial. Trials for Ebola and other emerging diseases “should have happened years ago”, he adds. He points out that the therapy is often considered old-fashioned and that there are neither big profits to be made nor cutting-edge-science interests at stake. “Convalescent plasma is not attractive to pharma, or the modern model of academia,” he says.

Results from the first safety and efficacy trials in West Africa are expected within weeks. If the therapy is effective, many of the thousands of Ebola survivors there will be potential donors, each capable of giving up to one litre of plasma every two weeks.

There is also growing evidence to support the broader testing of CPT. A 2006 review of 8 studies carried out during the 1918 flu pandemic[1], and a review published last July of 32 studies on SARS or severe influenza[2], both suggest that plasma can be an effective treatment. And a 2010 modelling study[3]

concluded that in a full-blown flu pandemic, the infrastructure of developed countries could probably harvest sufficient plasma from survivors for population-wide treatment of the ill. “It’s not the be-all and end-all, but it is certainly a potentially powerful and effective tool to add to our armamentarium,” says Stephen Hoffman, a co-author of the 2006 review and chief executive of malaria-vaccine company Sanaria in Rockville, Maryland.

Even relatively poor countries often have a good-enough infrastructure for processing blood to use the therapy, says Heymann, who was part of the team that fought the first Ebola outbreak in the Democratic Republic of the Congo in 1976. Plasma extraction can also be done in the field, he adds.

Related stories

- First trials of blood-based Ebola therapy kick off
- Ebola experts seek to expand testing
- Positive results spur race for Ebola vaccine

More related stories

Adequate screening for pathogens in donated blood can be an issue in poorer countries. In the CPT Ebola trials, a chemical is being added to the donated blood. When the mixture is exposed to ultraviolet light, the compound irreversibly crosslinks the DNA and RNA of pathogens, preventing their replication.

It is also getting easier to test CPT more broadly. The International Severe Acute Respiratory and Emerging Infection Consortium (ISARIC), a network of researchers based in Oxford, UK, was set up in 2011 to accelerate clinical research during outbreaks. It has now drafted a protocol for clinical trials of CPT that regulatory bodies can approve before an outbreak starts, allowing trials to be quickly carried out if necessary.

The protocol is being used in the Ebola trials and in clinical trials of CPT for MERS. These have begun in 20 patients in Saudi Arabia, and a larger trial of several hundred is planned over the next few months, says Yaseen Arabi, a physician and researcher at King Saud Bin Abdulaziz University for Health Sciences in Riyadh, who is coordinating the trials in collaboration with the World Health Organization and ISARIC. “Given the severity of illness and the lack of proven therapy, convalescent plasma has the potential of making a substantial difference,” says Arabi. “However, this needs to be tested.”

Nature **517,** 9–10 (01 January 2015) doi:10.1038/517009a

References

1. Luke, T. C. *et al*. *Ann. Intern. Med.* **145**, 599–609 (2006).
 Show context Article PubMed ISI
2. Mair-Jenkins, J. *et al*. *J. Infect. Dis.* http://dx.doi.org/10.1093/infdis/jiu396 (2014).
 Show context
3. Wu, J. T., Lee, C. K., Cowling, B. J. & Yuen, K. Y. *Proc. Natl Acad. Sci. USA* **107**, 3269–3274 (2010).

Show context Article PubMed ChemPort

Related stories and links

From nature.com

- **First trials of blood-based Ebola therapy kick off**
 15 December 2014
- **Ebola experts seek to expand testing**
 09 December 2014
- **Positive results spur race for Ebola vaccine**
 02 December 2014
- **Ebola trials to start in December**
 13 November 2014
- **Ethical dilemma for Ebola drug trials**
 11 November 2014
- **Blood transfusion named as priority treatment for Ebola**
 05 September 2014
- ***Nature* special: Ebola outbreak**

From elsewhere

- **ISARIC**
- **WHO interim guidance on use of CPT for Ebola (PDF)**
- **WHO Blood Regulators Network: position on Ebola blood therapy (PDF)**
- **WHO Ebola vaccines, therapies and diagnostics**

For the best commenting experience, please login or register as a user and agree to our Community Guidelines. You will be re-directed back to this page where you will see comments updating in real-time and have the ability to recommend comments to other users.

1 comment

Subscribe to comments



Peter Marchese • 2014-12-23 09:19 PM

The old vampire myths are beginning to be seen as having some element of truth with young blood being shown to have a rejuvenating effect and antibody containing blood to have a curative effect on otherwise untreatable diseases.

See other News & Comment articles from *Nature*

Nature ISSN 0028-0836 EISSN 1476-4687

© 2014 Nature Publishing Group, a division of Macmillan Publishers Limited. All Rights Reserved.
partner of AGORA, HINARI, OARE, INASP, CrossRef and COUNTER

emerging diseases "should have happened years ago", he adds. He points out that the therapy is often considered old-fashioned and that there are neither big profits to be made nor cutting-edge-science interests at stake. "Convalescent plasma is not attractive to pharma, or the modern model of academia," he says.

Results from the first safety and efficacy trials in West Africa are expected within weeks. If the therapy is effective, many of the thousands of Ebola survivors there will be potential donors, each capable of giving up to one litre of plasma every two weeks.

There is also growing evidence to support the broader testing of CPT. A 2006 review of 8 studies carried out during the 1918 flu pandemic[1], and a review published last July of 32 studies on SARS or severe influenza[2], both suggest that plasma can be an effective treatment. And a 2010 modelling study[3] concluded that in a full-blown flu pandemic, the infrastructure of developed countries could probably harvest sufficient plasma from survivors for population-wide treatment of the ill. "It's not the be-all and end-all, but it is certainly a potentially powerful and effective tool to add to our armamentarium," says Stephen Hoffman, a co-author of the 2006 review and chief executive of malaria-vaccine company Sanaria in Rockville, Maryland.

Even relatively poor countries often have a good-enough infrastructure for processing blood to use the therapy, says Heymann, who was part of the team that fought the first Ebola outbreak in the Democratic Republic of the Congo in 1976. Plasma extraction can also be done in the field, he adds.

"It's not the be-all and end-all, but it is certainly a potentially powerful and effective tool."

Adequate screening for pathogens in donated blood can be an issue in poorer countries. In the CPT Ebola trials, a chemical is being added to the donated blood. When the mixture is exposed to ultraviolet light, the compound irreversibly crosslinks the DNA and RNA of pathogens, preventing their replication.

It is also getting easier to test CPT more broadly. The International Severe Acute Respiratory and Emerging Infection Consortium (ISARIC), a network of researchers based in Oxford, UK, was set up in 2011 to accelerate clinical research during outbreaks. It has now drafted a protocol for clinical trials of CPT that regulatory bodies can approve before an outbreak starts, allowing trials to be quickly carried out if necessary.

The protocol is being used in the Ebola trials and in clinical trials of CPT for MERS. These have begun in 20 patients in Saudi Arabia, and a larger trial of several hundred is planned over the next few months, says Yaseen Arabi, a physician and researcher at King Saud Bin Abdulaziz University for Health Sciences in Riyadh, who is coordinating the trials in collaboration with the World Health Organization and ISARIC. "Given the severity of illness and the lack of proven therapy, convalescent plasma has the potential of making a substantial difference," says Arabi. "However, this needs to be tested." ■

1. Luke, T. C. *et al. Ann. Intern. Med.* **145,** 599–609 (2006).
2. Mair-Jenkins, J. *et al. J. Infect. Dis.* http://dx.doi.org/10.1093/infdis/jiu396 (2014).
3. Wu, J. T., Lee, C. K., Cowling, B. J. & Yuen, K. Y. *Proc. Natl Acad. Sci. USA* **107,** 3269–3274 (2010).

RESEARCH

What to expect in 2015

Nature *looks at what the New Year holds for science.*



MARK THIESSEN/NATIONAL GEOGRAPHIC

The souped-up Large Hadron Collider will resume its search for exotic particles.

PARTICLE SMASHER

The long wait is over: the Large Hadron Collider (LHC) will reboot in March after a two-year shutdown. The machine at CERN, Europe's particle-physics laboratory near Geneva, Switzerland, will restart with collisions at 13 trillion electronvolts — almost double the current record. Scientists hope that the extra firepower will help the collider to unearth phenomena that fill in gaps in the standard model of particle physics. The popular theory of supersymmetry, already in doubt, could lose further favour if the upgraded LHC cannot find evidence of the many heavy particles that the theory predicts.

CLIMATE DEAL

The United States and China, the world's biggest carbon emitters, made historic pledges in 2014 to reduce their greenhouse-gas emissions. That could clear the way for a new global climate deal at United Nations talks in Paris in December, where nations hope to finalize a legally binding post-2020 agreement. Meanwhile, the average annual level of heat-trapping carbon dioxide in the atmosphere could creep above 400 parts per million for the first time in millions of years.

© 2015 Macmillan Publishers Limited. All rights reserved

KEVIN FRAYER/GETTY



New climate commitments by China could help to reduce Beijing's signature smog.

END OF EBOLA EPIDEMIC

Health workers hope to stop the Ebola epidemic in Guinea, Liberia and Sierra Leone. That will require wider use of proven public-health measures — such as rapid detection and isolation of people with Ebola. Trials of vaccines are planned for early in the year; results should come by June. Tests are already under way on several drugs, as are trials of treatments that use the antibody-rich blood of people who have survived Ebola. The blood treatments could be rolled out quickly and widely if proved effective.

TRIPS TO DWARF PLANETS

Comets are out, dwarf planets are in. In March, NASA's Dawn probe will arrive at protoplanet Ceres, the most massive body in the asteroid belt between Mars and Jupiter. Ceres is thought to have water ice beneath its crust. And after travelling 5 billion kilometres, NASA's New Horizons craft will finally reach Pluto, making its closest approach on 14 July. The encounter promises the first intimate look at that rocky world and its moons, and new data on Pluto's atmosphere.

SHINY NEW LABS

The £650-million (US$1.0-billion) Francis Crick Institute will open in November in central London and house 1,250 researchers in its chromosome-shaped building. Farther north, the £61-million National Graphene Institute will open this spring at the University of Manchester, UK. The centre, funded in part by the British government, is a key element of Manchester's campaign to create what it calls Graphene City. And the US$100-million Allen Institute for Cell Science in Seattle, Washington, funded by Microsoft billionaire Paul Allen, will begin delving into the body's most basic unit.

CHOLESTEROL-BUSTING DRUGS

Drug companies are racing to bring a new class of cholesterol drug to market, and some may cross the finish line this year. The therapies, which reduce levels of low-density lipoprotein (LDL) cholesterol by targeting the protein PCSK9, have shown promise in clinical trials. Last year, two drugs moved to the front of the pack: one from Amgen of Thousand Oaks, California, which filed for US approval in October, and another from Paris's Sanofi, which has been assured of a speedy review by US regulators. Decisions on both drugs are expected by summer 2015.

WAVES IN SPACE-TIME

The hunt for ripples in the fabric of space-time will get better tools. Towards the end of the year, the Laser Interferometer Gravitational-Wave Observatory (LIGO) detectors in Richland, Washington, and Livingston, Louisiana, will emerge from a major upgrade to boost their sensitivity. After two decades of trying, the LIGO team hopes to glimpse the waves predicted by Albert Einstein almost a century ago. This autumn, the European Space Agency's Laser Interferometer Space Antenna (LISA) Pathfinder will start to test similar wave-hunting technologies for a mission set to launch in 2034.

ANSWERS TO ANCIENT RIDDLES

Palaeogeneticists hope to sequence the complete genome from the 400,000-year-old Sima de Los Huesos human, found in a deep cave in northern Spain. The ancient human's mitochondrial genome was published in 2013, the product of a Herculean effort given the specimen's deteriorated bones. Decoding the rest of the genome is expected to be even harder, because of the relative scarcity of nuclear DNA. But the results could help to clarify the evolutionary relationship between humans, Neanderthals and another ancient group called Denisovans, and to identify episodes of inbreeding between distantly related hominins.

POLITICAL MANOEUVRES

Big changes are afoot. The Russian government will review 450 research institutes at the Russian Academy of Sciences, after stripping the academy of its independence in 2013. UK citizens will go to the polls in May for the first general election since 2010, and Parliament will decide whether to allow three-parent *in vitro* fertilization — which would be a global first. The European Union will mull over how to replace the science-adviser position that was scrapped in 2014, and the United States will see its Congress move under Republican control.

OCEAN OUTLOOK

Two new US research vessels are going full steam ahead: the US National Science Foundation will formally commission its Arctic-bound *Sikuliaq*, and the Woods Hole Oceanographic Institution's *Neil Armstrong* will begin science operations. Germany also gets a new research vessel, which shares its name with its predecessor: *Sonne*. Elsewhere on the seas, the Ocean Observatories Initiative, a US push to monitor the seas in real time, will be completed in late May. And Japan is likely to restart "scientific" whaling in Antarctic waters after a hiatus imposed by the International Court of Justice. ■

COMPILED BY ELIZABETH GIBNEY

CORRECTION

The graph accompanying the News Feature 'Life — a status report' (*Nature* **516,** 158–161; 2014) incorrectly listed the number of described fungi as 48,500. The actual value is approximately 100,000.

© 2015 Macmillan Publishers Limited. All rights reserved

SCIENCE IN 2015

The global research enterprise is already vast, whether measured in people, publications, patents or refreshments. And it is getting bigger fast. Assuming current trends continue, here is what the New Year has in store.

BY MARK ZASTROW

R&D SPENDING

Global investments in research and development have been growing by some 7% annually for more than a decade.

2000 **$706 BILLION**

2005 **$954 BILLION**

2010 **$1.3 TRILLION**

2015 **~US$1.9 TRILLION**

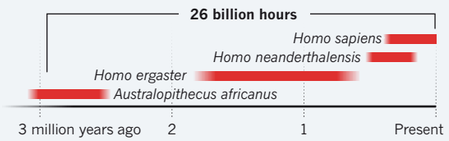
This year, the total should roughly equal the gross domestic product of India.

~2.6 MILLION PATENTS FILED

~1.2 MILLION PATENTS GRANTED

These key measures of innovation will have more than doubled since 2000.

~26 BILLION RESEARCHER HOURS



With some 10 million researchers averaging 50-hour working weeks, the global human effort going into R&D is equivalent to 2.9 million years — a span of time that would extend back to the heyday of *Australopithecus africanus*.

2 DWARF PLANETS VISITED

NASA's Dawn spacecraft will arrive at the dwarf planet Ceres, located in the asteroid belt between Mars and Jupiter, in March. The agency's New Horizon spacecraft will fly by the dwarf planet Pluto in July.

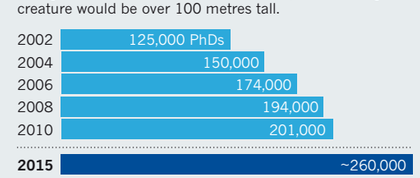
~920,000 PUBLICATIONS

~470 RETRACTIONS

The world's output of scientific articles is growing at about 2.8% per year. Only a tiny fraction are ever retracted — but that number also seems to be growing.

~260,000 NEW PhD HOLDERS WORLDWIDE

This is a crowd that could fill Beijing's 80,000-seat National Stadium more than 3 times over. If these new degree-holders were magically reassembled into a single 'Gradzilla' with the same volume, the resulting creature would be over 100 metres tall.



NATURE.COM
Learn more about these numbers at **go.nature.com/rdnns2**

~234,000 COOKIES CONSUMED AT McMURDO STATION

These easy-to-grab treats are a favourite fuel for those long hours in the laboratory. In Antarctica's McMurdo Station alone, cookies are devoured at the rate of 4,500 per week.

~1 BILLION CUPS OF COFFEE

Scientists consume this essential stimulant in vast quantities. The order-of-magnitude estimate of global consumption given here may well be on the low side, but it is enough to give every resident of the European Union a cup and a refill.

~1.5 TRILLION BASES FILED IN GENBANK

The online sequence-data repository has been doubling in size every two years or so, and the pace is picking up. By December it could reach the size of 500 human genomes — and will still represent only a fraction of the sequence data stored worldwide.

ARTWORK BY CHRIS RYAN/*NATURE*

© 2014 Macmillan Publishers Limited. All rights reserved

© Nature

COMMENT

CULTURE What are the must-see exhibitions, festivals, plays and films of 2015? **p.18**

METRICS Link between journal reputation and institutional performance questioned **p.21**

SUSTAINABILITY Biomass heating plan risks air quality and climate **p.21**

OBITUARY Hydrocarbon pioneer Paul von Ragué Schleyer, remembered **p.22**

ILLUSTRATION BY DAVID PARKINS



New year's resolutions

Nine scientific leaders share their goals for 2015, professional and personal.

ELLEN R. STOFAN
Step to Mars, inspire diversity

Chief scientist, NASA

By the end of 2015, I want NASA to have achieved significant progress towards sending humans safely to Mars by the 2030s, and I want to have inspired girls and other under-represented groups to pursue — and stick with — careers in science, technology, engineering and mathematics (STEM). These goals are sources of personal inspiration that keep me motivated.

To bring about my first resolution, we need major achievements on two fronts: scientific discoveries about the Martian environment, and advances in mitigating the effects of microgravity on humans in preparation for long-duration space flight. NASA's Curiosity rover will continue its ascent of Mars's Mount Sharp, studying its layered deposits to better understand the history of water on the planet, while the MAVEN orbiter will quantify the loss of atmospheric gases to space.

Starting in March, astronaut Scott Kelly and cosmonaut Mikhail Kornienko will spend one year on the International Space Station — a first for NASA's human research programme. Scott's identical twin, former astronaut Mark Kelly, will provide a valuable genetic control for the first microgravity twin study. My challenge will be to ensure that scientific studies such as these are tightly woven into the fabric of NASA's exploration road map, along with crucial technology development and international partnerships.

For my second resolution, I will continue to work as a role model and support effective STEM engagement programmes across the US government, including NASA's development of meaningful citizen-science opportunities. I will participate in events such as South Africa's national science festival Scifest Africa and an international summit of all-girls' schools, where I will talk about using scientific events, such as the July encounter of NASA's New Horizons craft with Pluto, to engage STEM students. I believe that, as a global community, we will not address the challenges ahead of us without the participation of all of our population. ▶

© 2015 Macmillan Publishers Limited. All rights reserved

SALLY DAVIES
Antimicrobial action, exercise

UK Chief Medical Officer

By the end of 2015, I want to see global action on antimicrobial resistance (AMR). Increasingly, lack of preparedness for the diminishing usefulness of antibiotics and antivirals is affecting economies and health systems. There has been too little research into the basic science, and too few companies, big and small, are focused on new therapeutics and diagnostics.

So this year, I will push — through the World Health Organization (WHO) and its executive board — to agree a global plan for AMR research, surveillance and action, and for this to be passed by the World Health Assembly with overwhelming support. This will take serious diplomacy, which will be supported by the UK government.

I will also be advocating laboratory surveillance of drug–microbe combinations and antibiotic-stewardship programmes — at the local, national and regional level. I will work with the independent AMR review, led by economist Jim O'Neill, on market mechanisms to stimulate the development of new therapeutics. By year's end, we hope to have a short list of proposals to debate with the Group of 20 countries and the WHO.

I also want to practise what I preach in 2015 — so I need to increase my own physical fitness. If fitness were a drug, we would all want it — to reduce risk of chronic diseases such as cancer, heart disease and dementia. But jogging on my own is boring and it affects my tendons. So, I resolve to run with a friend and take up pilates.

SUE DESMOND-HELLMANN
Fifteen-year plan, lift weights

Chief executive officer, Bill & Melinda Gates Foundation

My top resolution this year is for the Bill & Melinda Gates Foundation to help the world to meet major health and development challenges. These include halting the Ebola epidemic in West Africa and taking strides to prevent future outbreaks; moving closer to eradicating polio in Africa and accelerating progress against it in Afghanistan and Pakistan; and helping to persuade nations to generate strong funding for Gavi, the Vaccine Alliance, based in Geneva, Switzerland.

The foundation will continue to support scientific research on malaria and HIV, among other health priorities — including approaches that might be too risky or speculative for government or businesses to undertake. One example is infusing a common bacterium into the mosquito that transmits dengue fever. This could prevent the species from spreading dengue — and perhaps other diseases.

Another resolution is to ensure that we reflect on what the foundation has achieved and learned in its 15 years of existence, and what we can accomplish in the next 15. I want to make sure we think creatively and constructively about how we can maximize our impact.

On a personal level, running and cycling help me to maintain the clear head and the stamina required to do this work. As usual, I will resolve to add some weightlifting, and sustain it beyond the second week of January. And I will be more generous.

YI XIE
More energy, cross disciplines

Professor of chemistry, University of Science and Technology of China

As a step towards sustainable energy-generation, by the end of this year I want my laboratory to have substantially improved conversion efficiency for photo-, electro- and photoelectro-chemical energy. My personal goal is to communicate better with people outside my field. Collaborations across the disciplines are central to overcoming today's grand challenges.

To bring about the first resolution, we plan to design new ultrathin, two-dimensional semiconductor-based catalysts, which have increased density and mobility of carriers (electrons and holes). This can improve photon absorption and charge transfer, and eliminate the recombination of carriers, which hampers applications. Understanding the relationship between the structure and the function of these materials is key to their practical application. This understanding requires multidisciplinary collaborations.

Therefore, to keep my second resolution, I am going to explore topics beyond chemistry, such as synchrotron radiation and positron annihilation. I plan to read different journals, go to different conferences and visit different labs. I will strive to communicate my team's findings to those from other disciplines and the public through popular magazines and our website. Such outreach is important for inspiring the next generation to pursue science careers.

CHRISTIANA FIGUERES
Forge new climate agreement

Executive secretary, United Nations Framework Convention on Climate Change (UNFCCC)

Humans are responsible for climate change. Science has shown that beyond doubt. This simple, world-changing fact is why governments must reach a new climate-change agreement in Paris at the end of this year to achieve a state in which humans, on balance, add no further greenhouse gases into the atmosphere by the end of this century.

My task is to help countries to reach that goal. This means managing the process of the 195 countries under the UNFCCC, including many thousands of delegates and many thousands more observers from hundreds of non-governmental organizations and businesses, each with their own hopes for a new agreement. I will redouble my personal diplomatic efforts to ensure that all sides realize that a strong agreement is the only viable road to a sustainable, resilient, healthier and wealthier future for all.

Never before has there been such public support to act and political will to take action. The economics are clear: delayed action means higher future costs; immediate action means economic benefits. The finance and technology to act effectively exists. Already, as witnessed at September's UN climate-change summit in New York, there has been an outpouring of new commitments and pledges by governments, businesses, investors, cities and citizens to address the climate challenge.

What happens in the run-up to Paris will do more to determine the quality of life for generations to come than anything before. We have the opportunity to make decisions that put us either on a path of increasing human and economic cost, or on a path toward a safer, more stable future.

This is my job, and my personal commitment to the many thousands of scientists whose work on climate change has brought us to this tipping point.

ROLF-DIETER HEUER
Highest energy, smooth handover

Director-general, CERN

Today, I begin the last year of my mandate as director-general of CERN, Europe's particle-physics laboratory near Geneva, Switzerland.

© 2015 Macmillan Publishers Limited. All rights reserved



ILLUSTRATION BY DAVID PARKINS

In many ways it will be similar to my first year: we will be looking forward to setting the record for the world's highest-energy particle accelerator. By the time I leave office, I want to have witnessed the first collection of data from 13-teraelectronvolt collisions in the Large Hadron Collider (LHC).

After the huge amount of work over the past two years to ready the LHC, I am confident that these energetic events will happen in May. The machine has already cooled to its operating temperature. I hope that these collisions will open the way to discoveries as important as that of the Brout–Englert–Higgs mechanism.

I am also looking forward to working closely with my successor, great friend and colleague, Fabiola Gianotti, to ensure a smooth handover. Next year, safe in the knowledge that CERN is in good hands, one of my challenges will be my role as president of the German Physical Society, starting in April 2016. Meanwhile, I plan to enjoy my last year as director-general, as I have every one so far.

GLORIA BONDER

Keep gender in the centre

Director, Gender, Society and Policies Area of FLACSO Argentina (Latin American School of Social Sciences)

This year, I plan to devote much of my time to coordinating the Latin American focal point of an international, interdisciplinary programme called GenderInSITE (Gender in Science, Innovation, Technology and Engineering). Specifically, I will be honing strategies for data-gathering and project evaluation with SITE policy-makers. Our goal is to weave gender analysis and gender equality goals into mainstream policies, so that SITE fields can better serve women's and men's lives and livelihoods, and contribute to inclusive and sustainable development.

There have been important advances in Latin America in gender equality, particularly in the past ten years. I am particularly proud of innovative educational programmes developed in Argentina, Costa Rica and the Dominican Republic aimed at raising girls' and young women's interests in and capabilities for science and technology projects and products. Equality regulations for scientists in Chile and Argentina are also encouraging.

But hurdles remain. Crucial to overcoming them, is to recognize that, when dealing with gender issues, and especially in science, no 'success' is secure — resistance and backlashes are to be expected. After all, we are addressing power relations that influence the way that we perceive, interpret, value and deal with all dimensions of our lives, including science.

LANJUAN LI

Widen expertise, travel more

Director, State Key Laboratory for Infectious Diseases Diagnosis and Treatment, Zhejiang University School of Medicine

My main goal this year is to draw on a wider range of expertise. My own laboratory is a good example. We use tools from metagenomics and metatranscriptomics to clarify the role and construct interaction networks of microorganisms in the progression of liver diseases. These help us to provide fresh strategies to diagnose, treat and prevent diseases such as liver cirrhosis.

This year, we want to clarify the effect of antibiotics and probiotics on the liver. We have followed 80 people with liver cirrhosis for half a year, to elucidate the effects and mechanisms of probiotics such as lactulose on the disease's progression. We also followed 40 people with liver failure for one month, collecting samples every week, to elucidate the alterations of these patients' gut microbiomes. We hope to find new candidate probiotics for the treatment of liver disease.

This year I also hope to create more opportunities for my team to communicate and cooperate with people in different countries. We plan to attend more international conferences, among other things.

ATHENE DONALD

More women, more science blogs

Master of Churchill College, University of Cambridge

My aspiration this year, and for the next few years, is to bring Churchill College's undergraduate gender balance much closer to 50:50. The college has an excellent track record of welcoming applicants from state schools, yet only 35% of the students we admit are women, and even fewer in maths and engineering. It is simply not good enough. Attracting the best young women is fundamentally important, educationally and morally.

The college is obliged, by the terms of its foundation, to admit 70% of students in science, technology, engineering and mathematics fields. But we have no female lecturers in maths or engineering, a paucity that leads to a lack of female faces to welcome potential applicants at open days. So, starting in spring 2015, we will make sure that women doing master's degrees and PhDs in these subjects in particular will be more available to talk to prospective students. My goal is a noticeable improvement in our application statistics for women from our 2016 intake onwards.

At a personal level, I want to produce more blogposts purely about science (see go.nature.com/pcerpn). I frequently write about science culture and gender-related issues. But to take research that excites me (I work on soft-matter physics at the interface with biology) and write it clearly and succinctly for a public audience is a good way of improving my style, and public engagement is an essential part of an academic scientist's remit. In the past year, just one of the of eleven posts I published (on biomimetics and structural colour) could be called pure science. Now I will ensure that I read papers with this goal in mind. ■ SEE CAREERS P.111

© 2015 Macmillan Publishers Limited. All rights reserved



The Imagine Science Films festival in Abu Dhabi will showcase research in the Arab world and elsewhere.

LISTINGS

Science in culture 2015

Explore the gory glories of forensic science, grapple with Tom Stoppard's take on consciousness, learn what it takes to live on Mars, re-enter Jurassic Park, dive into a coral reef and dally with Robert Oppenheimer. **Daniel Cressey** reports.



***Oppenheimer* examines the Manhattan Project.**

MAIN PICTURE: BERIT MADSEN; OPPENHEIMER: HUGO GLENDINNING

Oppenheimer

Swan Theatre, Stratford-upon-Avon, UK
15 January – 7 March

The secret work of scientists in the Second World War has proved fertile ground for drama, from Michael Frayn's 1998 play *Copenhagen* to John Adams's opera *Doctor Atomic* (2005). The latest to explore that tension are British playwright Tom Morton-Smith and the Royal Shakespeare Company, who follow Adams by peering inside the Manhattan Project — the US programme that spawned the nuclear bomb. Morton-Smith has said that he sees something of the Bard's conflicted antiheroes in the "ambition, frailty and indecision" of nuclear pioneer Robert Oppenheimer. Whether the father of the bomb emerges as closer to Macbeth or Henry V remains to be seen.

Countdown to Zero: Defeating Disease

American Museum of Natural History, New York City
13 January – 12 July

Despite stunning medical advances, smallpox is the only human disease that has been eliminated worldwide. This exhibition at New York's natural history museum focuses on what could be the next conquest: guinea-worm disease. Debilitating and extremely painful, the condition is caused by migration of the nematode *Dracunculus medinensis* through tissues. In the mid-1980s, it affected 3.5 million people a year in Africa and Asia; incidence is now reduced by 99.9%. The show is a collaboration with the Carter Center in Atlanta, Georgia, established by former US president Jimmy Carter, which has led much of the global fight against the disease.

Imagine Science Films

New York University Abu Dhabi
19–21 February

Since 2008, Imagine Science Films has been pushing scientists into close collaboration

© 2015 Macmillan Publishers Limited. All rights reserved





Left: EXPO 2015 in Milan includes a digital 'augmented' supermarket; right: the Countdown to Zero exhibition looks at efforts to eradicate guinea-worm disease.

FRUIT: CARLO RATTI ASSOCIATI; READING: THE CARTER CENTER/L. GUBB

with film-makers for its annual multiregional festival. This year, the event — whose many sponsors include *Nature* — branches out with a satellite festival in Abu Dhabi, a relatively new arena for sci–art collaboration. Sessions have been organized for fiction and documentaries focused on issues of particular relevance to the Middle East. From science-fiction exploring the region's role on the world stage to factual forays into neuroscience and resource exploitation, the festival promises an edgy, multidimensional look at the Arab world now.

Forensics: The Anatomy of Crime
Wellcome Collection, London
26 February – 21 June

Flashy television programmes often warp the truth and obscure the uncertainty inherent in forensic techniques such as DNA analysis and fingerprinting. Bioscience-funding behemoth the Wellcome Trust promises a corrective in its blockbuster show, aiming to reveal the realities of teasing truth from what crimes leave behind. The trust's newly enlarged exhibition space will display disturbing evidence, including a sketch of a crime attributed to Jack the Ripper. Forensic instruments, artworks and films from the Wellcome's archive and beyond will be on show.

Emerge
Arizona State University
March 2015

Arizona State University is becoming a player in the confluence of science and art. Its annual Emerge festival, which launched in 2012, brings together artists and scientists, including digital-performance pioneer Lance Gharavi and roboticist Srikanth Saripalli, in a challenging public science carnival. This year's will examine "the future of choices and values" through "performance sci-fi". Art from dance to sculpture will appear across the enormous university campus, exploring how scientists are shaping the future alongside — or antagonistically to — the creative industries.

Arsenic and New Medicine: Paul Ehrlich's Pioneering Research
Berlin Museum of Medical History at the Charité
15 April – 27 September 2015

Nobel laureate Paul Ehrlich introduced fundamental biological concepts, such as the idea of cell-surface receptors and the necessity of quantifying data. He devised staining techniques to identify and distinguish immune cells, developed antisera for diseases such as diphtheria and, perhaps most famously, found a cure for syphilis with his 'magic bullet', Salvarsan (arsphenamine, **pictured**). On the centenary of his death, this joint exhibition by the Berlin Museum of Medical History at the Charité and the Historical Museum Frankfurt examines Ehrlich's extraordinary scientific life, and looks at how he has been memorialized. In his native Germany, for example, streets named after him were renamed during the Third Reich because he was Jewish. The show will move to the Frankfurt museum from 29 October 2015 to 3 April 2016.

CHRISTOPH WEBER, CHARITÉ/HOECHST ARCHIVE, FRANKFURT



EXPO 2015
Milan, Italy
1 May – 31 October

The world's fair comes to Milan to ponder a pressing global concern: food. Architect Carlo Ratti's Future Food District offers a digital 'augmented reality' experience of the supermarket as a nexus of products, producers and consumers. Arts & Foods, curated by radical critic Germano Celant, will examine the edible in art — and its cultural and industrial implications — since 1851. Biodiversity Park's 8 greenhouses will showcase agro-biodiversity in 250 plant types, and Pavilion Zero will trace the transformation of environments by agriculture from prehistory on. As the expo's tagline has it, "*Nutrire il pianeta, energia per la vita*" — "Feeding the planet, energy for life".

Jurassic World
Director: Colin Trevorrow
Opens 10 June

Resurrected dinosaurs, their photogenic victims and scientists playing God get another airing in *Jurassic World.* It is more than 20 years since Steven Spielberg's *Jurassic Park* (1993) ignited public fascination with the revivification of long-extinct species

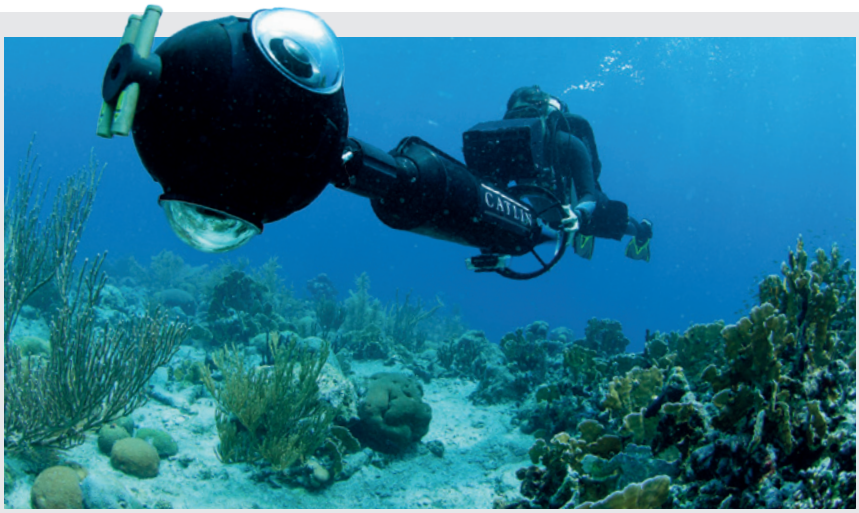
MY HIGHLIGHT OF THE YEAR

Philip Ball, science journalist and author of *Invisible: The Dangerous Allure of the Unseen*

The Hard Problem
National Theatre, London
21 January – 16 April

The "hard problem" is consciousness — just the sort of intellectual puzzle that excites playwright Tom Stoppard, whose dramas have probed chaos theory and quantum physics. In his latest work, starring Olivia Vinal and Jonathan Coy, a psychologist at a brain-research institute confronts this issue while grappling with a private sorrow, and is forced to question whether scanners and computers can provide all the answers about the human mind. Three major brain-research projects are currently hoping to do just that, so Stoppard has proved himself as timely as ever — and we can be sure that he will not be offering any glib resolution.

© 2015 Macmillan Publishers Limited. All rights reserved



CATLIN SEAVIEW SURVEY

The Catlin Seaview Survey explores a reef at Bonaire in the Caribbean Netherlands.

Coral Reefs: Secret Cities of the Sea
Natural History Museum, London
27 March – 13 September

One of nature's most enthralling tableaux, the coral reef, will be recreated alongside the dinosaurs in London's Natural History Museum. More than 200 individual denizens of reefs — both live and preserved — will be on show to create an artwork rivalling displays at the nearby design mecca, the Victoria and Albert Museum. Corals from Charles Darwin's collection will be joined by videos from the Catlin Seaview Survey — a global project to image the world's reefs involving Google and the University of Queensland, Australia. Although visitors will not be able to pop into the tank to join the live marine creatures, they are promised a virtual dive.

using DNA. How the franchise will fare in a world where genome science is mainstream rather than a strange new rarity remains to be seen. The fourth outing ups the role of genetic modification, as a new generation is introduced to heavy-handed warnings against tinkering with Mother Nature.

A Brief History of the Future
The Louvre, Paris
Mid-September – mid-December

Delving into the past to conjure what comes next is the focus of a major exhibition at the venerable Paris museum. A broad mix of ancient and contemporary art is promised, with specially commissioned pieces covering pioneers in engineering, science, architecture and the arts. The exhibition's overarching theme originated in a 2006 book of the same name by writer and civil servant Jacques Attali. That volume chronicles the trajectory of humankind from prehistory, ranging over innovations from printing in Belgium to the piston engine in Massachusetts, and extrapolating a technology-dominated future of shifting empires and nomadism.

UNIVERSAL/THE KOBAL COLLECTION

The Martian
Director: Ridley Scott
Opens 25 November

Ridley Scott, director of science-fiction blockbusters including *Blade Runner* (1982), is heading for Mars. His dramatization of Andy Weir's self-published 2012 sleeper hit *The Martian*, a scientifically grounded novel about an astronaut's struggle to survive on the red planet, is due to air in November. Although Scott received mixed reviews for 2012's *Prometheus*, his much-hyped return to science-fiction, his take on isolation in space in *Alien* (1979) has never been bettered. Hopes are high that he can translate Weir's protagonist's struggle to survive into compelling drama. ■

Daniel Cressey *is a reporter for* Nature *in London. Additional reporting by Alison Abbott.*

MY HIGHLIGHT OF THE YEAR

Danny Birchall, digital manager at the Wellcome Collection in London

Designers in Residence 2015: Migration
9 September 2015 – 28 February 2016
Design Museum, London

In a world on the move, immigration is top of many government agendas. But subtler forms of migration are always happening, as reflected in the eighth annual Designers in Residence exhibition, where product technology meets the art of form. With the museum itself moving across London next year to the former Commonwealth Institute, early-career designers in a range of disciplines have been invited to ponder mobility in everything from data to people, and to explore the neutrality of migration over the duality of emigration/immigration.

Ruth Wylie, assistant director of the Center for Science and the Imagination at Arizona State University, Tempe

It's Alive! — Frankenstein on Film
23–25 January
SIFF Film Center, Seattle, Washington

For nearly 200 years, Mary Shelley's *Frankenstein* has shaped how we see science and its ethical impacts. I am excited about this mega-screening of adaptations, co-hosted by the Seattle International Film Festival and my own university's Frankenstein Bicentennial Project. Among the offerings are James Whale's iconic 1930s *Frankenstein* and *Bride of Frankenstein* (**pictured**), and Paul Morrissey's transgressive *Flesh For Frankenstein* (1973). An electrifying weekend of film and analysis.



BRIEFLY NOTED

Marvellous Creatures
This exhibition at Qatar's Museum of Islamic Art in Doha, opening in March, looks at how animals real and unreal feature in art and fables such as *The Thousand and One Nights*.

Frida Kahlo's Garden
In a display of flowers, paintings and more starting in May, the New York Botanical Garden explores how artist Frida Kahlo's was inspired by the plants of her native Mexico.

Lava
A singing volcano stars in this short animation from Pixar, released with full-length film *Inside Out* in June. Geology has never looked so adorable.

The Francis Crick Institute, London
These interdisciplinary medical-research facilities promise to be an architectural highlight. Designed by HOK and PLP Architecture, they open towards the end of the year.

© 2015 Macmillan Publishers Limited. All rights reserved

Correspondence

New law risks release of invasive species

A new European Union (EU) regulation aiming to control invasive alien species comes into force on 1 January 2015 (see go.nature.com/ajiwtd). It could inadvertently promote — rather than deter — the release of exotic animals into the wild.

The regulation prohibits the keeping, breeding, sale, movement and release of listed invasive alien species. The EU has set September 2015 as the deadline for the preliminary list: after this, member states will be required to consider eradication of listed species from within national borders.

Many species that are now among the worst invaders in Europe originated from private collections, which are at present governed only by piecemeal legislation. It is likely that several animals, which include the North American bullfrog (*Lithobates catesbeianus*), the ruddy duck (*Oxyura jamaicensis*), northern raccoon (*Procyon lotor*) and Pallas's squirrel (*Callosciurus erythraeus*), will be added to the list under the new ruling.

There is a risk, therefore, that this could prompt owners to release their newly illegal holdings into the wild, as happened after the 1997 EU trade ban on red-eared slider turtles (*Trachemys scripta elegans*).

A carefully managed interim process to prevent deliberate releases by pet owners should therefore be an EU-wide priority.

Philip E. Hulme *Lincoln University, Canterbury, New Zealand.*
philip.hulme@lincoln.ac.nz

Harmful soot spurs climate-policy action

Julia Schmale and colleagues rightly call for more policy action on short-lived climate-forcing pollutants (SLCPs) leading up to December's Conference of the Parties in Paris (*Nature* **515,** 335–337; 2014). In fact, concerted action is already under way.

An alliance of countries, the Climate and Clean Air Coalition (www.ccacoalition.org), has made SLCPs a top priority. In November 2014, parties to the Montreal Protocol agreed to negotiate the phasing down of hydrofluorocarbons, one of the most potent SLCPs.

The substantial benefits of cutting these pollutants are now being recognized on many different fronts and in local and international arenas. Soot and other SLCPs kill millions of people and harm crops. Even countries that were once reluctant to adopt costly policies to mitigate climate change now find the political logic for action on SLCPs compelling.

Schmale *et al.* see tackling SLCPs as requiring new layers of international coordination. We see it differently: as a big opportunity to revitalize climate-change diplomacy, because action against SLCPs is seen by so many countries as being in their own interest.

David G. Victor, V. Ramanathan *University of California San Diego, California, USA.*
Durwood Zaelke *Institute for Governance and Sustainable Development, Washington DC, USA.*
david.victor@ucsd.edu

Green heating plan threatens air quality

The UK government's Renewable Heat Incentive (RHI) aims to transform domestic and non-domestic heating with affordable biomass-only boilers and pellet stoves. This could have unwanted consequences for air quality and climate change unless the RHI rapidly reduces its emissions limits (see also J. Schmale *et al. Nature* **515,** 335–337; 2014).

The RHI stipulates an air-quality limit for biofuel burning of 30 grams of particulate matter per gigajoule of net heat output. This means that a 10-kilowatt unit operating for 2.8 hours is allowed to emit as much as 3 g of particulates of up to 10 micrometres in size (PM_{10}) in a total of 27 cubic metres of boiler exhaust fumes (111 milligrams per cubic metre). Under current UK air-quality regulations, the permitted ambient PM_{10} level is about 2,000 times lower than this; the European PM_{10} limit is 5,000 times lower.

The RHI impact assessment suggests supporting 750,000 systems by 2020. Yet, if just 2.5% of the UK homes now heated by natural gas (500,000 boilers) were to switch to RHI-compliant 10-kW biomass boilers (enough to power five double radiators) and use them for 2.8 hours, this would generate the same mass of particulates as would be emitted in one day by the entire UK light-duty diesel fleet of 8.8 million vehicles were they to operate under the latest Euro 5 emissions regulations (see go.nature.com/mjpqmz).

Furthermore, much of the particulate matter emitted by biomass boilers is sooty black carbon — a climate-warming agent owing to its absorption of outgoing longwave radiation. So the intended positive effect of the RHI on climate will be compromised.

Gordon McFiggans *University of Manchester, UK.*
g.mcfiggans@manchester.ac.uk

Criteria for Nature Index questioned

The Nature Index gauges the performance of countries and research institutions by tracking the number of papers they publish in reputable journals (www.natureindex.com). We suggest that using absolute numbers and journal reputation can yield misleading results (see R. Haunschild and L. Bornmann *Scientometrics* (in the press) and at http://doi.org/xrg; 2014).

For example, the index ranks the Chinese Academy of Sciences above Harvard University in Cambridge, Massachusetts. Using the complete publication output from each of these in 2013 (31,428 and 17,836 articles, respectively, according to Thomson Reuters InCites), we calculate that only 8% (2,661) of papers from the Chinese Academy of Sciences contributed to the Nature Index, whereas 14% (2,555 papers) of Harvard papers contributed. This relative perspective is important, given that an institution with a high publication output would be expected to publish more papers in reputable journals.

In our view, it would also be better to measure the performance of countries and institutions on the basis of individual papers, rather than on the journals in which they are published (see http://am.ascb.org/dora). This is because the quality of a journal (as measured by peers or citations) is not a reliable proxy for the quality of each paper it publishes.

To illustrate this point, we counted citations over 5 years for papers published in 2008 in *Applied Physics Letters* — the journal contributing most articles to the Nature Index — using an in-house bibliometrics database maintained by the Max Planck Digital Library in Munich, Germany. We found that some 40% of the papers in *Applied Physics Letters* accounted for about 80% of the citations to this journal, suggesting an uneven distribution of quality.

Robin Haunschild *Max Planck Institute for Solid State Research, Stuttgart, Germany.*
Lutz Bornmann *Max Planck Society, Munich, Germany.*
r.haunschild@fkf.mpg.de

Editorial note: For details of Nature Index methodology, see *Nature* **515,** S52–S53 (2014). A response from Nature Publishing Group to R. Haunschild and L. Bornmann's forthcoming *Scientometrics* article is available at http://doi.org/xsf (2014).

© 2015 Macmillan Publishers Limited. All rights reserved

Paul von Ragué Schleyer

(1930–2014)

Chemist who launched the study of caged hydrocarbons.



UNIV. GEORGIA

The scientific career of Paul von Ragué Schleyer took off when, as a graduate student at Harvard University in Cambridge, Massachusetts, he discovered an astonishingly straightforward way to make adamantane, the simplest subunit of diamond and the simplest stable caged hydrocarbon.

In finding a way to synthesize kilograms of adamantane cheaply — by putting a compound called tetrahydrodicyclopentadiene into an acidic mixture — Schleyer paved the way for two best-selling drugs. One, memantine, improves cognitive abilities such as memory and attention in people with Alzheimer's disease. The other, saxagliptin, regulates insulin levels in people with diabetes. His work also launched a new field. The exploration of caged hydrocarbons led organic chemists, including Schleyer, to discover beautiful organic structures that no one had thought could be made, as well as leading to insights about chemical bonding.

Schleyer, who died on 21 November, was born in Cleveland, Ohio, in 1930, to parents of modest means. He obtained a degree in chemistry in 1951 from Princeton University in New Jersey, and then went to Harvard. By the time his adamantane paper was published in 1957, Schleyer was a faculty member at Princeton.

The next few years were taken up with experimental explorations of hydrocarbon rearrangements in organic molecules, and of the role of carbocations (positively charged organic ions) as reaction intermediates. When George Olah received the 1994 Nobel Prize in Chemistry for his research on carbocations, many of us felt that Schleyer might have received a share of the prize.

In 1969, Schleyer became Eugene Higgins Professor — Princeton's most prestigious chair in chemistry. He continued to produce experimental papers, but increasingly devoted his efforts to computational chemistry, in which mathematics, physics and computing are used to solve problems that are too difficult or dangerous to be solved experimentally.

In the 1960s, Schleyer began to make predictions about the molecular structures of known and unknown molecules using force-field methods — predictions that were later proved experimentally, in some cases by Schleyer himself. He treated molecules as mechanically connected systems of atoms, and mapped their structures according to the energy of all the atom–atom interactions.

A turning point in Schleyer's career came when he started working with John Pople, then at the Carnegie Mellon University in Pittsburgh, Pennsylvania. Pople was using more-rigorous theoretical methods that factored in quantum mechanics.

Schleyer's entry into the young field of computational chemistry dismayed many of those who admired his experimental research. It also irritated a few theorists who falsely claimed that Pople's methods were not sufficiently reliable for real-world chemical problems, such as solving the structures of long-established, diatomic molecules. But most theorists, myself included, appreciated the attention and credibility that Schleyer brought to theoretical chemistry. Indeed, many in the field believe that without the collaborations with Schleyer, Pople might not have received the 1998 Nobel Prize in Chemistry.

In 1976, Schleyer horrified some by moving to a 'provincial' university: he left Princeton to take a post at the University of Erlangen-Nuremberg in Germany. At Erlangen, Schleyer continued to synthesize molecules that had never been made before. With exclusive use of a powerful computer on nights and weekends, he also devoted more time than ever to computational chemistry. In 1983, Schleyer made the remarkable prediction that the seemingly bizarre carbon–lithium molecule CLi_6 could be made. The prediction was confirmed experimentally nine years later (H. Kudo *Nature* **355,** 432–434; 1992).

Schleyer loathed administration and officialdom. Instead of attending the endless committee meetings that assail professors at German universities, Schleyer spent time talking to his students and postdocs, writing papers and listening to classical music. His passion for research was contagious. By the time he left it in 1998, Erlangen had one of the most distinguished chemistry departments in Germany.

In 1990, Schleyer accepted a part-time appointment at the University of Georgia in Athens, where I had arrived three years earlier from the University of California, Berkeley. In 1998, he joined us permanently as a professor of chemistry and professorial fellow at the Center for Computational Quantum Chemistry. Far from radically slowing down, Schleyer worked about 60 hours a week, instead of his previous 80. He collaborated with several of the faculty members, myself included, and published around 400 papers.

Everyone who worked in Paul's lab had to listen to classical music. He had an encyclopaedic knowledge of it and could identify the composer of any piece, and often the orchestra that had performed it. Paul could be intimidating to students and colleagues, but formed warm friendships with many. He was never bitter at having 'just missed' two Nobels.

Of the many tributes to Paul that I received after his death, that of Roald Hoffmann, who shared the 1981 chemistry Nobel for his theoretical work on chemical reactions, captures his essence best: "What Paul had to say was always so honest, so clearly imbued with a drive to understand, that his friends and colleagues valued every opportunity to talk to him, from the time of letters in real ink to e-mails." ■

Henry F. Schaefer *is professor of chemistry and director of the Center for Computational Chemistry at the University of Georgia, Athens, Georgia, USA. He was a colleague of Paul Schleyer's for 24 years. e-mail: ccq@uga.edu*

© 2015 Macmillan Publishers Limited. All rights reserved

MOLECULAR BIOLOGY

Entry signals control development

Certain structural elements allow messenger RNAs not usually processed by the protein-synthesis apparatus to be translated. It now seems that they also control the expression of genes involved in embryonic development. SEE ARTICLE P.33

JONATHAN D. DINMAN

The discrepancy between organismal complexity and genome size, known as the C-value paradox[1], is a classic problem in molecular biology. The solution to achieving complexity from a few genes is to control their expression at multiple levels. The genes responsible for driving complex pattern formation in highly developed organisms, called homeobox (*Hox*) genes, are particularly subject to layers of regulation[2]. In this issue, Xue *et al.*[3] (page 33) reveal a surprising mechanism by which *Hox* expression is controlled during embryonic development to ensure proper formation of the body plans of multicellular animals.

There is a common misconception that gene expression begins and ends with the synthesis of messenger RNA, perhaps because of the preponderance of studies based on yeast and tumour-derived cells grown in the presence of unlimited nutrients. This is akin to drawing conclusions about driving from observing cars on the Autobahn. Real life, however, is more like cross-town traffic: although mRNA transcription is the first and essential step in gene expression, the journey to protein synthesis can be complex and elaborate. This is particularly evident in developmental programs and responses to environmental cues or stresses, and in cases where proteins must be localized to specific regions of a cell. mRNA stability is also an important factor in governing protein synthesis. The regulation of gene expression at levels beyond mRNA synthesis is generally referred to as post-transcriptional control[4].

Like a good story, protein synthesis has a beginning (initiation), a middle (protein elongation) and an end (termination). Because it lies at the beginning, initiation represents a crucial control nexus. Initiation of protein synthesis from most mRNAs in eukaryotes (organisms that include plants, animals and fungi) requires covalent modifications called 5′ caps and poly(A) tails to be added to the beginnings and ends of mRNAs, respectively[5]. These are recognized by a preinitiation complex (PIC), which contains the small subunit of the protein-synthesizing ribosome apparatus, together with an initiator transfer RNA and additional accessory factors. The PIC scans along the mRNA in the 5′-to-3′ direction until it encounters the nucleotide sequence (AUG) that specifies where translation should begin. Such 'cap-dependent' translation confers several opportunities for control: it enables cells to distinguish between self and non-self mRNAs to subvert viral RNA infection; it can be used to modify mRNA stability; and structural barriers between the cap and AUG can be used to control initiation.

Not having caps and tails can also be advantageous. For example, many RNA viruses, especially positive-sense RNA viruses, whose genomes resemble mRNAs, directly deposit their genomes into a host cell's cytoplasm to be used as mRNAs. Because these genomes do not have access to the host cell's nucleus (which harbours the machinery that attaches 5′ caps and poly(A) tails to the host's mRNAs), many viruses have evolved alternative ways of recruiting ribosomes that use highly structured RNA elements called internal ribosome entry signals (IRESs). In the presence of viral enzymes that inactivate cap-dependent translation, cellular ribosomes are driven to the viral IRES-containing mRNAs. But IRESs are not just used by viruses: IRES-containing cellular mRNAs are also preferentially translated under conditions in which cells inactivate cap-dependent translation. This happens in response to a variety of stresses and during cell division. The list of IRES-containing cellular mRNAs continues to grow[6].

Xue and colleagues now show that IRESs are used to control gene expression during mammalian development. Vertebrate genomes harbour four clusters of *Hox* genes, *HoxA*–*HoxD*. The chromosomal region corresponding to the *HoxA* cluster contains 11 genes encoding transcription factors, each of which is involved in the development of different parts of the vertebrate body, from

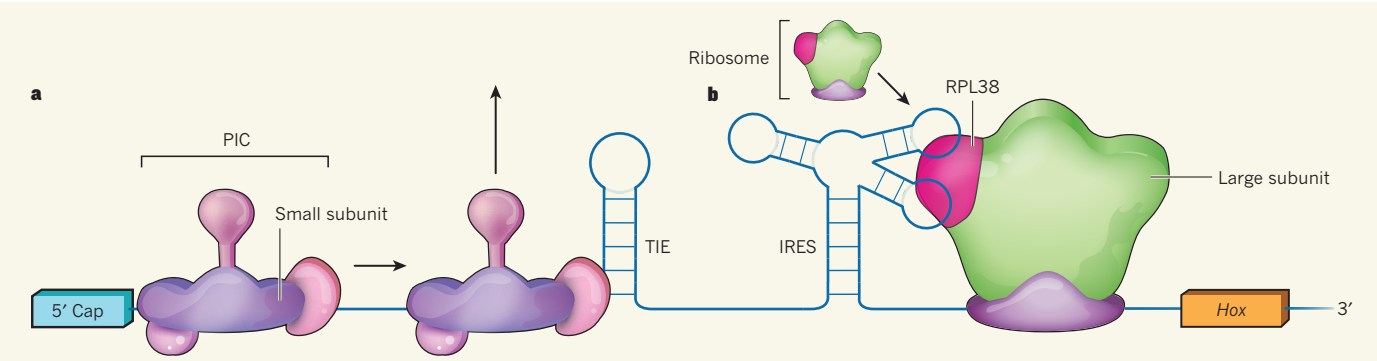


Figure 1 | Regulating the translation of certain *Hox* genes. **a**, A preliminary step in the translation of many messenger RNAs is the loading of a preinitiation complex (PIC, which includes the small subunit of the ribosomal protein-synthesis apparatus) onto cap structures at the 5′ end of the mRNAs. The PIC then scans along the mRNA in the 5′-to-3′ direction (horizontal arrow) searching for a nucleotide sequence that specifies where translation should begin. Xue *et al.*[3] report that translation inhibitory elements (TIEs) located in the 5′ untranslated regions of selected *Hox* mRNAs block the PIC's progress, and may cause it to detach from the mRNA (vertical arrow). **b**, They also find that RNA elements called internal ribosome entry signals (IRESs), located downstream of TIEs, directly recruit ribosomes to initiate translation of these *Hox* genes, perhaps with assistance from ribosomal protein RPL38 on the ribosome's large subunit.

© 2015 Macmillan Publishers Limited. All rights reserved

the hindbrain to the sacrum (the bone at the base of the spine)[7]. Although the mRNAs that encode these *HoxA* genes are equipped with 5′ caps and poly(A) tails, they are poor substrates for translation. Previous work[8] demonstrated that ribosomal protein RPL38 facilitates translation of a subset of *Hox* mRNAs, suggesting that translation of some of the *HoxA* mRNAs may require direct interaction with the ribosome.

In their study, Xue and co-workers used a series of ingenious experiments not only to characterize IRES activity in 5 of the 11 *HoxA* mRNAs, but also to identify mRNA motifs that they call translation inhibitory elements (TIEs), located between the 5′ caps and IRESs. These motifs seem to impede scanning by the PIC (Fig. 1). The combination of TIEs and IRESs enables a previously unknown mode of translational regulation in these key developmental regulatory genes.

The authors used state-of-the-art methods to structurally characterize the IRESs and to demonstrate that, at least in cell lysates, ribosomes can be directly recruited to the mRNAs. Most intriguingly, they found that complete loss of the IRES in the *Hoxa9* gene, which has a crucial role in effecting the transition between the thoracic and lumbar regions of the spine, results in loss of the terminal rib anchored to the thirteenth thoracic vertebra (T13) but does not affect the distribution of the *Hoxa9* mRNA in the developing mouse fetus. Indeed, Xue *et al.* observed that T13 is partly transformed into L1 (the first lumbar vertebra) in mice carrying only one IRES-containing *Hoxa9* gene rather than the normal two. This finding emphasizes the part played by the newly discovered regulatory mechanism in the development of the mammalian body plan.

Xue and colleagues' groundbreaking study raises many questions. Does ribosome recruitment involve the whole ribosome or only the large subunit? If the latter is true, then how is the small subunit engaged for initiation of translation? Structurally, RPL38 lies along the solvent-accessible 'back side' of the large ribosomal subunit[9]; are other ribosomal proteins or soluble factors that interact with the protein-synthesis apparatus involved in the translation of IRES-containing *Hox* mRNAs, and what might they be?

RPL38 is not essential in yeast[10], so another question is whether RPL38-containing ribosomes in multicellular organisms are specialized to decode IRES-containing mRNAs. And are such *Hox* mRNAs ever translated by cap recognition and scanning? If so, how are the TIEs inactivated? If not, are these mRNAs translated only at specific stages in development when cap-dependent translation is suppressed? These questions will drive a diverse set of research efforts in the future. ■

Jonathan D. Dinman *is in the Department of Cell Biology and Molecular Genetics, University of Maryland, College Park, Maryland 20742, USA.*
e-mail: dinman@umd.edu

1. Mirsky, A. E. & Ris, H. *J. Gen. Physiol.* **34,** 451–462 (1951).
2. Mallo, M. & Alonso, C. R. *Development* **140,** 3951–3963 (2013).
3. Xue, S. *et al. Nature* **517,** 33–38 (2015).
4. Hershey, J. W. B., Sonenberg, N. & Mathews, M. B. *Cold Spring Harb. Perspect. Biol.* **4,** a011528 (2012).
5. Sonenberg, N. & Hinnebusch, A. G. *Cell* **136,** 731–745 (2009).
6. Mokrejš, M. *et al. Nucleic Acids Res.* **38** (Suppl. 1), D131–D136 (2010).
7. Alexander, T., Nolte, C. & Krumlauf, R. *Annu. Rev. Cell Dev. Biol.* **25,** 431–456 (2009).
8. Kondrashov, N. *et al. Cell* **145,** 383–397 (2011).
9. Jenner, L. *et al. Curr. Opin. Struct. Biol.* **22,** 759–767 (2012).
10. Giaever, G. *et al. Nature* **418,** 387–391 (2002).

This article was published online on 19 November 2014.

MATERIALS SCIENCE

Like cartilage, but simpler

The properties of articular cartilage, which lines bones in joints, depend partly on repulsion between components of the material. A new synthetic gel that mimics this feature has rare, direction-dependent properties. SEE LETTER P.68

ANNE LADEGAARD SKOV

The work of materials scientists usually focuses on attractive forces, which underpin the reinforcement of polymers by strong fibres or particles[1], and the self-repairing abilities of rubbery materials through hydrogen bonding[2]. But on page 68 of this issue, Liu *et al.*[3] report their use of repulsive forces in the design of a hydrogel — a water-swollen polymer network — that exhibits fascinating direction-dependent behaviour. The material might be useful in applications that require a reduction of vibrations.

The new hydrogel contains nanometre-scale sheets of a titanium oxide known as titanate(IV) nanosheets (TiNS), arranged cofacially (in planes with their faces aligned towards each other). TiNS consist of only surface atoms, and adopt an ultrathin (7.5-ångström)

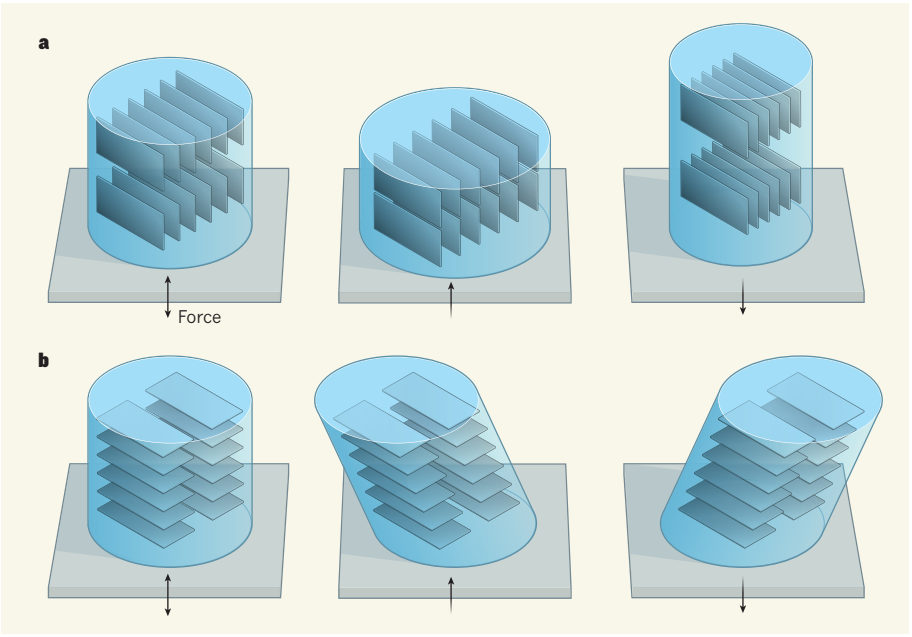


Figure 1 | Direction-dependent behaviour of a hydrogel. Liu *et al.*[3] have prepared a hydrogel — a water-swollen polymer network — that contains nanoscale sheets of a titanium oxide, aligned in planes with their faces parallel to each other. **a**, When an oscillatory force is applied up and down to cylindrical samples of the material parallel to the nanosheet planes, the hydrogel undergoes cycles of compression and expansion. Single-headed arrows indicate movement of the platform on which the sample rests. **b**, But when the same force is applied orthogonal to the nanosheet planes, the material undergoes almost completely horizontal deformation. Nanosheets are not shown to scale.

© 2015 Macmillan Publishers Limited. All rights reserved

two-dimensional crystal-like structure — 150 stacked nanosheets would have the same thickness as a human hair. In water-based media, the surfaces have a high density of negative charges, which are balanced by an overlayer of positively charged ions, thus forming electric double layers that repel each other and ensure efficient dispersion of the nanosheets.

If TiNS were simply mixed into a hydrogel, they would adopt the thermodynamically most favourable orientation, in which the sheets are orthogonal to each other. But Liu and colleagues observed that TiNS align cofacially when placed in a magnetic field strong enough to overcome the energy barrier to the formation of this arrangement. They therefore magnetically aligned TiNS in a solution of a hydrogel precursor, and then polymerized the precursor, trapping the nanosheets in the resulting polymer network so that they did not orient back to the orthogonal position.

The hydrogel turned out to have some remarkable properties. First, a simple visual inspection revealed that it is almost transparent from one angle, but completely opaque from another. This is clear evidence of strong orientation (structural order) in the material, and confirms that the nanosheets are ideally aligned. Such perfect structural order is rarely seen.

Second, Liu and co-workers observed that the hydrogel exhibits impressive mechanical behaviour, even though the concentration of the nanosheets is a mere 0.8% by weight. When the authors compressed the material orthogonal to the nanosheet plane, the resistance from the hydrogel was several times higher than that from compression parallel to that plane. This is the opposite of what happens in conventional fibre-reinforced materials, which are more resistant to compression parallel to the axis of alignment of the fibres. This unusual behaviour of the new material arises from the repulsive forces between the nanosheets, which prevents the layers of sheets from getting closer when compressed. And when the researchers applied shear (a force coplanar with the cross-section of the material) parallel to the nanosheet plane, resistance was about four times less than when shear was applied orthogonal to that plane. This is because the layers of nanosheets can slide across each other with almost no friction when parallel shear is applied.

Liu *et al.* report that the material's unusual mechanical behaviour has excellent vibration-damping properties when a large, continuous oscillatory motion is applied vertically to cylindrical samples that carry a load on top. Conventional hydrogels would initially compress and then undergo cycles of expansion and compression — this was also what happened when the authors applied an oscillatory force parallel to the nanosheet planes of their material (Fig. 1a). But when they applied such a force orthogonally to the nanosheet planes, the hydrogel counterintuitively showed restricted, almost solely horizontal deformation (Fig. 1b).

The hydrogel can thus efficiently direct force from one direction to the plane orthogonal to the force — in Liu and colleagues' words it is an excellent vibration isolator. An explanation for this rare behaviour is that, when a vertical force is applied to the hydrogel, the easiest way for the material to dissipate the energy is by shearing in the plane orthogonal to the deformation. Such efficient vibration isolation is reminiscent of a trampolinist at the end of a competitive routine, when the gymnast needs to become perfectly still after landing on the elastic trampoline. Gymnasts achieve this through tremendous body control largely involving technique, but also assisted by articular cartilage that isolates vertical movement in the soft joints of the body.

Articular cartilage is a complex hydrogel consisting of proteoglycan gel — essentially a protein-based substance that underpins the extracellular matrix of connective tissue — within which chondroitin sulphate (which consists of chains of sugars) is dissolved. The load-bearing and damping properties required for joints are provided by systematic structuring of collagen fibres and chondrocytes (the cells that maintain cartilage), along with repulsive forces between the negatively charged proteoglycan molecules[4]. The load-bearing and damping properties of Liu and co-workers' hydrogel closely resemble those of articular cartilage, although its structure is much simpler than that of the natural material.

So could the new hydrogel, or another material that exploits repulsive forces, be used as artificial cartilage? It is estimated that a human knee or hip joint can experience one million loading cycles per year. These large, cyclic stresses and strains may cause tiny cracks on the surface of articular cartilage or within the bulk material. These cracks can be repaired by chondrocytes, but may grow and accumulate into microscopically observable damage[4]. It would therefore probably be too ambitious to replace articular cartilage with the hydrogel unless a self-healing mechanism for the new material can be developed. But self-healing mechanisms are based on attractive forces; exploiting such forces in a system based on repulsion may not be easy without destroying desirable properties. Even so, the new hydrogel will surely be developed into many interesting products — for example, it could be used in microelectronic applications, in which the hydrogel could act as a matrix between electronic elements to strongly reduce harmful vibrations. ■

Anne Ladegaard Skov *is in the Danish Polymer Centre, Department of Chemical and Biochemical Engineering, Technical University of Denmark, Kongens Lyngby 2800, Denmark.*
e-mail: al@kt.dtu.dk

1. Vudayagiri, S. *et al. Smart Mater. Struct.* **23,** 105017 (2014).
2. Cordier, P., Tournilhac, P., Soulié-Ziakovic, C. & Leibler, L. *Nature* **451,** 977–980 (2008).
3. Liu, M. *et al. Nature* **517,** 68–72 (2015).
4. Mow, V. C., Ratcliffe, A. & Poole, A. R. *Biomaterials* **13,** 67–97 (1992).

STRUCTURAL BIOLOGY

Photosynthetic complex in close-up

Photosystem II, a photosynthetic protein complex, is prone to X-ray damage during crystallography. A high-resolution structure of the undamaged complex now offers a detailed view of its catalytic centre. SEE LETTER P.99

ILME SCHLICHTING

The oxygen we breathe is produced by photosystem II, a large protein complex located in the thylakoid membranes of photosynthetic organisms (Fig. 1). In this issue (page 99), Suga *et al.*[1] describe the first high-resolution crystal structure of undamaged photosystem II, obtained using an X-ray source called a free-electron laser. Their structure provides unprecedented insight into the oxygen-evolving complex of the photosynthetic apparatus.

Photosystem II transforms the energy of sunlight into chemical energy. In this process, the absorption of a photon results in a charge separation in the photosynthetic reaction centre of the protein complex, and the generation of a high-energy electron. This electron is ultimately used to chemically reduce plastoquinone molecules, as part of the electron-transport chain of the light-dependent reactions of photosynthesis.

The electron is replaced by the oxygen-evolving complex (OEC) of photosystem II: the OEC is oxidized with each photon-absorption event until it has been oxidized four times, and then resets itself by splitting water into an oxygen molecule, four protons and four electrons. Understanding the water-splitting reaction and the detailed arrangement of the atoms in the catalytic OEC required for energy-,

© 2015 Macmillan Publishers Limited. All rights reserved

two-dimensional crystal-like structure — 150 stacked nanosheets would have the same thickness as a human hair. In water-based media, the surfaces have a high density of negative charges, which are balanced by an overlayer of positively charged ions, thus forming electric double layers that repel each other and ensure efficient dispersion of the nanosheets.

If TiNS were simply mixed into a hydrogel, they would adopt the thermodynamically most favourable orientation, in which the sheets are orthogonal to each other. But Liu and colleagues observed that TiNS align cofacially when placed in a magnetic field strong enough to overcome the energy barrier to the formation of this arrangement. They therefore magnetically aligned TiNS in a solution of a hydrogel precursor, and then polymerized the precursor, trapping the nanosheets in the resulting polymer network so that they did not orient back to the orthogonal position.

The hydrogel turned out to have some remarkable properties. First, a simple visual inspection revealed that it is almost transparent from one angle, but completely opaque from another. This is clear evidence of strong orientation (structural order) in the material, and confirms that the nanosheets are ideally aligned. Such perfect structural order is rarely seen.

Second, Liu and co-workers observed that the hydrogel exhibits impressive mechanical behaviour, even though the concentration of the nanosheets is a mere 0.8% by weight. When the authors compressed the material orthogonal to the nanosheet plane, the resistance from the hydrogel was several times higher than that from compression parallel to that plane. This is the opposite of what happens in conventional fibre-reinforced materials, which are more resistant to compression parallel to the axis of alignment of the fibres. This unusual behaviour of the new material arises from the repulsive forces between the nanosheets, which prevents the layers of sheets from getting closer when compressed. And when the researchers applied shear (a force coplanar with the cross-section of the material) parallel to the nanosheet plane, resistance was about four times less than when shear was applied orthogonal to that plane. This is because the layers of nanosheets can slide across each other with almost no friction when parallel shear is applied.

Liu *et al.* report that the material's unusual mechanical behaviour has excellent vibration-damping properties when a large, continuous oscillatory motion is applied vertically to cylindrical samples that carry a load on top. Conventional hydrogels would initially compress and then undergo cycles of expansion and compression — this was also what happened when the authors applied an oscillatory force parallel to the nanosheet planes of their material (Fig. 1a). But when they applied such a force orthogonally to the nanosheet planes, the hydrogel counterintuitively showed restricted, almost solely horizontal deformation (Fig. 1b).

The hydrogel can thus efficiently direct force from one direction to the plane orthogonal to the force — in Liu and colleagues' words it is an excellent vibration isolator. An explanation for this rare behaviour is that, when a vertical force is applied to the hydrogel, the easiest way for the material to dissipate the energy is by shearing in the plane orthogonal to the deformation. Such efficient vibration isolation is reminiscent of a trampolinist at the end of a competitive routine, when the gymnast needs to become perfectly still after landing on the elastic trampoline. Gymnasts achieve this through tremendous body control largely involving technique, but also assisted by articular cartilage that isolates vertical movement in the soft joints of the body.

Articular cartilage is a complex hydrogel consisting of proteoglycan gel — essentially a protein-based substance that underpins the extracellular matrix of connective tissue — within which chondroitin sulphate (which consists of chains of sugars) is dissolved. The load-bearing and damping properties required for joints are provided by systematic structuring of collagen fibres and chondrocytes (the cells that maintain cartilage), along with repulsive forces between the negatively charged proteoglycan molecules[4]. The load-bearing and damping properties of Liu and co-workers' hydrogel closely resemble those of articular cartilage, although its structure is much simpler than that of the natural material.

So could the new hydrogel, or another material that exploits repulsive forces, be used as artificial cartilage? It is estimated that a human knee or hip joint can experience one million loading cycles per year. These large, cyclic stresses and strains may cause tiny cracks on the surface of articular cartilage or within the bulk material. These cracks can be repaired by chondrocytes, but may grow and accumulate into microscopically observable damage[4]. It would therefore probably be too ambitious to replace articular cartilage with the hydrogel unless a self-healing mechanism for the new material can be developed. But self-healing mechanisms are based on attractive forces; exploiting such forces in a system based on repulsion may not be easy without destroying desirable properties. Even so, the new hydrogel will surely be developed into many interesting products — for example, it could be used in microelectronic applications, in which the hydrogel could act as a matrix between electronic elements to strongly reduce harmful vibrations. ■

Anne Ladegaard Skov *is in the Danish Polymer Centre, Department of Chemical and Biochemical Engineering, Technical University of Denmark, Kongens Lyngby 2800, Denmark.*
e-mail: al@kt.dtu.dk

1. Vudayagiri, S. *et al. Smart Mater. Struct.* **23,** 105017 (2014).
2. Cordier, P., Tournilhac, P., Soulié-Ziakovic, C. & Leibler, L. *Nature* **451,** 977–980 (2008).
3. Liu, M. *et al. Nature* **517,** 68–72 (2015).
4. Mow, V. C., Ratcliffe, A. & Poole, A. R. *Biomaterials* **13,** 67–97 (1992).

STRUCTURAL BIOLOGY

Photosynthetic complex in close-up

Photosystem II, a photosynthetic protein complex, is prone to X-ray damage during crystallography. A high-resolution structure of the undamaged complex now offers a detailed view of its catalytic centre. SEE LETTER P.99

ILME SCHLICHTING

The oxygen we breathe is produced by photosystem II, a large protein complex located in the thylakoid membranes of photosynthetic organisms (Fig. 1). In this issue (page 99), Suga *et al.*[1] describe the first high-resolution crystal structure of undamaged photosystem II, obtained using an X-ray source called a free-electron laser. Their structure provides unprecedented insight into the oxygen-evolving complex of the photosynthetic apparatus.

Photosystem II transforms the energy of sunlight into chemical energy. In this process, the absorption of a photon results in a charge separation in the photosynthetic reaction centre of the protein complex, and the generation of a high-energy electron. This electron is ultimately used to chemically reduce plastoquinone molecules, as part of the electron-transport chain of the light-dependent reactions of photosynthesis.

The electron is replaced by the oxygen-evolving complex (OEC) of photosystem II: the OEC is oxidized with each photon-absorption event until it has been oxidized four times, and then resets itself by splitting water into an oxygen molecule, four protons and four electrons. Understanding the water-splitting reaction and the detailed arrangement of the atoms in the catalytic OEC required for energy-,

© 2015 Macmillan Publishers Limited. All rights reserved


DENNIS KUNKEL MICROSCOPY, INC./VISUALS UNLIMITED/CORBIS

Figure 1 | Thylakoid membranes of *Nostoc* cyanobacteria. The photosynthetic protein complex known as photosystem II resides in the thylakoid membranes (shown here in bright green) of plants, algae and cyanobacteria. Suga *et al.*[1] report a high-resolution X-ray crystal structure of photosystem II from the cyanobacterium *Thermosynechococcus vulcanus*.

electron- and proton-transfer reactions is crucial for basic science, and has implications for the design of light-driven batteries.

X-rays are extremely useful for structure determination, but they inflict radiation damage that can destroy the sample being investigated, sometimes before data collection is complete. Previous X-ray crystallographic studies[2,3] had provided detailed insight into the molecular architecture of photosystem II and the OEC, using crystals kept at cryogenic temperature during data collection to slow radiation damage. However, spectroscopic studies[4] showed that X-ray doses from the synchrotron sources used for structure determination result in serious damage to the OEC, indicating that the manganese atoms in the crystal structures are reduced[2] by the ionizing effects of X-rays and by radicals formed during data collection.

This problem now seems to have been solved with the advent of X-ray free-electron lasers (FELs), X-ray sources that provide ultra-bright femtosecond X-ray pulses (1 femtosecond is 10^{-15} seconds). They allow 'diffraction before destruction' — the ability to detect diffraction patterns before damage occurs. This has led to the development of a technique called serial femtosecond crystallography (SFX)[5], in which individual samples are exposed to a single pulse of X-rays; the samples are destroyed by the exposure, and so are replaced after each pulse. Data are thus collected from thousands of micrometre-scale crystals in a serial fashion. Randomly oriented microcrystals are conveniently and efficiently delivered to the X-ray beam in liquid microjets, which allows data to be collected at room temperature using crystals kept in the mother liquor from which they were grown.

Other groups have previously used FELs to collect SFX data from streams of photosystem II microcrystals[6–8]. Spectroscopic measurements[9] taken simultaneously with the SFX data showed that the OEC was not damaged, even though the microcrystals absorbed an extremely high dose of X-rays from the femtosecond pulses. However, no detailed information about the OEC's architecture could be derived from the diffraction data because the microcrystals did not diffract to high resolution. Poor diffraction is a common problem in macromolecular crystallography, in particular with membrane proteins. Because of their large size, macromolecules typically form crystals that have a high solvent content and that are held together by relatively few weak interactions. This explains their high fragility and often poor crystalline order.

In their quest to obtain a high-resolution structure of the undamaged OEC, Suga and co-workers used not only the advantages of damage-free data collection afforded by X-ray FELs (in this case, the SACLA instrument in Harima, Japan), but also their expertise in improving the quality of large crystals of photosystem II by dehydration[3]. Crystal packing, and thus diffraction properties, can be optimized by slow, controlled dehydration of crystals, an approach that has been applied successfully even to large macromolecular complexes.

An additional advantage of using large crystals is that it allows more than one diffraction pattern to be obtained from the same crystal by shifting it to expose a fresh spot. Suga *et al.* obtained data of excellent quality by rotating crystals for each X-ray exposure, so that each rotation represented a fraction of the crystal's mosaicity (a measure of the spread of crystal-plane orientations). This approach, which can be described as serial femtosecond rotation crystallography (SF-ROX), has previously been used[10] to collect data from crystals of the enzyme cytochrome *c* oxidase, another acutely radiation-sensitive system that evaded analysis using synchrotrons.

The new high-resolution structure depicts undamaged photosystem II in its dark-stable resting state (the S_1 state). It reveals the detailed arrangement of the OEC (see Fig. 1a of the paper), which consists of a cluster of four manganese ions and one calcium ion, with five oxygen atoms bridging the metals. Several water molecules are tightly bound close to the OEC. The authors observed slightly shorter distances between the manganese ions, compared to the previously determined high-resolution X-ray-damaged structure[3].

Notably, the distances between one of the oxygen atoms (designated O5) and its neighbouring manganese ions are longer than those of the other oxygen atoms — this had previously been observed[3], but it was unclear whether this was caused by radiation damage. This observation suggests that O5 is a hydroxide ion (OH^-), rather than an oxo ligand (O^{2-}), and so may be one of the OEC's substrate oxygen atoms. The researchers confirmed the accuracy and precision of their structures by obtaining two independent data sets, and by separately analysing data from the two monomers of the dimeric photosystem II complex.

Suga and colleagues' structure provides detailed information that will aid our understanding of the OEC's spectroscopic data, serve as a new starting point for computational studies of the water-splitting reaction, and provide invaluable clues about the mechanism of that reaction. An exciting next step would be to obtain time-resolved measurements using the SF-ROX approach, to provide an equally detailed view of the OEC at work. ■

Ilme Schlichting *is at the Max Planck Institute for Medical Research, Department of Biomolecular Mechanisms, 69120 Heidelberg, Germany.*
e-mail: ilme.schlichting@mpimf-heidelberg.mpg.de

1. Suga, M. *et al. Nature* **517,** 99–103 (2015).
2. Loll, B., Kern, J. Saenger, W., Zouni, A. & Biesiadka, J. *Nature* **438,** 1040–1044 (2005).
3. Umena, Y., Kawakami, K., Shen, J. R. & Kamiya, N. *Nature* **473,** 55–60 (2011).
4. Yano, J. *et al. Proc. Natl Acad. Sci. USA* **102,** 12047–12052 (2005).
5. Chapman, H. N. *et al. Nature* **470,** 73–77 (2011).
6. Kern, J. *et al. Proc. Natl Acad. Sci. USA* **109,** 9721–9726 (2012).
7. Kupitz, C. *et al. Nature* **513,** 261–265 (2014).
8. Kern, J. *et al. Nature Commun.* **5,** 4371; http://dx.doi.org/10.1038/ncomms5371 (2014).
9. Kern, J. *et al. Science* **340,** 491–495 (2013).
10. Hirata, K. *et al. Nature Methods* **11,** 734–736 (2014).

This article was published online on 26 November 2014.

© 2015 Macmillan Publishers Limited. All rights reserved

50 Years Ago

The Television Research Committee was appointed by the Home Secretary in July 1963, to initiate and co-ordinate research into the part which television plays, or could play, as a medium of communication and in fostering attitudes … The evidence seems fairly clear that television does not stimulate interest or broaden horizons to any greater degree than would happen in its absence … Several studies show that the heavy use of escapist material is associated with tendencies to anxiety, social maladjustment and frustration … There appears to be no evidence that television makes children passive and there is little to make us believe that violent programmes on television reduce the likelihood of violence in real life … On the whole the weight of evidence is behind the conclusion that the heavy dosage of violence in the mass media, while not a major determinant of crime or delinquency, heightens the probability that someone in the audience will act aggressively in a later situation.

From *Nature* 2 January 1965

100 Years Ago

Plague and Pestilence in Literature and Art. By Dr. Raymond Crawford — Dr. Crawford has treated his subject as much in its mental and moral aspects as in its physical, and the result is a wise and very interesting book … From century to century … theories of its causation are rife. It is the work of malignant demons; it is sent from heaven in punishment for sin; it is the result of evil magic exercised by man on man; it is engendered in the clouds … The contagious character of the disease was recognised by lay observers long before it was accepted by science … Science does move, moreover, even though it be but slowly, slowly.

From *Nature* 31 December 1914

MICROBIOLOGY

Diverted on the way to memory

The finding that protein A of *Staphylococcus aureus* diverts the immune response so that it ineffectively responds to other structures from the bacterium explains the failure of ongoing attempts to develop working *S. aureus* vaccines.

GORDON Y. C. CHEUNG & MICHAEL OTTO

Staphylococcus aureus is a global pathogen of great importance, causing thousands of deaths each year in the United States alone. The main problems with *S. aureus* infections are frequent resistance to antibiotics and the large repertoire of molecules produced by the pathogen to subvert human immune defences[1,2]. Notably, there is no protective immunity towards *S. aureus*, meaning that previous *S. aureus* infection does not defend an individual against subsequent infections. Writing in the *Journal of Experimental Medicine*, Pauli *et al.*[3] describe a mechanism by which one *S. aureus* molecule, protein A, overwhelms the host's immune machinery through excessively stimulating certain immune responses while suppressing reactivity toward other key virulence determinants of the bacterium. These findings explain the weak protective immune responses and lack of immunological memory observed with *S. aureus* infections.

The human immune system has two ways to combat bacterial invaders. One is innate immunity, so-called because the response mechanisms involved do not require adaptation; rather, the immune cells recognize structures that are evolutionarily conserved among pathogens, resulting in the pathogens' quick elimination. *S. aureus* has a large repertoire of 'weapons' to subvert this aspect of human immune defence — such as toxins that kill white blood cells — and the battle between the bacterium and the innate immune response determines whether an *S. aureus* invasion develops into a longer-lasting infection.

The other system is adaptive immunity, which mostly involves T cells and B cells. In B cells, adaptive immune responses lead to genetic rearrangements that result in differentiation into plasma cells, which produce antibodies that are specific to certain structures (antigens) and that trigger mechanisms to remove the pathogens expressing those structures. About 10% of plasma cells survive after an infection is cleared; these 'memory B cells' provide protective immunity against further infections with the same pathogen. Adaptive responses kick in about a week after the initial infection and normally provide long-lasting immunity.

In the case of *S. aureus*, the role of adaptive immunity is poorly understood, but it is clear that long-lasting protective memory is not generated. This is not only reflected by recurring *S. aureus* infections, but also by the fact

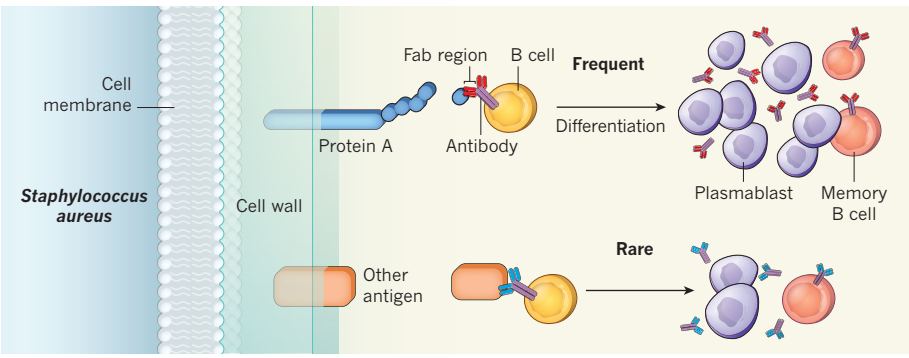


Figure 1 | Protein-A-dependent immune evasion. Protein A of *Staphylococcus aureus* contains a region of repetitive domains, part of which binds to the Fab region of antibodies in a nonspecific, 'superantigenic' manner. Pauli *et al.*[3] propose that this superantigenic binding biases the B-cell immune response to *S. aureus* towards protein A. They observe that, of the B cells that differentiate to become antibody-producing plasmablasts during an *S. aureus* infection, the majority bind to, and produce antibodies against, protein A; very few B cells that bind to other *S. aureus* antigens undergo this differentiation process. This means that the memory B cells that remain after an infection, and that are 'primed' to mount immune responses to repeat infections, will also be mostly specific for protein A. This may explain the lack of protective memory against *S. aureus* infections, because such protection requires immune activity against multiple virulence determinants of the bacterium.

© 2015 Macmillan Publishers Limited. All rights reserved

that vaccine development against *S. aureus* has always failed at the stage of clinical trials[4]. Although the mechanisms underlying this situation are still being unravelled, protein A, which is located on the surface of *S. aureus* cells, is believed to have a key role. Protein A contains repetitive sequences consisting of two parts: one binds to the Fc (constant) part of human antibodies and the other binds to the Fab (variable) antibody region. This Fab-region binding is 'superantigenic', meaning that it is nonspecific and has excessive potential to stimulate immune responses[5].

Binding of protein A to the Fc region was reported many years ago[6] and results in what has been called a 'camouflage coat' of non-specific antibodies on the *S. aureus* surface that prevents binding of specific antibodies and thus a targeted immune response. Pauli *et al.*[3] now show that the superantigenic binding of protein A to the Fab domain is so overwhelming that it strongly hampers the production of antibodies to other *S. aureus* antigens (Fig. 1).

To reach this conclusion, the authors characterized the antigen specificity of plasmablasts — an immature form of plasma B cells that are produced only during infections and that play a crucial part in active immune responses — in large cohorts of people with and without *S. aureus* infections. They found that, in principle, nothing was wrong with the plasmablast response in the infected individuals, inasmuch as the cells underwent normal maturation on exposure to *S. aureus* antigens. However, when the investigators isolated the antibody-encoding genes of the responding plasmablasts, they found that almost all targeted protein A, and very few were specific for other *S. aureus* toxins or cell-surface virulence determinants. On the basis of these results, Pauli *et al.* propose that the superantigenic action of protein A prevents the production of specific and effective antibodies to other *S. aureus* antigens.

Unfortunately, mouse models cannot be used to substantiate this proposal, because the murine immune response differs considerably in details of adaptive immunity that matter in this case[7]. However, it has been shown in a mouse model that protein A contributes significantly to immune evasion[8] and that monoclonal antibodies against protein A neutralize the Fc-binding and Fab-binding activities of protein A[9]. These studies suggest that protein A would be a valuable target for the development of vaccines against *S. aureus*. However, it is commonly thought that a successful *S. aureus* vaccine will need to be multivalent — in other words, it will need to target several of the many molecules that the bacterium uses for virulence and immune evasion. For example, the vaccine should also include strategies to address the fact that *S. aureus* produces several toxins that can circumvent immune elimination even when specific antibody responses are mounted[10]. Pauli and colleagues' findings suggest that, by adding protein A-specific components in such preparations, we may finally be able to develop a working *S. aureus* vaccine. ■

Gordon Y. C. Cheung *and* **Michael Otto** *are in the Laboratory of Human Bacterial Pathogenesis, National Institute of Allergy and Infectious Diseases, NIH, Bethesda, Maryland 20892, USA.*
e-mail: motto@niaid.nih.gov

1. Lowy, F. D. *J. Clin. Invest.* **111,** 1265–1273 (2003).
2. Rooijakkers, S. H., van Kessel, K. P. & van Strijp, J. A. *Trends Microbiol.* **13,** 596–601 (2005).
3. Pauli, N. T. *et al. J. Exp. Med.* **211,** 2331–2339 (2014).
4. Pier, G. B. *Hum. Vaccine Immunother.* **9,** 1865–1876 (2013).
5. Graille, M. *et al. Proc. Natl Acad. Sci. USA* **97,** 5399–5404 (2000).
6. Forsgren, A. & Nordström, K. *Ann. NY Acad. Sci.* **236,** 252–266 (1974).
7. Goodyear, C. S. & Silverman, G. J. *J. Exp. Med.* **197,** 1125–1139 (2003).
8. Falugi, F., Kim, H. K., Missiakas, D. M. & Schneewind, O. *mBio* **4,** e00575-13 (2013).
9. Kim, H. K. *et al. Infect. Immun.* **80,** 3460–3470 (2012).
10. DeLeo, F. R. & Otto, M. *J. Exp. Med.* **205,** 271–274 (2008).

This article was published online on 10 December 2014.

CELL CYCLE

It takes three to find the exit

Mitotic cell division separates chromosome pairs into two genetically identical daughter cells. A study in fission yeast reveals that this separation is guided by the sequential activation of three phosphatase enzymes. SEE LETTER P.94

MATHIEU BOLLEN

The ultimate aim of most cells is to become two cells[1], through a cell-division process that occurs following phases of cell growth and chromosome duplication. Cell division requires the ordered assembly, disassembly and reorganization of numerous cellular components. These structural rearrangements are coordinated by kinase and phosphatase enzymes, which regulate proteins by attaching phosphate molecules or removing them, respectively. Many proteins are phosphorylated during early cell division, and most are dephosphorylated again at the exit from division, but it is unclear how the phosphatases involved in this process are regulated. In this issue, Grallert *et al.*[2] (page 94) show that the end of cell division in fission yeast (*Schizosaccharomyces pombe*) is driven by three phosphatases that are organized in a relay, whereby one enzyme sequentially activates another.

During the first part of cell division, called mitosis, chromosomes from each chromosome pair are pulled towards opposite poles of the cell, culminating in the formation of two separate nuclei. The ensuing cytoplasmic division generates two daughter cells. Work over the past two decades[3] has revealed that, in budding yeast, the phosphatase Cdc14 opposes the activity of Cdk1 kinase, the master regulator of mitosis. However, this mitotic function of Cdc14 is not evolutionarily conserved in fission yeast and animals. Instead, complexes of protein phosphatases 1 (PP1) and 2A (PP2A) have emerged as key regulators of the exit from mitosis in these organisms[3].

Grallert and colleagues report that PP1 and PP2A are largely inactive at the beginning of mitosis in fission yeast. PP1 inactivity comes about because it is phosphorylated by Cdk1, which not only reduces the phosphatase's activity, but also promotes its degradation. The authors did not investigate the mechanism underlying the low PP2A activity in early mitosis. However, they did examine how these phosphatases are activated at mitotic exit, and uncovered an unexpected regulatory cascade (Fig. 1).

PP2A complexes comprise a catalytic and scaffolding subunit and a regulatory B subunit. The researchers discovered unanticipated docking sites for PP1 on two PP2A complexes that have structurally unrelated B subunits — B55 and B56. They found that, just before the start of chromosome separation, when Cdk1 becomes inactive, PP2A-B55-associated PP1 removes its own inhibitory phosphate group and then activates and releases the PP2A-B55 to which it is bound. Subsequently, PP2A-B55 removes a phosphate group from the PP1-binding site on PP2A-B56. The efficient dephosphorylation of this site is delayed, however, because PP2A-B55 activity is counteracted by an opposing kinase, Plk1. When Plk1 is inactivated in late mitosis, the B56 subunit is efficiently dephosphorylated and PP1 binds, resulting in the activation of PP2A-B56 and its release from PP1. Grallert and co-workers provide evidence that interference with this regulatory cascade causes chromosome-segregation defects, highlighting its importance for cell division.

These findings raise exciting questions.

© 2015 Macmillan Publishers Limited. All rights reserved

that vaccine development against *S. aureus* has always failed at the stage of clinical trials[4]. Although the mechanisms underlying this situation are still being unravelled, protein A, which is located on the surface of *S. aureus* cells, is believed to have a key role. Protein A contains repetitive sequences consisting of two parts: one binds to the Fc (constant) part of human antibodies and the other binds to the Fab (variable) antibody region. This Fab-region binding is 'superantigenic', meaning that it is nonspecific and has excessive potential to stimulate immune responses[5].

Binding of protein A to the Fc region was reported many years ago[6] and results in what has been called a 'camouflage coat' of non-specific antibodies on the *S. aureus* surface that prevents binding of specific antibodies and thus a targeted immune response. Pauli *et al.*[3] now show that the superantigenic binding of protein A to the Fab domain is so overwhelming that it strongly hampers the production of antibodies to other *S. aureus* antigens (Fig. 1).

To reach this conclusion, the authors characterized the antigen specificity of plasmablasts — an immature form of plasma B cells that are produced only during infections and that play a crucial part in active immune responses — in large cohorts of people with and without *S. aureus* infections. They found that, in principle, nothing was wrong with the plasmablast response in the infected individuals, inasmuch as the cells underwent normal maturation on exposure to *S. aureus* antigens. However, when the investigators isolated the antibody-encoding genes of the responding plasmablasts, they found that almost all targeted protein A, and very few were specific for other *S. aureus* toxins or cell-surface virulence determinants. On the basis of these results, Pauli *et al.* propose that the superantigenic action of protein A prevents the production of specific and effective antibodies to other *S. aureus* antigens.

Unfortunately, mouse models cannot be used to substantiate this proposal, because the murine immune response differs considerably in details of adaptive immunity that matter in this case[7]. However, it has been shown in a mouse model that protein A contributes significantly to immune evasion[8] and that monoclonal antibodies against protein A neutralize the Fc-binding and Fab-binding activities of protein A[9]. These studies suggest that protein A would be a valuable target for the development of vaccines against *S. aureus*. However, it is commonly thought that a successful *S. aureus* vaccine will need to be multivalent — in other words, it will need to target several of the many molecules that the bacterium uses for virulence and immune evasion. For example, the vaccine should also include strategies to address the fact that *S. aureus* produces several toxins that can circumvent immune elimination even when specific antibody responses are mounted[10]. Pauli and colleagues' findings suggest that, by adding protein A-specific components in such preparations, we may finally be able to develop a working *S. aureus* vaccine. ■

Gordon Y. C. Cheung *and* **Michael Otto** *are in the Laboratory of Human Bacterial Pathogenesis, National Institute of Allergy and Infectious Diseases, NIH, Bethesda, Maryland 20892, USA.*
e-mail: motto@niaid.nih.gov

1. Lowy, F. D. *J. Clin. Invest.* **111,** 1265–1273 (2003).
2. Rooijakkers, S. H., van Kessel, K. P. & van Strijp, J. A. *Trends Microbiol.* **13,** 596–601 (2005).
3. Pauli, N. T. *et al. J. Exp. Med.* **211,** 2331–2339 (2014).
4. Pier, G. B. *Hum. Vaccine Immunother.* **9,** 1865–1876 (2013).
5. Graille, M. *et al. Proc. Natl Acad. Sci. USA* **97,** 5399–5404 (2000).
6. Forsgren, A. & Nordström, K. *Ann. NY Acad. Sci.* **236,** 252–266 (1974).
7. Goodyear, C. S. & Silverman, G. J. *J. Exp. Med.* **197,** 1125–1139 (2003).
8. Falugi, F., Kim, H. K., Missiakas, D. M. & Schneewind, O. *mBio* **4,** e00575-13 (2013).
9. Kim, H. K. *et al. Infect. Immun.* **80,** 3460–3470 (2012).
10. DeLeo, F. R. & Otto, M. *J. Exp. Med.* **205,** 271–274 (2008).

This article was published online on 10 December 2014.

CELL CYCLE

It takes three to find the exit

Mitotic cell division separates chromosome pairs into two genetically identical daughter cells. A study in fission yeast reveals that this separation is guided by the sequential activation of three phosphatase enzymes. SEE LETTER P.94

MATHIEU BOLLEN

The ultimate aim of most cells is to become two cells[1], through a cell-division process that occurs following phases of cell growth and chromosome duplication. Cell division requires the ordered assembly, disassembly and reorganization of numerous cellular components. These structural rearrangements are coordinated by kinase and phosphatase enzymes, which regulate proteins by attaching phosphate molecules or removing them, respectively. Many proteins are phosphorylated during early cell division, and most are dephosphorylated again at the exit from division, but it is unclear how the phosphatases involved in this process are regulated. In this issue, Grallert *et al.*[2] (page 94) show that the end of cell division in fission yeast (*Schizosaccharomyces pombe*) is driven by three phosphatases that are organized in a relay, whereby one enzyme sequentially activates another.

During the first part of cell division, called mitosis, chromosomes from each chromosome pair are pulled towards opposite poles of the cell, culminating in the formation of two separate nuclei. The ensuing cytoplasmic division generates two daughter cells. Work over the past two decades[3] has revealed that, in budding yeast, the phosphatase Cdc14 opposes the activity of Cdk1 kinase, the master regulator of mitosis. However, this mitotic function of Cdc14 is not evolutionarily conserved in fission yeast and animals. Instead, complexes of protein phosphatases 1 (PP1) and 2A (PP2A) have emerged as key regulators of the exit from mitosis in these organisms[3].

Grallert and colleagues report that PP1 and PP2A are largely inactive at the beginning of mitosis in fission yeast. PP1 inactivity comes about because it is phosphorylated by Cdk1, which not only reduces the phosphatase's activity, but also promotes its degradation. The authors did not investigate the mechanism underlying the low PP2A activity in early mitosis. However, they did examine how these phosphatases are activated at mitotic exit, and uncovered an unexpected regulatory cascade (Fig. 1).

PP2A complexes comprise a catalytic and scaffolding subunit and a regulatory B subunit. The researchers discovered unanticipated docking sites for PP1 on two PP2A complexes that have structurally unrelated B subunits — B55 and B56. They found that, just before the start of chromosome separation, when Cdk1 becomes inactive, PP2A-B55-associated PP1 removes its own inhibitory phosphate group and then activates and releases the PP2A-B55 to which it is bound. Subsequently, PP2A-B55 removes a phosphate group from the PP1-binding site on PP2A-B56. The efficient dephosphorylation of this site is delayed, however, because PP2A-B55 activity is counteracted by an opposing kinase, Plk1. When Plk1 is inactivated in late mitosis, the B56 subunit is efficiently dephosphorylated and PP1 binds, resulting in the activation of PP2A-B56 and its release from PP1. Grallert and co-workers provide evidence that interference with this regulatory cascade causes chromosome-segregation defects, highlighting its importance for cell division.

These findings raise exciting questions.

© 2015 Macmillan Publishers Limited. All rights reserved

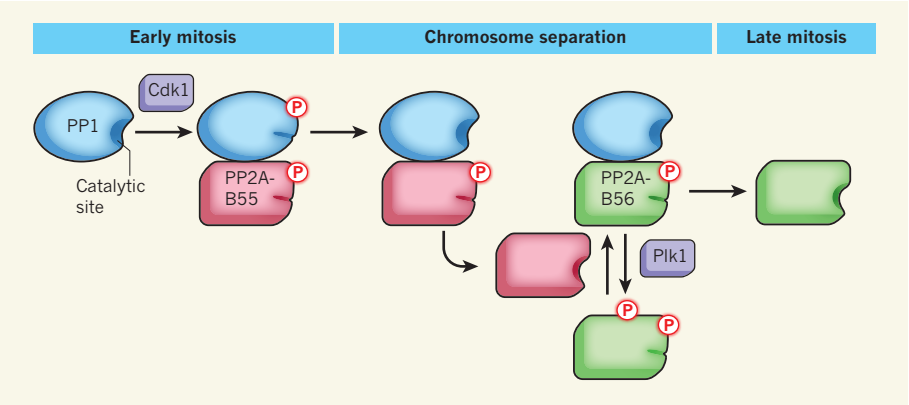


Figure 1 | A mitotic enzyme relay. Grallert *et al.*[2] report that during early mitosis, the kinase enzyme Cdk1 adds a phosphate group (P) to PP1, a phosphatase enzyme, thereby inactivating it. Active and inactive phosphatases are indicated by an open (half circle) or closed catalytic site, respectively. Cdk1 is inactivated just before the beginning of chromosome separation, causing PP1 that is bound by another phosphatase, PP2A-B55, to dephosphorylate and activate both itself and the bound PP2A-B55. Subsequently, PP2A-B55 dephosphorylates an amino-acid residue in the B56 subunit of PP2A-B56 phosphatase. This dephosphorylation is inefficient during chromosome separation, because Plk1 kinase opposes the action of PP2A-B55. At the end of chromosome separation, Plk1 is inactivated, and the resulting efficient dephosphorylation of B56 enables this subunit to recruit PP1, which subsequently activates PP2A-B56. Activation of the PP2A phosphatases results in their dissociation from PP1.

What are the mechanisms by which the relay-controlled pool of PP2A-B55 and PP2A-B56 is inactivated during early mitosis, and exactly how are these complexes activated in late mitosis? Because PP1 is implicated in the activation process, it seems likely that these mitotic PP2A complexes are activated by dephosphorylation of their B subunits[4], but the authors did not define the sites at which these modifications occur. Studies in other model organisms[5] indicate that mitotic PP2A can be restrained by inhibitory proteins that are removed by dephosphorylation at mitotic exit, but it is not known whether this applies to fission yeast.

How can the B55 and B56 subunits form a complex with PP1, given that their PP1-binding sites are buried deep in the hydrophobic core of well-folded protein domains[6]? With the structural data available[6], it is difficult to envisage how this can be achieved without disrupting the folding of the B subunits. The authors speculate that B55 and B56 can adopt alternative conformations that expose their PP1-binding sites. Some proteins are indeed known to undergo substantial conformational changes following ligand binding[7,8], but it is unclear whether this also applies to the PP1–PP2A-B55 and PP1–PP2A-B56 interactions. Furthermore, given the strong associations between PP1 and the PP2A complexes, it is somewhat counterintuitive that PP2A activation coincides with dissociation from PP1. How is this achieved? One possibility is that PP1 release occurs because of a reversal of the conformational change in B55 or B56, burying the PP1-binding sites in the hydrophobic core once again.

The elegance of the reported phosphatase relay is that it functions as a timer for the orderly dephosphorylation of proteins at the end of division. The cascade may be evolutionarily conserved, because Grallert and colleagues demonstrated that PP1 and PP2A-B56 can also interact in human cells. The relay affects only part of the cellular pool of PP1 and PP2A, explaining why other sources of these phosphatases fulfil independent functions throughout cell division[5]. In fact, recent data[9] hint at the existence of another relay system, which controls a cell-division step that occurs before chromosome separation, and which involves the recruitment of a chromosome-associated pool of PP1 by PP2A-B56. In animals, an additional layer of regulation of phosphatase relays may come from 'scaffolding' proteins that bind and coordinate local pools of both PP1 and PP2A[5]. Overall, this research implies that although budding yeast and other organisms, including fission yeast, employ distinct phosphatases to coordinate the mitotic exit, control of this process in the different organisms shares a similar precision. ■

Mathieu Bollen *is in the Laboratory of Biosignaling and Therapeutics, Department of Cellular and Molecular Medicine, KU Leuven, 3000 Leuven, Belgium.*
e-mail: mathieu.bollen@med.kuleuven.be

1. Monod, J. in *Chance and Necessity: Essay on the Natural Philosophy of Modern Biology* 3–22 (Vintage Books, 1972).
2. Grallert, A. *et al. Nature* **517,** 94–98 (2015).
3. Mocciaro, A. & Schiebel, E. *J. Cell Sci.* **123,** 2867–2876 (2010).
4. Schmitz, M. H. A. *et al. Nature Cell Biol.* **12,** 886–893 (2010).
5. Qian, J., Winkler, C. & Bollen, M. *Curr. Opin. Cell Biol.* **25,** 697–703 (2013).
6. Shi, Y. *Cell* **139,** 468–484 (2009).
7. Mapelli, M., Massimiliano, L., Santaguida, S. & Musacchio, A. *Cell* **131,** 730–743 (2007).
8. Whisstock, J. C. & Bottomley, S. P. *Curr. Opin. Struct. Biol.* **16,** 761–768 (2006).
9. Nijenhuis, W., Vallardi, G., Teixeira, A., Kops, G. J. & Saurin, A. T. *Nature Cell Biol.* **16,** 1257–1264 (2014).

This article was published online on 10 December 2014.

EARTH SCIENCE

Ocean circulation and rapid climate change

High-resolution data on ocean circulation during the last glacial cycle suggest that the formation of North Atlantic Deep Water and associated heat transport may be more stable than previously thought. SEE LETTER P.73

ELLEN E. MARTIN

Data from ice cores drilled on Greenland in the 1980s revealed alternating warm (interstadial) and cold (stadial) intervals embedded within the last glacial period[1], which occurred from about 70,000 to 17,000 years ago. Subsequent studies suggested that these millennial-scale climate variations were linked to changes in the formation and export of deep water in the North Atlantic[2], which is associated with ocean transport of heat to high northern latitudes. Three modes of circulation of deep water were identified and correlated to climate regimes[3]. These modes include: formation and flow of North Atlantic Deep Water, the dominant water mass in the Atlantic, during interstadials; a slower, shallower circulation system during stadial events; and a shutdown of North Atlantic Deep Water formation during extreme cooling and ice-rafting events known as Heinrich stadials (Fig. 1). On page 73 of this issue, Böhm *et al.*[4] present high-resolution data sets of ocean palaeocirculation that call into question the existence of three distinct modes and challenge our understanding of the coupling between climate and ocean circulation on millennial timescales.

The concept of multiple modes of ocean circulation during the last glacial period developed from nutrient-based proxy data, such as

© 2015 Macmillan Publishers Limited. All rights reserved

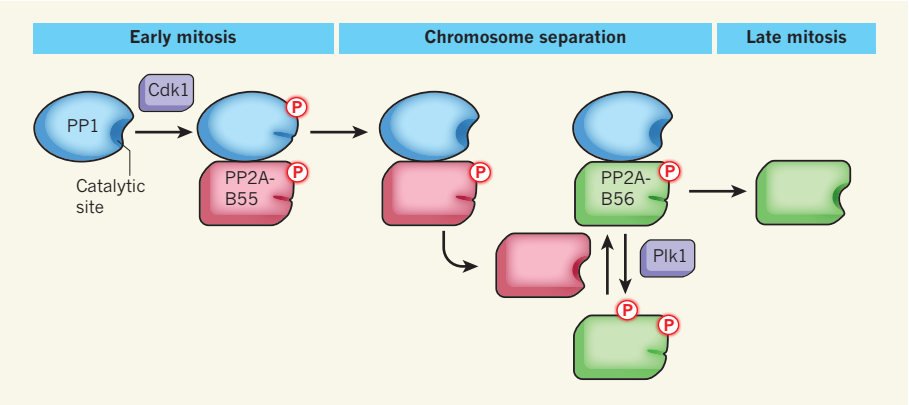


Figure 1 | A mitotic enzyme relay. Grallert *et al.*[2] report that during early mitosis, the kinase enzyme Cdk1 adds a phosphate group (P) to PP1, a phosphatase enzyme, thereby inactivating it. Active and inactive phosphatases are indicated by an open (half circle) or closed catalytic site, respectively. Cdk1 is inactivated just before the beginning of chromosome separation, causing PP1 that is bound by another phosphatase, PP2A-B55, to dephosphorylate and activate both itself and the bound PP2A-B55. Subsequently, PP2A-B55 dephosphorylates an amino-acid residue in the B56 subunit of PP2A-B56 phosphatase. This dephosphorylation is inefficient during chromosome separation, because Plk1 kinase opposes the action of PP2A-B55. At the end of chromosome separation, Plk1 is inactivated, and the resulting efficient dephosphorylation of B56 enables this subunit to recruit PP1, which subsequently activates PP2A-B56. Activation of the PP2A phosphatases results in their dissociation from PP1.

What are the mechanisms by which the relay-controlled pool of PP2A-B55 and PP2A-B56 is inactivated during early mitosis, and exactly how are these complexes activated in late mitosis? Because PP1 is implicated in the activation process, it seems likely that these mitotic PP2A complexes are activated by dephosphorylation of their B subunits[4], but the authors did not define the sites at which these modifications occur. Studies in other model organisms[5] indicate that mitotic PP2A can be restrained by inhibitory proteins that are removed by dephosphorylation at mitotic exit, but it is not known whether this applies to fission yeast.

How can the B55 and B56 subunits form a complex with PP1, given that their PP1-binding sites are buried deep in the hydrophobic core of well-folded protein domains[6]? With the structural data available[6], it is difficult to envisage how this can be achieved without disrupting the folding of the B subunits. The authors speculate that B55 and B56 can adopt alternative conformations that expose their PP1-binding sites. Some proteins are indeed known to undergo substantial conformational changes following ligand binding[7,8], but it is unclear whether this also applies to the PP1–PP2A-B55 and PP1–PP2A-B56 interactions. Furthermore, given the strong associations between PP1 and the PP2A complexes, it is somewhat counterintuitive that PP2A activation coincides with dissociation from PP1. How is this achieved? One possibility is that PP1 release occurs because of a reversal of the conformational change in B55 or B56, burying the PP1-binding sites in the hydrophobic core once again.

The elegance of the reported phosphatase relay is that it functions as a timer for the orderly dephosphorylation of proteins at the end of division. The cascade may be evolutionarily conserved, because Grallert and colleagues demonstrated that PP1 and PP2A-B56 can also interact in human cells. The relay affects only part of the cellular pool of PP1 and PP2A, explaining why other sources of these phosphatases fulfil independent functions throughout cell division[5]. In fact, recent data[9] hint at the existence of another relay system, which controls a cell-division step that occurs before chromosome separation, and which involves the recruitment of a chromosome-associated pool of PP1 by PP2A-B56. In animals, an additional layer of regulation of phosphatase relays may come from 'scaffolding' proteins that bind and coordinate local pools of both PP1 and PP2A[5]. Overall, this research implies that although budding yeast and other organisms, including fission yeast, employ distinct phosphatases to coordinate the mitotic exit, control of this process in the different organisms shares a similar precision. ■

Mathieu Bollen *is in the Laboratory of Biosignaling and Therapeutics, Department of Cellular and Molecular Medicine, KU Leuven, 3000 Leuven, Belgium.*
e-mail: mathieu.bollen@med.kuleuven.be

1. Monod, J. in *Chance and Necessity: Essay on the Natural Philosophy of Modern Biology* 3–22 (Vintage Books, 1972).
2. Grallert, A. *et al. Nature* **517,** 94–98 (2015).
3. Mocciaro, A. & Schiebel, E. *J. Cell Sci.* **123,** 2867–2876 (2010).
4. Schmitz, M. H. A. *et al. Nature Cell Biol.* **12,** 886–893 (2010).
5. Qian, J., Winkler, C. & Bollen, M. *Curr. Opin. Cell Biol.* **25,** 697–703 (2013).
6. Shi, Y. *Cell* **139,** 468–484 (2009).
7. Mapelli, M., Massimiliano, L., Santaguida, S. & Musacchio, A. *Cell* **131,** 730–743 (2007).
8. Whisstock, J. C. & Bottomley, S. P. *Curr. Opin. Struct. Biol.* **16,** 761–768 (2006).
9. Nijenhuis, W., Vallardi, G., Teixeira, A., Kops, G. J. & Saurin, A. T. *Nature Cell Biol.* **16,** 1257–1264 (2014).

This article was published online on 10 December 2014.

EARTH SCIENCE

Ocean circulation and rapid climate change

High-resolution data on ocean circulation during the last glacial cycle suggest that the formation of North Atlantic Deep Water and associated heat transport may be more stable than previously thought. SEE LETTER P.73

ELLEN E. MARTIN

Data from ice cores drilled on Greenland in the 1980s revealed alternating warm (interstadial) and cold (stadial) intervals embedded within the last glacial period[1], which occurred from about 70,000 to 17,000 years ago. Subsequent studies suggested that these millennial-scale climate variations were linked to changes in the formation and export of deep water in the North Atlantic[2], which is associated with ocean transport of heat to high northern latitudes. Three modes of circulation of deep water were identified and correlated to climate regimes[3]. These modes include: formation and flow of North Atlantic Deep Water, the dominant water mass in the Atlantic, during interstadials; a slower, shallower circulation system during stadial events; and a shutdown of North Atlantic Deep Water formation during extreme cooling and ice-rafting events known as Heinrich stadials (Fig. 1). On page 73 of this issue, Böhm *et al.*[4] present high-resolution data sets of ocean palaeocirculation that call into question the existence of three distinct modes and challenge our understanding of the coupling between climate and ocean circulation on millennial timescales.

The concept of multiple modes of ocean circulation during the last glacial period developed from nutrient-based proxy data, such as

© 2015 Macmillan Publishers Limited. All rights reserved



GEORGE F. MOBLEY/NATL GEOGR./GETTY

Figure 1 | Icebergs raft past Augpilagtoq, Greenland. Böhm and colleagues' study[4] suggests that massive ice rafting associated with climate events known as Heinrich stadials reduced ocean-density contrasts in the North Atlantic enough to shut down deep-water formation only during the few events that coincided with the most extreme glacial maxima. This unexpected result may have implications for the climate-system response to glacial meltwater associated with high-latitude anthropogenic warming.

carbon isotopes in ancient marine sediments, which indicate that deep waters in the North Atlantic were young, and therefore locally sourced, during interstadial events. This young water was confined to shallower depths during cooler, stadial events, and was replaced by older water, presumably sourced from the Southern Ocean, during Heinrich stadials. Although nutrient proxies provide information about the age of a water mass, they can be altered by biological processes and cannot be used to identify water-mass sources or the strength of circulation. By contrast, the ratio of isotopes of neodymium ($^{143}Nd/^{144}Nd$) — reported as ε_{Nd}, the deviation of this ratio from a mean chemical composition, known as the Chondritic Uniform Reservoir, in parts per 10,000 — are quasi-conservative tracers of water mass that clearly distinguish between North Atlantic Deep Water (ε_{Nd} about −13.5; ref. 5) and water sourced from the Southern Ocean (ε_{Nd} about −9; ref. 6). In addition, the ratio of protactinium to thorium isotopes ($^{213}Pa/^{230}Th$) monitors the strength of circulation, such that higher ratios indicate slower circulation.

Both these proxies have been applied to studies in the North Atlantic for the last glacial maximum (the peak of the last glacial period, around 20,000 years ago) and into the Holocene epoch (11,700 years ago to today), illustrating the expected patterns for warm, cold and shutdown (or 'off') circulation modes[7,8]. The high-quality, high-resolution data sets produced by Böhm *et al.*, from a site on Bermuda Rise in the northeastern Sargasso Sea, extend these records back through the last glacial and interglacial periods into the penultimate glacial maximum (140,000 years ago). The data allow the authors to study ocean circulation and its relationship to climate change throughout the last glacial cycle.

Böhm and colleagues' data reveal two surprising findings. First, the cold-mode circulation — southern-sourced deep water accompanied by relatively rapid, northern-sourced flow in a shallower ocean layer that delivers less heat to high northern latitudes — existed only during glacial maxima that occurred at the end of each glacial period (see Fig. 1b of ref. 4). Second, the off mode of circulation, expected during all Heinrich stadials and defined by the increased presence of southern-sourced deep waters and sluggish circulation rates, occurred only during Heinrich stadials that, again, coincided with maximum ice extent (see Fig. 1c of ref. 4). Contrary to expectation, most of the cool stadials and Heinrich stadials coincided with intermediate values of ε_{Nd} and $^{213}Pa/^{230}Th$, suggesting that they occurred during gradual transitions between warm interstadial and off modes, rather than as a distinct cold mode of circulation and oceanic heat transport as previously thought.

The significance of this transitional configuration is the implication that the North Atlantic continued to produce deep waters despite evidence that the region of modern deep-water formation was covered by ice, and, more surprisingly, when massive iceberg discharge is expected to have freshened surface waters in the deep-water source regions. Such freshening is thought to reduce ocean-density contrasts that lead to transport of North Atlantic surface waters to depth. Böhm *et al.* point out that the continued strength of North Atlantic Deep Water formation and its flow throughout climate variations indicate that this mode of circulation may be more stable in response to freshwater inputs than models imply[9]. On the basis of this stability, the authors suggest that North Atlantic Deep Water formation may also be less susceptible to shutdown in response to freshening by glacial meltwaters during modern global warming, a process that, if carried to the extreme, could eliminate oceanic northward heat transport and produce icy scenarios similar to that in the Hollywood film *The Day After Tomorrow*.

One word of caution, however, is that the climate-system response to freshening in a cold climate may be very different from that in a warm climate. The view of continuous North Atlantic Deep Water formation and flow during the last glacial period presented by Böhm *et al.* requires a re-evaluation of the relationship between ocean circulation and climate over millennial timescales. This may ultimately help us to understand the fundamental causes of short-term climate variability.

Finally, another intriguing observation that emerges from this study is that, during past interglacials and interstadials, the ε_{Nd} value of North Atlantic Deep Water was often much lower than that today (−15 to −18, compared with −13.5 today). Modern North Atlantic Deep Water is composed of a mixture of North Atlantic water masses, with the relative proportions of each responding to local climate impacts. Most of these waters have ε_{Nd} values higher than −13.5, but water from the Labrador Sea region has lower values and thus explains why North Atlantic Deep Water is the major water mass with the lowest ε_{Nd} value[5]; a low ε_{Nd} indicates weathering contributions of old continental material to the source regions.

The past composition of North Atlantic Deep Water is crucial for reconstructing changes in the relative proportions of northern- and southern-sourced waters through time. Previous studies[10,11] have argued for a stable North Atlantic Deep Water Nd isotopic composition across intervals of glacial climate variability. The ε_{Nd} values identified by Böhm and co-workers for past interglacials and interstadials suggest a variable, rather than a stable, North Atlantic Deep Water Nd isotopic composition, prompting a revision of the relative proportions of northern- and southern-sourced waters through time and their impact on heat transport. ■

Ellen E. Martin *is in the Department of Geological Sciences, University of Florida, Gainesville, Florida 32611, USA.*
e-mail: eemartin@ufl.edu

1. Dansgaard, W. *et al. Nature* **364,** 218–220 (1993).
2. Bond, G. *et al. Nature* **365,** 143–147 (1993).
3. Ramstorf, S. *Nature* **419,** 207–214 (2002).
4. Böhm, E. *et al. Nature* **517,** 73–76 (2015).
5. Lacan, F. & Jeandel, C. *Geochem. Geophys. Geosys.* **6,** Q12008 (2005).
6. Jeandel, C. *Earth Planet. Sci. Lett.* **117,** 581–591 (1993).
7. McManus, J., Oppo, D. & Cullen, J. *Science* **283,** 971–975 (1999).
8. Roberts, N. L., Piotrowski, A. M., McManus, J. F. & Keigwin, L. D. *Science* **327,** 75–78 (2010).
9. Manabe, S. & Stouffer, R. J. *J. Clim.* **1,** 841–866 (1988).
10. van de Flierdt, T., Robinson, L. F., Adkins, J. F., Hemming, S. R. & Goldstein, S. L. *Paleoceanography* **21,** PA4102 (2006).
11. Foster, G., Vance, D. & Prytulak, J. *Geology* **35,** 37–40 (2007).

This article was published online on 15 December 2014.

© 2015 Macmillan Publishers Limited. All rights reserved

ARTICLE

doi:10.1038/nature14010

RNA regulons in *Hox* 5′ UTRs confer ribosome specificity to gene regulation

Shifeng Xue[1,2,3], Siqi Tian[4], Kotaro Fujii[1,2], Wipapat Kladwang[4], Rhiju Das[4,5] & Maria Barna[1,2]

Emerging evidence suggests that the ribosome has a regulatory function in directing how the genome is translated in time and space. However, how this regulation is encoded in the messenger RNA sequence remains largely unknown. Here we uncover unique RNA regulons embedded in homeobox (*Hox*) 5′ untranslated regions (UTRs) that confer ribosome–mediated control of gene expression. These structured RNA elements, resembling viral internal ribosome entry sites (IRESs), are found in subsets of *Hox* mRNAs. They facilitate ribosome recruitment and require the ribosomal protein RPL38 for their activity. Despite numerous layers of *Hox* gene regulation, these IRES elements are essential for converting *Hox* transcripts into proteins to pattern the mammalian body plan. This specialized mode of IRES–dependent translation is enabled by an additional regulatory element that we term the translation inhibitory element (TIE), which blocks cap–dependent translation of transcripts. Together, these data uncover a new paradigm for ribosome–mediated control of gene expression and organismal development.

An important layer of post-transcriptional control of gene expression may be conferred through regulatory functions of the ribosome[1–6]. For example, RPL38, one of 80 ribosomal proteins of the eukaryotic ribosome, helps establish the mammalian body plan by selectively facilitating the translation of subsets of *Hox* mRNAs[1], genes critically required for formation of the body plan[7]. However, how ribosome-mediated regulation of gene expression is encoded within mRNA sequence remains an unanswered question.

All eukaryotic cellular mRNAs are capped, and cap-dependent translation is considered a highly efficient and predominant means for translation of most transcripts in the mammalian genome[8,9]. In many viral mRNAs that are not capped, IRESs provide an alternative mechanism for ribosome recruitment to promote translation initiation[8,10]. Interestingly, IRES elements have also been discovered in a handful of cellular mRNAs, including *c-myc*, *XIAP*, *Apaf-1* and *p53* (refs 11–16). As these cellular mRNAs are capped, their IRES elements act as a 'fail-safe' mechanism to promote translation under stress conditions, such as apoptosis or hypoxia, when cap-dependent translation is downregulated[17,18]. Cellular IRES elements have little sequence or structural homology[19], and their relevance for translational control and gene expression in normal cell physiology, tissue patterning, or organismal development is unclear.

We report below the unexpected identification of IRES elements within *Hox* mRNAs, particularly those regulated by RPL38, which are critically required for accurate gene expression during normal development. We also identify the TIE, an additional regulatory element in these mRNAs, which modulates the dependence of individual transcripts on canonical cap-dependent translation. This mechanism enables the IRES to become the predominant mode of translation initiation and confers greater gene regulatory potential by the ribosome.

RPL38–regulated *Hox* mRNAs possess IRES elements

To address the nature of specific *cis*-regulatory elements within transcripts that confer greater regulation by the ribosome, we studied RPL38-mediated control of *Hox* mRNA translation. We showed previously that although RPL38 haploinsufficiency within the developing mouse embryo does not affect general cap-dependent translation, the translation of a subset of the eleven *HoxA* mRNAs (*Hoxa4*, *Hoxa5*, *Hoxa9*, *Hoxa11*) is perturbed (Fig. 1a)[1]. We employed a bicistronic reporter assay in the murine mesenchymal stem cell line C3H10T1/2, which expresses *Hox* transcripts[20], to delineate whether *Hox* 5′ UTRs direct cap-independent translation (Fig. 1a, b). In this reporter system, the first cistron (*Renilla* luciferase, RLuc) is translated by a cap-dependent mechanism, and the second cistron (Firefly luciferase, FLuc) is translated only if the preceding 5′ UTR element can recruit ribosomes by a cap-independent mechanism (Fig. 1a); the latter is considered to reflect IRES-dependent translation initiation[21].

These experiments revealed that many *Hox* 5′ UTRs possess IRES activity that is as strong as, or even stronger than, the hepatitis C virus (HCV) IRES element, a bona fide viral IRES element (Fig. 1b). To ensure that *Hox* 5′ UTRs do not contain putative promoters or splice sites that may produce a monocistronic capped FLuc transcript, we performed additional controls. As expected for a single transcript containing both Rluc and Fluc: (i) the RNA levels of the two reporters are expressed in the same ratio among all bicistronic constructs; (ii) a short hairpin RNA (shRNA) against RLuc downregulated both Rluc and Fluc expression; (iii) these transcripts do not contain cryptic splice sites; and (iv) no ribosome read-through of the first reporter is evident (Extended Data Fig. 1). There is good correlation between RPL38 regulation and the presence of IRES elements; all RPL38-regulated mRNAs in the *HoxA* locus possess IRES elements. These include *Hoxa4*, which we show by 5′ rapid amplificiation of cloned ends (RACE) possesses an IRES-containing 5′ UTR of 1.1 kb, which is longer than previously annotated.

To test whether cap-independent translation from the *Hox* 5′ UTRs is controlled by RPL38 in C3H10T1/2 cells, a copy of *Rpl38* was disrupted by transcription activator-like effector nucleases (TALENs), yielding a 40% reduction in RPL38 protein expression (Fig. 1c, Extended Data Fig. 2a). In these cells, although there is no change in cap-dependent translation, there is a specific decrease in IRES-dependent translation of *Hox* target mRNAs that are regulated by RPL38 *in vivo* (Fig. 1c,

[1]Department of Developmental Biology, Stanford University, Stanford, California 94305, USA. [2]Department of Genetics, Stanford University, Stanford, California 94305, USA. [3]Tetrad Graduate Program, University of California, San Francisco, San Francisco, California 94158, USA. [4]Department of Biochemistry, Stanford University, Stanford, California 94305, USA. [5]Department of Physics, Stanford University, Stanford, California 94305, USA.

©2015 Macmillan Publishers Limited. All rights reserved

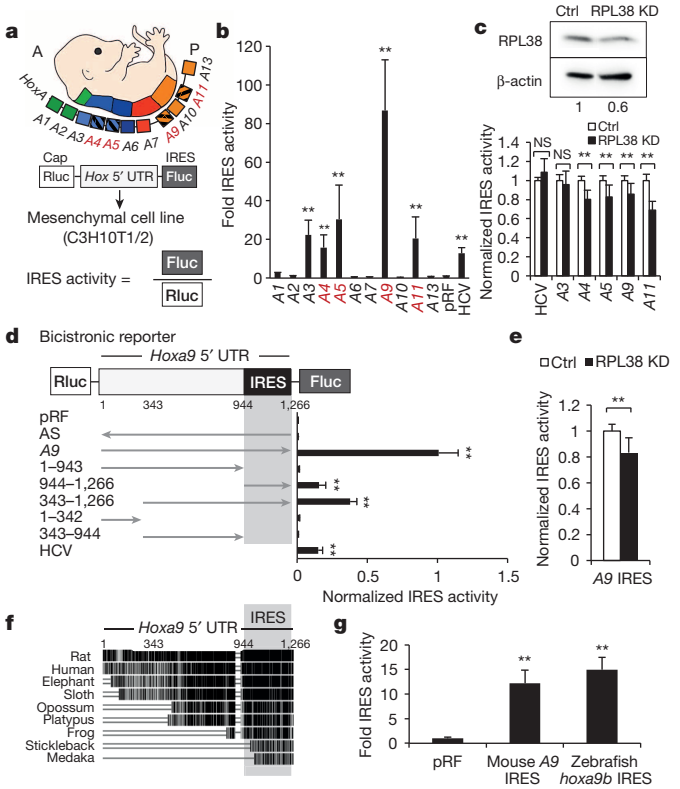


Figure 1 | Select *HoxA* 5′ UTRs contain IRES elements regulated by RPL38. **a**, *HoxA* genes are located in tandem along a chromosomal locus, and their location directs their anterior expression boundaries along the embryo. Striped boxes, *Hox* genes translationally regulated by RPL38. IRES activity is the ratio between Fluc and Rluc. **b**, IRES activity of *HoxA* 5′ UTRs. IRES activity of UTRs was normalized to that of empty vector (pRF) and RPL38-regulated *Hox* genes are denoted in red. $^{**}P < 0.01$ (χ^2 test against pRF), $n = 5$. **c**, RPL38 regulates translation of specific *HoxA* IRES elements. Bicistronic reporters were transfected into control cells (Ctrl) or cells where one copy of *Rpl38* was deleted (RPL38 KD). Top, western blot of RPL38 and β-actin with quantification of RPL38 levels below the blot. Bottom, IRES activity of specific *Hox* 5′ UTRs in RPL38 knockdown cells normalized to that of control cells. $^{**}P < 0.01$ (*t*-test), $n = 3$. **d**, Deletion analysis of the *Hoxa9* 5′ UTR. IRES activity was normalized to that of the full-length *Hoxa9* 5′ UTR (*A9*). AS, antisense. $^{**}P < 0.01$ (χ^2 test against pRF), $n = 3$. **e**, IRES activity of the *Hoxa9* IRES (nt 944–1,266) in RPL38 knockdown cells. $^{**}P < 0.01$ (*t*-test), $n = 3$. **f**, Alignment of the *Hoxa9* 5′ UTR in vertebrates. **g**, The 5′ UTR of one of two zebrafish *Hoxa9* paralogues (*hoxa9b*) has similar IRES activity as the mouse *Hoxa9* IRES. IRES activity was normalized to pRF. $^{**}P < 0.01$ (*t*-test as compared to pRF), $n = 3$. All experiments were performed in triplicates. Data represent mean ± s.d.

Extended Data Fig. 2b). Consistent with the fact that RPL38 control of IRES-dependent translation is transcript-specific, *Hoxa3* IRES-dependent translation, which is not regulated by RPL38 within the embryo[1], and the HCV IRES, are similarly unaffected by RPL38 knockdown (Fig. 1c). These results reveal the unexpected presence of IRES elements within *Hox* 5′ UTRs and a critical function of RPL38 in regulating their IRES-dependent translation.

The *Hoxa9* minimal IRES is evolutionarily conserved

To further understand IRES-dependent regulation of *Hox* mRNAs, we made a series of deletions within the 1.2-kb *Hoxa9* 5′ UTR. We localized the minimum fragment for RPL38-dependent IRES activity to nucleotides (nt) 944–1,266 (which we term the *Hoxa9* IRES element) (Fig. 1d). Although this fragment does not fully recapitulate the IRES activity observed with full-length *Hoxa9* 5′ UTR, it has strong IRES activity on its own and its removal abolishes all IRES activity (Fig. 1d, e). This region of the *Hoxa9* 5′ UTR shows remarkable evolutionary conservation in all vertebrates (from fish to mammals) that is greater than sequence conservation in the remaining 5′ UTR or the 3′ UTR sequence (Fig. 1f, Extended Data Fig. 3). IRES function is also evolutionarily conserved, as the zebrafish *hoxa9b* 5′ UTR shows strong IRES activity in murine C3H10T1/2 cells (Fig. 1g). These findings suggest that the *Hoxa9* IRES element may have arisen early during vertebrate evolution for post-transcriptional regulation of *Hox* expression.

Hoxa9 IRES is an RNA structure that recruits ribosomes

Many viral IRESs possess structures such as conserved helices, asymmetric bulges, and pseudoknots that interact with initiation factors or the ribosome to promote translation initiation[22–24]. We therefore examined whether the *Hoxa9* IRES element has structural properties *in vitro* that are functionally important.

Within the full-length *Hoxa9* 5′ UTR, protections of sub-regions of the 944–1,266 domain from selective 2′-hydroxyl acylation analysed by primer extension (SHAPE)[25] were consistent with the minimal IRES domain forming a specific RNA structure *in vitro* (Extended Data Fig. 4). Automated modelling indicated that this domain formed a four-way junction with two long hairpin arms (P3 and P4; Fig. 2a, Extended Data Fig. 6) and a 'right-angle' asymmetric bulge (between P3b and P3c), but with little interaction with other domains of the 5′ UTR (Extended Data Fig. 4). Analogous chemical mapping and functional studies on the 5′ UTR from a different *Hox* mRNA, *Hoxa5*, also revealed a structured subdomain (nt 77–132) necessary for its full IRES activity (Extended Data Fig. 5a, d, e). Deletion of the subdomain substantially reduces IRES activity (Extended Data Fig. 5b). Structural conservation between different cellular IRES elements has so far been poorly defined[19]. Interestingly, the 'right angle' asymmetric bulges observed in *Hoxa5* and *Hoxa9* (Extended Data Fig. 5c) bear qualitative similarity to asymmetric bulges in, for example, the HCV IRES[26], suggesting at least certain common structural features are present amongst cellular *Hox* IRESs and viral IRESs.

To gain further insight into structural and functional properties of a *Hox* IRES, we applied multidimensional chemical mapping to the *Hoxa9* minimal IRES subdomain (Fig. 2a, Extended Data Fig. 6). Comprehensive mutate-and-map analysis[27] gave strong independent evidence for the same structural topology seen in the context of the full-length 5′ UTR, revealing exposure of RNA segments upon mutation of their predicted pairing partners (Extended Data Fig. 6a–c). Importantly, compensatory mutation analysis[28] unambiguously confirmed specific base pairs in the P3 and P4 segments (green circles, Fig. 2a, and Extended Data Fig. 7). After this *in vitro Hoxa9* structural characterization, we tested the functional significance of these hairpins for IRES-dependent translation through bicistronic assays. Deletion of P3, P4, or both hairpins in the context of the full-length *Hoxa9* 5′ UTR resulted in a significant reduction in IRES activity. Most strikingly, the mutation of nucleotides in the base of P3a reduced IRES activity, whereas compensatory mutations gave quantitative rescue of IRES activity (Fig. 2b). These results demonstrate the importance of the P3 and P4 hairpins in IRES function and connect the detailed *in vitro Hoxa9* IRES structural model to functional activity. Many viral IRES elements contain pseudoknots that may position the ribosome at the initiation codon[29]. A potential pseudoknot was suggested by mutate-and-map analysis (Fig. 2a), but this awaits further analysis. Together, these data confirm a structure defined at base-pair resolution for a *Hox* IRES element and indicate that a specific RNA structure is important for cellular *Hox* IRES activity.

To date, only a small class of viral IRES elements have been shown to interact with both the large and small ribosome subunits to form a translationally competent 80S ribosome[30,31]. However, a biotinylated full-length *Hoxa9* 5′ UTR, as well as the minimal IRES element contained within nt 944–1,266, are able to pull down ribosomal proteins from both the large and small subunits, including RPL38 (Fig. 2c, d). The full-length 5′ UTR also pulls down both 28S and 18S rRNAs (Fig. 2e), suggesting that the 80S ribosome is able to form on the

©2015 Macmillan Publishers Limited. All rights reserved

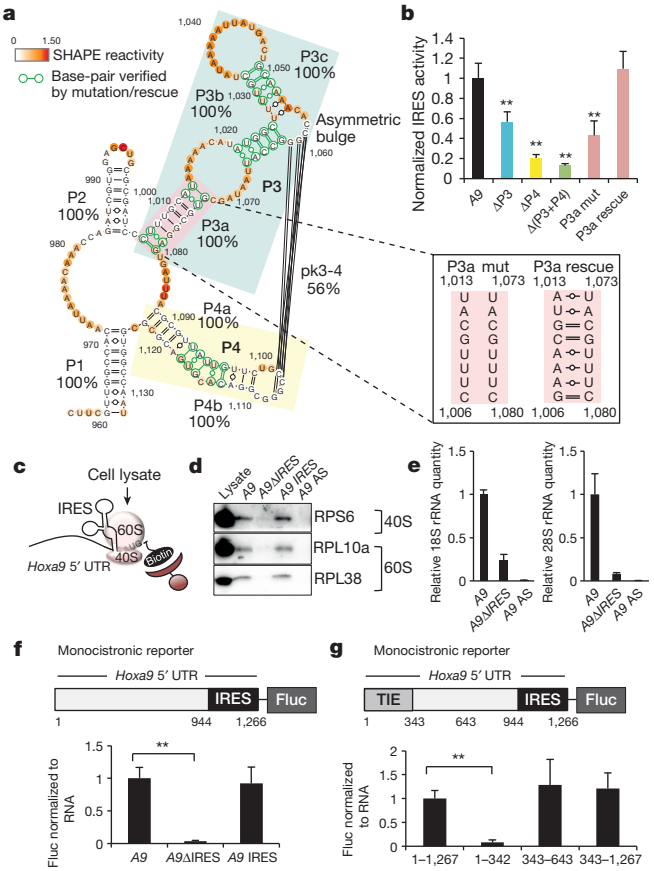


Figure 2 | The *Hoxa9* IRES is an RNA structure that facilitates recruitment of the ribosome and is required for normal translation. **a**, Secondary structure of *Hoxa9* 5′ UTR (nt 957–1,132) by SHAPE and mutate-and-map analysis. Nucleotides are coloured with SHAPE reactivities. Percentages give bootstrap support values for each helix, including a tentative pseudoknot (pk). Base-pairs verified by mutation and rescue are circled green. Inset, mutations made in helix P3a for functional testing in **b**. **b**, Deletions as well as mutation-and-rescue of specific hairpins identified in *Hoxa9* IRES structure shown in **a** affects IRES activity in bicistronic reporter assays. IRES activity was normalized to full-length *Hoxa9* 5′ UTR (*A9*, set to 1). $^{**}P < 0.01$ (*t*-test as compared to *A9*). $n = 3$ and experiments performed in triplicates. **c**, Schematic of RNA pull-down experiments. **d**, **e**, Representative western blot for RPs (**d**) and qPCR for rRNA (**e**) from eluted material of two independent RNA pull-down experiments. The 18S and 28S rRNA amounts of all *Hoxa9* deletion mutants were normalized to amount of full-length *Hoxa9* 5′ UTR (set to 1) eluted from beads, $n = 2$. **f**, Deletions within the *Hoxa9* 5′ UTR in a monocistronic reporter assay. Fluc activity was normalized to amount of luciferase mRNA determined by quantitative PCR (qPCR). All values are normalized to *Hoxa9* full-length 5′ UTR (*A9*), set to 1; $n = 4$. **g**, A TIE that inhibits cap-dependent translation was identified in the *Hoxa9* 5′ UTR (nt 1–342); $n = 3$ and experiments were performed in duplicates. Data represent mean ± s.d.

uncapped *Hoxa9* 5′ UTR. Importantly, the full-length *Hoxa9* 5′ UTR lacking the nt 944–1,266 IRES element (*A9ΔIRES*) or an antisense *Hoxa9* 5′ UTR (*A9* AS) is no longer able to efficiently recruit ribosomal proteins or ribosomal RNA (Fig. 2d, e), consistent with the fact that these fragments do not possess IRES activity (Fig. 1d). These data support the idea that a structured element from a *Hox* IRES facilitates 80S ribosome recruitment to the mRNA, either directly or through intermediary RNA-binding proteins.

TIE inhibits cap-dependent translation

Because all eukaryotic mRNAs are capped and translated by a cap-dependent mechanism[8], the function of an IRES-element in normal translational control remains unclear. Surprisingly, removing the IRES element from a *Hoxa9* 5′ UTR monocistronic reporter construct dramatically decreases translational efficiency by 70-fold, despite the fact that the mRNA remains capped (Fig. 2f). We therefore hypothesized that the *Hoxa9* 5′ UTR may contain additional element(s) that intrinsically inhibit cap-dependent translation. The *Hoxa9* 5′ UTR contains 14 putative upstream open reading frames (uORFs), which are generally thought to inhibit the translation of the main open reading frame[32]. However, mutating all 14 ATGs to TTGs in the *Hoxa9* 5′ UTR (*A9ΔIRESΔuORF*) (Extended Data Fig. 8a) does not affect cap-dependent translation of *Hoxa9*. We therefore placed various regions of the *Hoxa9* 5′ UTR upstream of a monocistronic reporter to assay for effects on cap-dependent translation. Strikingly, nt 1–342 of the *Hoxa9* 5′ UTR strongly inhibit cap-dependent translation (Fig. 2g) despite this region not being particularly GC-rich (55%) and therefore unlikely to impede ribosome scanning. Other similarly sized pieces of the 5′ UTR (nt 343–643), or the very long remaining portion of the 5′ UTR (nt 343–1,266), do not inhibit cap-dependent translation and are probably translated by a combination of cap and IRES-mediated translation. To our knowledge, the 1–342 fragment of the *Hoxa9* 5′ UTR is a unique example of a 5′ UTR regulon that is sufficient to strongly inhibit cap-dependent translation under physiological conditions. We termed this 5′ UTR mRNA element the translation inhibitory element (TIE). SHAPE analysis of the full-length *Hoxa9* 5′ UTR lacks evidence for structural interactions between the TIE and the minimal IRES (Extended Data Fig. 4a), suggesting they function as independent modules. These findings reveal that the TIE enables a more specialized mode of translation initiation directed by the IRES.

5′ UTR topology allows for specialized translation

We next asked whether the unique 5′ UTR topology of both a TIE close to the 5′ end of the mRNA and an IRES element is a more generalizable mechanism of translational regulation. Our findings reveal that all the minimal IRES domains of *HoxA* 5′ UTRs lie within the 100–300 nt closest to the AUG, with the exception of *Hoxa5* (Fig. 3). Deletions of these minimal IRES domains in monocistronic reporter constructs reveal that they are critically required for normal translation (Fig. 4a–c). In addition, within these *HoxA* 5′ UTRs, a TIE is also present near the mRNA cap (Fig. 4a–c). Moreover, although the *Hoxa3*, *Hoxa4*, *Hoxa9* and *Hoxa11* TIEs do not share obvious sequence similarity, they all strikingly block translation from the β-globin (*Hbb*) 5′ UTR (Fig. 4d), which initiates translation exclusively by a cap-dependent mechanism[33]. *Hoxa5* is the only 5′ UTR that does not appear to possess a TIE and a putative uORF also does not decrease cap-dependent translation (Extended Data Fig. 8b). However, *Hoxa5* has the shortest 5′ UTR (237 nt) and almost the entire UTR is required for IRES activity, leaving little space for an additional TIE (Fig. 3c). Interestingly, the *Hoxa5* transcript can be produced as a bicistronic mRNA with the neighbouring *Hoxa6* gene[34] and therefore may not need a TIE to inhibit cap-dependent translation in this context. These findings reveal a unique topology to *Hox* 5′ UTRs that suppresses a more generic mode of cap-dependent translational control and facilitates specialized, ribosome-mediated control of protein expression.

Hoxa9 IRES is essential for translation *in vivo*

To determine whether IRES-dependent translation is critically required for the conversion of the *Hoxa9* transcript into protein *in vivo*, we generated the first targeted mouse knockout of a cellular IRES by removing nt 944–1,193 of the *Hoxa9* 5′ UTR, leaving the Kozak sequence and the rest of the 5′ UTR intact (Fig. 5a, Extended Data Fig. 8c, d). A caveat to the previously generated HOXA9 targeted knockout is the retention of a neomycin (Neo) cassette[35,36], which can have indirect effects on the expression of neighbouring *Hox* genes[37]. Indeed, our current genetic studies reveal that the presence of the Neo cassette within the *Hoxa9* targeting locus is sufficient to produce phenotypes previously attributed to *Hoxa9* loss-of-function (Extended Data Fig. 9).

©2015 Macmillan Publishers Limited. All rights reserved

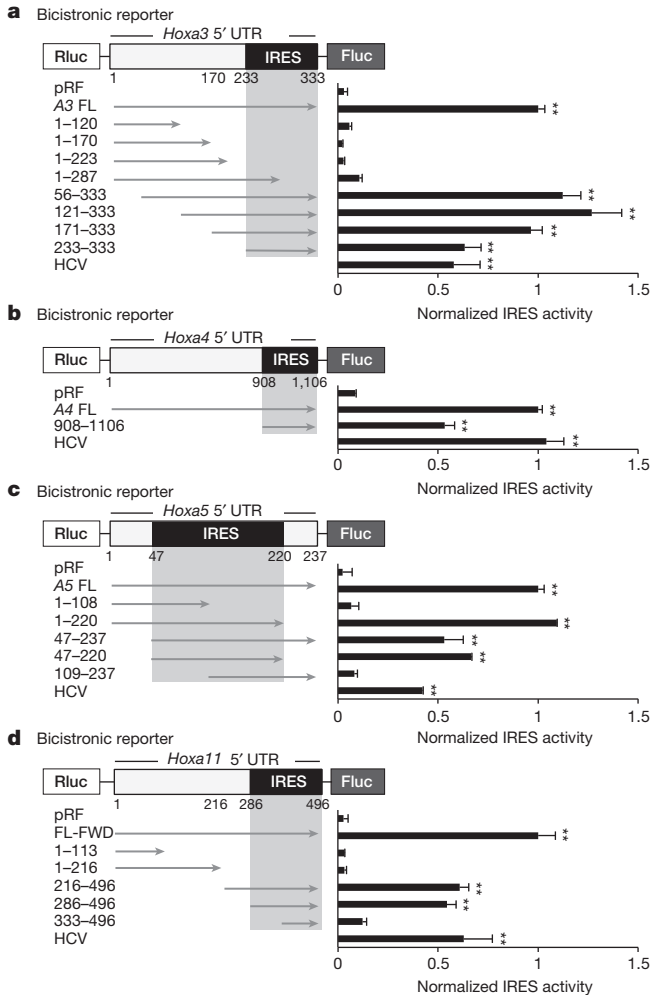


Figure 3 | Identification of minimal IRES domains in all IRES-containing *HoxA* 5′ UTRs. **a**–**d**, Deletion analysis of *HoxA* 5′ UTRs performed in bicistronic constructs maps the IRES element in *Hoxa3* (**a**), *Hoxa4* (**b**), *Hoxa5* (**c**) and *Hoxa11* (**d**). IRES activity was normalized to full-length 5′ UTRs (FL). $^{**}P < 0.01$ (χ^2 test against pRF). $n = 3$ and experiments were performed in triplicate. Data represent mean ± s.d.

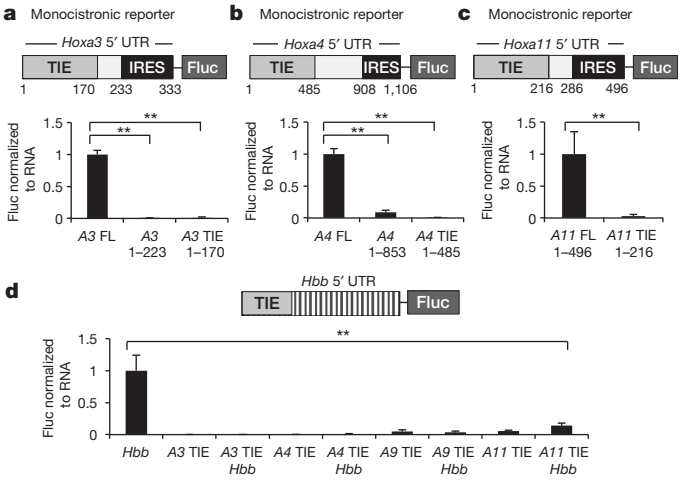


Figure 4 | Identification of a common TIE that blocks cap-dependent translation of *Hox* IRES-mRNAs. **a**–**c**, Deletion of the minimal IRES elements within monocistronic reporters of *HoxA* 5′ UTR and identification of TIEs close to the mRNA cap in *Hoxa3* (**a**), *Hoxa4* (**b**) and *Hoxa5* (**c**). All values are normalized to the full-length constructs (FL); $n = 3$. **d**, *HoxA* TIEs were placed upstream of the β-globin 5′ UTR (*Hbb*) in a monocistronic reporter to assay inhibition of cap-dependent translation, $n = 3$. All experiments were performed in duplicate. Data represent mean ± s.d. $^{**}P < 0.01$ (*t*-test).

Therefore, in our $Hoxa9^{\Delta IRES/\Delta IRES}$ mouse, we were careful to remove the Neo cassette from the targeted locus by Cre-mediated excision.

$Hoxa9^{\Delta IRES/\Delta IRES}$ embryos do not show any major change in *Hoxa9* transcript boundaries or expression levels (Fig. 5b, c). Strikingly, however, these mice show a fully penetrant homeotic transformation of the thirteenth thoracic vertebra (T13) to the first lumbar vertebra (L1), in which a full set of ribs normally present on T13 is missing (Fig. 5d). Although we cannot at present ascertain whether the *Hoxa9* IRES deletion completely phenocopies a *Hoxa9* knockout mouse, this dramatic homeotic transformation is precisely at the anterior boundary of *Hoxa9* expression at the thoracic to lumbar transition[35]. This transformation is also evident in ~50% of $Hoxa9^{\Delta IRES/+}$ mice, although small rudimentary ribs can still form on T13. Consistently, there is a striking decrease in HOXA9 protein levels in the neural tube and somites of $Hoxa9^{\Delta IRES/\Delta IRES}$ embryos from the thoracic to sacral level (Fig. 6a) revealing a block in HOXA9 protein production. Furthermore, in $Hoxa9^{\Delta IRES/\Delta IRES}$ embryos there is a dramatic decrease in ribosome association of the *Hoxa9* transcript. The majority of the *Hoxa9* transcript in $Hoxa9^{\Delta IRES/\Delta IRES}$ embryos, but not control transcripts such as β-actin, accumulates in pre-polysomal fractions, reflecting an accumulation of mRNA not bound by translationally active ribosomal subunits (Fig. 6b, Extended Data Fig. 10). These findings reveal that the *Hoxa9* IRES element is crucial in recruiting the ribosome to this transcript to pattern the mammalian body plan *in vivo*.

Discussion

Our studies reveal how expression information encoded within the mRNA template is sufficient to confer greater gene regulatory potential by the ribosome. In particular, our findings suggest that IRES elements are key regulatory elements within the mammalian genome that facilitate important, ribosome-mediated control of gene expression in development (Fig. 6c). Cellular IRES elements have been controversial because of their weak IRES activity as compared to viral

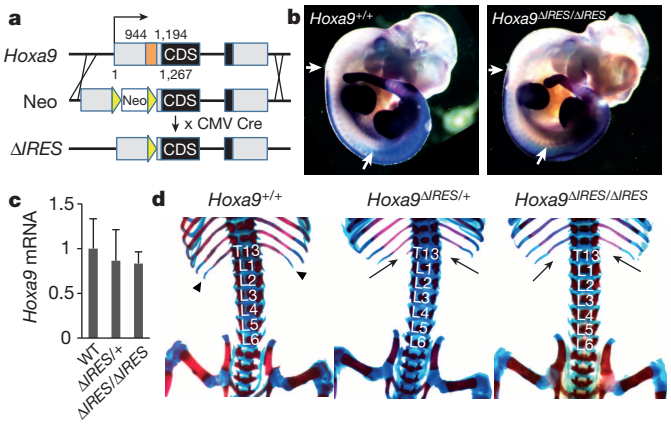


Figure 5 | The *Hoxa9* IRES is required for axial skeleton patterning but not for *Hoxa9* mRNA expression. **a**, Scheme of *Hoxa9* IRES targeted deletion in the mouse. *LoxP* sites are depicted by yellow triangles. The region deleted is highlighted in orange. **b**, Representative *in situ* hybridization of *Hoxa9* mRNA expression at E11.5, $n = 3$ embryos of each genotype. Arrows indicate the anterior boundaries of expression in the neural tube and somites. **c**, qPCR shows little difference in *Hoxa9* transcript levels in neural tube and somites between $Hoxa9^{+/+}$, $Hoxa9^{\Delta IRES/+}$ and $Hoxa9^{\Delta IRES/\Delta IRES}$ embryos. $Hoxa9^{\Delta IRES/+}$, $P = 0.06$; $Hoxa9^{\Delta IRES/\Delta IRES}$, $P = 0.03$, *t*-test as compared to $Hoxa9^{+/+}$. $n = 5$ embryos of each genotype. **d**, Representative skeletons of $Hoxa9^{+/+}$, $Hoxa9^{\Delta IRES/+}$ and $Hoxa9^{\Delta IRES/\Delta IRES}$ mice. Arrows point to the missing rib(s) on T13, normally present in WT mice (arrowheads), revealing a posterior homeotic transformation to L1. $n = 5$ mice of each genotype.

©2015 Macmillan Publishers Limited. All rights reserved

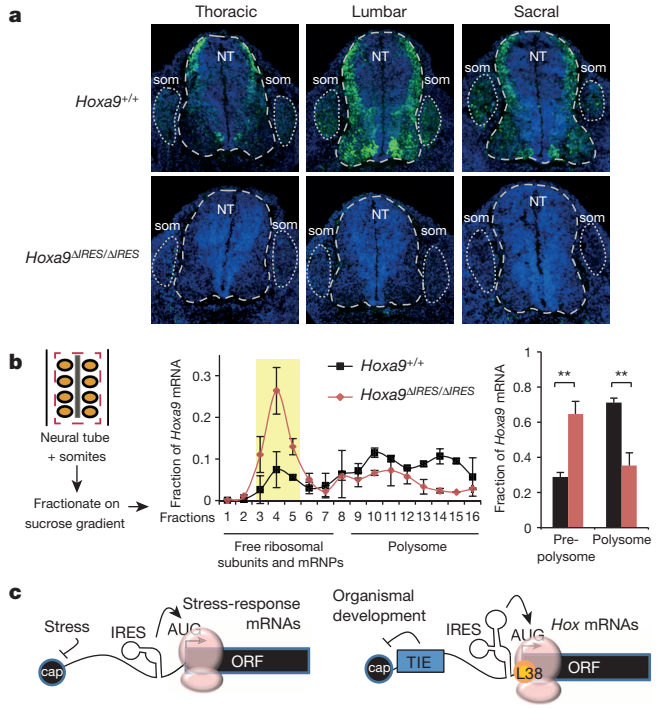


Figure 6 | The *Hoxa9* IRES is critically required for *Hoxa9* translation *in vivo*. **a**, Representative immunostaining of HOXA9 (green) in cross-section of E11.5 $Hoxa9^{+/+}$ (top) and $Hoxa9^{\Delta IRES/\Delta IRES}$ (bottom) embryos from the thoracic to sacral levels. DAPI (4′,6-diamidino-2-phenylindole) staining is in blue. NT, neural tube; som, somite. $n = 3$ embryos of each genotype. **b**, Somites and neural tubes of E11.5 $Hoxa9^{+/+}$ and $Hoxa9^{\Delta IRES/\Delta IRES}$ embryos were microdissected and fractionated on a sucrose gradient. Middle, qPCR of *Hoxa9* mRNA from each fraction. Early pre-polysome fractions are highlighted. Right, quantification of *Hoxa9* mRNA in fractions. Fractions 1–8 are pre-polysome and 9–16 polysome fractions. $^{**}P < 0.01$ (*t*-test compared to $Hoxa9^{+/+}$). $n = 3$ embryos of each genotype. **c**, Model for how ribosome-mediated regulation of gene expression is encoded within the mRNA sequence. Stress-responsive cellular IRES elements are only active when cap-dependent translation is downregulated through a decrease in eIF4F activity. *HoxA* mRNAs possess a TIE, which normally inhibits cap-dependent translation. The TIE enables ribosome-mediated control of *HoxA* IRES expression during embryonic development.

IRES elements under non-stress conditions. Their relevance to normal gene regulation is also poorly understood, as all eukaryotic mRNAs are capped and undergo cap-dependent translation[21,38]. Importantly, the requirement for *Hox* IRES elements is explained by our identification of the TIE within these transcripts, which strongly inhibits general, cap-dependent translation (Fig. 6c). We speculate that such IRES elements may be more widespread in the genome and suggest a two-state mechanism for gene regulation, controlled by transcription and an additional layer of *cis*-acting RNA regulons within 5′ UTRs that direct protein production. Both IRES and TIE elements may be differentially regulated, providing a versatile toolbox for controlling the ultimate expression of transcripts. Although *Hox* IRES elements are highly conserved, and may already be present in *Drosophila* orthologues[39], the TIE lacks conservation and is absent even in vertebrate species such as fish and amphibians (Fig. 1f). These species often lay their eggs in harsh environments[40] and may have originally used IRES elements as a fail-safe mechanism to ensure proper expression of key transcripts under stress conditions. Therefore, the acquisition of a TIE later in evolution may have enabled an additional, independent level of regulatory control to IRES-dependent translation and gene expression during normal development. A mechanism that regulates whether a pre-existing transcript is converted into a protein offers a fast and dynamic means to provide greater variation and control to gene expression.

It will be interesting to determine if additional ribosomal proteins may promote specialized translation through control of unique subsets of IRES-containing mRNAs, either directly or through RNA-binding proteins. For example, RPS25 is required for IRES-dependent translation of certain viral IRES mRNAs[41]. Moreover, rRNA modifications both at the level of pseudouridylation and RPL13a-dependent methylation also appear to regulate the translation of certain cellular IRES-containing mRNAs[14,16,42,43]. We therefore speculate that similar to the complex and highly regulated system of transcriptional control, in which specific DNA sequences and histone marks regulate gene expression, *cis*-acting RNA regulons, in conjunction with more specialized ribosome activity, provide newfound regulatory control to gene expression critical for mammalian development.

Online Content Methods, along with any additional Extended Data display items and Source Data, are available in the online version of the paper; references unique to these sections appear only in the online paper.

Received 11 March; accepted 30 October 2014.
Published online 19 November 2014.

1. Kondrashov, N. *et al.* Ribosome-mediated specificity in Hox mRNA translation and vertebrate tissue patterning. *Cell* **145,** 383–397 (2011).
2. Lee, A. S., Burdeinick-Kerr, R. & Whelan, S. A ribosome-specialized translation initiation pathway is required for cap-dependent translation of vesicular stomatitis virus mRNAs. *Proc. Natl Acad. Sci. USA* **110,** 324–329 (2013).
3. Vesper, O. *et al.* Selective translation of leaderless mRNAs by specialized ribosomes generated by MazF in *Escherichia coli*. *Cell* **147,** 147–157 (2011).
4. Xue, S. & Barna, M. Specialized ribosomes: a new frontier in gene regulation and organismal biology. *Nature Rev. Mol. Cell Biol.* **13,** 355–369 (2012).
5. Dinman, J. D. The eukaryotic ribosome: current status and challenges. *J. Biol. Chem.* **284,** 11761–11765 (2009).
6. Komili, S., Farny, N. G., Roth, F. P. & Silver, P. A. Functional specificity among ribosomal proteins regulates gene expression. *Cell* **131,** 557–571 (2007).
7. Alexander, T., Nolte, C. & Krumlauf, R. Hox genes and segmentation of the hindbrain and axial skeleton. *Annu. Rev. Cell Dev. Biol.* **25,** 431–456 (2009).
8. Sonenberg, N. & Hinnebusch, A. G. Regulation of translation initiation in eukaryotes: mechanisms and biological targets. *Cell* **136,** 731–745 (2009).
9. Livingstone, M., Atas, E., Meller, A. & Sonenberg, N. Mechanisms governing the control of mRNA translation. *Phys. Biol.* **7,** 021001 (2010).
10. Plank, T.-D. M. & Kieft, J. S. The structures of nonprotein-coding RNAs that drive internal ribosome entry site function. *Wiley Interdiscip. Rev. RNA* **3,** 195–212 (2012).
11. Stoneley, M., Paulin, F. E., Le Quesne, J. P., Chappell, S. A. & Willis, A. E. C-Myc 5′ untranslated region contains an internal ribosome entry segment. *Oncogene* **16,** 423–428 (1998).
12. Riley, A., Jordan, L. E. & Holcik, M. Distinct 5′ UTRs regulate XIAP expression under normal growth conditions and during cellular stress. *Nucleic Acids Res.* **38,** 4665–4674 (2010).
13. Ungureanu, N. H. *et al.* Internal ribosome entry site-mediated translation of Apaf-1, but not XIAP, is regulated during UV-induced cell death. *J. Biol. Chem.* **281,** 15155–15163 (2006).
14. Yoon, A. *et al.* Impaired control of IRES-mediated translation in X-linked dyskeratosis congenita. *Science* **312,** 902–906 (2006).
15. Ray, P. S., Grover, R. & Das, S. Two internal ribosome entry sites mediate the translation of p53 isoforms. *EMBO Rep.* **7,** 404–410 (2006).
16. Bellodi, C., Kopmar, N. & Ruggero, D. Deregulation of oncogene-induced senescence and p53 translational control in X-linked dyskeratosis congenita. *EMBO J.* **29,** 1865–1876 (2010).
17. Pyronnet, S., Dostie, J. & Sonenberg, N. Suppression of cap-dependent translation in mitosis. *Genes Dev.* **15,** 2083–2093 (2001).
18. Holcik, M., Sonenberg, N. & Korneluk, R. G. Internal ribosome initiation of translation and the control of cell death. *Trends Genet.* **16,** 469–473 (2000).
19. Xia, X. & Holcik, M. Strong eukaryotic IRESs have weak secondary structure. *PLoS ONE* **4,** e4136 (2009).
20. Phinney, D. G., Gray, A. J., Hill, K. & Pandey, A. Murine mesenchymal and embryonic stem cells express a similar Hox gene profile. *Biochem. Biophys. Res. Commun.* **338,** 1759–1765 (2005).
21. Thompson, S. R. So you want to know if your message has an IRES? *Wiley Interdiscip. Rev. RNA* **3,** 697–705 (2012).
22. Fraser, C. S. & Doudna, J. A. Structural and mechanistic insights into hepatitis C viral translation initiation. *Nature Rev. Microbiol.* **5,** 29–38 (2007).
23. Kieft, J. S., Zhou, K., Jubin, R. & Doudna, J. A. Mechanism of ribosome recruitment by hepatitis C IRES RNA. *RNA* **7,** 194–206 (2001).
24. Spahn, C. M. T. *et al.* Cryo-EM visualization of a viral internal ribosome entry site bound to human ribosomes: the IRES functions as an RNA-based translation factor. *Cell* **118,** 465–475 (2004).
25. Wilkinson, K. A., Merino, E. J. & Weeks, K. M. Selective 2′-hydroxyl acylation analyzed by primer extension (SHAPE): quantitative RNA structure analysis at single nucleotide resolution. *Nature Protocols* **1,** 1610–1616 (2006).
26. Lukavsky, P. J., Kim, I., Otto, G. A. & Puglisi, J. D. Structure of HCV IRES domain II determined by NMR. *Nature Struct. Biol.* **10,** 1033–1038 (2003).

©2015 Macmillan Publishers Limited. All rights reserved

27. Kladwang, W., VanLang, C. C., Cordero, P. & Das, R. A two-dimensional mutate-and-map strategy for non-coding RNA structure. *Nat. Chem.* **3,** 954–962 (2011).
28. Tian, S., Cordero, P., Kladwang, W. & Das, R. High-throughput mutate-map-rescue evaluates SHAPE-directed RNA structure and uncovers excited states. *RNA* **20,** 1815–1826 (2014).
29. Berry, K. E., Waghray, S. & Doudna, J. A. The HCV IRES pseudoknot positions the initiation codon on the 40S ribosomal subunit. *RNA* **16,** 1559–1569 (2010).
30. Jan, E. & Sarnow, P. Factorless ribosome assembly on the internal ribosome entry site of cricket paralysis virus. *J. Mol. Biol.* **324,** 889–902 (2002).
31. Stupina, V. A., Yuan, X., Meskauskas, A., Dinman, J. D. & Simon, A. E. Ribosome binding to a 5′ translational enhancer is altered in the presence of the 3′ untranslated region in cap-independent translation of turnip crinkle virus. *J. Virol.* **85,** 4638–4653 (2011).
32. Calvo, S. E., Pagliarini, D. J. & Mootha, V. K. Upstream open reading frames cause widespread reduction of protein expression and are polymorphic among humans. *Proc. Natl Acad. Sci. USA* **106,** 7507–7512 (2009).
33. Fletcher, L., Corbin, S. D., Browning, K. S. & Ravel, J. M. The absence of a m^7G cap on β-globin mRNA and alfalfa mosaic virus RNA 4 increases the amounts of initiation factor 4F required for translation. *J. Biol. Chem.* **265,** 19582–19587 (1990).
34. Coulombe, Y. *et al.* Multiple promoters and alternative splicing: *Hoxa5* transcriptional complexity in the mouse embryo. *PLoS ONE* **5,** e10600 (2010).
35. Fromental-Ramain, C. *et al.* Specific and redundant functions of the paralogous *Hoxa-9* and *Hoxd-9* genes in forelimb and axial skeleton patterning. *Development* **122,** 461–472 (1996).
36. Chen, F. & Capecchi, M. R. Targeted mutations in *Hoxa-9* and *Hoxb-9* reveal synergistic interactions. *Dev. Biol.* **181,** 186–196 (1997).
37. Boulet, A. M. & Capecchi, M. R. Targeted disruption of *hoxc-4* causes esophageal defects and vertebral transformations. *Dev. Biol.* **177,** 232–249 (1996).
38. Komar, A. A. & Hatzoglou, M. Internal ribosome entry sites in cellular mRNAs: mystery of their existence. *J. Biol. Chem.* **280,** 23425–23428 (2005).
39. Oh, S. K., Scott, M. P. & Sarnow, P. Homeotic gene *Antennapedia* mRNA contains 5′-noncoding sequences that confer translational initiation by internal ribosome binding. *Genes Dev.* **6,** 1643–1653 (1992).
40. Johnston, I. A. Environment and plasticity of myogenesis in teleost fish. *J. Exp. Biol.* **209,** 2249–2264 (2006).
41. Landry, D. M., Hertz, M. I. & Thompson, S. R. RPS25 is essential for translation initiation by the *Dicistroviridae* and hepatitis C viral IRESs. *Genes Dev.* **23,** 2753–2764 (2009).
42. Bellodi, C. *et al.* Loss of function of the tumor suppressor DKC1 perturbs p27 translation control and contributes to pituitary tumorigenesis. *Cancer Res.* **70,** 6026–6035 (2010).
43. Chaudhuri, S. *et al.* Human ribosomal protein L13a is dispensable for canonical ribosome function but indispensable for efficient rRNA methylation. *RNA* **13,** 2224–2237 (2007).

Supplementary Information is available in the online version of the paper.

Acknowledgements We would like to thank members of the Barna laboratory and D. Ruggero for discussion and critical reading of the manuscript. We thank E. Sarinay Cenik for advice with RNA pull-down experiments; and Y. Rim, A. Sapiro and A. Mateo for technical assistance. This work was supported by the Agency of Science, Technology and Research of Singapore (S.X.), Stanford Graduate Fellowship (S.T.), Human Frontier Science Program Fellowship (K.F.), NIH R01 GM102519 (R.D.), NIH Director's New Innovator Award, 7DP2OD00850902 (M.B.), Alfred P. Sloan Research Fellowship (M.B.) and Pew Scholars Award (M.B.).

Author Contributions M.B. conceived and supervised the project; S.X. and M.B. designed experiments; S.X. performed all experiments with help from K.F. for 5′ RACE and sucrose gradient fractionation; S.T. and R.D. designed the RNA structure experiments; S.T. and W.K. performed the RNA structure experiments and analysed results; S.X. and M.B. wrote the manuscript with contributions from all authors.

Author Information *Hoxa4* 5′ UTR sequence has been deposited in GenBank under accession number KM596709. All chemical mapping datasets have been deposited at the RNA Mapping Database (http://rmdb.stanford.edu) under the following accession codes: (1) Full-length: HOXA5_STD_0000, HOXA9_STD_0000; (2) *Hoxa9* TIE: HOXA9A_STD_0001; (3) *Hoxa9* IRES: HOXA9D_STD_0001, HOXA9D_STD_0002, HOXA9D_1M7_0001, and HOXA9D_RSQ_0001. Reprints and permissions information is available at www.nature.com/reprints. The authors declare no competing financial interests. Readers are welcome to comment on the online version of the paper. Correspondence and requests for materials should be addressed to M.B. (mbarna@stanford.edu).

©2015 Macmillan Publishers Limited. All rights reserved

METHODS

Plasmids. *Hox* 5′ UTRs were amplified from mouse E10.5–12.5 cDNA and cloned into the bicistronic pRF vector[14] using EcoRI and NcoI sites. For monocistronic assays, *Hox* 5′ UTRs are cloned into pGL3 control vector (Promega) using HindIII and NcoI sites. 5′ UTRs of *Hoxa3* and *Hoxa10* were made by gene synthesis (IDT). pRF-HCV was a kind gift from D. Ruggero (UCSF). Zebrafish *hoxa9b* 5′ UTR was amplified from zebrafish 24 hpf cDNA. Sequences were based off the Ensembl database[44]. See Supplementary Table 1 for a list of PCR primers used.

To ensure no ribosome read-through of the first cistron in bicistronic assays, a hairpin with a linker (GAATTCAGATCTGGTACCGAGCTCCCCGGGCTGC AGGATATCCTGCAGCCCGGGGACCTCGGTACCAGATCTAGGATCCGG ATCCGGCGACACTCCACCATGAATCACTCCCCTGTGAGGAACTACTGT CTTCACGCAGAAAGCGTCTAGCCATGG) was synthesized and ligated into the pRF vector at the EcoRI and NcoI sites. *Hox* 5′ UTRs and HCV IRES were cloned into this new vector pRF-hpC in the NcoI site. Clones were sequenced to ensure directionality.

5′ RACE. RNA was purified from dissected E11.5 neural tubes and somites using TRIzol (Invitrogen). The reverse transcription template was produced using ExactSTART Eukaryotic mRNA 5′-& 3′-RACE Kit (Epicentre) and reverse transcribed using Superscript III (Invitrogen) with a primer in the coding region of *Hoxa4*. The 5′ UTR fragment was amplified using Phusion High-Fidelity DNA polymerase (Thermo Scientific) with a gene specific reverse primer and a forward primer at the 5′ linker. PCR products were adenylated, gel-extracted and subcloned into TOPO TA cloning vector (Invitrogen) for sequencing.

TALEN. 2 sets of TALEN pairs were designed against the second and third exons of *Rpl38*. TALENs were generated towards the following sequences: F1 5′-GC GGACGCCAGAGCCGA, R1 5′- CCCTCGTCCCGCACTCA, F2 5′- CATCTT CTGTCCCTC, R2 5′- TGATCTCCTCAATTTTC. Intermediate arrays were produced for each TALEN-pair and assembled into pC-GoldyTALEN[45]. The 2 sets of TALEN pairs were transfected together into C3H10T1/2 cells. Cells were trypsinized into single cell suspension and plated for clonal expansion 2 days after transfection. Positive clones were identified by PCR followed by restriction digest. *Rpl38* disruption was confirmed by Sanger sequencing and western blotting.

Luciferase assay. C3H10T1/2 cells were transfected in 24-well plates with various pRF constructs using Lipofectamine 2000 (Invitrogen) as per manufacturer instructions. Cells were collected 24 h post-transfection and assayed using Dual luciferase kit (Promega). IRES activity is expressed as a ratio between Fluc and Rluc. To verify the integrity of the bicistronic construct, an shRNA plasmid against Rluc or scrambled plasmid[16] was cotransfected with the pRF constructs. Cells were harvested 72 h post-transfection for luciferase assays. For monocistronic luciferase assays, various pGL3 constructs were transfected as above into 12-well plates. Cells were collected 24 h later. Then 50% of the cells were used for qPCR analysis with Fluc primers to quantify total transcript abundance, the rest for luciferase assays. Fluc activity was normalized to total luciferase mRNA expression levels.

RNA pull down. Template DNA was made by PCR from pRF-HoxA9 using a 5′ primer containing the T7 promoter and a 3′ primer containing a linker sequence T2 (Supplementary Table 1). Biotinylated RNA was *in vitro* transcribed with Megascript T7 kit (Ambion) using a final concentration of 6.8 mM each of ATP, CTP and GTP, 6.5 mM UTP and 0.3 mM Biotin-16-UTP (Roche). Synthesized RNAs were treated with TURBO DNase (Ambion) and purified by phenol/chloroform extraction. Unincorporated nucleotides were removed by running the RNA through a G50 column (GE Healthcare). The RNA was analysed by electrophoresis for quality and Nanodrop for quantity.

A total of four 15-cm dishes of subconfluent C3H10T1/2 cells were collected for analysis using trypsinization. Cell pellets were washed and lysed on ice with 1.5 ml lysis buffer (10 mM Tris pH 7.5, 10 mM $MgCl_2$, 150 mM NaCl, 0.1% TritonX, 0.25% NP40, 10 mM DTT, RNaseOUT, Halt Protease inhibitor) for 30 min. Lysate was centrifuged at 14,000 rpm for 10 min, 4 °C. Supernatant was transferred to new tube and cleared with 400 µl avidin-agarose beads (Thermo) for 50 min, 4 °C. Cleared lysate was transferred to new tube and quantified by spectrometry.

Folding buffer was added to 100 pmol of biotinylated RNA of each species to a final concentration of 100 mM Tris pH8, 100 mM NaCl, 10 mM $MgCl_2$. RNA was heated to 95 °C for 1.5 min, ice for 2 min and 37 °C for 20 min. Then 100 pmol of folded RNA and 1 mg cleared lysate were incubated together with 100 µg ml^{-1} heparin and 100 µg ml^{-1} yeast tRNA in 2 ml lysis buffer for 1 h at room temperature.

Streptavidin M280 Dynabeads (Invitrogen) were washed according to manufacturer's instructions. 100 µl beads were incubated with each RNA per lysate sample for 1.5 h at 4 °C. Beads were then washed with lysis buffer with increasing concentrations of salt up to 600 mM NaCl. One-tenth of the bead sample was kept for RNA and the rest was used for protein analysis. RNA was eluted with 50 µl RNA denaturing buffer (95% formamide, 10 mM EDTA) at 65 °C for 5 min. Eluted RNA was purified by phenol/chloroform extraction. RNA was converted to cDNA and analysed by qPCR using primers *HoxA9* 5′ UTR F and *HoxA9* 342 R (Supplementary Table 1). Proteins were eluted with 40 µl protein elution buffer (5 mM biotin, 3× SDS sample buffer) at 95 °C for 5 min. Proteins were analysed by western blotting.

Western blotting. Western blots were performed with antibodies against RPS6 (Cell Signaling no. 2217) and RPL10a (Santa Cruz sc-100827). Polyclonal RPL38 antibodies were generated against C-EKAEKLKQSLPPGLAVKDLK.

RNA structural probing and data analysis. Double-stranded DNA templates were prepared by PCR assembly of DNA oligomers with maximum length of 60 nt ordered from IDT (Integrated DNA Technologies). DNA templates for mutate-and-map (M^2) and mutation/rescue were designed as previously described using NA_Thermo (https://github.com/DasLab/NA_thermo) and HiTRACE[27,28]. DNA template and RNA transcript preparation and quality checks were carried out as previously described[27,28].

All chemical mapping were carried out in 96-well format as described previously[27,28,46]. Briefly, before chemical modification, RNA was heated to 90 °C for 30 seconds, cooled on the bench top to room temperature to remove secondary structure heterogeneity, and folded for 20 min at 37 °C in 10 mM $MgCl_2$, 50 mM Na-HEPES, pH 8.0. RNA was modified by adding 1/4 volume freshly made 5 mg ml^{-1} 1-methyl-7-nitroisatoic anhydride (1M7)[47] in anhydrous DMSO or neat anhydrous DMSO as control. Modification reactions were incubated at room temperature and then quenched with 0.5 M Na-MES, pH 6.0. Quenches also included poly(dT) magnetic beads (Ambion) and FAM-labelled Tail2-A20 primer for reverse transcription. Samples were separated and purified using magnetic stands, washed with 70% ethanol twice, and air-dried. Beads were resuspended in ddH_2O and reverse transcription mix, then incubated at 55 °C for 30 min. RNA was degraded by addition of 1 volume of 0.4 M NaOH and incubation at 90 °C for 3 minutes, then cooled and neutralized with an additional volume of acid quench (prepared as 2 volumes of 5 M NaCl, 2 volumes of 2 M HCl, and 3 M NaOAc pH 5.2). Fluorescent labelled cDNA was recovered by magnetic bead separation, rinsed twice with 70% ethanol and air-dried. The beads were resuspended in Hi-Di formamide containing ROX-350 ladder (Applied Biosystems), then loaded on capillary electrophoresis sequencer (ABI3100).

For full-length *Hox* transcripts, an Illumina MiSeq-based ligSHAPE (ligation-based SHAPE) on long RNAs was carried out, using a protocol analogous to Mod-seq[48]. RNA was folded similarly and probed by SHAPE as above, then recovered by ethanol precipitation. To obtain 3′ ends for ligating primer-binding sites at unstructured regions, modified RNA was folded again and fragmented by 5 mM $TbCl_3$ for 5 min (or no Tb^{3+} as control)[49], quenched by 0.5 M Na-EDTA pH 8.0, then purified by RNA cleanup and concentration columns (Zymo Research). Fragmented RNA was prepared through 3′ end phosphate removal by treatment with T4 polynucleotide kinase (New England Biolabs), T4 RNA-ligase-based ligation of a 5′-adenylated universal miRNA cloning linker (New England Biolabs) to the RNA 3′ end, reverse transcription to cDNA using sequencing primers, and circLigase-based Illumina adapter ligation to the cDNA 3′ end as described[50].

The HiTRACE 2.0 package was used to analyse CE data, available as MATLAB toolbox at (https://github.com/hitrace)[51] and web server at (http://hitrace.org)[52]. Electrophoretic traces were aligned and baseline subtracted using linear and non-linear alignment routines as previously described[53]. Band intensities were fitted to Gaussian peaks, then background subtracted, signal attenuation corrected and normalized. MiSeq results were analysed using the MAPseeker software package[50,54]. The SHAPE reactivity profile was generated by projection of pair-ended reads. Briefly, a correction factor of 0.25 was used for full-length read ligation bias correction, accounting for the empirically observed low circLigase ligation efficiency for full-length cDNAs ending in CC[55]. Reads shorter than 8 nt were discarded due to ambiguity in their positional alignment in the full-length RNA. Modification fractions were determined by the number of cDNAs in which reverse transcription stopped at a given nucleotide divided by the number of cDNAs in which reverse transcription stopped or proceeded beyond that nucleotide[55]. Traces were background subtracted (SHAPE minus no-SHAPE data; and SHAPE-Tb minus Tb-alone data) and normalized through a boxplot-based heuristic[56] for *Hoxa5*, or using a scanning window of 350 nt for *Hoxa9*. Errors were estimated as the standard deviation between SHAPE/no-SHAPE and SHAPE-Tb/Tb-alone measurements.

Data-guided secondary structure models were obtained using the Fold executable of the RNAstructure package[57]. Pseudo-energy parameters of RNAstructure version 5.4 were used by default. To obtain 2D-data-guided secondary structure models, *Z* score matrices for mutate-and-map data sets were calculated and used as base-pair-wise pseudo-energies with a slope and intercept of 1.0 kcal mol^{-1} and 0 kcal mol^{-1} as previously described[27]. The ShapeKnots executable of RNA structure version 5.6 (ref. 58) enables modelling of pseudoknots but with different parameters for using SHAPE data in the modelling; this newer method was used for pseudoknot prediction of *Hoxa9* nt 957–1,132 when using 1D and 2D SHAPE data combined. Extension of ShapeKnots to accept 2D data are being incorporated into the next version of RNAstructure. Helix-wise confidence values were calculated via bootstrapping as described previously[27,28]. All predictions were

©2015 Macmillan Publishers Limited. All rights reserved

modelled in context with full-length sequences. Secondary structures were visualized by the VARNA software[59].

Mice. A 2.8-kb 5′ arm and a 4.9-kb 3′ arm of *Hoxa9* were cloned into PGKneolox2DTA.2 (P. Soriano, Addgene plasmid 13449). This results in a replacement of nt 945–1,194 of *Hoxa9* 5′ UTR with a *LoxP*-flanked Neo cassette in the same transcriptional direction as *Hoxa9* (Extended Data Fig. 8c). The plasmid was linearized with XhoI and electroporated into JM8NA3.N1 ESCs for homologous recombination by the UCSF ES cell core. The correctly targeted ESC clones were identified by long-range PCR and confirmed by Southern blotting. The clones were injected into C57BL/6 blastocysts by the Gladstone Institute Transgenic Core Facility. Resulting chimaeras were crossed with C57BL/6 mice to generate F1 ($Hoxa9^{Neo/+}$). $Hoxa9^{Neo/+}$ were crossed with CMV-Cre mice (Jackson Laboratory) to precisely remove the *LoxP*-flanked Neo cassette within the 5′ UTR to generate $HoxA9^{\Delta IRES/+}$ mice. All mice used for experiments were between 2 and 6 months old. All animal studies were performed in accordance with Stanford University Animal Care and Use guidelines.

Sucrose gradient fractionation. E11.5 neural tubes and somites were dissected and trypsinized as previously described[1]. The neural tube and somites of each embryo were lysed on ice in 200 µl of lysis buffer (20 mM Tris pH 7.5, 200 mM NaCl, 15 mM $MgCl_2$, 1 mM DTT, 8% glycerol, 1% Triton X-100, 100 µg ml^{-1} cycloheximide, 100 µg ml^{-1} heparin, 200 U ml^{-1} SUPERase In (Ambion)). After lysis, nuclei and membrane debris was removed by centrifugation (1,300*g*, 5 min at 4 °C, and then 14,000 rpm, 5 min, at 4 °C). The supernatant was layered onto a linear sucrose gradient (10–40% sucrose(w/v), 20 mM Tris, pH 7.5, 100 mM NaCl, 15 mM $MgCl_2$, 100 µg ml^{-1} cycloheximide) and centrifuged in a SW41Ti rotor (Beckman) for 2.5 h at 40,000 rpm at 4 °C. Fractions were collected by Density Gradient Fraction System (Brandel).

qPCR analysis. For cells, RNA was isolated using NucleoSpin RNA kit (Clontech) and DNase-treated on column. For embryos, E11.5 neural tubes and somites were dissected and trypsinized as previously described[1]. RNA was isolated using TRIzol (Invitrogen) and treated with TURBO DNA-free kit (Ambion). For sucrose gradient fractions, RNA was purified by acid phenol/chloroform followed by isopropanol precipitation. 0.5 µg of RNA was converted to cDNA using iScript supermix (BioRad). cDNA was diluted twofold and 1 µl used to run a SYBR green detection qPCR assay (SsoAdvanced SYBR Green supermix and CFX384, BioRad). Data was analysed and converted to relative RNA quantity using CFX manager (BioRad). For sucrose gradient fractions, amount of RNA from individual fractions was expressed as a fraction of the total RNA collected from all fractions. Primers were used at 250 nM per reaction. β-actin and *Hoxa9* qPCR primers were previously described[1]. Fluc F 5′-CATCACGTACGCGGAATACTT, Fluc R 5′-AAGAGATA CGCCCTGGTTC. 18S F 5′-ACATCCAAGGAAGGCAGCAG, 18S R 5′-CATTC CAATTACAGGGCCTC. 28S F 5′-GGGGAGAGGGTGTAAATCTC, 28S R 5- T CCTTATCCCGAAGTTACGG.

Whole mount *in situ* hybridization. Whole mount *in situ* hybridization was carried out using digoxygenin-labelled antisense RNA probes as previously described[1]. *Hoxa9* probe was amplified from mouse embryo cDNA. Primers sequences are described in Supplementary Table 1.

Skeletal staining. Alcian blue and alizarin red staining of cartilage and bone were performed on neonates as previously described[1].

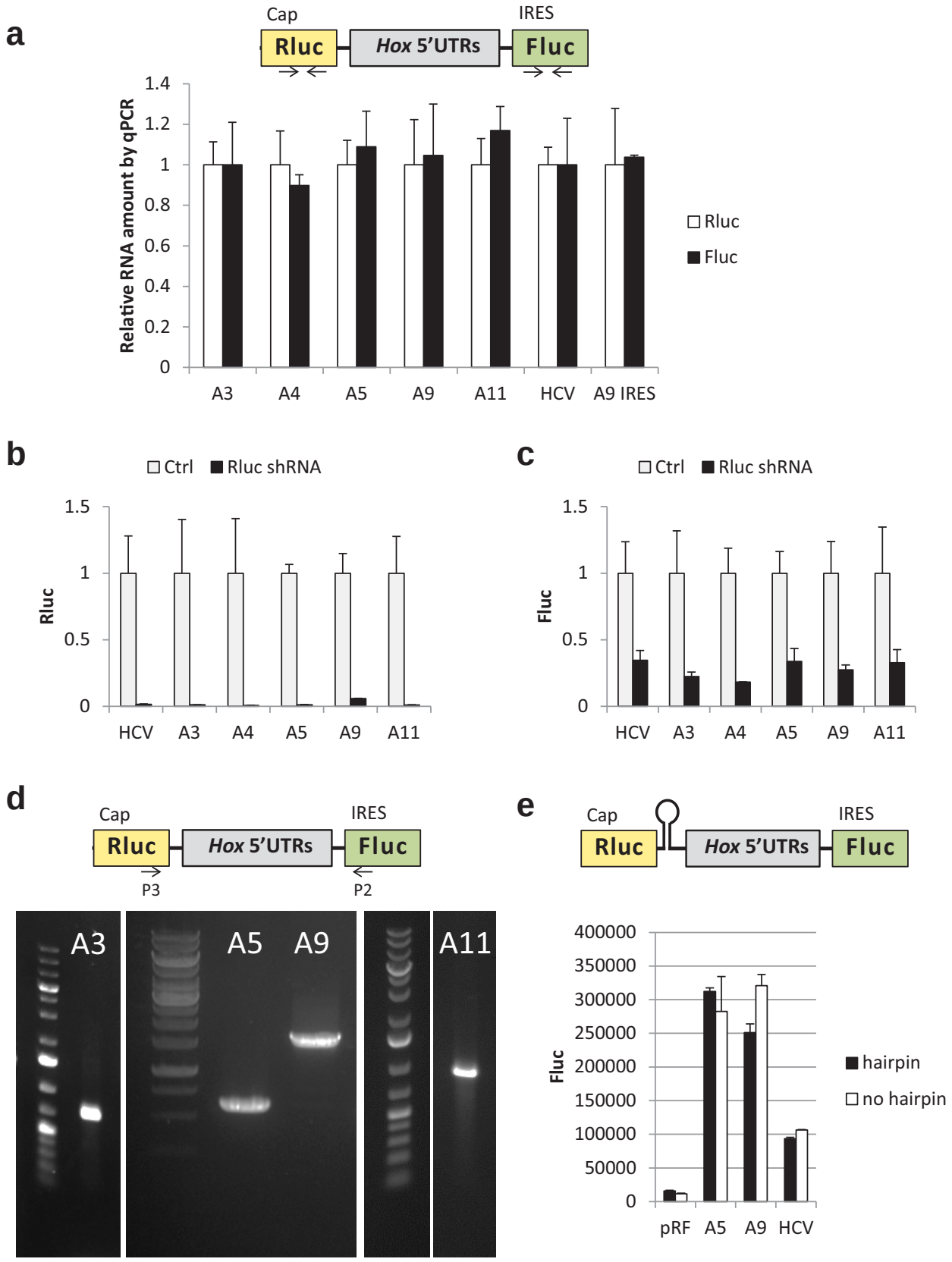
Immunofluorescence. E11.5 embryos were dissected, fixed and cryosectioned as previously described[1]. WT and $Hoxa9^{\Delta IRES/\Delta IRES}$ littermates sections were placed onto the same slide for direct comparison and identical processing. Sections were equilibrated to room temperature and rehydrated in blocking buffer (1% heat-inactivated goat serum, 0.1% Triton X-100 in PBS) for 1 h at room temperature. Sections were incubated with anti-HOXA9 antibody (Abcam ab140631) at 1:1,000 in blocking buffer overnight at 4 °C, washed three times, 30 min each and incubated with Alexa 488 anti-rabbit secondary antibodies (Invitrogen) for 1 h at room temperature. Slides were washed with blocking buffer three times, 30 min each and incubated with 1 µg ml^{-1} DAPI (Cell Signaling) for 15 min at room temperature. They were washed again in blocking buffer for 20 min and mounted with VectaShield Mounting Media (Vector Laboratories).

Statistical analysis. No normalization, blinding or exclusion was used in any experiments. No statistical method was used to predetermine sample size. In all cases, multiple independent experiments were performed on different days to verify the reproducibility of experimental findings. For mice experiments, embryos from multiple litters were used to avoid litter-specific bias.

Each variable was analysed using the two-tailed unpaired Student's *t* test. For all analyses, a *P* value of less than 0.05 was considered significant. Results are given as means ± s.d.

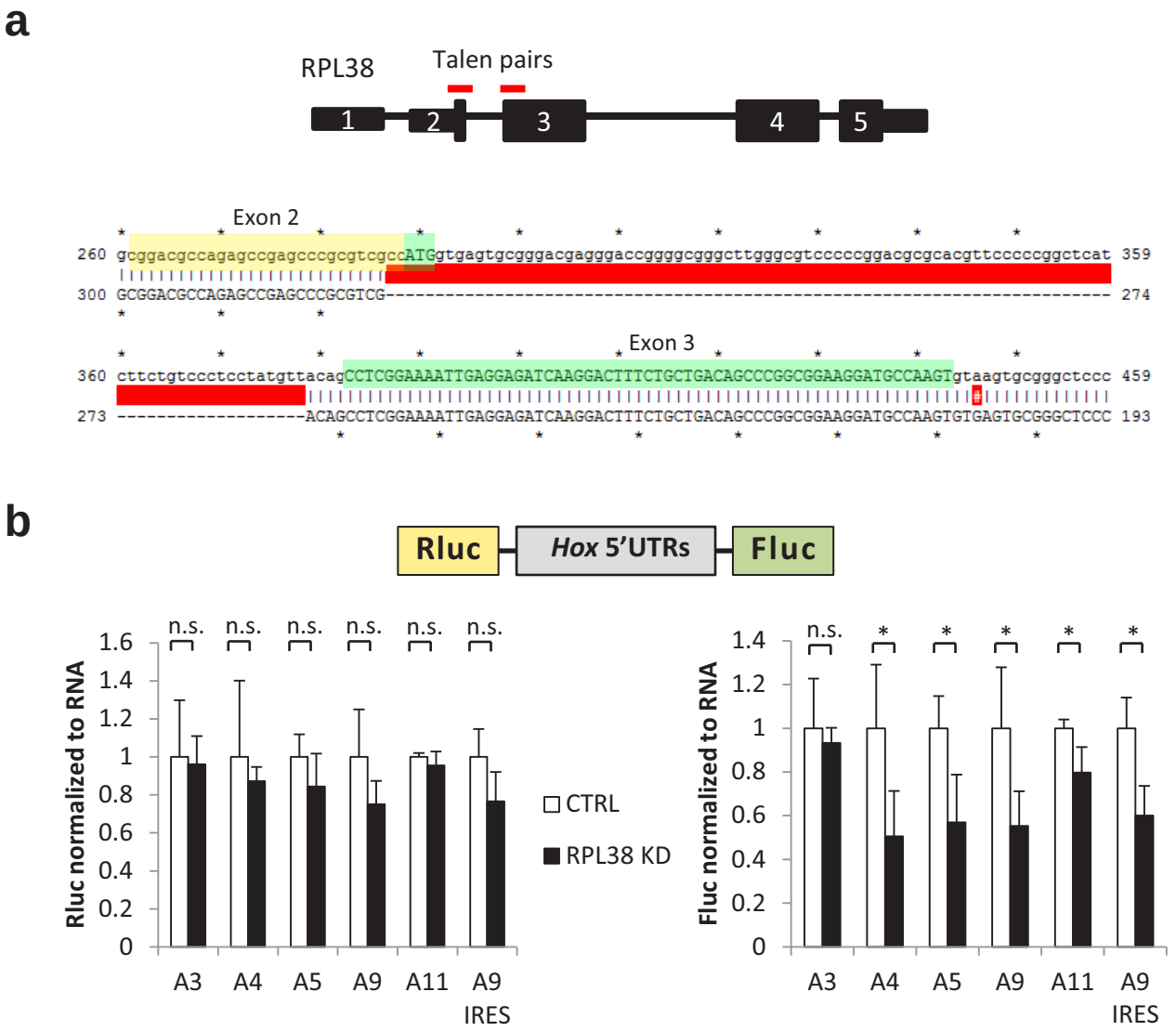
44. Flicek, P. *et al.* Ensembl 2014. *Nucleic Acids Res.* **42,** D749–D755 (2014).
45. Carlson, D. F. *et al.* Efficient TALEN-mediated gene knockout in livestock. *Proc. Natl Acad. Sci. USA* **109,** 17382–17387 (2012).
46. Kladwang, W., Cordero, P. & Das, R. A mutate-and-map strategy accurately infers the base pairs of a 35-nucleotide model RNA. *RNA* **17,** 522–534 (2011).
47. Mortimer, S. A. & Weeks, K. M. A fast-acting reagent for accurate analysis of RNA secondary and tertiary structure by SHAPE chemistry. *J. Am. Chem. Soc.* **129,** 4144–4145 (2007).
48. Talkish, J., May, G., Lin, Y., WoolFord J. L. Jr & McManus, C. J. Mod-seq : high-throughput sequencing for chemical probing of RNA structure. *RNA* **20,** 713–730 (2014).
49. Harris, D. A. & Walter, N. G. Probing RNA structure and metal-binding sites using Terbium (III) footprinting. *Curr. Protoc. Nucleic Acid Chem.* http://dx.doi.org/10.1002/0471142700.nc0608s13 (2003).
50. Cheng, C., Chou, F. & Kladwang, W. MOHCA-seq : RNA 3D models from single multiplexed proximity-mapping experiments. Preprint at *bioRxiv* http://dx.doi.org/10.1101/004556 (2014).
51. Yoon, S. *et al.* HiTRACE: high-throughput robust analysis for capillary electrophoresis. *Bioinformatics* **27,** 1798–1805 (2011).
52. Kim, H., Cordero, P., Das, R. & Yoon, S. HiTRACE-Web: an online tool for robust analysis of high-throughput capillary electrophoresis. *Nucleic Acids Res.* **41,** W492–W498 (2013).
53. Kim, J. *et al.* A robust peak detection method for RNA structure inference by high-throughput contact mapping. *Bioinformatics* **25,** 1137–1144 (2009).
54. Seetin, M., Kladwang, W., Bida, J. & Das, R. in *RNA Folding: Methods and Protocols* (ed. Waldsich, C.) **1086,** 95–117 (Humana Press, 2014).
55. Kladwang, W. *et al.* Standardization of RNA chemical mapping experiments. *Biochemistry* **53,** 3063–3065 (2014).
56. Deigan, K. E., Li, T. W., Mathews, D. H. & Weeks, K. M. Accurate SHAPE-directed RNA structure. *Proc. Natl Acad. Sci. USA* **106,** 97–102 (2009).
57. Reuter, J. S. & Mathews, D. H. RNAstructure: software for RNA secondary structure prediction and analysis. *BMC Bioinformatics* **11,** 129 (2010).
58. Hajdin, C. E. *et al.* Accurate SHAPE-directed RNA secondary structure modeling, including pseudoknots. *Proc. Natl Acad. Sci. USA* **110,** 5498–5503 (2013).
59. Darty, K., Denise, A. & Ponty, Y. VARNA: interactive drawing and editing of the RNA secondary structure. *Bioinformatics* **25,** 1974–1975 (2009).

©2015 **Macmillan Publishers Limited. All rights reserved**



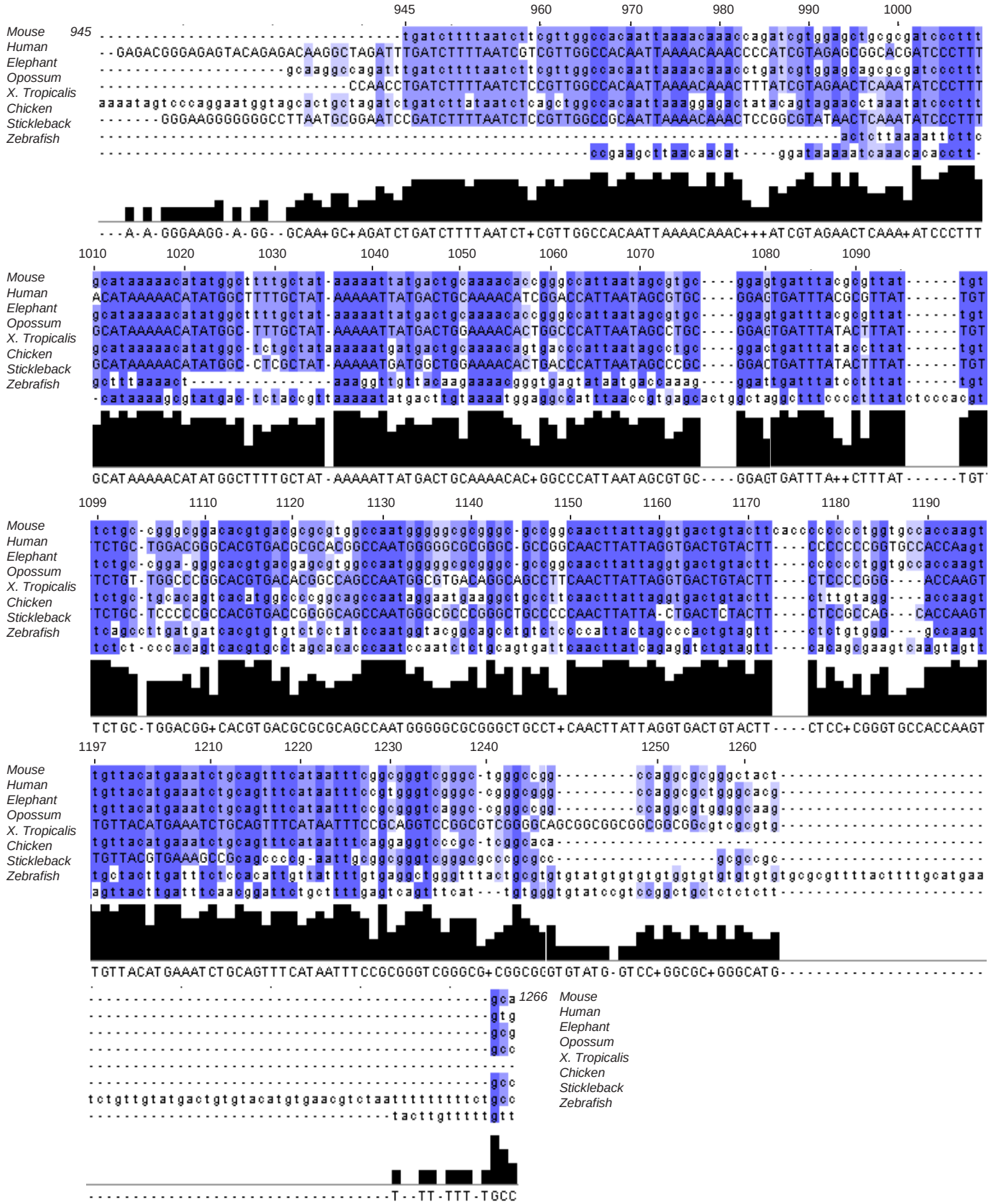
Extended Data Figure 1 | *HoxA* IRES controls confirming that Fluc activity from bicistronic vector is due to IRES activity. **a**, qPCR of both Rluc and Fluc from transfected cells shows that Rluc and Fluc are produced at the same ratio. All Rluc and Fluc values are normalized to that of HCV (set to 1). $n = 3$, individual experiments performed in duplicate. **b**, **c**, shRNA against Rluc decreased reporter activity of both Rluc (**a**) and Fluc (**b**), confirming that Rluc and Fluc were transcribed on the same mRNA. $n = 3$, individual experiments performed in triplicate. **d**, RT–PCR using primers in Rluc and Fluc show that there is no cryptic splice site in the cloned *Hox* 5′ UTR. Primer locations are shown as arrows in the diagram. **e**, Inserting a strong hairpin (-67 kcal mol^{-1}) after the Rluc reporter did not affect Fluc activity, suggesting that Fluc activity was not due to ribosome read-through.

©2015 Macmillan Publishers Limited. All rights reserved



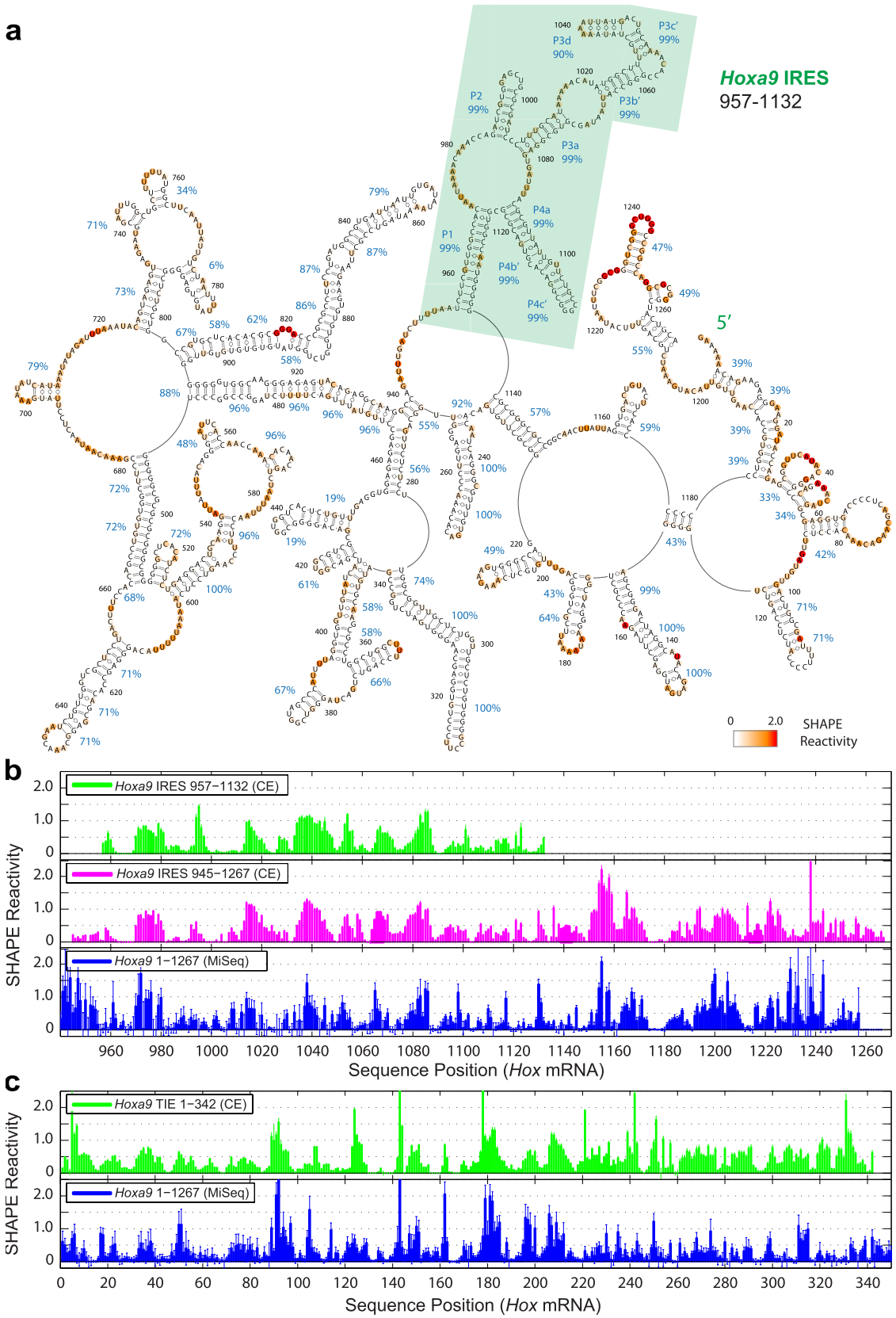
Extended Data Figure 2 | Disruption of *Rpl38* in C3H10T1/2 by TALEN nucleases. a, Location of TALEN pairs. Two pairs of TALENs were designed to bind at the end of exon 2 and the beginning of exon 3 to make a genomic break close to the ATG. Sequencing of a positive clone shows a deletion of the ATG and most of the intron after it. Coding sequence is highlighted in green. **b,** *Rpl38* knockdown does not change cap-dependent translation (Rluc) but decreases IRES-dependent translation (Fluc) from specific *Hox* 5′ UTRs. Luciferase activity was normalized to amount of Fluc RNA in the cells as quantified by qPCR. $^*P < 0.05$ (*t*-test compared to control). $n = 2$, individual experiments performed in duplicate.

©2015 Macmillan Publishers Limited. All rights reserved



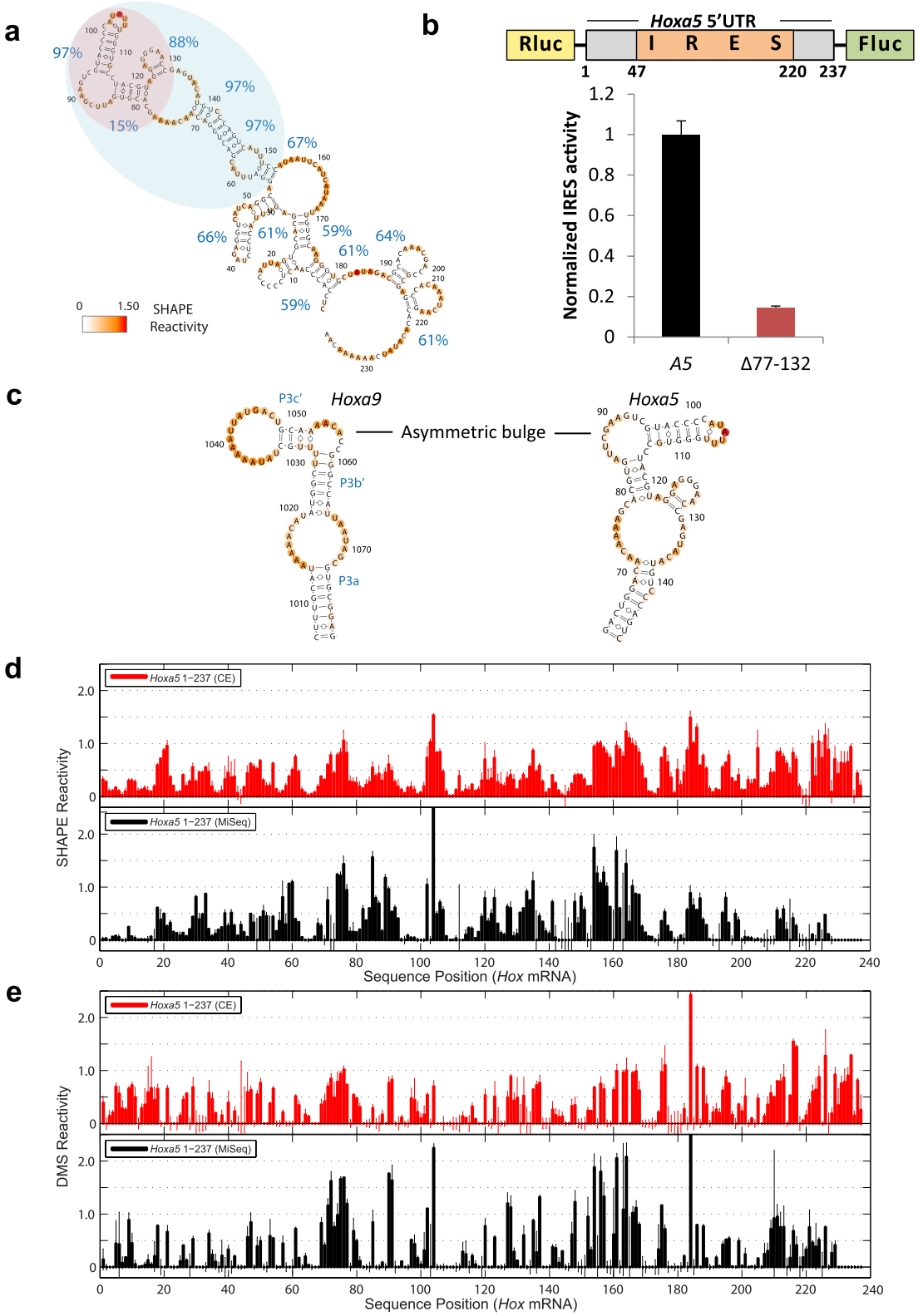
Extended Data Figure 3 | Alignment of the *Hoxa9* IRES element between vertebrate species. Nucleotides 945 to 1,266 of the mouse *Hoxa9* 5′ UTR were aligned with sequences from other vertebrates and show high sequence homology. Nucleotides are coloured based on their homology, with darker colours representing higher conservation.

©2015 Macmillan Publishers Limited. All rights reserved



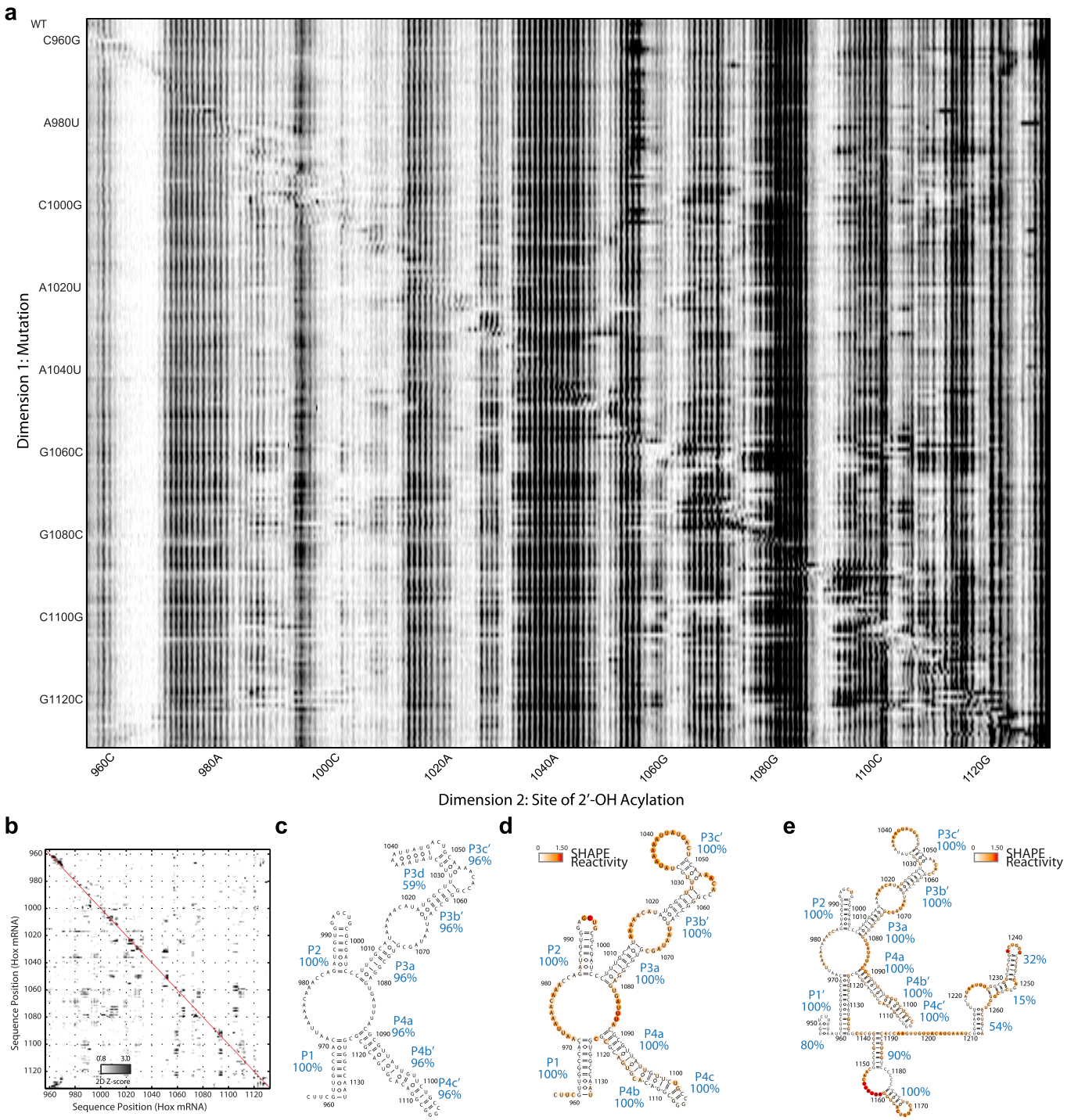
Extended Data Figure 4 | Chemical mapping and secondary structure prediction of full-length *Hoxa9* 5′ UTR. **a**, Secondary structure modelling of full-length *Hoxa9* using ligSHAPE data. The *Hoxa9* IRES element (nt 957–1,132, shaded in green) is modelled as the same secondary structure shown in Fig. 2a. Confidence values from bootstrapping (bulge percentages) exceed 90% for this element, suggesting a well-determined subdomain, but are generally low outside this region, indicating poor certainty in other regions. **b**, Normalized SHAPE reactivity of *Hoxa9* IRES (nt 957–1,132 and 944–1,266 from one-dimensional SHAPE read out through capillary electrophoresis (CE), full-length 1–1,266 from MiSeq-based ligSHAPE). **c**, Normalized SHAPE reactivity of *Hoxa9* TIE (nt 1–342 from CE-based one-dimensional SHAPE, full-length 1–1,266 from MiSeq-based ligSHAPE).

©2015 Macmillan Publishers Limited. All rights reserved



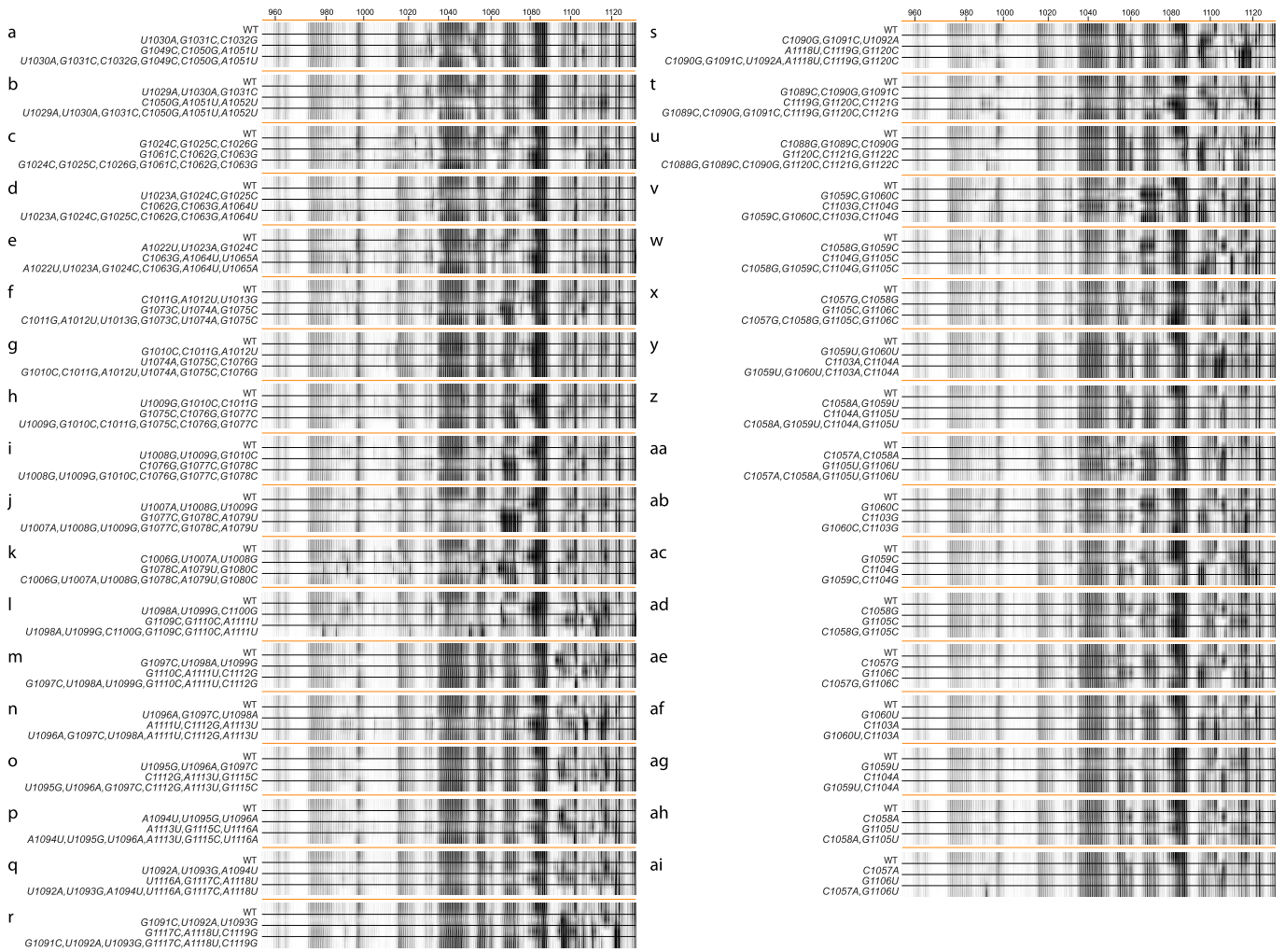
Extended Data Figure 5 | Chemical mapping and secondary structure model of full-length *Hoxa5* 5′ UTR. **a**, Secondary structure modelling of *Hoxa5* using one-dimensional SHAPE data. Nucleotides are coloured with SHAPE reactivities. Percentage labels give bootstrap support values for each helix. The feature highlighted in blue resembles P3 in *Hoxa9* and the tip highlighted in pink is deleted in **b**. **b**, The deletion of the tip identified in *Hoxa5* IRES structure shown in **a** decreases IRES activity in bicistronic reporter assays. IRES activity was normalized to full length *Hoxa5* 5′ UTR (*A5*, set to 1). $^{**}P < 0.01$ (*t*-test as compared to *A5*). $n = 2$ experiments, performed in triplicate. **c**, Both *Hoxa9* and *Hoxa5* contain an asymmetric bulge in a region important for IRES activity. **d**, **e**, Normalized SHAPE (**d**) and DMS (**e**) reactivity of *Hoxa5* (CE-based and MiSeq-based).

©2015 Macmillan Publishers Limited. All rights reserved



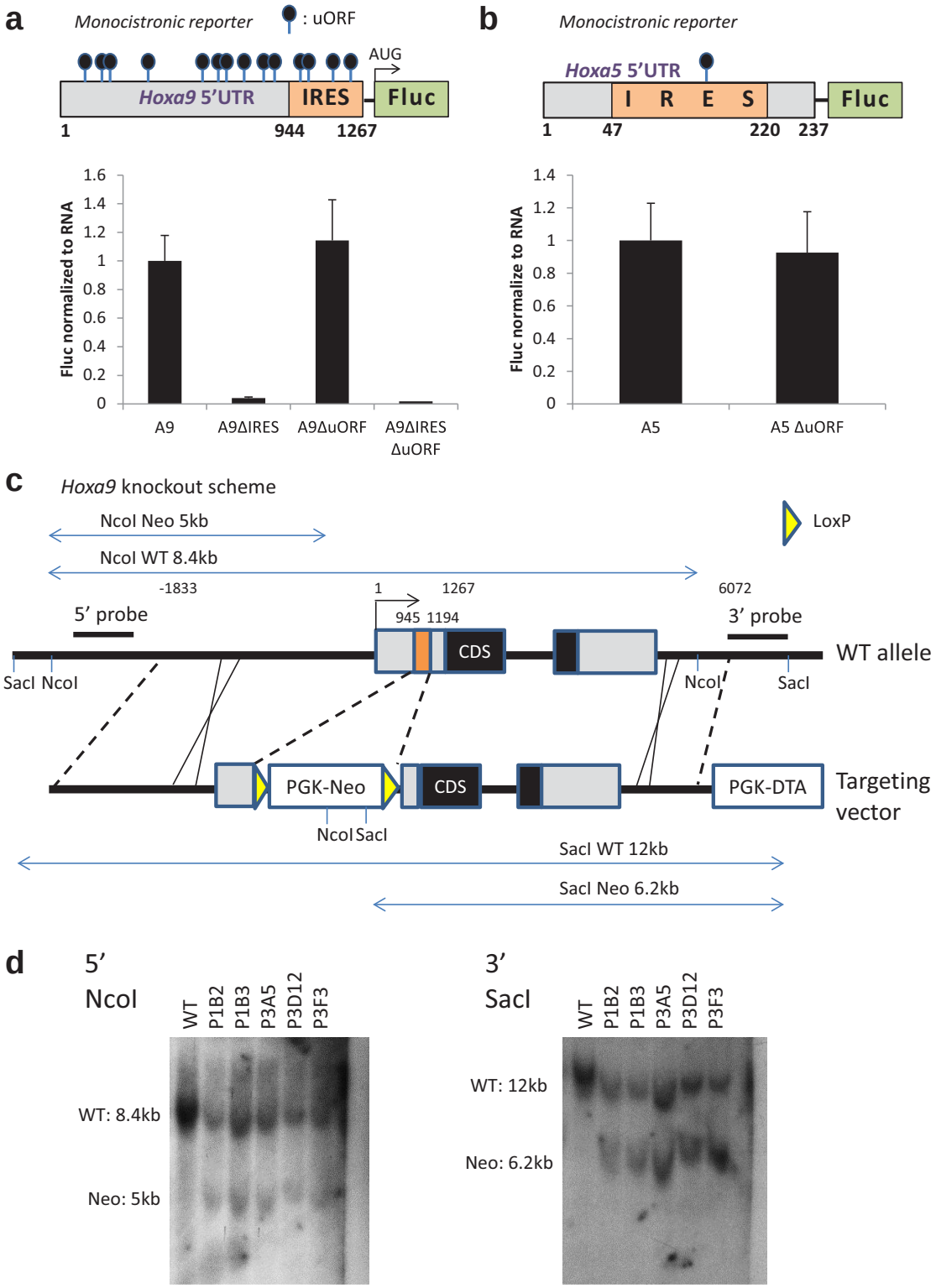
Extended Data Figure 6 | Secondary structure model and mutate-and-map (M^2) data set of *Hoxa9* IRES element. **a**, **b**, Entire M^2 data set and *Z*-score contact-map of *Hoxa9* nt 957–1,132 across 177 single mutants probed by 1M7. **c**, Secondary structure model of *Hoxa9* nucleotides 957–1,132 using M^2 data alone. **d**, Secondary structure model of *Hoxa9* nt 957–1,132 using one-dimensional SHAPE data alone. Nucleotides are coloured with SHAPE reactivity. **e**, Secondary structure model of *Hoxa9* nt 944–1,266 using one-dimensional SHAPE data. The models in **c**–**e** contain the same helices as the model from combined SHAPE/M^2 analysis in Fig. 2a, up to register shifts and edge base pairs; the small rearrangements are labelled P3b', P3c', P3d, P4b' and P4c'.

©2015 Macmillan Publishers Limited. All rights reserved



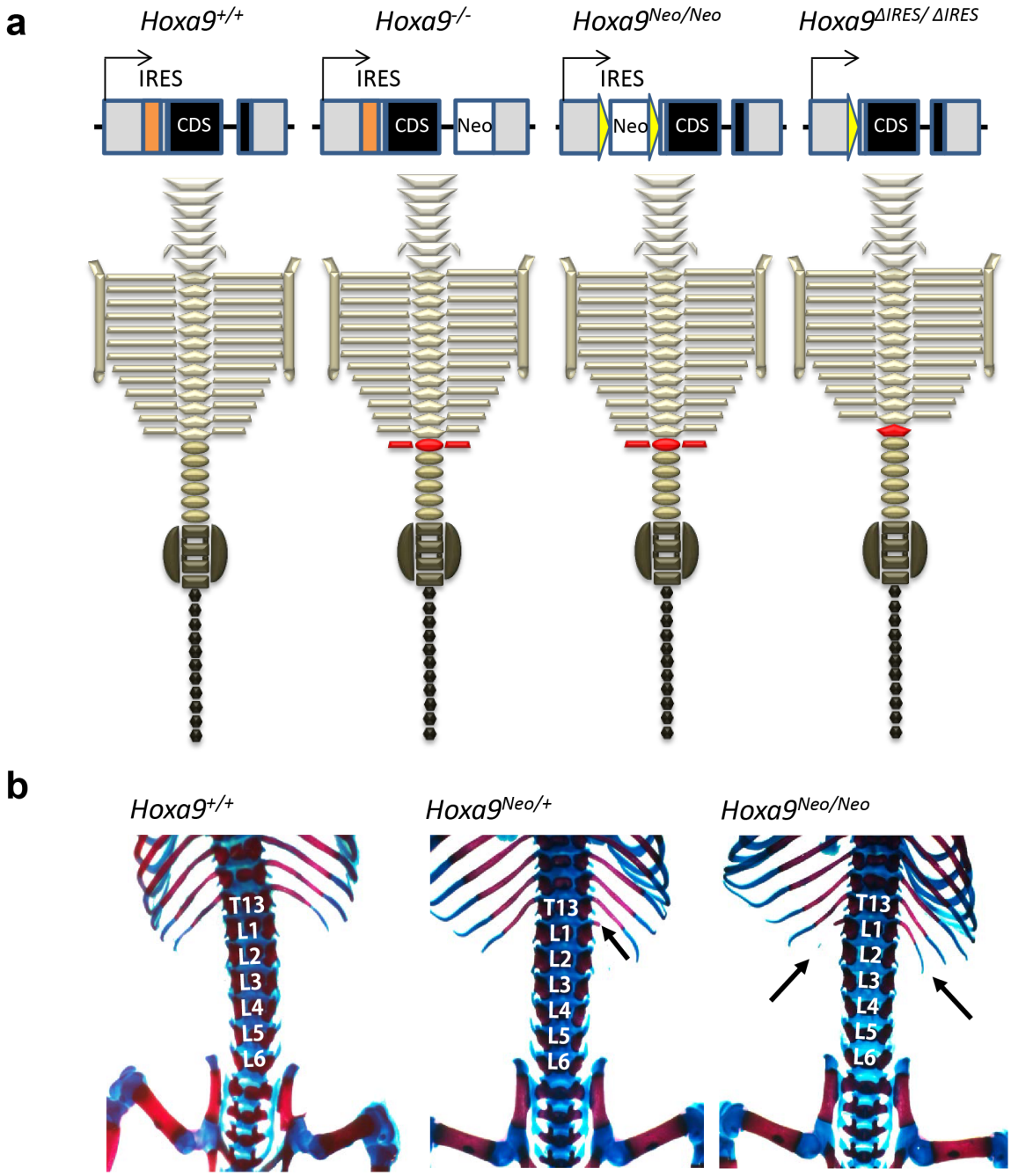
Extended Data Figure 7 | Mutation/rescue results of *Hoxa9* IRES structure (nt 944–1,266) probed by 1M7. Electropherograms of mutation/rescue to test base-pairings in P3c (**a, b**), P3b (**c**–**e**), P3a (**f**–**k**), P4b (**l**–**o**), P4a (**p**–**u**) and pk3-4 (**v**–**ai**). Perturbation of the chemical mapping reactivities by mutations of one strand and restoration by mutations in the other strand provide strong evidence for the tested pairings in P3c (**a**, **b**), P3b (**c**–**e**), P3a (**f**–**k**), P4b (**m**–**o**) and P4a (**p**–**q**, **t**). Near-perfect restoration by compensatory mutations in (**x**) and (**ad**) support pseudoknot pk3-4. Lack of rescue in other tested pairings is consistent with either absence of those pairings or higher-order structure (for example, base triples) interacting with those pairings.

©2015 Macmillan Publishers Limited. All rights reserved



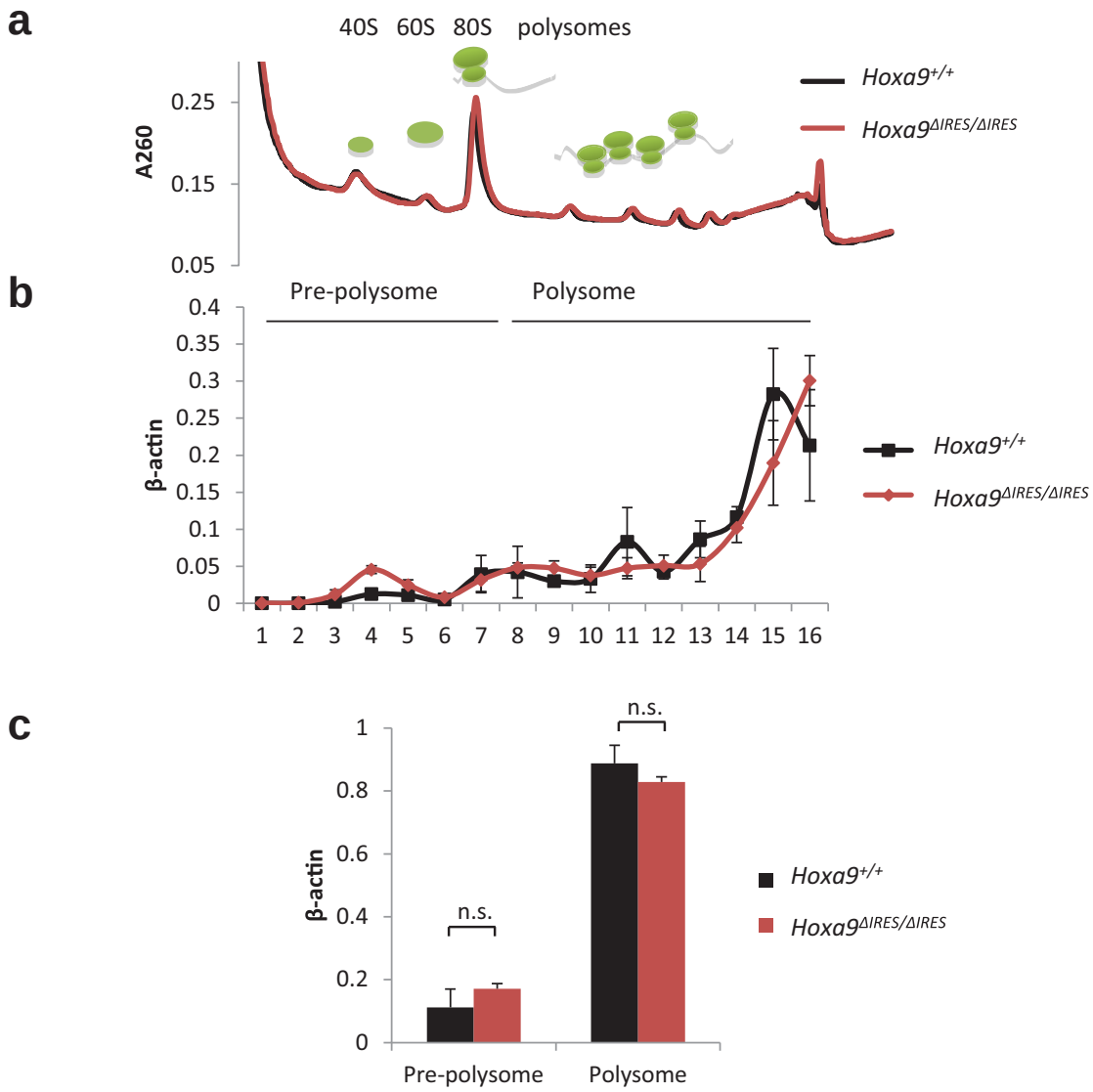
Extended Data Figure 8 | Putative uORFs within the 5′ UTRs of *Hoxa9* and *Hoxa5* do not inhibit cap-dependent translation and *Hoxa9*$^{\Delta IRES}$ targeting strategy. uORFs are marked by black circles on the diagram of monocistronic reporter for the *Hoxa9* (**a**) and *Hoxa5* (**b**) 5′ UTR. All the ATGs in the 5′ UTR were mutated to TTG in *A9ΔuORF* construct and GTG in *A5ΔuORF*. The IRES element (944–1,266) was removed in *A9ΔIRES* construct. The IRES element was removed from the *A9ΔuORF* construct in *A9ΔIRESΔuORF*. $n = 3$ individual experiments in duplicates. Data represent mean ± s.d. **c**, Diagrams of the *Hoxa9* locus and the targeting vector. Boxes represent exons, grey boxes represent UTRs, and black boxes represent the coding sequence. Nucleotides 944–1,145 were replaced by a floxed Neo cassette in the targeting vector. Locations of Southern blot probes, restriction enzymes used for Southern analysis and expected sizes are marked on the diagrams. **d**, Southern blot analysis of targeted cells using both the 5′ and 3′ probes showing that both arms integrated correctly into the *Hoxa9* locus. Mice were generated from clone P3A5.

©2015 Macmillan Publishers Limited. All rights reserved



Extended Data Figure 9 | The presence of a Neo cassette in the *Hoxa9* locus is linked to the presence of an L1 → T13 homeotic transformation. **a**, Diagram of the *Hoxa9* locus (top) and axial skeleton phenotype (bottom) in different *Hoxa9* mouse mutants. The original $Hoxa9^{-/-}$ was made by replacing the homeodomain with a Neo cassette. Vertebra with homeotic transformation is coloured red. **b**, Representative skeletons of $Hoxa9^{+/+}$, $Hoxa9^{Neo/+}$ and $Hoxa9^{Neo/Neo}$. Arrows point to the additional rib(s) on L1, revealing a homeotic transformation to T13. These results show that it is the presence of Neo in the targeting locus, which may affect the expression of neighbouring Hox gene, that is sufficient to cause the L1 → T13 phenotype. When the Neo cassette is removed from the targeting locus by crossing the $Hoxa9^{Neo/+}$ mouse with a CMV Cre line, the L1 → T13 phenotype is no longer present. $n = 3$ skeletons of each genotype.

©2015 Macmillan Publishers Limited. All rights reserved



Extended Data Figure 10 | Sucrose gradient fractionation shows no difference in β-actin association with polysomes in *Hoxa9*$^{+/+}$ and *Hoxa9*$^{\Delta IRES/\Delta IRES}$ embryos. **a**, Overlay of A_{260} trace during fractionation showing no difference in polysome profiles between E11.5 *Hoxa9*$^{+/+}$ and *Hoxa9*$^{\Delta IRES/\Delta IRES}$ embryos. **b**, qPCR from each fraction reveals no difference in β-actin mRNA accumulation between *Hoxa9*$^{+/+}$ and *Hoxa9*$^{\Delta IRES/\Delta IRES}$ embryos. **c**, Quantification of β-actin mRNA in fractions. Fractions 1–8 are pre-polysomes and 9–16 are polysome fractions. $n = 3$ embryos of each genotype.

©2015 Macmillan Publishers Limited. All rights reserved

ARTICLE

doi:10.1038/nature13916

Architecture and conformational switch mechanism of the ryanodine receptor

Rouslan G. Efremov[1,2,3], Alexander Leitner[4], Ruedi Aebersold[4,5] & Stefan Raunser[1]

Muscle contraction is initiated by the release of calcium (Ca^{2+}) from the sarcoplasmic reticulum into the cytoplasm of myocytes through ryanodine receptors (RyRs). RyRs are homotetrameric channels with a molecular mass of more than 2.2 megadaltons that are regulated by several factors, including ions, small molecules and proteins. Numerous mutations in RyRs have been associated with human diseases. The molecular mechanism underlying the complex regulation of RyRs is poorly understood. Using electron cryomicroscopy, here we determine the architecture of rabbit RyR1 at a resolution of 6.1 Å. We show that the cytoplasmic moiety of RyR1 contains two large α-solenoid domains and several smaller domains, with folds suggestive of participation in protein–protein interactions. The transmembrane domain represents a chimaera of voltage-gated sodium and pH-activated ion channels. We identify the calcium-binding EF-hand domain and show that it functions as a conformational switch allosterically gating the channel.

Calcium ions control many physiological processes, in particular key steps during transcription, cell cycle, apoptosis and muscular contraction. Therefore, their concentration and spatial distribution within living cells is regulated with high accuracy[1]. In striated muscles, calcium concentrations of several hundred micromolar are stored in the sarcoplasmic reticulum. Triggered by an action potential, which travels along the T-tubules of skeletal and cardiac muscles, voltage-gated calcium channels (Ca_v) activate ryanodine receptors (RyRs) that release large amounts of Ca^{2+} within several milliseconds[2] from the sarcoplasmic reticulum to induce contraction of the muscle. RyRs are the largest known ion channels, which are primarily triggered by Ca^{2+} and regulated by several factors, including Mg^{2+}, ATP, phosphorylation, the redox potential and via the interaction with other proteins such as Ca_v, FK506 binding proteins (FKBP) and calmodulin[3,4]. Among the three isoforms of RyRs identified in mammals, RyR1 is abundant in skeletal muscle, RyR2 is predominant in cardiac myocytes, and RyR3, the least studied isoform, is found in several cell types[5]. RyRs share structural and sequence homology with another important calcium channel, the inositol-1,4,5-triphosphate receptor ($Ins(1,4,5)P_3$ or IP_3 receptor)[6]. IP_3 receptors reside in the endoplasmic reticulum and form a part of the intracellular signalling system converting external stimuli into calcium signals[7]. More than 300 mutations in RyRs have been associated with human diseases, including malignant hyperthermia, fatal cardiac arrhythmias, cardiac sudden death and neurological disorders[3,8,9]. For these reasons, RyRs are important pharmacological targets. However, little is known about the molecular mechanism underlying the complex regulation of RyR, largely because high-resolution structures are lacking.

Structure determination

To further our understanding of ryanodine receptors and their gating mechanism, we used electron cryomicroscopy (cryo-EM) and single particle analysis to determine the structure of rabbit RyR1 in the open state at a resolution of 8.5 Å, allowing us to resolve the architecture of most of the domains. However, the assignment of some of the domains was ambiguous at this resolution. We therefore also determined the structure of the calcium channel in its closed state to an average resolution of 6.1 Å (Fig. 1a and Extended Data Fig. 1) using new direct electron detector technology. In both cases we reconstituted RyR1 into lipid nanodiscs to provide a near-to-native lipid environment that is particularly important for the structural integrity of ion channels[10].

To build a model of RyR1 at a resolution of 6.1 Å we first fitted the known crystal structures of the amino-terminal ABC[11] and phosphorylation domains[12,13] (Extended Data Table 1) in the cryo-EM density map. Then, we used well recognizable patterns of secondary structure element arrangements to identify α-solenoid and transmembrane domains for which the approximate sequence was assigned based on secondary structure prediction, hydrophobicity profile identification and topology mapping experiments[14] (Extended Data Figs 2 and 3 and Supplementary Information). Finally, homology models of the remaining domains were positioned into the cryo-EM density. To assign positions of structurally homologous domains we used chemical cross-linking mass spectrometry experiments that provided additional restraints on the distances between cross-linked amino acids (Supplementary Information and Extended Data Fig. 4). On the basis of the determined arrangement of the individual domains (Fig. 1a), we divided the 2.2-megadalton (MDa) homotetramer of RyR1 into triangular shaped protomers with relatively small contact surface between each other.

Architecture of RyR1

The cytoplasmic moiety of RyR1 constituting ~80% of the protein can be subdivided into core and peripheral regions. The central core is formed by the N-terminal AB domain folded into two β-trefoil subdomains located at the central rim of RyR1 (ref. 11). It is continued by a large α-solenoid domain, termed α-solenoid 1, that is formed by 30 α-helices packed in two parallel layers.

The α-solenoid 1 forms a structural scaffold for the cytoplasmic domain of RyR1. It extends towards the surface of the RyR1 handle, that is, to the periphery of the cytoplasmic domain, and bends under the AB domain (Fig. 1b and Extended Data Fig. 5g). α-Solenoid domains are formed by several repeats of helical hairpin motifs creating extended flat domains and are common in eukaryotic organisms[15]. Analysis of the structure allowed the approximate sequence assignment for the α-solenoid domains

[1]Department of Structural Biochemistry, Max Planck Institute of Molecular Physiology, 44227 Dortmund, Germany. [2]Structural Biology Research Center, Vlaams Instituut voor Biotechnologie (VIB), 1050 Brussels, Belgium. [3]Structural Biology Brussels, Vrije Universiteit Brussel (VUB), 1050 Brussels, Belgium. [4]Department of Biology, Institute of Molecular Systems Biology, ETH Zurich, 8093 Zurich, Switzerland. [5]Faculty of Science, University of Zurich, 8057 Zurich, Switzerland.

©2015 Macmillan Publishers Limited. All rights reserved

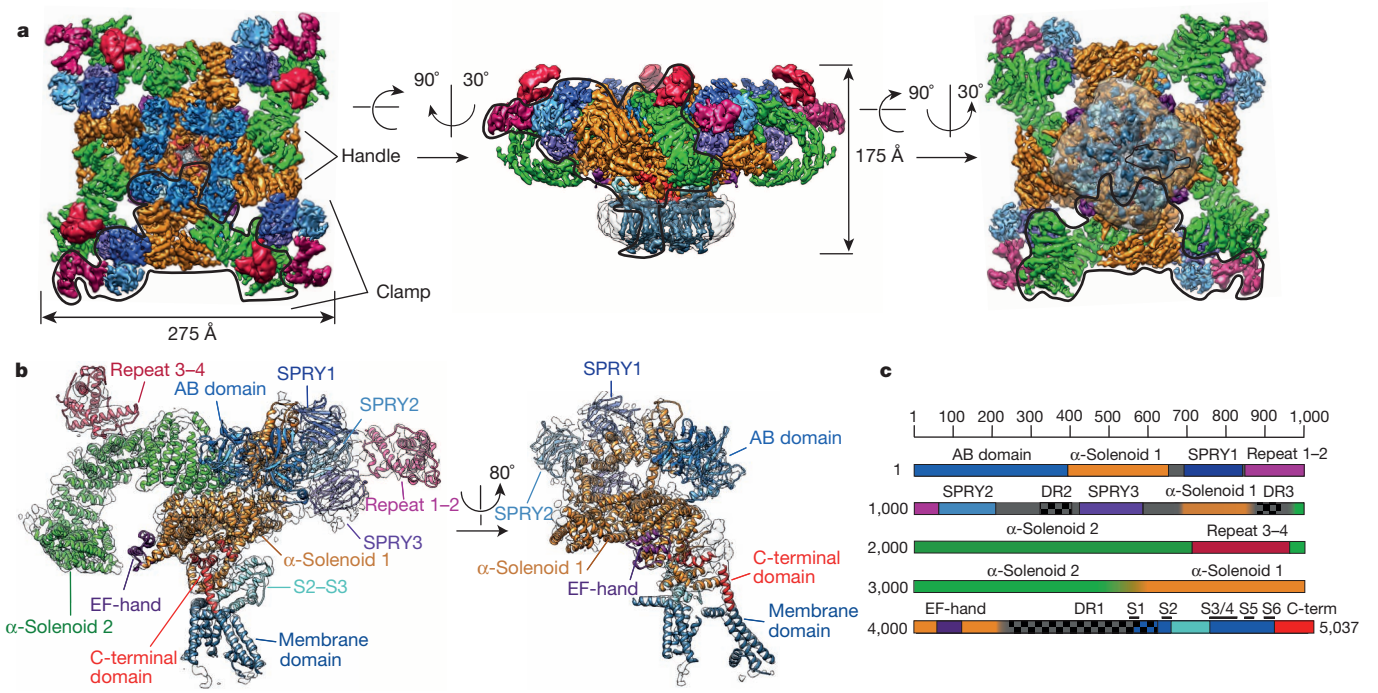


Figure 1 | Architecture of RyR1. **a**, Cryo-EM density map of RyR1 at an average resolution of 6.1 Å coloured by domains. The contour of a most probable protomer is outlined. The density of the nanodisc surrounding the membrane domain is shown in transparent grey. **b**, Molecular model and density of a protomer. The colours correspond to the colour code used in **a**. In the second side view of the protomer, the α-solenoid 2 and repeat 3–4 domains are omitted for clarity. See Extended Data Table 1 for sequence assignment details. **c**, Positions of domains are indicated on the schematically represented primary structure of the protomer. The colour coding is as in **b**. Divergent regions are marked by a chessboard-like pattern. The long sequence regions absent in the model are shown in grey. Colour gradients between domains indicate that the sequence has been assigned only approximately in these regions. The largest unassigned stretch coincides with DR1 and is most likely disordered. See Extended Data Fig. 2 for more details.

(Fig. 1c and Supplementary Information). Their fragmented sequence is probably the result of an insertion of peripheral domains during the evolution of RyR1 from an initially smaller protein. The bundle of up to 80-Å-long helices in the centre of α-solenoid 1 forms a characteristic solvent-exposed protrusion of the handle complemented by four shorter perpendicularly oriented α-helices (Extended Data Figs 5g and 6a). Interestingly, the protrusion comprises amino acids with approximate numbers 3,550–3,650. This region of RyR1 binds calmodulin (CaM)[16,17], which regulates the probability of RyR1 gate opening[3].

Three SPRY domains (SPRY1, SPRY2 and SPRY3), originally found in the dual-specificity kinase splA and RyRs[18], form a cluster adjacent to the periphery of α-solenoid 1 (Fig. 1). A cross-link between lysines 1,032 and 1,079 (Extended Data Fig. 4) allowed us to assign the domain that is the most remote from the centre to SPRY2. Multiple cross-links within the sequence region encompassing SPRY domains and sequence mapping experiments[19] place SPRY1 on top of the α-solenoid 1 domain, and SPRY3 below SPRY1 and SPRY2 (Fig. 1, Extended Data Fig. 4 and Supplementary Information). SPRY domains have one of the most common β-sandwich folds in eukaryotes and a broad range of functions. They are found as central domains in ligases, act as binders of regulatory proteins, and facilitate the assembly of macromolecular complexes[20]. The function of SPRY domains in RyRs is still poorly understood. However, their positions in RyR1 suggest that among other possible functions they maintain structural integrity by mediating contacts between two large α-solenoid domains and provide a scaffold for the repeat 1–2 domain.

A second α-solenoid domain, termed α-solenoid 2, forms the edges of the square-like RyR1 cytoplasmic domain. This ~200-Å-long strongly curved domain corresponds to the amino acid region between ~1,920 and ~3,500, and comprises 38 helices (Fig. 1, Extended Data Fig. 5g and Supplementary Information). It extends between the SPRY domains on one protomer and the α-solenoid 1 domain on the other. The best known function of α-solenoid domains is binding of other proteins[21]. Thus, it is very likely that at least some of the many binding partners of RyR1 interact with this exposed domain.

In the sequence of RyR1, four repeats of ~110 amino acids are organized in two tandems[22,23] (Fig. 1c). Each tandem folds into distinct V-shaped domains, termed here as repeat 1–2 and repeat 3–4 (also known as the phosphorylation domain)[12,13]. Repeat 1–2 was localized at the corners of the square-shaped cytoplasmic domain by cross-linking mass spectrometry (Supplementary Text) and interacts with SPRY2, whereas repeat 3–4 is positioned on the top central region of α-solenoid 2 (Fig. 1). Repeat 1–2 is probably involved in mediating RyR1–RyR1 interactions that result in a previously observed checkboard-like pattern on the membrane surface[24,25]. Repeat 3–4 contains a phosphorylation site at Ser 2,843 (ref. 13) in a surface-exposed loop that faces the SPRY1 domain (Extended Data Fig. 6b) and seven disease-causing mutations have been identified on the solvent-exposed surface of the domain[13]. A possible explanation for this prominent role of repeat 3–4 would be a direct interaction of RyR1 with $Ca_v1.1$ to bridge the narrow cytoplasmic space between T-tubules and membranes of the sarcoplasmic reticulum[3]. Protruding from the RyR1 surface, repeat 3–4 and SRPY1 are ideally positioned to enable such an interaction.

We found that the functionally important 50-residue-long calcium-binding EF-hand domain[26,27], containing paired EF-hands similar to CaM, is inserted into the last segment of the α-solenoid 1 domain (Fig. 1b). Such domains are known to operate as a calcium-activated conformational switch[28]. As micromolar concentrations of calcium trigger the opening of RyR1, the position of the EF-hand in the proximity of the ion gate immediately suggests an allosteric Ca^{2+}-induced molecular switch gating mechanism for RyR1.

The last 80 residues of RyR1, which are highly conserved and indispensible for the stability of the complex[29], fold into two short α-helices harboured underneath the C-terminal region of α-solenoid 1. The interaction between the carboxy terminus and the α-solenoid 1 domain

©2015 Macmillan Publishers Limited. All rights reserved

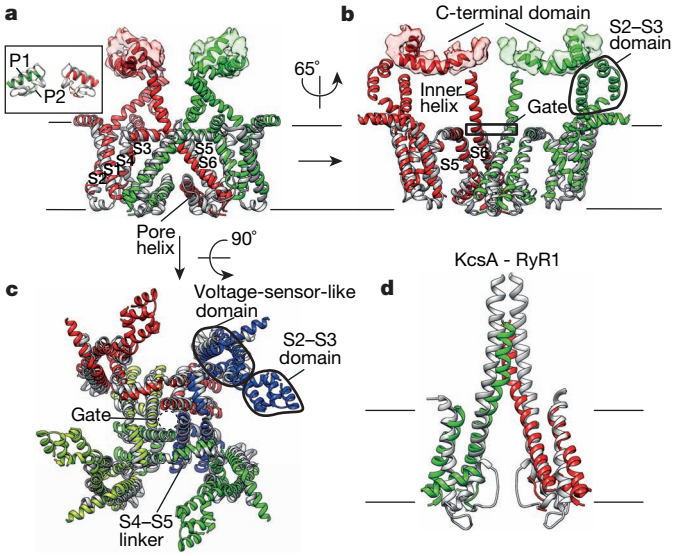


Figure 2 | Similarity between the architecture of RyR1 membrane domain and other ion channels. **a**–**c**, Comparison of the backbone of the RyR1 membrane and the C-terminal domain with the voltage-gated sodium channel Na_v (ref. 30). The corresponding root mean squared deviation is 3.7 Å for the Cα atoms of 168 residues. Views of dimers parallel (**a**, **b**) and perpendicular (**c**) to the plane of the lipid bilayer. The density of the RyR1 C-terminal domain is shown to indicate its extension in **a** and **b**. The protomers are coloured in red, yellow, green and blue. Na_v is depicted in grey. Insert in **a** shows a close-up view of filter regions in RyR1. **d**, The long inner helices continuing into the cytoplasm are similar to the regulatory helices in the prokaryotic potassium channel KcsA, suggesting that the gate in RyR1 can be similarly regulated by conformational changes in these helices. KcsA is depicted in grey.

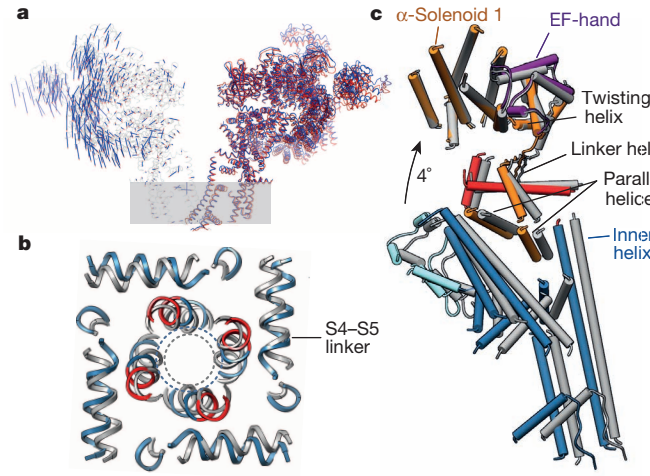


Figure 3 | Calcium-induced conformational changes in RyR1. **a**, Conformational changes between the closed state (1 mM EGTA) shown in blue and the open state (10 mM Ca^{2+}) shown in red involves global rocking movements of the clamp domain. On the right, protomers of the two states are shown in cartoon representation, on the left, the conformational changes between them are depicted as vector field. The vectors are drawn between Cα atoms and their amplitude is multiplied by a factor of 3 for better visualization. **b**, Transition from the closed (in grey) to the open (in blue for the membrane domain and in red for the C-terminal domain) state induces conformational changes that result in an 8° rotation of the linker helix and a 2 Å dilation of the gate. **c**, Transmission of conformational changes from the EF-hand to the gate of the channel. The α-solenoid 1 domain, EF-hand, C-terminal domain and membrane domain are depicted in the closed and open state (coloured as in **b**). The two structures are aligned by the α-solenoid 1 domain preceding the helices that embed the EF-hand. Rearrangement of helices in the EF-hand upon binding of calcium results in twisting of the last two α-helices of α-solenoid 1. This twist coincides with a rotation of the domain between the EF-hand domain and the membrane shifting helices separating α-solenoid 1 from the membrane surface by ~2 Å parallel to the lipid bilayer relative to the core of the α-solenoid 1 domain. Simultaneously the inner helix bends and dilates the gate.

provides a tight coupling between the position and conformation of α-solenoid 1 and the ion gate via the long inner pore helices protruding from the membrane into the cytoplasm (Figs 2a, b, 3c and Extended Data Fig. 7a).

The cryo-EM density map of the protein moiety embedded into the rounded square-shaped nanodisc (edge length ~100 Å) clearly resolves 24 transmembrane helices (Fig. 1a). Although there is no significant sequence similarity to any other ion channel of known structure, the arrangement of the helices is similar to voltage-gated ion channels, with the highest similarity to the voltage-gated sodium channel Na_v in its closed state[30] (Fig. 2a–c). Na_v is closely related to voltage-gated calcium channels Ca_v, and can be converted into a calcium-selective channel by four mutations in the selectivity filter[31].

When compared to the transient receptor potential channel TRPV1 (ref. 32), another calcium channel (Extended Data Fig. 6d, e), the overall similarity in the arrangement of helices is lower. However, the arrangement of the inner helices, especially in the gate region, together with the pore helices and loops bear similarities (Extended Data Fig. 6e), despite the apparently larger size of the pore in RyR1 compared to TRPV1.

In Na_v the ion pore is formed by the transmembrane segments S5 and S6, the pore helix (P-helix) and the filter-forming P-loop. The pore is surrounded by the four helical voltage sensors S1–S4 (Fig. 2a–c, Extended Data Fig. 5 and Supplementary Information). In spite of a ~10° larger tilt of the inner helices (S6) relative to the membrane normal in RyR1, the pore at the gate region has almost the same diameter in both proteins, consistent with both structures representing the closed state of the channels. The geometry of the filter is well resolved in RyR1 (Extended Data Fig. 5b) and is very similar in both channels. However, at the current resolution the unusual second pore helix found in Na_v is not observed in RyR1 (Fig. 2a, inset), and the overall size of the filter region is larger in RyR1 consistent with a high and unspecific cation conductance of RyR.

RyR1 and Na_v differ in regions that protrude from the membrane. In RyR1 an insertion of a 114-amino-acid-long loop that is not found in any other ion channels connects helices S2 and S3 (Fig. 2a, b). The loop folds in a α-helical domain and protrudes ~20 Å from the membrane interacting with the EF-hand domain of a neighbouring protomer and the C-terminal domain (Figs 1a and 2b). Another significant difference is that the inner helix in RyR1 continues into the cytoplasm forming a 70-Å-long continuous helix (Fig. 2). Notably, this long highly conserved helix is absent in other voltage-gated ion channels, but present in the pH-regulated prokaryotic potassium channel KcsA where it mediates gating[33] (Fig. 2d). This suggests that the long helix of RyR1 also has an important role in the gating mechanism of the channel. Thus, somewhat unexpectedly the membrane domain of RyR1 shares folds with both voltage-gated and pH-regulated ion channels, suggesting a novel mechanism of RyR1 gating.

Functional core and homology with IP_3 receptor

The structure of RyR1 has important implications for understanding the architecture of the IP_3 receptor. IP_3 receptors (IP_3Rs) are evolutionarily related to RyR channels, but have a smaller cytoplasmic domain (Extended Data Figs 7 and 8). Rigid body fitting of evolutionarily related RyR1 domains into a previously published cryo-EM structure of IP_3R1 (ref. 34) demonstrates that with only slight shifts of the domains the truncated RyR1 model explains nearly the entire density of IP_3R1, suggesting a highly conserved architecture of the two proteins (Extended Data Fig. 7b, c). The most conserved core between RyRs and IP_3Rs (Extended Data Fig. 7a, d) includes the ion filter, the inner helix, the C-terminal domain, and the C terminus of the α-solenoid 1 domain. It probably presents an ancient precursor of the channels. This core mediates most of the contacts between protomers, has an important role in

©2015 Macmillan Publishers Limited. All rights reserved

channel stability and probably forms a conserved pathway for the propagation of channel gating conformational changes. Consistently, disease-causing mutations in IP_3Rs and RyRs concentrate in these regions[3,11].

Calcium–induced conformational changes

To determine the mechanism of ion gating further we compared the two cryo-EM structures of RyR1, one determined in the absence and the other at saturating concentrations of calcium (10 mM; Extended Data Fig. 1). At 10 mM Ca^{2+}, purified RyR1 was shown to be in the state with a high open probability of the channel[35].

We first noticed that this reconstruction displayed additional density corresponding to a previously mapped binding site[36] for FKBP. Indeed, the size and shape of the density corresponded well with FKBP (Extended Data Figs 5 and 6c), which apparently represents endogenous protein co-purified with RyR1 and is present at low occupancy. FKBP interacts with the α-solenoid 1 and SPRY2 domains (Extended Data Fig. 6c), bridging these two otherwise not interacting domains.

Comparison of the structure of the closed state with the structure of the open state revealed considerable conformational changes in RyR1. The largest movement involves a collective motion of the peripheral regions of RyR1. Clamp and handle domains rotate downwards with an amplitude of ~5 Å at the periphery (Fig. 3a). This movement coincides with an expansion of the bundle of the inner pore helices by 2 Å and an outward rotation of the linker helix S4–S5 by ~8° in the membrane domain (Fig. 3b). Although conformational changes are relatively small (~1 Å) in the centre of RyR1, we could identify specific conformational changes originating from the EF-hand domain and coinciding with a relative rearrangement of α-solenoid 1 and the membrane domain underneath. These relative domain movements are best visualized when the helices of the C-terminal region of α-solenoid 1 preceding the EF-hand are structurally aligned between two conformations (Fig. 3c and Supplementary Video 1).

Transition from Ca^{2+}-free to Ca^{2+}-bound states involves a shift of α-helices in the EF-hand by ~1.5 Å, with a simultaneous twist of the last two helices of α-solenoid 1 that embed the EF-hand domain with similar amplitude (Fig. 3c). This rearrangement results in a rotation of α-solenoid 1 by ~4° relative to the domain beneath it causing displacement of the linker helix, parallel helices and the C-terminal domain (Fig. 3c). These helices are directly connected to the long inner helix that reaches through the membrane and forms the central pore. The dislocation is therefore transmitted to the inner helix and the other helices in the membrane domain resulting in a dilation of the gate. In this way, a small conformational change in the EF-hand is amplified and allosterically transmitted to the gate of the channel (Fig. 3b, c and Supplementary Video 1).

Conformational heterogeneity

Analysis of the conformational heterogeneity within the data sets revealed three different conformations for the closed and four for the open state (Extended Data Fig. 1 and Supplementary Video 2). Comparing the different conformations in the closed state we observed one major motion mode characterized by global rocking movements of the peripheral domains with an amplitude of up to 8 Å. This is very similar to the collective conformational changes between the average structures of closed and open states. This conformational change does not involve any specific rearrangement around the EF-hand, nor is it associated with a dilation of the gate (Extended Data Fig. 9a).

The four conformations identified in the presence of calcium reveal two motion modes. The most pronounced mode is characterized by a radial contraction involving a horizontal movement of 12 Å at the periphery accompanied by a similar expansion in height and a 6.6 Å upward movement of the AB domain in the centre. Although the domains move relative to each other, the overall movement can be approximated by a rigid body rotation of ~3.4° around the horizontal axis above the surface of the membrane. The transition from the more compacted to the more expanded state is also accompanied by a dilation of the four-helical bundle at the gate region by ~2 Å (Extended Data Fig. 9b). The second mode involves rocking of the upper layer on the surface of the α-solenoid 1 domain with an amplitude of ~6 Å (Extended Data Fig. 9c) and a downward movement that coincides with a dilation of the helical bundle at the gate region with an amplitude of ~2 Å. Thus, although they differ in their respective movements, both transitions in the presence of calcium result in the modification of the channel gate. Neither of these two movement modes, however, is associated with a specific domain rearrangement around the EF-hand domain.

There might be various causes for the observed conformational heterogeneity such as for example differences in post-translational modifications of individual proteins. However, because transitions between different conformations do not involve a specific rearrangement of the domains, we suggest that the main reason for conformational heterogeneity is an inherent flexibility of α-solenoids constituting the central scaffold of RyR1. Therefore we propose that the observed conformations reflect slow modes of collective thermal motions of the protein. Our hypothesis is supported by the similarity of the motions with low-frequency normal modes of the protein.

Mechanism of calcium–induced calcium release

Taken together, these data allow us to suggest the following mechanism of calcium induced gating of RyR1. Binding of Ca^{2+} to the EF-hand domain induces conformational changes that alter the position of α-solenoid 1 relative to the C-terminal and membrane domains, which increases the average gate diameter. However, like other large protein complexes[37], the 2.2-MDa RyR1 undergoes thermal collective movements occurring in the millisecond time frame that are observed here as different conformers. These thermal motions temporary open the ion gate (Fig. 4), resulting in conductivity spikes of millisecond duration

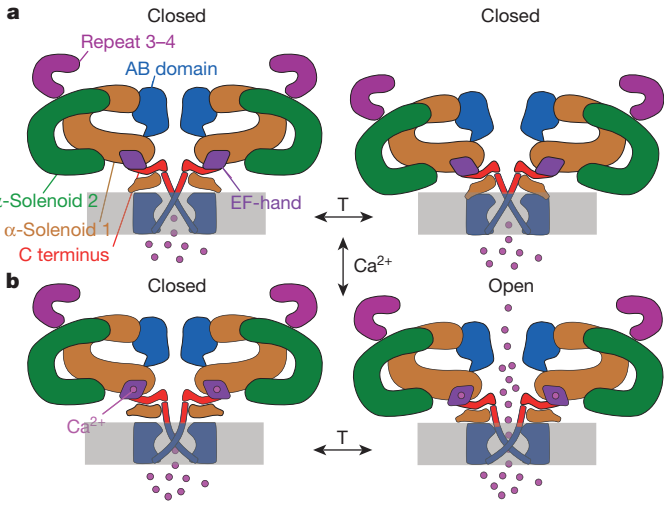


Figure 4 | Mechanism of calcium release. **a**, **b**, Schematic mechanism of Ca^{2+}-induced Ca^{2+} gating by RyR1. Dynamics of RyR1 in the absence (**a**) and presence (**b**) of cytoplasmic calcium are dominated by thermal motions. Only two states are shown representing a continuum of states in reality. The transition between the states is indicated by the letter T. Binding of Ca^{2+} ions (pink) to the EF-hand domain (purple) induces conformational changes that are transmitted to the domains underneath the α-solenoid 1 (orange) and the C-terminal domain (red). This alters the 'average' conformation of the protein and increases the probability of gate opening during collective thermal motions of the channel. The upper layer of the structure consists of the regulatory and protein–protein interaction domains (only α-solenoids, repeat 3–4 and AB domains are shown). The channel regulation through binding of accessory or regulatory proteins to these domains or their chemical modification through post-translational modifications alters the properties of thermal fluctuations and hence allosterically modifies the times and probability of opening of the RyR1 gate. The colour coding of domains is similar to Fig. 1.

©2015 Macmillan Publishers Limited. All rights reserved

observed in single-channel current measurements[35]. In this mechanism the probability of channel opening depends on the protein conformation around the inner helices and is allosterically regulated by the EF-hand, which operates as a Ca^{2+}-triggered conformational switch[28]. In the Ca^{2+}-bound state the EF-hand adjusts the conformation of the transmembrane helices forming the pore (Fig. 4b). This increases the probability of gate opening with every large-amplitude collective motion. This mechanism elegantly explains how Ca^{2+} binding increases the probability of channel opening but does not change the period of each opening event[38].

The proposed mechanism also explains the effect on gating induced by the binding of regulators to the cytoplasmic domain of RyR. FKBP, for instance, binds ~100 Å away from the gate and stabilizes both open and closed states of the channel[39,40]. It clamps two RyR domains and therefore increases friction of collective protein motions slowing them down. Disease-causing mutations altering the interfaces between the cytoplasmic domains[11] probably have similar effects, changing the properties of the collective thermal motions and consequently channel current.

In summary, the results allow us to understand the three-dimensional organization of Ca^{2+} release channels and the structural determinants of their regulation. The architecture and dynamics of RyR1 reveal how calcium binding to the EF-hand domain regulates the channel opening and facilitates calcium-induced calcium release. Our results point towards a gating mechanism that is conserved between RyR and IP_3R protein families, and provide the structural framework for further experiments towards resolving the molecular details of cellular calcium signalling.

Online Content Methods, along with any additional Extended Data display items and Source Data, are available in the online version of the paper; references unique to these sections appear only in the online paper.

Received 12 July; accepted 6 October 2014.

Published online 1 December 2014.

1. Schwaller, B. in *Calcium Signaling* (ed. Islam, M. S.) Ch. 1, 1–25 (Springer, 2012).
2. Baylor, S. M. & Hollingworth, S. Sarcoplasmic reticulum calcium release compared in slow-twitch and fast-twitch fibres of mouse muscle. *J. Physiol. (Lond.)* **551,** 125–138 (2003).
3. Lanner, J. T., Georgiou, D. K., Joshi, A. D. & Hamilton, S. L. Ryanodine receptors: structure, expression, molecular details, and function in calcium release. *Cold Spring Harb. Perspect. Biol.* **2,** a003996 (2010).
4. Kimlicka, L. & Van Petegem, F. The structural biology of ryanodine receptors. *Sci. China. Life Sci.* **54,** 712–724 (2011).
5. Hamilton, S. L. & Serysheva, I. I. Ryanodine receptor structure: progress and challenges. *J. Biol. Chem.* **284,** 4047–4051 (2009).
6. Van Petegem, F. Ryanodine receptors: allosteric ion channel giants. *J. Mol. Biol.* http://dx.doi.org/10.1016/j.jmb.2014.08.004 (15 August 2014).
7. Parys, J. B. & De Smedt, H. Inositol 1,4,5-trisphosphate and its receptors. *Adv. Exp. Med. Biol.* **740,** 255–279 (2012).
8. Mackrill, J. J. Ryanodine receptor calcium channels and their partners as drug targets. *Biochem. Pharmacol.* **79,** 1535–1543 (2010).
9. Betzenhauser, M. J. & Marks, A. R. Ryanodine receptor channelopathies. *Pflugers Arch.* **460,** 467–480 (2010).
10. Gulbis, J. M. & Doyle, D. A. Potassium channel structures: do they conform? *Curr. Opin. Struct. Biol.* **14,** 440–446 (2004).
11. Tung, C. C., Lobo, P. A., Kimlicka, L. & Van Petegem, F. The amino-terminal disease hotspot of ryanodine receptors forms a cytoplasmic vestibule. *Nature* **468,** 585–588 (2010).
12. Sharma, P. *et al.* Structural determination of the phosphorylation domain of the ryanodine receptor. *FEBS J.* **279,** 3952–3964 (2012).
13. Yuchi, Z., Lau, K. & Van Petegem, F. Disease mutations in the ryanodine receptor central region: crystal structures of a phosphorylation hot spot domain. *Structure* **20,** 1201–1211 (2012).
14. Du, G. G., Sandhu, B., Khanna, V. K., Guo, X. H. & MacLennan, D. H. Topology of the Ca^{2+} release channel of skeletal muscle sarcoplasmic reticulum (RyR1). *Proc. Natl Acad. Sci. USA* **99,** 16725–16730 (2002).
15. Marcotte, E. M., Pellegrini, M., Yeates, T. O. & Eisenberg, D. A census of protein repeats. *J. Mol. Biol.* **293,** 151–160 (1999).
16. Huang, X., Fruen, B., Farrington, D. T., Wagenknecht, T. & Liu, Z. Calmodulin-binding locations on the skeletal and cardiac ryanodine receptors. *J. Biol. Chem.* **287,** 30328–30335 (2012).
17. Maximciuc, A. A., Putkey, J. A., Shamoo, Y. & Mackenzie, K. R. Complex of calmodulin with a ryanodine receptor target reveals a novel, flexible binding mode. *Structure* **14,** 1547–1556 (2006).
18. Ponting, C., Schultz, J. & Bork, P. SPRY domains in ryanodine receptors (Ca^{2+}-release channels). *Trends Biochem. Sci.* **22,** 193–194 (1997).
19. Liu, Z., Zhang, J., Wang, R., Wayne Chen, S. R. & Wagenknecht, T. Location of divergent region 2 on the three-dimensional structure of cardiac muscle ryanodine receptor/calcium release channel. *J. Mol. Biol.* **338,** 533–545 (2004).
20. Perfetto, L. *et al.* Exploring the diversity of SPRY/B30.2-mediated interactions. *Trends Biochem. Sci.* **38,** 38–46 (2013).
21. Kobe, B. & Kajava, A. V. When protein folding is simplified to protein coiling: the continuum of solenoid protein structures. *Trends Biochem. Sci.* **25,** 509–515 (2000).
22. Takeshima, H. *et al.* Primary structure and expression from complementary DNA of skeletal muscle ryanodine receptor. *Nature* **339,** 439–445 (1989).
23. Zorzato, F. *et al.* Molecular cloning of cDNA encoding human and rabbit forms of the Ca^{2+} release channel (ryanodine receptor) of skeletal muscle sarcoplasmic reticulum. *J. Biol. Chem.* **265,** 2244–2256 (1990).
24. Ferguson, D. G., Schwartz, H. W. & Franzini-Armstrong, C. Subunit structure of junctional feet in triads of skeletal muscle: a freeze-drying, rotary-shadowing study. *J. Cell Biol.* **99,** 1735–1742 (1984).
25. Yin, C. C., Blayney, L. M. & Lai, F. A. Physical coupling between ryanodine receptor-calcium release channels. *J. Mol. Biol.* **349,** 538–546 (2005).
26. Fessenden, J. D., Feng, W., Pessah, I. N. & Allen, P. D. Mutational analysis of putative calcium binding motifs within the skeletal ryanodine receptor isoform, RyR1. *J. Biol. Chem.* **279,** 53028–53035 (2004).
27. Lewit-Bentley, A. & Rety, S. EF-hand calcium-binding proteins. *Curr. Opin. Struct. Biol.* **10,** 637–643 (2000).
28. Kuboniwa, H. *et al.* Solution structure of calcium-free calmodulin. *Nature Struct. Biol.* **2,** 768–776 (1995).
29. Gao, L., Tripathy, A., Lu, X. & Meissner, G. Evidence for a role of C-terminal amino acid residues in skeletal muscle Ca^{2+} release channel (ryanodine receptor) function. *FEBS Lett.* **412,** 223–226 (1997).
30. Payandeh, J., Scheuer, T., Zheng, N. & Catterall, W. A. The crystal structure of a voltage-gated sodium channel. *Nature* **475,** 353–358 (2011).
31. Tang, L. *et al.* Structural basis for Ca^{2+} selectivity of a voltage-gated calcium channel. *Nature* **505,** 56–61 (2014).
32. Liao, M., Cao, E., Julius, D. & Cheng, Y. Structure of the TRPV1 ion channel determined by electron cryo-microscopy. *Nature* **504,** 107–112 (2013).
33. Uysal, S. *et al.* Mechanism of activation gating in the full-length KcsA K^+ channel. *Proc. Natl Acad. Sci. USA* **108,** 11896–11899 (2011).
34. Ludtke, S. J. *et al.* Flexible architecture of IP_3R1 by Cryo-EM. *Structure* **19,** 1192–1199 (2011).
35. Smith, J. S. *et al.* Purified ryanodine receptor from rabbit skeletal muscle is the calcium-release channel of sarcoplasmic reticulum. *J. Gen. Physiol.* **92,** 1–26 (1988).
36. Samsó, M., Shen, X. & Allen, P. D. Structural characterization of the RyR1–FKBP12 interaction. *J. Mol. Biol.* **356,** 917–927 (2006).
37. Fischer, N., Konevega, A. L., Wintermeyer, W., Rodnina, M. V. & Stark, H. Ribosome dynamics and tRNA movement by time-resolved electron cryomicroscopy. *Nature* **466,** 329–333 (2010).
38. Sitsapesan, R. & Williams, A. J. Gating of the native and purified cardiac SR Ca^{2+}-release channel with monovalent cations as permeant species. *Biophys. J.* **67,** 1484–1494 (1994).
39. Gaburjakova, M. *et al.* FKBP12 binding modulates ryanodine receptor channel gating. *J. Biol. Chem.* **276,** 16931–16935 (2001).
40. Ahern, G. P., Junankar, P. R. & Dulhunty, A. F. Single channel activity of the ryanodine receptor calcium release channel is modulated by FK-506. *FEBS Lett.* **352,** 369–374 (1994).

Supplementary Information is available in the online version of the paper.

Acknowledgements We are grateful to O. Hofnagel for assistance with electron microscopy facilities and R. S. Goody for continuous support and useful comments on the manuscript. R.G.E. thanks R. Chaves and K. Willegems for assistance with particle selection. We gratefully acknowledge R. Matadeen and S. de Carlo (FEI Company) for image acquisition at the National Center for Electron Nanoscopy in Leiden (NeCEN) which is co-financed by grants from the Nederlandse Organisatie voor Wetenschappelijk Onderzoek (project 175.010.2009.001) and by the European Union's Regional Development Fund through 'Kansen voor West' (project 21Z.014). This work was funded by Humboldt Foundation (to R.G.E.), by the 'Deutsche Forschungsgemeinschaft' Grant RA 1781/1-1 (to S.R.), the Max Planck Society (to S.R. and R.G.E.), VIB and Vrij Universiteit Brussel (to R.G.E.).

Author Contributions R.G.E. designed the project and performed research, S.R. and R.G.E. managed the project, analysed data and wrote the manuscript, A.L. and R.A. performed cross-linking mass spectrometry experiments in the laboratory of R.A.

Author Information The coordinates and electron microscopy density maps for closed and open states have been deposited in the RCSB Protein Data Bank under the accession codes 4UWA and 4UWE, and in the Electron Microscopy Data Bank under the accession codes EMD-2751 and EMD-2752, respectively. Reprints and permissions information is available at www.nature.com/reprints. The authors declare no competing financial interests. Readers are welcome to comment on the online version of the paper. Correspondence and requests for materials should be addressed to R.G.E. (rouslan.efremov@vib-vub.be) or S.R. (stefan.raunser@mpi-dortmund.mpg.de).

©2015 Macmillan Publishers Limited. All rights reserved

METHODS

Purification of RyR1. RyR1 was isolated from rabbit fast twitch muscles following a modified protocol based on the method described previously[41]. Sarcoplasmic reticulum vesicles were purified first. Muscle tissue (100–300 g) was minced, suspended in 700 ml of 20 mM Tris-maleate, pH 7.0, 100 mM NaCl, 0.3 M sucrose, 1 mM EGTA, 2 mM dithiothreitol (DTT) and a cocktail of inhibitors: 4 μM leupeptine, 1 mM benzamidine, 0.1 μM aprotinin, 1 μM pepstatin, 2 μM calpain I inhibitor and 1 mM phenylmethylsulphonyl fluoride (PMSF). The suspension was homogenized in a Waring blender (3 × 15 s) and centrifuged for 30 min at 8,500*g* at 4 °C. Crystalline KCl was added to the supernatant filtered through cheesecloth to a final concentration of 0.5 M and stirred for 10 min on ice. After ultracentrifugation at 130,000*g* for 30 min the pellet was resuspended in 350 ml of buffer A (20 mM MOPS, pH 7.4, 0.6 M KCl, 0.3 M sucrose, 1 mM EGTA, 2 mM DTT and protease inhibitor cocktail) and stirred for 30 min on ice. The pellet was collected by ultracentrifugation, resuspended in 20 mM MOPS, pH 7.4, and applied on a 25–45% sucrose gradient prepared in buffer A in which PMSF was replaced by 200 μM Pefabloc. The sucrose gradient was centrifuged at 96,500*g* for 16 h at 4 °C, and fractionated into 2 ml fractions. The fractions were monitored by 4–18% SDS–PAGE and by a ^{3}H-ryanodine binding assay, and those containing RyR1 were pooled. After dilution with 20 mM MOPS, pH 7.4, sarcoplasmic reticulum vesicles were pelleted by ultracentrifugation (130,000*g* for 30 min, 4 °C), frozen in liquid nitrogen and kept at −80 °C or used for solubilization directly.

Sarcoplasmic reticulum vesicles (2 ml) were diluted in buffer B (20 mM MOPS, pH 7.4, 700 mM NaCl, 2 mM DTT, 1 mM EGTA, 1 mM PMSF, 10% sucrose and inhibitor cocktail) with 4% CHAPS (Glycon) and 1% soy lecithin (Avanti Polar Lipids) to a final volume of 5 ml. The solution was stirred for 1 h at 4 °C and centrifuged at 100,000*g* for 30 min. The filtered supernatant was first purified from an excess of Ca-ATPases by gel filtration over a 16/60 Superdex-200 column in buffer B containing 0.8% CHAPS and 0.2% lipids. Peak fractions containing RyR1 were applied on a 15–35% sucrose gradient in buffer B with 0.8% CHAPS and 0.2% lipids and separated at 154,000*g* for 14 h at 4 °C. Fractions containing RyR1 were pooled, concentrated and further purified by gel filtration on a 10/300 Superose-6 column in buffer B with 0.8% CHAPS. The purest fractions were pooled, concentrated in 100 kilodaltons (kDa) molecular mass cut-off Millipore concentrators and frozen in liquid nitrogen. The protein concentration was determined by a Pierce 660 assay (Thermo Scientific).

Reconstitution into nanodiscs. Membrane scaffold protein MSP1E3D1 was expressed and purified as described elsewhere[42]. The plasmid was a gift from M. Engelhard. A mixture of 400 nM solubilized RyR1, 800 nM membrane scaffold protein and 56 μM POPC was prepared in buffer B with 0.5% CHAPS and incubated for 2 h at 4 °C. The detergent was removed by adsorption to Bio-Beads (Bio-Rad) overnight at 4 °C.

Sample vitrification. RyR1 was vitrified in two different buffers stabilizing the channel in open and closed states, respectively. Buffer containing 10 mM MOPS, pH 7.4, 200 mM NaCl, 2 mM DTT and 10 mM $CaCl_2$ was used to prepare RyR1 in the open state, and 10 mM MOPS, pH 7.4, 200 mM NaCl and 1 mM EGTA was used to prepare RyR1 in its closed state. Just before applying the protein solution onto the electron microscopy grid, 0.2% of fluorinated octyl-maltoside, a non-solubilizing detergent, was added to the buffer to improve distribution of protein molecules in ice. Between 1 and 2 μl of RyR1 at a concentration of 1–2 mg ml^{-1} was applied onto glow discharged C-flat CF-1.2/1.3-4C carbon grids (Protochips), automatically blotted and plunged using a cryoplunge CP3 (Gatan).

Electron microscopy. Images of RyR1 in its open state were collected with a JEM-3200FSC electron microscope (JEOL) equipped with a field emission gun (FEG) at an acceleration voltage of 200 kV and an electron dose of 20–30 e^{-} Å^{-2}; the specimen was kept at liquid-nitrogen temperature. Micrographs were recorded on an 8 k × 8 k CMOS TemCam-F816 camera (TVIPS) at a magnification of 124,500 (1.253 Å per pixel). An in-column omega energy filter was used for zero-loss filtration with an energy width of 15 eV. A total number of 1,041 micrographs with a defocus range of 0.9–3.9 μm were recorded manually and with the aid of automated software EM-TOOLS (TVIPS).

A single-particle data set of RyR1 in its closed state was collected at the Netherlands Centre for Electron Nanoscopy (NeCEN) on a TITAN KRIOS electron microscope equipped with Cs corrector and high brightness FEG operating at an acceleration voltage of 300 kV. Images with an electron dose of 20 e^{-} Å^{-2} were acquired at liquid-nitrogen temperature on a Falcon 2 direct electron detector (FEI) at a magnification of 96,550, corresponding to a pixel size of 1.45 Å. In addition to the integrated image corresponding to the total exposed electron dose we collected seven consecutive frames during each exposure corresponding to a dose of 2.6 e^{-} Å^{-2} per frame. The first 83 ms of exposure, corresponding to ~2 e^{-} Å^{-2} and associated with the highest radiation induced drift[43] were not recorded. A total number of 2,320 images with a defocus range of 1.0–3.0 μm were acquired automatically using the EPU software (FEI).

Single particle data processing. The defocus of the micrographs was determined in CTFFIND3 (ref. 44), and 101,175 particles were picked semi-automatically with SIGNATURE[45] for the open state and 75,297 particles were picked manually in E2BOXER[46] for the closed state. For the open state, the particle alignment, classification and three-dimensional reconstruction were carried out in SPARX[46]. Following a coarse alignment, a 'gold standard' refinement[47] was performed to reduce noise amplification. Specifically, particle images were separated into two sets. Refinement of orientation parameters and reconstruction for each of the sets were performed independently. The resulted volumes were aligned after each round of refinement and the cross volume Fourier shell correlation (FSC) was calculated. An FSC-based filter was applied to each volume[47]. The final reconstruction was calculated from 94,354 particles to an average resolution of 8.5 Å (Extended Data Fig. 1i, k). The resolution of the electron microscopy map is not homogeneous over the volume of the structure. It is the highest close to the centre of mass of the molecule decreasing towards peripheral parts of the tetramer and towards membrane embedded region (Extended Data Fig. 1g).

The frames of the micrographs collected with the Falcon II detector were first aligned to each other using the program MotionCorr[48] to reduce beam-induced blurring of the images. Next, the data set of the closed state was aligned, classified and an initial three-dimensional reconstruction was performed in SPARX after which the three-dimensional reconstruction was refined to a resolution of 6.1 Å from the best 25,000 particles using RELION[49] (Extended Data Fig. 1a–e).

Variance analysis. Conformational variance was analysed in the data set of open RyR1 using SPARX[50]. Four conformational states were identified based on the eigenvalues principal components of the set of resampled three-dimensional volumes (only symmetry preserving modes have been analysed). Following three-dimensional classification and refinement, the data set was separated into four subsets with 23,064, 23,631, 29,957 and 24,523 particles. Refinement of particle orientation was done independently for each subset using the gold standard procedure after local randomization of parameters. The final resolution based on the FSC at 0.143 was 8.7, 9.0, 8.8 and 8.9 Å, respectively (Extended Data Fig. 1i, k). The distribution of defocuses is nearly identical in all four conformers. Conformational variance of the data set of the closed state was analysed by three-dimensional classification, which revealed three conformational classes corresponding to a transition between two different conformations. Two classes with 6,400 and 6,300 particles refined to a resolution of 9.9 and 9.7 Å, respectively, correspond to more extreme conformations, and one class with 12,300 particles refined to resolution of 9.0 Å corresponds to an intermediate conformation (Extended Data Fig. 1d, k). Local resolutions of the electron microscopy maps were calculated in ResMap[51].

Density map analysis. α-Helices were positioned into the cryo-EM density map using the find_helix_strands routine of the protein crystallography package PHENIX[52] as well as manually in Coot[53]. For analysis and visualization the density was segmented in Segger[54]. Chimera[55] was used for rigid body real space refinement of individual domain positions.

Bioinformatics tools. The following web servers were used for RyR1 secondary structure prediction: PredictProtein (http://www.predictprotein.org), SABLE (http://sable.cchmc.org/)[56], and PBIL (http://pbil.univ-lyon1.fr). Sequences were aligned in CLUSTALW v2 (ref. 57). Missing loops in the ABC domain were modelled in MODELLER[58]. SPRY domains were modelled using web server ROBETTA[59], models of repeat 1–2 and the EF-hand domain were generated with PHYRE v0.2 (ref. 60). Disordered protein regions were predicted with the IUPRED server[61]. Transmembrane helices were predicted using HMMTOP[62], TMHMM[63], PredictProtein and TMpred (http://www.ch.embnet.org/software/TMPRED_form.html).

Analysis of the ion channel sizes was performed using program PoreWalker[64]. For visualization, analysis, and preparation of electron microscopy figures, we used Chimera[55] and Pymol[65].

Chemical cross-linking and sample processing. RyR1 was cross-linked at a concentration of approximately 2 mg ml^{-1} in 20 mM MOPS, pH 7.4, 700 mM NaCl, 2 mM DTT, 200 μM EGTA, 0.8% CHAPS and 20% sucrose, by adding a 25 mM stock solution of disuccinimidyl suberate-d_0/d_{12} (Creative Molecules) in dimethyl formamide to a final concentration of 1 mM. After incubation for 30 min at 37 °C, ammonium bicarbonate was added to a final concentration of 50 mM to quench remaining cross-linking reagent. Two independent cross-linking experiments using 100 μg protein each were performed.

To avoid interferences from the detergent during mass spectrometric analysis, two different procedures were used to reduce the CHAPS concentration.

In method 1, the sample was diluted twofold with water below the critical micellar concentration of CHAPS (0.5–0.6%, w/v) and passed through a Zeba spin column (7 kDa molecular mass cut-off, Pierce/ThermoFisher Scientific) according to the manufacturer's instructions. The eluate was evaporated to dryness in a vacuum centrifuge and resuspended in 100 μl of 8 M urea solution. Disulphide bonds were reduced by addition of Tris(2-carboxyethyl)phosphine (TCEP) to a final concentration of 2.5 mM, followed by incubation at 37 °C for 30 min. The solution was

©2015 Macmillan Publishers Limited. All rights reserved

allowed to cool down to room temperature, and iodoacetamide was added to a final concentration of 5 mM to alkylate free cysteine thiol groups. The sample was incubated at room temperature for 30 min, protected from light. The reduced and alkylated sample was then diluted to 5.5 M urea by addition of 150 mM ammonium bicarbonate solution, and endoproteinase Lys-C (Wako) was added at an enzyme-to-substrate ratio of 1:100. The sample was incubated for 2 h at 37 °C, followed by an additional dilution step to 1 M urea with 50 mM ammonium bicarbonate solution. Trypsin (Promega) was added at an enzyme-to-substrate ratio of 1:50 and the sample was incubated at 37 °C overnight.

After overnight digestion, the solution was acidified with pure formic acid to a final concentration of 2% (v/v), and the sample was purified by solid-phase extraction using 50 mg SepPak tC18 cartridges (Waters). Peptides were eluted from the column with 500 µl acetonitrile/water/formic acid (50:50:0.1, by volume). The eluate was evaporated to dryness in a vacuum centrifuge and subjected to fractionation by size-exclusion chromatography (see below).

In method 2, the sample was directly digested in the presence of CHAPS. Thus, 50 µg of solid urea were added to the quenched, cross-linked sample to achieve a final urea concentration of approximately 8 M. The following steps (reduction, alkylation, Lys-C and trypsin digestion) were performed as described above. For the solid-phase extraction step, a reduced elution volume of 250 µl was used to prevent desorption of most of the detergent from the sorbent.

Samples processed using both method 1 and 2 were then fractionated individually by size-exclusion chromatography on a Superdex Peptide column (GE Healthcare) as described previously[66,67]. Fractions corresponding to elution volumes 1.0–1.1 ml and 1.1–1.2 ml were individually collected for mass spectrometry analysis and evaporated to dryness. Monitoring of the UV absorption at 214 nm during size-exclusion chromatography separation revealed a slightly higher digestion efficiency for the sample prepared according to method 1, although both samples were subsequently analysed by liquid chromatography–tandem mass spectrometry (LC–MS/MS).

Liquid chromatography-tandem mass spectrometry. Approximately 1 µg of each sample (two size-exclusion fractions from two cross-linking experiments) was analysed in duplicate on two different Orbitrap mass spectrometers (ThermoFisher Scientific).

The configuration of instrument 1 consisted of a Thermo Easy-nLC HPLC system connected to a LTQ Orbitrap XL mass spectrometer. Peptides were separated on a 11 cm self-packed column (75 µm inner diameter) filled with 3µm Magic C_{18} particles at a flow rate of 300 nl min^{-1}. The mobile phase gradient was set from 7 to 35%B (93 to 65%A) in 90 min, in which A denotes water/acetonitrile/formic acid (98:2:0.1, v/v/v) and B denotes acetonitrile/water/formic acid (98:2:0.1, v/v/v).

Mass spectrometry (MS) spectra were acquired in the orbitrap with a resolution of 60,000, and MS/MS spectra were acquired in the linear ion trap at normal scan speed following collision-induced dissociation of the five most abundant precursors per cycle (charge state ≥ 3, isolation width 2.0 m/z, normalized collision energy 35%).

The set-up for instrument 2 was a Thermo Easy-nLC 1000 HPLC system connected to an Orbitrap Elite mass spectrometer. Peptides were separated on a 15 cm Acclaim PepMap RSLC column (75 µm inner diameter, 2 µm particle size, Thermo Fisher Scientific) at a flow rate of 300 nl min^{-1}. The mobile phase gradient was set from 9 to 35%B (91 to 65%A) in 60 min, in which A denotes water/acetonitrile/formic acid (98:2:0.15, v/v/v), and B denotes acetonitrile/water/formic acid (98:2:0.15, v/v/v).

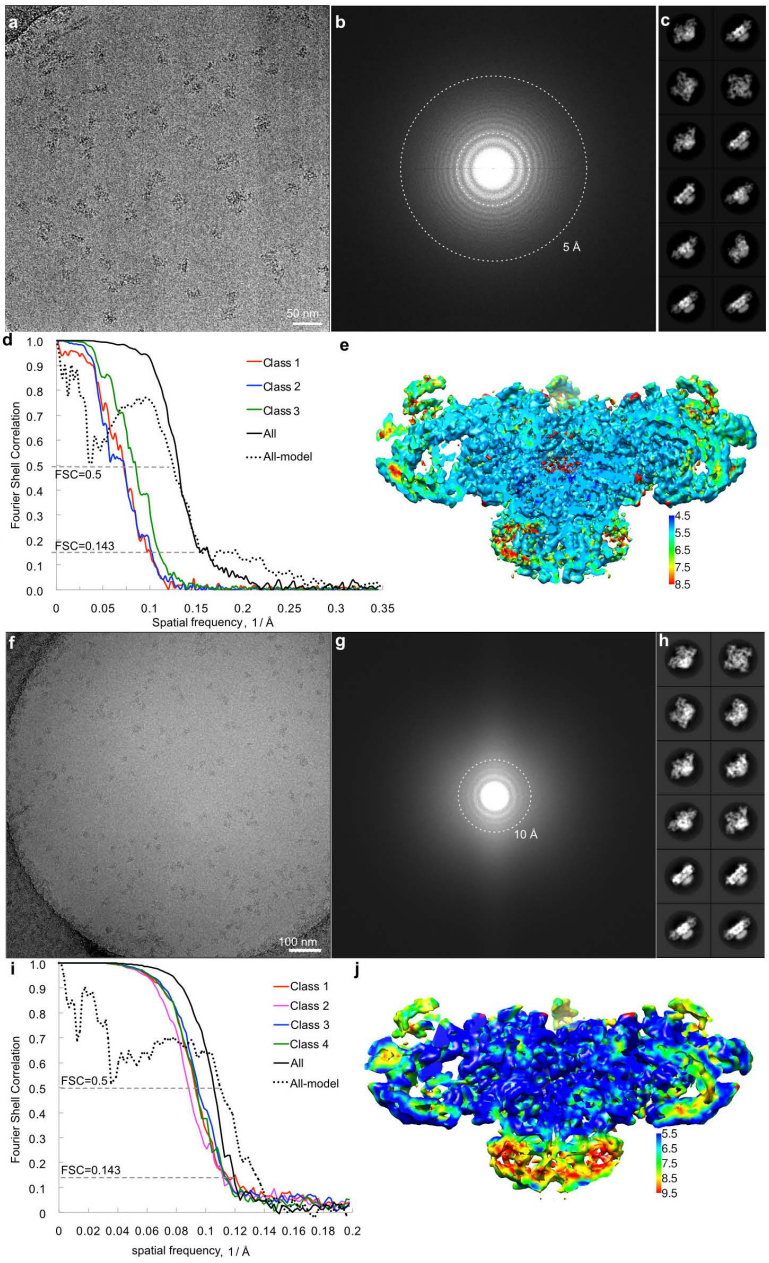
MS spectra were acquired in the orbitrap with a resolution of 120,000, and MS/MS spectra were acquired in the linear ion trap at normal scan speed following collision-induced dissociation of the ten most abundant precursors per cycle (charge state ≥ 3, isolation width 2.0 m/z, normalized collision energy 35%).

Identification of cross-linked peptides. LC–MS/MS data was searched using xQuest[68,69] against a database containing the target protein (RYR1_RABIT) as well as five contaminants (AT2A1, ADT1, G1U2E7, FKB1A and G1TZN7) identified from the analysis of a non-cross-linked sample. All protein sequences were obtained from UniProt.

Search settings included trypsin cleavage specificity and a maximum of two missed cleavage sites. All MS/MS spectra were manually evaluated and filtered according to a minimum peptide length of six residues, a minimum number of bond cleavages of four (or three adjacent ones) per chain, and a mass error of −1/+9 p.p.m. (LTQ Orbitrap XL) or −4/+5 p.p.m. (Orbitrap Elite). The lower xQuest score threshold was set to 16, which corresponds to a false discovery rate of <5% for intra-protein cross-links for a database of this size.

41. Hawkes, M. J., Diaz-Munoz, M. & Hamilton, S. L. A procedure for purification of the ryanodine receptor from skeletal muscle. *Membr. Biochem.* **8,** 133–145 (1989).
42. Ritchie, T. K. *et al.* Chapter 11 - Reconstitution of membrane proteins in phospholipid bilayer nanodiscs. *Methods Enzymol.* **464,** 211–231 (2009).
43. Campbell, M. G. *et al.* Movies of ice-embedded particles enhance resolution in electron cryo-microscopy. *Structure* **20,** 1823–1828 (2012).
44. Mindell, J. A. & Grigorieff, N. Accurate determination of local defocus and specimen tilt in electron microscopy. *J. Struct. Biol.* **142,** 334–347 (2003).
45. Chen, J. Z. & Grigorieff, N. SIGNATURE: a single-particle selection system for molecular electron microscopy. *J. Struct. Biol.* **157,** 168–173 (2007).
46. Hohn, M. *et al.* SPARX, a new environment for Cryo-EM image processing. *J. Struct. Biol.* **157,** 47–55 (2007).
47. Scheres, S. H. & Chen, S. Prevention of overfitting in cryo-EM structure determination. *Nature Methods* **9,** 853–854 (2012).
48. Li, X. *et al.* Electron counting and beam-induced motion correction enable near-atomic-resolution single-particle cryo-EM. *Nature Methods* **10,** 584–590 (2013).
49. Scheres, S. H. RELION: implementation of a Bayesian approach to cryo-EM structure determination. *J. Struct. Biol.* **180,** 519–530 (2012).
50. Penczek, P. A., Kimmel, M. & Spahn, C. M. Identifying conformational states of macromolecules by eigen-analysis of resampled cryo-EM images. *Structure* **19,** 1582–1590 (2011).
51. Kucukelbir, A., Sigworth, F. J. & Tagare, H. D. Quantifying the local resolution of cryo-EM density maps. *Nature Methods* **11,** 63–65 (2014).
52. Adams, P. D. *et al.* PHENIX: building new software for automated crystallographic structure determination. *Acta Crystallogr. D* **58,** 1948–1954 (2002).
53. Emsley, P. & Cowtan, K. Coot: model-building tools for molecular graphics. *Acta Crystallogr. D* **60,** 2126–2132 (2004).
54. Pintilie, G. & Chiu, W. Comparison of Segger and other methods for segmentation and rigid-body docking of molecular components in cryo-EM density maps. *Biopolymers* **97,** 742–760 (2012).
55. Pettersen, E. F. *et al.* UCSF chimera – a visualization system for exploratory research and analysis. *J. Comput. Chem.* **25,** 1605–1612 (2004).
56. Adamczak, R., Porollo, A. & Meller, J. Accurate prediction of solvent accessibility using neural networks-based regression. *Proteins* **56,** 753–767 (2004).
57. Larkin, M. A. *et al.* Clustal W and Clustal X version 2.0. *Bioinformatics* **23,** 2947–2948 (2007).
58. Fiser, A., Do, R. K. & Sali, A. Modeling of loops in protein structures. *Protein Sci.* **9,** 1753–1773 (2000).
59. Kim, D. E., Chivian, D. & Baker, D. Protein structure prediction and analysis using the Robetta server. *Nucleic Acids Res.* **32,** W526–W531 (2004).
60. Kelley, L. A. & Sternberg, M. J. Protein structure prediction on the Web: a case study using the Phyre server. *Nature Protocols* **4,** 363–371 (2009).
61. Dosztányi, Z., Csizmok, V., Tompa, P. & Simon, I. IUPred: web server for the prediction of intrinsically unstructured regions of proteins based on estimated energy content. *Bioinformatics* **21,** 3433–3434 (2005).
62. Tusnády, G. E. & Simon, I. The HMMTOP transmembrane topology prediction server. *Bioinformatics* **17,** 849–850 (2001).
63. Krogh, A., Larsson, B., von Heijne, G. & Sonnhammer, E. L. Predicting transmembrane protein topology with a hidden Markov model: application to complete genomes. *J. Mol. Biol.* **305,** 567–580 (2001).
64. Pellegrini-Calace, M., Maiwald, T. & Thornton, J. M. PoreWalker: a novel tool for the identification and characterization of channels in transmembrane proteins from their three-dimensional structure. *PLOS Comput. Biol.* **5,** e1000440 (2009).
65. DeLano, W. L. The PyMOL Molecular Graphics System version 1.3r1 (Schrödinger, LLC, 2010).
66. Leitner, A. *et al.* Expanding the chemical cross-linking toolbox by the use of multiple proteases and enrichment by size exclusion chromatography. *Mol. Cell. Proteomics* **11,** M111.014126 (2012).
67. Leitner, A., Walzthoeni, T. & Aebersold, R. Lysine-specific chemical cross-linking of protein complexes and identification of cross-linking sites using LC–MS/MS and the xQuest/xProphet software pipeline. *Nature Protocols* **9,** 120–137 (2014).
68. Rinner, O. *et al.* Identification of cross-linked peptides from large sequence databases. *Nature Methods* **5,** 315–318 (2008).
69. Walzthoeni, T. *et al.* False discovery rate estimation for cross-linked peptides identified by mass spectrometry. *Nature Methods* **9,** 901–903 (2012).

©2015 Macmillan Publishers Limited. All rights reserved



k

Dataset	Ca^{2+} /EGTA concen-tration	Number of particles	Resolution ($FSC_{1/2MAP-1/2MAP}$ 0.143), Å	Resolution ($FSC_{map-model}$ 0.5), Å	Image pixel size, Å	Defocus range, mm	Detector
JEOL all	10 mM Ca^{2+}	94,354	8.5	9.0	2.53	0.9-3.9	TemCam-F816
JEOL class 1		23,064	8.7				
JEOL class 2		23,631	9.0				
JEOL class 3		29,957	8.8				
JEOL class 4		24,523	8.9				
FEI all	1mM EGTA	25,000	6.1	8.0	1.45	1.0-3.0	Falcon II
FEI class 1		6,400	9.9				
FEI class 2		6,300	9.7				
FEI class 3		12,300	9.0				

Extended Data Figure 1 | Quality of electron microscopy data. **a**–**j**, Data collected on a FEI Titan Krios in 1 mM EGTA (**a**–**e**) and on a JEOL 3200 microscope in 10 mM $CaCl_2$ (**f**–**j**). **a**, **f**, Typical low dose cryo-EM micrographs of RyR1 vitrified in holey carbon grid recorded at an accelerating voltage of 300 kV (**a**) and 200 kV (**f**). **b**, **g**, Power spectra of the low dose micrographs. Thon rings are visible up to a resolution of 5 Å (**b**) and 10 Å (**g**). **c**, **h**, Representative two-dimensional class averages calculated in SPARX (**c**) and RELION (**h**) show characteristic views of RyR1. **d**, **i**, FSC curves between two independently refined half data sets (gold standard) shown for a set of all particles (solid black) and different conformational states (coloured curves). FSC between the volume calculated from all particles and the molecular model of RyR1 are shown as dotted black curves. FSC levels of 0.143 and 0.5 corresponding to the resolution cut off for density maps and the model are indicated. According to the 0.5 criterion the resolution of the model is 8.0 and 9.0 Å for the RyR1 reconstructions of closed and open states. The resolution is slightly lower than that of the map because of incompleteness of the model (the polyalanine model accounts for only about half of all the atoms of RyR1). **e**, **j**, Three-dimensional map of RyR1 coloured according to the local resolution calculated in ResMap from two unmasked volumes calculated from independently refined halves of the data sets. The resolution of the electron micoscropy map is heterogeneous with the highest resolution close to the centre of the molecule and the lowest resolution at the periphery. **k**, Statistics of single particle data.

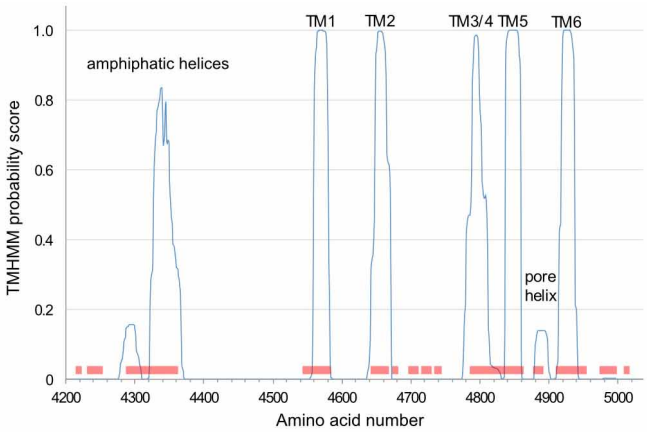
©2015 Macmillan Publishers Limited. All rights reserved



Extended Data Figure 2 | Consensus secondary structure prediction for rabbit RyR1 generated in SABLE. Extension of domains is indicated by rectangles colour-coded as in Fig. 1. Except for the N-terminal AB domain and the three SPRY domains located in the first 1,650 residues, RyR1 is predicted to fold mainly in α-helices connected with coiled structures. The 165 amino acid sequence between residues 4,375 and 4,540, connecting the amphipathic region with the transmembrane domain, is glycine- and proline-rich and predicted to be disordered.

©2015 Macmillan Publishers Limited. All rights reserved

a



b

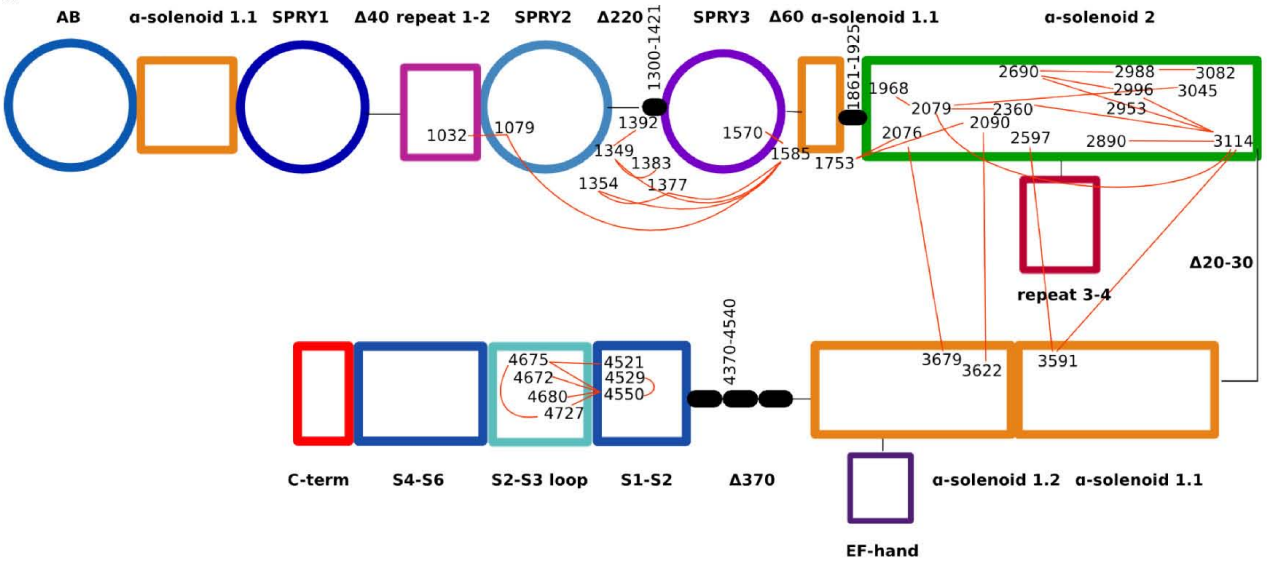
TM helix No.	Experimental topology mapping model	Uniprot	HMMTOP	TMHMM	Predict Protein	TMpred
Amph*		4,330-4,350	4,333-4,350	4,327-4,349	4,333-4,354	4,327-4,353
1	**4,557-4,576**	**4,559-4,579**	**4,567-4,584**	**4,558-4,580**	**4,561-4,578**	**4,567-4,585**
2	**4,637-4,662**	**4,641-4,661**	**4,648-4,665**	**4,648-4,670**	**4,646-4,663**	**4,646-4,666**
3	**4,776-4,800**	**4,780-4,800**	**4,794-4,811**	**4,789-4,811**	**4,790-4,814**	**4,785-4,809**
4	**4,803-4,825**	**4,807-4,827**				
5	**4,834-4,854**	**4,839-4,859**	**4,842-4,859**	**4,837-4,859**	**4,840-4,857**	**4,841-4,861**
6	**4,911-4,935**	**4,920-4,940**	**4,919-4,936**	**4,918-4,937**	**4,918-4,936**	**4,919-4,942**

*Amph – amphipathic region predicted as TM helix.

Extended Data Figure 3 | Positions of transmembrane helices. **a**, The probability for the formation of transmembrane helices calculated by the program TMHMM is shown for the C-terminal region of RyR1. Red bars indicate α-helices predicted in SABLE. The consensus transmembrane (TM) helices are unambiguously recognized and clearly separated, except of TM3 and TM4, which have nearly no solvent exposed loop in between. The amphipathic and pore helices are also clearly indicated, but have lower hydrophobicity scores than the transmembrane helices. **b**, Experimental mapping and prediction of transmembrane helices. Sequence ranges of computationally predicted, annotated and experimentally mapped transmembrane helices. Consensus helices between experimental mapping and computational prediction are indicated in bold. Although computational methods suggest just one TM3 helix instead of TM3/4, the width of the hydrophobic region corresponding to helix TM3 is consistent with the presence of two joint transmembrane helices as observed in the topology mapping experiments[14].

©2015 Macmillan Publishers Limited. All rights reserved

a

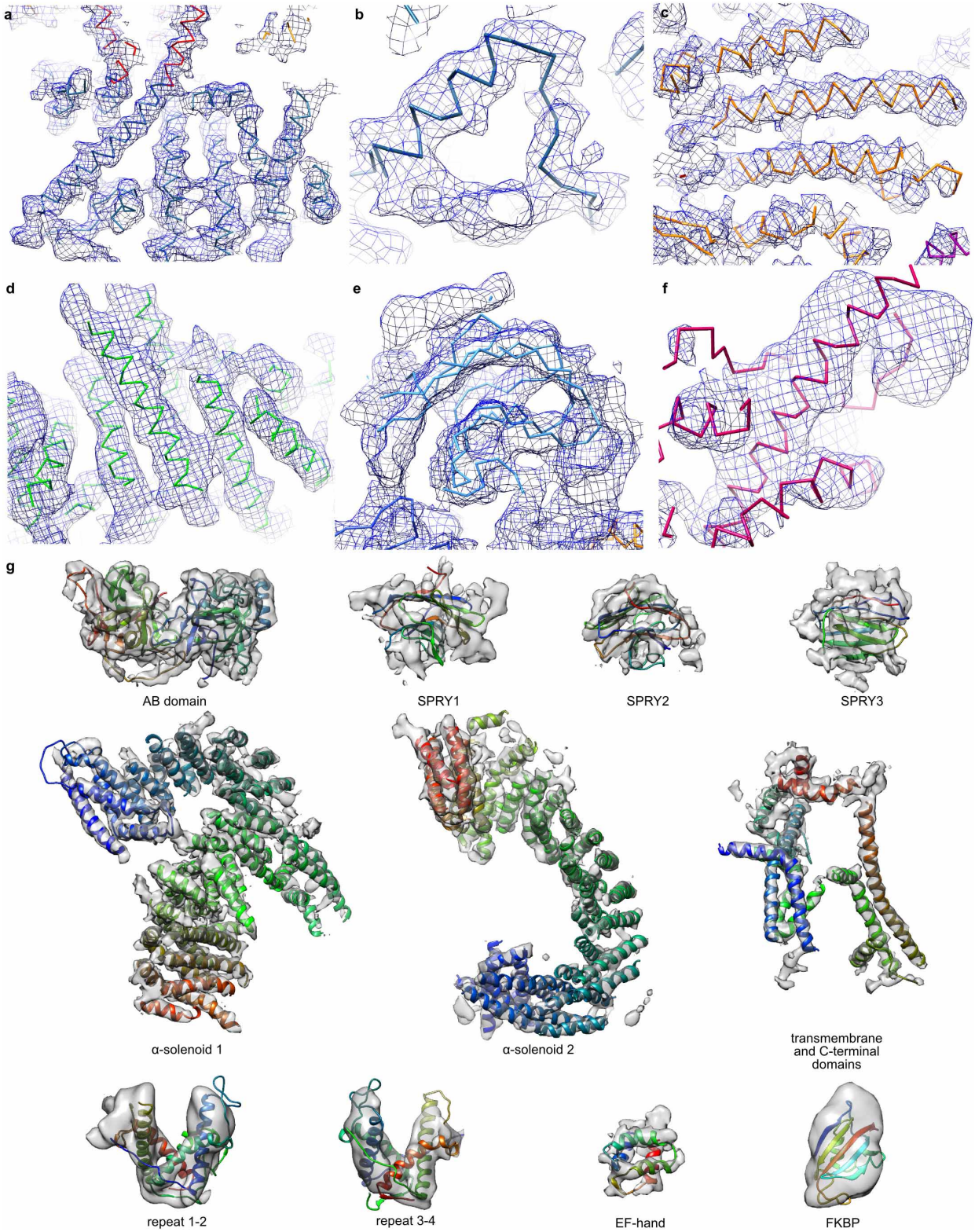


b

Residue 1	Residue 2	ID score	Distance/position in the model
SPRY and repeat domains			
1032	1079	29.04	24 Å
1354	1377	18.59	
1349	1383	24.52	DR2 is compact, SPRY2-SPRY3 close to each other
1349	1392	27.2	
1349	1585	25.04	
1395	1585	21.07	C-terminus of SPRY2 and C-terminus of SPRY3 are relatively close
1354	1585	26.24	
1570	1585	23.04	
1079	1585	26.38	$Cα_{1079}$-$Cα_{1571}$ 28 Å, N-terminus of SPRY2 close to C-terminus of SPRY3
α-solenoid 2			
1753	2076	27.18	Cross-links to N-terminal region
1753	2090	19.24	
1968	2079	22.29	Intra α-solenoid cross-links
2079	2360	27.19	
2079	3045	18.4	
2079	3114	20.39	
2360	3114	24.48	
2890	3114	19.12	
2690	3114	24.31	
2690	2988	25.92	
2988	3082	25.13	
2690	2996	24.31	
2953	3114	29.47	
2076	3679	20.74	Cross-links to C-terminal region
2090	3622	17.08	
2597	3591	23.44	
3114	3591	17.6	
S2-S3 loop			
4521	4675	22.39	
4675	4550	28.87	25 Å
4672	4550	32.28	21 Å
4680	4550	17.53	33 Å
4727	4550	21.54	28 Å
4727	4675	29.75	15 Å

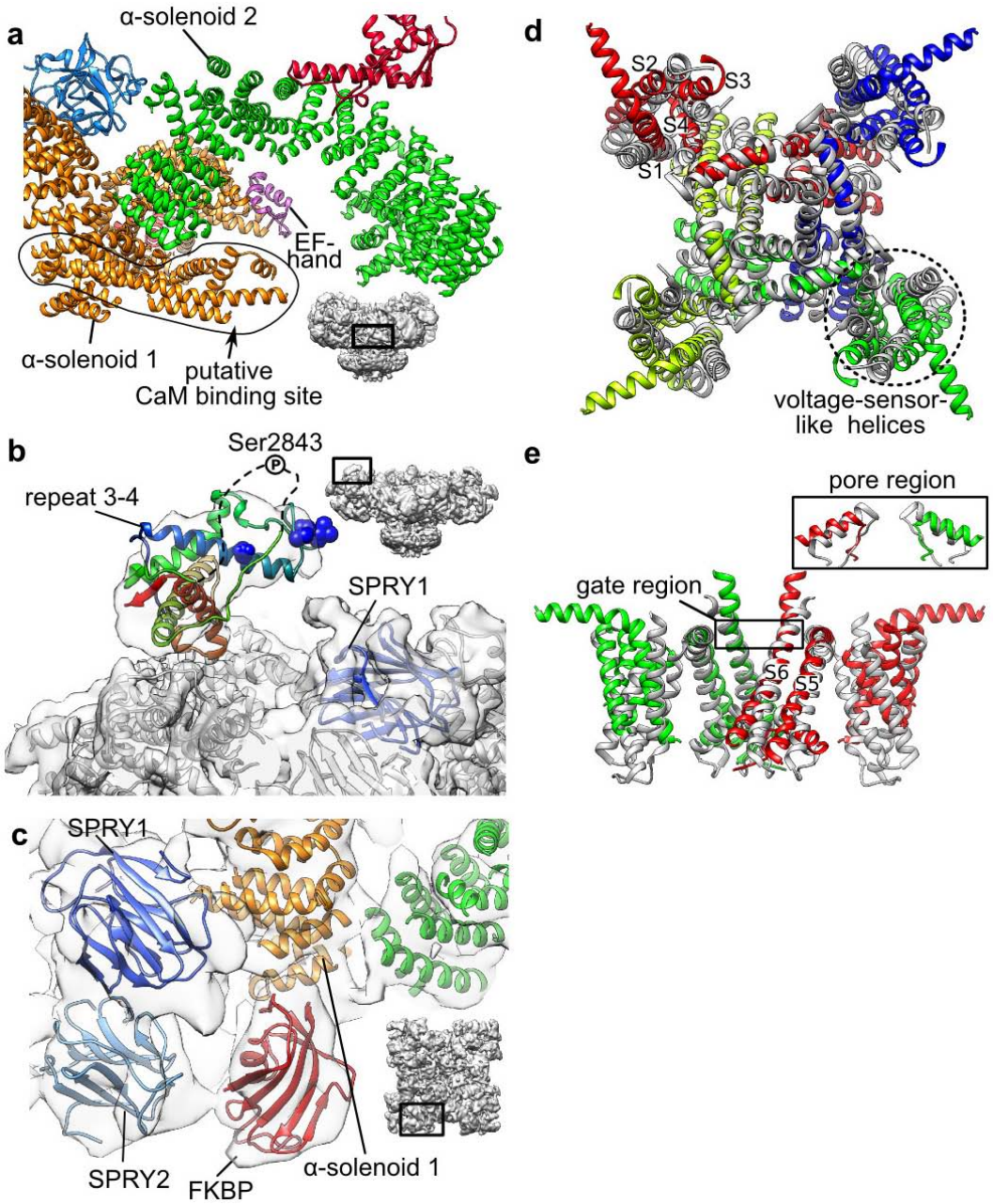
Extended Data Figure 4 | Cross-links identified within RyR1. **a**, **b**, Graphical representation (**a**) and table (**b**) summarizing cross-links identified in cross-linking mass spectrometry experiments. **a**, Schematic representation of RyR1 domains colour-coded similar to domains in Fig. 1. The repeat 3–4 and EF-hand domains are shown as inserts into the α-solenoid 1.1 and α-solenoid 1.2 domains, respectively. The cross-links are shown by red lines. The approximate length of linkers joining domains is indicated by 'Δ' followed by the number of residues. Disordered regions of linking fragments are shown as fat dotted lines and their positions in the amino acid sequence are indicated. Domains containing β-sheets are depicted as circles, α-helical domains are shown as squares. **b**, Cross-linked residues are shown with ID score and their distances in the built model (see Supplementary Table 1 for complete list of identified cross-links).

©2015 Macmillan Publishers Limited. All rights reserved



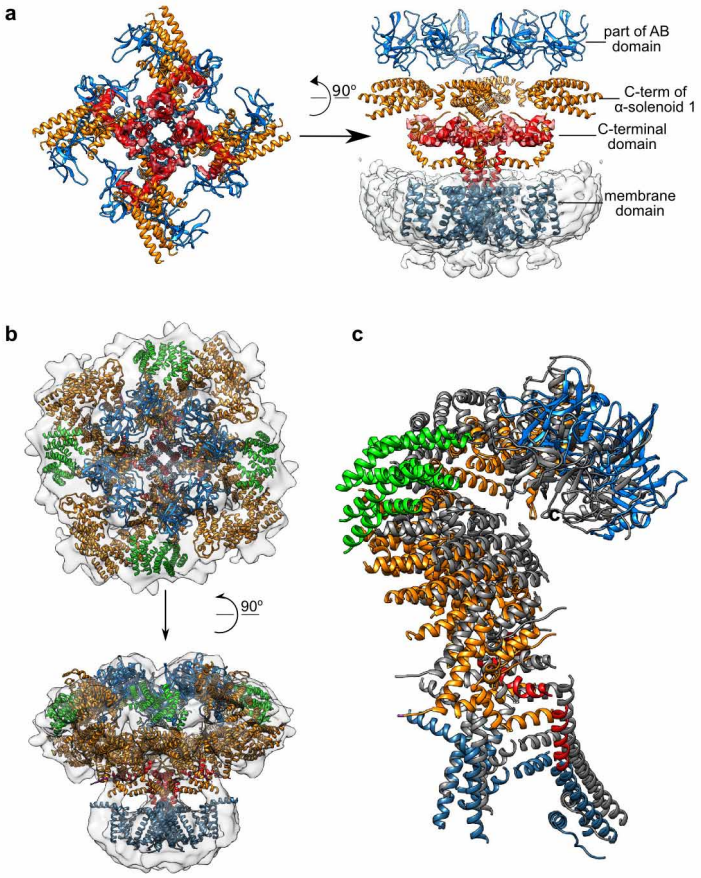
Extended Data Figure 5 | Cryo-EM density map of RyR1 at 6.1 Å resolution. **a**–**f**, Backbone of the model in ribbon representation coloured as in Fig. 1 and cryo-EM density map from different regions of the structure are shown. **a**, Transmembrane region showing the inner helix and the helices of the voltage-sensor-like domain. The cytoplasmic part of the inner helix (in red) is resolved as good as the transmembrane helices indicating that the resolution inside the lipid nanodisc is similar to the nearby cytoplasmic regions. **b**, Pore helix and pore loops showing the absence of the second pore helix found in structurally homologous Na_v channels. **c**, **d**, Helices of α-solenoid domains 1 (**c**) and 2 (**d**). **e**, Fit of the SPRY2 domain in the density. **f**, One of the least resolved domains, repeat 1–2, rod-shaped densities corresponding to α-helices are visible. **g**, Structure and density maps of individual domains. Segments of the 6.1 Å RyR1 density map corresponding to individual domains of RyR1 are shown together with the ribbon models of the domains in rainbow colouring from the N terminus (blue) to the C terminus (red). The excellent fitting of the crystallographic model of the N-terminal AB domain (residues 12–532)[11] into the density, even revealing conformation of loops that were disordered in the crystal structure, indicates the high quality of our electron microscopy map. The density segment for FKBP bound to RyR1 was extracted from the 8.5 Å cryo-EM map of RyR1 in its open state.

©2015 Macmillan Publishers Limited. All rights reserved



Extended Data Figure 6 | Details of the RyR1 structure. **a**, The α-helical protrusion in α-solenoid 1 (contoured) includes an 80-Å-long α-helix and a bundle of helices exposed to solvent and represents a potential CaM-binding site. **b**, The phosphorylation loop (shown schematically since it was not resolved in the crystal structure) of repeat 3–4 (shown in rainbow colouring from N to C terminus) is exposed to solvent. Mutations of seven residues (four of which are shown as blue spheres) close to the potential phosphorylation site cause human diseases suggesting functional importance of this region and its potential involvement in the interaction with $Ca_v1.1$ channels. **c**, FKBP (red) bound to RyR1 resolved in the cryo-EM map of RyR1 in presence of 10 mM Ca^{2+}. It interacts with the SPRY2 and the α-solenoid 1 domains. **d**, **e**, Comparison of the backbone of the RyR1 (coloured in red, yellow, green and blue) membrane domain with the TRPV1 channel (grey). Views perpendicular to (**d**) and parallel to (**e**) the membrane plane are shown. The tilt of transmembrane helices in the voltage-sensor domain (S1–S4) is different between the two proteins, while positions of inner helices (S6) in the gate region and architecture of the pore region shown as insert in **e** are similar.

©2015 Macmillan Publishers Limited. All rights reserved

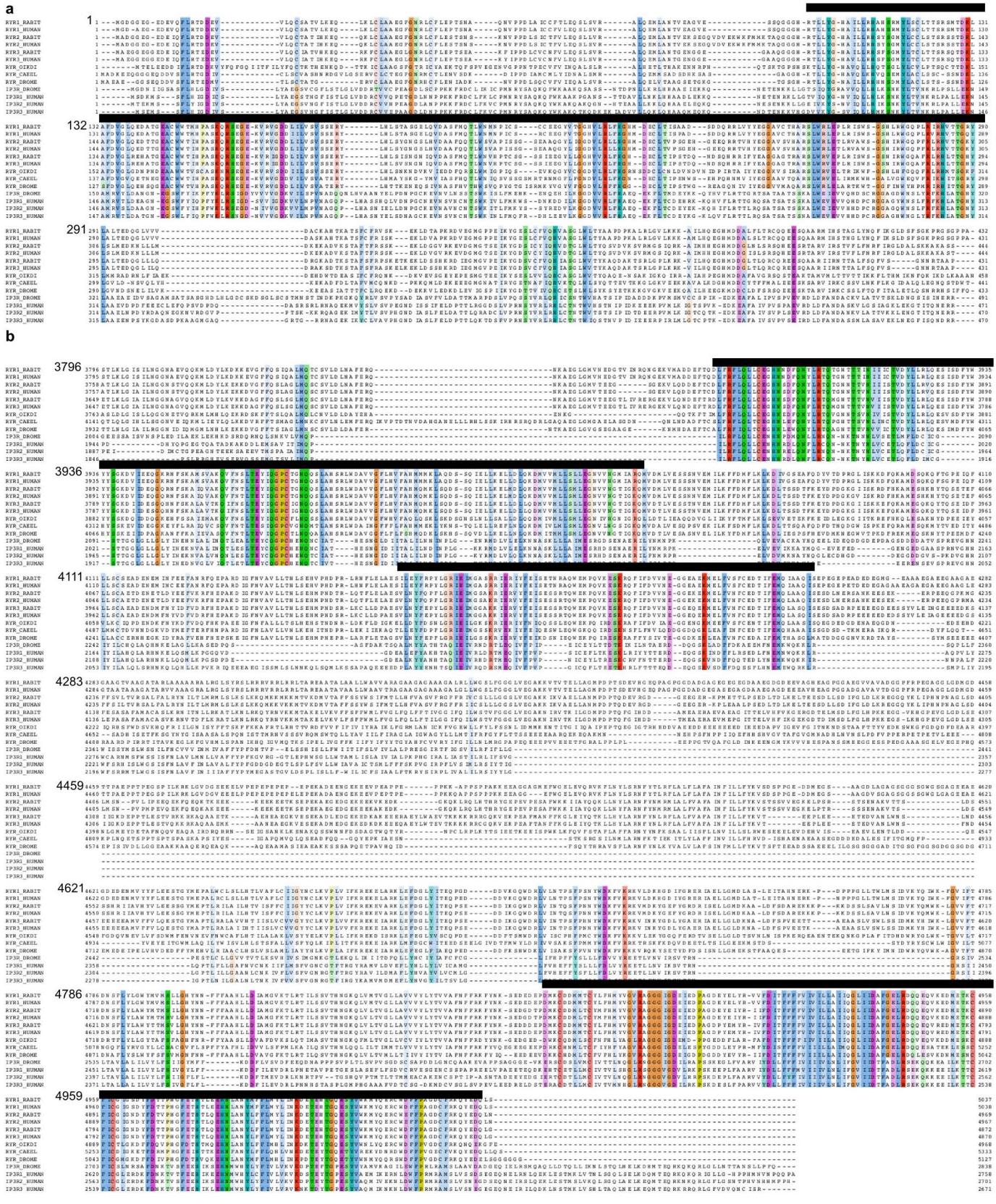


d

Domain	Residue Range	
	Rabbit RyR1	Human IP3R1
part of AB domain	**99 – 293**	**113 – 314**
RIH1 (part of α-solenoid 1)	441 – 633	473 – 664
RIH2 (part of α-solenoid 2)	2,155 – 2,477	1,186 – 1,426
RIH3 (part of α-solenoid 1)	**3,884 – 4,050** **4,171 – 4,251**	**1,977 – 2,023** **2,194 – 2,268**
S2	4,639 – 4,686	2,358 – 2,406
S3	4,781 – 4,802	2,446 – 2,467
Filter, S5-S6, C-terminus	**4,873 – 5,034**	**2,433 – 2,695**

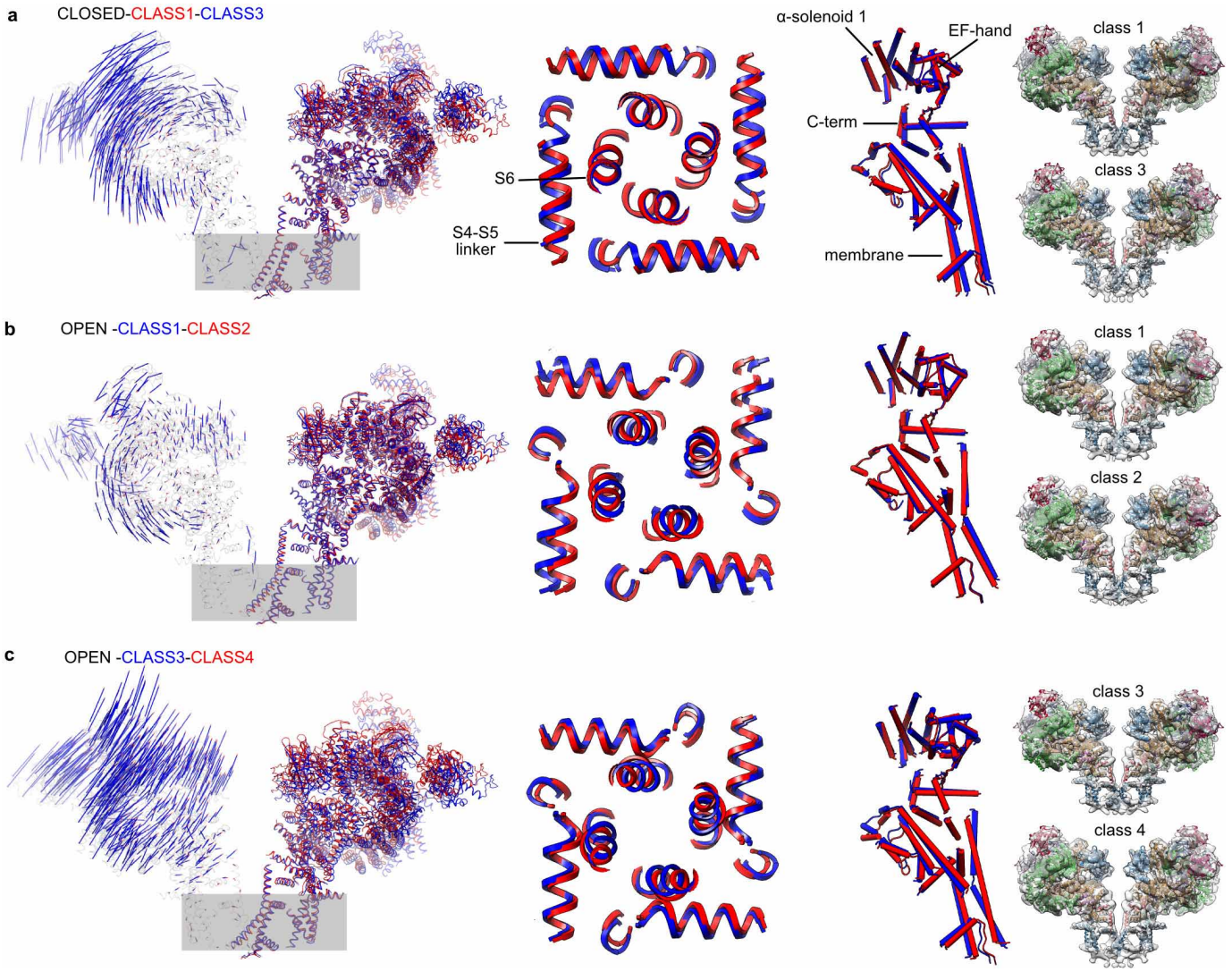
Extended Data Figure 7 | Conserved architecture of RyR and IP_3R channels. **a**, Conserved core between RyRs and IP_3Rs. The evolutionarily most conserved and likely functionally important core includes part of the AB domain bridging the C-terminal regions of the α-solenoid 1 (blue), the C terminus of α-solenoid 1 (orange), which is in direct contact with the C-terminal domain (red). To indicate better the extent of the C-terminal domain the corresponding density segments are shown. The helices of the membrane domain are shown in dark blue. In the side view the density of the nanodisc is shown in light grey. The colour coding is identical to Fig. 1. **b**, **c** Fit of RyR1 domains in the IP_3R1 density map. **b**, Rigid body fit of the RyR1 domains conserved between IP_3Rs and RyRs into the 17 Å resolution cryo-EM density map of IP_3R1 (ref. 34) shows a high correlation coefficient of 0.90. **c**, Positions of the individual domains in RyR1 (grey) compared to their positions in IP_3R1 (coloured). The colour coding is the same as in Fig. 1. Although the middle part of the α-solenoid 1 domain is not conserved, the secondary structure prediction of this region in IP_3R1 is similar to RyR1 containing mainly α-helices. We therefore included it in the fit and it agrees well with the density. The complete transmembrane region was included in the fit as the architecture of the ion-channel domain is extremely conserved even between more distant channels. With the exception of RIH2 (2155–2477), which shifted by ~70 Å (this domain for RyR1 corresponds to the α-solenoid 2 domain and is omitted from the figure), all other domains had only minor shifts. The large shift of RIH might be caused by the actual shift that occurred as α-solenoid 2 evolved or by reverse directionality of the solenoid domain (Supplementary Information). **d**, Conserved sequence regions between RyR1 and IP_3R1. Numbering corresponds to rabbit RyR1 and human IP_3R1, respectively. The most conserved regions are highlighted in bold.

©2015 Macmillan Publishers Limited. All rights reserved



Extended Data Figure 8 | Sequence conservation between RyRs and IP_3Rs. **a**, **b**, The most conserved regions between RyRs and IP_3Rs are in the N-terminal (**a**, residues 1–432 rabbit RyR1) and C-terminal (**b**, residues 3,796–5,037 rabbit RyR1) sequence regions. Amino acid sequences were aligned in CLUSTALW2, the amino acids with conservation >50% were coloured in clustalw colour scheme. Domains with the highest conservation are indicated with black bars. Aligned sequences from top to bottom are: rabbit RyR1, human RyR1, rabbit RyR2, human RyR2, rabbit RyR3, human RyR3, *Oikopleura dioica* RyR, *Caenorhabditis elegans* RyR, *Drosophila melanogaster* RyR, *Drosophila melanogaster* IP_3R and human IP_3R1, 2 and 3.

©2015 Macmillan Publishers Limited. All rights reserved



Extended Data Figure 9 | Conformational dynamics of RyR1 in closed and open states. **a**–**c**, Collective motions, changes in the gate region and relative domain movements between different conformations in the closed (**a**) and open (**b**, **c**) states. Left panels: on the right, protomers of the respective two states are shown in cartoon representation, on the left, the conformational changes between them are depicted as vector field. Second panel from left: top view on the pore region depicting the S4–S5 linker and the inner pore helices. Third panel form left: membrane domain, C-terminal domain, α-solenoid 1, and EF-hand of two different conformations in solid-cylinder representation. As in Fig. 3c the structures were aligned to the core of the α-solenoid 1 domain preceding the helices that embed the EF-hand. Similarities between the structures point towards an absence of the specific conformational changes between the conformers from the same data set. Right panels show densities of RyR1 dimers corresponding to different conformations with fitted RyR1 models.

©2015 Macmillan Publishers Limited. All rights reserved

Extended Data Table 1 | Structural domains of RyR1

Domain	Amino acid sequence range	Number of residues	Cross correlation coefficient *	Source of the molecular model
AB	**1-394**	**394**	**0.88**	**Crystal structure PDB code 2AOX**
α-solenoid 1	395-~590 ~1,646 - ~1,860 ~3,500 - ~4,080 ~ 4,135 - ~4,250	~ 1,100	0.88	Crystal structure of C domain, PDB code 2AOX is the N-terminal region of a continuous pattern of α-helical arrangement corresponding to an α-solenoid with a core made of 30 α-helices
SPRY1	**646-842**	**197**	**0.81**	**Residues 650-799 modelled in ROBETTA**
Repeat 1-2	**851-1,053**	**202**	**0.86**	**Modelled in PHYRE 2**
SPRY2	**1,070-1,310**	**240**	**0.84**	**Residues 1,074-1,210 modelled in ROBETTA**
DR2	1,342-1,403	62	NA	Predicted as disordered 1300-1421, 122 residues, not built
SPRY3	**1,420-1,571**	**152**	**0.76**	**Residues 1420-1571 modelled in ROBETTA**
DR3	1,872-1,923	52	NA	Predicted as disordered 1861-1925, 65 residues, not built
α-solenoid 2	~1,920-~2,730 ~2,940-~3,500	~1,600	0.91	Unambiguous pattern of α-helical arrangement corresponding to α-solenoid made of 38 α-helices
Repeat 3-4 (phosphorylation domain)	**2,734-2,939**	**205**	0.90	**Crystal structure PDB code 4ERT**
EF-hand	**4,084-4,135**	**52**	0.85	**Modelled in PHYRE2 residues 4069-4123**
DR1	4,254 – 4,631	378	NA	Predicted as disordered 4370-4540, 170 residues, not built
Transmembrane domain	4,540-4,936	397	0.92	Polyalanine model with approximate sequence based on structural homology with Shaker channel PDB code 2R9R Map segmentation, secondary structure prediction (4 α-helices), constructed poly-alanine model
Inter S2-S3 domain	4,666-4,779	114		
C-terminal domain	4,947-5,037	91		Density connectivity and fragmentation, consistent with secondary structure prediction, predicting 3 α-helices
FKBP			**0.85**	**PDB code: 1D6O**

Sequence region corresponding to each domain and correlation coefficient between the domain and the map as well as source of the domain model are indicated. Domains, with known structure or modelled structure are shown in bold.
* The cross correlation coefficient was calculated between the segment of the experimental map that corresponds to the domain and the density calculated from the model to resolution of 6.1 Å. For FKBP the density of the RyR1 in its partially open state was used and the model density was calculated with maximum resolution of 8.5 Å.

©2015 Macmillan Publishers Limited. All rights reserved

ARTICLE

doi:10.1038/nature13950

Structure of a mammalian ryanodine receptor

Ran Zalk[1]*, Oliver B. Clarke[2]*, Amédée des Georges[2]*, Robert A. Grassucci[2,3], Steven Reiken[1], Filippo Mancia[1], Wayne A. Hendrickson[1,2], Joachim Frank[2,3,4] & Andrew R. Marks[1,5,6]

Ryanodine receptors (RyRs) mediate the rapid release of calcium (Ca^{2+}) from intracellular stores into the cytosol, which is essential for numerous cellular functions including excitation–contraction coupling in muscle. Lack of sufficient structural detail has impeded understanding of RyR gating and regulation. Here we report the closed-state structure of the 2.3-megadalton complex of the rabbit skeletal muscle type 1 RyR (RyR1), solved by single-particle electron cryomicroscopy at an overall resolution of 4.8 Å. We fitted a polyalanine-level model to all 3,757 ordered residues in each protomer, defining the transmembrane pore in unprecedented detail and placing all cytosolic domains as tertiary folds. The cytosolic assembly is built on an extended α-solenoid scaffold connecting key regulatory domains to the pore. The RyR1 pore architecture places it in the six-transmembrane ion channel superfamily. A unique domain inserted between the second and third transmembrane helices interacts intimately with paired EF-hands originating from the α-solenoid scaffold, suggesting a mechanism for channel gating by Ca^{2+}.

Ryanodine receptors (RyRs) are intracellular Ca^{2+} release channels on the sarcoplasmic and endoplasmic reticula required for fundamental cellular functions in most tissues, including skeletal and cardiac muscle excitation–contraction coupling, synaptic transmission and pancreatic beta cell function[1]. The type 1 ryanodine receptor (RyR1) mediates excitation–contraction coupling in skeletal muscle. It is a homotetramer of four ~565-kilodalton (kDa) channel-forming protomers, as well as regulatory subunits, enzymes and their respective targeting/anchoring proteins, forming a macromolecular complex that exceeds 3,000,000 daltons[2]. In most tissues, RyRs are activated by the inward flow of Ca^{2+} via plasma-membrane Ca^{2+} channels, resulting in a massive and rapid release of Ca^{2+} from intracellular stores (a process known as Ca^{2+}-induced Ca^{2+} release). By contrast, in skeletal muscle, approximately 50% of RyR1 channels are mechanically activated by direct interaction with voltage-gated Ca^{2+} channels (VGCCs) on the plasma membrane[3]. RyR1 is also activated by Ca^{2+} *in vitro*, and hence those RyR1s not associated with VGCCs are presumably activated by Ca^{2+}, possibly together with coupled gating between adjacent RyRs, amplifying Ca^{2+} release[4–6].

RyR channels are subject to stress-induced Ca^{2+} leak, which is critically involved in heart failure[2], cardiac arrhythmias[7], post-traumatic stress disorder[8], age-dependent loss of muscle function[9], and muscular dystrophy[10]. RyRs have recently become therapeutic targets for some of these disorders[11,12].

Previous single-particle electron cryomicroscopy (cryo-EM) studies revealed that RyR1 adopts a four-fold symmetric mushroom-like superstructure, with about 80% of the mass in the cytosol (the 'cap' of the mushroom) and a 'stalk' embedded in the sarcoplasmic and endoplasmic reticula membrane. The highest-resolution reconstruction obtained for intact RyR1 before this study was 9.6 Å (ref. 13), which, although giving a good picture of the overall dimensions of the molecule and approximate protomer boundaries, was insufficient to identify secondary structural elements, or locate key domains.

Architecture of RyR1 at 4.8 Å resolution

The calcium-free (low nanomolar free Ca^{2+}) RyR1–calstabin2 (also known as FKBP12.6) complex was purified from rabbit (*Oryctolagus cuniculus*) skeletal muscle by calstabin-affinity chromatography (see Methods and Extended Data Fig. 1 for details). Recent advances in cryo-EM detector technology and data processing[14] have allowed us to obtain three-dimensional reconstructions at overall resolutions as high as 4.8 Å (Extended Data Fig. 2).

Three-dimensional classification using RELION 1.2 (ref. 15) identified distinct classes of particles (Extended Data Fig. 3) differing in the cytosolic assembly conformation but not in the transmembrane pore. The best-resolved class yielded a reconstruction with C_4 symmetry and a resolution of 4.8 Å according to the Fourier shell correlation (FSC) = 0.143 gold standard criterion[15] (Extended Data Fig. 4a).

The quality of the density map was excellent in the transmembrane region, and lower in the cytoplasmic region. A reconstruction obtained from dephosphorylated (see Methods for details) RyR1 at 5.0 Å resolution had considerably improved density in regions that were poorly defined in the original sample (Fig. 1a and Extended Data Figs 4b–e and 5). This map has been used for most of the interpretation and model building (model–map correlation in Extended Data Fig. 6).

The architecture of RyR1 consists of four protomers surrounding a central transmembrane pore coincident with the four-fold symmetry axis of the tetramer. Each protomer is built around an extended scaffold of α-solenoid repeats[16]. This scaffold is extraordinary in scale, comprising 37 repeats in three contiguous segments, totaling 2,217 residues, or 56% of the ordered residues in the polypeptide. The α-solenoid scaffold is capped at the amino terminus by two β-trefoil domains, N-terminal domain (NTD)-A and NTD-B, which form a central cytosolic vestibule; and at the carboxy terminus by the transmembrane pore that adopts a fold placing it in the six-transmembrane (6TM) superfamily of ion channels, which includes the voltage-gated sodium and potassium channels and the transient receptor potential (TRP) channels (Fig. 1b). The

[1]Department of Physiology and Cellular Biophysics, Columbia University, New York, New York 10032, USA. [2]Department of Biochemistry and Molecular Biophysics, Columbia University, New York, New York 10032, USA. [3]Howard Hughes Medical Institute, Columbia University, New York, New York 10032, USA. [4]Department of Biological Sciences, Columbia University, New York, New York 10027, USA. [5]Department of Medicine, Columbia University, New York, New York 10032, USA. [6]Wu Center for Molecular Cardiology, College of Physicians and Surgeons of Columbia University, New York, New York 10032, USA.

*These authors contributed equally to this work.

©2015 Macmillan Publishers Limited. All rights reserved

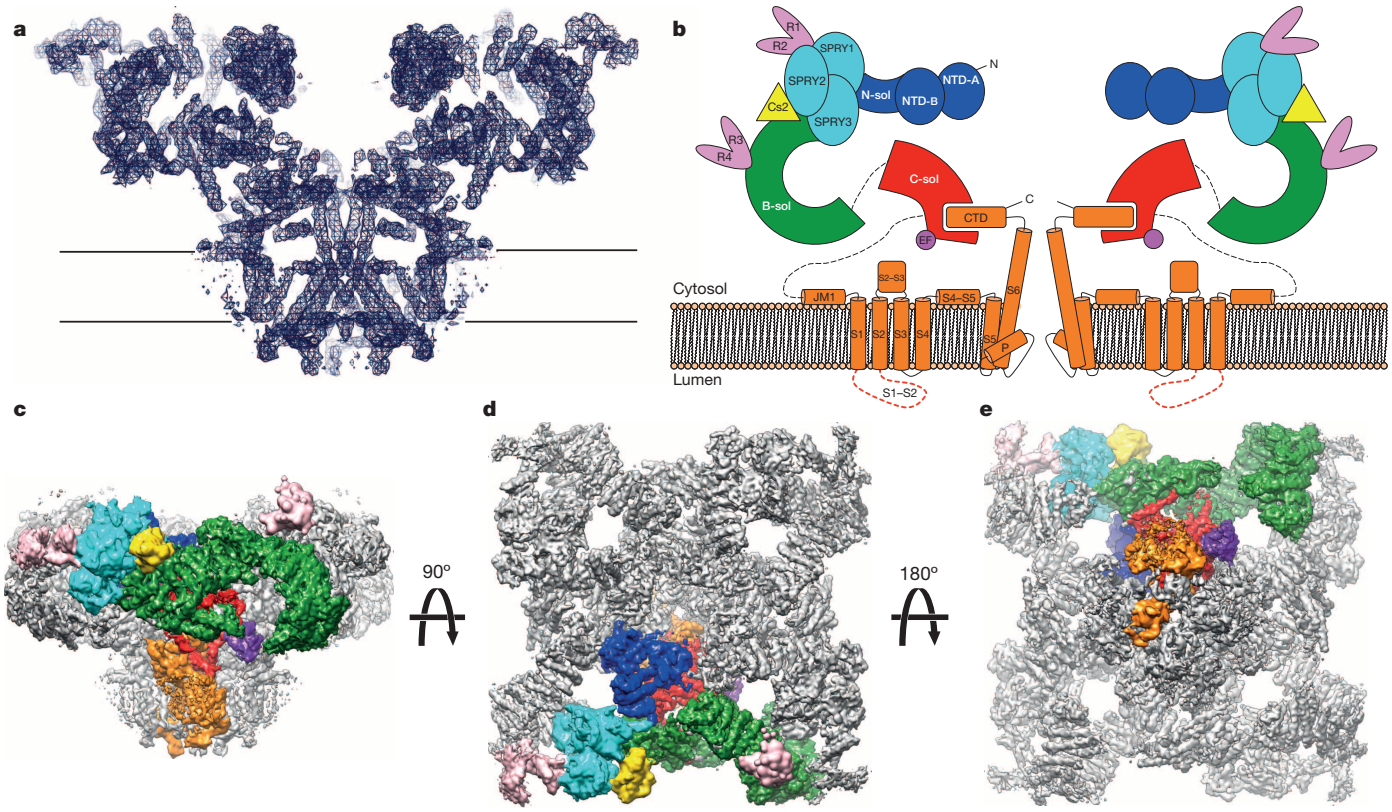


Figure 1 | The architecture of RyR1 at 4.8 Å. **a**, View from the plane of the sarcoplasmic reticulum membrane of a slab of density (blue mesh) coinciding with the channel axis. **b**, Colour-coded schematic representation of the RyR1. B-sol, bridge solenoid; C-sol, core solenoid; N-sol, N-terminus solenoid. **c**, View in the plane of the sarcoplasmic reticulum membrane. **d**, View from the cytosol. **e**, View from the lumen of the density map of skeletal muscle RyR1 at 5.0 Å resolution, with one protomer segmented according to the domains assigned in the model, coloured as follows: blue, N-terminal domain; cyan, SPRY1, SPRY2 and SPRY3; salmon, clamp region (RY12 repeats), and phosphorylation domain (RY34 repeats); yellow, calstabin; green, the bridge solenoid scaffold; red, the core solenoid; and orange, transmembrane and C-terminal domains; purple, putative Ca^{2+}-binding domain (EF). Dashed lines represent major disordered segments.

α-solenoid scaffold incorporates five major domains: three SPRY domains (SPRY1–3), and two pairs of RyR repeats (RY12 and RY34, the latter containing a regulatory protein kinase A phosphorylation site at Ser 2843). Several smaller insertions were also identified, including most importantly a previously predicted EF-hand pair[17] that constitutes the presumed conserved Ca^{2+}-binding domain in RyRs (Fig. 1b). The RyR1 model exhibits well-defined protomer boundaries (Fig. 1c–e).

The flexible α-solenoid scaffold of RyR1

The α-solenoid scaffold of RyR1 can be divided into three major segments (Extended Data Fig. 7). The smallest of these is the N-terminal solenoid (N-Sol), consisting of four repeats, linking the central cytosolic vestibule of the channel to the three SPRY domains at the outer corner of the tetramer (Fig. 1b). The first two of these repeats were present in the crystal structure of the N-terminal fragment, in which they were assigned as 'domain C' of this fragment[18].

The second and largest of the three major α-solenoid regions is the bridging solenoid, which curls around the periphery of the cytosolic assembly in a right-handed superhelix towards the SPRY domains of the adjacent protomer. The bridging solenoid may be further subdivided into N-terminal, central and C-terminal subdomains, denoted BrA, BrB and BrC, respectively (Extended Data Fig. 8).

The N-terminal subdomain, BrA, adopts a distinctly different architecture from the rest of the bridging solenoid, in which distorted, interlocking α-solenoid repeats wrap around a 72-Å-long central helix that projects towards the three SPRY domains. An additional feature of interest in BrA is the calstabin-binding helix, which projects out from the central helix, with its N terminus buried in calstabin2 (Extended Data Fig. 9).

Midway along BrB, the second RyR-repeat pair (RY34) projects away from the sarcoplasmic reticulum membrane into the cytosol. The connections between RY34 and BrB are not clearly resolved, leading to uncertainty in the numbering of this region. BrC, the C-terminal subdomain of the bridging solenoid, interacts closely with the SPRY3 domain of the neighbouring subunit, before terminating in a disordered segment.

The last of the major solenoid regions, which we have termed the core solenoid (Fig. 1b), begins with a linker helix (starting approximately at residue 3679) embedded in BrA, and progresses through eight repeats towards the transmembrane pore (Extended Data Fig. 8b). An EF-hand pair, described in detail below, is inserted in the seventh repeat of the core solenoid (Extended Data Fig. 10). Between the seventh and eighth repeats, the core solenoid is interrupted by an extended loop (4180–4200), which probably adopts a β-hairpin structure. The β hairpin and the eighth repeat of the core solenoid form a 'vice' surrounding the C-terminal domain of RyR1, as described in detail below.

Inspection of the initial model suggested that the fold of three major regions of the polypeptide could be categorized into one of the many families of α-solenoid repeat proteins. We used the polyalanine model of each region to search the Protein Data Bank (PDB; using the DALI web server[19]). For all three major solenoid regions, the top hits (Z scores > 15) were Armadillo repeat-containing proteins, including adenomatous polyposis coli (APC) and β-catenin (Extended Data Fig. 7b–d).

Previously characterized Armadillo and HEAT repeats are flexible protein–protein interaction modules[20,21]. We suggest that the flexible α-solenoid scaffold of RyR1 could facilitate assembly of regulatory proteins, and allow coupling of conformational changes of the scaffold, induced by either protein binding or post-translational modifications, to RyR1 activity.

©2015 Macmillan Publishers Limited. All rights reserved

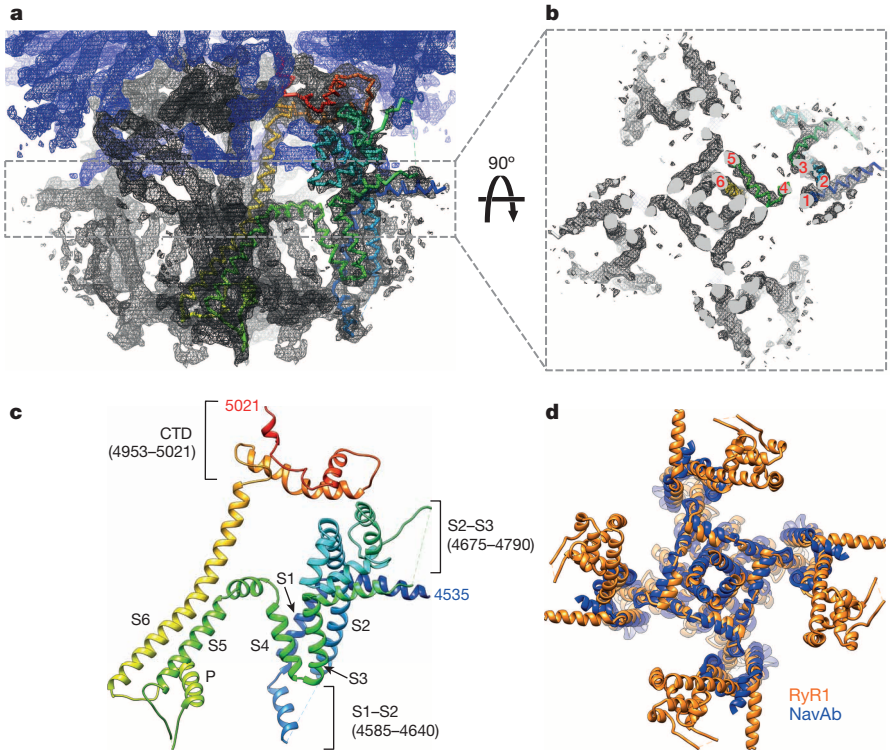


Figure 2 | RyR1 transmembrane pore and CTD. **a**, Density map of the pore region (black mesh) and the core solenoid (blue mesh), displayed with the transmembrane region of one protomer in spectral colouring (N terminus is blue, C terminus is red). **b**, A 90° slab through the plane of the membrane, with numbering indicating the positions of the six transmembrane helices. **c**, The transmembrane region of a protomer in spectral colouring, as labelled. **d**, Superposition of the RyR1 pore with the structure of a voltage-gated sodium channel (NavAB, PDB code 3RVY). The two structures were aligned using SUPERPOSE[40], giving a core root mean squared deviation (r.m.s.d.) of 3.42 Å across 628 aligned Cα atoms.

RyR1 is a 6TM ion channel

The transmembrane domain is one of the best-resolved regions of the map (Fig. 2a, b), allowing us to identify all secondary structural elements. The architecture of the pore clearly identifies it as a member of the 6TM ion channel superfamily[22], with six transmembrane helices per protomer surrounding a central pore. An extended peptide (the P-segment), structurally analogous to the selectivity filter of potassium and sodium channels, delineates the luminal aperture (Fig. 2c). The transmembrane region contains two domains: the pore domain, formed by S5, S6, the pore helix and the P-segment; and a pseudo voltage-sensor domain (pVSD), formed by S1–S4 that interfaces with the pore domain of the adjacent subunit (Fig. 2b). The RyR1 pore domain most closely resembles that of the voltage-gated sodium channel, NavAb (Fig. 2d), although the P-segment is more similar to the equivalent region of the TRPV1 cation channel[23,24] (Fig. 3a). Moreover, the luminal aperture is comparable to that of the highly Ca^{2+}-permeable[25] TRPV1 channel. The brevity of the constriction suggests that it may accommodate only one Ca^{2+}-binding site.

The P-segment contains many acidic residues that are expected to be anionic under physiological conditions, probably contributing to the high conductance of RyR1 (for example, 110 pS for Ca^{2+}, >700 pS for K^{+})[26]. Seven additional negatively charged residues are located along the cytosolic extension of S6, presumably serving a similar function (Fig. 3b).

The transmembrane region includes three apparently amphipathic helices (JM1, the first helix of the S2–S3 insertion and the S4–S5 linker helix) that are expected to lie in the plane of the cytosolic surface of the membrane.

There is a single cytosolic constriction in the ion conduction pathway, at the S6 bundle crossing. The Cα–Cα distance at this point is 11 Å, similar to the minimal Cα–Cα distance observed in the structure of NavAb (10.41 Å at Cys 217). On the basis of structural alignment with the closed NavAb pore (Fig. 2d), and the diameter of hydrated Ca^{2+} (8.2 Å; ref. 27), we conclude that the pore is in a non-conducting state.

The S6 helix has a 24° kink in the middle, centred on Gly 4934 near the cytosolic face of the membrane, which orients the cytosolic extension of S6 roughly parallel to the channel axis (Fig. 3c). Conserved glycine residues in the pore-lining helices of other 6TM ion channels may operate as 'glycine-hinges', facilitating reorientation of the pore-lining helix and consequent alteration in the cytosolic aperture of the channel[28]. Gly 4934 is conserved in all RyR isoforms and in a closely related channel, the inositol-1,4,5-trisphosphate receptor.

The S6 helix extends ~30 Å into the cytosol, terminating in the C-terminal domain (CTD), a small α-helical domain that extends laterally from the channel axis into the core solenoid (Fig. 1b). The CTD is secured by an extended loop and a pair of helices that are reminiscent of a thumb and forefingers (Fig. 4).

An additional helix, in weaker density, may correspond to half of the predicted transmembrane hairpin located between amino acids 4325 and 4370 (Extended Data Fig. 6).

A cytosolic Ca^{2+} sensor contacts the pore

Unlike other 6TM channels, RyR1 possesses a compact, folded cytosolic domain inserted within the pVSD, between helices S2 and S3 (residues 4675–4790). A curved, cytosolic extension of S2 leads into a bundle of four short helices, which are separated by an unresolved segment spanning 31 amino acids from an amphipathic helix leading into S3 (Fig. 2c). The S2–S3 helical bundle lies in close proximity to the putative Ca^{2+}-binding domain and the CTD (Fig. 4), suggesting that this domain may be involved in transmitting conformational changes in the cytosolic assembly to the pore.

RyR1 is activated by increased cytosolic Ca^{2+} concentration[29]. A calmodulin-like domain inserted within the core solenoid was previously suggested to be a Ca^{2+} sensor[17]. This region is highly conserved

©2015 Macmillan Publishers Limited. All rights reserved

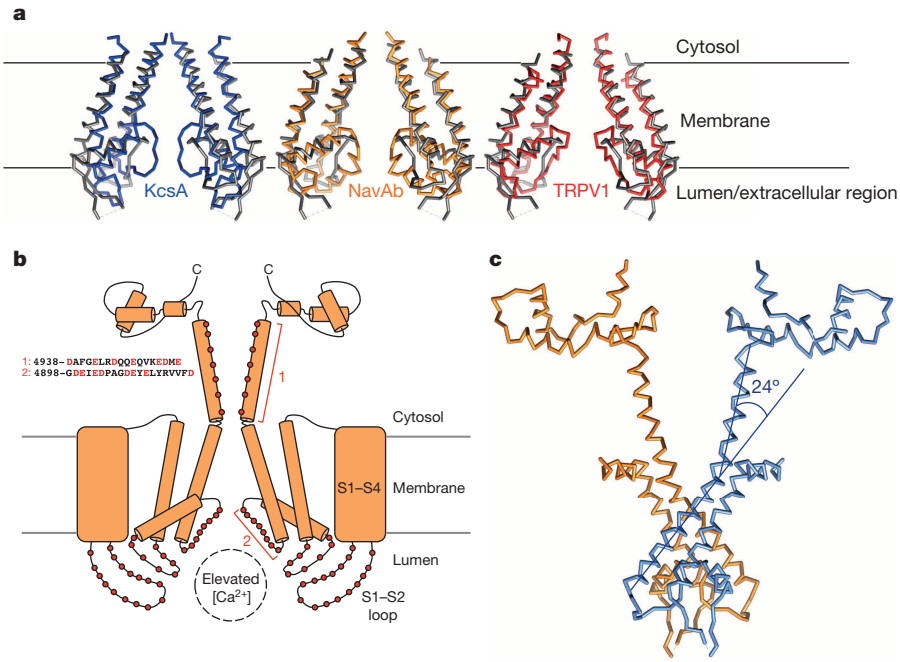


Figure 3 | The RyR1 conduction pathway. **a**, Superposition of the RyR1 pore domain (grey) with structures of the potassium channel KcsA (blue), the voltage-gated sodium channel NavAB (yellow), and TRPV1 (red) pores. Only two subunits are shown for clarity. The core r.m.s.d. values of the three alignments, calculated using SUPERPOSE are 3.44 Å (over 306 aligned Cα atoms), 3.42 Å (over 628 aligned Cα atoms) and 4.80 Å (over 635 aligned Cα atoms), respectively. **b**, Scheme indicating the relative positioning of all the negatively charged residues in the ionic pathway (red dots) and the sequence of the P-loop and the cytosolic helix extending from S6 indicating in red the negatively charged residues. **c**, Model of two opposing pore regions of RyR1 indicating the bundle crossing and the 24° kink in S6.

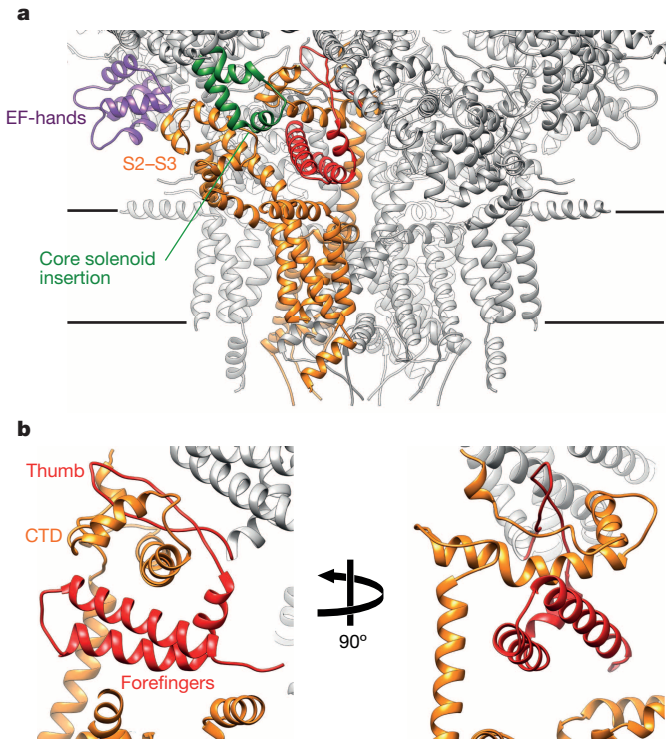


Figure 4 | The Ca^{2+}-sensing machinery. **a**, Colour-coded representation of elements in the RyR1 structure that may participate in Ca^{2+} sensing and allosteric Ca^{2-} dependent force transduction to the channel gate. Purple, calmodulin-like domain/EF-hand pair; orange, CTD and S1–S6; green, core solenoid hairpin insertion. **b**, Two views of the 'thumb and forefingers' motif originating from the core solenoid that engulfs the CTD.

in all RyRs, and shares 26% sequence identity with the C-lobe of human calmodulin (Extended Data Fig. 10a). Six of the eight residues that coordinate Ca^{2+} in calmodulin are conserved in the putative Ca^{2+}-binding domain of RyR1.

The putative Ca^{2+}-binding domain of RyR1 is adjacent to the S2–S3 insertion from a neighbouring protomer and the CTD of the originating protomer (Fig. 4a), suggesting a mechanism for Ca^{2+}-mediated gating in which Ca^{2+}-dependent changes in the conformation of the Ca^{2+}-binding domain are transmitted to the pore via contacts with the S2–S3 loop and/or the CTD, inducing a conformational change that alters the cytosolic aperture of the channel.

NTDs form the cytosolic vestibule

A prominent feature of the RyR1 structure, already evident at lower resolution[30,31], is a large cytosolic vestibule around the four-fold axis above the pore in the cytosolic domain (Fig. 5). We docked the crystal structure of the three-domain N-terminal fragment of RyR1 (ref. 18) into the density map in the same location as previously proposed. Several loops that were unresolved in the crystal structure are now clearly visible and were added into the model, as were residues 533–603 of NTD-C, which were not resolved in the previous structure. This addition completes the N-terminal solenoid, which connects to the beginning of SPRY1 through a short linker that is well resolved in the density map (Fig. 5a).

The NTDs make key interactions stabilizing the cytosolic assembly, both with other domains in the same protomer, and with domains contributed by neighbouring protomers. NTD-A contacts the fifth repeat in the core solenoid of the adjacent protomer via interactions mediated by Arg 76 and Glu 177 (Fig. 5b), and interacts with NTD-B of the neighbouring protomer via Gln 156 (NTD-A) and Asp 385 (NTD-B) (Fig. 5a). NTD-A interfaces with the sixth repeat of BrB in the bridging solenoid of the adjacent protomer, in an interaction involving the 121–134 loop on NTD-A, as well as Phe 195, Met 196 and Ser 175 (Fig. 5a). Arg 392 and Gln 465 in NTD-C contribute to an interface with the core solenoid of the same protomer (Fig. 5b). NTD-C forms a structurally contiguous segment of α-solenoid repeats with the first set of repeats in the

©2015 Macmillan Publishers Limited. All rights reserved

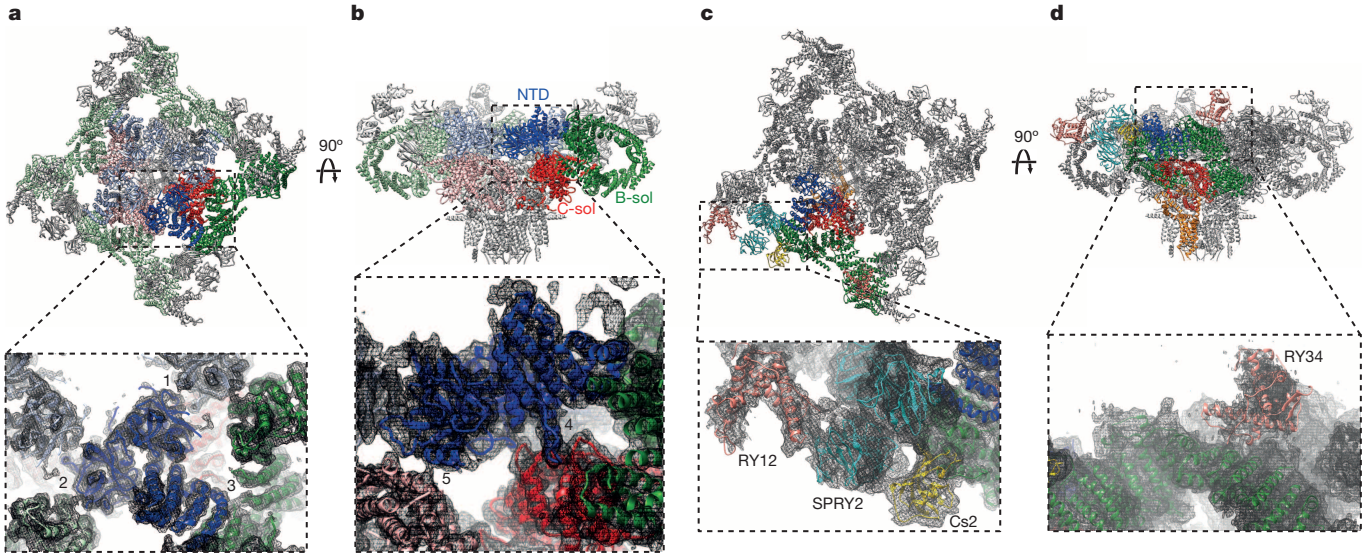


Figure 5 | Intra- and inter-protomer interactions formed by cytosolic domains. Views from the cytosol and in the membrane plane of RyR1, with regions coloured as follows: the N-terminal domain (blue), core solenoid (red), and bridge solenoid (green). For clarity, one protomer is depicted in brighter colouring. In the view parallel to the membrane, most of the front subunit has been clipped for clarity. **a**, View from the cytosol, showing contacts between NTD-A and NTD-B of the neighbouring protomer (1), NTD-B with the bridging solenoid of the adjacent protomer (2), and NTD-C forming a structurally contiguous solenoid with the bridging solenoid of the same protomer (3). **b**, View in the plane of the membrane showing interactions formed by NTD-C with the core solenoid of the same protomer (4), and of NTD-B with the core solenoid of the adjacent protomer (5). **c**, Views in the membrane plane and from the cytosol of RyR1 with the following domains coloured as in Fig. 1b; core solenoid, the bridging solenoid scaffold, the RY34 repeats phosphorylation domain, SPRY domains 1, 2 and 3, RY12 repeats, and the N-terminal domain. Position of the docked RY34 phosphorylation domain (salmon) abutting the bridge solenoid (dark green) within the density map (grey mesh). **d**, Locations of SPRY domains 1, 2 and 3 (cyan), calstabin2 (yellow), and RY12 (salmon) within the density map.

bridging solenoid region following SPRY3 (Fig. 5a). A major feature of the cytosolic domain are four prominent openings in the structure (one in each protomer) that are bounded by outer edges of the NTDs, the inner edges of the SPRY domains, and the bridging solenoid from the adjacent protomer (Fig. 5a).

RYR repeats, SPRY and calstabin interactions

RyR1 contains two pairs of RYR repeats, RY12 (residues 850–1055) and RY34 (residues 2734–2941). RY12 is located between SPRY1 and SPRY2, whereas RY34 is inserted in BrB (Fig. 1b). RY12 and RY34 are expected to adopt the same overall fold, as they share 29% sequence identity. The structure of RY34 (which contains a regulatory PKA phosphorylation site at Ser 2843) has been solved by two independent groups, and both placed it in the distinctly 'U-shaped' density located at the extreme outer corners of the receptor, also referred to as the 'clamp' region[32,33].

In our 5.0 Å map, we see two densities that share this distinctive shape. One is located in the previously identified location, abutting the SPRY domains, and another, less well-resolved density with the same overall shape protrudes upwards from the bridging solenoid. In the primary sequence, RY12 is located between SPRY1 and SPRY2. Therefore, we place RY12 at the corner of the channel, and RY34 (containing the PKA phosphorylation site) protrudes from BrB on top of the cytosolic assembly projecting into the cytosol (Fig. 5c, d). This assignment agrees with the observation that RY34, which seems to be the most exposed and flexible of the RYR repeat pairs, is also the most susceptible to proteolysis[34].

Interestingly, the location of RY12 (Fig. 5c), projecting laterally from the corners of the cytosolic assembly, places it in an appropriate position to serve as a contact site between neighbouring channels in the paracrystalline RyR arrays that have been shown to assemble on the sarcoplasmic reticulum membrane[35].

RyR1 contains three SPRY domains, SPRY1 (residues 643–794), SPRY2 (residues 1073–1205) and SPRY3 (residues 1419–1567). Structures of SPRY domains from other proteins have shown that the domain adopts a distinctive β-sandwich structure consisting of two antiparallel 7- or 8-stranded β-sheets[36]. In our 5.0 Å map of dephosphorylated RyR1, we identify the three SPRY domains on the basis of the two curved sheets that form the β-sandwich (Fig. 5c, d). The plane of the triangle is oriented roughly perpendicular to the channel axis, and parallel to the edge of the cytoplasmic assembly.

High-affinity binding of calstabin1 and 2 has a critical role in stabilizing the closed states of RyR1 and RyR2, respectively, and in preventing pathological intracellular calcium leak[2,37]. Calstabin2 binds with high affinity to both RyR1 and RyR2 (but is not expressed in skeletal muscle), and calstabin1 binds preferentially to RyR1 (ref. 38). Calstabin1 and calstabin2 differ at only 18 positions out of 108 residues. The calstabin-binding site is located at the mutual interface of the bridging solenoid, SPRY1 and SPRY2 (Extended Data Fig. 9). The N-terminal end of a helix originating from subdomain BrA is located in the hydrophobic binding pocket of calstabin2. Calstabin binding may stabilize the connection between the cytoplasmic regulatory domains and the pore by rigidifying the BrA–SPRY1–SPRY2 interface and possibly altering the relative orientation of these domains.

Concluding remarks

The model and density maps presented here provide, to our knowledge, a first glimpse of the transmembrane architecture of ryanodine receptors. Our analysis confirms that RyR1 is a 6TM ion channel, reveals a flexible cytosolic α-solenoid scaffold of remarkable size, and places every previously known domain, including a putative calcium-binding domain. This structure is of RyR1 in the closed state, but its features provide a foundation for understanding the open state and the process of Ca^{2+}-activation for all members of the RyR family.

Note added in proof: While this paper was in press, high-resolution structures of the SPRY2 domains from RyR1 and RyR2 were published[39]. These authors placed the SPRY2 domain in the location where we have assigned the SPRY3 domain. Now, having the authentic SPRY2 structure

©2015 Macmillan Publishers Limited. All rights reserved

instead of a homology model, we find equally good fittings to our map for either alternative, leaving some ambiguity about the connectivity in this region.

Online Content Methods, along with any additional Extended Data display items and Source Data, are available in the online version of the paper; references unique to these sections appear only in the online paper.

Received 16 July; accepted 8 October 2014.

Published online 1 December 2014.

1. Zalk, R., Lehnart, S. E. & Marks, A. R. Modulation of the ryanodine receptor and intracellular calcium. *Annu. Rev. Biochem.* **76,** 367–385 (2007).
2. Marx, S. O. *et al.* PKA phosphorylation dissociates FKBP12.6 from the calcium release channel (ryanodine receptor): defective regulation in failing hearts. *Cell* **101,** 365–376 (2000).
3. Paolini, C., Protasi, F. & Franzini-Armstrong, C. The relative position of RyR feet and DHPR tetrads in skeletal muscle. *J. Mol. Biol.* **342,** 145–153 (2004).
4. Meissner, G. & Lu, X. Dihydropyridine receptor-ryanodine receptor interactions in skeletal muscle excitation-contraction coupling. *Biosci. Rep.* **15,** 399–408 (1995).
5. Stern, M. D., Pizarro, G. & Rios, E. Local control model of excitation-contraction coupling in skeletal muscle. *J. Gen. Physiol.* **110,** 415–440 (1997).
6. Marx, S. O., Ondrias, K. & Marks, A. R. Coupled gating between individual skeletal muscle Ca^{2+} release channels (ryanodine receptors). *Science* **281,** 818–821 (1998).
7. Wehrens, X. H. *et al.* FKBP12.6 deficiency and defective calcium release channel (ryanodine receptor) function linked to exercise-induced sudden cardiac death. *Cell* **113,** 829–840 (2003).
8. Liu, X. *et al.* Role of leaky neuronal ryanodine receptors in stress-induced cognitive dysfunction. *Cell* **150,** 1055–1067 (2012).
9. Andersson, D. C. *et al.* Ryanodine receptor oxidation causes intracellular calcium leak and muscle weakness in aging. *Cell Metab.* **14,** 196–207 (2011).
10. Bellinger, A. M. *et al.* Hypernitrosylated ryanodine receptor calcium release channels are leaky in dystrophic muscle. *Nature Med.* **15,** 325–330 (2009).
11. Marks, A. R. Calcium cycling proteins and heart failure: mechanisms and therapeutics. *J. Clin. Invest.* **123,** 46–52 (2013).
12. Andersson, D. C. & Marks, A. R. Fixing ryanodine receptor Ca leak — a novel therapeutic strategy for contractile failure in heart and skeletal muscle. *Drug Discov. Today Dis. Mech.* **7,** e151–e157 (2010).
13. Serysheva, I. I. *et al.* Subnanometer-resolution electron cryomicroscopy-based domain models for the cytoplasmic region of skeletal muscle RyR channel. *Proc. Natl Acad. Sci. USA* **105,** 9610–9615 (2008).
14. Fernández, I. S. *et al.* Molecular architecture of a eukaryotic translational initiation complex. *Science* **342,** 1240585 (2013).
15. Scheres, S. H. RELION: implementation of a Bayesian approach to cryo-EM structure determination. *J. Struct. Biol.* **180,** 519–530 (2012).
16. Groves, M. R. & Barford, D. Topological characteristics of helical repeat proteins. *Curr. Opin. Struct. Biol.* **9,** 383–389 (1999).
17. Xiong, L., Zhang, J. Z., He, R. & Hamilton, S. L. A. Ca^{2+}-binding domain in RyR1 that interacts with the calmodulin binding site and modulates channel activity. *Biophys. J.* **90,** 173–182 (2006).
18. Tung, C. C., Lobo, P. A., Kimlicka, L. & Van Petegem, F. The amino-terminal disease hotspot of ryanodine receptors forms a cytoplasmic vestibule. *Nature* **468,** 585–588 (2010).
19. Holm, L. & Rosenstrom, P. Dali server: conservation mapping in 3D. *Nucleic Acids Res.* **38,** W545–W549 (2010).
20. Groves, M. R. & Barford, D. Topological characteristics of helical repeat proteins. *Curr. Opin. Struct. Biol.* **9,** 383–389 (1999).
21. Huber, A. H., Nelson, W. J. & Weis, W. I. Three-dimensional structure of the armadillo repeat region of β-catenin. *Cell* **90,** 871–882 (1997).
22. Yu, F. H., Yarov-Yarovoy, V., Gutman, G. A. & Catterall, W. A. Overview of molecular relationships in the voltage-gated ion channel superfamily. *Pharmacol. Rev.* **57,** 387–395 (2005).
23. Payandeh, J., Scheuer, T., Zheng, N. & Catterall, W. A. The crystal structure of a voltage-gated sodium channel. *Nature* **475,** 353–358 (2011).
24. Liao, M., Cao, E., Julius, D. & Cheng, Y. Structure of the TRPV1 ion channel determined by electron cryo-microscopy. *Nature* **504,** 107–112 (2013).
25. Owsianik, G., Talavera, K., Voets, T. & Nilius, B. Permeation and selectivity of TRP channels. *Annu. Rev. Physiol.* **68,** 685–717 (2006).
26. Tripathy, A., Xu, L., Mann, G. & Meissner, G. Calmodulin activation and inhibition of skeletal muscle Ca^{2+} release channel (ryanodine receptor). *Biophys. J.* **69,** 106–119 (1995).
27. Volkov, A. G., Paula, S. & Deamer, D. W. Two mechanisms of permeation of small neutral molecules and hydrated ions across phospholipid bilayers. *Bioelectrochem. Bioenerg.* **42,** 153–160 (1997).
28. Jiang, Y. *et al.* X-ray structure of a voltage-dependent K^+ channel. *Nature* **423,** 33–41 (2003).
29. Bezprozvanny, I., Watras, J. & Ehrlich, B. E. Bell-shaped calcium-response curves of $Ins(1,4,5)P_3$- and calcium-gated channels from endoplasmic reticulum of cerebellum. *Nature* **351,** 751–754 (1991).
30. Ludtke, S. J., Serysheva, I. I., Hamilton, S. L. & Chiu, W. The pore structure of the closed RyR1 channel. *Structure* **13,** 1203–1211 (2005).
31. Samsó, M., Wagenknecht, T. & Allen, P. D. Internal structure and visualization of transmembrane domains of the RyR1 calcium release channel by cryo-EM. *Nature Struct. Mol. Biol.* **12,** 539–544 (2005).
32. Yuchi, Z., Lau, K. & Van Petegem, F. Disease mutations in the ryanodine receptor central region: crystal structures of a phosphorylation hot spot domain. *Structure* **20,** 1201–1211 (2012).
33. Sharma, P. *et al.* Structural determination of the phosphorylation domain of the ryanodine receptor. *FEBS J.* **279,** 3952–3964 (2012).
34. Marks, A. R., Fleischer, S. & Tempst, P. Surface topography analysis of the ryanodine receptor/junctional channel complex based on proteolysis sensitivity mapping. *J. Biol. Chem.* **265,** 13143–13149 (1990).
35. Yin, C. C., Han, H., Wei, R. & Lai, F. A. Two-dimensional crystallization of the ryanodine receptor Ca^{2+} release channel on lipid membranes. *J. Struct. Biol.* **149,** 219–224 (2005).
36. Woo, J.-S. *et al.* Structural and functional insights into the B30.2/SPRY domain. *EMBO J.* **25,** 1353–1363 (2006).
37. Brillantes, A. B. *et al.* Stabilization of calcium release channel (ryanodine receptor) function by FK506-binding protein. *Cell* **77,** 513–523 (1994).
38. Gaburjakova, M. *et al.* FKBP12 binding modulates ryanodine receptor channel gating. *J. Biol. Chem.* **276,** 16931–16935 (2001).
39. Lau, K. & van Petegem, F. Crystal structures of wild type and disease mutant forms of the ryanodine receptor SPRY2 domain. *Nature Comm.* **5,** 5937 (2014).
40. Krissinel, E. & Henrick, K. Secondary-structure matching (SSM), a new tool for fast protein structure alignment in three dimensions. *Acta Crystallogr. D* **60,** 2256–2268 (2004).

Acknowledgements We thank R. Axel for discussions and M. Thomas for assistance with the preparation of illustrations. This work was supported by grants from the National Institutes of Health (R01AR060037 and R01HL061503 to A.R.M., U54GM095315 to W.A.H., R01GM29169 to J.F.), and the Howard Hughes Medical Institute (to J.F.). R.Z. was a fellow of the American Heart Association (0625919T), and O.B.C. was supported by an overseas biomedical fellowship (NHMRC; Australia) and a Charles H. Revson Senior Fellowship (Charles H. Revson Foundation).

Author Contributions A.R.M. conceived the project, designed experiments, analysed data and wrote the manuscript. W.A.H. conceived the project, designed experiments, analysed data and wrote the manuscript. J.F. designed the cryo-EM experiments, analysed data and wrote the manuscript. R.Z. designed experiments, isolated the RyR1 used in this work, analysed data and wrote the manuscript. O.B.C. designed experiments, analysed data, built the atomic model and wrote the manuscript. F.M. designed experiments. A.G. designed experiments and conducted the cryo-EM experiments, including data acquisition and processing, and wrote the manuscript. R.A.G. conducted the cryo-EM experiments. S.R. conducted phospho-RyR immunoblot experiments.

Author Information Cryo-EM reconstructions of RyR1 have been deposited in the Electron Microscopy Data Bank under the accession numbers EMD-6106 (EGTA-treated RyR1) and EMD-6107 (EGTA- and CIP-treated RyR1). The Cα coordinates of the model have been deposited in the Protein Data Bank (PDB) under accession number 3J8E. Reprints and permissions information is available at www.nature.com/reprints. The authors declare no competing financial interests. Readers are welcome to comment on the online version of the paper. Correspondence and requests for materials should be addressed to A.R.M. (arm42@columbia.edu), J.F. (jf2192@columbia.edu) or W.A.H. (wayne@xtl.cumc.columbia.edu).

©2015 Macmillan Publishers Limited. All rights reserved

METHODS

RyR1 purification from rabbit skeletal muscle. Detergent-solubilized RyR1 was purified from rabbit (*Oryctolagus cuniculus*) skeletal muscle by calstabin-affinity chromatography using a procedure modified from ref. 41. The protein was eluted using calstabin2 (also known as FKBP12.6), rather than the physiological binding partner calstabin1 (FKBP12), owing to the higher affinity of the former for the RyR1 channel. Importantly, calstabin1 and calstabin2 share the same binding site on RyRs, and both have the same effects on RyR1 function. Addition of EGTA reduced the concentration of free Ca^{2+} in the sample to the low nanomolar range, such that the channel is closed according to functional studies using purified RyR1 reconstituted into planar lipid bilayers[29].

Rabbit skeletal muscle (100 g) flash-frozen in liquid nitrogen was blended for 90 s in 500 ml of ice-cold buffer containing 10 mM Tris-maleate, pH 6.8, 1 mM dithiothreitol, 1 mM EDTA, 150 μM PMSF (phenylmethylsulphonyl fluoride) and 1 mM benzamidine. The mixture was then centrifuged for 10 min at 8,000*g*. The supernatant was centrifuged for 20 min at 40,000*g*. Pellets were solubilized in 50 ml buffer containing 10 mM HEPES, pH 7.5, 1% (w/v) CHAPS, 1 M NaCl, 2 mM EGTA, 2 mM Tris(2-carboxyethyl)phosphine (TCEP) and a protease inhibitor cocktail (Roche). The solubilized membranes were then diluted 1:1 in the same buffer without NaCl and centrifuged for 30 min at 100,000*g*. The supernatant was then filtered using a 0.2-μm filter and allowed to bind overnight at 4 °C to a pre-equilibrated 5 ml GSTrap (GE healthcare) column with bound glutathione *S*-transferase (GST)–calstabin1 (derived from 0.5 l BL-21 cells overexpressing GST–calstabin1). The column was then washed with 10 column volumes of cold solubilization buffer (with the following alterations: 0.5% (w/v) CHAPS and 0.5 M NaCl) and RyR1 was eluted with two column volumes of 10 μM calstabin2 in the same buffer. The eluent was pre-cleared with 0.5 ml glutathione beads and treated with calf intestinal alkaline phosphatase (CIP, NEB, 100 U ml^{-1}) for 4 h at room temperature. The CIP-treated RyR1 was concentrated in a 100-kDa cut-off centrifugal filter unit (Millipore) to less than 500 μl, loaded on a size-exclusion column (Tosoh G4SWXL) and eluted in solubilization buffer with the following alterations and substitutions: 5 mM EGTA, 0.25% (w/v) CHAPS and 0.001% (w/v) DOPC (Avanti). The fractions corresponding to the RyR1 peak (Extended Data Fig. 3b) were then combined and concentrated in a 100-kDa cut-off centrifugal filter unit (Millipore) to a concentration of ~10 mg ml^{-1} as determined using spectroscopy ($A_{280\,nm}$ at 1 mg ml^{-1} = 1.018, measured using a Nanodrop spectrophotometer).

Grid preparation and data collection. Three microlitres of each sample was applied to holey carbon grids (C-flat CF-1.2/1.3-2C-T, Protochips Inc.) without prior plasma cleaning. After a 30-s incubation time on the grids, sample was blotted with filter paper (Whatman; pre-treated with 1 mM EGTA to remove trace Ca^{2+}) for 0.5–2 s at 100% humidity and vitrified by rapidly plunging into liquid ethane at −180 °C with a Vitrobot (FEI)[42,43]. Data acquisition was performed on a FEI Tecnai F30 Polara (FEI) operating at 300 kV and at a nominal magnification of ×31,000. Data sets were collected with the automated data collection system Leginon[44] on a K2 Summit direct electron detector (Gatan) with a physical pixel size of 5 μm, corresponding to a calibrated pixel size of 1.255 Å per pixel at the specimen when operating in electron counting mode. Micrographs were recorded in dose-fractionation mode as a series of 23 frames, with an accumulation time of 0.2 s per frame. The dose rate was set to 8 counts per physical pixel per second (~10e^- $pixel^{-1}$ s^{-1}). The total exposure time was 4.6 s, leading to a total accumulated dose of approximately 25 e^- $Å^{-2}$ on the specimen.

Image processing, three-dimensional classification and refinement. Dose-fractionated image stacks were aligned using dosefgpu_driftcorr[45] and a sum of frames 3–20 in each image stack was used for further processing. The first two frames were omitted as they contained motions greater than 4 Å per frame on average. For the EGTA data set, 3,423 micrographs were collected in total. After visual assessment of the micrographs and their power spectra, 3,190 micrographs were selected for subsequent processing. For the CIP-treated data set, 6,194 micrographs were collected in total and 5,243 micrographs were selected for further processing.

The data were then preprocessed using pySPIDER and Arachnid (http://www.arachnid.us; R. Langlois and J.F., unpublished observations). Arachnid is a Python-encapsulated version of SPIDER[46], replacing SPIDER batch files with Python scripts. It also contains novel procedures such as Autopicker[47], which was used for the reference-free automated particle selection (Extended Data Fig. 2a). Then, 230,000 particles were extracted from a first data set of RyR1 prepared in the presence of EGTA. Those particles were aligned and refined using the RELION 1.2 autorefine procedure[48]. Map quality was good in the transmembrane region but lower in the most peripheral parts of the cytoplasmic region, suggesting the presence of conformational heterogeneity. The particles were therefore subjected to three-dimensional classification using RELION[15] without symmetry imposed, and yielded different classes (Extended Data Fig. 3a) with the cytoplasmic assembly of RyR1 in different conformations. Class 1 (46,860 particles) was the most homogeneous and yielded a reconstruction at 4.8 Å using the autorefine procedure implemented in RELION 1.2 with C_4 symmetry imposed. The distribution of particle orientations in the ice was very homogeneous (Extended Data Fig. 2c), and all views could be recovered following reference-free two-dimensional classification (Extended Data Fig. 3d). This map allowed us to determine the transmembrane topology of the channel, place the previously solved structures of the N-terminal fragment and the two RYR repeat pairs, and build a preliminary Cα trace for the protomer. A class of particles was identified in this data set in which the entire cytosolic region of a single protomer was disordered (Extended Data Fig. 3a). A difference map calculated between this class and a class in which all protomers were ordered supports the protomer boundaries assigned in our model (Extended Data Fig. 3c). Although the quality of the density was excellent in the transmembrane region in this data set, with helices distinctly defined and some bulky side chains visible, the quality of the map in the cytoplasmic region was lower, impeding model completion.

RyR1 is regulated by phosphorylation[49], and we were concerned that heterogeneous phosphorylation could contribute to the observed structural heterogeneity. In an attempt to improve the conformational homogeneity of the sample, as well as the overall resolution, we treated purified RyR1 with CIP to obtain a uniformly dephosphorylated sample (Extended Data Fig. 1c). From this sample, we collected a data set from which 322,400 particles were extracted. Three-dimensional classification of CIP-treated RyR1 performed following the same procedure as for the original sample gave several well-populated classes (Extended Data Fig. 3b), with different conformations of the cytoplasmic assembly, similar to those observed in the first data set. The best-resolved class had an overall resolution of 5.0 Å, refined as a C_4-symmetric particle. Although the overall resolution did not improve, the local resolution improved substantially in some regions compared to the previous protein preparation (Extended Data Fig. 4c, d). This map has been used for most of the map interpretation and model building described here. It is important to note that the observed improvements in the map may relate to dephosphorylation of the sample, but may also be due to the larger size of this data set.

Notably, the local resolution in the cytosolic assembly was greatly improved in reconstruction obtained from the CIP-treated sample (Extended Data Fig. 4b, c), and this map was used for completion of the model, as described below. The local resolution, as measured using the program ResMap, varies between 4.5 and 6 Å across most of the map (Extended Data Fig. 4b–d).

Reported resolutions are based on the gold-standard FSC = 0.143 criterion, and were corrected for the effects of a soft mask on the FSC curve using high-resolution noise substitution[50]. Before visualization, all density maps were sharpened by applying a negative B-factor that was estimated using automated procedures[51].

Density maps segmentation and display. Cryo-EM reconstructions were segmented using the SEGGER module[52] implemented in UCSF Chimera[53]. Segments were manually combined to generate segmented densities corresponding to individual structural domains, as represented in Fig. 1c–e and Extended Data Fig. 5. All other maps were left unsegmented. All density figures were rendered and displayed using UCSF Chimera.

Model building. The 5.0 Å map of dephosphorylated RyR1 (Fig. 1a) has allowed us to place all domains in RyR1 (Fig. 1b), as well as to define the boundaries of the four identical protomers that comprise the channel (Fig. 1c–e), and to build a largely complete Cα model for each protomer, comprising 3,757 of the 5,027 residues that constitute the full-length polypeptide chain, in addition to the 105 residues comprising the co-purified subunit, calstabin2. Most of the unassigned residues are located in regions of the sequence that are predicted to be disordered or to lack regular secondary structure. In addition, several of the regions that are either not present in the model or are less well ordered (for example RY34) have previously been shown to be highly accessible to proteolysis consistent with their surface exposure[34].

Given the absence of homologous structures for most domains in RyR1 it is important to address the limitations of our model. In some regions, specifically NTD A-C, the RY12 and RY34 repeat pairs, and the EF-hand pair, we were able to place a crystal structure or high sequence identity homology model. For the SPRY1–3 domains, we placed homology models, and the numbering within the SPRY domains is consequently uncertain because of limited sequence identity with template structures. In all other areas, we built the model *de novo* as a polyalanine trace, and did not attempt to model side chains, even where visible. Helices are clearly defined in the density in most regions of the map; in the best areas, the pitch and curvature of the helices is clearly defined and bulky side chains are visible, although not identifiable (Extended Data Fig. 5). Features of the map correspond well to the local resolution measured using the program ResMap (Extended Data Fig. 4b–d). The model is of good quality in most regions, as demonstrated by analyses of the local correlation with the map (Extended Data Fig. 6). The two main regions where the correlation of the model with the map is lower are the SPRY domains (which are subject to the difficulties described above), and an unmodelled rod of density on the periphery of the transmembrane region. The final model has been presented as a Cα trace, with sequence assignments based on the distance from known landmarks in the sequence, such as the NTDs, for which high-resolution crystal structures are available.

©2015 Macmillan Publishers Limited. All rights reserved

These sequence assignments should be considered provisional owing to the absence of identifiable side chains and the presence of multiple disordered regions (Extended Data Fig. 5).

Model building was performed manually in Coot[54]. First, the high-resolution structure of the N-terminal three-domain fragment of RyR1 (PDB code 2XOA) was placed in the previously assigned location, and the orientation of the domain was determined using the 'jiggle-fit' algorithm implemented in Coot, using 1,000 random candidate orientations of the domain followed by rigid body fitting. Homology models for the three SPRY domains were generated using the PHYRE2 web server, and fitted to the density using the same procedure as for the N-terminal fragment, assigned as SPRY1–3 according to the rationale described in the main text. The two pairs of RyR repeats (RY12 and RY34) were modelled based on the structure of RY34 (ref. 18) and fitted to the density in a similar fashion.

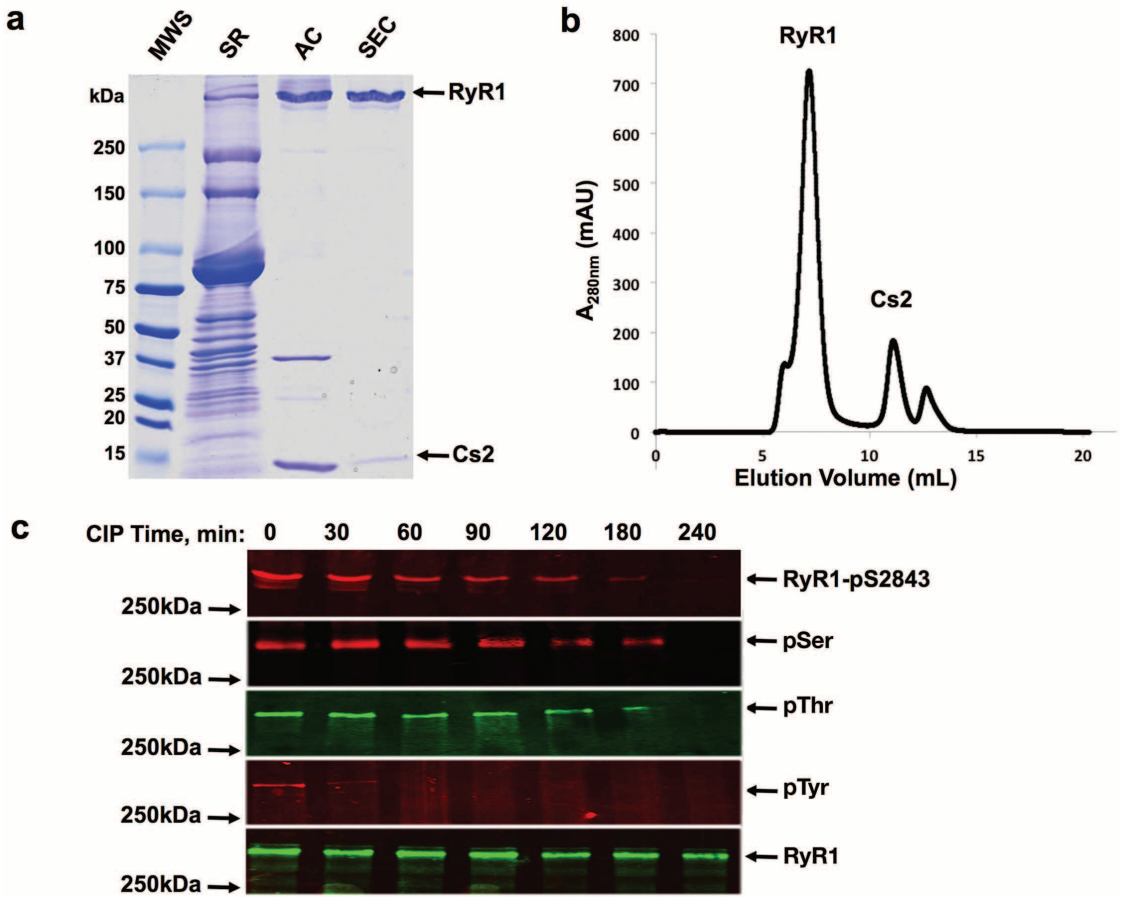
One of the SPRY domains is directly connected to the N-terminal solenoid via an ordered, α-helical linker, identifying it as SPRY1. Another of the SPRY domains is directly connected to RY12, placing it as SPRY2, and the remaining SPRY domain has been assigned as SPRY3. The three SPRY domains pack side-by-side in a triangular arrangement near the corner of the cytoplasmic assembly.

In the primary sequence, RY12 is located between SPRY1 and SPRY2, whereas RY34 is located ~1,000 residues after SPRY3, inserted in the stretch of sequence we have assigned to the bridging solenoid. Two densities of an appropriate size and shape to accommodate RyR repeat pairs are present in the map; one is located at the corner of the tetramer, contacting the SPRY domains, and the other is directly adjacent to the bridging solenoid. On the basis of these observations, we have revised the assignment of the position of RyR repeats such that RY12 is located at the extreme outer corner of the channel (directly adjacent to the SPRY domains), and RY34 (containing the PKA phosphorylation site) projects upward from the bridging solenoid (Fig. 5c, d).

The putative Ca^{2+}-binding domain was placed in a similar fashion to the other domains for which template structures were available, using the structure of the C-lobe of yeast calmodulin (PDB code 1LKJ) as a starting model. The rest of the model was built manually in Coot, using the secondary structure recognition algorithms in Coot to place and extend helices and build the linkages between them. Directionality was determined based on extension of the structure from known fragments, most importantly the N-terminal fragment, and secondary structure predictions[55] were used to guide alignment of the sequence with the model. After an initial build, segments of the structure were flexibly fit to the density using the real-space refinement algorithms implemented in Coot, with ProSMART restraints (on the basis of high-resolution reference structures where available, otherwise on the assigned secondary structure) applied to allow for deformation and curvature of helices without degrading local geometry. The final model is presented as a Cα trace, comprising in full 3,757 ordered residues for each of the four RyR protomers, and 105 residues for each of the four bound calstabin2 subunits.

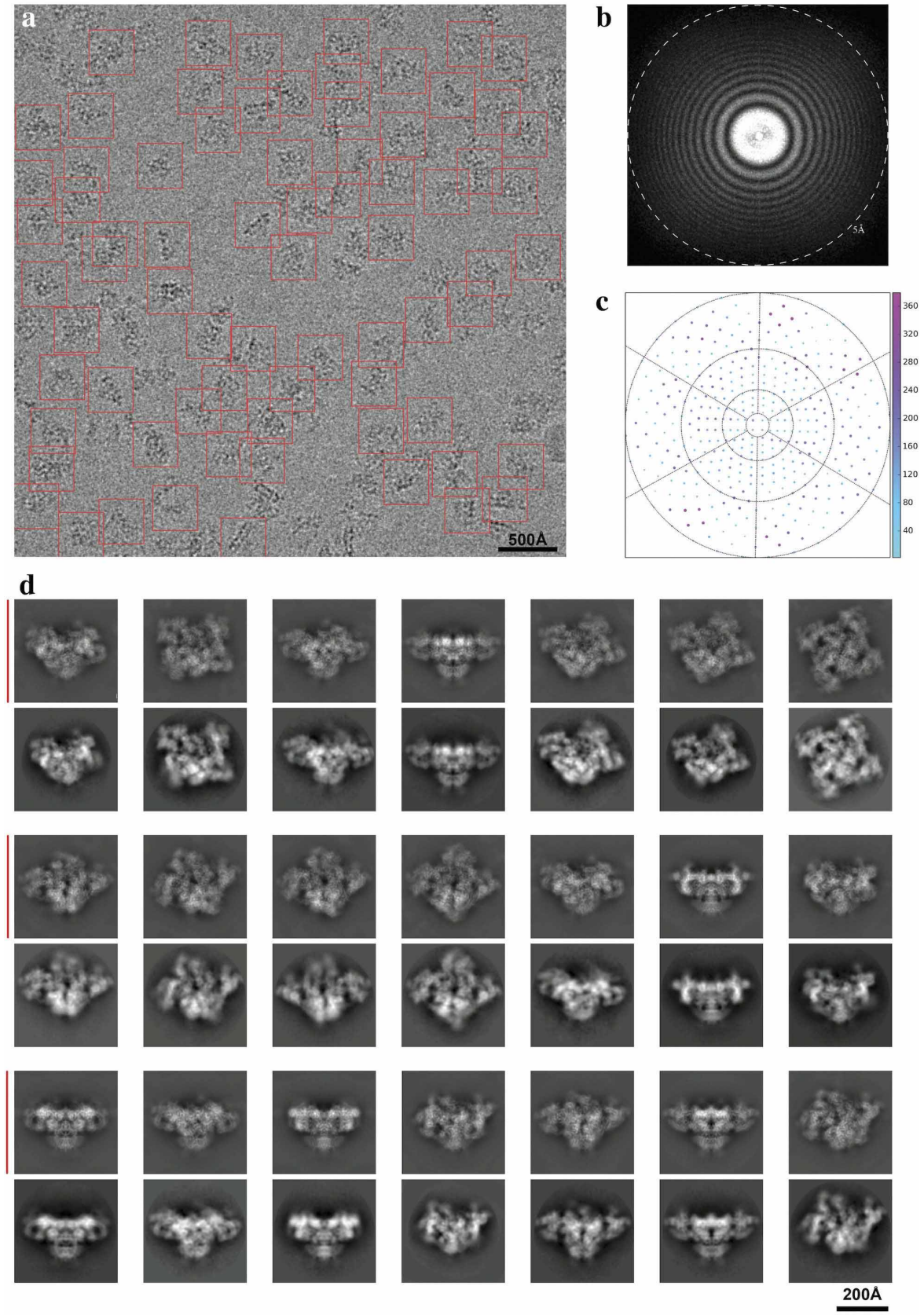
41. Xin, H. B., Timerman, A. P., Onoue, H., Wiederrecht, G. J. & Fleischer, S. Affinity purification of the ryanodine receptor/calcium release channel from fast twitch skeletal muscle based on its tight association with FKBP12. *Biochem. Biophys. Res. Commun.* **214,** 263–270 (1995).
42. Dubochet, J. *et al.* Cryo-electron microscopy of vitrified specimens. *Q. Rev. Biophys.* **21,** 129–228 (1988).
43. Wagenknecht, T., Frank, J., Boublik, M., Nurse, K. & Ofengand, J. Direct localization of the tRNA–anticodon interaction site on the *Escherichia coli* 30 S ribosomal subunit by electron microscopy and computerized image averaging. *J. Mol. Biol.* **203,** 753–760 (1988).
44. Suloway, C. *et al.* Automated molecular microscopy: the new Leginon system. *J. Struct. Biol.* **151,** 41–60 (2005).
45. Li, X. *et al.* Electron counting and beam-induced motion correction enable near-atomic-resolution single-particle cryo-EM. *Nature Methods* **10,** 584–590 (2013).
46. Frank, J. *et al.* SPIDER and WEB: processing and visualization of images in 3D electron microscopy and related fields. *J. Struct. Biol.* **116,** 190–199 http://dx.doi.org/10.1006/jsbi.1996.0030 (1996).
47. Langlois, R. *et al.* Automated particle picking for low-contrast macromolecules in cryo-electron microscopy. *J. Struct. Biol.* **186,** 1–7 (2014).
48. Scheres, S. H. A Bayesian view on cryo-EM structure determination. *J. Mol. Biol.* **415,** 406–418 (2012).
49. Reiken, S. *et al.* PKA phosphorylation activates the calcium release channel (ryanodine receptor) in skeletal muscle: defective regulation in heart failure. *J. Cell Biol.* **160,** 919–928 (2003).
50. Chen, S. *et al.* High-resolution noise substitution to measure overfitting and validate resolution in 3D structure determination by single particle electron cryomicroscopy. *Ultramicroscopy* **135,** 24–35 (2013).
51. Rosenthal, P. B. & Henderson, R. Optimal determination of particle orientation, absolute hand, and contrast loss in single-particle electron cryomicroscopy. *J. Mol. Biol.* **333,** 721–745 (2003).
52. Pintilie, G. D., Zhang, J., Goddard, T. D., Chiu, W. & Gossard, D. C. Quantitative analysis of cryo-EM density map segmentation by watershed and scale-space filtering, and fitting of structures by alignment to regions. *J. Struct. Biol.* **170,** 427–438 (2010).
53. Pettersen, E. F. *et al.* UCSF Chimera–a visualization system for exploratory research and analysis. *J. Comput. Chem.* **25,** 1605–1612 (2004).
54. Emsley, P., Lohkamp, B., Scott, W. G. & Cowtan, K. Features and development of Coot. *Acta Crystallogr. D* **66,** 486–501 (2010).
55. McGuffin, L. J., Bryson, K. & Jones, D. T. The PSIPRED protein structure prediction server. *Bioinformatics* **16,** 404–405 (2000).

©2015 **Macmillan Publishers Limited. All rights reserved**



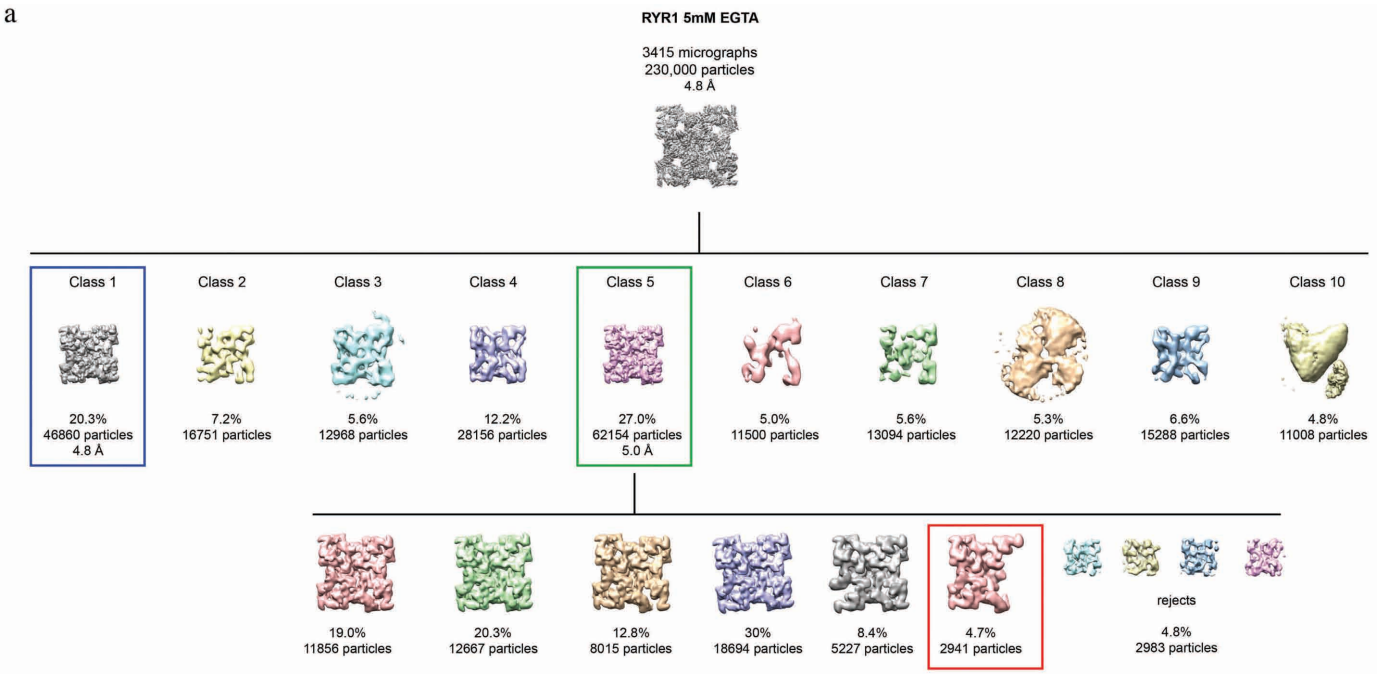
Extended Data Figure 1 | Skeletal muscle RyR1 purification. **a**, Coomassie blue staining of SDS–PAGE showing molecular weight standards (MWS), CHAPS-solubilized sarcoplasmic reticulum membrane (SR), RyR1 eluted with calstabin2 from a glutathione *S*-transferase (GST)–calstabin1 affinity chromatography column (AC), the eluted RyR1 from fast protein liquid chromatography (FPLC) size-exclusion chromatograph (SEC). **b**, FPLC plot showing the RyR1 peak at ~7 ml elution and the excess calstabin2 (Cs2) peak at ~12 ml elution. **c**, Immunoblot analysis of CIP-treated RyR1 probed at indicated time points with (from bottom) anti-RyR1 (34C) antibody, anti-phosphotyrosine antibody (pTyr; Abcam ab10321), anti-phosphothreonine antibody (pThr; Abcam ab79851), anti-phosphoserine antibody (pSer; Abcam ab9332) and anti-RyR phospho-specific antibody (RyR1-pS2843) that recognizes the PKA phosphorylated site on RyR1.

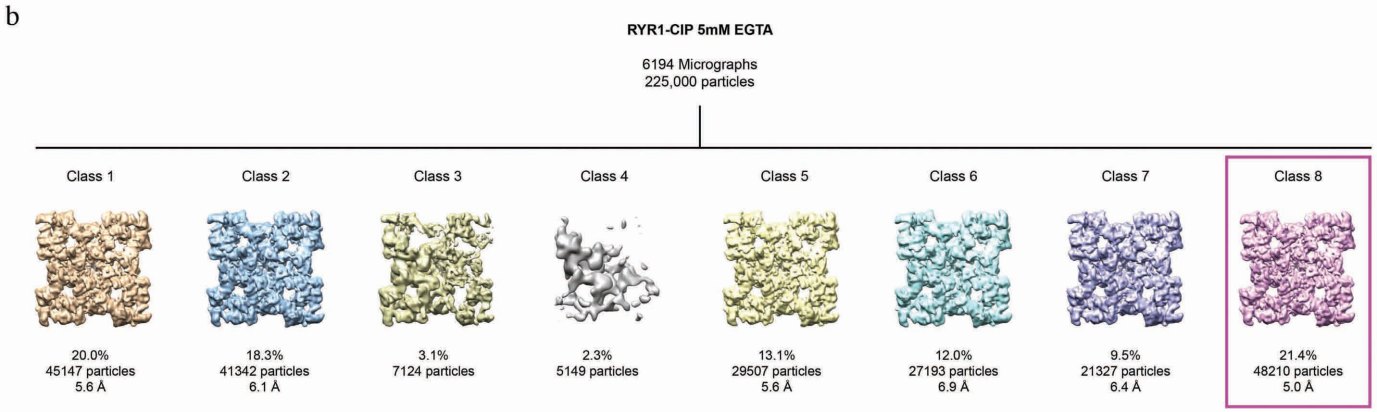
©2015 Macmillan Publishers Limited. All rights reserved

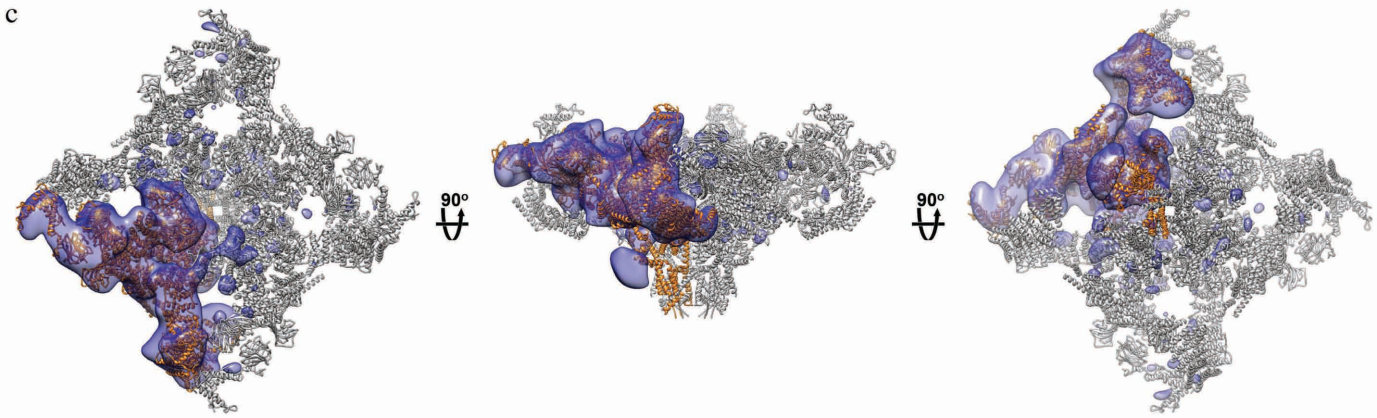


Extended Data Figure 2 | Particle picking and two-dimensional class averages. **a**, Sample micrograph of the RyR1-CIP-EGTA data set after motion correction, with red boxes around the particles picked by Autopicker[47]. Scale bar, 500 Å. **b**, Sample power spectrum of a twice-decimated micrograph after motion correction. **c**, Euler angle distribution before symmetry was imposed of the particles that went into the CIP-treated data set final reconstruction. Latitude (radial distance) corresponds to θ from 0 to 90°. Longitude (position on the circle) corresponds to ϕ, from 0 to 360°. The dots colour and area represent the number of particles in each view. **d**, Two-dimensional projections of the final CIP-treated map (upper rows; red lines) compared to their respective reference-free two-dimensional class averages (lower rows).

©2015 Macmillan Publishers Limited. All rights reserved

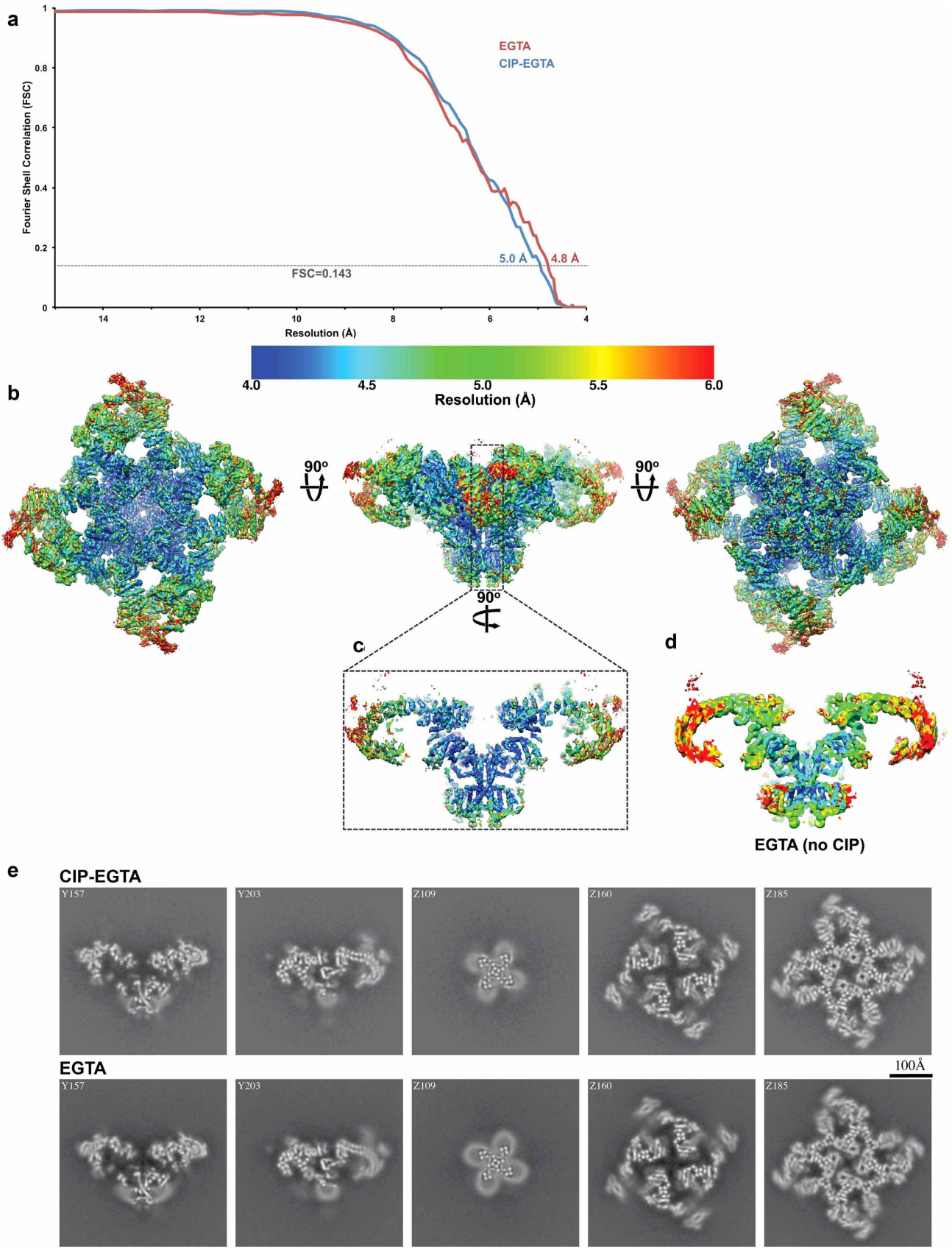






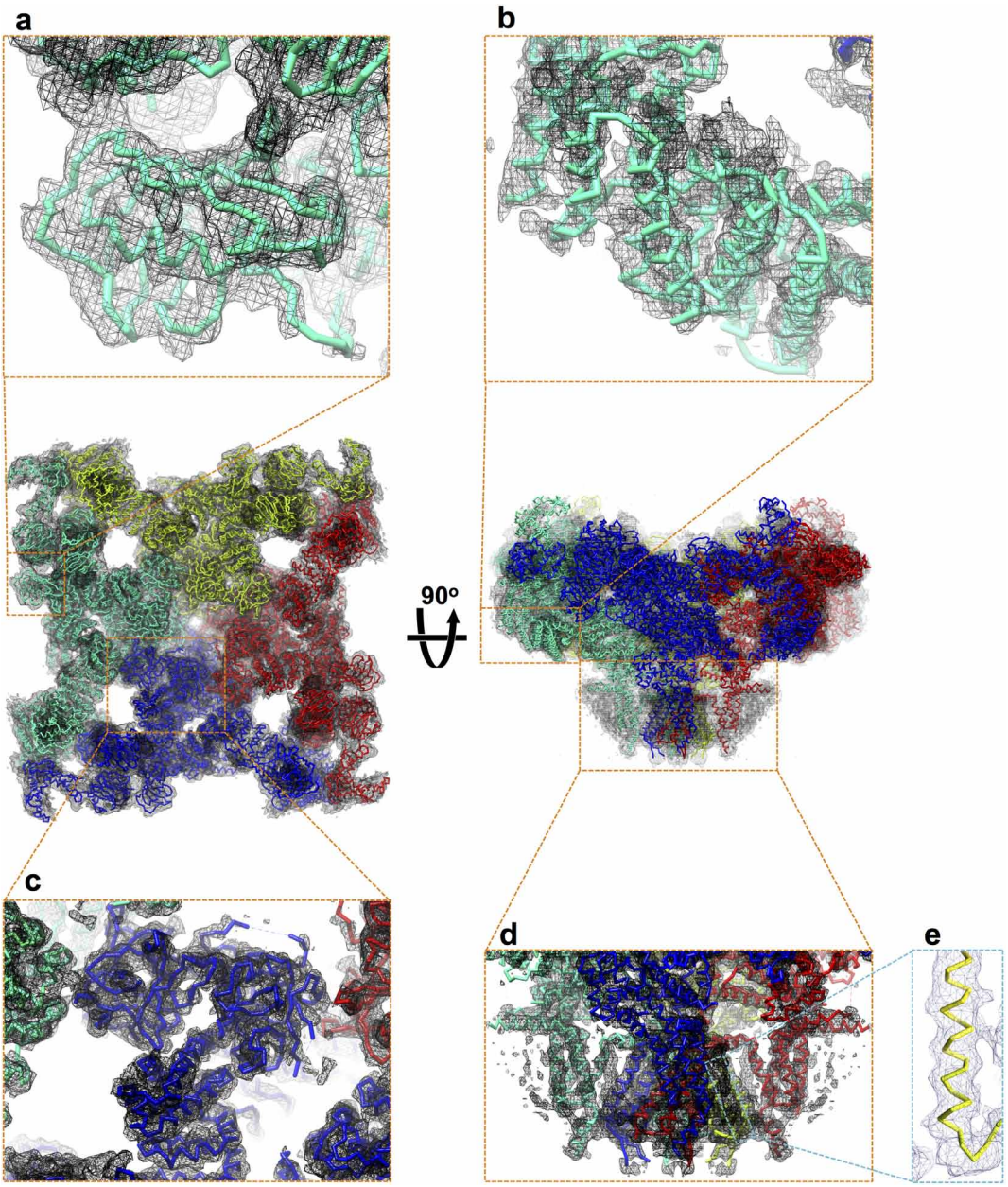
Extended Data Figure 3 | Classification and protomer boundaries. **a**, Classification of the RyR1-EGTA data set. First row, refined volume with all particles. Second row, primary classification with a number of classes ($K = 10$) giving rise to two major classes, one refined to 4.8 Å (blue box) and one refined to 5.0 Å (green box). This class (green box) was subclassified with $K = 10$ (third row), and yielded one class with a missing or disordered cytosolic portion of a protomer (red box). **b**, Classification of the RyR1-EGTA-CIP-treated data set with $K = 8$. Class 8 (purple box) was refined to 5.0 Å. **c**, Views from the cytosol, membrane plane and lumen of the RyR1 model superimposed with a difference map between the full tetramer map (blue box) and the map with the cytosolic region of one protomer missing or disordered (red box).

©2015 Macmillan Publishers Limited. All rights reserved



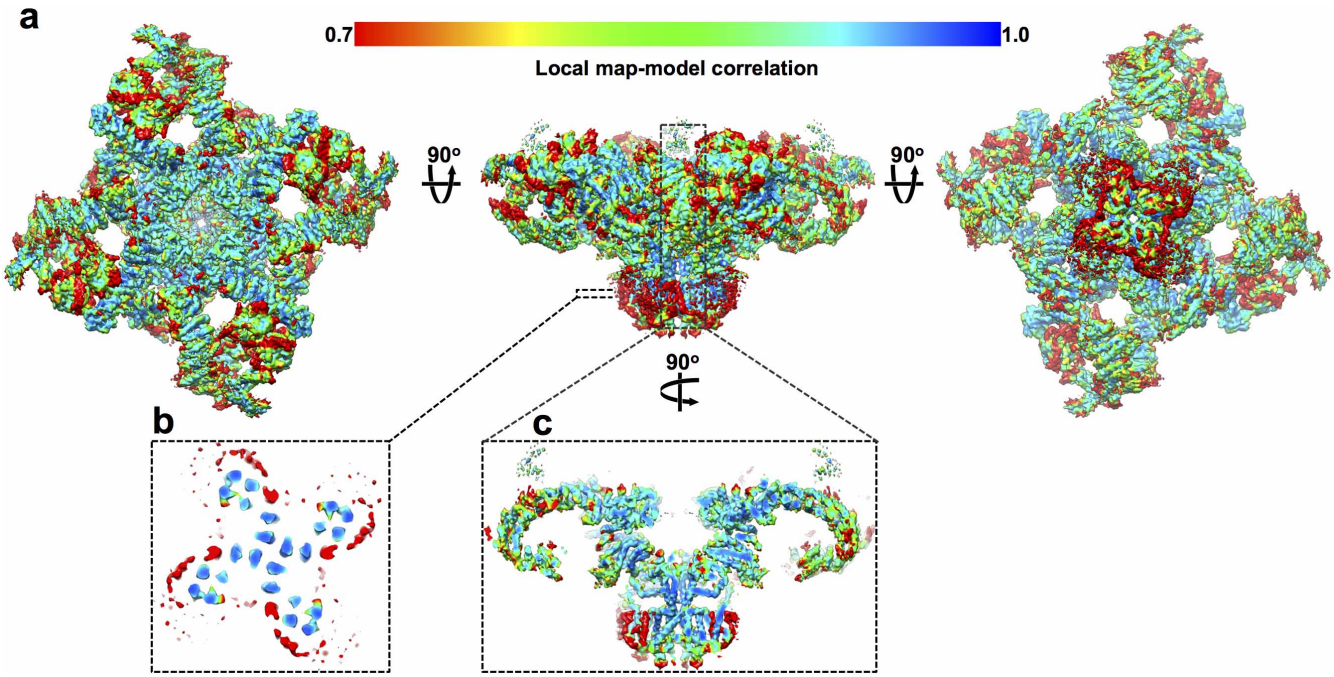
Extended Data Figure 4 | RyR1 cryo-EM local resolution map. **a**, Gold-standard FSC curve for the three-dimensional reconstructions, marked with resolutions corresponding to FSC = 0.143. **b**, Cytosolic, membrane plane and luminal views of RyR1 (EGTA- and CIP-treated data set) local resolution distribution from 4 (blue) to 6 (red) Å resolution. **c**, Local resolution distribution through a slab of density coincident with channel axis. **d**, Same slab as **c** for the EGTA-treated without CIP. **e**, Slices through the volume of the CIP-EGTA data set (top) and EGTA data set (bottom). Slice direction and number are indicated on the images.

©2015 Macmillan Publishers Limited. All rights reserved



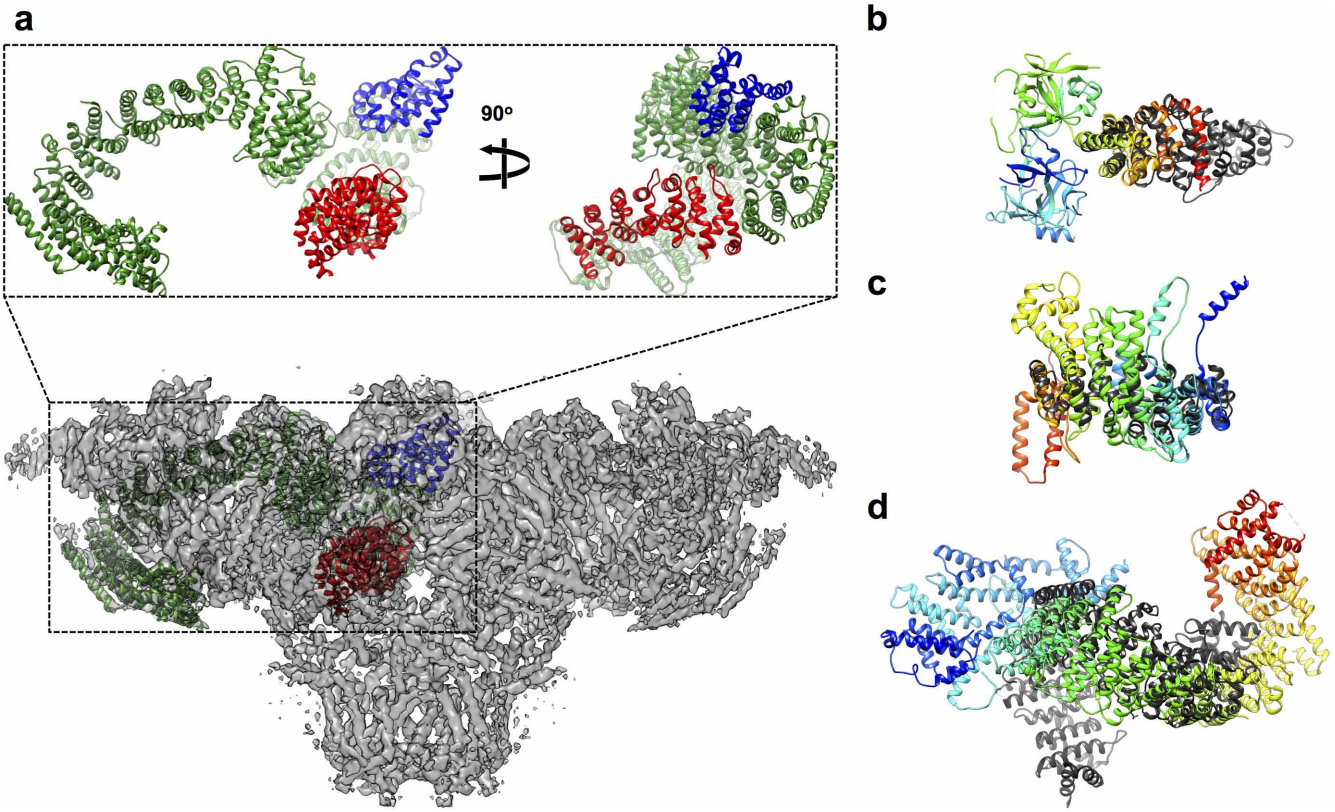
Extended Data Figure 5 | Representative densities of RyR1-selected regions. **a**–**e**, Representative density (grey mesh) in selected regions of the map. The protomers are represented as Cα traces, in different colours for clarity, with enlarged views of the following regions: calstabin2 (**a**), the bridge solenoid (**b**), NTD (**c**), the pore region (**d**) and S6 (**e**).

©2015 Macmillan Publishers Limited. All rights reserved



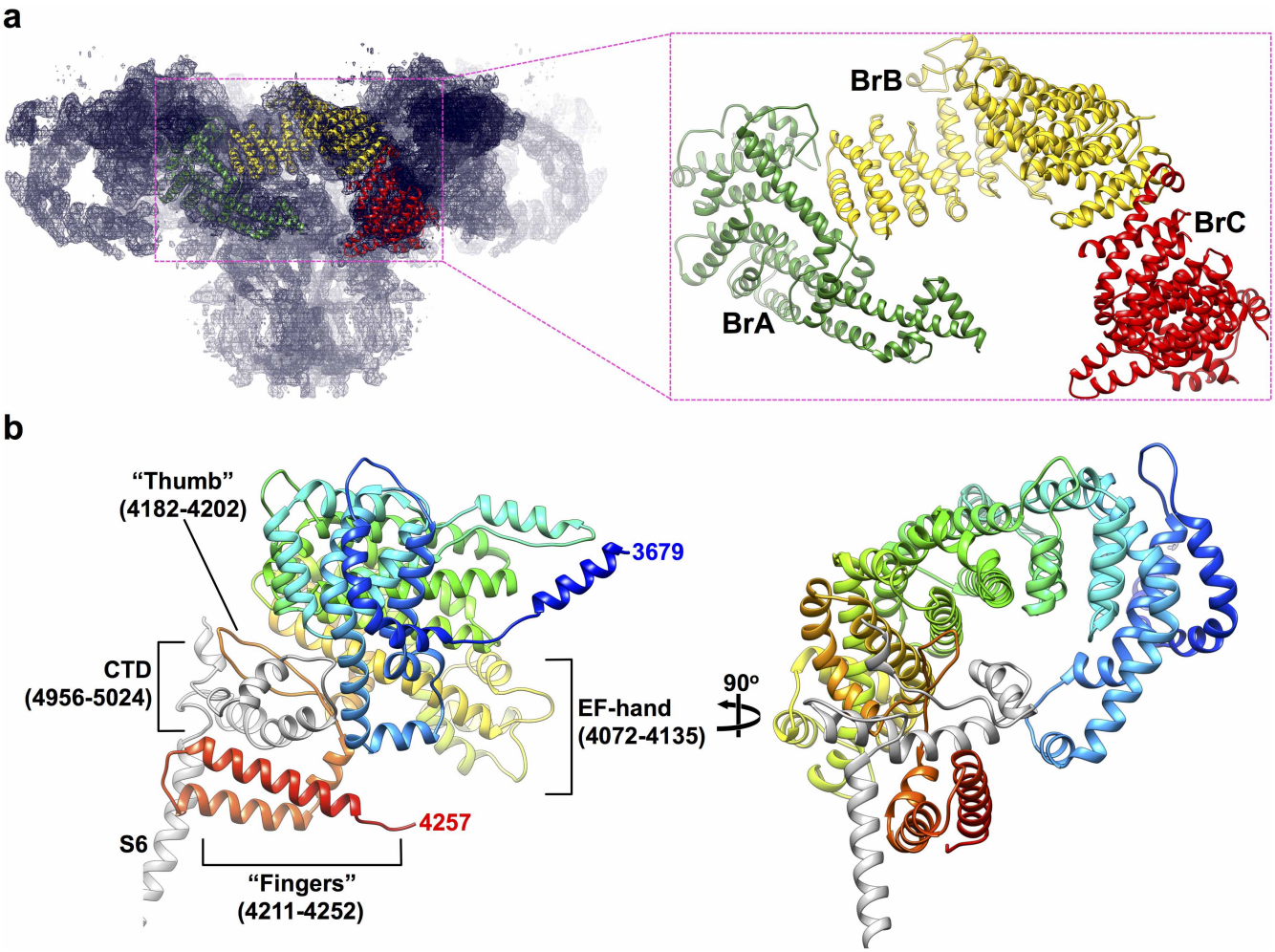
Extended Data Figure 6 | RyR1 local model to map correlation. **a**, Cytosolic, membrane plane and luminal views of the local correlation (calculated in a 5×5 voxel sliding window) between a map calculated from the model (filtered to 5 Å) and the density map of dephosphorylated RyR1, depicted in spectral colouring from 0.7 (red) to 1 (blue). **b**, **c**, Local model/density map correlation within a slab of density through the plane of the membrane, highlighting the unmodelled rod of density on the periphery of the transmembrane region (**b**) and a slab coinciding with the channel axis (**c**).

©2015 Macmillan Publishers Limited. All rights reserved



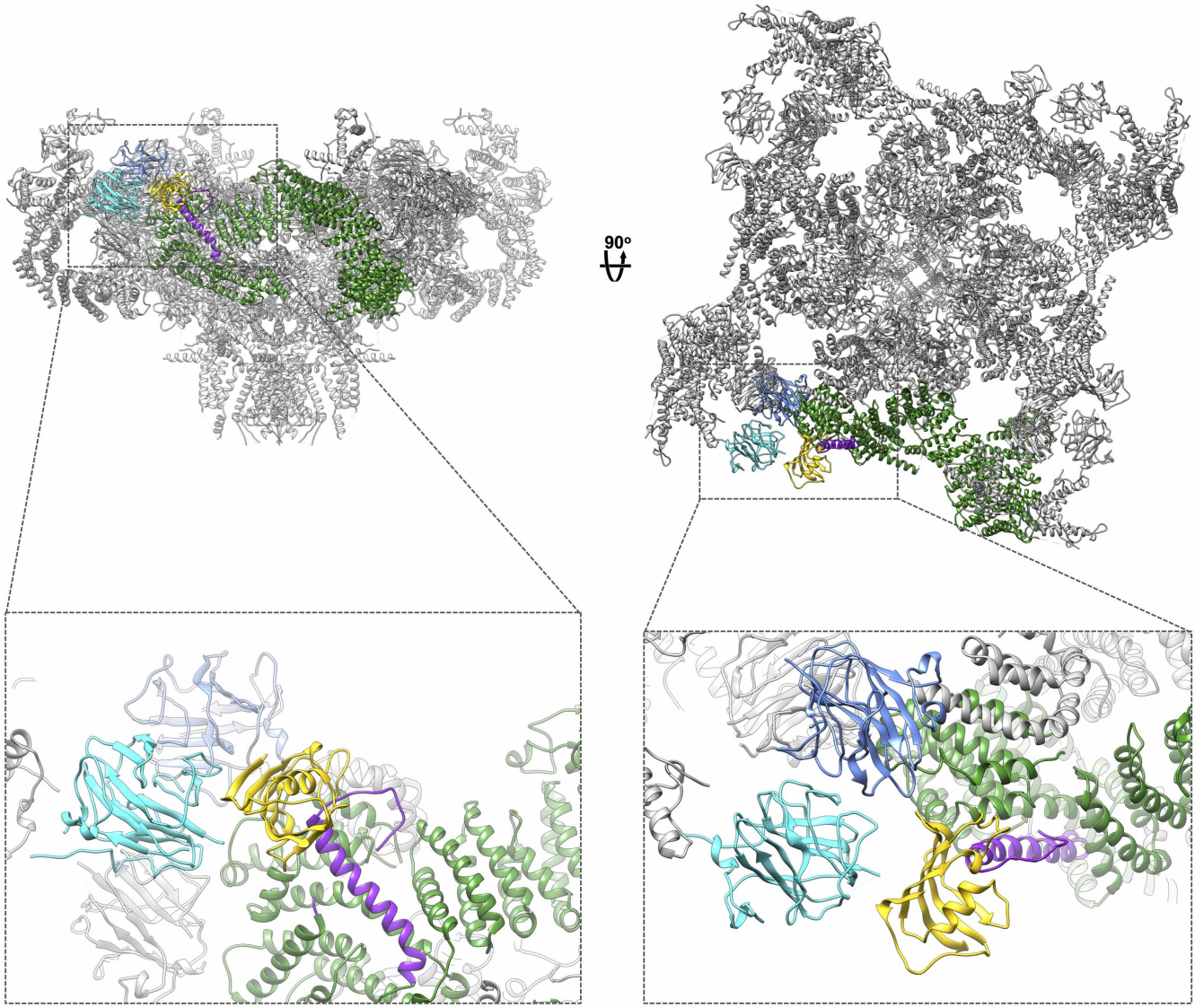
Extended Data Figure 7 | α- solenoid subdomains. RyR1 density map (grey semitransparent surface) superimposed with the α-solenoid scaffold of RyR1. **a**, Core of the α-solenoid scaffold (insertions and elaborations not shown). Green, bridging solenoid; blue, NTD solenoid; red, core solenoid. **b**, Alignment of NTD with an α-solenoid structure (PDB code 3NMX). **c**, Alignment of core solenoid with an α-solenoid structure (PDB code 1G3J). **d**, Overlay of bridging solenoid with an α-solenoid structure (PDB code 1WA5). In **b**–**d**, RyR1 α-solenoid repeats are depicted in spectral colouring from blue (N terminus) to red (C terminus), and the aligned α-solenoid protein is represented in dark grey.

©2015 Macmillan Publishers Limited. All rights reserved



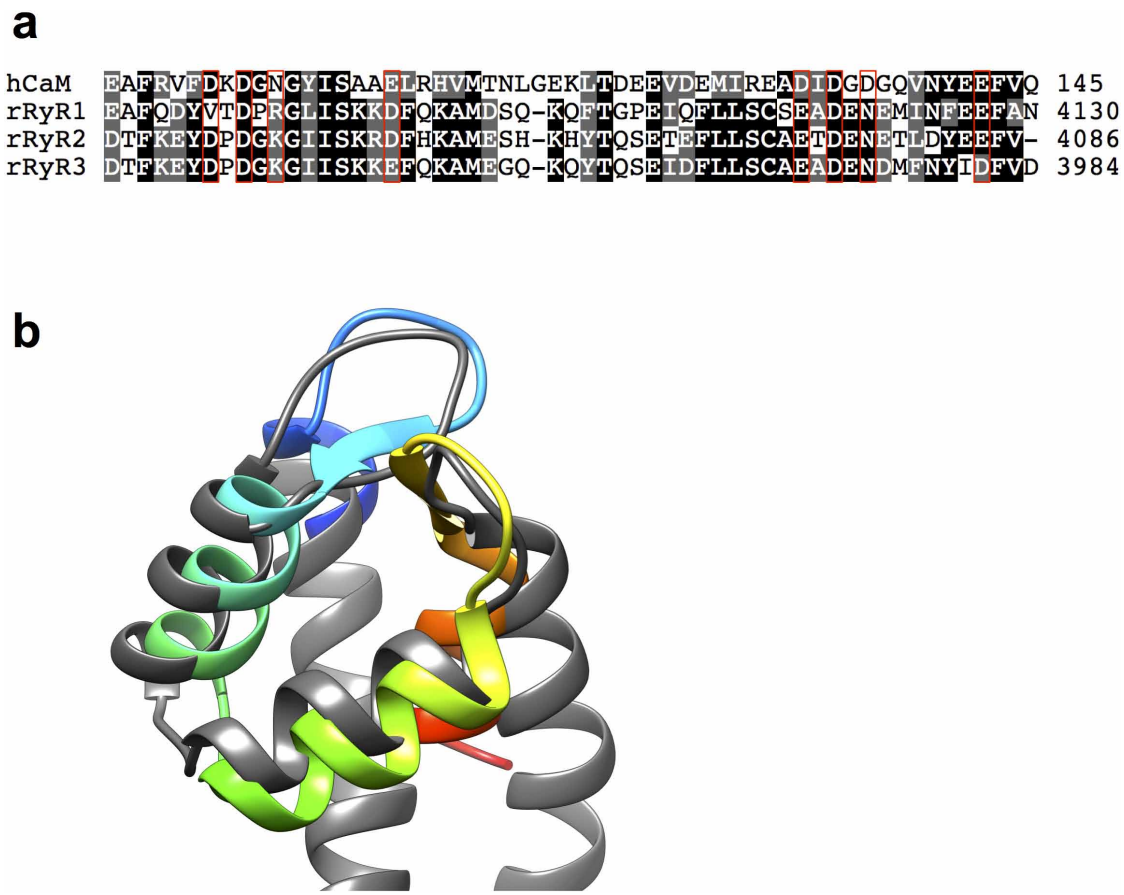
Extended Data Figure 8 | Architecture of bridging and core solenoids. **a**, Density map of RyR1 in dark blue mesh superimposed with the bridging solenoid shown in detail on right, as labelled. **b**, Two views of the interaction of the core solenoid (spectral colouring) containing the putative Ca^{2+}-binding domain with CTD (grey) as labelled.

©2015 Macmillan Publishers Limited. All rights reserved



Extended Data Figure 9 | Calstabin2-binding site. Views in the membrane plane and cytosol of RyR1 with enlarged views of calstabin2 (yellow) bound to RyR1. SPRY1 is depicted in light blue, SPRY2 in cyan, the bridging solenoid in green and the calstabin binding helix in purple.

©2015 Macmillan Publishers Limited. All rights reserved



Extended Data Figure 10 | Putative Ca^{2+}-binding domain in RyR1. **a**, Sequence alignment of rabbit RyR1–3 with the C-lobe of human calmodulin (hCaM). **b**, Structural alignment of the C-lobe of yeast calmodulin with the model of RyR1.

©2015 Macmillan Publishers Limited. All rights reserved

ARTICLE

doi:10.1038/nature14063

Structure of the rabbit ryanodine receptor RyR1 at near-atomic resolution

Zhen Yan[1,2,3]*, Xiao-chen Bai[4]*, Chuangye Yan[2,3]*, Jianping Wu[2,3], Zhangqiang Li[1,3], Tian Xie[2,3], Wei Peng[1,3], Chang-cheng Yin[5], Xueming Li[3], Sjors H. W. Scheres[4], Yigong Shi[2,3] & Nieng Yan[1,3]

The ryanodine receptors (RyRs) are high-conductance intracellular Ca^{2+} channels that play a pivotal role in the excitation–contraction coupling of skeletal and cardiac muscles. RyRs are the largest known ion channels, with a homotetrameric organization and approximately 5,000 residues in each protomer. Here we report the structure of the rabbit RyR1 in complex with its modulator FKBP12 at an overall resolution of 3.8 Å, determined by single-particle electron cryomicroscopy. Three previously uncharacterized domains, named central, handle and helical domains, display the armadillo repeat fold. These domains, together with the amino-terminal domain, constitute a network of superhelical scaffold for binding and propagation of conformational changes. The channel domain exhibits the voltage-gated ion channel superfamily fold with distinct features. A negative-charge-enriched hairpin loop connecting S5 and the pore helix is positioned above the entrance to the selectivity-filter vestibule. The four elongated S6 segments form a right-handed helical bundle that closes the pore at the cytoplasmic border of the membrane. Allosteric regulation of the pore by the cytoplasmic domains is mediated through extensive interactions between the central domains and the channel domain. These structural features explain high ion conductance by RyRs and the long-range allosteric regulation of channel activities.

RyRs are responsible for the rapid release of Ca^{2+} ions from sarcoplasmic and endoplasmic reticula into the cytoplasm, a key event that triggers muscle contraction[1–3]. Three mammalian isoforms, RyR1, RyR2 and RyR3, share about 70 per cent sequence identity. RyR1 and RyR2 are primarily expressed in skeletal and cardiac muscles, respectively, and RyR3 was originally found in the brain[4,5]. RyRs also share considerable sequence similarity with the inositol-1,4,5-triphosphate receptor ($Ins(1,4,5)P_3$ or IP_3 receptor), another major sarcoplasmic and endoplasmic reticula Ca^{2+} channel[6,7]. As the largest known ion channel, RyR has a molecular mass of more than 2.2 megadaltons (MDa) and consists of four identical protomers, each containing over 5,000 residues that are folded into a cytoplasmic region and a transmembrane region[4,8]. Four identical transmembrane segments enclose a central ion-conducting pore, whereas the cytoplasmic region senses interactions with diverse ligands ranging from ions, exemplified by Ca^{2+} and Mg^{2+}, to proteins such as the voltage-gated Ca^{2+} channel dihydropyridine receptor (DHPR, also known as $Ca_v1.1$). RyRs can therefore respond to a large number of stimuli with complex regulatory mechanisms[9–11].

Ca^{2+} ions represent a primary regulator of RyRs[10,12,13]. The probability plot of channel opening versus Ca^{2+} concentration is bell-shaped[14,15]. In cardiocytes, voltage-gated opening of $Ca_v1.2$ causes an influx of Ca^{2+} ions, which subsequently activates RyR2. In skeletal myocytes, action-potential-induced conformational changes of $Ca_v1.1$ are physically coupled to channel opening of RyR1. In essence, $Ca_v1.1$ serves as the voltage sensor for RyR1 (refs 16, 17). A variety of other chemicals and proteins modulate RyRs through independent or synergistic mechanisms. Among these modulators, the immunophilins FKBP12 and FKBP12.6 preferentially bind RyR1 and RyR2, respectively, and stabilize their closed states[18]. Because RyRs have an essential role in muscle contraction, their functional mutations are associated with several debilitating diseases. Aberrant function of RyR1 contributes to malignant hyperthermia and central core disease, whereas mutations in RyR2 may lead to heart disorders. Altogether, more than 500 disease-derived mutations have been mapped to the primary sequences of RyRs with several hotspots[11].

Electron microscopy has been applied to structural studies of RyRs[19–23]. In fact, RyRs were initially identified in the electron microscopy negative-staining images of the myocyte, which revealed the presence of 'feet' between the T-tubule and sarcoplasmic reticulum[24]. Among the published electron cryomicroscopy (cryo-EM) structures, the highest overall resolution achieved for RyR1 is approximately 10 Å, revealing a mushroom-shaped architecture and a transmembrane domain thought to resemble the structure of the $K_v2.1$ channel[23]. In addition, crystal structures of the amino-terminal fragments and a phosphorylation hotspot domain of RyRs have been reported[11].

Using direct electron detection and advanced image processing algorithms for cryo-EM[25–27], we have determined the structure of a closed-state RyR1 in complex with FKBP12 at an overall resolution of 3.8 Å. Near-atomic resolution is achieved at the channel domain (residues 4545–5037) and its adjoining domains in the cytoplasmic region, sufficient for *de novo* atomic model building. In total, 70% of the 2.2-MDa molecular mass of RyR1 was resolved.

Overall structure and domain assignment of RyR1

We used glutathione *S*-transferase (GST)–FKBP12 as an affinity bait to purify RyR1 (residues 1–5037) from rabbit muscle, and solved the structure by cryo-EM single-particle analysis (Extended Data Fig. 1). The tetrameric RyR1 has a pyramid appearance, with a square base of 270 × 270 Å and a height of 160 Å (Fig. 1a). Combining *de novo* model building and previous knowledge on isolated domains, the backbone of 3,685 residues and more than 3,100 specific side chains were assigned in each protomer (Extended Data Figs 2–5 and Supplementary Video 1).

[1]State Key Laboratory of Bio-membrane and Membrane Biotechnology, School of Life Sciences and School of Medicine, Tsinghua University, Beijing 100084, China. [2]Ministry of Education Key Laboratory of Protein Science, School of Life Sciences and School of Medicine, Tsinghua University, Beijing 100084, China. [3]Center for Structural Biology, Tsinghua-Peking Joint Center for Life Sciences, School of Life Sciences and School of Medicine, Tsinghua University, Beijing 100084, China. [4]MRC Laboratory of Molecular Biology, Cambridge Biomedical Campus, Cambridge CB2 0QH, UK. [5]Department of Biophysics, the Health Science Center & Center for Protein Science, Peking University, Beijing 100191, China.
*These authors contributed equally to this work.

©2015 Macmillan Publishers Limited. All rights reserved

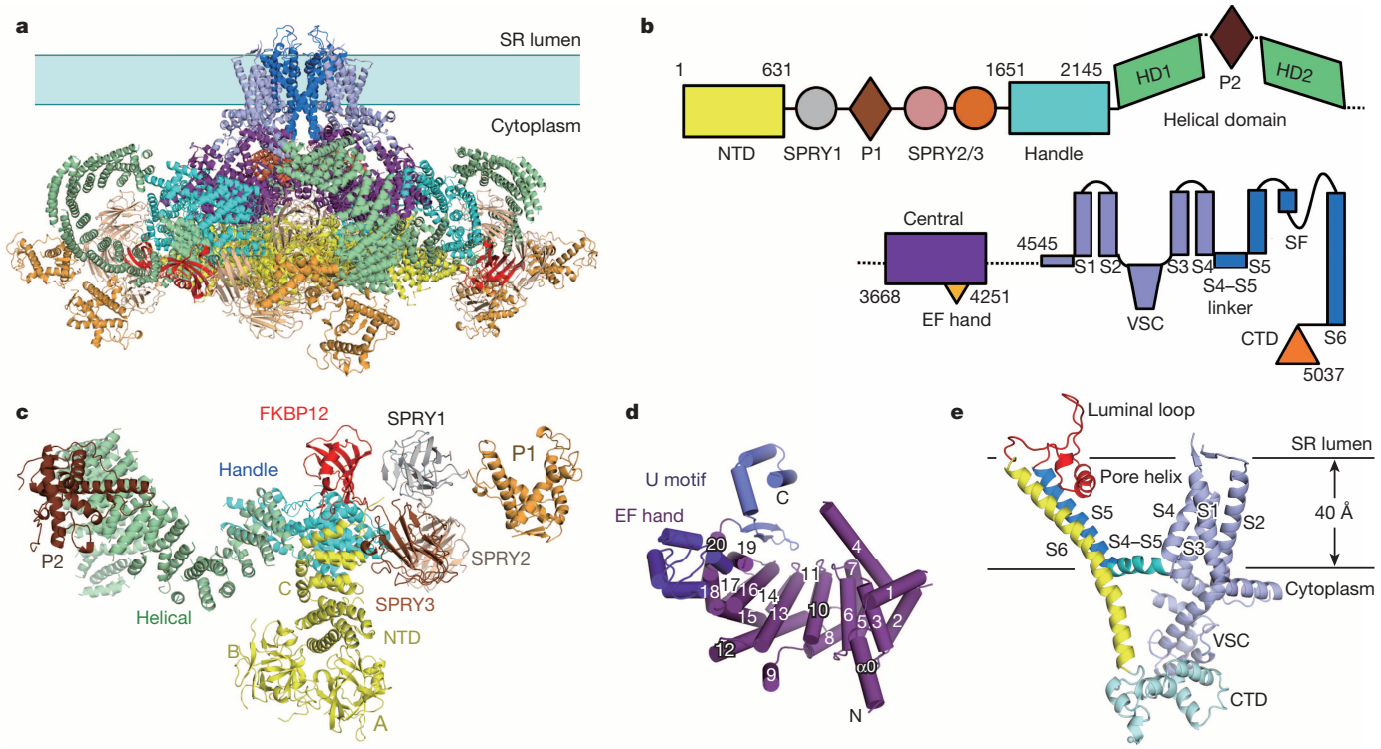


Figure 1 | Overall structure and domain organization of the rabbit RyR1. **a**, Structure of the tetrameric RyR1 in complex with FKBP12. In all side views, the structure is presented with the sarcoplasmic reticulum (SR) luminal side on the top. **b**, A schematic illustration of domain organization in one RyR1 protomer. The annotation for domain abbreviations and detailed boundaries are reported in Extended Data Fig. 2c. **c**, Spatial arrangement of the cytoplasmic domains preceding the central domain within one RyR1 protomer. Shown here is a cytoplasmic view. **d**, Structure of the central domain. The central domain comprises an armadillo repeat-like superhelical assembly of 20 α-helices, an EF-hand domain on the ridge of the assembly, and a U-motif at the C terminus. **e**, Structure of the channel domain from one RyR1 protomer. All structure figures were prepared using PyMol[43].

A total of nine distinct domains have been resolved in the cytoplasmic region of each protomer, including the N-terminal domain (NTD), three SPRY domains (originally identified in SplA kinase and RyRs), the P1 and P2 domains, and the handle, helical and central domains (Fig. 1b, c). The resolution and quality of the electron microscopy densities allowed side-chain assignment for the NTD (residues 1–631), the handle domain (residues 1651–2145) and the central domain (residues 3668–4251). Most of the helical domain (residues 2146–2712 for HD1 and 3016–3572 for HD2) only permitted tracing of the backbone. The density map for the three SPRY domains, P1 and P2 domains, and FKBP12, which are located at the periphery of the tetrameric assembly, is considerably poorer than that for the central regions, but still allowed domain assignment and homologous structure-based model building. The handle, helical and central domains are previously uncharacterized, whereas the NTD has five additional α-helices compared to that in the crystal structure[28] (Extended Data Figs 3–6).

The handle and helical domains are connected in both primary sequences and spatial arrangements (Fig. 1b, c). The handle domain is formed by 16 α-helices, among which five pairs are homologous to the armadillo repeats (Extended Data Fig. 6c, f). The helical domain, which comprises 17 α-helical hairpins and 7 α-helices at the carboxyl-terminal end, forms a right-handed superhelical assembly. The P2 domain (residues 2734–2940) bulges out from the outer surface of the assembly after the tenth repeat (Extended Data Fig. 6d).

In the central domain, the bulk of the sequences forms a horseshoe-shaped subdomain with 19 α-helices organized into helical repeats conforming to the armadillo repeat fold[29] (Extended Data Fig. 6g). The C-terminal ridge of the helical repeats is bound by an EF-hand subdomain (residues 4071–4131) corresponding to the previously identified EF-hands 1 and 2 (ref. 30) (Fig. 1d and Extended Data Fig. 5). The C-terminal sequences of the central domain form a U-shaped subdomain (U-motif) that is positioned above the concave side of the armadillo repeats. The U-motif consists of a β-hairpin, an α-helix hairpin at the C terminus, and an intervening short α-helix (Fig. 1d).

In the channel domain, the transmembrane segments S1 to S6 exhibit a voltage-gated ion channel superfamily fold (Fig. 1e). However, the RyR1 channel domain has three unique features. First, the extended S6 segment, with half in the membrane and the other half sticking into the cytoplasm, is immediately followed by a previously unknown small C-terminal subdomain (CTD). Second, the intervening sequences between S2 and S3 fold into a cytoplasmic subdomain, named VSC for cytoplasmic subdomain in the voltage-sensor like domain (VSL), which bridges CTD and the S1–S4 segments. Third, a hairpin loop between S5 and the pore helix projects into the sarcoplasmic reticulum lumen and is hence named the luminal loop. VSC, CTD and the central domain together constitute the previously defined 'column' in RyR1 (refs 21, 22) (Extended Data Fig. 2b).

Hierarchical organization of the RyR1 structure

The tetrameric RyR1 structure has a hierarchical organization (Fig. 2 and Supplementary Video 1). The overall structure can be divided into three zones: a central tower comprising the channel domain, the central domains and the NTDs (Fig. 2a), a corona formed by the handle and helical domains surrounding the central tower (Fig. 2b), and the peripheral domains comprising the three SPRY domains and P1 and P2 domains that attach to the corona (Fig. 2c).

The central tower displays a three-layered organization along the four-fold axis: transmembrane segments as layer 1, the cytoplasmic elements of the channel domain and central domains as layer 2, and NTDs as layer 3 (Fig. 2a). The NTD comprises subdomains A and B, which are rich in β-strands, and subdomain C, which consists exclusively of 12 α-helices conforming to the armadillo repeats (Extended Data Fig. 6a, e).

©2015 Macmillan Publishers Limited. All rights reserved

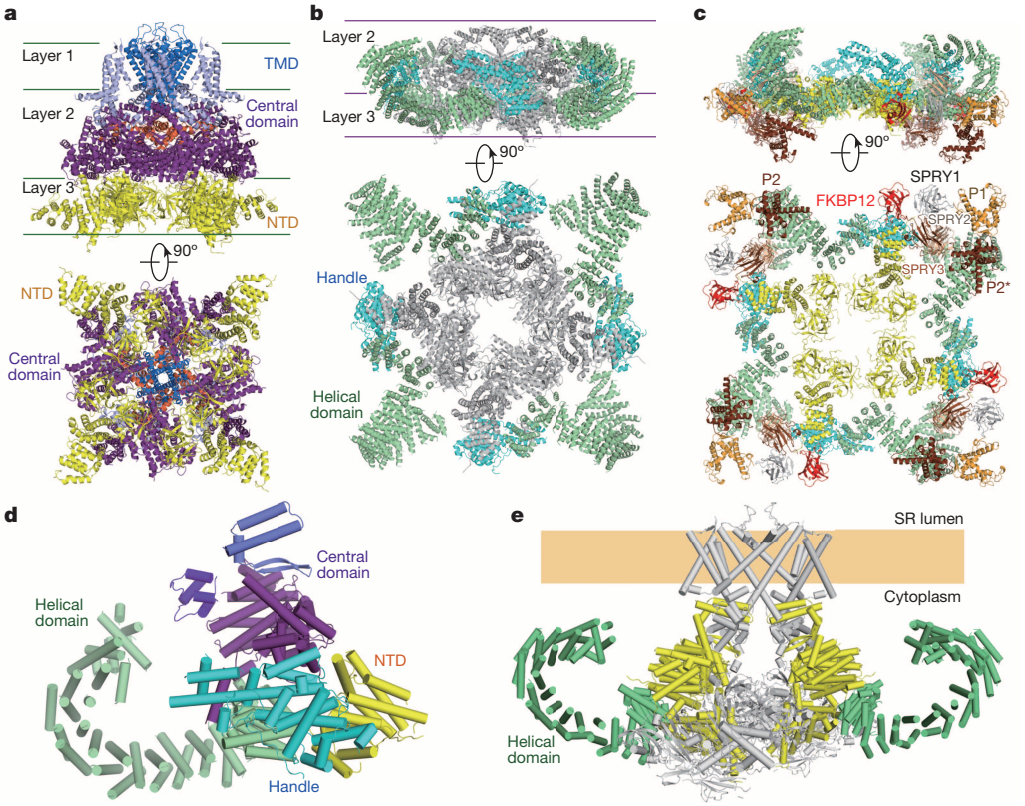


Figure 2 | Hierarchical organization of the tetrameric RyR1. **a**, A three-layered central tower forms the core of RyR1. The central domain is the only cytoplasmic structure that directly interacts with the channel domain. **b**, The handle and helical domains form a corona around the central tower. For visual clarity, the NTD and central domain are coloured grey and the channel domain is omitted. **c**, The peripheral domains of RyR1 attach to the corona. The central domains and channel domain are omitted. **d**, Two superhelical assemblies form a scaffold in the cytoplasmic region in each RyR protomer. The helical domain constitutes one superhelical assembly; the armadillo-like repeats from the NTD, the handle and central domains constitute the other. **e**, The two superhelical assemblies provide the binding scaffold and the adaptability for the propagation of conformational changes. Only two diagonal molecules are shown. The superhelical assemblies formed by the NTD, the handle and central domains are coloured yellow, the helical domains are coloured green, and the rest in grey.

The four NTDs associate with each other through their respective subdomains A and B to form a central vestibule[28]. By contrast, the central domains do not interact with each other. The N-terminal helical repeats of the central domain directly bind subdomain B and helix 3 of subdomain C in one NTD, and the C-terminal helices interact specifically with subdomain A of an adjacent NTD (Extended Data Fig. 6h–j). Notably, the central domain is the only cytoplasmic structure that directly interacts with the channel domain (Figs 1a and 2a), and thus must be responsible for allosteric coupling between conformational changes in the cytoplasmic region and the opening/closure of the channel.

The handle and helical domains form a discontinuous corona surrounding the lower two layers of the central tower (Fig. 2b). The gap is occupied by SPRY2 (Extended Data Fig. 6k). The corona interacts extensively with the central tower and provides the binding platform for the peripheral domains as well as RyR modulators such as FKBP12 (Fig. 2c and Extended Data Fig. 6l, m). The peripheral domains contribute to the interactions between adjacent protomers and expand the cytoplasmic surface of RyR1.

Notably, the armadillo repeats from the NTD, handle and central domains merge end-to-end to form an extended superhelical assembly, which interacts with the other superhelical structure — the helical domains — through an extensive interface (Fig. 2d and Extended Data Fig. 6h, j). The armadillo repeat fold, which belongs to the α-solenoid superfamily, is designed for binding to various cofactors and known for its inherent conformational adaptability[29]. Structural shifts caused by modulator binding may be propagated to other regions along the two superhelical assemblies, which ultimately affect the conformation of the central domain, and impact on the channel domain (Fig. 2e). RyR1 therefore has the structural support to sense and propagate conformational changes from any location of the cytoplasmic region.

A closed channel

The near-atomic resolution allows a detailed analysis of the RyR1 channel domain (Fig. 3a and Extended Data Fig. 7). The ion-conducting pathway is formed entirely by the S6 segment and the selectivity filter (Fig. 3b). In K^+ and transient receptor potential vanilloid 1 (TRPV1) channels, the selectivity filter is supported by a half-way pore-helix (P-helix) followed by a re-entrant loop, and an extra helix (the P2 helix) is present in Na_v and Ca_vAb channels (Extended Data Fig. 8a). The RyR1 protomer has only one intact pore-helix, and the pore-loop contains a helical turn at the entrance to the selectivity-filter vestibule, where the side chains of Asp 4899 and Glu 4900 may constitute an ion-binding site (Fig. 3c).

The selectivity-filter vestibule is approximately 10 Å in length (Fig. 3d). An inner ion-binding site may be formed by the carbonyl oxygen groups of Ala 4893, Gly 4894 and Gly 4895 (Fig. 3c). The observed selectivity filter composition is consistent with previous predictions derived from sequence and mutational analyses[31–35]. Despite distinct physical attributes of the selectivity-filter vestibule, the combination of an outer site by side-chain carboxylates and an inner site by C = O groups within the selectivity-filter vestibule is reminiscent of that in the Ca^{2+}-conducting channel TRPV1 (ref. 36) or Ca_vAb (ref. 37), suggesting a common principle for Ca^{2+} permeation. Consistent with its essential function, the selectivity filter is also a hotspot for disease-related mutations (Extended Data Figs 7 and 9 and Supplementary Table 1).

RyR1 has a hairpin loop between S5 and the P-helix (Fig. 3c). Seven residues at the turn of the hairpin loop exhibit poor electron microscopy

©2015 Macmillan Publishers Limited. All rights reserved

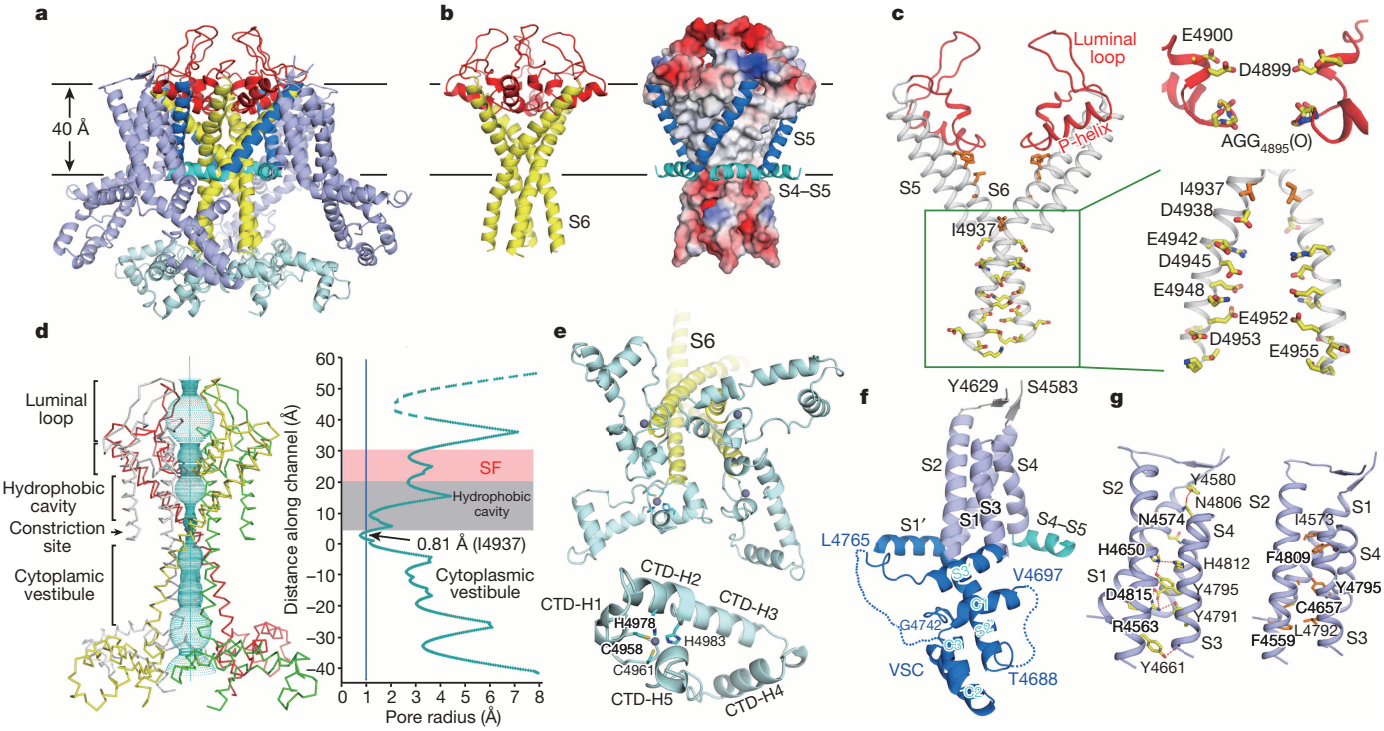


Figure 3 | Structure of the channel domain of RyR1. **a**, The transmembrane region of the RyR1 channel domain exhibits a voltage-gated ion channel fold. The structural elements are colour-coded as in Fig. 1e. **b**, The ion-conducting pore of RyR1 is formed by S6 segments and the selectivity filter. Shown here are cartoon representation (left) and electrostatic surface potential (right), calculated by PyMol[43]. **c**, Structural analysis of the ion-conducting pathway. Shown here are two diagonal protomers (left) and a close-up view on an enlarged selectivity-filter vestibule and the cytoplasmic segments of S6 (right). **d**, The RyR1 channel is closed at the cytoplasmic activation gate. The channel passage, calculated by HOLE[40], is depicted by cyan dots (left). The pore radii along the ion-conducting pathway are tabulated (right), in which the dashed lines indicate segments of poor electron microscopy densities. The position of the S4–S5 helical axis is set as the origin of the *y* axis. **e**, A unique C-terminal domain (CTD) is tightly connected to S6 in each RyR1 protomer. Bottom, structure of one CTD in which a C2H2-type zinc-finger motif is identified. The zinc atom is shown as a purple sphere. The helices in CTD are labelled from CTD-H1 to CTD-H5. **f**, Structure of the voltage sensor-like (VSL) domain in one protomer. The disordered sequences are indicated by dashed lines. **g**, The transmembrane segments S1–S4 interact closely with each other. Potential hydrogen bonds are shown as red dashed lines.

densities, indicating intrinsic flexibility. Six out of the seven residues are Asp or Glu (Extended Data Fig. 3e). The highly electronegative luminal loops above the entrance to the selectivity-filter vestibule may serve to attract cations and partially account for the store-overload-induced release[38,39]. Reflecting their functional importance, 8 out of the 16 residues in the luminal loop are targeted for disease-related mutations (Extended Data Figs 7 and 9 and Supplementary Table 1).

The extended S6 helices form a right-handed helical bundle with a bottleneck at the cytoplasmic edge of the sarcoplasmic reticulum membrane, which is encircled by the four S4–S5 linker helices (Fig. 3b). Analysis of the pore radii with the program HOLE[40] identified the constriction point at residue Ile 4937 (Fig. 3c, d). The pore radius at the constriction point is less than 1 Å, impermeable to a completely dehydrated Ca^{2+} ion. Therefore, the structure represents a closed state, consistent with the condition of sample preparation[15,23].

Owing to the elongated S6 segments and the luminal loops above the selectivity-filter vestibule, the conducting pathway of RyR1 is extraordinarily long, spanning approximately 90 Å from the sarcoplasmic reticulum lumen to the cytoplasm. Below the selectivity filter is a hydrophobic cavity (Fig. 3c), which represents a conserved feature observed in the K^+, Na_v and TRPV1 channels. Consistent with previous analysis[41], the cytoplasmic segment of S6 is highly enriched with Asp/Glu residues (Fig. 3c). The hydrophobic cavity and the high electronegativity along the cytoplasmic vestibule may facilitate rapid Ca^{2+} ion permeation from the sarcoplasmic reticulum lumen to the cytoplasm.

A zinc-finger-containing CTD and the VSL

The cytoplasmic CTD (residues 4957–5037) comprises five short α-helices. Two cysteine and two histidine residues, Cys 4958, Cys 4961, His 4978 and His 4983, together form a C2H2-type zinc-finger (Fig. 3e). In the context of the RyR1 homotetramer, the four CTDs are arranged like four blades of a windmill, in which the zinc-finger motifs are positioned close to the centre and guard the exit of the ion-conducting pore (Fig. 3e). The S6 segment is connected to the CTD through the zinc-finger motif, which may restrict relative movement between S6 and the CTD.

The VSL domain (residues 4545–4821) is so named because it exhibits the voltage-sensor fold but lacks the voltage-sensing elements such as the gating charges on S4 (Fig. 3f, g and Extended Data Fig. 8b). The sequences between S2 and S3 (residues 4663–4787) fold into the VSC domain, which comprises five helical segments, including the S2′ helix that is an extension of S2 into the cytoplasm, the S3′ helix that connects to S3 through a tight turn, and three short helices C1/2/3 in between (Fig. 3f and Extended Data Fig. 7). The four transmembrane segments closely interact with each other to form a compact helical bundle (Fig. 3g).

Interactions of the RyR1 channel domain

To understand the molecular mechanism of channel activation, we first examined the interactions between different segments of the channel domain and those between the channel domain and the cytoplasmic region (Fig. 4a–c and Extended Data Fig. 10). Within the same RyR1 protomer, several interfaces, including that between S5 and S6, between the S4–S5 linker and the pore domain, and between VSL and the pore domain, may contribute to allosteric regulation of channel opening. These interactions, involving predominantly van der Waals contacts (Extended Data Fig. 10a), provide the adaptability to propagate conformational changes within the channel domain.

In addition to the interactions within the lipid bilayer, VSC and CTD from the same protomer also contact each other. Therefore,

©2015 Macmillan Publishers Limited. All rights reserved

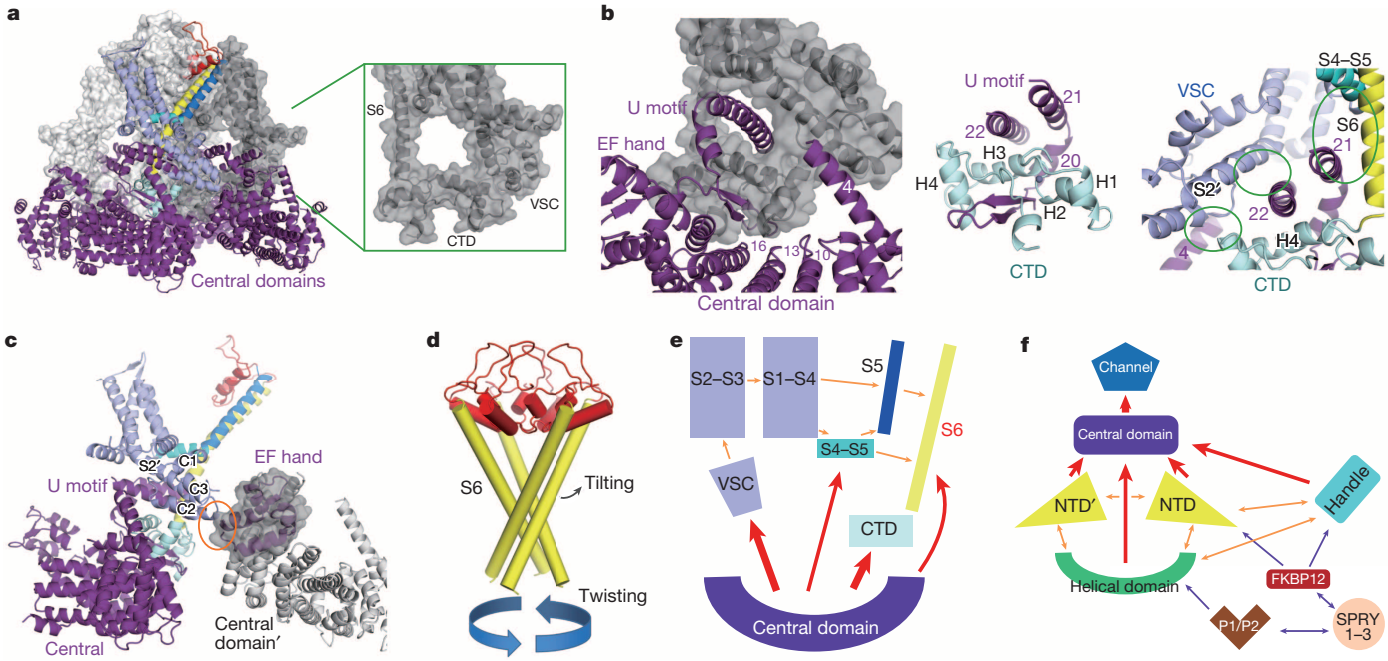


Figure 4 | The intra- and inter-domain contacts of the RyR1 channel domain may contribute to channel gating. **a**, The VSC and CTD mediate the interactions between the channel domain and the central domain in the cytoplasmic region of RyR1. Shown in the inset is a circle formed by the cytoplasmic fragment of S6, CTD and VSC that provides the primary accommodation site for the central domain. Only one protomer is domain-coloured, and the other three protomers are shown in light to dark grey in semi-transparent surface view. **b**, Analysis of the interactions between the channel and central domain. The green circles in the right panel indicate the interfaces between the central and channel domain. Detailed interactions can be found in Extended Data Fig. 10. **c**, The EF-hand subdomain in the central domain contacts VSC and may provide the molecular basis for Ca^{2+}-mediated modulation of RyR1. A semi-transparent surface is shown for the EF-hand subdomain. The potential interface is highlighted by the orange circle. The prime symbol denotes an adjacent central domain. **d**, Putative conformational changes of the S6 segments may result in the opening of the activation gate. **e**, A cartoon diagram to illustrate the actions from the surrounding domains and structural segments that may lead to conformational changes of S6. **f**, A cartoon illustration of the complex interactions among the different domains of RyR1. Each arrow denotes two mutually interacting domains. Single-headed arrows indicate the directions of allosteric changes, whereas double-headed arrows suggest two-way flow of conformational changes.

conformational shifts of VSC may be directly transmitted to S6 through the CTDs (Fig. 4a). The CTDs, VSCs and cytoplasmic portion of S6 provide the primary docking site for the central domains. Each U-motif in the central domain is hooked into a ring structure formed by the CTD, VSC and S6 (Fig. 4a, b), involving extensive hydrophobic and polar contacts (Extended Data Fig. 10b–d). The concave surface of the armadillo repeats of the central domain also interacts with the CTD to strengthen further the interface between the channel domain and cytoplasmic region (Fig. 4b). This extensive interface may serve as the primary transmitter for conformational changes from the cytoplasmic domain to the channel domain. Notably, the EF-hand subdomain in the adjacent central domain contacts the tip of the VSC (Fig. 4c), which may provide an important mechanism for Ca^{2+} ions to modulate the conductance of RyRs[42].

Discussion

The near-atomic resolution structure of the rabbit RyR1 provides an unprecedented opportunity for examination of the structural organization as well as the functional and regulatory mechanisms of high-conductance Ca^{2+} channels. The RyR1 structure is captured in a closed state with the four elongated S6 segments constricted at the inner activation gate, whereas the selectivity-filter vestibule appears in a conductive conformation (Fig. 3b–d). The activation of RyRs requires opening of the activation gate. The most intuitive activation model may simply entail twisting of the S6 bundle (Fig. 4d).

S6 is connected to the CTD through a potentially rigid zinc-finger joint. Change of the CTD position may lead to the relaxation of the activation gate. The CTD and VSC participate in extensive interactions with the central domains from the cytoplasmic region (Fig. 4b). Conformational shifts of the central domains probably impinge on the CTD and VSC simultaneously, whose consequent conformational changes may then be relayed to the transmembrane segments in VSL as well as the pore-forming elements, resulting in conductance change (Fig. 4e).

In the hierarchical organization of the RyR1 tetramer, the central domain probably serves as the central transmitter of conformational changes. The two extended superhelical assemblies in the cytoplasmic region and the intricate interaction network among the cytoplasmic domains provide the molecular platform to propagate any conformational changes induced by modulator binding to the central domain (Figs 2 and 4f).

The mechanisms of channel opening await further characterizations. Nevertheless, the analyses reported here reveal a molecular scaffold that allows long-range allosteric regulation of the activation gate. The near atomic resolution cryo-EM structure of the rabbit RyR1 serves as a framework for interpretation of a wealth of experimental observations over the last four decades and for understanding the function and disease mechanisms of RyRs.

Online Content Methods, along with any additional Extended Data display items and Source Data, are available in the online version of the paper; references unique to these sections appear only in the online paper.

Received 12 September; accepted 12 November 2014.
Published online 15 December 2014.

1. Pessah, I. N., Waterhouse, A. L. & Casida, J. E. The calcium-ryanodine receptor complex of skeletal and cardiac muscle. *Biochem. Biophys. Res. Commun.* **128,** 449–456 (1985).
2. Inui, M., Saito, A. & Fleischer, S. Purification of the ryanodine receptor and identity with feet structures of junctional terminal cisternae of sarcoplasmic reticulum from fast skeletal muscle. *J. Biol. Chem.* **262,** 1740–1747 (1987).
3. Lai, F. A., Erickson, H. P., Rousseau, E., Liu, Q. Y. & Meissner, G. Purification and reconstitution of the calcium release channel from skeletal muscle. *Nature* **331,** 315–319 (1988).

©2015 Macmillan Publishers Limited. All rights reserved

4. Takeshima, H. *et al.* Primary structure and expression from complementary DNA of skeletal muscle ryanodine receptor. *Nature* **339,** 439–445 (1989).
5. Rossi, D. & Sorrentino, V. Molecular genetics of ryanodine receptors Ca^{2+}-release channels. *Cell Calcium* **32,** 307–319 (2002).
6. Seo, M. D. *et al.* Structural and functional conservation of key domains in $InsP_3$ and ryanodine receptors. *Nature* **483,** 108–112 (2012).
7. Mignery, G. A., Sudhof, T. C., Takei, K. & De Camilli, P. Putative receptor for inositol 1,4,5-trisphosphate similar to ryanodine receptor. *Nature* **342,** 192–195 (1989).
8. Bhat, M. B., Zhao, J., Takeshima, H. & Ma, J. Functional calcium release channel formed by the carboxyl-terminal portion of ryanodine receptor. *Biophys. J.* **73,** 1329–1336 (1997).
9. Lanner, J. T., Georgiou, D. K., Joshi, A. D. & Hamilton, S. L. Ryanodine receptors: structure, expression, molecular details, and function in calcium release. *Cold Spring Harb. Perspect. Biol.* **2,** a003996 (2010).
10. Meissner, G. Ryanodine receptor/Ca- release channels and their regulation by endogenous effectors. *Annu. Rev. Physiol.* **56,** 485–508 (1994).
11. Van Petegem, F. Ryanodine receptors: allosteric ion channel giants. *J. Mol. Biol.* http://dx.doi.org/10.1016/j.jmb.2014.08.004 (2014).
12. Endo, M., Tanaka, M. & Ogawa, Y. Calcium induced release of calcium from the sarcoplasmic reticulum of skinned skeletal muscle fibres. *Nature* **228,** 34–36 (1970).
13. Fabiato, A. Calcium-induced release of calcium from the cardiac sarcoplasmic reticulum. *Am. J. Physiol.* **245,** C1–C14 (1983).
14. Bezprozvanny, I., Watras, J. & Ehrlich, B. E. Bell-shaped calcium-response curves of $Ins(1,4,5)P_3$- and calcium-gated channels from endoplasmic reticulum of cerebellum. *Nature* **351,** 751–754 (1991).
15. Smith, J. S., Coronado, R. & Meissner, G. Single channel measurements of the calcium release channel from skeletal muscle sarcoplasmic reticulum. Activation by Ca^{2+} and ATP and modulation by Mg^{2+}. *J. Gen. Physiol.* **88,** 573–588 (1986).
16. Rios, E. & Brum, G. Involvement of dihydropyridine receptors in excitation-contraction coupling in skeletal muscle. *Nature* **325,** 717–720 (1987).
17. Block, B. A., Imagawa, T., Campbell, K. P. & Franzini-Armstrong, C. Structural evidence for direct interaction between the molecular components of the transverse tubule/sarcoplasmic reticulum junction in skeletal muscle. *J. Cell Biol.* **107,** 2587–2600 (1988).
18. MacMillan, D. FK506 binding proteins: Cellular regulators of intracellular Ca^{2+} signalling. *Eur. J. Pharmacol.* **700,** 181–193 (2013).
19. Radermacher, M. *et al.* Cryo-EM of the native structure of the calcium release channel/ryanodine receptor from sarcoplasmic reticulum. *Biophys. J.* **61,** 936–940 (1992).
20. Radermacher, M. *et al.* Cryo-electron microscopy and three-dimensional reconstruction of the calcium release channel/ryanodine receptor from skeletal muscle. *J. Cell Biol.* **127,** 411–423 (1994).
21. Samsó, M., Wagenknecht, T. & Allen, P. D. Internal structure and visualization of transmembrane domains of the RyR1 calcium release channel by cryo-EM. *Nature Struct. Mol. Biol.* **12,** 539–544 (2005).
22. Serysheva, I. I. *et al.* Subnanometer-resolution electron cryomicroscopy-based domain models for the cytoplasmic region of skeletal muscle RyR channel. *Proc. Natl Acad. Sci. USA* **105,** 9610–9615 (2008).
23. Samsó, M., Feng, W., Pessah, I. N. & Allen, P. D. Coordinated movement of cytoplasmic and transmembrane domains of RyR1 upon gating. *PLoS Biol.* **7,** e85 (2009).
24. Franzini-Armstrong, C. STUDIES OF THE TRIAD: I. Structure of the junction in frog twitch fibers. *J. Cell Biol.* **47,** 488–499 (1970).
25. Scheres, S. H. W. RELION: Implementation of a Bayesian approach to cryo-EM structure determination. *J. Struct. Biol.* **180,** 519–530 (2012).
26. Bai, X. C., Fernandez, I. S., McMullan, G. & Scheres, S. H. W. Ribosome structures to near-atomic resolution from thirty thousand cryo-EM particles. *eLife* **2,** e00461 (2013).
27. Li, X. *et al.* Electron counting and beam-induced motion correction enable near-atomic-resolution single-particle cryo-EM. *Nature Methods* **10,** 584–590 (2013).
28. Tung, C. C., Lobo, P. A., Kimlicka, L. & Van Petegem, F. The amino-terminal disease hotspot of ryanodine receptors forms a cytoplasmic vestibule. *Nature* **468,** 585–588 (2010).
29. Tewari, R., Bailes, E., Bunting, K. A. & Coates, J. C. Armadillo-repeat protein functions: questions for little creatures. *Trends Cell Biol.* **20,** 470–481 (2010).
30. Xiong, H. *et al.* Identification of a two EF-hand Ca^{2+} binding domain in lobster skeletal muscle ryanodine receptor/Ca^{2+} release channel. *Biochemistry* **37,** 4804–4814 (1998).
31. Zhao, M. *et al.* Molecular identification of the ryanodine receptor pore-forming segment. *J. Biol. Chem.* **274,** 25971–25974 (1999).
32. Gao, L. *et al.* Evidence for a role of the lumenal M3–M4 loop in skeletal muscle Ca^{2+} release channel (ryanodine receptor) activity and conductance. *Biophys. J.* **79,** 828–840 (2000).
33. Du, G. G., Guo, X., Khanna, V. K. & MacLennan, D. H. Functional characterization of mutants in the predicted pore region of the rabbit cardiac muscle Ca^{2+} release channel (ryanodine receptor isoform 2). *J. Biol. Chem.* **276,** 31760–31771 (2001).
34. Wayne Chen, S. R., Li, P., Zhao, M., Li, X. & Zhang, L. Role of the proposed pore-forming segment of the Ca^{2+} release channel (ryanodine receptor) in ryanodine interaction. *Biophys. J.* **82,** 2436–2447 (2002).
35. Wang, Y., Xu, L., Pasek, D. A., Gillespie, D. & Meissner, G. Probing the role of negatively charged amino acid residues in ion permeation of skeletal muscle ryanodine receptor. *Biophys. J.* **89,** 256–265 (2005).
36. Cao, E., Liao, M., Cheng, Y. & Julius, D. TRPV1 structures in distinct conformations reveal activation mechanisms. *Nature* **504,** 113–118 (2013).
37. Tang, L. *et al.* Structural basis for Ca^{2+} selectivity of a voltage-gated calcium channel. *Nature* **505,** 56–61 (2014).
38. Palade, P., Mitchell, R. D. & Fleischer, S. Spontaneous calcium release from sarcoplasmic reticulum. General description and effects of calcium. *J. Biol. Chem.* **258,** 8098–8107 (1983).
39. Jiang, D. *et al.* RyR2 mutations linked to ventricular tachycardia and sudden death reduce the threshold for store-overload-induced Ca^{2+} release (SOICR). *Proc. Natl Acad. Sci. USA* **101,** 13062–13067 (2004).
40. Smart, O. S., Goodfellow, J. M. & Wallace, B. A. The pore dimensions of gramicidin A. *Biophys. J.* **65,** 2455–2460 (1993).
41. Xu, L., Wang, Y., Gillespie, D. & Meissner, G. Two rings of negative charges in the cytosolic vestibule of type-1 ryanodine receptor modulate ion fluxes. *Biophys. J.* **90,** 443–453 (2006).
42. Fessenden, J. D., Feng, W., Pessah, I. N. & Allen, P. D. Mutational analysis of putative calcium binding motifs within the skeletal ryanodine receptor isoform, RyR1. *J. Biol. Chem.* **279,** 53028–53035 (2004).
43. DeLano, W. L. The PyMOL Molecular Graphics System http://www.pymol.org (Schrödinger, LLC, 2002).

Supplementary Information is available in the online version of the paper.

Acknowledgements This work was supported by funds from the Ministry of Science and Technology of China (2015CB910101, 2011CB910501 and 2014ZX09507003006), National Natural Science Foundation of China (projects 31321062, 31130002 and 31125009), a European Union Marie Curie Fellowship (to X.B.), and the UK Medical Research Council (MC_UP_A025_1013, to S.H.W.S.). The research of N. Yan was supported in part by an International Early Career Scientist grant from the Howard Hughes Medical Institute and an endowed professorship from Bayer Healthcare.

Author Contributions Y.S. and N.Y. conceived the project. Z.Y., X.B., X.L., S.H.W.S., Y.S. and N.Y. designed experiments. Z.Y., X.B., C.Y., J.W., Z.L., T.X., W.P. and X.L. performed the experiments. All authors analysed the data and contributed to manuscript preparation. N.Y. and Y.S. wrote the manuscript.

Author Information The atomic coordinates of the RyR1–FKBP12 complex have been deposited in the Protein Data Bank with the accession code 3J8H. The 3.8 Å electron microscopy map has been deposited in the Electron Microscopy Data Bank with accession code EMD-2807. Reprints and permissions information is available at www.nature.com/reprints. The authors declare no competing financial interests. Readers are welcome to comment on the online version of the paper. Correspondence and requests for materials should be addressed to N.Y. (nyan@tsinghua.edu.cn), S.H.W.S. (scheres@mrc-lmb.cam.ac.uk), or Y.S. (shi-lab@tsinghua.edu.cn).

©2015 Macmillan Publishers Limited. All rights reserved

METHODS

Preparation of enriched skeletal sarcoplasmic reticulum fraction. To reduce the duration for protein purification, we modified the published protocols for the preparation of the enriched skeletal sarcoplasmic reticulum fraction from New Zealand white rabbits[44]. In brief, fresh skeletal muscles from rabbit legs were homogenized in the buffer containing 0.3 M sucrose, 10 mM MOPS-Na, pH 7.4, 0.5 mM EDTA, and protease inhibitors including 2 mM phenylmethylsulphonyl fluoride (PMSF), 2.6 μg ml^{-1} aprotinin, 1.4 μg ml^{-1} pepstatin and 10 μg ml^{-1} leupeptin. The homogenates were centrifuged at 6,000*g* (low speed) for 6 min to remove debris. The supernatant was then centrifuged at 200,000*g* for 1 h. The pellet containing enriched sarcoplasmic reticulum fraction was collected and frozen at −80 °C for storage.

Expression and purification of rabbit FKBP12. The GST-fused FKBP12 protein was expressed and purified as reported previously[45]. The complementary DNA of *FKBP12* from New Zealand white rabbit was inserted into the pGEX-4T-2 vector (Novagen). Overexpression of GST–FKBP12 was induced in *Escherichia coli* BL21 (DE3) with 0.2 mM isopropyl-β-D-thiogalactoside (IPTG) when the cell density reached an attenuance (*D*) at 600 nm of 1.2. After growth for 6 h at 37 °C, the cells were collected, re-suspended in the buffer containing 25 mM Tris-HCl, pH 8.0, and 150 mM NaCl, and disrupted by sonication. Cell debris was removed by centrifugation at 27,000*g* for 45 min. The supernatant was applied to glutathione Sepharose 4B resin (GS4B, GE Healthcare), which was subsequently washed three times, each with buffer containing 25 mM Tris-HCl, pH 8.0, 150 mM NaCl and 2 mM dithiothreitol (DTT) (Sigma). The protein, eluted from the affinity resin with wash buffer plus 10 mM glutathione, was further purified through anion-exchange column (Source 15Q, GE Healthcare) to remove reduced glutathione. The peak fractions were pooled for further use.

Pull-down of RyR1 by GST–FKBP12. The RyR1 bound to GST–FKBP12 was purified on the basis of the described protocols[3,46,47] with considerable modifications. The enriched sarcoplasmic reticulum fraction was solubilized at 4 °C for 1 h in the buffer containing 20 mM MOPS-Na, pH 7.4, 1 M NaCl, 2 mM DTT, 2 mM EDTA, 5% CHAPS, 2.5% (w/v) soybean phospholipids (Calbiochem) and protease inhibitors. During this process, GST–FKBP12 was added in excess. After ultra-centrifugation at 200,000*g* for 25 min, the supernatant was collected and incubated with GS4B resin at 4 °C for 2 h. The protein-loaded resin was washed with 20 mM MOPS-Na, pH 7.4, 500 mM NaCl, 2 mM DTT, 2 mM EGTA, 0.015% Tween20 and protease inhibitors. The target protein complex was eluted by the buffer containing 13 mM reduced glutathione, 80 mM Tris-HCl, pH 8.0, 2 mM DTT, 2 mM EGTA, 0.015% Tween20 and protease inhibitors. The target protein complex was then further purified through Mono S 5/50 GL (GE Healthcare). The fraction containing target protein complex was concentrated and applied to size-exclusion chromatography (Superdex-200, 10/30, GE Healthcare) in buffer containing 20 mM MOPS-Na, pH 7.4, 250 mM NaCl, 2 mM DTT, 2 mM EGTA, 0.015% Tween20 and protease inhibitors. The fractions containing the RyR1–FKBP12 complex were pooled for electron microscopy analysis.

Electron microscopy. Aliquots of 3 μl of purified RyR1 at a concentration of approximately 30 nM were placed on glow-discharged holey carbon grids (Quantifoil CuR2/2), on which a home-made continuous carbon film (estimated to be ~30 Å thick) had previously been deposited. Grids were blotted for 2 s and flash-frozen in liquid ethane using an FEI Vitrobot. Grids were transferred to an FEI Tecnai Polara electron microscope that was operating at 300 kV. Images were recorded manually using an FEI Falcon-II detector at a calibrated magnification of 104,478, yielding a pixel size of 1.34 Å. A dose rate of 20 electrons per Å^2 per second, and an exposure time of 2 s were used on the Falcon.

Image processing. The 34 frames of each video were aligned using the whole-image motion correction[27]. We used the particles picking tool in the RELION for automated selection of 245,850 particles from 1,500 micrographs. Contrast transfer function parameters were estimated using CTFFIND3 (ref. 48). All two- and three-dimensional classifications and refinements were performed using RELION[25]. We used reference-free two-dimensional class averaging and three-dimensional classification to discard bad particles, and selected 154,394 particles, for a first three-dimensional refinement.

A 60 Å low-pass filtered cryo-EM reconstruction of RyR1 (Electron Microscopy Data Bank (EMDB) accession 1606)[23] was used as an initial model for the three-dimensional refinement. In a subsequent three-dimensional classification run with four classes, an angular sampling of 0.9° was combined with local angular searches around the refined orientations, and the refined model from the first refinement was used as a starting model. This yielded a subset of 65,872 particles.

The 34 video frames for each micrograph were first aligned using whole-image motion correction[27]. Second, particle based beam-induced movement correction was performed using statistical movie processing in RELION. For these calculations, we used running averages of seven movie frames, and a standard deviation of one pixel for the translational alignment. To increase the accuracy of the per-particle movement correction further, we used RELION-1.3 to fit linear tracks through the optimal translations for all running averages, and included neighbouring particles on the micrograph in these fits. In addition, we used a resolution and dose-dependent model for the radiation damage, in which each frame is weighted with a different B-factor (temperature factor) as estimated from single-frame reconstructions[49].

Reported resolutions are based on the gold-standard Fourier shell correlation (FSC) 0.143 criterion, and FSC curves were corrected for the effects of a soft mask on the FSC curve using high-resolution noise substitution[50]. Before visualization, all density maps were corrected for the modulation transfer function of the detector, and then sharpened by applying a negative B-factor that was estimated using automated procedures[51]. Local resolution variations were estimated using ResMap[52].

Model building. Because of the uneven distribution of resolution, we combined *de novo* building and homologous structure docking to generate the structural model of RyR1. A simplified diagram of the procedure for model building is presented in Extended Data Fig. 2. The resolution and quality of electron density allows *de novo* generation of atomic models for the following regions, the C-terminal helices of the NTD (residues 560–639), the handle domain (residues 1651–2145), the N-terminal helices of the HD1 domain (residues 2146–2460), the central domain (residues 3668–4251), and the channel domain (residues 4545–5037). The atomic model was built in COOT[53]. The chemical properties of proteins and amino acids were considered to facilitate initial model building. For instance, the hydrophobic residues in the channel domain probably favour the interface between the transmembrane segments and lipids. Sequence assignment was guided mainly by bulky residues such as Phe, Tyr, Trp and Arg. Unique patterns of sequences were exploited for validation of residue assignment. The backbone of a large portion of the HD1 and HD2 domains can be traced, therefore poly-Ala residues were built.

The crystal structures of the NTD (residues 1–559)[28] and FKBP12 (ref. 54), with respective Protein Data Bank (PDB) accession codes 4JKQ and 2PPN, were docked into the corresponding density maps. The electron microscopy density at the tip of each RyR1 protomer is of relatively low resolution, but displays a characteristic V-shape, which is reminiscent of the overall structure of the phosphorylation hotspot domain (residues 2734–2940, also known as the RyR domain)[55–57]. Unfortunately, sequence analysis is against docking of the phosphorylation domain structure into this V-shaped electron microscopy density.

In the previously reported low-resolution electron microscopy maps[23,58], the cytoplasmic domain contains a few solvent-filled holes enclosed by a structural feature named 'clamp'[59]. The helical domain accounts for half of the clamp (Extended Data Fig. 2b). Three SPRY domains (residues 640–1634) were identified and assigned to the other half of the clamp. Sequence alignments provide useful information for the domain identification and model building of the SPRY domains. The initial structural model for the three SPRY domains were generated on the basis of the homologous structure Ash2L (PDB code 3TOJ)[60]. After structural docking, manual adjustment was performed to correct the polypeptide connections. Most of the side chains were able to be assigned for the three SPRY domains. Notably, the SPRY sequences are interrupted by residues 851–1055 that occupy the V-shaped electron microscopy density at the tip of each protomer and hence named the P1 domain. Consequently, the structurally homologous phosphorylation hotspot domain is referred to as the P2 domain (residues 2734–2940, PDB code 4ERT), which was assigned to a V-shaped density on the convex side of the helical domain. A homology model for P1 domain was generated on the basis of the structure of P2 domain, and is docked into the density with further manual adjustment.

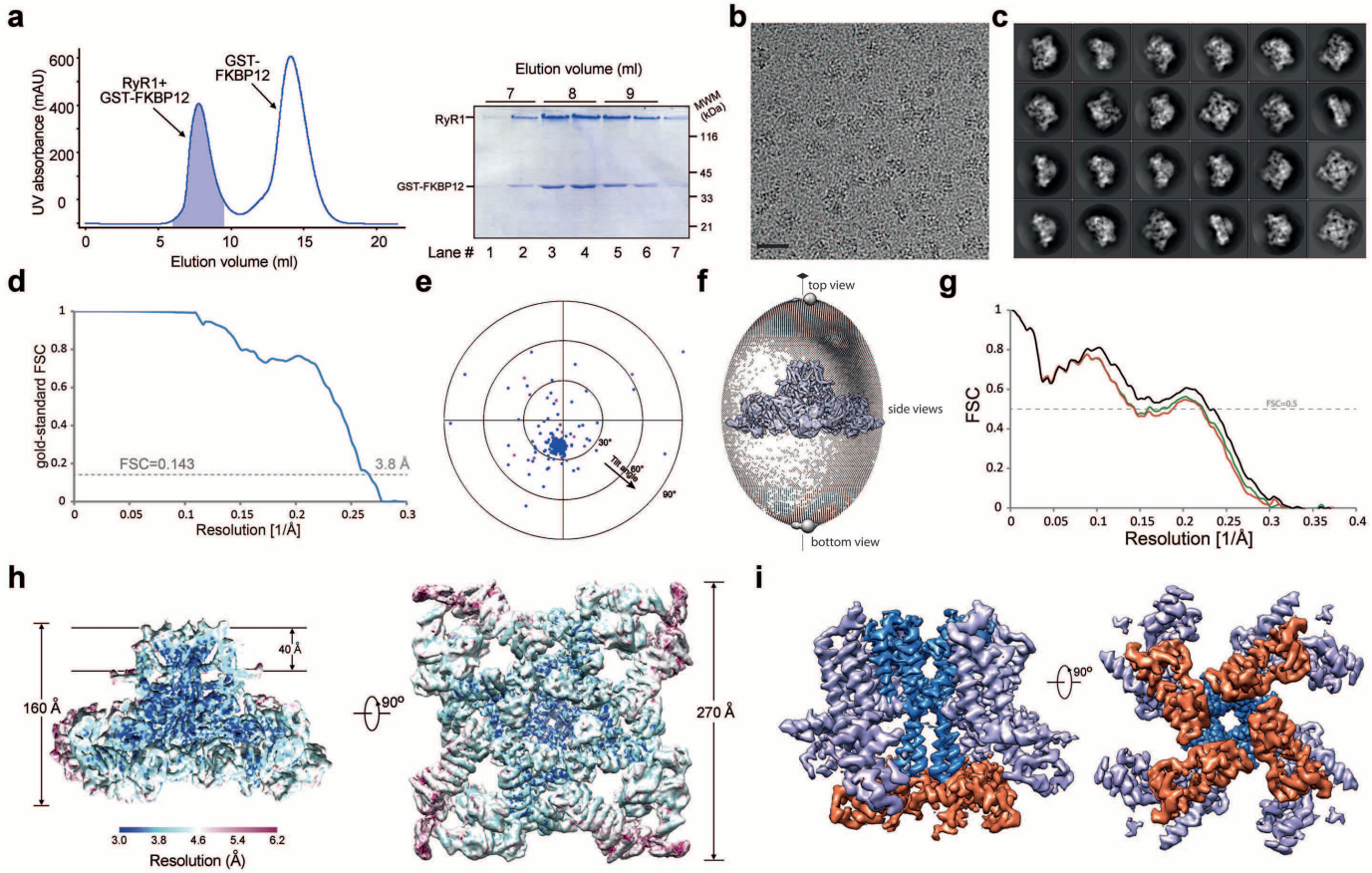
Structure refinement. Initial structure refinement was carried out by PHENIX in real space[61,62] with secondary structure and geometry restraint. To accelerate refinement, the EM map was transformed from *P*1 to *P*4 space group according the symmetry of tetrameric RyR1 by MAPMAN[63]. A reciprocal space refinement was carried out in REFMAC[64,65] with stereo-chemical and homology restraints, using the modified versions of the program for cryo-EM maps. To prevent overfitting, the optimal weight for refinement in REFMAC were determined by cross-validation as recently described[66].

44. Chu, A., Dixon, M. C., Saito, A., Seiler, S. & Fleischer, S. Isolation of sarcoplasmic-reticulum fractions referable to longitudinal tubules and junctional terminal cisternae from rabbit skeletal-muscle. *Methods Enzymol.* **157,** 36–46 (1988).
45. Wiederrecht, G. *et al.* Characterization of high-molecular-weight FK-506 binding activities reveals a novel FK-506-binding protein as well as a protein complex. *J. Biol. Chem.* **267,** 21753–21760 (1992).
46. Xin, H. B., Timerman, A. P., Onoue, H., Wiederrecht, G. J. & Fleischer, S. Affinity purification of the ryanodine receptor/calcium release channel from fast twitch skeletal muscle based on its tight association with FKBP12. *Biochem. Biophys. Res. Commun.* **214,** 263–270 (1995).
47. Meng, X. *et al.* CLIC2-RyR1 interaction and structural characterization by cryo-electron microscopy. *J. Mol. Biol.* **387,** 320–334 (2009).
48. Mindell, J. A. & Grigorieff, N. Accurate determination of local defocus and specimen tilt in electron microscopy. *J. Struct. Biol.* **142,** 334–347 (2003).
49. Scheres, S. H. Beam-induced motion correction for sub-megadalton cryo-EM particles. *eLife* **3,** e03665 (2014).

©2015 Macmillan Publishers Limited. All rights reserved

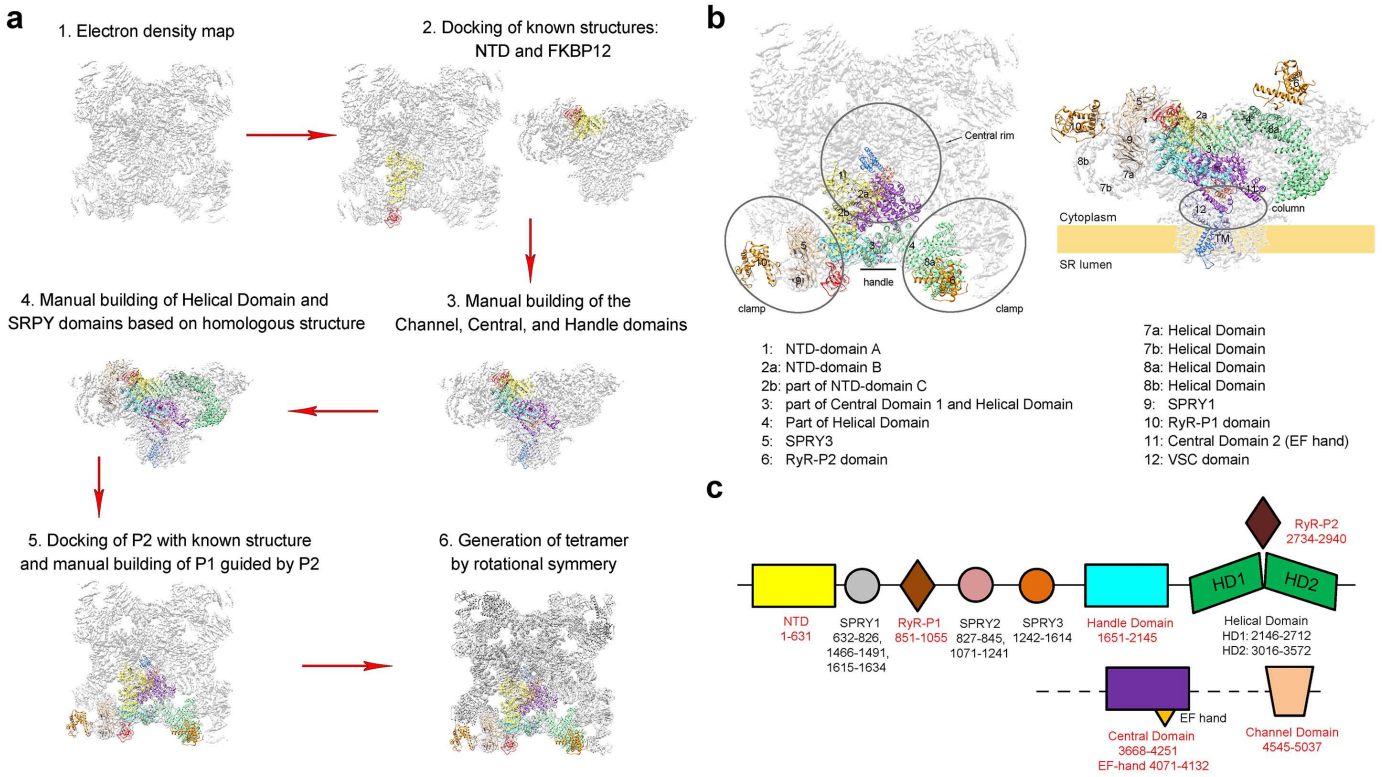
50. Chen, S. *et al.* High-resolution noise substitution to measure overfitting and validate resolution in 3D structure determination by single particle electron cryomicroscopy. *Ultramicroscopy* **135,** 24–35 (2013).
51. Rosenthal, P. B. & Henderson, R. Optimal determination of particle orientation, absolute hand, and contrast loss in single-particle electron cryomicroscopy. *J. Mol. Biol.* **333,** 721–745 (2003).
52. Kucukelbir, A., Sigworth, F. J. & Tagare, H. D. Quantifying the local resolution of cryo-EM density maps. *Nature Methods* **11,** 63–65 (2014).
53. Emsley, P., Lohkamp, B., Scott, W. G. & Cowtan, K. Features and development of Coot. *Acta Crystallogr. D* **66,** 486–501 (2010).
54. Szep, S., Park, S., Boder, E. T., Van Duyne, G. D. & Saven, J. G. Structural coupling between FKBP12 and buried water. *Proteins* **74,** 603–611 (2009).
55. Zorzato, F. *et al.* Molecular cloning of cDNA encoding human and rabbit forms of the Ca^{2+} release channel (ryanodine receptor) of skeletal muscle sarcoplasmic reticulum. *J. Biol. Chem.* **265,** 2244–2256 (1990).
56. Yuchi, Z., Lau, K. & Van Petegem, F. Disease mutations in the ryanodine receptor central region: crystal structures of a phosphorylation hot spot domain. *Structure* **20,** 1201–1211 (2012).
57. Sharma, P. *et al.* Structural determination of the phosphorylation domain of the ryanodine receptor. *FEBS J.* **279,** 3952–3964 (2012).
58. Ludtke, S. J., Serysheva, I. I., Hamilton, S. L. & Chiu, W. The pore structure of the closed RyR1 channel. *Structure* **13,** 1203–1211 (2005).
59. Serysheva, I. I. *et al.* Electron cryomicroscopy and angular reconstitution used to visualize the skeletal muscle calcium release channel. *Nature Struct. Biol.* **2,** 18–24 (1995).
60. Chen, Y., Cao, F., Wan, B., Dou, Y. & Lei, M. Structure of the SPRY domain of human Ash2L and its interactions with RbBP5 and DPY30. *Cell Res.* **22,** 598–602 (2012).
61. Adams, P. D. *et al.* PHENIX: a comprehensive Python-based system for macromolecular structure solution. *Acta Crystallogr. D* **66,** 213–221 (2010).
62. Afonine, P. V., Headd, J. J., Terwilliger, T. C. & Adams, P. D. New tool:phenix.real_space_refine. *Comput. Crystallogr. Newsl.* **4,** 43–44 (2013).
63. Kleywegt, G. J. & Jones, T. A. xdlMAPMAN and xdlDATAMAN - programs for reformatting, analysis and manipulation of biomacromolecular electron-density maps and reflection data sets. *Acta Crystallogr. D* **52,** 826–828 (1996).
64. Murshudov, G. N. *et al.* REFMAC5 for the refinement of macromolecular crystal structures. *Acta Crystallogr. D* **67,** 355–367 (2011).
65. Amunts, A. *et al.* Structure of the yeast mitochondrial large ribosomal subunit. *Science* **343,** 1485–1489 (2014).
66. Fernández, I. S., Bai, X. C., Murshudov, G., Scheres, S. H. & Ramakrishnan, V. Initiation of translation by cricket paralysis virus IRES requires its translocation in the ribosome. *Cell* **157,** 823–831 (2014).
67. Pettersen, E. F. *et al.* UCSF Chimera–a visualization system for exploratory research and analysis. *J. Comput. Chem.* **25,** 1605–1612 (2004).

©2015 **Macmillan Publishers Limited. All rights reserved**



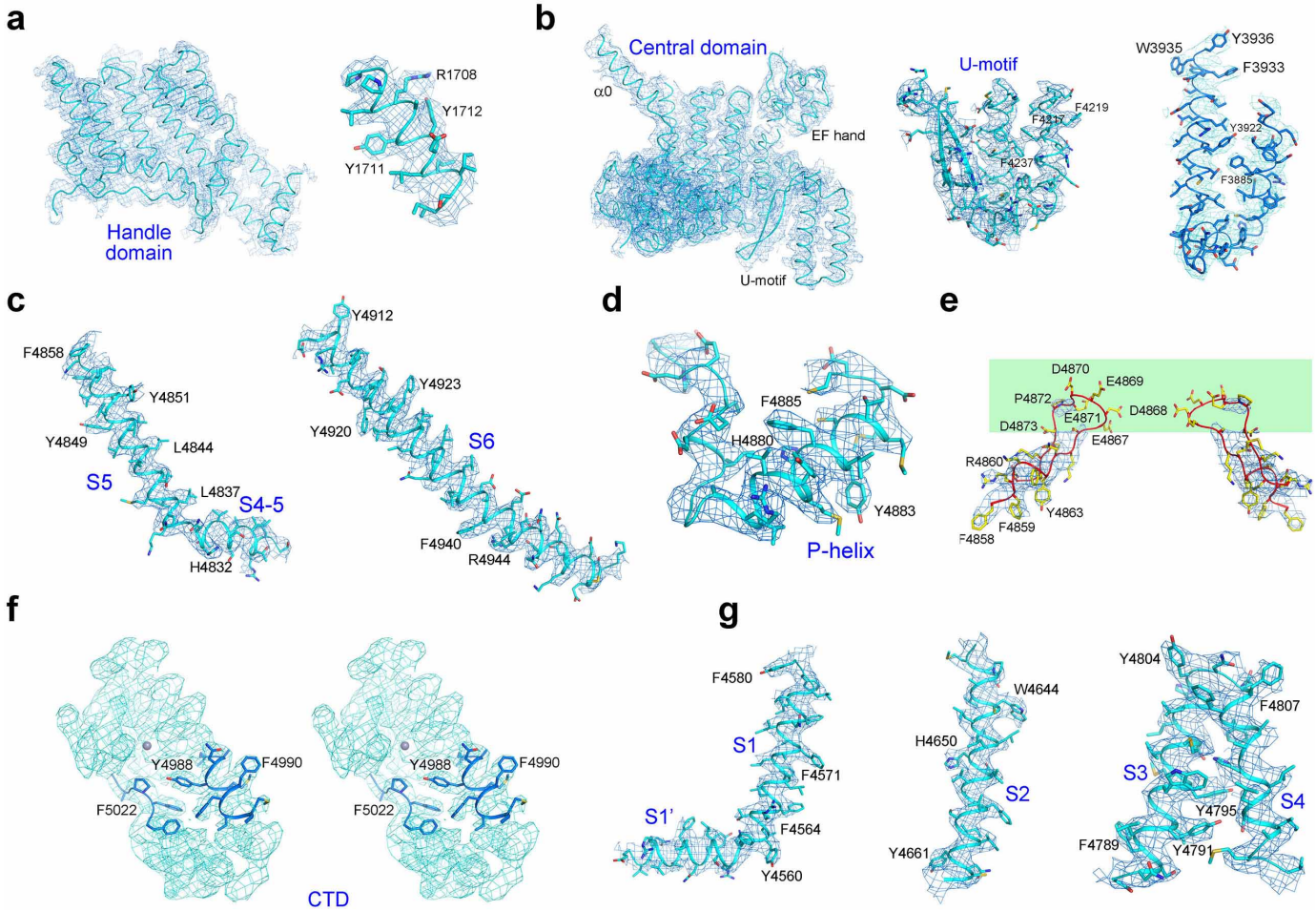
Extended Data Figure 1 | Purification and cryo-EM analysis of the rabbit RyR1 complex bound to the modulator FKBP12. **a**, The final step of purification of the rabbit RyR1 bound to FKBP12. Shown here are a size-exclusion chromatogram of the RyR1–FKBP12 complex (left) and a SDS–PAGE gel of the peak fractions visualized by Coomassie blue staining (right). The shaded fractions in the left panel were pooled for cryo-EM analysis. kDa, kilodaltons; UV, ultraviolet. **b**, A representative electron micrograph of the rabbit RyR1–FKBP12 complex. Scale bar, 20 nm. **c**, Two-dimensional class averages of the electron micrographs. **d**, Gold-standard FSC curves for the density maps. The overall resolution is estimated at 3.8 Å. **e**, Tilt-pair validation of the correctness of the map. Particles of RyR1 were imaged twice at 0° and 20° tilt angles. The position of each dot represents the direction and amount of tilting for a particle pair in polar coordinates. Blue and red dots correspond to in-plane and out-of-plane tilt transformations, respectively. Most of the blue dots cluster at a tilt angle of approximately 20°, which validates the structure. **f**, Angular distribution for the final reconstruction. Each sphere represents one view and the size of the sphere is proportional to the number of particles for that view. The azimuth angle only spans 90° because of the four-fold symmetry axis that runs from top to bottom. **g**, FSC curves between the model and the cryo-EM map. Shown here are the FSC curves between the final refined atomic model and the reconstruction from all particles (black), between the model refined in the reconstruction from only half of the particles and the reconstruction from that same half (FSC_{work}, green), and between that same model and the reconstruction from the other half of the particles (FSC_{test}, red). **h**, The overall electron microscopy density map of the RyR1–FKBP12 is colour-coded to indicate a range of resolutions. Much of the central region of RyR1 is resolved at resolutions better than the overall 3.8 Å, while the periphery of the structure is of much lower resolution. **i**, Electron microscopy density map for the channel domain of the rabbit RyR1.Two perpendicular views are shown. The electron microscopy density maps were generated in Chimera[67].

©2015 Macmillan Publishers Limited. All rights reserved



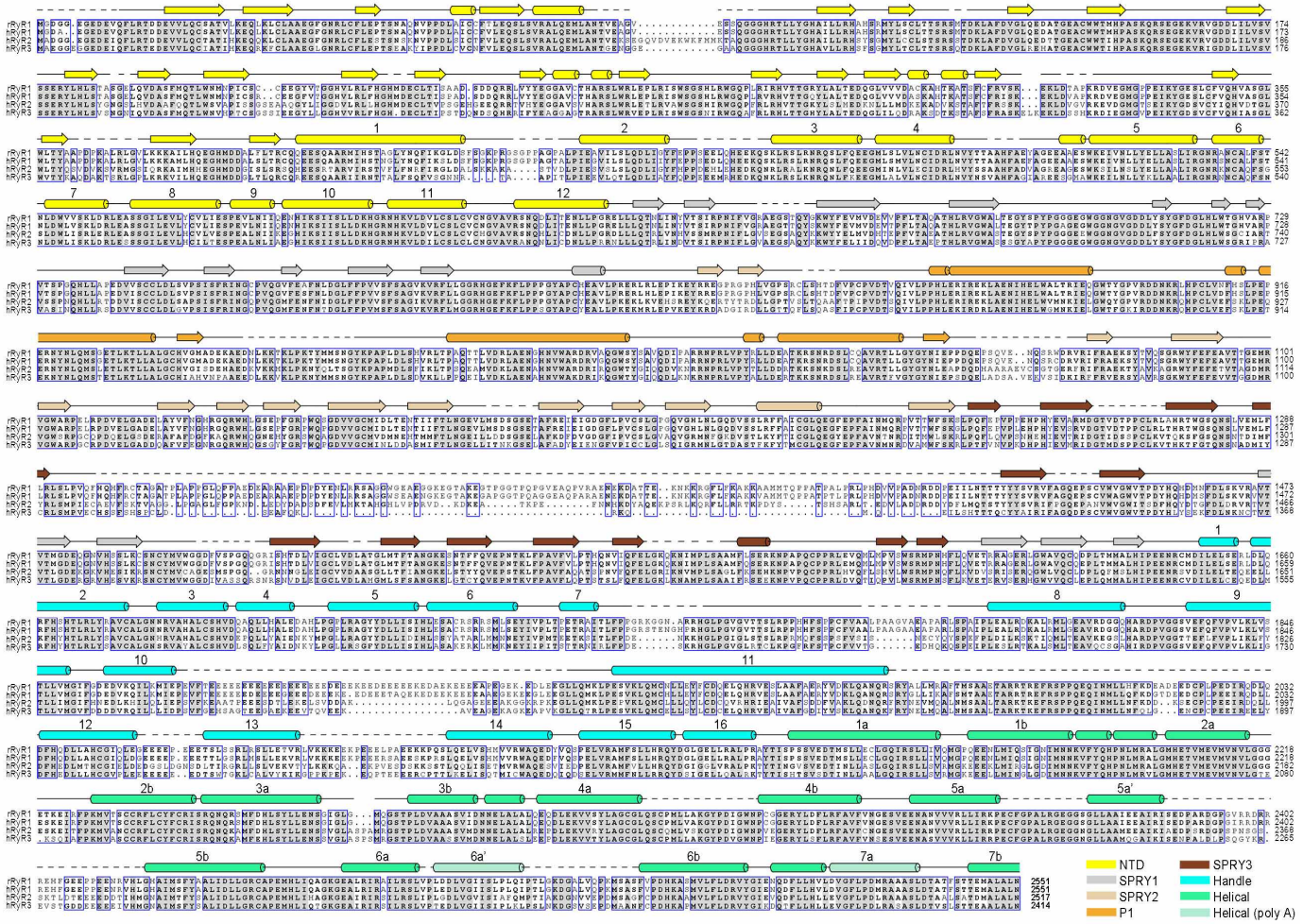
Extended Data Figure 2 | An illustration of the model-building procedures for the RyR1–FKBP12 complex into the electron microscopy density map. **a**, The step-by-step procedures for the generation of the overall structural model and domain assignment. Detailed descriptions can be found in Methods. **b**, Correlation between the previously assigned sub-regions[21,22] and the corresponding domains in our 3.8 Å structure. **c**, The boundaries of the identified domains in the current structure of RyR1. HD, helical domain. The P2 domain is a phosphorylation hotspot in RyRs. P1 shares homology with P2. The numbers below the domains indicate their sequence boundaries. Those labelled red were identified on the basis of well-defined electron microscopy density maps. It is of particular note that the three SPRY domains and P1 domain appear to be intertwined. See Extended Data Fig. 6b for the following structural descriptions. Each SPRY domain consists mainly of a β-sandwich. In addition to the core β-sandwich (residues 639–826), SPRY1 also contains two pairs of anti-parallel β-strands (residues 1466–1491, brown, and 1615–1634, magenta), the primary sequences of which are connected to those of SPRY3. Similarly, SPRY2 contains a pair of anti-parallel β-strands (residues 827–845, silver) from SPRY1. The sequences of SPRY2 are also interrupted by those of the P1 domain. Consequently, the N and C termini of the SPRY1–3 region (residues 639 and 1634) are both contained within the SPRY1 structure.

©2015 Macmillan Publishers Limited. All rights reserved



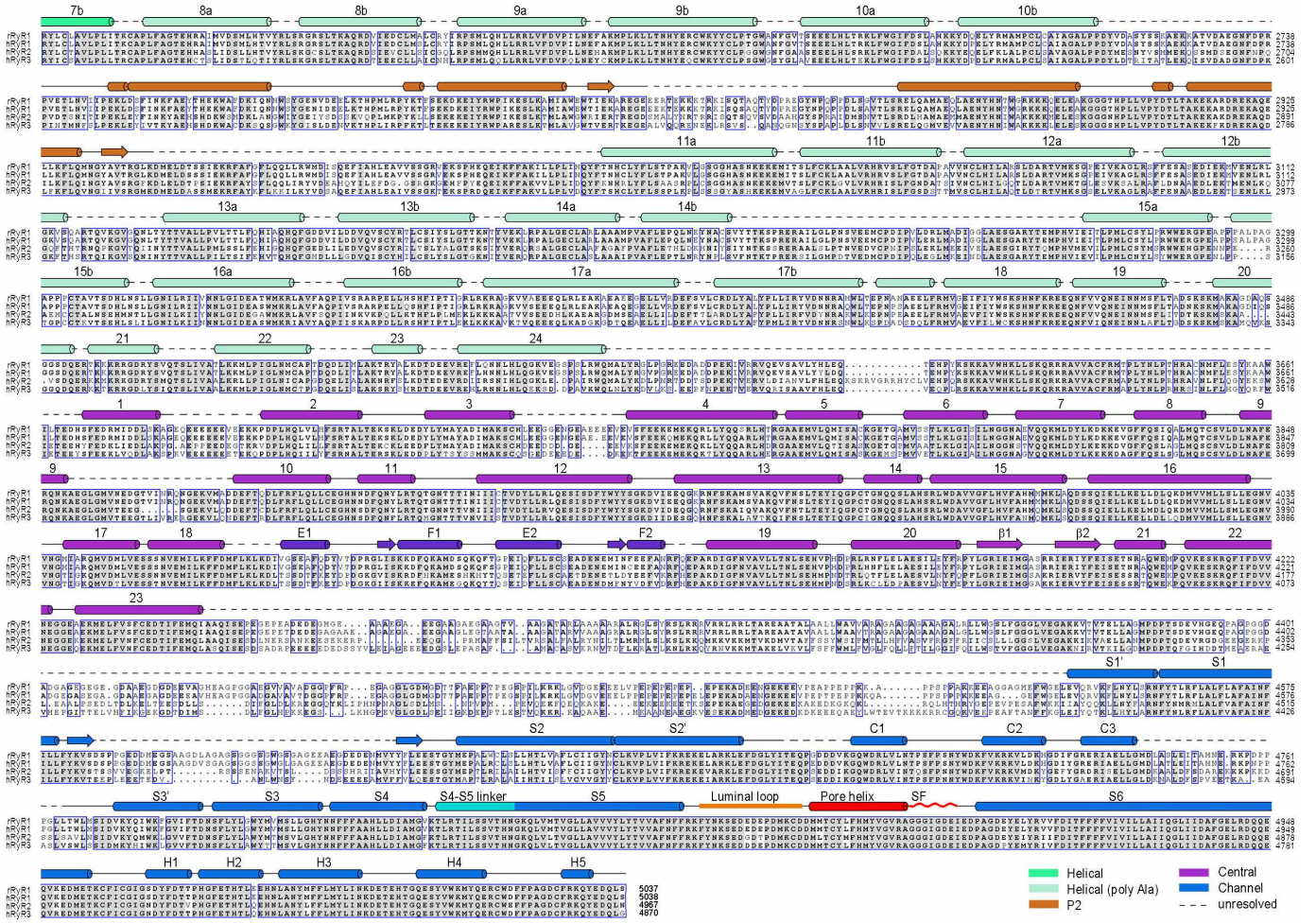
Extended Data Figure 3 | Electron microscopy density maps for the domains whose atomic structural models were generated *de novo*. **a**, The electron microscopy density maps for the handle domain. Representative density map for one helix in the handle domain is shown on the right. **b**, The electron microscopy density maps for the central domain. Left to right: the density maps for the overall domain, the U-motif, and one representative helical repeat in the central domain, respectively. **c**–**g**, The electron microscopy density maps for the segments in the channel domain. Shown here are the density maps for the pore forming elements (**c**), the selectivity filter (**d**), the luminal hairpin loop (**e**), the CTD shown in stereo views (**f**), and VSL domain (**g**). The maps, shown as blue mesh, are contoured at 4σ and made in PyMol. Representative bulky residues which were used to aid sequence assignment are shown as sticks and labelled.

©2015 Macmillan Publishers Limited. All rights reserved



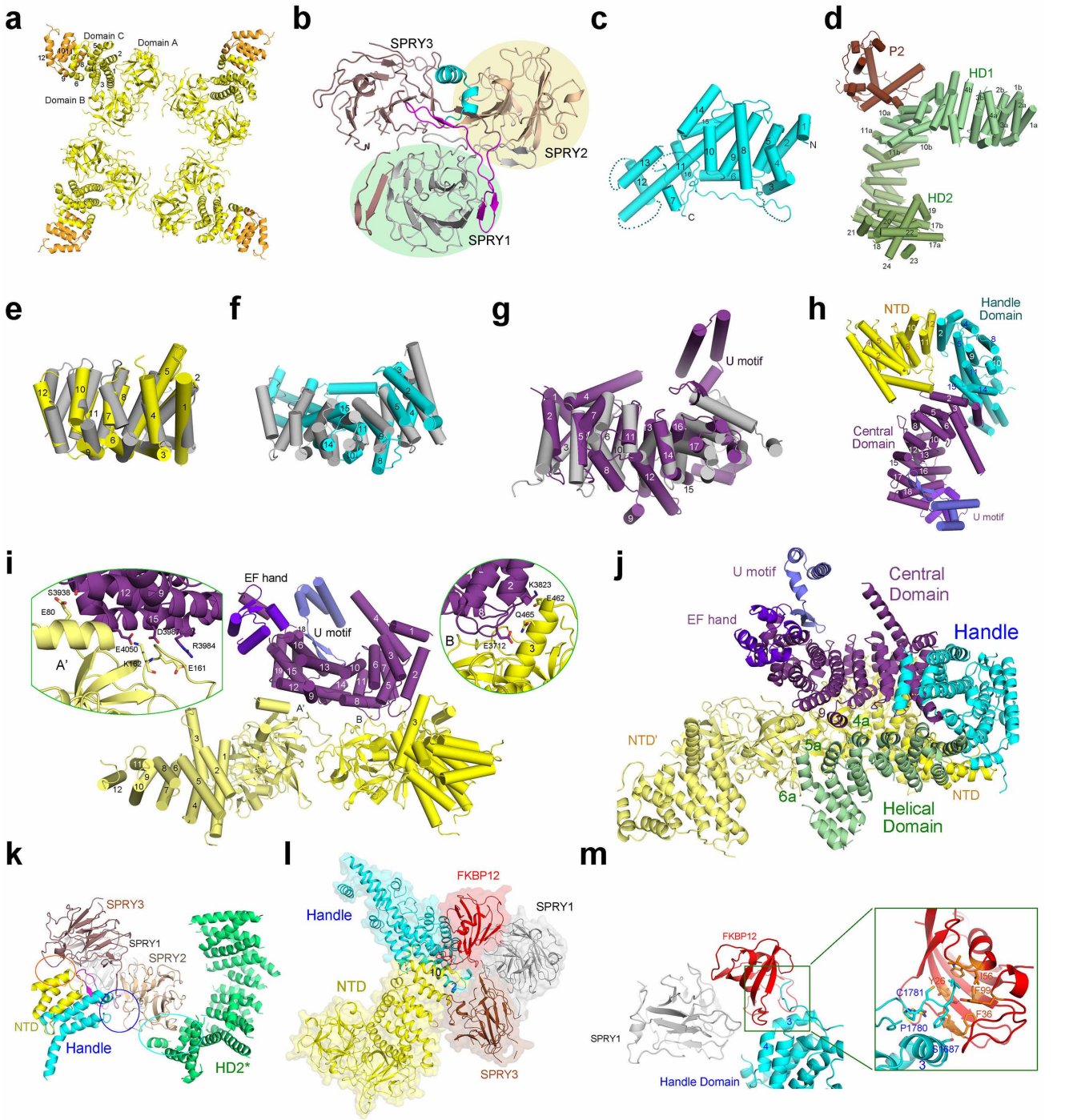
Extended Data Figure 4 | Sequence alignment of RyR orthologues. Secondary structural elements are indicated above the sequence alignment and domains are coloured the same as the structures shown in the main text figures. The numbering of the secondary elements refers to their sequential positions within the corresponding domains. Invariant amino acids are shaded light grey. The GenInfo Identifier (GI) codes for the sequences from top to bottom: rabbit RyR1 (156119408), human RyR1 (113204615), human RyR2 (308153558) and human RyR3 (325511382).

©2015 Macmillan Publishers Limited. All rights reserved



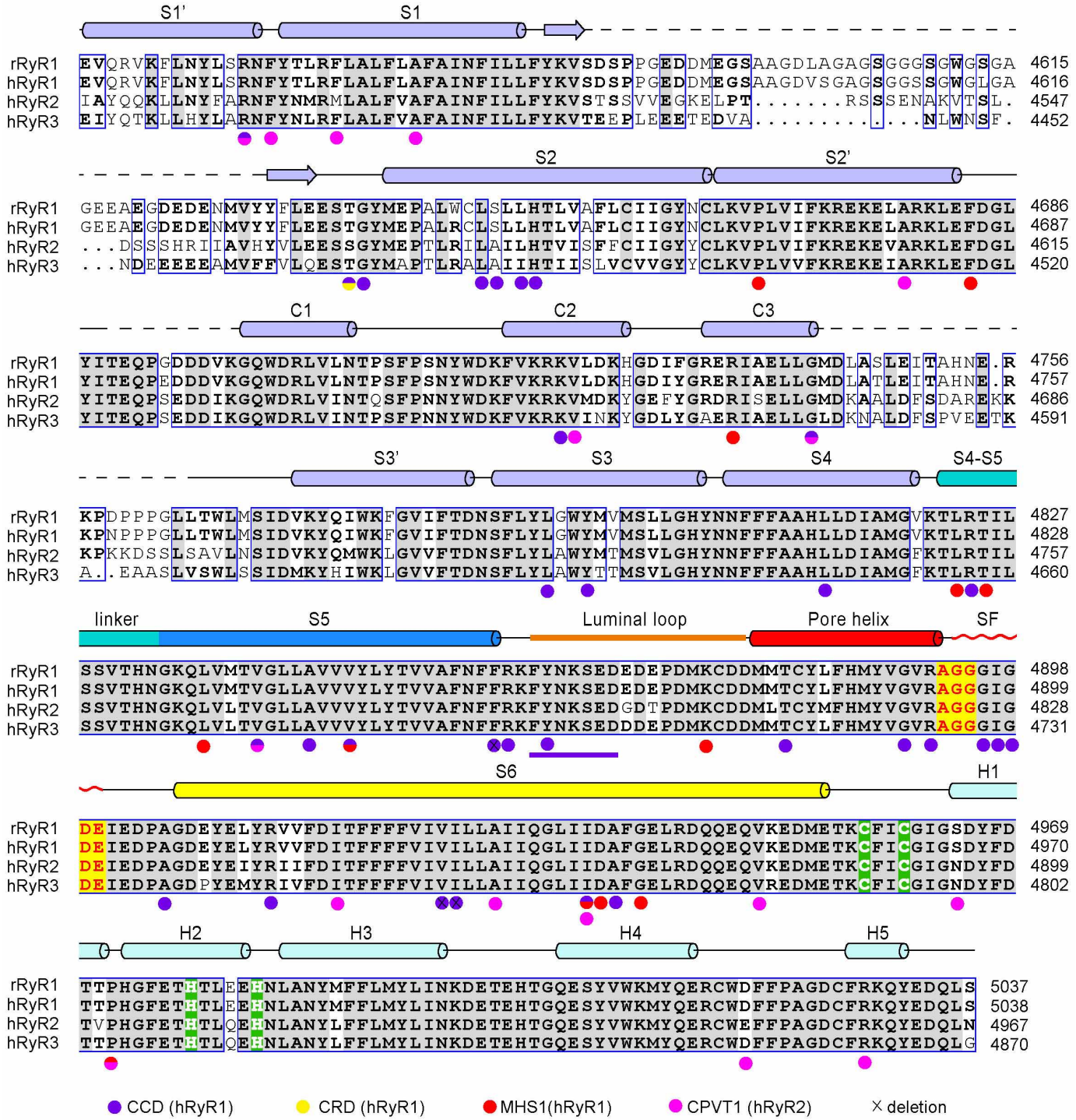
Extended Data Figure 5 | Continued sequence alignment of RyR orthologues. Owing to the enormous size of the proteins, the sequence alignment was divided into two figures with an overlap at the helix 7b from the helical domain. Notably, it was predicted that several EF-hand domains may exist between residues 4252 and 4545 (ref. 4). The lack of electron microscopy density for these domains may indicate their intrinsic flexibility in the absence of Ca^{2+}. The structure and mechanism of these putative EF-hand domains await further investigation.

©2015 Macmillan Publishers Limited. All rights reserved



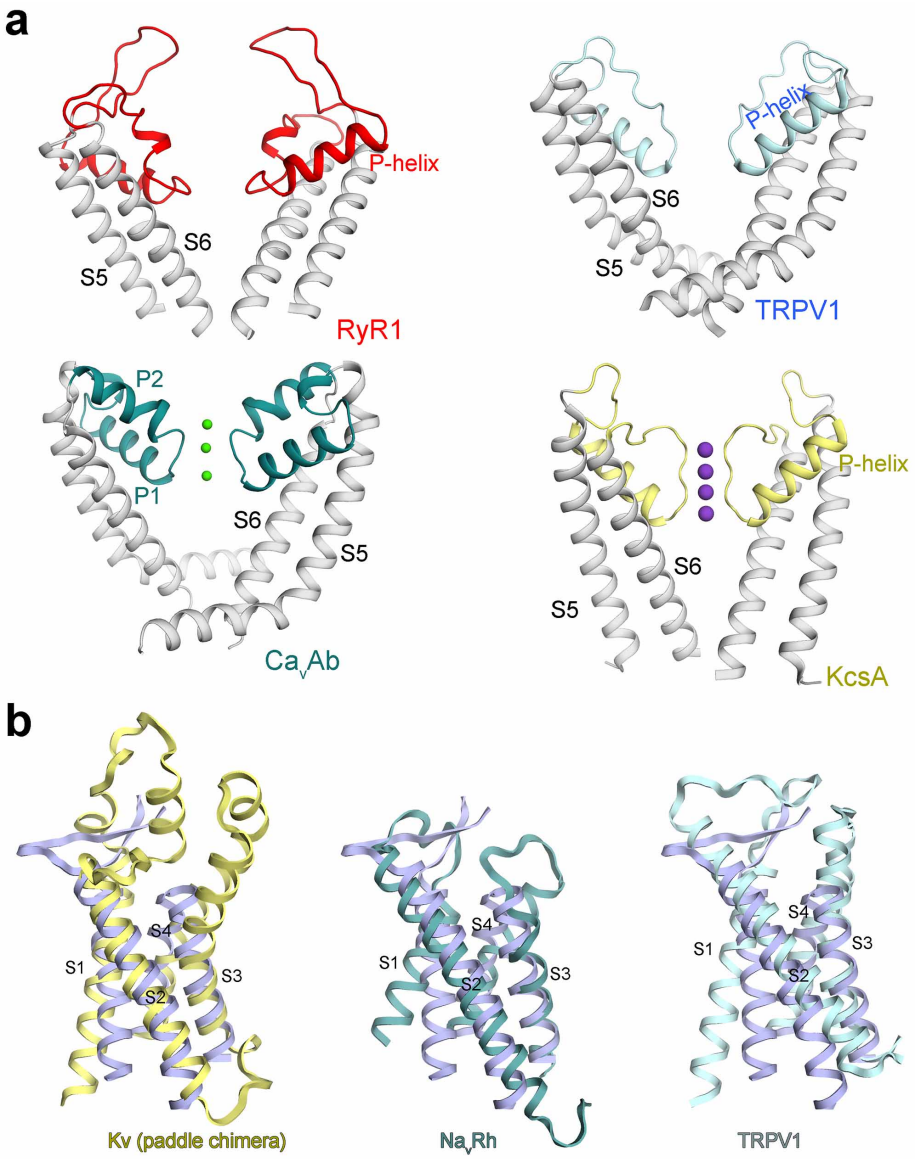
Extended Data Figure 6 | Organization of the cytoplasmic domains of RyR1. **a**, The NTD (yellow) participates in tetramerization. Compared to the previously reported crystal structure of the NTD[28], five additional α-helices (residues 560–631, orange) were identified in the electron microscopy structure. **b**, The structure of the SPRY1–3 domains. See Extended Data Fig. 2c for the sequence assignment of the three intertwined domains. Note that the N terminus of SPRY1 is preceded by the NTD, and its C terminus (magenta) is followed by the handle domain (cyan). **c**, Structure of the handle domain. The disordered sequences are indicated by dashed lines. **d**, The helical domain comprises two discontinuous sequence fragments, HD1 and HD2, which are disrupted by the P2 domain. **e**, The helical repeats in subdomain C of the NTD resemble the armadillo repeats. Shown here is a superposition with a designed armadillo protein (PDB code 4DB8). **f**, Structural superposition of the handle domain with β-catenin (PDB code 3IFQ) suggests that five pairs of helices, 1–2, 4–5, 8–9, 10–11 and 14–15, in the handle domain exhibit structural homology to the armadillo repeats. **g**, The helical repeats in the central domain are armadillo-like repeats. Shown here is the superposition of the central domain with the armadillo repeats of the anaphase-promoting complex (PDB code 3NMW). **h**, The armadillo-like repeats in the NTD, handle and central domains are joined end-to-end to form a superhelical assembly. The appearance of the superhelical assembly resembles a question mark. **i**, Each central domain directly interacts with two adjacent NTDs. The convex side of the helical repeats is involved in binding to the NTDs. Two close-up views are shown to highlight key residues that may form hydrogen bonds at the interfaces. **j**, The NTDs, central, handle and helical domains form multiple interfaces. Shown here are two adjacent NTDs (NTD and NTD′), one central domain, one handle domain, and the N-terminal fragment of the helical domain. **k**, SPRY2 bridges the spatial gap between the handle domain and HD2 from the adjacent protomer. **l**, FKBP12 is bound in a cleft formed by the handle, NTD and SPRY1/3 domains. **m**, An extended hydrophobic loop from the handle domain reaches into the ligand-binding pocket of FKBP12. A close-up view is shown to illustrate the residues that may mediate the interactions.

©2015 Macmillan Publishers Limited. All rights reserved



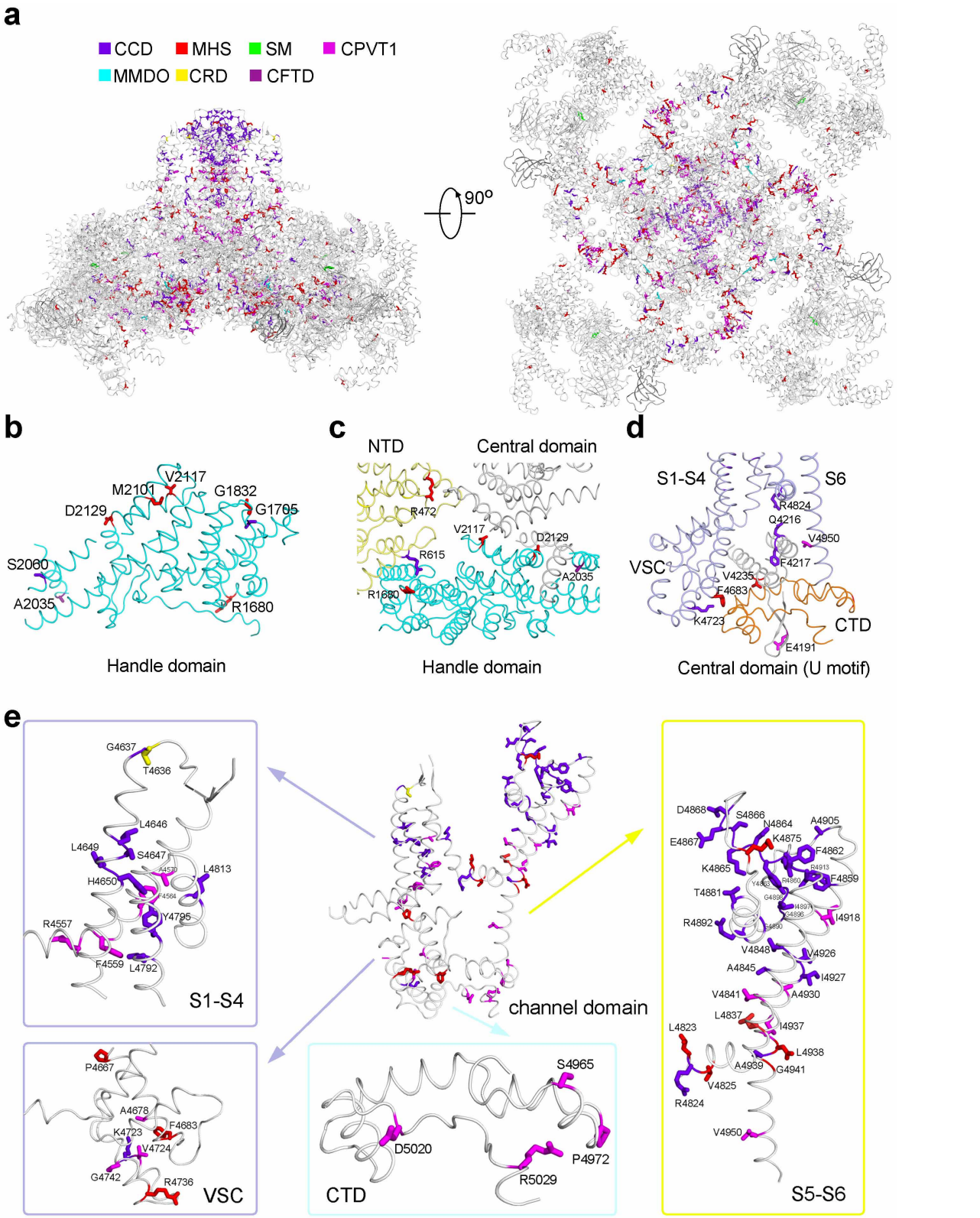
Extended Data Figure 7 | Alignment of the channel domain sequences of RyR orthologues. Secondary structural elements are indicated above the sequence alignment. Invariant amino acids are shaded in grey. The residues that may constitute potential cation-binding sites are in red. The C2H2 zinc-finger motif is highlighted by a green background. The residues whose mutations or deletions have been identified in patients are indicated with coloured circles below the sequences. The colour code is annotated at the bottom. CCD, central core disease; CPVT1, catecholaminergic polymorphic ventricular tachycardia type 1; CRD, core/rod disease; MHS, malignant hyperthermia susceptibility.

©2015 Macmillan Publishers Limited. All rights reserved



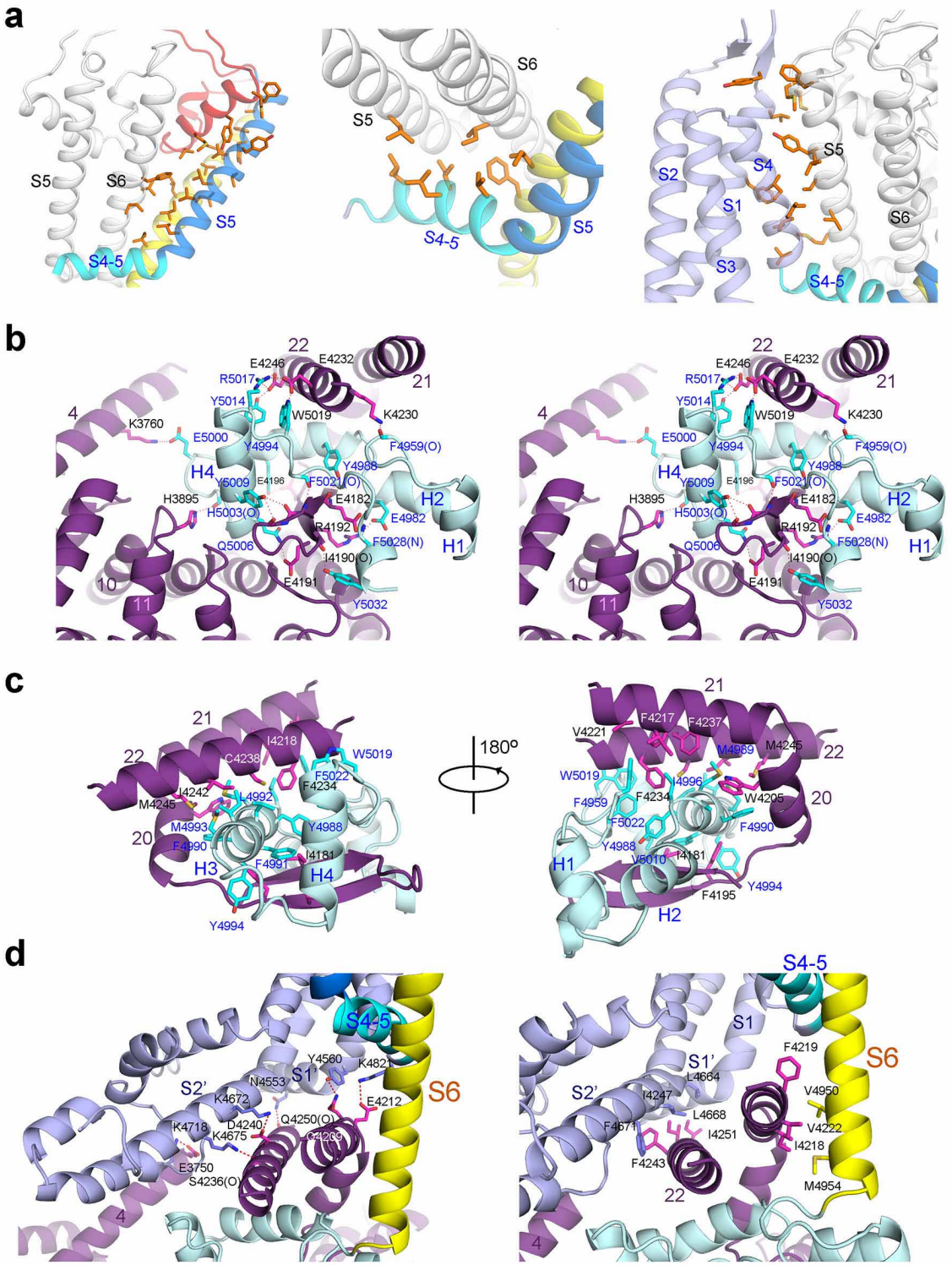
Extended Data Figure 8 | Structural comparison of the RyR1 channel domain with representative tetrameric cation channels of known structures. **a**, Structural comparison of the pore-forming elements from different tetrameric cation channels of known structures. Two diagonal protomers are shown. In all structures, the S5 and S6 segments are coloured grey. In the structures of Ca_vAb and KcsA, the bound ions are shown as spheres. PDB codes: 4MS2 for Ca_vAb, 3J5Q for TRPV1 and 1K4C for KcsA. **b**, Structural comparison of the transmembrane region of RyR1 VSL to the VSDs or like domains in the indicated tetrameric ion channels. Note that a hydrophilic sequence between S1 and S2 (residues 4579–4639) exhibits poor electron microscopy density and constitutes the least conserved DR1 region (DR for 'divergent') in the RyR1 channel domain[11] (Extended Data Fig. 7). The ordered segments within this sequence form a pair of short anti-parallel β-strands that extends into the sarcoplasmic reticulum lumen. PDB codes: 2R9R for the $K_v1.2/K_v2.1$ paddle chimaera, 4DXW for Na_vRh, and 3J5P for TRPV1.

©2015 Macmillan Publishers Limited. All rights reserved



Extended Data Figure 9 | Mapping of the disease-associated point mutations onto the structure of the RyR1 channel domain. **a**, The residues that are targeted for disease-derived mutations are highlighted by different colours: purple blue for CCD, red for MHS, green for SM (samaritan myopathy), cyan for MMDO (minicore myopathy with ophthalmoplegia), yellow for CRD, dark purple for CFTD (congenital fibre type disproportion), and magenta for CPVT1. See Supplementary Table 1 for details of these mutations. **b**, Disease-related mutations in the handle domain. The concerned residues, which are positioned on the surface of the handle domain, may be involved in the interaction with modulators or other domains within RyR1. **c**, Disease-related residues aligning the inter-domain interface between the NTD, handle and central domains. **d**, Representative disease-related residues involved in the interaction between the central domain and channel domain. **e**, The channel domain represents a hotspot for mutations associated with several diseases. See Extended Data Fig. 7 and Supplementary Table 1 for details of the mutations.

©2015 Macmillan Publishers Limited. All rights reserved



Extended Data Figure 10 | Intra- and inter-domain interactions that may be important for the long-range allosteric regulation of channel gating. **a**, Extensive van der Waals interactions exist between the pore-forming segments, and between the VSL of one protomer and S6 of adjacent protomer. These extensive interactions may aid the coupling of conformational changes within the channel domain. One protomer is colour-coded, whereas the adjacent one is coloured silver. **b**, A stereo view of the polar interaction network between the central domain and CTD. Potential H-bonds are shown as red dashed lines. **c**, The van der Waals contacts between the U-motif of the central domain and the CTD. Two opposite views are shown. **d**, Interactions between the central domain and the VSL. Polar and van der Waals contacts are shown on the left and right, respectively.

©2015 Macmillan Publishers Limited. All rights reserved

LETTER

doi:10.1038/nature14048

A higher-than-predicted measurement of iron opacity at solar interior temperatures

J. E. Bailey[1], T. Nagayama[1], G. P. Loisel[1], G. A. Rochau[1], C. Blancard[2], J. Colgan[3], Ph. Cosse[2], G. Faussurier[2], C. J. Fontes[3], F. Gilleron[2], I. Golovkin[4], S. B. Hansen[1], C. A. Iglesias[5], D. P. Kilcrease[3], J. J. MacFarlane[4], R. C. Mancini[6], S. N. Nahar[7], C. Orban[7], J.-C. Pain[2], A. K. Pradhan[7], M. Sherrill[3] & B. G. Wilson[5]

Nearly a century ago it was recognized[1] that radiation absorption by stellar matter controls the internal temperature profiles within stars. Laboratory opacity measurements, however, have never been performed at stellar interior conditions, introducing uncertainties in stellar models[2–5]. A particular problem arose[2,3,6–8] when refined photosphere spectral analysis[9,10] led to reductions of 30–50 per cent in the inferred amounts of carbon, nitrogen and oxygen in the Sun. Standard solar models[11] using the revised element abundances disagree with helioseismic observations that determine the internal solar structure using acoustic oscillations. This could be resolved if the true mean opacity for the solar interior matter were roughly 15 per cent higher than predicted[2,3,6–8], because increased opacity compensates for the decreased element abundances. Iron accounts for a quarter of the total opacity[2,12] at the solar radiation/convection zone boundary. Here we report measurements of wavelength-resolved iron opacity at electron temperatures of 1.9–2.3 million kelvin and electron densities of (0.7–4.0) × 10^{22} per cubic centimetre, conditions very similar to those in the solar region that affects the discrepancy the most: the radiation/convection zone boundary. The measured wavelength-dependent opacity is 30–400 per cent higher than predicted. This represents roughly half the change in the mean opacity needed to resolve the solar discrepancy, even though iron is only one of many elements that contribute to opacity.

In the region of the solar radiation/convection zone boundary[11], the electron temperature $T_e \approx 2.1 \times 10^6$ K, the electron density $n_e \approx 9 \times 10^{22}$ cm^{-3}, and the iron opacity arises mainly from L-shell bound–bound and bound–free transitions in the 6–16 Å spectral range. There are multiple processes involved in modelling these transitions, including the electron energy-level structure, photoionization, and continuum lowering. A theoretical challenge is an accurate description of excited atomic states, which are prevalent at solar interior temperatures. Plasma line-broadening models are both untested and important in this regime, because photons are more readily transported in the 'windows' between the lines and broader lines tend to close the opacity windows. Finally, there is at present no consensus on how to model the autoionizing levels adequately[13].

Stellar interior energy transport calculations require the Rosseland mean[14], a harmonic average over photon energy. The large range of stellar constituents and conditions makes it impractical to measure all the mean opacities that are needed. Therefore, here we measured wavelength-dependent opacities over a range of densities and temperatures in an attempt to understand the different physical processes.

There were three main impediments[15,16] to laboratory opacity measurements at stellar interior conditions that were surmounted by the Sandia Z facility[16–18]: (1) a macroscopic sample had to be uniformly heated to stellar interior conditions; (2) the sample had to contain an electron population distribution that could be described by the local thermodynamic equilibrium (LTE) (in the Sun, this distribution is enforced by the radiation field); and (3) a spectrally smooth X-ray backlight was needed that was sufficiently bright to overcome sample self-emission. A spectrometer that views the backlight directly and through the sample determines the spectrally resolved transmission. The opacity is inferred by taking the natural log of the transmission and dividing by the areal density. The first such measurements for high-energy-density matter[19] were published in 1988, at temperatures about a factor of four lower than at the solar radiation/convection zone boundary. Later experiments[15,20] refined the method, but the maximum temperature did not exceed approximately 0.9×10^6 K.

An important step forward was realized in 2007 when the Z-facility opacity science platform[16,17] provided iron transmission laboratory measurements at 1.8×10^6 K. These experiments created the iron charge states that exist in the solar radiation/convection zone boundary region, but T_e and n_e were still too low to test solar opacity models definitively. Higher-T_e and -n_e measurements have now been developed by exploiting the increased X-ray power at the Z facility[18] and sample design improvements[21]. The Fe/Mg sample foils are heated during the ~10 ns radiation source assembly phase (Fig. 1 and Methods) and backlit when the radiation source stagnation provides a backlight of duration ~3 ns and spectral radiance equivalent to a ~350 eV Planckian. The Planck-equivalent radiation flux of ~210 eV at the sample drives the electronic populations to form a replica of the LTE distribution. The conditions are controlled by tamping the sample expansion with different thicknesses of plastic (CH) and Be. The backlight time is fixed relative to the heating radiation, so heavily tamped samples that expand more slowly are at a higher density and temperature at the time the absorption spectrum is measured (Extended Data Fig. 1).

We performed measurements over a range of T_e/n_e values to gain an understanding of the physical processes that control the opacity (see Methods). The T_e/n_e values inferred using K-shell spectroscopic analysis[22] of Mg intermixed with the Fe were 1.91×10^6 K/7×10^{21} cm^{-3}; 1.97×10^6 K/2×10^{22} cm^{-3}; 2.11×10^6 K/3.1×10^{22} cm^{-3}; and 2.26×10^6 K/4×10^{22} cm^{-3}. The T_e and n_e accuracies are ±4% and ±25%, respectively. The highest T_e reported here exceeds the radiation/convection zone boundary temperature by approximately 4%, whereas n_e is a factor of ~2.3 lower.

The measurements at these four conditions (Fig. 2) show that as the T_e/n_e values are increased, the opacity rises, the prominent line features shrink with respect to the nearby quasi-continuum, the 'windows' between the lines fill in, and the lines become broader. The SCRAM[23] opacity model (Fig. 2) predicts similar trends, but the degree of change effected by raising T_e and n_e is strikingly smaller. The agreement is best at the lowest T_e/n_e conditions and deteriorates as T_e and n_e increase.

A comparison of the 2.11×10^6 K/3.1×10^{22} cm^{-3} measured opacity spectrum with several opacity models is shown in Fig. 3. The OPAL[24]

[1]Sandia National Laboratories, 1515 Eubank SE, Albuquerque, New Mexico 87185-1196, USA. [2]Commissariat à l'Énergie Atomique (CEA) et aux Énergies Alternatives, F-91297 Arpajon, France. [3]Los Alamos National Laboratory, Bikini Atoll Road, Los Alamos, New Mexico 87545, USA. [4]Prism Computational Sciences, 455 Science Drive, Suite 140, Madison, Wisconsin 53711, USA. [5]Lawrence Livermore National Laboratory, 7000 East Avenue, Livermore, California 94550-9234, USA. [6]University of Nevada, 1664 North Virginia Street, Reno, Nevada 89557, USA. [7]Ohio State University, 140 West 18th Avenue, Columbus, Ohio 43210, USA.

©2015 Macmillan Publishers Limited. All rights reserved

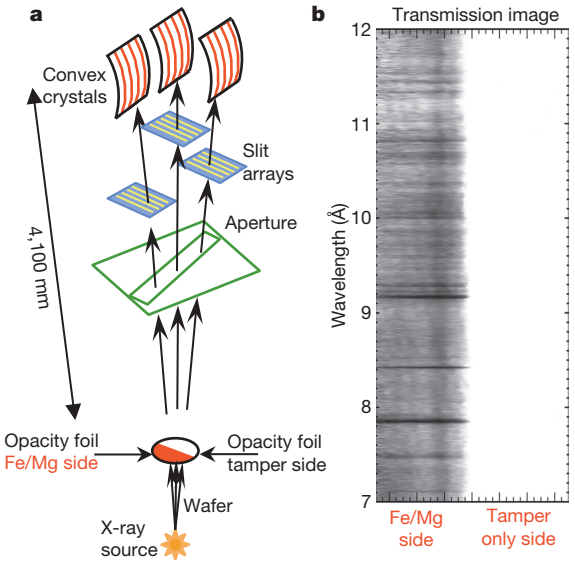


Figure 1 | Experiment diagram and example transmission image. **a**, Three to four spectrometers view the 'half-moon'-shaped tamped iron/magnesium sample (not to scale). Each uses multiple slits to project spatially resolved images onto a convex crystal that disperses the spectrum before recording on film (not shown). The set-up measures the unattenuated (tamper only) and the attenuated (tamper plus FeMg) spectra in the same experiment. **b**, A spatially resolved and spectrally resolved transmission image is obtained by dividing the attenuated spectral image by the unattenuated image. Darker regions correspond to higher absorption. The white portion of the image corresponds to ~100% transmission.

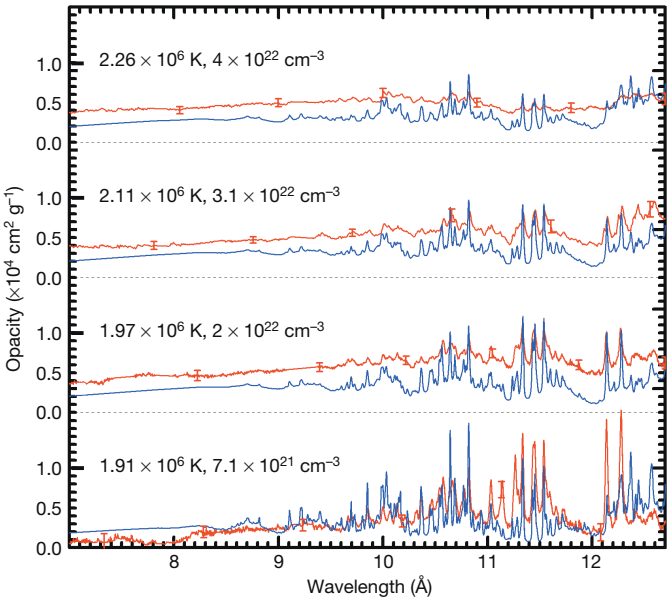


Figure 2 | Measured iron opacity spectra at four T_e/n_e values compared with calculations. The SCRAM[23] model calculations (blue lines) account for the instrument resolution. Red lines denote the measurements and the error bars represent 1σ uncertainties. The measurements combine information from 22 separate experiments, each with three or four independent spectrometers that each record 4–6 spectra. The numbers of experiments used to infer the average opacities presented here were as follows: six for the 1.91×10^6 K/7×10^{21} cm^{-3} results; one for the 1.97×10^6 K/2×10^{22} cm^{-3} results; five for the 2.11×10^6 K/3.1×10^{22} cm^{-3} results; and ten for the 2.26×10^6 K/4×10^{22} cm^{-3} results.

and OP[25,26] models are most frequently used in astrophysics, although the OPAS model has recently been used[12] to calculate solar opacities. Unfortunately, wavelength-dependent OPAL calculations are no longer available. OP calculations generally yield values lower than the data values and the wavelengths of the strong spectral features disagree (Fig. 3a). The latter implies that the OP energy-level structure is not sufficiently accurate and the former is consistent with a hypothesis that OP does not account for all of the transitions present in the actual solar plasma. Comparisons with the ATOMIC[27], OPAS[12], and SCO-RCG[28] models (Fig. 3b) show that these models also yield values notably lower than the data values over most of the spectral range. The strong bound–bound feature wavelengths agree reasonably well, but none of these models reproduces the measured opacity spectra. These models have been more recently formulated or updated than the OP model and they exploit the advances in computing power that have occurred in the last decade. OP and ATOMIC use line-by-line atomic physics calculations while the other models employ a hybrid approach that combines line-by-line calculations for the strongest transitions and a statistical treatment for the myriad weaker transitions.

The predicted Rosseland mean opacities for iron are lower than the measured Rosseland mean values by 1.75, 1.67, 1.53, 1.75, and 1.57 for the OP, SCRAM, OPAS, ATOMIC, and SCO-RCG models, respectively. These comparisons use the Be-tamped measurement conditions (2.11×10^6 K/3.1×10^{22} cm^{-3}), account for the instrument resolution effect, and are restricted to the 7.0–12.7 Å range reported here. The Be-tamper data reflect the measurements at high T_e/n_e with the best accuracy and they generally support the validity of the thick-CH measurements (see Methods). These differences are large compared to the roughly ±11% experimental uncertainty in the Rosseland mean. Ratios of the experimental and model opacities as a function of wavelength further quantify the discrepancies (Fig. 3c). The differences between the ratios calculated for the various models at specific wavelengths can help formulate hypotheses for the discrepancies.

First, the predicted opacity is lower than the measurement by a factor of 1.3–1.9 in the short-wavelength (7–10 Å) range. Models predict that bound–free transitions dominate over bound–bound transitions for wavelengths shorter than ~9.5 Å (Extended Data Fig. 3). If the data are correct (see below and Methods), then two possible explanations are that (1) models neglect additional bound–bound features in the short wavelength range or (2) predictions for the photoionization bound–free contribution are low in this spectral range. Second, the measured opacities in the windows between the strong spectral features are higher than the model predictions. At the same time, the peak opacity agreement of the strong spectral features varies from feature to feature and from model to model. We note that even among the model predictions there are ~50% variations in the strength of certain strong spectral features. Furthermore, the measured widths of the strong prominent line features are broader than the predictions. These facts together suggest that there are missing transitions from the models, the Stark and/or autoionization broadening of the line features is larger than predicted, or both.

The comparisons imply that revisions are needed to the current descriptions of photon absorption by atoms in high-energy-density plasmas. This finding has broad implications for astrophysics and in the laboratory, so it is essential to determine whether the problem lies with the experimental methods. We established experimental reliability and reproducibility by incorporating approximately 450 spectra recorded in 22 separate experiments. We examined many possible systematic errors, including transmission errors, plasma diagnostic accuracy, departures from LTE, extraneous background, sample flaws, spatial and temporal gradients, and tamper attenuation and emission. These effects were found to be too small to influence the conclusions drawn above.

The measured iron opacity affects our understanding of the solar interior. We evaluate the impact by first computing the wavelength-dependent opacity for the solar interior composition[9] and the OP opacities[25,26] at $T_e = 2.11 \times 10^6$ K and $n_e = 3.1 \times 10^{22}$ cm^{-3} (Fig. 4), the values of the Be-tamped experiment. We then replace the OP iron contribution in the measured wavelength range with the experimental results, while the opacity contributions from the other solar matter constituents are kept the same. The impact on the solar mixture Rosseland mean depends

©2015 Macmillan Publishers Limited. All rights reserved

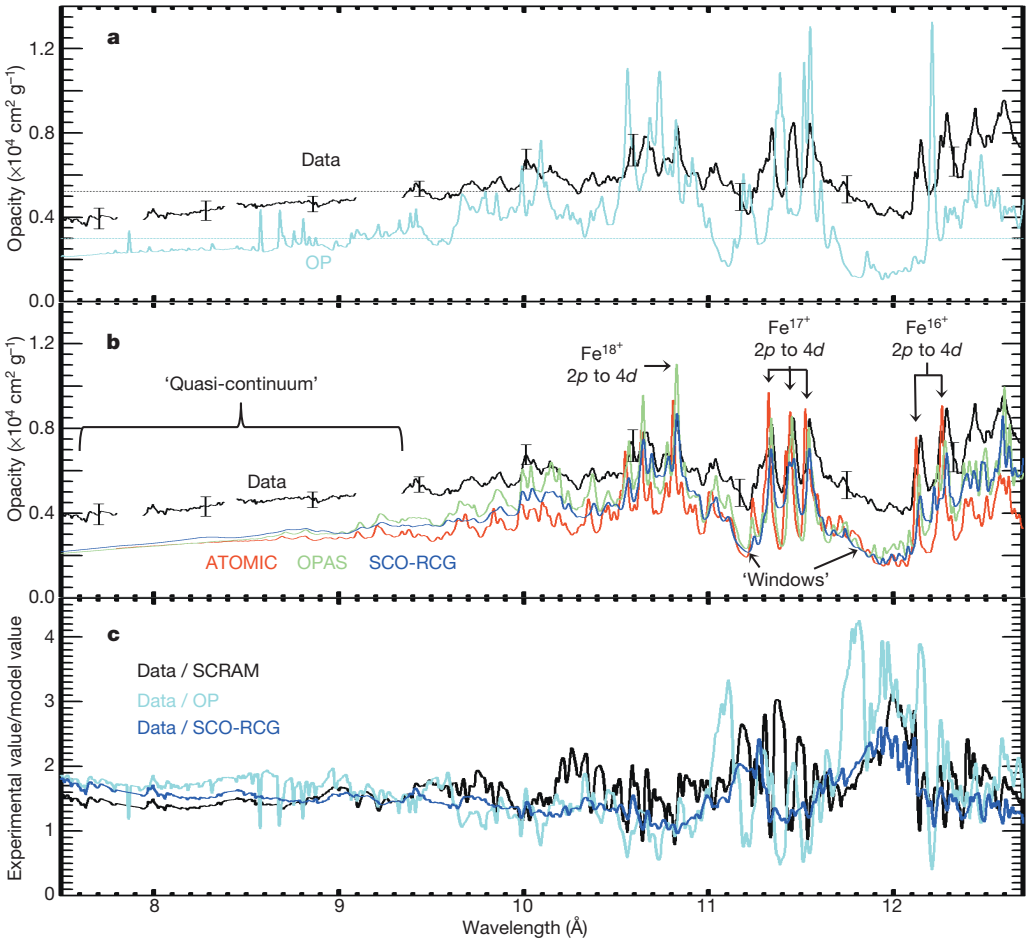


Figure 3 | Comparisons of iron opacity spectra with multiple models at the solar radiation/convection zone boundary temperature. The $T_e = 2.11 \times 10^6$ K, $n_e = 3.1 \times 10^{22}$ cm^{-3} conditions displayed here were deemed to be the most accurate; the opacity represents an average obtained by combining information from five separate experiments with four independent spectrometers. The calculations account for the instrument resolution and the experiment error bars represent 1σ uncertainties. **a**, Comparison with the OP model[25,26] that is used for solar modelling. The dashed lines are the Rosseland mean opacities calculated for this wavelength range. **b**, Comparisons with the ATOMIC, OPAS and SCO-RCG models. **c**, Ratio of the experiment opacity to the opacities modelled by SCRAM, OP and SCO-RCG.

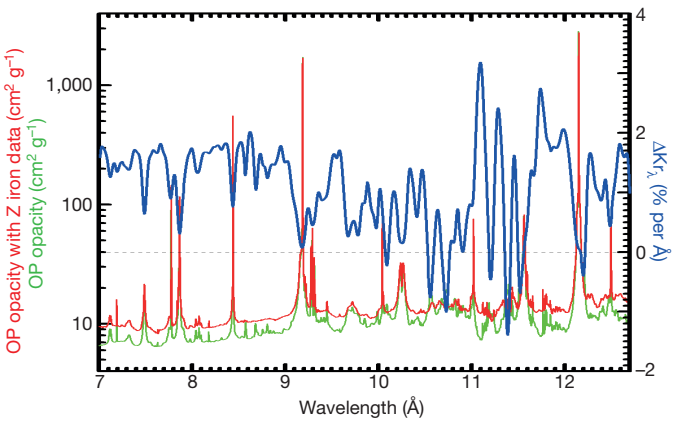


Figure 4 | Measured iron opacity impact on solar mixture Rosseland mean. The opacity of a plasma with solar composition[9] is calculated with OP[25,26] (green line; log scale on left axis) at the experiment conditions ($T_e = 2.11 \times 10^6$ K, $n_e = 3.1 \times 10^{22}$ cm^{-3}). The opacity for the same plasma using the measured iron opacity is generally higher (red line; log scale on left axis). The Rosseland mean opacity percentage change per unit wavelength (ΔKr_λ) is denoted with a blue line (linear scale on right axis). Spectral features where the blue curve is below the dashed line reduce the solar mixture Rosseland mean and features above the dashed line raise it.

on the ratio of the measured to calculated iron opacity (Fig. 3c), the Rosseland mean weighting function, and the relative importance of the iron contribution to the total opacity at each wavelength. The percentage change per unit wavelength in the Rosseland mean caused by using the experimental iron measurement as a function of wavelength (Fig. 4) helps to identify which spectral features have the most impact on the Sun's opacity. Integrated over wavelength, the Rosseland mean for this mixture of solar constituents is 7 ± 3% higher when the experimental iron opacity is used. This is about half of the opacity adjustment required[8] to restore agreement between standard solar models[11] and helioseismology.

The present experiments imply that model corrections are probably needed for all the solar constituents ionized into the L-shell, including Ni, Cr, Ti, and Ca. Experiments with Ni and Cr are in progress, both to help evaluate hypotheses for the model–experiment discrepancy observed for iron and to determine whether additional revisions to the solar opacity are appropriate. Future work will attempt to increase the experimental electron density by a factor of 2.3, to achieve opacity measurements at the T_e and n_e that are believed to exist at the solar radiation/convection zone boundary region.

Online Content Methods, along with any additional Extended Data display items and Source Data, are available in the online version of the paper; references unique to these sections appear only in the online paper.

Received 17 September; accepted 3 November 2014.

1. Eddington, A. S. *The Internal Constitution of the Stars* (Cambridge Univ. Press, 1926).

©2015 Macmillan Publishers Limited. All rights reserved

2. Basu, S. & Antia, H. M. Helioseismology and solar abundances. *Phys. Rep.* **457,** 217–283 (2008).
3. Basu, S., Grevesse, N., Mathis, S. & Turck-Chièze, S. Understanding the internal chemical composition and physical processes of the solar interior. *Space Sci. Rev.* http://dx.doi.org/ 101007/s11214-014-0035-9 (2014).
4. Christensen-Dalsgaard, J. in *Proc. IAU Symp. No. 258*, *The Ages of Stars (2008)* (eds Mamajek, E. E., Soderblom, D. R. & Wyse, R. F. G.) 431–442 (International Astronomical Union, 2009).
5. Delahaye, F. & Pinsonneault, M. Comparison of radiative accelerations obtained with atomic data from OP and OPAL. *Astrophys. J.* **625,** 563–574 (2005).
6. Bahcall, J. N., Serenelli, A. M. & Pinsonneault, M. How accurately can we calculate the depth of the solar convective zone? *Astrophys. J.* **614,** 464–471 (2004).
7. Turck-Chièze, S. *et al.* Surprising Sun: a new step towards a complete picture? *Phys. Rev. Lett.* **93,** 211102 (2004).
8. Serenelli, A. M., Basu, S., Ferguson, J. W. & Asplund, M. New solar composition: the problem with solar models revisited. *Astrophys. J.* **705,** L123–L127 (2009).
9. Asplund, M., Grevesse, N., Sauval, J. A. & Scott, P. The chemical composition of the Sun. *Annu. Rev. Astron. Astrophys.* **47,** 481–522 (2009).
10. Caffau, E. *et al.* Solar chemical abundances determined with a CO5BOLD 3D model atmosphere. *Sol. Phys.* **268,** 255–269 (2011).
11. Bahcall, J. N. *et al.* Standard solar models and the uncertainties in predicted capture rates of solar neutrinos. *Rev. Mod. Phys.* **54,** 767–799 (1982).
12. Blancard, C., Cosse, Ph. & Faussurier, G. Solar mixture opacity calculations using detailed configuration and level accounting treatments. *Astrophys. J.* **745,** 10 (2012).
13. Nahar, S. N., Pradhan, A. K., Chen, G.-X. & Eissner, W. Highly excited core resonances in photoionization of Fe XVII: implications for plasma opacities. *Phys. Rev. A* **83,** 053417 (2011).
14. Rosseland, S. Note on the absorption of radiation within a star. *Mon. Not. R. Astron. Soc.* **84,** 525–528 (1924).
15. Perry, T. S. *et al.* Absorption experiments on x-ray-heated mid-Z constrained samples. *Phys. Rev. E* **54,** 5617–5631 (1996).
16. Bailey, J. E. *et al.* Experimental investigation of opacity models for stellar interior, inertial fusion, and high energy density plasmas. *Phys. Plasmas* **16,** 058101 (2009).
17. Bailey, J. E. *et al.* Iron-plasma transmission measurements at temperatures above 150 eV. *Phys. Rev. Lett.* **99,** 265002 (2007).
18. Rochau, G. A. *et al.* ZAPP: the Z Astrophysical Plasma Properties collaboration. *Phys. Plasmas* **21,** 056308 (2014).
19. Davidson, S. J. *et al.* Investigation of the opacity of hot, dense aluminum in the region of its K edge. *Appl. Phys. Lett.* **52,** 847–849 (1988).
20. Foster, J. M. *et al.* L-shell absorption spectrum of an open-M-shell germanium plasma: comparison of experimental data with a detailed configuration-accounting calculation. *Phys. Rev. Lett.* **67,** 3255–3258 (1991).
21. Nash, T. J., Rochau, G. A. & Bailey, J. E. Design of dynamic Hohlraum opacity samples to increase measured sample density on Z. *Rev. Sci. Instrum.* **81,** 10E518 (2010).
22. Nagayama, T. *et al.* Control and diagnosis of temperature, density, and uniformity in x-ray heated iron/magnesium samples for opacity measurements. *Phys. Plasmas* **21,** 056502 (2014).
23. Hansen, S., Bauche, J., Bauche-Arnoult, C. & Gu, M. Hybrid atomic models for spectroscopic plasma diagnostics. *High Energy Density Phys.* **3,** 109–114 (2007).
24. Iglesias, C. A. & Rogers, F. J. Opacities for the solar radiative interior. *Astrophys. J.* **371,** 408–417 (1991).
25. Seaton, M. J., Yu, Y., Mihalas, D. & Pradhan, A. K. Opacities for stellar envelopes. *Mon. Not. R. Astron. Soc.* **266,** 805–828 (1994).
26. Badnell, N. R. *et al.* Updated opacities from the opacity project. *Mon. Not. R. Astron. Soc.* **360,** 458–464 (2005).
27. Colgan, J. *et al.* Light element opacities from ATOMIC. *High Energy Density Phys.* **9,** 369–374 (2013).
28. Porcherot, Q., Pain, J.-C., Gilleron, F. & Blenski, T. A consistent approach for mixed detailed and statistical calculation of opacities in hot plasmas. *High Energy Density Phys.* **7,** 234–239 (2011).

Acknowledgements Sandia is a multiprogramme laboratory operated by Sandia Corporation, a Lockheed Martin Company, for the United States Department of Energy under contract DE-AC04-94AL85000. The Los Alamos National Laboratory is operated by Los Alamos National Security, LLC, for the NNSA of the US DOE under contract number DE-AC5206NA25396. J.E.B. acknowledges support from a DOE High Energy Density Laboratory Plasmas grant. A.K.P. and C.O. also acknowledge support from a DOE High Energy Density Laboratory Plasmas grant. We appreciate the efforts of the entire Z facility team. We thank S. Turck-Chièze, H. Morris, and M. Pinsonneault for discussions. We also thank R. W. Lee for critiquing the manuscript. We appreciate support for the experiments provided by R. J. Leeper, J. L. Porter, M. K. Matzen and M. Herrmann.

Author Contributions These measurements were conceived and planned by J.E.B. and G.A.R. J.E.B. was the primary author of the manuscript, with important contributions from T.N. Experiments were conducted by J.E.B., G.A.R. and G.P.L. The Z-facility data were analysed by T.N., J.E.B. and G.P.L., with assistance from G.A.R., C.A.I., B.G.W., I.G., J.J. M. and R.C.M. OPAS calculations were performed by C.B., G.F. and Ph.C. ATOMIC calculations were performed by J.C., with assistance from C.F., D.P.K. and M.S. SCRAM calculations were provided by S.B.H. SCO calculations were performed by J.-C.P. and F.G. OP calculations were performed by C.O., with assistance from A.K.P. and S.N.N. All authors discussed the results, commented on the manuscript, and contributed to the interpretation.

Author Information Reprints and permissions information is available at www.nature.com/reprints. The authors declare no competing financial interests. Readers are welcome to comment on the online version of the paper. Correspondence and requests for materials should be addressed to J.E.B. (jebaile@sandia.gov).

©2015 **Macmillan Publishers Limited. All rights reserved**

METHODS

Experimental methods. The Z-facility opacity science platform[16–18,22,29,30] samples consist of thin 'half-moon'-shaped FeMg films sandwiched by low-Z tamper materials (Extended Data Fig. 1, Extended Data Table 1). Optical microscopy confirmed that the samples were free of non-uniformities that can artificially reduce the inferred opacity. Profilometry verified that the 'half-moon' boundary sharpness was approximately 10 μm or less. Profilometry and interferometry sample thickness measurements provided an upper bound on the sample areal density, because the fabrication methods produce thin films with densities lower than the bulk density. Rutherford backscattering spectrometry (RBS)[31] provided primary areal density measurements with an accuracy of better than ~4% for the individual sample constituents. Three separate RBS laboratories measured many of the sample areal densities with an average standard deviation of ±3%. A small group of samples was also measured by weighing a precisely determined sample area. This measurement agreed with the RBS measurements.

The results described here are based on 22 Z experiments conducted over a three-year period. The diagnostic configuration was refined over the course of this work and the transmission determination method depends on the configuration. Four X-ray crystal spectrometers were employed, configured to view the backlight at a combination of angles with respect to the Z-pinch axis: +9°, −9° and 0°. These spectrometers provide multiple simultaneous measurements of the attenuated and unattenuated backlight spectra from each single experiment. Here, the term 'attenuated' refers to the reduction in backlight intensity by the FeMg layer; all signals include the attenuation by the low-Z tamper plasma.

The spectrometer fields of view were restricted by a aperture 1 mm wide located 17 mm above the sample. An array of either four or six 50-μm-wide slits provided a spatial resolution of ~100 μm perpendicular to the 'half-moon' boundary. Each slit projects a nominally identical spatially resolved and spectrally resolved image onto the detector. The collection of slit-imaged spectra enables an *in situ* determination of any crystal artefacts and the variance of the multiple nominally identical spectra determines the spectral radiance random uncertainty. The potassium acid phthalate crystals were cylindrically bent to a radius of either 15.24 cm or 22.86 cm and are located 410 cm from the source. The data are recorded on Kodak RAR 2492 film. The instrument spectral resolution is limited by the crystal and was measured[32] in the wavelength $\lambda \approx 7$–10 Å range to be $\lambda/\delta\lambda \approx 800$–$1{,}000$. Each spectrometer covers a range of approximately 5–6 Å. The data were recorded over 6–16 Å, but here we report only data from 7–12.7 Å. At shorter wavelengths the data require additional corrections for backlight variability and at longer wavelengths the data require corrections for second-order crystal reflections and possibly sample self-emission. Work to perform these corrections is in progress.

Transmission and opacity analysis. The spectrometers record 20–24 spectrally resolved and spatially resolved images from each experiment, from different viewing angles and with different spectral ranges. The 22 experiments discussed here required analysis of more than 450 spectral images. We regard this data set as the minimum needed to provide benchmark-quality opacity tests, because such tests require[15,16]

(1) multiple measurements to determine simultaneously the attenuated and unattenuated signals, to provide random uncertainty evaluations, and to reject artificial features from crystal defects;

(2) transmission measurements with different areal densities, in order to extend the dynamic range and verify proper scaling with sample thickness according to the Beer–Lambert–Bouguer Law;

(3) repeated experiments to verify reproducibility;

(4) tamper-only experiments to verify the transmission accuracy;

(5) measurements with different T_e/n_e conditions to help unravel multiple entangled processes; and

(6) experiments with different tamper materials to evaluate possible systematic errors.

Each spectrally resolved image is digitized and corrected for the spatial magnification and spectral dispersion. The film optical density is converted to exposure[33] and agreement among measurements obtained at varying exposures with different diagnostic configurations and sample thicknesses confirmed the conversion accuracy. Multiple methods were developed to obtain the transmission. Here, we summarize the method for the five experiments conducted with a CH + Be tamper (Extended Data Fig. 2 and Extended Data Table 1). Four spectrometers recorded data at ±9° on each experiment, two with crystals of radius 15.24 cm (designated CCP4a and CCP10a) and two with crystals of radius 22.86 cm (designated CCP4b and CCP10b). Three of these experiments employed a FeMg 'half-moon' design and two used a tamper-only sample. The 9° spectrometer angle of view combined with the measured ~1.5 mm backlight-to-sample distance[34] implies that the +9° spectrometer views the backlight centre through the FeMg portion of the 'half-moon' sample and the −9° spectrometer views the backlight centre through the tamper-only portion. Thus, the spectrally resolved transmission can be inferred by dividing the +9° spectrometer signal by the −9° spectrometer signal.

The measurements using the crystals of radii 15.24 cm and 22.86 cm are analysed as two separate groups to avoid possible crystal reflectivity differences. The unattenuated measurements demonstrate the reproducibility for these five experiments (Extended Data Fig. 2a). The absolute fractional percentage standard deviation $[\sigma/I]_{abs}$ averaged over 8–12 Å was ±5.8% and the relative fractional percentage standard deviation $[\sigma/I]_{rel}$ was ±3.3%. Therefore, we use the mean spectral intensity to represent the unattenuated spectrum.

The attenuated and unattenuated spectral intensities used to determine the transmission on experiment Z2624 are shown in Extended Data Fig. 2b. The transmissions from each crystal on Z2624 are shown in Extended Data Fig. 2c. The error bars represent 1σ uncertainties obtained by convolving the uncertainties in the attenuated and unattenuated measurements. The dashed lines correspond to the fractional transmission uncertainty. The transmission uncertainty averaged over the 8.5–12.5 Å range that provides the best accuracy is ±10% for both the CCP10a and CCP10b spectrometers. These are independent measurements of the same physical quantity and the uncertainty in the mean absolute transmission is therefore approximately ±7%. The relative uncertainty as a function of wavelength is of the order of ±2%, but the exact value depends on the wavelength range considered.

The optical depth obtained by taking the natural log of the mean transmission measured on Z2624 (Extended Data Fig. 2d) includes Fe and Mg contributions. To proceed, we calculate the Mg optical depth with the PrismSPECT model[35] using the Mg areal densities determined with RBS. The iron optical depth is inferred by subtracting the Mg calculation from the FeMg result. The mean opacity from the three Be-tamped iron opacity experiments is shown in Extended Data Fig. 2e, along with the fractional uncertainties. These results are then combined (Extended Data Fig. 2f) to infer an overall mean opacity for the Be-tamped experiment conditions. The opacity uncertainty is ±10% over a broad wavelength range, rising to ±15% near the short-wavelength end of the spectrum. This relatively small uncertainty is obtained by averaging repeated experiments that each provide multiple opacity measurements.

Systematic error evaluation. The estimated ±10% opacity uncertainty over the 8.5–12.5 Å range is small compared to the 30–400% differences between the Be-tamped measurement and the opacity models (Fig. 3). Discrepancies of this order, their persistence for all tested opacity models, and their importance for both astrophysics and laboratory experiments make it essential to consider possible systematic errors. An additional concern is that the data exceed the cold opacity[36] by ~36% (Extended Data Fig. 3a) averaged over the 7–8 Å range. Revisiting the opacity of room-temperature iron may be warranted because the stated uncertainty of generally accepted[37] cold iron opacity measurements is ±10%, but recent measurements[38] are approximately 40% higher. Nevertheless, it is only possible for the hot iron plasma opacity to exceed the cold opacity in a particular wavelength range if there is an important contribution from either bound–bound or resonant bound–free transitions. According to the SCRAM model, the bound–bound contribution falls to 50% at ~9.5 Å and it shrinks for shorter wavelengths (Extended Data Fig. 3b). Furthermore, the combination of bound–bound and bound–free features is expected to obey the oscillator strength sum rule[39]. This states that the total oscillator strength for a given initial state to all final states is equal to the number of electrons. Accordingly, if models underpredict the opacity in a certain wavelength range, then there should be a compensating overprediction in another wavelength range. Work is in progress to measure opacity values for the strong $n = 2$ to $n = 3$ (n is the principal quantum number) iron L-shell transition arrays that fall in the 12.5–16 Å range. This could provide insight into the most suitable interpretation of the sum rule.

The systematic error evaluation comprised the majority of the work conducted for this project and here we provide only a synopsis of the results. The systematic errors are divided into three categories according to the direction in which they bias the result with respect to the true value: those that always reduce inferred opacity, those that always increase the inferred opacity, and those that can do either, depending on the conditions. The systematic error evaluation incorporates both experimental tests and experimentally benchmarked simulations. The simulations were performed using the HELIOS[40] one-dimensional radiation-hydrodynamics code using measured radiation source characteristics and the experimental geometry. The simulation credibility was supported by the calculated sample temperature and density, which match the experimentally measured values for a wide variety of experiments that included changes in the tamper and sample thicknesses and compositions.

Initial systematic error tests evaluated whether the transmission scaled with the areal density according to the Beer–Lambert–Bouguer Law[16]. This scaling was obeyed within the experiment uncertainties (Extended Data Fig. 4), which mitigates concerns[15,16] from transmission determination errors, extraneous background, tamper self-emission, and spatial non-uniformities. Satisfying this relationship is necessary, but not always sufficient, to detect possible systematic errors. Therefore, alternative experimental and simulation-based tests were conducted.

©2015 Macmillan Publishers Limited. All rights reserved

Sample contamination and tamper shadowing are possible systematic errors that can cause an overestimate of the inferred opacity. The RBS sample characterization verified that the oxygen contamination was 10–100 times lower than the amount needed to cause a 10% change in the opacity. Other contaminants were smaller and their contamination did not notably bias the result. We reiterate that the incident heating radiation, backlight radiation, diagnostic set-up, and data analysis methods are the same for all the experiments. The tamper is the only experimental set-up change between the lower-T_e/n_e results that agree reasonably well with opacity calculations[17] to the present higher-T_e/n_e results that strongly disagree. Therefore, we investigated whether increasing the tamper thickness biases the experimental result.

Tamper shadowing can occur when the tamper used to infer the unattenuated spectrum is hotter than the tamper behind the FeMg layer, because the FeMg absorbs some fraction of the incident photons. If the attenuation in the shadowed tamper is larger, then the inferred iron opacity would be larger than the true value. The quantitative influence of tamper shadowing on the opacity depends on the T_e and n_e values. The shadowing effect on the opacity grows monotonically with increasing wavelength, is smaller for thinner FeMg layers, and smaller for thinner or less-attenuating tampers. Simulations[40] estimate negligible effects for all the CH tampers at wavelengths less than approximately 10.5 Å. However, at longer wavelengths, tamper shadowing is calculated to cause a significant (>5%) change in the inferred opacity for the 70-μm-thick CH tamper. This concern motivated our replacement of part of the thick CH tamper with Be. The Be attenuation is less than for an equivalent mass of CH and is negligible for the range of possible T_e/n_e conditions. A comparison of the Be-tamped results with the thick-CH-tamped results confirmed that there was little difference in the inferred opacity below 10.5 Å. The thick-CH-tamped results presented here were corrected for the shadowing effect in the 10.5–12.7 Å range using the simulation results. However, this introduces a possible error that is difficult to quantify. Therefore, we regard the Be-tamped results to be the most accurate.

Possible systematic errors that cause an underestimate of the inferred opacity include extraneous background, tamper self-emission, and iron self-emission. The first two effects are similar: they both add an extra signal that is not altered by the iron absorption to both the attenuated and unattenuated spectra, causing the inferred iron opacity to be lower than the true value. The imaging spectrometers account for the spatially homogeneous background, but spatially imaged extraneous background could arise, for example, from plasma that emerges from the Z-pinch dynamic hohlraum near the end of the experiment. Tamper self-emission is also expected to be small. However, both the emerging Z-pinch plasma and the tamper might emit over a long time in comparison to the backlight duration. The 1-mm-wide Ti aperture installed between the sample and the spectrometer lines of sight restricts the observed plasma volume and helps mitigate these effects.

Nevertheless, there is one finding that could suggest that either extraneous background or tamper self-emission is present: for some experiments the observed Mg Heα and Heβ transmissions are approximately 15% higher at the line centre than models predict. This might suggest that the true opacity near these wavelengths is higher than reported here, increasing the discrepancy with iron opacity model predictions. This observation could also be affected by the large optical depths of these lines at the line centre; for these lines the radiation transport calculations are complex. Furthermore, Beer–Lambert–Bouguer scaling tests with varying thickness of iron provide evidence that extraneous background and tamper self-emission are not important. In addition, the general agreement between iron opacities inferred with CH and CH + Be tampers indicates that tamper self-emission is unimportant. Finally, HELIOS simulations also predict small contributions from the CH self-emission. These multiple investigations provide evidence that extraneous background and tamper self-emission are unimportant, but a definitive conclusion awaits an explanation for the higher-than-expected Mg Heα and Heβ transmission values.

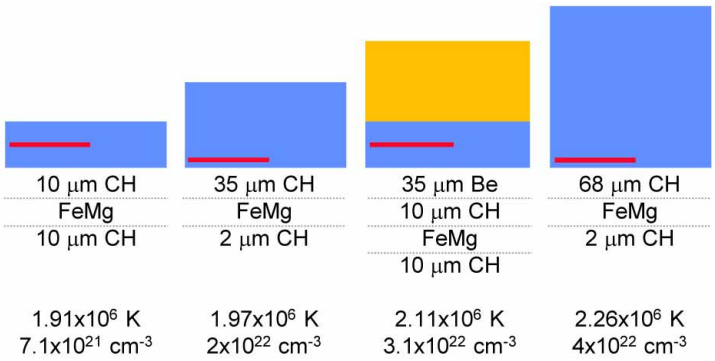
The effect of iron self-emission tends to be largest for optically thick lines and for the long wavelength portion of the spectrum. Calculations using HELIOS[40] simulations that account for the fact that the iron self-emission might persist longer than the backlight duration show that iron self-emission causes less than a 20% effect on the inferred opacity in the 7–12.7 Å region. Both Beer–Lambert–Bouguer scaling tests and the lack of any observed iron emission lines from the portion of the sample that is heated, but not backlit, provide experimental evidence that the iron self-emission is small. We therefore do not correct the inferred opacity reported here for self-emission.

Effects that could either raise or lower the inferred opacity include sample areal density errors, transmission errors, spatial non-uniformities, temporal non-uniformities, deviations from LTE, and plasma diagnostic errors. Sample areal density errors are precluded by the RBS and interferometry measurements described above. Systematic transmission errors were investigated by analysing tamper-only experiments—where the transmission is known to equal unity—with the same methods applied to the FeMg 'half-moon' samples. The transmission deviations were found to be comparable to or less than the estimated uncertainty. Spatial non-uniformities were directly measured using specially designed samples[41] and were estimated using HELIOS simulations[40]. The effects were found to be small. Temporal non-uniformity effects estimated using HELIOS simulations were small. Deviations from LTE were investigated using the PrismSPECT model[35] to calculate the FeMg plasma transmission in both LTE and non-LTE at the plasma T_e and n_e values inferred from the LTE Mg K-shell spectral analysis. The non-LTE calculations included the radiation field at the sample using measurements of the time-dependent radiation source spatial distribution and the geometric dilution. The main effects predicted by these calculations are a slight decrease in the average ionization and a ground-state population increase. The latter increases the strong spectral feature opacities, decreases the valleys between these strong features and therefore notably increases the discrepancy between model predictions and measurements of iron opacity. Finally, the displayed model–experiment comparisons employed the nominal T_e/n_e values obtained from an LTE analysis of the Mg K-shell spectra[22]. Iron opacity calculations were also done using the SCRAM model over the range of the T_e/n_e uncertainties (Extended Data Fig. 5). The calculations at the lowest T_e value and the highest n_e value agree slightly better with the measurements, but the improvement is small compared to the model–experiment discrepancy.

Eleven different potential systematic errors were evaluated. None appears to explain the reported discrepancy between opacity model calculations and the iron opacity data. If the data are correct, then our understanding of radiation interactions with atoms in high-energy-density plasma must be revised. Given the impact on both astrophysics and laboratory physics, continued scrutiny of the existing data and execution of new experiments designed to test hypotheses for the model–experiment discrepancies is warranted.

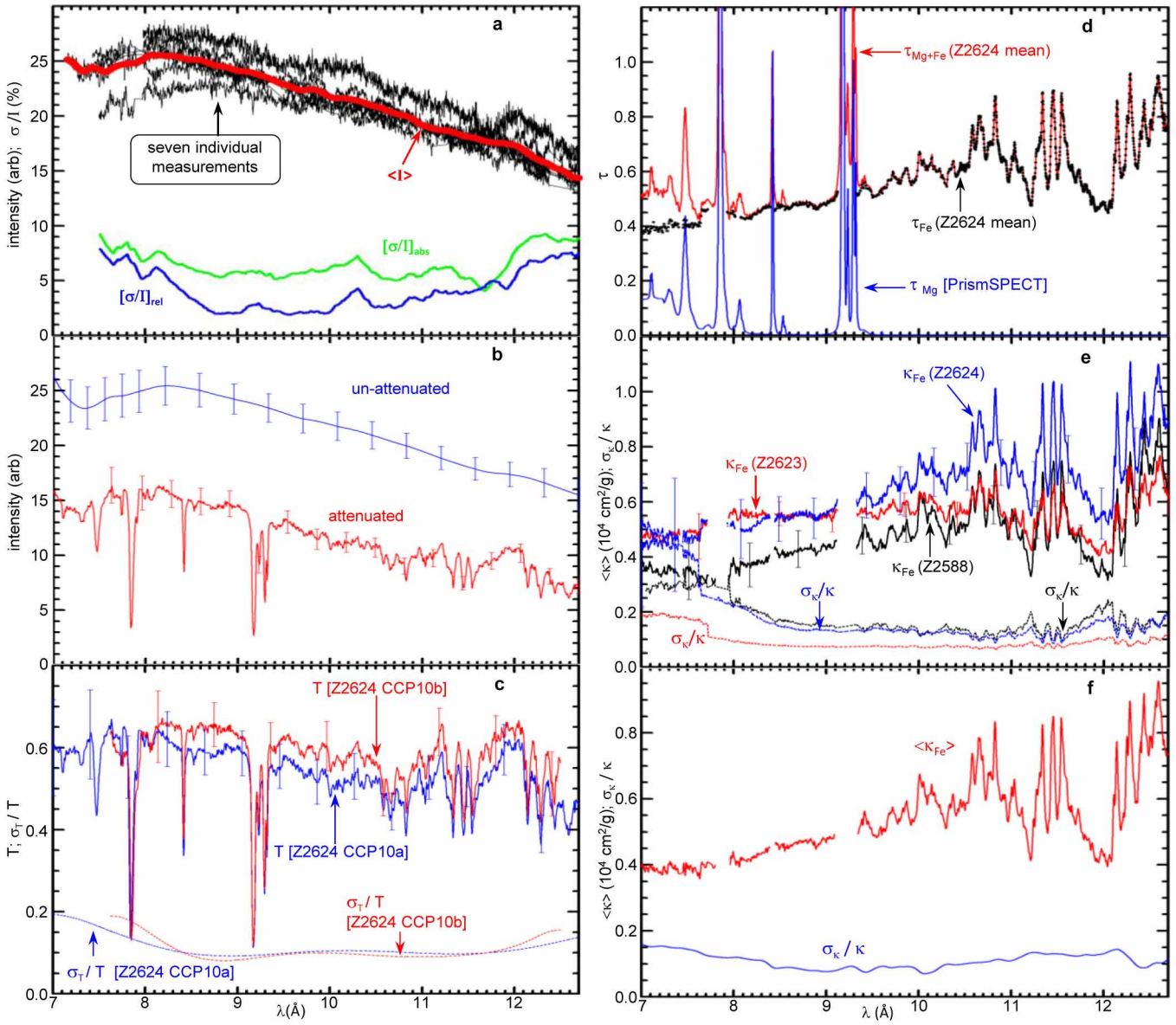
29. Bailey, J. E. *et al.* Dynamic hohlraum radiation hydrodynamics. *Phys. Plasmas* **13,** 056301 (2006).
30. Bailey, J. E. *et al.* Diagnosis of x-ray heated Mg/Fe opacity research plasmas. *Rev. Sci. Instrum.* **79,** 113104 (2008).
31. Jeynes, C., Barradas, N. P. & Szilágyi, E. Accurate determination of quantity of material in thin films by Rutherford backscattering spectrometery. *Anal. Chem.* **84,** 6061–6069 (2012).
32. Loisel, G. *et al.* A methodology for calibrating wavelength dependent spectral resolution for crystal spectrometers. *Rev. Sci. Instrum.* **83,** 10E133 (2012).
33. Henke, B. L. *et al.* Low-energy x-ray response of photographic films. II. Experimental characterization. *J. Opt. Soc. Am. B* **1,** 828–849 (1984).
34. Nagayama, T. *et al.* Parallax diagnostics of radiation source geometric dilution for iron opacity experiments. *Rev. Sci. Instrum.* **85,** 11D603 (2014).
35. MacFarlane, J. J. *et al.* in *Proc. Int. Symp. on Inertial Fusion Science and Applications (Monterey, California, 2003)* 457–464 (American Nuclear Society, 2003).
36. Henke, B. L., Gullikson, G. M. & Davis, J. C. X-ray interactions: photoabsorption, scattering, transmission, and reflection at E=50-30,000 eV, Z=1-92. *At. Data Nucl. Data Tables* **54,** 181–342 (1993).
37. del Grande, N. K. L Shell photoabsorption spectroscopy for solid metals: Ti, V, Cr, Fe, Ni, Cu. *Phys. Scr.* **41,** 110–114 (1990).
38. Zheng, L., Cui, M.-Q., Zhu, J. & Zhao, Y.-D. Determination of the photoabsorption cross-sections of Al and Fe films in the soft x-ray region using synchrotron radiation. *High Energy Phys. Nuclear Phys.* **28,** 1121–1125 (2004).
39. Cowan, R. D. *The Theory of Atomic Structure and Spectra* (Univ. California Press, 1981).
40. MacFarlane, J. J., Golovkin, I. E. & Woodruff, P. R. HELIOS-CR—a 1-D radiation-magnetohydrodynamics code with inline atomic kinetics modeling. *J. Quant. Spectrosc. Radiat. Transf.* **99,** 381–397 (2006).
41. Nagayama, T. *et al.* Investigation of iron opacity experiment plasma gradients with synthetic data analyses. *Rev. Sci. Instrum.* **83,** 10E128 (2012).

©2015 Macmillan Publishers Limited. All rights reserved



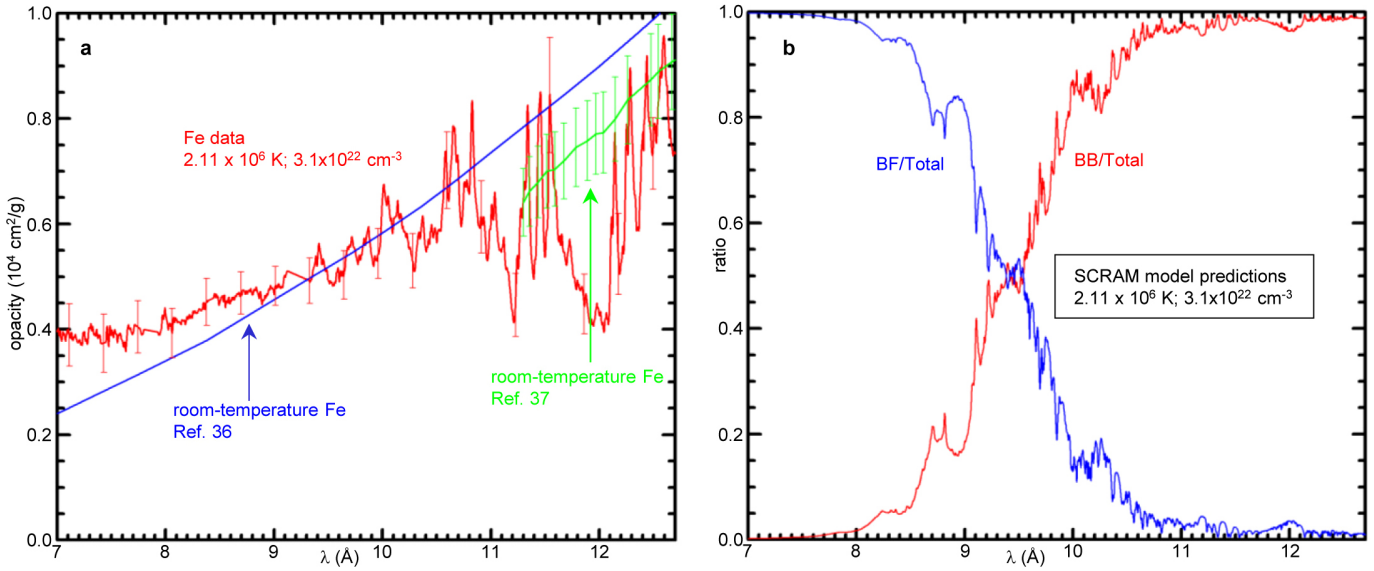
Extended Data Figure 1 | Schematic diagram of four sample configurations used in Z opacity experiments. The FeMg layer (red line) is completely encapsulated by the CH (blue) in order to avoid exposure to atmosphere during the experiment preparation. One sample type employed a Be tamper (yellow) to provide additional tamping while greatly reducing both the attenuation and emission in comparison with CH. T_e and n_e both increase as the tamper mass increases. The tamper thicknesses and the resulting average T_e and n_e values[22] are listed below each sample type. Experiments were also conducted using the same tamper construction, but without the FeMg layer, to provide calibrations of the opacity measurement accuracy.

©2015 Macmillan Publishers Limited. All rights reserved



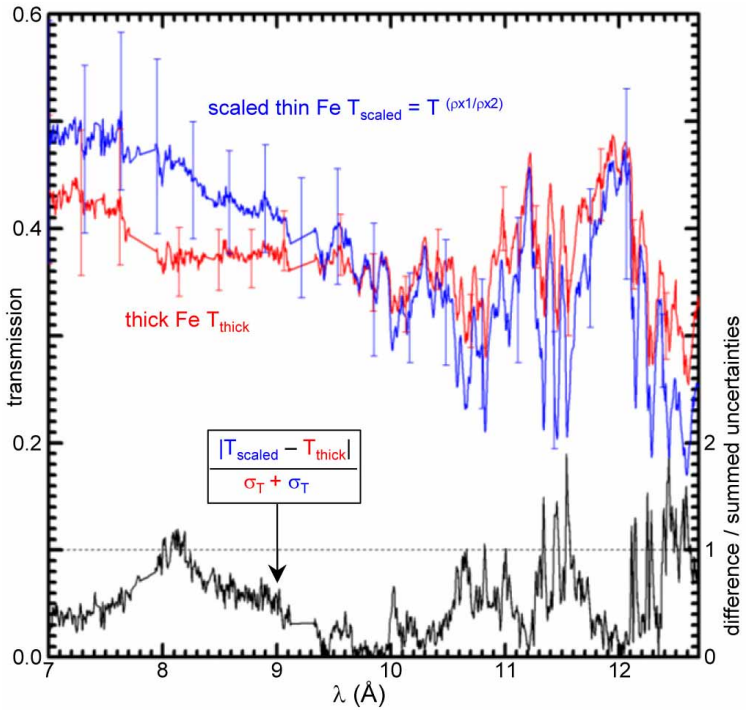
Extended Data Figure 2 | Data illustrating the transmission determination method. The five experiments shown here were conducted with a CH + Be tamper. **a**, The seven measurements of the unattenuated spectral intensity I from five experiments using the CCP4a and CCP10a spectrometers are denoted with black lines. The mean spectral intensity $<I>$ (red) is used to determine transmission, $[\sigma/I]_{abs}$ represents the absolute percentage unattenuated spectrum 1σ uncertainty (green), and $[\sigma/I]_{rel}$ represents the relative percentage 1σ uncertainty as a function of wavelength (blue). A similar collection of data are obtained from the seven CCP4b and CCP10b spectrometer measurements. (arb, arbitrary units.) **b**, The attenuated (red) and unattenuated (blue) spectral intensities used to determine the transmission on experiment Z2624. These data were recorded with the CCP4a and CCP10a crystals and a similar data set (not shown) was recorded with the CCP4b and CCP10b crystals. **c**, The transmissions T measured on Z2624 agree within the 1σ uncertainties. **d**, The optical depth (τ, red) inferred by taking the natural log of the mean transmission measured on Z2624 includes contributions from both Fe and Mg. The optical depth corresponding to the iron contribution only (black) is inferred by subtracting the Mg contribution calculated with PrismSPECT[35] (blue) from the FeMg mixture measurement. **e**, The mean opacities κ inferred from the three Be-tamped iron opacity measurements (solid), along with 1σ fractional absolute uncertainties (dashed). **f**, These measurements are combined to infer the overall mean opacity ($<\kappa>$, red) and associated 1σ fractional uncertainty (blue) for these conditions. The error bars in **b**, **c**, and **e** represent the 1σ uncertainty.

©2015 Macmillan Publishers Limited. All rights reserved



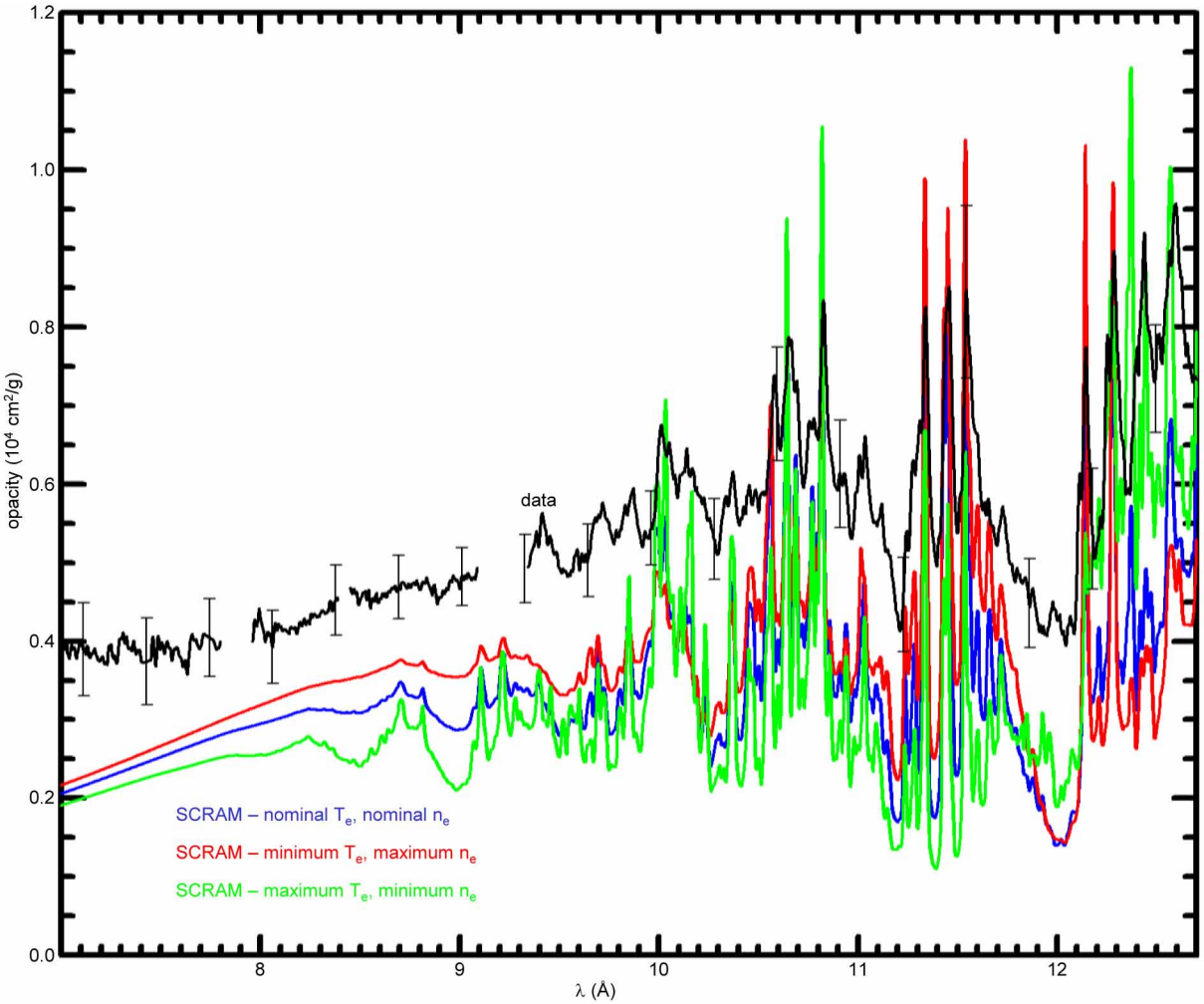
Extended Data Figure 3 | The measured Z iron opacity exceeds the room-temperature value[36] for wavelengths where models predict the opacity is dominated by photoionization. **a**, The measured iron opacity from the Be-tamped result is larger than the room-temperature value[36,37] for wavelengths shorter than approximately 9 Å. The error bars correspond to 1σ uncertainties. **b**, The SCRAM opacity model predicts that the ratio of the bound–free (BF) opacity contribution with the total opacity (blue) is larger than the ratio of the bound–bound (BB) opacity contribution with the total (red) for wavelengths less than approximately 9.5 Å.

©2015 Macmillan Publishers Limited. All rights reserved



Extended Data Figure 4 | Beer–Lambert–Bouguer scaling test for Be-tamped iron opacity data. The transmission should scale according to $T_2 = T_1^{Nx2/Nx1}$, where $Nx1$ and $Nx2$ are areal densities associated with transmissions T_1 and T_2. The thick iron sample transmission T_{thick} ($NX \approx 1.91 \times 10^{18}$ atoms per cm^2) is shown in red (left axis). The average transmission for the two experiments using a thin iron sample ($NX \approx 0.98 \times 10^{18}$ atoms per cm^2) was scaled by the ratio of the areal densities (T_{scaled}; blue). The error bars represent 1σ uncertainties. A quantitative evaluation is provided by taking the ratio of the transmission difference with the summed 1σ uncertainties (black; right axis). Values below unity (dashed black) satisfy the scaling test.

©2015 Macmillan Publishers Limited. All rights reserved



Extended Data Figure 5 | Evaluation of changes in the model–data comparisons at the error bounds determined for the plasma conditions. The measured iron opacity at $T_e = 2.11 \times 10^6$ K and $n_e = 3.1 \times 10^{22}$ cm^{-3} is denoted with a black line, with error bars corresponding to the 1σ uncertainty. SCRAM[23] calculations are shown at the nominal conditions in blue, at the minimum T_e, maximum n_e in red and at the maximum T_e, minimum n_e in green. The minimum T_e, maximum n_e values lead to the lowest ionization and the maximum T_e, minimum n_e values lead to the highest ionization.

©2015 Macmillan Publishers Limited. All rights reserved

Extended Data Table 1 | Sample specifications for Z opacity experiments

Shot	Date	Top Be (μm)	Top CH (μm)	Bottom CH (μm)	Total CH (μm)	Fe (x10^{18} cm^{-2})	Mg (x10^{18} cm^{-2})	construction
2176	March 2011	-----	67	2	69	2.065 ±0.095	1.02 ±0.022	5 layers Mg/Fe; Fe; 5 layers Al/Fe
2219	June 2011	-----	-----	-----	20	-----	-----	CH only
2221	June 2011	-----	10	10	20	0.640 ±0.034	0.746 ±0.045	10 layers Fe//Mg
2242	August 2011	-----	67	2	69	1.307 ±0.04	1.260 ±0.03	10 layers Fe//Mg
2243	August 2011	-----	-----	-----	70	-----	-----	CH only
2244	August 2011	-----	67	2	69	2.967 ±0.08	1.187 ±0.005	10 layers Fe//Mg
2267	Dec. 2011	-----	67	2	69	2.837 ±0.045	1.32 ±0.065	20 layers Fe//Mg
2268	Dec. 2011	-----	69	2	71	-----	-----	CH only; ~250Å NaF in middle
2270	Dec. 2011	-----	68	2	70	1.277 ±0.095	1.330 ±0.091	20 layers Fe//Mg
2299	Feb. 2012	-----	10	10	20	-----	-----	CH only; ~250Å NaF in middle
2301	Feb. 2012	-----	10	10	20	0.382 ±0.017	0.828 ±0.038	Co-sputtered FeMg
2309	March 2012	-----	10	10	20	-----	-----	CH only; ~250Å NaF in middle
2363	June 2012	-----	35	2	37	1.295 ±0.005	1.29 ±0.01	Co-sputtered FeMg
2364	June 2012	-----	70	2	72	0.659 ±0.002	1.24 ±0.0	Co-sputtered FeMg
2365	June 2012	-----	67	2	69	-----	-----	CH only; ~250Å NaF in middle
2366	June 2012	-----	70	2	72	0.659 ±0.002	1.24 ±0.0	Co-sputtered FeMg
2389	July 2012	-----	10	10	20	-----	-----	CH only; ~250Å NaF in middle
2588	Dec. 2013	35	10	10	20	1.04	1.25	Co-sputtered FeMg
2589	Dec. 2013	35	10	10	20	-----	-----	Be+CH Tamper; ~250Å NaF in middle of CH
2623	March 2014	35	10	10	20	1.91	1.17	Co-sputtered FeMg
2624	March 2014	35	10	10	20	0.926	1.40	Co-sputtered FeMg
2625	March 2014	35	10	10	20	-----	-----	Be+CH Tamper; ~250Å NaF in middle of CH

The areal density uncertainties correspond to the standard deviation of multiple RBS measurements. A dash denotes that the component was not present.

©2015 Macmillan Publishers Limited. All rights reserved

LETTER

doi:10.1038/nature14088

Higher-than-predicted saltation threshold wind speeds on Titan

Devon M. Burr[1], Nathan T. Bridges[2], John R. Marshall[3], James K. Smith[4], Bruce R. White[5] & Joshua P. Emery[1]

Titan, the largest satellite of Saturn, exhibits extensive aeolian, that is, wind-formed, dunes[1,2], features previously identified exclusively on Earth, Mars and Venus. Wind tunnel data collected under ambient and planetary-analogue conditions inform our models of aeolian processes on the terrestrial planets[3,4]. However, the accuracy of these widely used formulations in predicting the threshold wind speeds required to move sand by saltation, or by short bounces, has not been tested under conditions relevant for non-terrestrial planets. Here we derive saltation threshold wind speeds under the thick-atmosphere, low-gravity and low-sediment-density conditions on Titan, using a high-pressure wind tunnel[5] refurbished to simulate the appropriate kinematic viscosity for the near-surface atmosphere of Titan. The experimentally derived saltation threshold wind speeds are higher than those predicted by models based on terrestrial-analogue experiments[6,7], indicating the limitations of these models for such extreme conditions. The models can be reconciled with the experimental results by inclusion of the extremely low ratio of particle density to fluid density[8] on Titan. Whereas the density ratio term enables accurate modelling of aeolian entrainment in thick atmospheres, such as those inferred for some extrasolar planets, our results also indicate that for environments with high density ratios, such as in jets on icy satellites or in tenuous atmospheres or exospheres, the correction for low-density-ratio conditions is not required.

Data from NASA's Cassini spacecraft show extensive linear dunes covering Titan's low latitudes[1,2]. Unlike the silicate material that comprises most sand on terrestrial planets[4], the dune sand on Titan is either organic or organic-coated water ice[9], with likely densities of 0.4–1.5 g cm^{-3} (see discussion in ref. 10). In view of the deposition of organic aerosols from the atmosphere, the distinct compositions of dune and interdune surfaces suggest recent dune activity[9]. However, models of the present-day atmosphere give predominantly easterly (east-to-west) winds on the basis of conservation of angular momentum (see discussion in ref. 11), in contrast to the westerly (west-to-east) flow inferred from the streamlined appearance of dunes around topographic obstacles to the flow[1,12].

Knowledge of the threshold wind speed on Titan is fundamental to resolving this and other questions in Titan science. The dunes constitute one of the largest organic material reservoirs in the outer Solar System, and understanding how this material is mobilized across Titan depends on accurate understanding of threshold values. Knowledge of threshold wind speed is also necessary to model sand fluxes and dune migration rates[13], as well as the relative effectiveness of competing resurfacing processes[2], including aeolian sedimentation and abrasion.

Threshold friction wind speed (u^*_t) is defined[3,4] as a function of A, a dimensionless proportionality parameter dependent on both the particle Reynolds number at threshold friction wind speed ($\mathrm{Re}^*_t = u^*_t D_p/\nu$; D_p, particle diameter; ν, kinematic viscosity) and the interparticle forces ($I_p \equiv I_p(D_p)$), and also as a function of particle, fluid and gravity characteristics:

$$u^*_t = A(\mathrm{Re}^*_t, I_p)\sqrt{\frac{\rho_p - \rho}{\rho} g D_p} \approx A(\mathrm{Re}^*_t, I_p)\sqrt{\frac{\rho_p}{\rho} g D_p} \quad (1)$$

Here ρ_p and ρ are respectively the particle and fluid densities and g is the acceleration due to gravity at the surface of Titan. Most of these functional parameters can be either set or derived in boundary-layer wind tunnels[3,4] to quantify threshold wind speeds under a variety of boundary conditions. Compensation for functional parameters that cannot be set, for example g, is accomplished through data analysis and modelling. Experimental similitude parameters with values that approximate those of the natural setting ensure that atmospheric conditions are similar for the aeolian processes under investigation. Wind tunnel studies have yielded threshold wind speeds for particle motion on Earth, Mars and Venus[4]. For this work, we refurbished, and conducted experiments in, the high-pressure boundary-layer wind tunnel formerly used to simulate Venusian conditions[5]. The purpose was to simulate the conditions of aeolian saltation threshold on Titan. We refer to this facility as the Titan Wind Tunnel (TWT; Fig. 1 and Methods).

Previous publications have been equivocal in stating or suggesting the correct similitude parameter—kinematic viscosity[14,15], static pressure[4,16,17] or density[5]—for saltation threshold experiments. We infer that the correct similitude parameter for determining threshold is kinematic viscosity, the ratio of molecular viscosity (μ) to fluid density (Methods). To match the kinematic viscosity of the surface atmosphere on Titan at terrestrial temperatures requires an absolute air pressure of $\sim 1.25 \times 10^6$ Pa (Extended Data Table 1). With this simulation, the fundamental physics governing particle threshold on Titan is reproduced. This physics is not achieved in wind tunnels designed to simulate conditions on Earth and Mars, and so model extrapolations to Titan conditions from experiments in those tunnels are questionable.

Our methodology for deriving threshold wind speeds on Titan (see Extended Data Fig. 1 for a flowchart) begins with the derivation of threshold friction wind speeds in the TWT (u^*_{tTWT}) for sediments of various sizes and densities (Methods and Extended Data Table 2). The experimentally derived values of u^*_{tTWT} were compared with predictions of the experimental conditions from two recognized models of threshold fiction wind speeds, one model originally published by Iversen and White[6] and the other by Shao and Lu[7] (Methods). This comparison shows that the experimentally derived values are consistently ~40–50% higher, outside of uncertainty estimates, than predicted by either model (Extended Data Fig. 5; for calculation of uncertainty estimates, see Methods). These TWT threshold friction speeds were then converted to threshold friction speeds for the Titan surface (u^*_{tTitan}) for both models (Methods) and again compared with predictions from the two models (Fig. 2 and Table 1). We modified the Iverson–White model to give the interparticle force term the same dependence on D_p as in the Shao–Lu model (Methods), to facilitate comparison between the model results. The modified Iversen–White model underestimates the experimentally based values of u^*_{tTitan} by ~40–50%. The Shao–Lu model also

[1]Earth and Planetary Sciences Department, University of Tennessee-Knoxville, 306 EPS Building, 1412 Circle Drive, Knoxville, Tennessee 37996, USA. [2]Space Department, Johns Hopkins University Applied Physics Laboratory, Laurel, Maryland 20723, USA. [3]SETI Institute, 189 Bernardo Avenue, Suite 100, Mountain View, California 94043, USA. [4]Arizona State University, Tempe, Arizona 85287-1404, USA. [5]Department of Mechanical Engineering, University of California Davis, California 95616, USA.

©2015 Macmillan Publishers Limited. All rights reserved

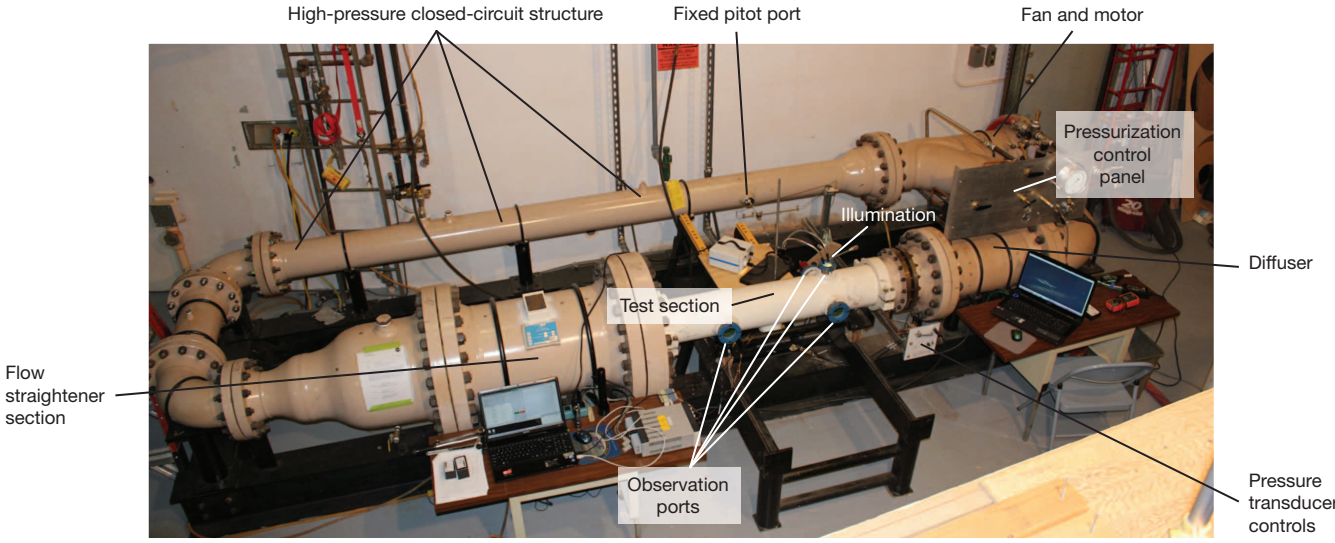


Figure 1 | Titan Wind Tunnel with important components labelled. The downwind observation side port through which the data of record are observed is the rightmost of the labelled observation ports.

underestimates the values by ~40–50% (Methods). Thus, the experimentally based threshold values for Titan conditions are higher than predicted by either model.

Correcting the models requires shifting the model curves to match the experimental results. Algebraic analyses of various model formulations[6,8,18] suggest the most reasonable approach to accomplishing this shift. As a specific form of equation (1), the complete formulation may be written

$$u^*_t = A_1\sqrt{\left(\frac{1+A_4 I_p/\rho_p g D_p^3}{f(\mathrm{Re}^*_t)+\mathcal{G}(\rho_p/\rho)}\right)\frac{\rho_p g D_p}{\rho}} \qquad (2)$$

where A_4 is a constant that quantifies the interparticle force and $\mathcal{G}(\rho_p/\rho)$ is a density ratio term (note the distinction between g and $\mathcal{G}$). The value for A_4 in the various model formulations varied by roughly an order of magnitude (Extended Data Table 4) depending on whether the exponent for the particle diameter was fitted to the data or assumed, but this variation did not significantly change the magnitude of the curve. The Reynolds number dependence, $f(\mathrm{Re}^*_t)$, has been derived on the basis of fitting to diverse data sets for discrete Reynolds number ranges[4,6], and so is unlikely to be significantly in error. A ~40–50% increase in the value of A_1 would correct the underestimation by the Iversen–White model, but the A_1 values have also been derived from fitting to a broad experimental data set, and a physical reason to change its value by 40–50% is not obvious.

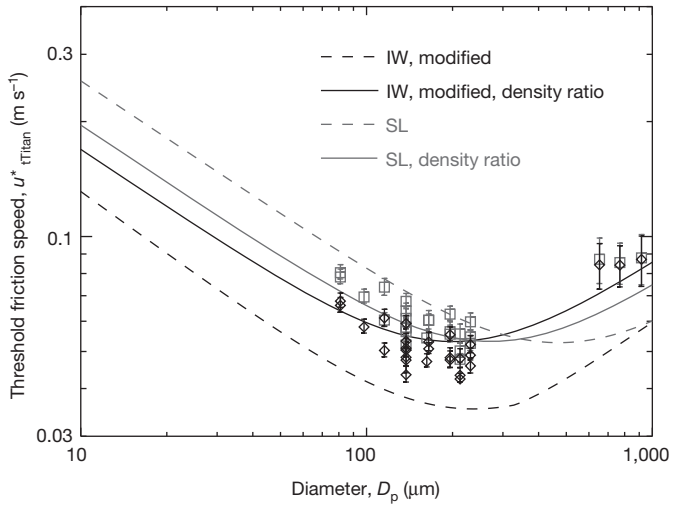


Figure 2 | Experimentally derived threshold fiction wind speeds on Titan. The dashed lines are the nominal models by Iversen and White[6] (IW) and by Shao and Lu[7] (SL). The solid lines are the nominal models with the density ratio term[8]. For the nominal Iversen–White model, we use $K = 0.055\ \mathrm{g\,s^{-2}}$, where K is equivalent to $A_4 I_p$ in the interparticle force term, and $n = 2$, where n is the exponent of D_p in the generalized interparticle force term (equation (6) in Methods, following ref. 8; Extended Data Table 4). This modification makes the interparticle force (I_p) proportional to D_p as in the Shao–Lu model, thereby facilitating comparison between the two models. The modified Iversen–White model (experimentally derived data in black symbols) is plotted for equations 5 ($0.03 \le \mathrm{Re}^*_p \le 10$) and 6 ($10 \le \mathrm{Re}^*_p$) in ref. 6 (equations (7) and (8) in Methods), with the transition between the two particle friction Reynolds number regimes at ~200 μm. The Shao–Lu model (experimentally derived data in grey symbols) is plotted for equation 24 in ref. 7 (equation (9) in Methods) for the nominal value of A_N (0.0123), where A_N is the dimensionless proportionality parameter for the Shao–Lu model, and the lowest value for γ ($0.1\ \mathrm{g\,s^{-2}}$), where γ controls the interparticle force, as determined from optimizing the fit of the u^*_{tTWT} data to the model (Extended Data Fig. 5). Vertical bars show standard deviation uncertainties in speed for the number of data points indicated in Extended Data Table 2; see Methods for the approach to calculating the uncertainty.

The magnitude of the modified Iversen–White model curve may also be increased through the inclusion of a density ratio term, $\mathcal{G}(\rho_p/\rho)$. This term was introduced to improve the model fit to experimental data for Venus-analogue conditions, data that, like the TWT data, were higher in value than predicted[8]. The density ratios for the TWT experiments (~80–200) and for Titan (~200) are similar to each other and to the value for the Venus-analogue experiments (~40), which (under density similitude) matches the value for Venus. In comparison, the density ratios for Earth and Mars are of orders 10^3 and 10^5, respectively. Inclusion of the density ratio for Titan conditions shifts the modified Iversen–White model curve up, increasing the minimum u^*_{tTitan} value by ~50%, to a value approximately equal to that of the Shao–Lu model (Table 1). Inclusion of the density ratio term in the Shao–Lu model similarly shifts the corresponding curve up, although the model still underestimates the experimentally derived data, especially at large particle sizes (Fig. 2). The median value of the interparticle force coefficient suggested by Shao and Lu[7] ($\gamma = 0.3\ \mathrm{g\,s^{-2}}$) predicts a larger optimal particle diameter than is derived here, and so we use their minimum value of $0.1\ \mathrm{g\,s^{-2}}$, shifting the optimal diameter to smaller sizes (Table 1). Whereas the Iversen–White model and the Shao–Lu model compare well for Earth and the various Martian conditions[7], they show an observable difference for Venus[7] and, with the modified Iversen–White model, an even greater difference (~100% around a near-optimum D_p of ~200 μm) for Titan (Fig. 2). That both Venus and Titan have comparably lower

©2015 Macmillan Publishers Limited. All rights reserved

Table 1 | Comparison of u^*_{tTitan} values derived from both models

Value	Modified Iversen–White	Modified Iversen–White with density ratio	Iversen–White change	Shao–Lu	Shao–Lu with density ratio	Shao–Lu change
Minimum u^*_{tTitan} (m s^{-1})	0.035	0.053	~50% increase	0.053	0.053	None
Optimum D_p (μm)	236	206	~10% change	475	272	~40% decrease

In order to facilitate comparison between the two models, the Iversen-White model[6] is modified to use the same dependence of interparticle force on D_p as in the Shao–Lu[7] model (see Extended Data Table 4), using the formulation from refs 8, 18.

density ratios than both Earth and Mars substantiates the use of the density ratio to correct the Titan model curves.

The density ratio term was originally derived algebraically from a balance of forces for threshold conditions that include grain impacts[8]. However, the data of record in our TWT experiments were the observations made during increasing wind speeds, before significant upwind saltation began. Thus, they probably correspond to the fluid threshold, that is, the wind speed at which particles are first entrained by the fluid flow. By analogy with Titan (and Venus)[19], the fluid threshold in the TWT (and Venus Wind Tunnel) experiments is lower than the impact threshold, that is, the lowest wind speed necessary to maintain saltation after initiation, and so would be encountered first as wind speed is increased. We thus infer that our experimental data, probably like those for the Venus Wind Tunnel[5], record fluid thresholds without contributions from grain impacts. We infer A_1 to be a function of drag and moment[18]. That both A_1 and the density ratio term shift the Iversen–White model curve implies that a low density ratio affects the drag and moment in some fashion.

Our experimentally derived results provide parameters for improved modelling of sand transport on Titan. The threshold friction wind speeds (Fig. 2), translated into fluid shear stress ($\tau_t = \rho u^{*2}_t$) (Fig. 3), provide values for numerical simulation of aeolian sediment flux. They can also be translated into threshold freestream wind speeds (no longer affected by surface friction) at specific elevations (Fig. 3) for use in atmospheric modelling or for comparison with model results. Greater threshold wind speeds increase the geomorphic effectiveness of winds that are strong enough to exceed threshold speeds, while eliminating the effect of weaker, although possibly more frequent, winds. Thus, the higher-than-predicted threshold wind speeds on Titan support a scenario in which only rare strong westerly winds, instead of prevailing easterlies, control the elongation of Titan dunes[11]. However, our experimentally derived threshold values at an altitude of 300 m (Fig. 3) exceed the reported model threshold values at this height[11], and so use of the new threshold values in modelling dune elongation is necessary to test this hypothesis. Although the interparticle force is unknown on Titan, it is unlikely to be less than on Earth (Methods). If the dune sand on Titan is 'sticky'[20], then the experimentally derived high threshold wind speeds would underestimate the true threshold wind speeds, potentially further enhancing both the geomorphic effectiveness of stronger (westerly) winds and the difference between the experimentally derived and modelled threshold winds.

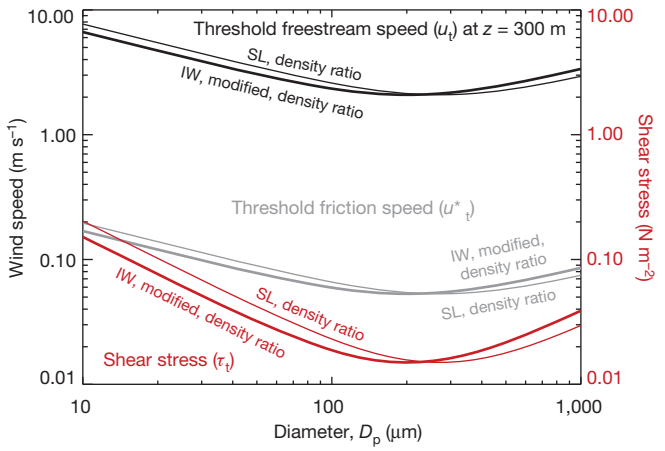


Figure 3 | Derived parameters from Titan threshold fiction speeds. The u^*_{tTWT} data (grey lines) from Fig. 2 are presented as both shear stress values at threshold, $\tau_t = \rho u^{*2}_t$ (red lines and right ordinal scale), and as freestream wind speed, $u(z)$, at $z = 300$ m altitude (black lines).

These results demonstrate the importance of including the density ratio term in calculating threshold friction speeds in thick atmospheres, as are likely to occur on some near-Earth-size extrasolar planets[21,22]. Conversely, they help to substantiate its relative unimportance[8] in modelling high-density-ratio conditions ($\rho_p/\rho > 1{,}000$). Thus, for other extreme aeolian conditions, including transport by plumes on Triton[23], jets on comets[24] or winds on Pluto, entrainment may be modelled by the modified Iversen–White[6,8] formulation without the density ratio term. Under such low-gravity, low-sediment-density conditions, correct formulation of the interparticle force becomes especially significant. Whether either the modified Iversen–White model or the Shao–Lu model adequately represents the interparticle force term, given its complex dependence on particle characteristics[25], is a question for future research.

Online Content Methods, along with any additional Extended Data display items and Source Data, are available in the online version of the paper; references unique to these sections appear only in the online paper.

Received 7 April; accepted 17 November 2014.
Published online 8 December 2014.

1. Lorenz, R. D. *et al.* The sand seas of Titan: Cassini RADAR observations of longitudinal dunes. *Science* **312,** 724–727 (2006).
2. Lopes, R. M. C. *et al.* Distribution and interplay of geologic processes on Titan from Cassini radar data. *Icarus* **205,** 540–558 (2010).
3. Bagnold, R. A. *The Physics of Blown Sand and Desert Dunes* 1–106 (Methuen, 1941).
4. Greeley, R. & Iversen, J. D. *Wind as a Geological Process: on Earth, Mars, Venus and Titan* Vol. 4, 67–106 (Cambridge Univ. Press, 1985).
5. Greeley, R. *et al.* Windblown sand on Venus: preliminary results of laboratory simulations. *Icarus* **57,** 112–124 (1984).
6. Iversen, J. D. & White, B. R. Saltation threshold on Earth, Mars and Venus. *Sedimentology* **29,** 111–119 (1982).
7. Shao, Y. & Lu, H. A simple expression for wind erosion threshold friction velocity. *J. Geophys. Res.* **105,** 22437–22443 (2000).
8. Iversen, J. D., Greeley, R., Marshall, J. R. & Pollack, J. B. Aeolian saltation threshold: the effect of density ratio. *Sedimentology* **34,** 699–706 (1987).
9. Barnes, J. W. *et al.* Spectroscopy, morphometry, and photoclinometry of Titan's dunefields from Cassini/VIMS. *Icarus* **195,** 400–414 (2008).
10. Burr, D. M., Emery, J. P., Lorenz, R. D., Collins, G. C. & Carling, P. A. Sediment transport by liquid surficial flow: application to Titan. *Icarus* **181,** 235–242 (2006).
11. Tokano, T. Relevance of fast westerlies at equinox for the eastward elongation of Titan's dunes. *Aeolian Res.* **2,** 113–127 (2010).
12. Lorenz, R. D. & Radebaugh, J. Global pattern of Titan's dunes: radar survey from the Cassini prime mission. *Geophys. Res. Lett.* **36,** L03202 (2009).
13. White, B. R. Soil transport by winds on Mars. *J. Geophys. Res. Solid Earth* **84,** 4643–4651 (1979).
14. Greeley, R., Iversen, J. D., Pollack, J. B., Udovich, N. & White, B. Wind tunnel studies of Martian aeolian processes. *Proc. R. Soc. Lond. A* **341,** 331–360 (1974).
15. Iversen, J. D., Greeley, R., White, B. R. & Pollack, J. B. The effect of vertical distortion in the modeling of sedimentation phenomena - Martian crater wake streaks. *J. Geophys. Res.* **81,** 4846–4856 (1976).
16. Greeley, R., Leach, R., White, B., Iversen, J. & Pollack, J. Mars - wind friction speeds for particle movement. *Geophys. Res. Lett.* **3,** 417–420 (1976).
17. Greeley, R., Leach, R., White, B., Iversen, J. & Pollack, J. Threshold windspeeds for sand on Mars: wind tunnel simulations. *Geophys. Res. Lett.* **7,** 121–124 (1980).
18. Iversen, J. D., Pollack, J. B., Greeley, R. & White, B. R. Saltation threshold on Mars: the effect of interparticle force, surface roughness, and low atmospheric density. *Icarus* **29,** 381–393 (1976).
19. Kok, J. F. Parteli, E. J. R., Michaels, T. I. & Karam, D. B. The physics of wind-blown sand and dust. *Rep. Prog. Phys.* **75,** 106901 (2012).
20. Rubin, D. M. & Hesp, P. A. Multiple origins of linear dunes on Earth and Titan. *Nature Geosci.* **2,** 653–658 (2009).
21. Quintana, E. V. *et al.* An Earth-sized planet in the habitable zone of a cool star. *Science* **344,** 277–280 (2014).
22. Charbonneau, D. *et al.* A super-Earth transiting a nearby low-mass star. *Nature* **462,** 891–894 (2009).

©2015 Macmillan Publishers Limited. All rights reserved

23. Sagan, C. & Chyba, C. Triton's streaks as windblown dust. *Nature* **346,** 546–548 (1990).
24. Cheng, A. F., Lisse, C. M. & A'Hearn, M. Surface geomorphology of Jupiter family comets: a geologic process perspective. *Icarus* **222,** 808–817 (2013).
25. Jones, R., Pollock, H. M., Cleaver, J. A. S. & Hodges, C. S. Adhesion forces between glass and silicon surfaces in air studied by AFM: effects of relative humidity, particle size, roughness, and surface treatment. *Langmuir* **18,** 8045–8055 (2002).

Acknowledgements This research was supported by grants from NASA's Planetary Geology and Geophysics Program and the Outer Planets Research Program. We dedicate this manuscript to our colleague R. Greeley, who was the motivating force behind the construction of the Planetary Aeolian Laboratory at the NASA Ames Research Center and used it over several decades to make fundamental and long-lasting contributions to understanding aeolian processes on other bodies.

Author Contributions D.M.B. is the principal investigator on the NASA grants that funded this work. She conceived the work, defined the objectives, oversaw the wind tunnel refurbishment, oversaw and participated in the data collection, analysis and reduction, and led the writing of the manuscript. N.T.B. contributed fundamental ideas and calculations during wind tunnel refurbishment, participated in the data collection, analysis and reduction, and contributed to writing the manuscript. The Titan Wind Tunnel is housed in the Planetary Aeolian Laboratory at the NASA Ames Research Center. J.R.M. and J.K.S. provided practical assistance, in conjunction with NASA personnel, to complete the wind tunnel refurbishment and calibration. J.K.S., the engineer at the Planetary Aeolian Laboratory, provided sieved sediments for the experiments, maintained and operated the wind tunnel during all runs, and provided data logs from all runs. B.R.W. contributed ideas during project design, wind tunnel refurbishment and data collection. J.P.E. provided assistance in data reduction and analysis, and contributed to writing the manuscript.

Author Information Reprints and permissions information is available at www.nature.com/reprints. The authors declare no competing financial interests. Readers are welcome to comment on the online version of the paper. Correspondence and requests for materials should be addressed to D.M.B. (dburr1@utk.edu.).

©2015 Macmillan Publishers Limited. All rights reserved

METHODS

Titan Wind Tunnel. The TWT (Fig. 1), a remodel of the Venus Wind Tunnel[5,26], is a closed-circuit, high-pressure, boundary-layer tunnel. Flow is generated by an eight-bladed fan rotating at a rate of up to 2,500 r.p.m. Downwind of the fan, ten curved tubes, each 5 cm in diameter, prevent flow separation and minimize turbulence and secondary flow. Downwind of these flow straighteners, a settling chamber further damps turbulence and traps material before entering the test section. In the test section, at pressures necessary to simulate Titan kinematic viscosity at standard temperature (12 bar; Extended Data Table 1), the fan drives air flow at freestream speeds ($u(z)$) of up to ~6.5 m s^{-1}. Downwind of the test section, a diffuser expansion section prevents material from recirculating with the gas flow and impinging on the fan or plugging the fixed pitot tube, located downwind of the fan.

The test section is 122 cm in length and 20.3 cm in interior diameter, and moves laterally on rails into or out of its position within the wind tunnel. Floor plates—either the calibration plate with a traversable pitot tube or the experimental test plate with no pitot tube—have the same length as the test section and are 18 cm in width. When inserted into the test section (Extended Data Figs 2 and 3), they rest against the inside walls. The test section has two stations for observing the test bed: a single upwind observation port 30 cm from the upwind end of the test section, and three downwind observation ports, including two ports on either side of the test section identical to the upwind port and a smaller port on top to enable illumination of the test bed.

The TWT operates with pressurized air that is desiccated by an Airtek TW250 dryer to dew point of −40 °C. Temperature variations are negligible given the large fluid mass within the tunnel. Static pressure is monitored visually using a calibrated gauge.

The TWT is fitted with a custom-made, high-pressure, high-temporal-resolution transducer supplied by the Tavis Corporation. Wind speed data, both for calibrations and threshold wind speed information, were collected using pitot tubes (see, for example, Extended Data Fig. 3b) connected to this transducer. Pneumatic lines from the pitot tube exit from beneath the plate to a signal pass-through port in the bottom of the test section. The electrical lines that supply power and control to the instrument and enable data capture are run to a laptop computer through the same pass-through. The pneumatic lines run through the stack valve to the dynamic pressure transducer. Transducer output consists of voltage as a function of dynamic pressure according to manufacturer-supplied calibration curves. These dynamic pressures, in turn, are converted to freestream wind speeds at height z as

$$u(z) = (2P_{\mathrm{dyn}}/\rho)^{1/2} \quad (3)$$

where P_{dyn} is the dynamic pressure of the gas (air) and is a function of z ($P_{\mathrm{dyn}} = P_{\mathrm{dyn}}(z)$).

TWT calibration. Derivation of threshold friction wind speeds in the TWT entailed initial collection of wind tunnel calibration data (Extended Data Fig. 4). Different types of calibration data were required.

(i) Although wind speed (dynamic pressure) data were required in the test section, where threshold was observed, the traversable pitot tube in the test section had to be removed during experiments to prevent clogging or disruption of air flow. Dynamic pressure data were collected instead using the fixed pitot tube on the opposite side of the wind tunnel (Fig. 1). Thus, a correlation curve was derived to convert the freestream wind speed data collected during experiments with the fixed pitot tube into equivalent freestream wind speed data in the test section. We constructed this curve from three separate calibration runs (interspersed with threshold data collection runs) at fan motor speeds up to 105% of maximum rated speed in 20% increments. During these runs, voltage data from the transducer were collected independently and alternately from the traversable pitot tube and from the fixed pitot tube by switching the stack valve to read either the fixed pitot or traversable pitot for the same fan motor speed increment. Those voltage data were converted to dynamic pressures using the manufacturer's curves and then from dynamic pressures into freestream wind speeds using equation (3). The resultant correction curve is $u(z)_{\mathrm{TWT}} = 1.49u(z)_{\mathrm{fixed\ pitot}} - 0.426$, where $u(z)_{\mathrm{fixed\ pitot}}$ is the freestream wind speed at the fixed pitot and $u(z)_{\mathrm{TWT}}$ is the freestream wind speed in the test section. Both the fixed pitot and (during this calibration) the traverse pitot in the test section are within the boundary layer, and so record freestream wind speeds.

(ii) Freestream wind speed at height z, $u(z)$, is related to friction wind speed, u^*, according to the 'law of the wall',

$$u(z) = (u^*/\kappa)\ln(z/z_0) \quad (4)$$

where κ is the von Kármán constant (0.41) and z_0 is the roughness height, that is, the distance above the surface at which the wind speed is zero. Thus, to convert the freestream wind speeds at threshold ($u(z)_{\mathrm{t}}$) into the desired friction wind speeds at threshold (u^*_{t}) requires knowledge of the roughness height. Equation (4) can be linearized to

$$\ln(z) = (\kappa/u^*)u(z) + \ln(z_0) \quad (5)$$

In aeolian studies, this roughness height is commonly derived by measuring a wind speed profile to construct the relationship between height and freestream wind speed[3]. As indicated by equation (5), the y intercept of a plot of $\ln(z)$ versus $u(z)$ is $\ln(z_0)$, such that the value of $e^{(y\ \mathrm{intercept})}$ gives the roughness height.

To derive the roughness height, we performed a series of calibration runs to determine the boundary-layer profiles. A calibration plate of aluminium was covered with 100-grit sand paper (grain diameters of 125 μm), and a traversable pitot tube assembly with a stepping motor assembly was installed at the downwind end of the plate (Extended Data Fig. 3b). The stepping motor raised the pitot tube in logarithmically increasing steps above the plate to a maximum height of ~4.3 cm, well into the freestream (Extended Data Fig. 4). At each step, the dynamic pressure from the pitot tube was read over a 10 s interval by the transducer. The voltage from the transducer was sent to a data acquisition module manufactured by Measurement Computing Corporation, and was processed and recorded by TracerDAQ software on a laptop computer. After data collection, voltages were converted to dynamic pressures using the appropriate pressure-dependent correlation curve provided by the transducer manufacturer (Tavis Corporation), and these dynamic pressures were in turn converted to freestream wind speeds using equation (3). These boundary-layer data taken at different wind speeds show that the freestream boundary layer begins at $z \approx 1.9$ cm, such that the pitot tube reached well into the freestream and the boundary layer was fully developed, and that $z_0 \approx 0.003$ cm (Extended Data Fig. 4).

These calibration runs were conducted at fan motor speeds of 20% to 80% of the maximum rated speed, increasing in 10% increments. We used the average value of these multiple calibration runs. The same data are also used to derive u^*, which is used in uncertainty estimates (see below).

Kinematic viscosity as similitude parameter for threshold experiments. Kinematic viscosity (ν), is the ratio of molecular viscosity (μ) to fluid density (ρ). For a particle of a given diameter, kinematic viscosity is a fundamental control on the relative importance of lift and drag forces, which is quantified by the particle friction Reynolds number:

$$\mathrm{Re}^*_{\mathrm{p}} = u^* D_{\mathrm{p}}/\nu = u^* D_{\mathrm{p}}\rho/\mu$$

Here D_{p} is the particle diameter and u^* is the friction wind speed. The particle friction Reynolds number is a controlling parameter in the formulation for threshold friction wind speed (equation (1)). For smaller particles, threshold is controlled largely by the viscous (or laminar) sublayer, of thickness δ_{ν}, within which the flow regime is linear and the mechanics of particle detachment differ from those in the turbulent regime[19]. The thickness of this viscous sublayer is proportional to the kinematic viscosity and inversely proportional to the friction speed:

$$\delta_{\nu} \approx 5\nu/u^* \approx 5\mu/\rho u^*$$

Thus, correctly simulating the kinematic viscosity is necessary in deriving threshold friction wind speeds, providing the correct ratio of lift and drag forces, and simulating the viscous sublayer thicknesses.

Selection and preparation of experimental sediments. The experimental sediments were chosen to encompass a range of densities, median particle diameters (D_{p}) and particle diameter ranges (Extended Data Table 2). This distribution includes sediments believed to be similar in size to the sand on Titan and of equivalent weight for both organic and water ice compositions. In addition, the experimental matrix includes several sediments of both larger and smaller grain sizes and various densities, to give more complete coverage of the wind-speed/particle-diameter space for more robust comparison with threshold models.

After sieving, the experimental sediments were added to the test plate within the test section and smoothed to ensure complete coverage with a consistent thickness (~1 cm) (Extended Data Fig. 2). The test section was rolled back into alignment with the tunnel, which was sealed and pressurized with dry air (dew point at −40° C).

Relative interparticle forces of experimental and Titan conditions. We set conditions in the TWT to mimic cohesive forces expected for Titan. The largest contributor to interparticle force on Earth (that is, humidity) is due to the polarity of water molecules, but water vapour and other polar molecules are lacking in Titan's atmosphere. Thus, the experimental sediments in the TWT are dry, as noted above, so that cohesive forces due to the polarity of the water molecules are negligible, as is the case for sediments on Titan. The values for interparticle force in the threshold models that were fitted to the TWT data can be computed as the product of the interparticle force term (Extended Data Table 4) and a representative grain diameter, taken to be ~200 μm, the approximate optimal particle size for saltation on Titan (Fig. 2). In the modified Iversen–White model, the interparticle force at that particle size is ~11 nN, and for the Shao–Lu model the value is ~20 nN. For comparison,

©2015 Macmillan Publishers Limited. All rights reserved

atomic force microscopy experiments derive pull-off forces for ~200 μm-diameter hydrophobic particles under dry conditions of ~10 to 500 nN (refs 25, 27). Calculation of interparticle force for 'clean' particles of that diameter using relationships derived from lunar soils[28] suggests even higher values, of ~3,600 nN. On terrestrial bodies, sediment cohesion may be enhanced by electrostatic forces generated by friction between both rocky and icy (snow) particles[29], and the blown sands on Titan, being composed of organic compounds or water ice (or both), probably experience similar electrostatic forces. Other processes, such as wetting by liquid hydrocarbons, may enhance these high cohesion values even further. Thus, it is unlikely that the cohesive forces on Titan will be less strong than in these wind tunnel experiments. Therefore, the threshold wind speed models derived from these experiments probably represent minimum values, exacerbating the mismatch between the data and the models. The morphology of the dunes, which could be interpreted as evidence for unusually high sand cohesion[20], provides some supporting evidence for high cohesive forces on Titan. Further work is required to quantify the magnitude of interparticle forces for wind-blown sediments on any planetary body[19,29].

Collection of threshold wind speed data. Following established procedures[5,16,18], we momentarily increased the wind speed until motion was briefly observed, to remove perched grains or otherwise easily moved grains from the bed, thereby making the surface similar to that expected to exist at equilibrium in an aeolian environment. Threshold wind speed data were then collected by observation of motion in the test section. Our interest is in the fluid (or static) threshold, the wind speed at which particles are first entrained by the fluid flow, as distinct from impact threshold, the lowest wind speed necessary to maintain saltation after initiation. For these fluid threshold data, fan motor speed was gradually increased while visual observations were made of five stages of grain motion, namely first motion, flurries, patches, motion of ~50% of the longitudinally central portion of the bed, and motion of ~100% of the bed (Extended Data Table 3). The fan motor speed was then decreased as similar stages were noted in reverse.

We define threshold as 50% of the bed in motion, indicating that one-half of the grains have exceeded threshold and the other half have not. We focus on the longitudinally central portion of the bed to avoid effects along the walls. Early work defined threshold as "the lowest … speed at which the majority of exposed particles … are set in motion" and "general motion of the exposed particles"[18] or "movement of particles over the entire bed"[16], consistent with ref. 3. If 'general motion' indicates that the entire bed is in motion, our definition of 50% of the bed in motion is equally or more conservative—tending towards lower wind speeds—than the definitions in these references. Later work by some of the same authors defined threshold as the wind speed at which "groups of grains began to saltate" such that "at slightly higher wind speeds, saltation was a continuous cloud of particles"[5]. In our observations, motion of 50% of the bed occurred as groups of saltating grains and immediately preceded continuous saltation over the entire bed. Thus, our definition of threshold seems qualitatively consistent with this definition as well. Because of our focus on fluid threshold, we use the value for motion of 50% of the bed during increasing wind speeds.

Observations of grain motion were made by two independent observers at both the upwind and downwind viewing ports to provide confirmation of motion. The observations from the downwind port are considered the threshold data of record because the ~80 cm fetch allows for development of the turbulent boundary layer and for any anomalous effects from the leading edge of the test plate to damp out. The observations focused on roughly the central third of the bed along its horizontal axis (that is, perpendicular to the wind stream) within the field of view to avoid anomalous conditions associated with the side walls of the test section.

Voltages from a high-precision, high-pressure transducer connected to the fixed pitot tube in the freestream were continuously recorded throughout each experiment. As each grain motion stage was observed in the test section, the time and fan motor speed were noted. Data on grain motion stages were collected during three successive runs from the same bed of material and showed excellent reproducibility.

The continuous voltage data were then converted to threshold friction wind speeds in the test section. This conversion entailed first using the manufacturer-supplied calibration curves of transducer voltage verses applied pressure to derive the dynamic pressure. These dynamic pressures were then converted to freestream wind speeds (using equation (3)), effectively creating a look-up table of wind speed by time. The recorded times for each grain motion stage were used to query this look-up table to find the wind speeds at each grain motion stage, including threshold. The correlation curve to convert freestream wind speeds derived from the fixed pitot tube into equivalent freestream wind speeds in the test section was then applied (see Fig. 1 for pitot tube locations). Finally, these threshold freestream wind speeds were translated into threshold friction wind speeds, u^*_{tTWT}, according to the 'law of the wall', (equation (4), in which z, the freestream wind speed height, is derived from appropriate boundary layer curves (Extended Data Fig. 4)).

Models used for comparison of TWT threshold friction wind speeds. Model of Iversen and White. This model[4,6] is based on mathematically fitting data from terrestrial and low-pressure planetary-analogue wind tunnel experiments. The form of the model is

$$u^*_t = A_1 f(\mathrm{Re}^*_t)([1 + K/(\rho_p g D_p^n)](\rho_p/\rho) g D_p)^{1/2} \quad (6)$$

where $u^*_t = A((\rho_p/\rho) g D_p)^{1/2}$ is the original equation (derived in ref. 3). Comparison with equation (1) shows that $A = A_1 f(\mathrm{Re}^*_t)$ and that the term $(1 + K/(\rho_p g D_p^n))^{1/2}$, in which $K = 0.006\ \mathrm{g\,cm^{0.5}\,s^{-2}}$ and $n = 2.5$, is an expression for the importance of interparticle forces relative to gravity. However, previous[18] and subsequent iterations[8] of this model used an a priori proportionality of I_p to D_p ($n = 2$), for which the (fitted) value of K is $0.055\ \mathrm{g\,s^{-2}}$ (Extended Data Table 4). In this work, we modify the Iversen–White model by using $K = 0.055\ \mathrm{g\,s^{-2}}$ and $n = 2$ (after ref. 8) to facilitate its comparison with the Shao–Lu model[7].

Model of Shao and Lu. This model[7] is a deliberate simplification of the Iversen–White model[4,6], replacing the modest dependence of A on Reynolds number with a constant. Unlike Iversen and White[4,6] but consistent with the previous[18] and subsequent[8] iterations of the Iversen–White model, the Shao–Lu model sets I_p proportional to D_p.

Conversion to threshold friction wind speed on Titan. The TWT simulates the kinematic viscosity of flow around the grains but not the atmospheric density, the gravity of Titan nor the variation in A, as required in the model of Iversen and colleagues[6,8,18] (formulated in equations (1) and (2)). On the basis of equation (1), conversion of the threshold friction speed from the wind tunnel, u^*_{tTWT}, to the threshold friction speed on the surface of Titan, u^*_{tTitan}, may be implemented as:

$$u^*_{tTitan} = u^*_{tTWT}(A_{Titan}/A_{TWT})[(g_{Titan}/g_{TWT})(\rho_{TWT}/\rho_{Titan})]^{1/2}$$

Although the direct correction for gravity and particle density is trivial, correcting for A (which depends also on the particle Reynolds number and the particle size) is more complex. Our approach was to compute theoretical values of u^*_{tTitan} and u^*_{tTWT} as functions of particle size using the appropriate expression for A and corresponding parameters[4,6]. We then multiplied the u^*_{tTWT} values (Extended Data Fig. 5) by the ratio $(u^*_{tTitan}/u^*_{tTWT})_{theoretical}$ (Extended Data Fig. 6) to translate these experimentally derived wind speeds to Titan surface conditions (u^*_{tTitan}), using a density for Titan sediment of $1\ \mathrm{g\,cm^{-3}}$.

Comparison of u^*_{tTitan} with models. Model of Iversen and White[6]. For the modified Iversen–White model, we use $K = 0.055\ \mathrm{g\,s^{-2}}$ and $n = 2$ (following ref. 8). This modification to the Iversen–White model gives the same dependence of interparticle force (I_p) on D_p as the Shao–Lu model, thereby facilitating comparison between the two models. For this model, u^*_{tTitan} was found by first determining the Reynolds number range ($\mathrm{Re}^*_t \geq 3$) for the relevant particle sizes ($10\ \mu\mathrm{m} \leq D_p \leq 1{,}000\ \mu\mathrm{m}$) and flow speeds on Titan. For this range of particle Reynolds number, both expressions for A from the Iversen–White model are used. These expressions are

$$A = 0.129\left(1 + \frac{0.055}{\rho_p g D_p^2}\right)^{1/2}\left(1.928\mathrm{Re}^{*\,0.092}_t - 1\right)^{1/2} \quad (7)$$

for $3 \leq \mathrm{Re}^*_t \leq 10$ and

$$A = 0.120\left(1 + \frac{0.055}{\rho_p g D_p^2}\right)^{1/2}\left(1 - 0.0858e^{\left[-0.0617\left(\mathrm{Re}^*_t - 10\right)\right]}\right) \quad (8)$$

for $\mathrm{Re}^*_t \geq 10$ (refs 4, 6). From equations (1), (7) and (8), we calculated values of u^*_{tTWT} and u^*_{tTitan} for the actual values of D_p used in our experiments, calculated the ratio of u^*_{tTitan} to u^*_{tTWT} as a function of grain size (Extended Data Fig. 6), and multiplied these ratios by u^*_{tTWT} to get u^*_{tTitan} as a function of grain size.

Model of Shao and Lu[7]. The Shao–Lu model assumes that the coefficient A is only weakly dependent on the particle friction Reynolds number. In addition, aerodynamic drag and lift are balanced by cohesion and gravity (both functions of grain size), so that the threshold is dependent only on grain size. Thus, A is reduced to a constant (A_N) and the remainder of the expression may be expressed as a function of particle size with an empirical constant (γ) for interparticle forces, as follows:

$$u^*_t = (A_N[(\rho_p/\rho) g D_p + \gamma/(\rho D_p)])^{1/2} \quad (9)$$

Here A_N has a value of approximately 0.0123 and γ is approximately $0.3\ \mathrm{g\,s^{-2}}$.

For the Shao–Lu model, like the Iversen–White model, conversion of u^*_{tTWT} to u^*_{tTitan} entailed multiplying by $(u^*_{tTitan}/u^*_{tTWT})_{theoretical}$ (Extended Data Fig. 6) and using the given value of A_N (0.0123) and the lowest value within the indicated range of values for γ ($0.1\ \mathrm{g\,s^{-2}}$) as derived for the TWT data (Extended Data Fig. 5). Lower γ values effectively decrease the interparticle force, causing the transition between dominance by interparticle forces and dominance by gravity to shift to smaller grain sizes. This shift leaves the curve unchanged at the largest particle diameters and moves it down at smaller particle diameters. With this shift, the nominal Shao–Lu model underestimates u^*_{tTitan} by 40–50% at all particle diameters. Lower

©2015 Macmillan Publishers Limited. All rights reserved

values of γ are outside the range indicated by Shao and Lu[7] on the basis of data on terrestrial planets.

Uncertainty estimates. We calculate uncertainties in our results for the TWT (Extended Data Fig. 5) as explained below. In this explanation, we provide example values for one sediment type, 175–250 μm silica sand (see, for example, Extended Data Fig. 2). Data for this sediment were collected on three runs (T-13-135, T-13-136 and T-13-137). Threshold (50% of the bed in motion) was not observed during T-13-136. That is, as fan motor speed was increased during the experiments, we were not always able to identify accurately or quickly enough when the bed transitioned from less than 50% of the bed in motion ('patches'; see Extended Data Table 3) to more than 50% of the bed in motion. Such non-identifications, as for T-13-136, reduced the number of data points for any series of three or four runs per sediment type.

A. Voltage as measured at the fixed pitot at threshold. The uncertainty in the voltage recorded at the time that threshold is observed is due to two factors.

• Transducer uncertainty. We quantify this fractional uncertainty as the ratio of the 'Deviation (mV)' and the 'Output Voltage (VDC)' (VDC, d.c. voltage in volts) recorded in the manufacturer's transducer calibration data. The maximum fractional uncertainty over the entire range of test pressures is always ≤1%. 1% is taken as a standard, conservative value.

• Voltage variability. The fractional uncertainty in the voltage variability is the standard deviation of the population divided by the average voltage. This uncertainty is calculated for the ten seconds after threshold is observed. For T-13-135, the average voltage is −0.73 VDC, the standard deviation is 0.019 VDC and the fractional uncertainty is 0.024 or 2.4%. For T-13-137, the average voltage is −0.77 VDC, the standard deviation is 0.019 VDC and the fractional uncertainty is 0.027 or 2.7%.

Because these uncertainties in the voltage at threshold are random and independent, they are added in quadrature. For the two runs of 175–250 μm silica sand for which threshold was observed, the results are 2.6% and 2.9%.

B. Conversion from fixed pitot voltages to pressures. Conversion from voltage to dynamic pressure is done using the manufacturer-supplied linear calibration curves, for which the uncertainty is <0.01%. Given the linear shape of the curves and their small uncertainty, we consider this uncertainty to be negligible.

C. Conversion from fixed pitot pressures to fixed pitot freestream wind speeds. Dynamic pressure from the fixed pitot tube as recorded by the transducer is converted to wind speed according to equation (3), where ρ is calculated using the universal gas law (as indicated in Extended Data Table 1). The static pressure (P) for this calculation is measured with a precision of <0.5% using a calibrated gauge. The temperature in the wind tunnel is taken as the temperature in the room (the Planetary Aeolian Laboratory), which is measured with a calibrated thermometer. Thus, the fractional uncertainty in density ($\delta\rho/\rho$) is the fractional uncertainty in the static pressure ($\delta P/P$), and is taken to be 0.5%.

The fractional uncertainty in the wind speed ($\delta u/u$) at the fixed pitot is derived by propagating uncertainties in the dynamic pressure (P_{dyn}) and the density (ρ):

$$\delta u/u = (1/2)[(2\delta P_{dyn}/P_{dyn}) + \delta\rho/\rho]$$

To average these uncertainties for the two runs for 175–250 μm silica sand which threshold was observed, the fractional uncertainties in wind speed were converted into absolute uncertainties, added in quadrature and converted back to fractional uncertainties. For 175–250 μm silica sand, the result is 3.7%.

D. Conversion of fixed pitot freestream wind speeds to equivalent freestream wind speed in the test section. The freestream wind speeds at the fixed pitot tube are converted to equivalent freestream wind speeds in the test section using an average correlation curve. This correlation curve was derived from data collected during three calibration runs interspersed with data collection runs. The data used in the curve were those at which threshold was observed (~1–2 m s^{-1}). The fractional uncertainty in the correlation curves derived from these three runs is used as the uncertainty in this correlation. This fractional uncertainty is estimated to be the ratio of the standard deviation of the population and the average wind speed. For threshold speeds of 1–2 m s^{-1}, the result ranges from 1.5% to 0.3%. 1.5% is used as a standard, conservative value.

The uncertainties in these two conversions above are independent and so are added in quadrature. For 175–250 μm silica sand, the result is 4.0%.

E. Determination of observational uncertainty in the freestream wind speed. Threshold is determined to occur in the wind tunnel by visual observation of 50% bed motion. Three or four experiments were run for each sediment type (unique combination of material and size). For each sediment type, the variability of the wind speed at which threshold was observed is quantified as the standard deviation of the population, which was divided by the threshold wind speeds to yield fractional uncertainty. For three sediment types, threshold was observed during only one run, and so a standard deviation could not be calculated. Without the standard deviation, the uncertainties depicted in Extended Data Figs 5 for these three (out of 27) data points slightly underestimate the true uncertainties. For silica sand (runs T-13-135 and T-13-137), the standard deviation of the population is 0.030 m s^{-1}, corresponding to a fractional uncertainty of 2.2%.

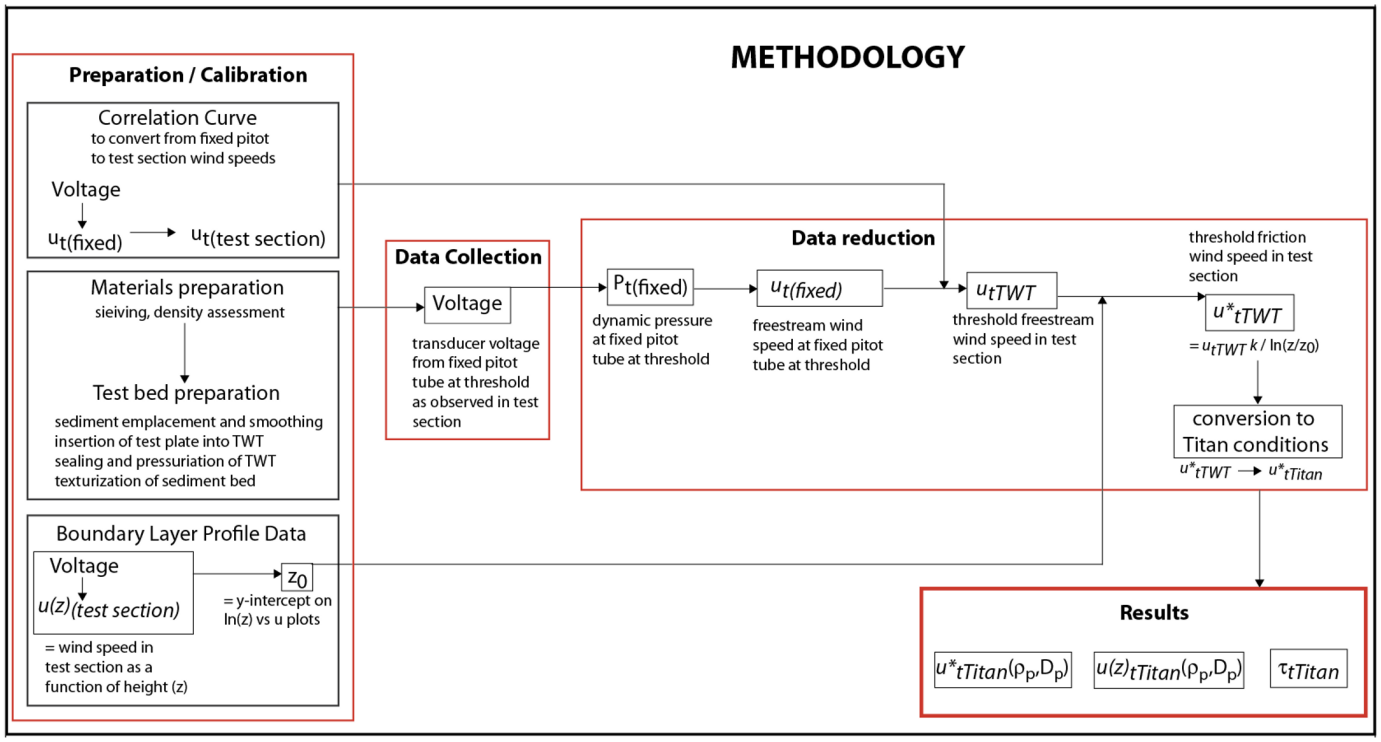
F. Conversion of freestream wind speed in the test section to TWT friction wind speed. The freestream wind speeds are converted into friction wind speeds using the 'law of the wall' (equation (4)). The uncertainty in this conversion derives from uncertainty in the roughness height. We used the value of z_0 derived from the calibration runs for the wind speeds at which threshold was observed (20%–30% of the maximum rated fan motor speed). These values can be checked against theoretical values for z_0. For a roughness Reynolds number (Re_r) >60, $z_0 = k_s/30$, where k_s is the Nikuradse roughness; roughness in the transitional regime down to $Re_r = 4$ is similar to roughness in the aerodynamically rough regime, and so the same formulation is commonly used[19]. In the aerodynamically smooth regime where $Re_r < 4$, $z_0 = \mu/9\rho u^*$. To capture the variability in z_0, we averaged six different values: the roughness heights at 20%, 30%, 40%, 50%, 60% and 80% of the maximum rated fan motor speed (see, for example, Extended Data Fig. 4). The uncertainty in z_0 was characterized as the standard deviation of these values. That absolute uncertainty, ~0.0016 mm, was both added and subtracted from the average z_0 to get absolute positive and negative uncertainties, which were then converted to fractional uncertainties. Adding these uncertainties in quadrature with the previous uncertainties from step E gave the final fractional uncertainties for each sediment type. For silica sand, the TWT fractional uncertainties are 5.4% (run T-13-135) and 4.8% (run T-13-137).

G. Conversion of TWT friction wind speed to Titan friction wind speed. The TWT friction wind speeds were converted to Titan friction wind speeds through scaling by the ratio of the TWT threshold friction speeds and the Titan threshold friction wind speeds. For silica sand (runs T-13-135 and T-13-137), this ratio is 0.4796. Because this step consists of multiplication by a constant, the fractional uncertainties do not change. For plotting in Fig. 2, all the values for each sediment type and grain size were averaged together.

The results of this error analysis are shown in Extended Data Table 2.

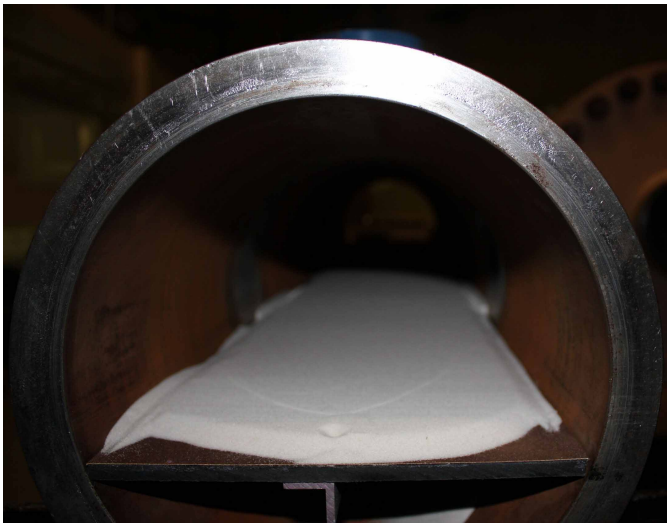
26. Marshall, J. R. & Greeley, R. An experimental-study of aeolian structures on Venus. *J. Geophys. Res. Planets* **97,** 1007–1016 (1992).
27. Hodges, C. S., Cleaver, J. A. S., Ghadiri, M., Jones, R. & Pollock, H. M. Forces between polystyrene particles in water using the AFM: pull-off force vs particle size. *Langmuir* **18,** 5741–5748 (2002).
28. Scheeres, D. J., Hartzell, C. M., Sánchez, P. & Swift, M. Scaling forces to asteroid surfaces: the role of cohesion. *Icarus* **210,** 968–984 (2010).
29. Merrison, J. P. Sand transport, erosion and granular electrification. *Aeolian Res.* **4,** 1–16 (2012).

©2015 Macmillan Publishers Limited. All rights reserved



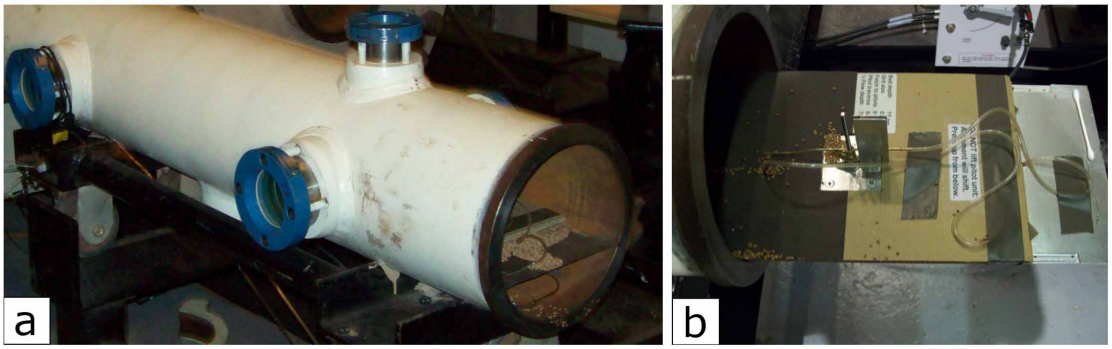
Extended Data Figure 1 | Flow chart of methodology showing the steps used in this work. The results are threshold friction wind speed on Titan, u^*_{tTitan}, and freestream wind speed at height z, $u(z)_{tTitan}$, as a function of particle density (ρ_p) and diameter (D_p), and the shear stress at the surface at threshold (τ_{tTitan}). Upright font denotes calibration data or informational text. Italic font indicates measured wind speeds or parameters derived from measured wind speeds.

©2015 Macmillan Publishers Limited. All rights reserved



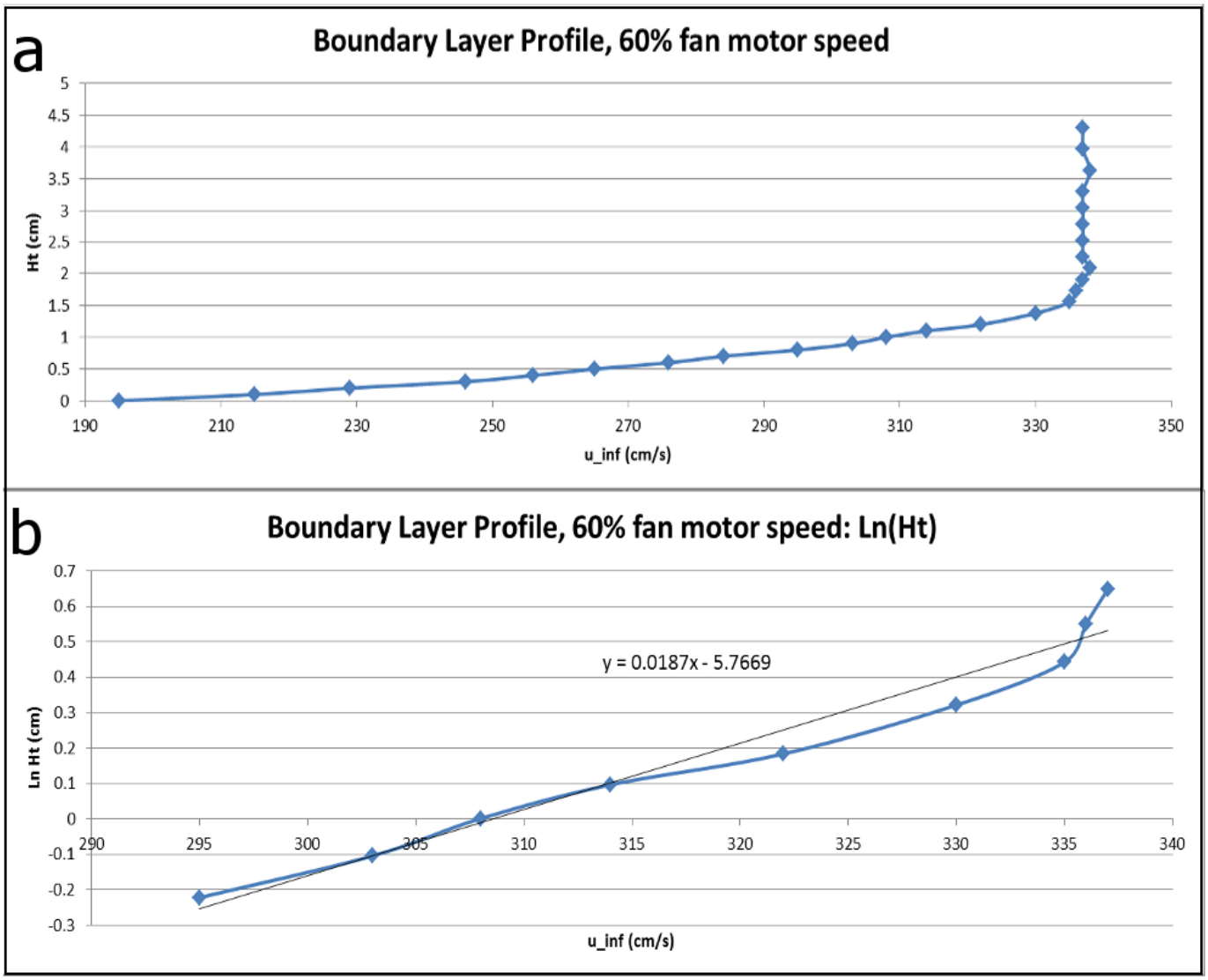
Extended Data Figure 2 | A view into the test section with the test plate inserted. In this photo, the test plate is prepared for an experimental run with silica sand.

©2015 Macmillan Publishers Limited. All rights reserved



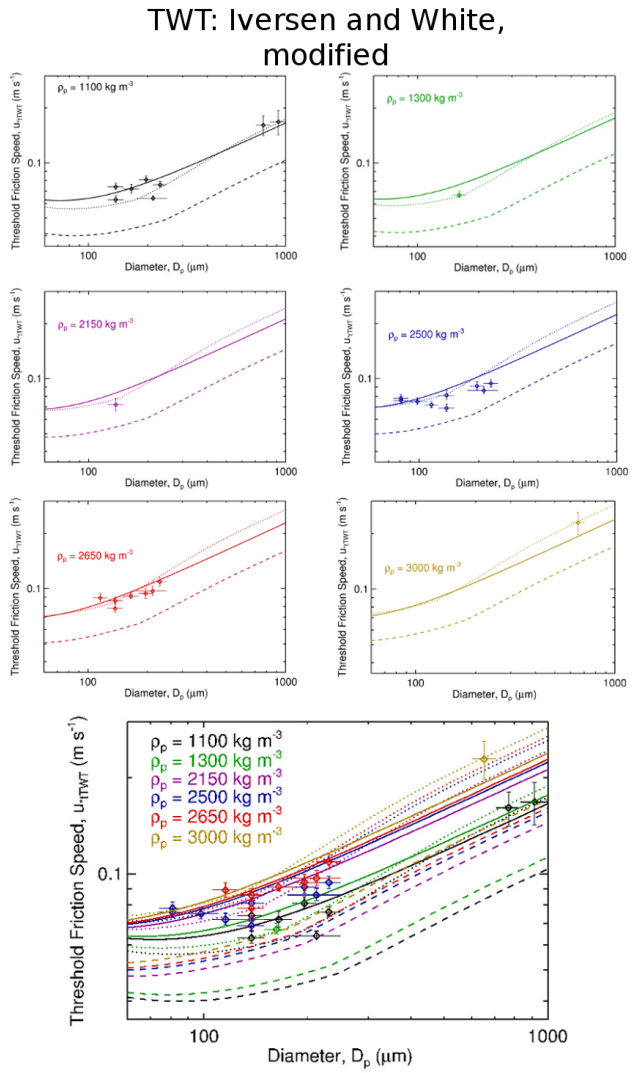
Extended Data Figure 3 | Close-up views of some wind tunnel elements. **a**, View of the downwind end of the test section rolled out from the wind tunnel, showing the single upwind viewing port (far left) and the three downwind viewing ports (top of third port visible on far side of test section). The downwind end of the calibration plate is seen within the test section (lower right), with walnut shell and pneumatic lines visible (traversable pitot tube within test section not visible). **b**, Oblique view of downstream end of test plate after partial removal from the test section (opening visible at far left) showing the traversable pitot tube assembly (in centre of photo). 100-grit (125 μm-diameter grains) sandpaper, for ensuring development of a representative boundary layer, is visible to the left (upwind side) of the pitot tube assembly.

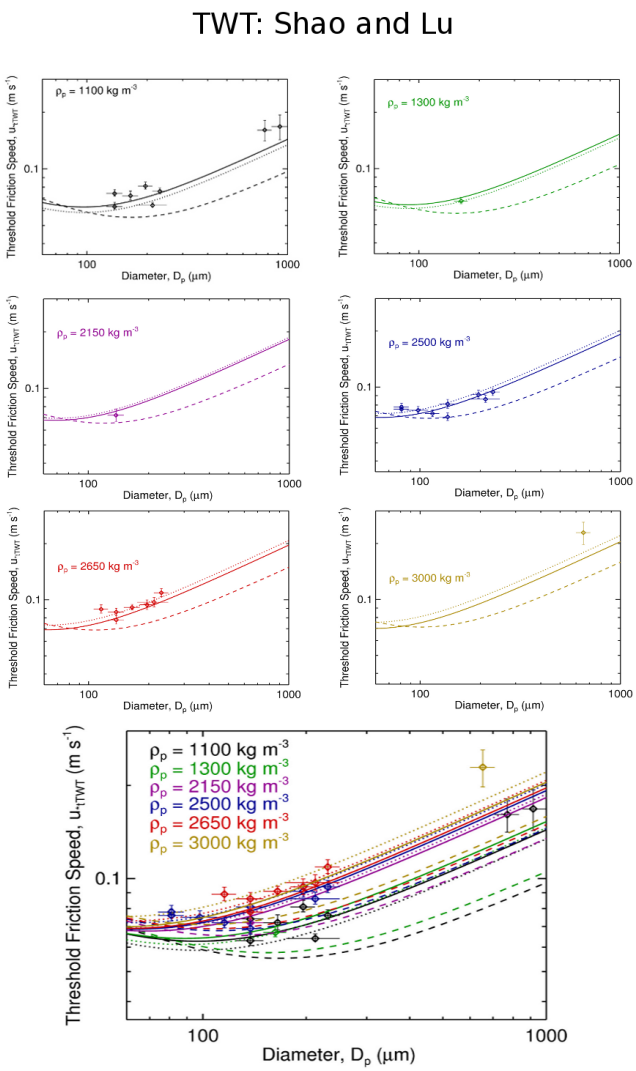
©2015 Macmillan Publishers Limited. All rights reserved



Extended Data Figure 4 | Example plot (at 60% of the maximum rated fan motor speed) of boundary layer data collected with the traversable pitot tube. **a**, Data showing that the boundary layer is fully developed with a freestream wind speed, $u(z)$, of ~3.35 m s^{-1} at a height of ~1.9 cm. **b**, Linearized data illustrating how values of roughness height (z_0) are derived. Fitting a straight line to the data gives the equation $y = 0.00187x - 5.7669$ in centimetres. Comparison with equation (5) shows that $\ln(z_0) = -5.7669$, such that $z_0 = \sim 0.003$ cm.

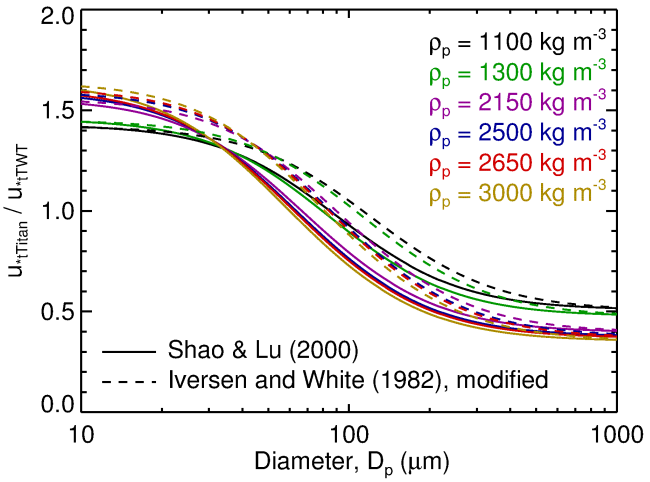
©2015 Macmillan Publishers Limited. All rights reserved





Extended Data Figure 5 | Plots of experimentally derived threshold fiction wind speeds in the TWT for the Iversen–White and Shao–Lu models. For each plot, the dashed line represents the nominal model, the solid line shows the model matched to the data using the density ratio term of ref. 8, and the dotted line shows the model fitted to the data (χ^2 minimization). For the modified Iversen–White model, we use $K = 0.055\,\mathrm{g\,s^{-2}}$ and $n = 2$ (following ref. 8; see Extended Data Table 4). This modification makes the interparticle force (I_p) proportional to D_p as in the Shao–Lu model[7], thereby facilitating comparison between the two models. The modified Iversen–White model[6] is plotted for their equations 5 ($0.03 \leq \mathrm{Re}^*_p \leq 10$) and 6 ($10 \leq \mathrm{Re}^*_p$) (see equations (7) and (8) here), with the transition between the two particle friction Reynolds number regimes at ~200 μm. The Shao–Lu model[7] is plotted for their nominal value for A_N (0.0123) and for their lowest value for γ ($1 \times 10^{-4}\,\mathrm{kg\,s^{-2}}$) to optimize the fit. The proximity of the models with the density ratio term (solid lines) and the models fitted to the data (dotted lines) indicates the power of the density ratio term to match the models to the data. Horizontal bars indicate the range of grain sizes (Extended Data Table 2). Vertical bars show the standard deviation uncertainty in speed for the number of data points indicated in Extended Data Table 2; see Methods for calculation of uncertainties.

©2015 Macmillan Publishers Limited. All rights reserved



Extended Data Figure 6 | Plot of the u^*_t ratios used for converting the u^*_{tTWT} to u^*_{tTitan}. See Methods ('Comparison of u^*_{tTitan} with models') for details.

©2015 Macmillan Publishers Limited. All rights reserved

Extended Data Table 1 | Conditions necessary to achieve similitude of kinematic viscosity with the Titan near-surface atmosphere

PARAMETER	TITAN	TITAN WIND TUNNEL
Atmospheric composition	~95% N_2, ~5% CH_4	~79% N_2, ~20% O_2
Static pressure, P (Pa)	1.44×10^5	***1.25×10^6***
Temperature, T (K)	94	293
Molecular (dynamic) viscosity, μ (Pa s)[a]	6.25×10^{-6}	1.85×10^{-5}
Atmospheric Density, ρ (kg m^{-3})[b]	5.3	14.5
Kinematic viscosity, ν (m^2 s^{-1}) = μ / ρ	**1.2×10^{-6}**	**1.2×10^{-6}**

©2015 Macmillan Publishers Limited. All rights reserved

Extended Data Table 2 | Experimental matrix of sediments with 23 unique combinations of particle diameter (D_p) and density

Material	Density (kg m^{-3})	D_p (microns)	Average D_p (microns)	Date (YYYY)	Error		$u_{t(fixed)}$	u_{tTWT}	u^*_{tTWT}	u^*_{tTitan}
					Value (s.d.)	n	units for all wind speeds are m s^{-1}			
Walnut shell	1100	125-150	138	2012	+3.1% -3.0%	3	0.99	1.04	0.063	0.058
				2013	+2.7% -2.7%	1	1.11	1.23	0.074	0.068
		150-180	165	2013	+3.5% -3.5%	2	1.10	1.21	0.072	0.060
		180-212	196	2013	+5.1% -5.1%	3	1.19	1.34	0.081	0.063
		175-250	213	2012	+3.4% -3.4%	3	1.00	1.06	0.064	0.048
		212-250	231	2013	+1.5% -1.5%	1	1.14	1.27	0.076	0.055
		707-833	770	2013	+12.3% -12.3%	4	2.09	2.69	0.161	0.085
		833-1000	917	2013	+15.0% -15.0%	4	2.16	2.79	0.168	0.088
GC *	1300†	150-175	163	2012	+3.2% -3.2%	3	1.03	1.11	0.067	0.054
	2150	125-150	138	2013	+7.2% -7.2%	3	1.09	1.20	0.072	0.056
Glass spheres (solid)	2500	74-88	81	2012	+3.6% -3.6%	4	1.14	1.27	0.076	0.078
				2013	+3.7% -3.7%	2	1.16	1.29	0.078	0.080
		88-106	97	2013	+5.1% -5.1%	3	1.13	1.26	0.075	0.069
		106-125	116	2013	+4.5% -4.4%	3	1.10	1.21	0.072	0.060
		125-150	138	2012	+3.6% -3.6%	3	1.06	1.15	0.069	0.052
				2013	+4.2% -4.2%	3	1.20	1.36	0.081	0.061
		180-212	196	2013	+3.8% -3.8%	2	1.30	1.51	0.091	0.055
		175-250	213	2012	+4.1% -4.1%	3	1.25	1.43	0.086	0.050
		212-250	231	2013	+4.2% -4.2%	2	1.20	1.36	0.094	0.053
Silica Sand	2650	106-125	116	2013	+4.7% -4.7%	3	1.28	1.48	0.089	0.074
		125-150	138	2012	+3.6% -3.6%	3	1.16	1.30	0.086	0.064
				2013	+5.4% -5.4%	3	1.24	1.44	0.078	0.058
		150-180	165	2013	+5.6% -5.6%	2	1.30	1.51	0.091	0.060
		180-212	196	2013	+2.8% -2.8%	1	1.34	1.57	0.094	0.056
		175-250	213	2012	+4.8% -4.8%	2	1.37	1.62	0.097	0.056
		212-250	213	2013	+4.9% -4.9%	3	1.51	1.82	0.109	0.060
Basaltic sand	3000	600-707	654	2013	+13.6% -13.6%	4	2.85	3.82	0.229	0.087

This distribution of materials includes predominately materials of similar equivalent weight (mass × gravity) to organic materials of the predicted grain size on Titan, as well as some heavier and larger particles to constrain the threshold curve at higher grain sizes (Fig. 2 and Extended Data Fig. 5). This table also shows the measured and derived threshold wind speeds, where $u_{t(fixed)}$ is the freestream threshold wind speed at the fixed pitot, u_{tTWT} is the freestream threshold wind speed in the test section, u^*_{tTWT} is the friction threshold wind speed in the test section, and u^*_{tTitan} is the friction threshold wind speed on Titan scaled to a particle density of 1,000 kg m^{-3}. The error values are calculated as standard deviations (Methods) and are shown in Fig. 2 and Extended Data Fig. 5. n is the number of data points, which is the number of runs for which threshold was observed.

* Gas chromatograph column-packing material.

† Calcined diatomite.

©2015 Macmillan Publishers Limited. All rights reserved

Extended Data Table 3 | Description of each stage of grain motion during data collection

STAGE	**DESCRIPTION** (*focused on the central ~one-third of the bed within the field of view*)
INCREASING WIND SPEED	
First motion	The first perception of individual grain motion, including vibrating in place or rolling (observed as twinkling) or saltation
Flurries	Sporadic or episodic grain motion, commonly saltation
Patches	Continuous grain motion but occurring over less than 50% of the bed
50% of bed in motion	Continuous grain motion occurring over ~50% of the longitudinally central portion of the bed in motion → designated as ***threshold***
100% of bed in motion	Continuous grain motion occurring over the entire bed
DECREASING WIND SPEED	
50% of bed in motion	Continuous grain motion occurring over ~50% of the longitudinally central portion of the bed in motion
Patches	Continuous grain motion but occurring over less than 50% of the bed
Flurries	Sporadic or episodic grain motion, commonly saltation
Twinkling	Flashes of sparkling, interpreted as limited or individual grain motion, including vibrating in place or rolling (observed as twinkling) or saltation
No motion	No perceived change in the field of view

©2015 **Macmillan Publishers Limited. All rights reserved**

Extended Data Table 4 | Values for the interparticle force parameters in various formulations of the models used here

Publication	Parameter	Value	Origin
Iversen et al. 1976, Iversen et al. 1987	K^*	0.055 g s^{-2}	Fitted
	n	2†	Assumed
Iversen and White 1982, Greeley and Iversen 1985	K^*	0.006 g $cm^{0.5}$ s^{-2}	Fitted
	n	2.5	Fitted
Shao and Lu 2000	γ	0.10 g s^{-2}	Fitted

* For comparison with equation (2), $K = A_4 I_p$.
† The value of $n = 2$ results in I_p being proportional to D_p.

©2015 Macmillan Publishers Limited. All rights reserved

LETTER

doi:10.1038/nature14049

Observation of quantized conductance in neutral matter

Sebastian Krinner[1], David Stadler[1], Dominik Husmann[1], Jean-Philippe Brantut[1] & Tilman Esslinger[1]

In transport experiments, the quantum nature of matter becomes directly evident when changes in conductance occur only in discrete steps[1], with a size determined solely by Planck's constant *h*. Observations of quantized steps in electrical conductance[2,3] have provided important insights into the physics of mesoscopic systems[4] and have allowed the development of quantum electronic devices[5]. Even though quantized conductance should not rely on the presence of electric charges, it has never been observed for neutral, massive particles[6]. In its most fundamental form, it requires a quantum-degenerate Fermi gas, a ballistic and adiabatic transport channel, and a constriction with dimensions comparable to the Fermi wavelength. Here we report the observation of quantized conductance in the transport of neutral atoms driven by a chemical potential bias. The atoms are in an ultra-ballistic regime, where their mean free path exceeds not only the size of the transport channel, but also the size of the entire system, including the atom reservoirs. We use high-resolution lithography to shape light potentials that realize either a quantum point contact or a quantum wire for atoms. These constrictions are imprinted on a quasi-two-dimensional ballistic channel connecting the reservoirs[7]. By varying either a gate potential or the transverse confinement of the constrictions, we observe distinct plateaux in the atom conductance. The conductance in the first plateau is found to be equal to the universal conductance quantum, $1/h$. We use Landauer's formula to model our results and find good agreement for low gate potentials, with all parameters determined a priori. Our experiment lets us investigate quantum conductors with wide control not only over the channel geometry, but also over the reservoir properties, such as interaction strength, size and thermalization rate.

As pointed out by Landauer in 1957, conduction is the transmission of carriers from one terminal to another[8,9]. At the heart of this idea is the separation of a conducting channel region from the terminals, which have the role of carrier reservoirs. Inelastic processes in these reservoirs keep them in a steady state, and a fast and dissipative dynamics ensures incoherent emission of the carriers into the channel. A criterion for the observation of quantized conductance is the suppression of both inelastic and elastic scattering processes in the channel, as well as an adiabatic connection of the channel to the reservoirs (Methods). These criteria are met in only very few systems, such as high-mobility two-dimensional (2D) electron gases[2,3], atomic-sized break junctions in metals[10], and carbon nanotubes[11]. The conducting channel is then described by a discrete set of modes in the transverse directions and a continuum along the transport direction. Each transverse mode contributes a maximum value of $1/h$ to the conductance G, reflecting the maximum phase-space occupation allowed by the Pauli principle. This gives

$$G = \frac{1}{h}\sum_n f(E_n - \mu) \quad (1)$$

where f is the Fermi–Dirac distribution, E_n is the energy of the nth transverse mode and μ is the chemical potential in the unbiased reservoirs. When the temperature is sufficiently low compared with the energy spacing of the transverse modes, the contribution of individual modes can be isolated in a transport measurement, leading to quantized plateaux in the conductance.

The composite nature of the Landauer picture of transport has long prevented its realization with cold atoms[12], even though one-dimensional systems have been extensively investigated[13–18]. A situation opposite to the Landauer picture had been realized by placing Bose–Einstein condensates into a double–well potential, where the transport is governed by the coherence between the reservoirs[19]. Fermion reservoirs connected to 2D channels have recently been realized, but so far it has been possible to study transport only in the semi-classical regime, where individual transport modes are not resolved[7,20,21]. In sharp contrast to their solid-state counterparts, the atomic reservoirs are isolated systems, in which energy and particle number are strictly conserved and the dynamics is governed by free-particle motion interrupted only by rare elastic collisions between the particles.

The basis of our experiment is the transport set-up[7]. In brief, a weakly interacting gas of $N = 7.5(3) \times 10^4$ fermionic ^{6}Li atoms is prepared in a cigar-shaped trap (the number in parentheses is the uncertainty (s.d.) in the final digit), which is then split into two reservoirs connected by a 2D channel using the repulsive potential of a TEM_{01}-like (transverse electromagnetic) mode of a laser operating at 532 nm (Fig. 1a). The Fermi temperature in this trapping geometry is $T_F = 385(12)$ nK and the temperature is $T = 42(8)$ nK $= 0.11(2)T_F$.

A quantum point contact[22] (QPC) is created by lithographically projecting a split-gate structure onto the 2D channel (Fig. 1a, b). To do so, the negative of a slit with a width of 12 μm is printed on a binary mask and illuminated with a laser beam at 532 nm. A projection system, consisting of an achromatic lens and a high-numerical-aperture microscope objective, shrinks the object by a factor of 11. The width of the resulting QPC in the channel region is measured to be 1.5(3) μm (full-width at half-maximum) in the x direction, using a second, identical microscope placed opposite the first[23]. Because this width is comparable to the Fermi wavelength of 2.0 μm in our system, a single-mode regime should be accessible. The finite width of the diffraction-limited point spread function of the projection system leads to a harmonically confining potential along the x axis. The overall shape of the projected QPC potential is given by the Gaussian profile of the illuminating laser beam, whose waists are 5.6(3) μm and 33.6(6) μm along the y and x axes, respectively, in the image plane.

The QPC is characterized by ν_z and ν_x, the trap frequencies along z and x at the centre of the QPC, which originate from the harmonic confinement of the TEM_{01}-like laser beam and the lithographically imprinted constriction, respectively. Typical values are $\nu_z = 10.0(4)$ kHz and $\nu_x = 30(3)$ kHz. The three lowest modes are thus separated by $h\nu_z \approx 0.5$ μK, which is much more than the energy equivalent to the temperature of the gas. The zero-point energy in the QPC is $E_0 = (h\nu_z + h\nu_x)/2 \approx 1.0$ μK, which is larger than the chemical potential $\mu = 370(11)$ nK imposed by the reservoirs. We use an additional laser beam creating an attractive gate potential V_g at the position of the QPC to successively populate its otherwise empty transverse modes (Fig. 1c–e). This laser beam has a wavelength of 767 nm and a waist of 25.0(6) μm, and is propagating along the z axis.

[1]Institute for Quantum Electronics, ETH Zurich, 8093 Zurich, Switzerland.

©2015 Macmillan Publishers Limited. All rights reserved

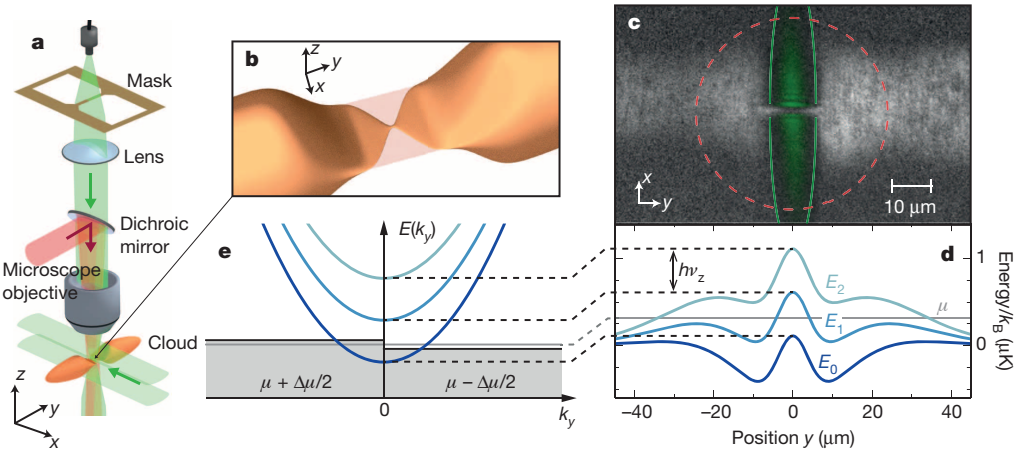


Figure 1 | An atomic QPC. **a**, Lithographic imprinting of the QPC (vertical green beam). An achromatic lens and a high-numerical-aperture microscope objective are used to shrink the QPC structure onto the 2D channel region in the atomic cloud. An attractive gate potential is created by a red detuned laser beam (red beam). It is combined with the green beam on a dichroic mirror and focused onto the centre of the QPC. The TEM_{01}-like laser mode, which creates the 2D channel and sets the confinement frequency ν_z of the QPC, is shown as a horizontal green beam propagating along the $-x$ axis. **b**, Close-up view of the channel region: reservoirs, 2D channel and QPC are smoothly connected to each other. **c**, Imaged atomic density in the QPC for $\nu_z = 4.6$ kHz, $\nu_x = 29$ kHz and $V_g = 1.4$ μK in grey scale. The overlaid elliptical green region with the horizontal cut is an image of the projected split-gate structure. The green solid line and red dashed line are $1/e^2$ contours of the intensity profiles of the laser beams creating the split-gate structure and the gate potential, respectively. **d**, Effective potential along the transport axis, consisting of the transverse-mode energy and the gate potential (Methods). The energy levels corresponding to the three lowest transverse modes are labelled E_0, E_1 and E_2. The depicted situation corresponds to the first plateau of the $\nu_z = 10.4$ kHz data of Fig. 2. **e**, Energy dispersion relation of the particles in the QPC. The parabolas are offset by the quantized transverse-mode energies. Left and right reservoirs are represented by grey boxes, having chemical potentials $\mu \pm \Delta\mu/2$.

To measure the conductance, we prepare an initial particle number imbalance $\Delta N_0 = (N_L - N_R)_0 = 0.40(2)N$ between the two reservoirs, with N_L and N_R denoting the particle numbers in the left and right reservoirs, respectively. This leads to a chemical potential bias $\Delta\mu = 94(7)\,\text{nK} \ll h\nu_z$ driving a current $I = G\Delta\mu$ across the QPC. We access the conductance by measuring the relative particle number imbalance after 1.5 s of transport, assuming a linear response, and evaluating the compressibility of the reservoirs (Methods).

Figure 2 presents the measured conductance as a function of V_g for two different vertical confinement frequencies, $\nu_z = 10.4$ kHz and $\nu_z = 8.2$ kHz. The confinement frequency along x is set to $\nu_x = 31.8$ kHz. Both curves start at zero conductance (note that the 8.2 kHz curve is artificially offset for clarity) because the QPC is entirely closed at small gate potentials owing to its zero-point energy. The conductance starts to rise at the point where V_g compensates the zero-point energy, and saturates very close to the universal value $1/h$ as soon as the ground-state mode is tuned below the chemical potential of the reservoirs. Higher modes follow accordingly on further increasing V_g. We clearly resolve the first two conductance plateaux in the case of $\nu_z = 10.4$ kHz (open blue circles), corresponding to the population of the $(n_x = 0; n_z = 0, 1)$ modes, where n_x and n_z are the quantum numbers in the harmonic potentials in the x and z directions. For $\nu_z = 8.2$ kHz (filled red squares), the plateaux are narrower because the modes are more closely spaced in energy. In this case, we resolve the first three modes $(n_x = 0; n_z = 0, 1, 2)$ and even the onset of the (0, 3) mode is visible.

The inset in Fig. 2 shows a close-up view of the first conductance plateau (with no offset). When V_g is replaced with the total energy $E_{tot} = V_g + \mu$ of the particles minus E_0 and this value is normalized to $h\nu_z$, the two data sets fall on top of each other as a consequence of universality, with the width of the plateau given by $h\nu_z$. The absolute accuracy of our conductance measurement is limited by the uncertainty in the compressibility of the reservoirs, which amounts to 11% (Methods).

The quantization of conductance is universal and should not depend on the control parameter. To demonstrate this, we next use the horizontal confinement frequency ν_x of the QPC as a tuning parameter and keep the gate potential fixed. This is the counterpart of the measurement in solid-state physics where the split-gate voltage is tuned to reveal quantized conductance[2,3]. The blue data points in Fig. 3 present this measurement

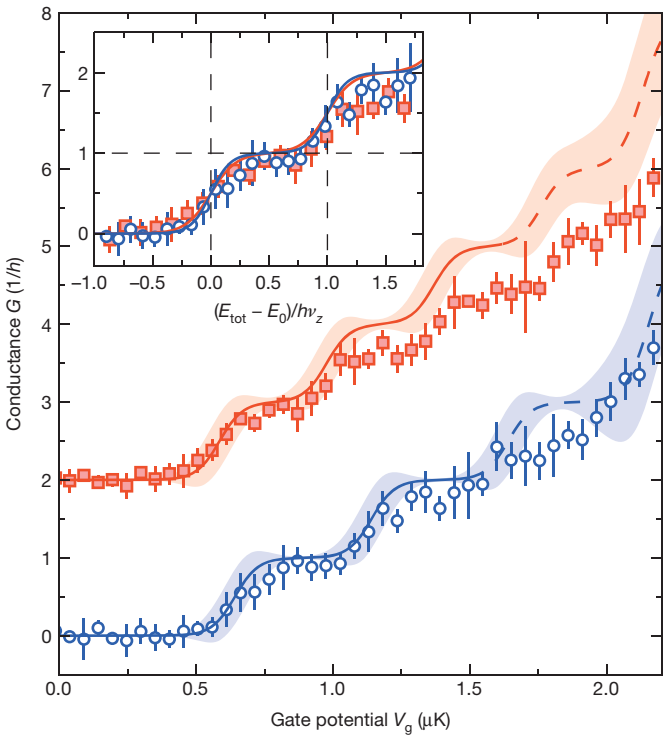


Figure 2 | Conductance as a function of gate potential. Open blue circles correspond to a vertical confinement frequency of $\nu_z = 10.4$ kHz. Filled red squares correspond to $\nu_z = 8.2$ kHz and are vertically shifted by two units for clarity. Each data point represents the mean of six measurements, and error bars indicate one standard deviation. Solid lines are theoretical predictions based on the Landauer formula of conductance. The shaded regions reflect the uncertainties in the input parameters (see text). Dashed lines are continuations of the solid lines and correspond to a change in the effective potential (Methods). Inset, first conductance plateau as a function of reduced energy, showing universal scaling. Vertical dashed lines indicate the width of the first plateau, and the horizontal dashed line indicates the universal conductance value $1/h$.

©2015 Macmillan Publishers Limited. All rights reserved

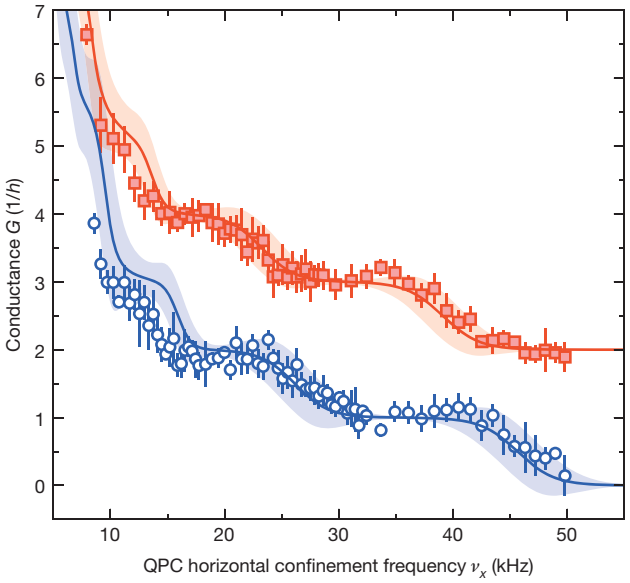


Figure 3 | Conductance as a function of horizontal confinement. Open blue circles correspond to a vertical confinement frequency of $\nu_z = 10.9$ kHz and a gate potential of $V_g = 1.0(1)$ μK. Filled red squares correspond to $\nu_z = 9.2$ kHz and $V_g = 0.8(1)$ μK, and are vertically shifted by two units for clarity. Solid lines are theoretical predictions based on the Landauer formula of conductance. The shaded regions reflect the uncertainties in the input parameters (see text). Data averaging and error bars are the same as in Fig. 2.

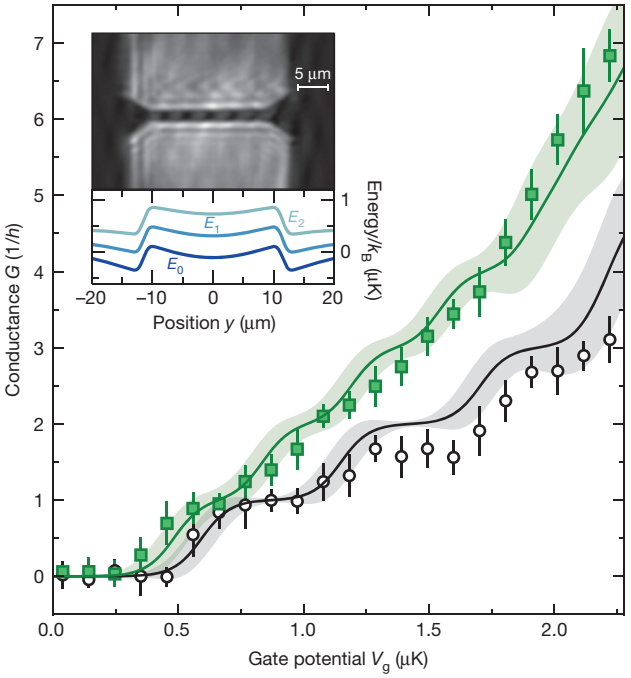


Figure 4 | Quantum wire: conductance as a function of gate potential. Open black circles correspond to a vertical confinement frequency of $\nu_z = 8.7$ kHz, and filled green squares to a lower confinement frequency of $\nu_z = 5.5$ kHz. For the stronger confinement, clear conductance plateaux are observed. The weaker confinement illustrates the onset of the contribution from the first excited mode along the x direction (see text). Solid lines are theoretical predictions based on the Landauer formula of conductance. Shaded regions, data averaging and error bars are the same as in Fig. 2. The inset shows the lithographically imprinted wire as imaged by a second, identical microscope objective. Below it, the corresponding effective potentials are drawn for the three lowest transverse modes, E_0, E_1 and E_2, for the parameters at the first plateau of the $\nu_z = 8.7$ kHz data.

for $\nu_z = 10.9$ kHz and $V_g = 1.0(1)$ μK. We identify two increasingly wider plateaux centred at $\nu_x = 20$ and 35 kHz. They correspond to the presence of two or one conductance modes, respectively. The bending at $\nu_x = 12$ kHz is due to the population of a third mode, the (1, 0) mode. When widening the QPC further, the conductance rises quickly because the next transverse energy levels (n_x, n_z) are energetically very close. The red data points in Fig. 3 correspond to $\nu_z = 9.2$ kHz and $V_g = 0.8(1)$ μK, and show the same features as the blue data, with a reduced plateau width owing to a smaller ν_z.

We compare our data with theoretical predictions (solid lines in Figs 2 and 3) of the Landauer formula in the limit of entirely adiabatic and ballistic transport (equation (1)) without any fit parameters (Methods). The input parameters T, μ, $\Delta\mu$, ν_x, ν_z and V_g are all independently measured quantities. The positions and widths of the plateaux are in general well predicted. The conductances on the plateaux reach the universal values for moderate gate potentials. For larger gate potentials (Fig. 2), the measured conductance is lower than predicted. Possible reasons could be the presence of additional contact resistances in the 2D tapered regions connecting the reservoirs with the QPC (Methods and Extended Data Fig. 4), or a small non-adiabaticity in the motion of the particles introduced by the gate potential, which accelerates the particles more and more towards the QPC as its strength is increased.

The sharpness of the transition from one plateau to the next is set by the finite temperature. We checked numerically within the adiabatic approximation that broadening due to tunnelling below the barrier or reflections above it[24] is much smaller than the relevant thermal broadening of the Fermi edge of $\sim 4k_BT$ (ref. 5; k_B, Boltzmann's constant). Furthermore, we do not observe any nonlinear effects[25] due to the applied finite bias $\Delta\mu$ because it is also smaller than $\sim 4k_BT$.

Even with isolated reservoirs, which cannot dissipate energy, our QPC features quantized conductance that can be described by Landauer's theory. This is remarkable because our reservoirs are close to a collisionless regime, with a collision mean free path of approximately 12 mm, which is about 40 times larger than the size of the cloud and corresponds to a scattering time of about 400 ms (Methods and Extended Data Fig. 1). We attribute this to the three-dimensional nature and anharmonicity of the trapping potential, which should prevent closed particles orbits when the longitudinal and transverse degrees of freedom are mixed at the connections with the reservoirs (Methods and Extended Data Fig. 3). To further illuminate the role of mixing of the motional degrees of freedom, compared with thermalization via collisions, we measured the conductance with the scattering length set to zero during transport, such that the entire system became non-interacting and its evolution coherent. We could again observe clear quantized steps in the conductance (Methods and Extended Data Fig. 2). This is in a regime not covered by the usual assumptions of the Landauer theory because the latter relies on incoherent reservoirs to prevent particles from keeping their energy and reversing their motion. From that we conclude that the incoherence of our reservoirs is most probably mimicked by the above-described geometric effects, and that interparticle collisions have a minor role.

The chemical potential or voltage in a ballistic constriction drops at its contacts[26], leading to universal conductance values independent of the length of the constriction. We demonstrate this by creating a long quantum wire (Fig. 4, upper inset). It has a length of 19.0(6) μm and the same width of 1.5(3) μm as the QPC. The projected structure is spatially smoothed by the low-pass filtering of the projection system. The triangular openings further smoothen the transition from the quantum wire to the 2D channel to avoid reflections at the openings[27,28]. The resulting effective potential, with the openings modelled by an error function, is shown in the lower inset in Fig. 4. It is highest at the entrance and exit of the quantum wire, which is a consequence of the nearly uniform confinement in combination with the Gaussian envelope of the attractive gate beam. The detection of single quanta of conductance is found to be less robust in this configuration, most probably because the points of highest potential are located at positions where the spatial profile of the gate potential has a slope. Nevertheless, quantized conductance plateaux

©2015 Macmillan Publishers Limited. All rights reserved

are observed for tight confinement ($v_x = 24.6$ kHz and $v_z = 8.7$ kHz; black circles in Fig. 4), using the gate potential as a tuning parameter. They are well reproduced by theory, up to a 10–20% reduction in height for the second and third plateaux. Possible interference effects, such as above-barrier resonances[27], are not observed, probably because the finite temperature leads to an atomic coherence length of 7(1) μm, which is less than the length of the quantum wire.

The green data in Fig. 4 demonstrate how the plateaux disappear when v_z is lowered to 5.5 kHz. The conductance starts to increase at a lower gate potential because of the reduced zero-point energy. Well-defined plateaux are no longer visible owing to the reduced ratio of hv_z to temperature. However, we observe a change in the slope of the conductance by a factor of ~2 at $V_g \approx 1.75$ μK, which is where the first excited mode along the x direction begins to contribute. More precisely, when V_g is increased from 0.25 to 1.75 μK the ($n_x = 0$; $n_z = 0, 1, 2, 3$) modes begin to contribute, whereas above $V_g = 1.75$ μK the ($n_x = 0, n_z = 4, 5, \ldots$) modes and the ($n_x = 1, n_z = 0, 1, \ldots$) modes begin to contribute, giving rise to a change in slope by a factor of ~2. This feature is accurately predicted by theory.

With our projection technique, channels shorter than the Fermi wavelength can be straightforwardly implemented to study the breakdown of the adiabatic assumption and to produce structured tunnel contacts as building blocks for quantum dots or interferometers. Increasing the interactions should allow us to investigate a possible breakdown of quantized conductance and the Landauer picture in the strongly correlated regime[29]. The detection of conductance at the level of single quanta provides access to the physics of topological edge states[30], transport in the vicinity of a quantum phase transition[31], and universal conductance fluctuations[32].

Online Content Methods, along with any additional Extended Data display items and Source Data, are available in the online version of the paper; references unique to these sections appear only in the online paper.

Received 12 April; accepted 1 November 2014.

1. Imry, Y. in *Directions in Condensed Matter* (eds Grinstein, G. & Mazenko, G.) 120–145 (World Scientific, 1986).
2. van Wees, B. J. *et al.* Quantized conductance of point contacts in a two-dimensional electron gas. *Phys. Rev. Lett.* **60,** 848–850 (1988).
3. Wharam, D. A. *et al.* One-dimensional transport and the quantisation of the ballistic resistance. *J. Phys. C* **21,** L209 (1988).
4. Imry, Y. *Introduction to Mesoscopic Physics* (Oxford Univ. Press, 2002).
5. Ihn, T. *Semiconductor Nanostructures* (Oxford Univ. Press, 2010).
6. Sato, Y., Eom, B.-H. & Packard, R. On the feasibility of detecting quantized conductance in neutral matter. *J. Low Temp. Phys.* **141,** 99–109 (2005).
7. Brantut, J.-P., Meineke, J., Stadler, D., Krinner, S. & Esslinger, T. Conduction of ultracold fermions through a mesoscopic channel. *Science* **337,** 1069–1071 (2012).
8. Landauer, R. Spatial variation of currents and fields due to localized scatterers in metallic conduction. *IBM J. Res. Develop.* **1,** 223–231 (1957).
9. Büttiker, M., Imry, Y., Landauer, R. & Pinhas, S. Generalized many-channel conductance formula with application to small rings. *Phys. Rev. B* **31,** 6207–6215 (1985).
10. Krans, J. M., van Ruitenbeek, J. M., Fisun, V. V., Yanson, I. K. & de Jongh, L. J. The signature of conductance quantization in metallic point contacts. *Nature* **375,** 767–769 (1995).
11. Frank, S., Poncharal, P., Wang, Z. L. & de Heer, W. A. Carbon nanotube quantum resistors. *Science* **280,** 1744–1746 (1998).
12. Thywissen, J. H., Westervelt, R. M. & Prentiss, M. Quantum point contacts for neutral atoms. *Phys. Rev. Lett.* **83,** 3762–3765 (1999).
13. Görlitz, A. *et al.* Realization of Bose-Einstein condensates in lower dimensions. *Phys. Rev. Lett.* **87,** 130402 (2001).
14. Moritz, H., Stöferle, T., Köhl, M. & Esslinger, T. Exciting collective oscillations in a trapped 1D gas. *Phys. Rev. Lett.* **91,** 250402 (2003).
15. Paredes, B. *et al.* Tonks–Girardeau gas of ultracold atoms in an optical lattice. *Nature* **429,** 277–281 (2004).
16. Kinoshita, T., Wenger, T. & Weiss, D. S. Observation of a one-dimensional Tonks-Girardeau gas. *Science* **305,** 1125–1128 (2004).
17. Bouchoule, I., van Druten, N. & Westbrook, C. in *Atom Chips* (eds Reichel, J. & Vuletic, V.) 331–363 (Wiley, 2010).
18. Serwane, F. *et al.* Deterministic preparation of a tunable few-fermion system. *Science* **332,** 336–338 (2011).
19. Albiez, M. *et al.* Direct observation of tunneling and nonlinear self-trapping in a single bosonic Josephson junction. *Phys. Rev. Lett.* **95,** 010402 (2005).
20. Stadler, D., Krinner, S., Meineke, J., Brantut, J.-P. & Esslinger, T. Observing the drop of resistance in the flow of a superfluid Fermi gas. *Nature* **491,** 736–739 (2012).
21. Krinner, S., Stadler, D., Meineke, J., Brantut, J.-P. & Esslinger, T. Superfluidity with disorder in a thin film of quantum gas. *Phys. Rev. Lett.* **110,** 100601 (2013).
22. van Houten, H. & Beenakker, C. Quantum point contacts. *Phys. Today* **49,** 22–27 (1996).
23. Zimmermann, B., Müller, T., Meineke, J., Esslinger, T. & Moritz, H. High-resolution imaging of ultracold fermions in microscopically tailored optical potentials. *New J. Phys.* **13,** 043007 (2011).
24. Glazman, L. I. & Lesovik, G. B. Khmel'Nitskiĭ, D. E. & Shekhter, R. I. Reflectionless quantum transport and fundamental ballistic-resistance steps in microscopic constrictions. *JETP Lett.* **48,** 238–241 (1988).
25. Kouwenhoven, L. P. *et al.* Nonlinear conductance of quantum point contacts. *Phys. Rev. B* **39,** 8040–8043 (1989).
26. Ulreich, S. & Zwerger, W. Where is the potential drop in a quantum point contact? *Superlattices Microstruct.* **23,** 719–730 (1998).
27. Szafer, A. & Stone, A. D. Theory of quantum conduction through a constriction. *Phys. Rev. Lett.* **62,** 300–303 (1989).
28. Yacoby, A. & Imry, Y. Quantization of the conductance of ballistic point contacts beyond the adiabatic approximation. *Phys. Rev. B* **41,** 5341–5350 (1990).
29. Vignale, G. & Di Ventra, M. Incompleteness of the Landauer formula for electronic transport. *Phys. Rev. B* **79,** 014201 (2009).
30. Hasan, M. Z. & Kane, C. L. Topological insulators. *Rev. Mod. Phys.* **82,** 3045–3067 (2010).
31. Sachdev, S. *Quantum Phase Transitions* 260–290 (Cambridge Univ. Press, 2011).
32. Lee, P. A. & Stone, A. D. Universal conductance fluctuations in metals. *Phys. Rev. Lett.* **55,** 1622 (1985).

Acknowledgements We acknowledge discussions with G. Blatter, K. Ensslin, C. Glattli, T. Giamarchi, C. Grenier and M. Lebrat, and thank C. Chin, T. Ihn, Y. Imry, and W. Zwerger for their careful reading of the manuscript and for discussions. We acknowledge financing from NCCR QSIT, the ERC Project SQMS, the FP7 project SIQS and ETHZ. J.-P.B. is supported by the Ambizione program of SNF.

Author Contributions All authors contributed equally to this work.

Author Information Reprints and permissions information is available at www.nature.com/reprints. The authors declare no competing financial interests. Readers are welcome to comment on the online version of the paper. Correspondence and requests for materials should be addressed to J.-P.B. (brantutj@phys.ethz.ch).

©2015 Macmillan Publishers Limited. All rights reserved

METHODS

Experimental set-up. Our experiment uses the system described in refs 7, 33. In brief, a degenerate Fermi gas of ^{6}Li atoms is produced by evaporative cooling of a balanced spin mixture of the lowest and third-lowest hyperfine states in a hybrid magnetic and optical dipole trap in a homogenous magnetic field of 388 G, using a magnetic field gradient[34]. The dipole trap operates at a wavelength of 1,064 nm, and has a waist of 70 μm and a trap depth of 1.2 μK. The experiments are performed in a homogeneous magnetic field of 552 G, where the scattering length is $-187a_0$, a_0 denoting the Bohr radius. This allows for sufficiently fast thermalization of the reservoirs, and at the same time ensures a ballistic transport channel. All quantities in the text are stated for a single hyperfine state, implying that the conductance plateaux appear in multiples of $1/h$ and not $2/h$.

Transport sequence. During the preparation of the degenerate gas, a magnetic field gradient of 0.2 mT m^{-1} is applied along the y axis to shift the trap with respect to the QPC. A repulsive elliptic gate beam focused on the centre of the QPC is used to separate the two reservoirs as in ref. 33. The powers of the laser beams creating the 2D channel and the QPC are consecutively ramped from zero to their final values within 200 ms. Then evaporative cooling is enforced by using a magnetic field gradient along the z axis[34]. This procedure results in a well-defined particle number imbalance between the two reservoirs. Next the dipole trap is adiabatically decompressed from a trap depth of 5.6 μK to a final depth of 1.2 μK within 200 ms to further reduce the absolute temperature of the gas. During the same time interval the attractive gate potential is ramped from zero to V_g. Finally, the magnetic field gradient along y is ramped to zero within 60 ms, resulting in a well-defined chemical potential difference $\Delta\mu$ between the two reservoirs. We start the transport process by removing the repulsive gate beam. After a transport time of 1.5 s we switch the repulsive gate beam back on to stop the transport process, and we measure the atom number in both reservoirs via absorption imaging along the x direction.

Conductance evaluation. From the equation for the current, $I = G\Delta\mu$, we find that the temporal evolution of the particle number imbalance between the left and right reservoirs, $\Delta N = N_L - N_R$, is governed in linear response by the equation

$$\frac{\mathrm{d}}{\mathrm{d}t}(\Delta N/N) = -\frac{G}{C_{\mathrm{eff}}}(\Delta N/N) \qquad (2)$$

where $N = N_L + N_R$ is the total atom number and $C_{\mathrm{eff}} = (1/C_L + 1/C_R)^{-1}$ is an effective compressibility determined by the respective compressibilities of the single reservoirs at equilibrium. In agreement with this equation we observe an exponential decay of the relative particle number imbalance as a function of time, the time constant being $\tau = C_{\mathrm{eff}}/G$. We evaluate G by measuring τ and evaluating C_{eff}. The error made when replacing $\Delta\mu$ with $\Delta N/C_{\mathrm{eff}}$ to obtain the linear response equation (equation (2)) is smaller than 5% at the largest value of $\Delta N/N$, which is 0.4.

We determine τ by measuring the relative particle number imbalance at $t = 0$ and again after a transport time of $t_{\mathrm{tr}} = 1.5$ s. From the solution of equation (2) we obtain

$$\frac{1}{\tau} = \frac{1}{t_{\mathrm{tr}}}\log\left(\frac{\Delta N}{N}(t=0)\right) - \frac{1}{t_{\mathrm{tr}}}\log\left(\frac{\Delta N}{N}(t=t_{\mathrm{tr}})\right)$$

where a constant offset of $-0.20(1)$ is subtracted from both imbalances. This offset originates partly from the relative alignment of the gate beam and the lithographic system, and for the data of Fig. 2 it varied linearly from -0.20 to -0.16 over the range shown.

The compressibilities $C_L = C_R = C$ of the identical reservoirs are calculated from the trap geometry, particle number and temperature, assuming a non-interacting Fermi gas. In brief, the trapping potential is harmonic along the x and z directions and half-harmonic along the y direction[33], with respective trapping frequencies of 194, 23.5 and 157 Hz along the x, y and z directions. The effect of the repulsive potential of the TEM$_{01}$-like laser mode, creating the 2D channel, is to shift the Fermi energy and chemical potential by 17% towards larger values with respect to the unperturbed cloud. The compressibility is almost not affected. The systematic uncertainty in C_{eff} is 11%, which is due to the calibration error in the total particle number and an uncertainty in the overall trapping potential.

Trapping frequencies of the QPC and the quantum wire. The transverse trapping frequencies of the QPC and quantum wire, ν_x and ν_z, are measured by parametric heating in a dipole trap created by a laser beam with a waist of 8 μm and a wavelength of 767 nm, propagating along the z axis. The observed resonances have relative widths (full-widths at half-maximum) of $\delta\nu_z/\nu_z = 0.05$ and $\delta\nu_x/\nu_x = 0.30(5)$, respectively. ν_z is found to depend weakly on ν_x. This is because the darkness of the projected QPC structure decreases as a result of diffraction when moving out of focus along the z axis, thus creating an additional confinement along z. We measure this contribution to be $\tilde{\nu}_z = 0.16\,\nu_x$. Hence, ν_z is given by $\nu_z = \sqrt{\nu_{z,0}^2 + (0.16\,\nu_x)^2}$, where $\nu_{z,0}$ is the trapping frequency in the absence of the QPC. The values of ν_z stated in the text for the data of Fig. 3 are evaluated for $\nu_x = 31.8$ kHz to be comparable to the values set for the data of Fig. 2. For the shown range of $\nu_x \in [10\,\mathrm{Hz}, 50\,\mathrm{Hz}]$, ν_z varies by 12% around its mean value for the $\nu_z = 10.9$ kHz data and by 16% around its mean value for the $\nu_z = 9.2$ kHz data

Adiabatic approximation and theory curves. The computation of the conductance makes use of the adiabatic approximation[5,24], allowing for a separation of longitudinal (y) and transverse (x, z) variables. It neglects scattering between different transverse modes and is justified if the confinement of the constriction varies smoothly along the transport direction. This is to a good approximation the case for both the QPC, with its Gaussian envelope, and the quantum wire, with its triangular openings that are smoothed by the inherent low-pass filtering of the projection system. In the resulting one-dimensional Schrödinger equation the transverse energy $E_n(y) = E_{n_x,n_z}(y) = h\nu_x f_x(y)(n_x + 1/2) + h\nu_z f_z(y)(n_z + 1/2)$, with $f_x(y)$ and $f_z(y)$ describing the spatial variations of the corresponding trapping frequencies, acts as an additional potential. Together with the gate potential $V_g(y)$ it forms the effective potential drawn in Fig. 1d and in the inset of Fig. 4. For the QPC we have $f_{x,z}(y) = \exp\left(-y^2/w_{x,z}^2\right)$, with $w_x = 5.6(3)$ μm and $w_z = 30(1)$ μm, whereas for the quantum wire f_x is constant along the wire, with its edges modelled by an error function.

The theory lines in Fig. 2 are dashed above $V_g \approx 1.5$ μK because at this point the maximum of the effective potential moves from the centre to the sides of the QPC, which is not taken into account in the theory. This effect is not expected to explain the observed shift of the conductance below the universal values for large gate potentials.

The conductance is calculated from equation (1), which we obtain from the two-terminal Landauer formula in the adiabatic regime[5]

$$G = \frac{1}{h}\sum_n \int_{-\infty}^{\infty} \mathrm{d}E\, T_n(E)\left(-\frac{\partial f}{\partial E}(E-\mu)\right)$$

by setting the transmission probability to be $T_n(E) = \Theta(E - E_n)$, with $\Theta(E - E_n)$ the Heaviside step function. This substitution corresponds to the semiclassical approximation, where the transmission probability for particles is 1 if their total energy is larger than their transverse energy, and is 0 otherwise. It neglects tunnelling below the barrier and reflections above it[24], which would lead to a broadening of $T_n(E)$. We checked numerically that for our geometry this broadening is much smaller than the thermal broadening of the Fermi-Dirac distribution and can thus be neglected.

Taking into account the gate potential for the conductance evaluation, equation (1) reads

$$G = \frac{1}{h}\sum_n f\left(\frac{E_n - V_g - \mu}{k_B T}\right)$$

In the case of the quantum wire V_g is multiplied by a factor of $\exp(-2 \times 9.5^2/25^2)$ to account for the fact that the points of largest effective potential are located 9.5 μm from the centre of the gate potential and the quantum wire. The shaded error regions in Figs 2–4 cover statistical and systematic errors of the input parameters and are determined using Gaussian error propagation. The main contribution in Figs 2 and 4 is the uncertainty in ν_x, whereas in Fig. 3 it is the uncertainty in V_g.

Timescales in the reservoirs. Here we discuss the timescales and associated length scales relevant to the evolution of the coupled reservoirs, as sketched in Extended Data Fig. 1.

The shortest timescale is the Fermi time $h/k_B T_F \approx 125$ μs. On this timescale the atoms exiting the channel into the reservoirs travel a distance of the order of the Fermi wavelength. Recent calculations in a geometry similar to our experimental configuration, where a one-dimensional channel enters a wider region, show that it takes a time of only $10h/k_B T_F$ for a steady flow pattern to establish[35]. Importantly, it was shown that this is the case in the presence of an incoherent bath as well as in a complete microcanonical picture.

The next-longest timescale is the coherence time $h/k_B T \approx 1.1$ ms. This timescale is about an order of magnitude smaller than the oscillation period in the reservoirs $1/\bar{\nu} \approx 8.5$ ms, where $\bar{\nu}$ is the mean trap frequency in the reservoirs. This prevents interference patterns from developing in the reservoirs. The dephasing of the interferences is due to thermal averaging, and not due to inelastic scattering with phonons, as can happen in solid-state systems.

Because the reservoirs are three-dimensional and the trapping potential is anharmonic, it is unlikely that trajectories will be closed, and we should instead expect complex orbits leading to escape times much larger than the oscillation period[36].

The thermalization of the incident particles from the QPC occurs on the scale of the scattering time $\tau_s = (1/\bar{n}\sigma v_F)(T/T_F) \approx 400$ ms, where $\bar{n}$ is the peak density at the trap centre, σ is the scattering cross-section for interparticle collisions and v_F is the Fermi velocity. This timescale does not account for the finite bias, and should thus be considered an upper bound. Here we are concerned with the decay of excitations above the Fermi surface and not with a generic particle in the trap, and the Pauli principle thus leads to suppression of scattering by a factor T/T_F and not $(T/T_F)^2$. This situation is similar to the case of evaporative cooling where the exit states are empty[37]. Note that this scattering is elastic, and that the many-body evolution of

©2015 Macmillan Publishers Limited. All rights reserved

the reservoir remains coherent. The interparticle scattering ensures that the energy distribution follows Fermi–Dirac statistics. While theoretically possible, revivals due to the coherent many-body evolution of the reservoirs should take place only on extremely long timescales. The corresponding collision mean free path is about 12 mm, showing that many oscillations in the reservoirs take place before collisions redistribute the energy. This also shows that in our experiment, the decay of excitations introduced by the transport is non-local.

The timescale for current flow corresponds to the timescale τ_{RC} of the equivalent RC circuit. In our case, $\tau_{RC} \approx 8$ s for the first conductance plateau. We measure the decay of the atom number imbalance in the reservoirs after an observation time of typically $t_{obs} = 1.5$ s.

Inelastic processes take place on even longer timescales. Three-body recombinations are strongly inhibited by the Pauli principle. All the available estimates for the loss coefficient in the BEC–BCS crossover (with much stronger interactions than in our present work) suggest a timescale larger than 1,000 s (ref. 38). Spontaneous emission in the far-detuned optical dipole trap takes place on a timescale of $\tau_{trap} \approx 580$ s. The attractive gate potential has a spontaneous emission timescale of $\tau_{gate} \approx 63$ s. Yet only a tiny fraction of the atoms are exposed to this potential (<1%), which reduces accordingly the actual probability for an atom to scatter from this beam. The finite depth of the optical dipole trap allows in principle for free evaporation of high-energy atoms. This effect is controlled by an effective truncation parameter $\eta = (U - k_B T_F)/k_B T \approx 19$, which is large enough that escape of atoms can be neglected.

Non-interacting reservoirs. We took another set of data with parameters similar to the ones of Fig. 2, with the interaction strength tuned to zero. The reservoirs are prepared as described in the main text, with the same initial particle numbers and a temperature of $T = 50(10)$ nK $= 0.13 T_F$. The confinement in the QPC was $\nu_z = 10.4$ kHz and $\nu_x = 31.8$ kHz, and the observation time was set to 4 s. Before starting the transport process, the magnetic field was ramped to 567.8 G, where the scattering length amounts to $a = -4a_0$ (ref. 39). This corresponds to an elastic scattering time of 850 s for atoms above the Fermi level, placing the reservoirs in non-interacting conditions. Even though the cloud is prepared in thermal equilibrium, the subsequent evolution of the reservoirs is non-thermal. Applying the same data processing as for the weakly interacting gas, we obtain the same step features, as presented in Extended Data Fig. 2 (filled magenta squares). The data was taken simultaneously with a reference data set (open blue circles in Extended Data Fig. 2), where the scattering length was set to $a = -187a_0$, as it was for all the data presented in the main text. By comparison, we see that the complete absence of interactions does not lead to any noticeable change in the conductance. The theory curve in Extended Data Fig. 2 includes a common shift of 150 nK in the local chemical potential in the QPC for both scattering lengths, arising most probably from a finite contrast in the intensity profile of the QPC.

Note that formally, the absence of thermal equilibrium prevents us from defining a chemical potential in the reservoirs. Thus, the conductance cannot be deduced from the ratio of current to particle number imbalance and compressibility. For clarity, to allow for a direct comparison of weakly and non-interacting gases, we nevertheless present the data in the same way because they result from the same data processing procedure.

Adiabaticity estimate. In the Laudauer picture, the observation of quantized conductance relies on the fact that no transitions between transverse modes take place inside the point contact. In principle, this could be the case because in their rest frame, the moving atoms see a time-dependent confinement leading to possible transitions between modes when this change is too fast. Specifically, atoms will stay in the same transverse energy state $E_n = \hbar\omega_n$ if, in the frame moving with the atoms, the temporal change of this energy $\hbar\dot{\omega}_n$ relative to the level spacing $\Delta E = \hbar\Delta\omega$ is small compared to $\Delta\omega$ itself[40]:

$$\left|\frac{\dot{\omega}_n}{\Delta\omega}\right| \ll \Delta\omega \tag{3}$$

Because $\Delta\omega$ is very small far away from the QPC, this criterion can be fulfilled only in the region of the QPC and necessarily fails at its entrance and exit. The criterion to observe quantized conductance is then that the breakdown of adiabaticity should take place inside the reservoirs, that is, where many modes are populated[28]. The non-adiabatic motion of atoms entering the reservoir ensures that the longitudinal and transverse degrees of freedom are coupled. Then atoms move in the anharmonic reservoirs with random initial momenta, leading to open trajectories and effectively randomizing the momentum directions. This mechanism redistributes the energy of an atom between its different degrees of freedom, independently of the presence of interactions.

We now calculate the extent to which equation (3) is satisfied for the atoms moving through our QPC. We present the analysis only for the transverse energy states along the x direction, which are the limiting case because they vary faster along y than do their counterparts along the z direction. Taking into account the Gaussian envelope of the QPC confinement, $f_x(y) = e^{-y^2/w_y^2}$ (see above), equation (3) reads

$$\left|\frac{\nu_{x,0}(n_x + 1/2)\dot{f}_x(y)}{\nu_{x,0} f_x(y)}\right| \ll 2\pi\nu_{x,0} f_x(y)$$

where $\nu_{x,0}$ is the central trapping frequency of the QPC along x, which was referred to as simply ν_x in the main text. For $n_x = 0$ we obtain

$$\left|\frac{y}{w_y^2}\dot{y}\right| \ll 2\pi\nu_{x,0} f_x(y) \tag{4}$$

where the velocity $\dot{y}$ is determined by the kinetic energy along the transport axis, which is the local chemical potential $\mu + V_g$ minus the transverse energy E_{n_x,n_y}. On the qth plateau the modes ($n_x = 0$; $n_z = 0, \ldots, q-1$) are populated and their corresponding longitudinal velocities are

$$\dot{y} = \sqrt{2[q - (n_z + 1/2)]h\nu_z/m} \tag{5}$$

with m the mass of the lithium atoms. Inserting equation (5) into equation (4), we plot both sides of the inequality as functions of y, as shown in Extended Data Fig. 3 for the case of $q = 3$. At a distance of $y_s \approx 1.5 w_y$ from the centre of the QPC the $\dot{\omega}_{x,n_x=0}/\Delta\omega_x$ curves intersect $\Delta\omega_x$, defining an interval $[-y_s, y_s]$ within which adiabatic motion of the atoms is assumed. This interval is larger than the width $\sim 2w_y$ of the QPC. Note that for a given q, the mode with the largest quantum number n_z, that is, $n_z = q - 1$, fulfils the adiabaticity criterion best because it has least kinetic energy along the transport direction and, thus, the smallest velocity $\dot{y}$ entering in equation (5). It is represented by the dash–dot line in Extended Data Fig. 3. For the same reason, counting downwards in n_z leads to successive increases in the slope of the $\dot{\omega}_{x,n_x=0}/\Delta\omega_x$ curve in Extended Data Fig. 3, and, thus, to a slightly smaller value of y_s.

The criterion for exact conductance quantization can be formulated more precisely when considering an adiabatic opening of the constriction, terminating in a sudden opening to the reservoirs. Then the condition for full transmission of the mode n_x is that at the position y_0 of the sudden opening n_x is much smaller than the maximum mode number $n_{x,\max} \approx (\mu + V_g)/(h\nu_{x,0} f_x(y = y_0))$ available at the sudden opening[28]. Applying this to our case by setting $y_0 \approx y_s$, we obtain $n_{x,\max} \approx 10$ for $q = 3$. This consideration shows that transport through our QPC should be adiabatic within the presented framework.

Possible series resistance to the QPC. In this section we investigate whether an additional resistance in series with the QPC can explain the deviation of the conductance from the universal values at large gate potential, as observed in Fig. 2 and Extended Data Fig. 2. This additional resistance can arise as a contact resistance due to the connection of the reservoirs to the 2D channel if a remixing of transverse modes occurs between the tapered 2D region and the QPC.

Let us consider the effective potential drawn in Fig. 1d. At distances of ~20 μm to the left and right of the central maximum, there are side maxima, which are the result of the combined potential of the 2D confinement and the gate potential. They can be regarded as constrictions in series with the QPC. If transport through the entire structure is phase coherent, the resistance is determined by the largest barrier, which is in our case the central confinement of the QPC. However, if there is a remixing of transverse modes between the individual constrictions, their resistances add[41]. Phase randomization in general can occur as a result of inelastic scattering or effectively in our case by a sufficiently rapidly varying geometry along the transport axis (see 'Adiabaticity estimate'), which leads to intermode transitions[42] and, thus, to a randomization of the relevant longitudinal momentum and the associated phase. Applying this scenario to our geometry, the minima in the effective potential next to the central maximum, which appear for large gate potential, would act as incoherent reservoirs and we could write the measured conductance as

$$G = \left(\frac{1}{G_{QPC}} + \frac{2}{G_{2D}}\right)^{-1}$$

where G_{QPC} is the conductance of the QPC only and G_{2D} is the conductance associated with one of the side maxima of the effective potential. We measured G_{2D} in the absence of the QPC, assuming that transport through the rather smooth effective potential of 2D confinement and gate potential is phase coherent. It is plotted in Extended Data Fig. 4a for the same 2D confinement as for the data of Extended Data Fig. 2 and for a scattering length of $a = -187a_0$. Tuning the scattering length to zero has no effect. Above $V_g \approx 1$ μK the gate potential leads to atom losses in the absence of the QPC, most probably because in this case many more atoms reside in the centre of the gate potential, which can introduce a leak in the trapping potential owing to the potential gradient produced by an imperfectly collimated gate laser beam. To evaluate G_{QPC} from equation (5) for the entire range of gate potentials presented in Extended Data Fig. 2, we linearly extrapolate G_{2D} towards larger values.

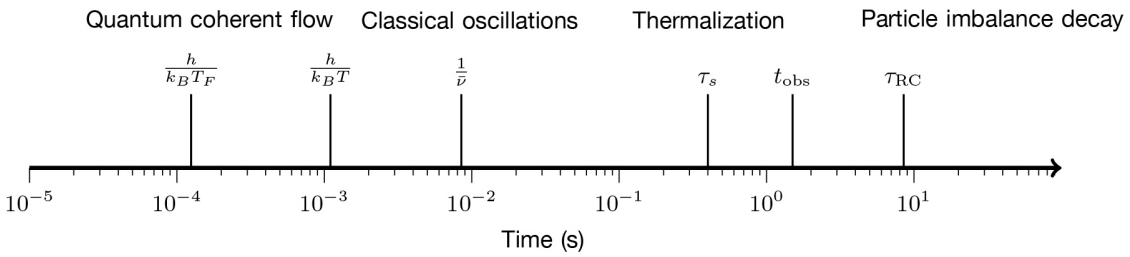
The resulting G_{QPC} is plotted in Extended Data Fig. 4b, and we see that the second plateau of G_{QPC} is now also in agreement with the universal value. It is of course possible that we are in an intermediate situation between phase-coherent transport

©2015 Macmillan Publishers Limited. All rights reserved

and the regime where the resistances of subsequent constrictions add, in which case G would be given by a formula interpolating between the two regimes[41]. Furthermore, the latter regime might be reached only for large gate potentials, in which case equation (5) should be applied only for large gate potentials. However, for small gate potentials, that is, for small conductances G, the contribution of G_{2D} in the evaluation of G_{QPC} is anyway very small, because the resistor $1/G_{QPC}$ then dominates the two resistors $1/G_{2D}$.

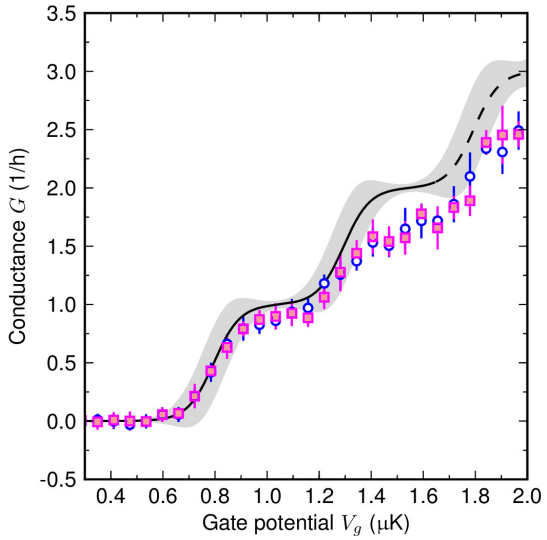
33. Brantut, J.-P. *et al.* A thermoelectric heat engine with ultracold atoms. *Science* **342,** 713–715 (2013).
34. Hung, C.-L., Zhang, X., Gemelke, N. & Chin, C. Accelerating evaporative cooling of atoms into Bose-Einstein condensation in optical traps. *Phys. Rev. A* **78,** 011604 (2008).
35. Beria, M., Iqbal, Y., Di Ventra, M. & Müller, M. Quantum-statistics-induced flow patterns in driven ideal Fermi gases. *Phys. Rev. A* **88,** 043611 (2013).
36. Gattobigio, G. L., Couvert, A., Georgeot, B. & Guéry-Odelin, D. Exploring classically chaotic potentials with a matter wave quantum probe. *Phys. Rev. Lett.* **107,** 254104 (2011).
37. O'Hara, K. M., Gehm, M. E., Granade, S. R. & Thomas, J. E. Scaling laws for evaporative cooling in time-dependent optical traps. *Phys. Rev. A* **64,** 051403 (2001).
38. Du, X., Zhang, Y. & Thomas, J. E. Inelastic collisions of a fermi gas in the BEC-BCS crossover. *Phys. Rev. Lett.* **102,** 250402 (2009).
39. Zürn, G. *et al.* Precise characterization of Li^6 Feshbach resonances using trap-sideband-resolved RF spectroscopy of weakly bound molecules. *Phys. Rev. Lett.* **110,** 135301 (2013).
40. Migdal, A. *Qualitative Methods in Quantum Theory* 115–118 (Perseus, 2000).
41. Büttiker, M. Role of quantum coherence in series resistors. *Phys. Rev. B* **33,** 3020–3026 (1986).
42. Ulreich, S. *Transport Durch Ballistische Leiter* 44–52, PhD thesis, LMU München (1997).

©2015 **Macmillan Publishers Limited. All rights reserved**



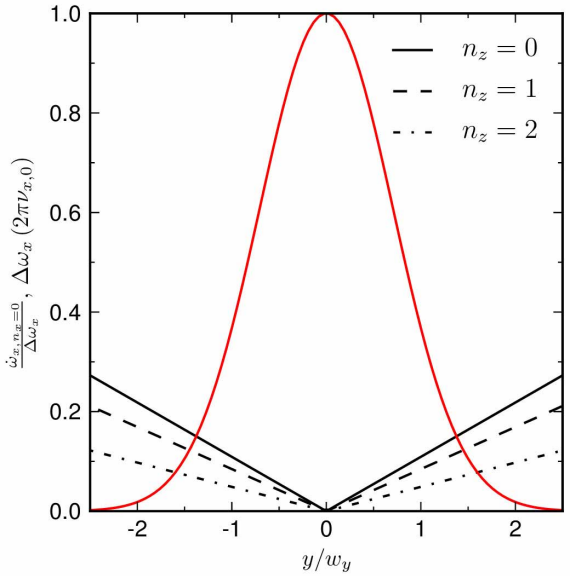
Extended Data Figure 1 | Distribution of timescales in the reservoirs. The corresponding physical phenomena are indicated on the time line. The meanings of the different notations are defined in the text.

©2015 Macmillan Publishers Limited. All rights reserved



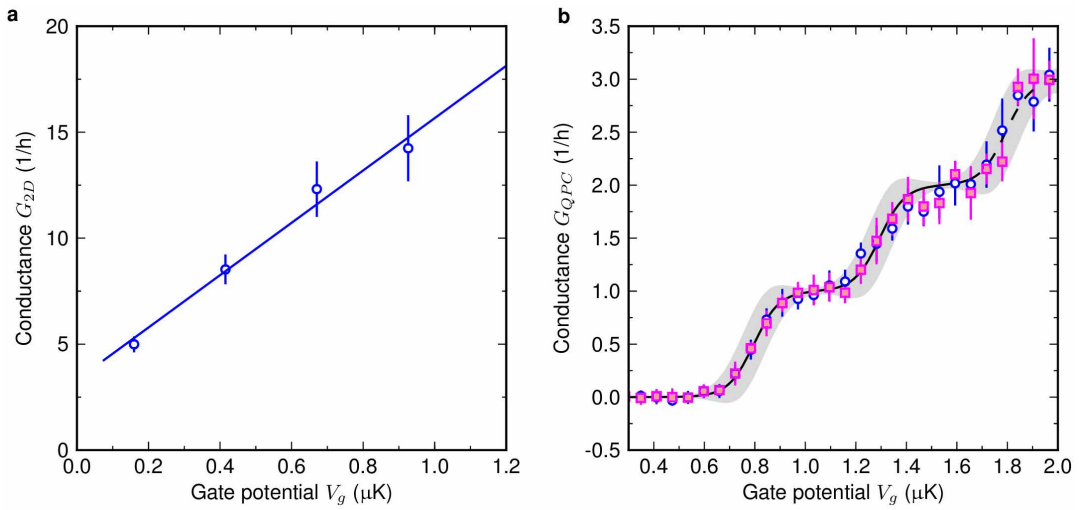
Extended Data Figure 2 | Conductance as a function of gate potential for non-interacting reservoirs. Filled magenta squares correspond to a scattering length of $a = -4a_0$, whereas open blue circles represent a reference data set for weakly interacting reservoirs, where $a = -187a_0$. Each data point is the mean of nine measurements, and error bars indicate one standard deviation. The black line is a theoretical prediction based on the Landauer formula of conductance, and the shaded region reflects the uncertainties in the input parameters.

©2015 Macmillan Publishers Limited. All rights reserved



Extended Data Figure 3 | Illustration of the adiabaticity criterion. Transverse energy level spacing $\Delta\omega_x = \Delta E_x/h$ along the tightly confined QPC direction (solid red line), and corresponding temporal change in the ground-state trapping frequency in the moving frame of the atoms $\dot{\omega}_{x,n_x=0}/\Delta\omega$ as a function of position along the QPC for the three possible values of n_z when $q = 3$ modes are populated.

©2015 Macmillan Publishers Limited. All rights reserved



Extended Data Figure 4 | Conductance of the 2D region and of the QPC as a function of gate potential. **a**, Conductance G_{2D} as a function of gate potential in the absence of the QPC. The solid line is a linear fit to the data. **b**, Conductance G_{QPC} of the QPC only, when considering the contact resistances of the 2D confinement as series resistors to the QPC. The data set, colour code, solid line and shaded region are the same as in Extended Data Fig. 2. Error bars are obtained by propagating the errors in G and G_{2D}.

©2015 Macmillan Publishers Limited. All rights reserved

LETTER

doi:10.1038/nature14060

An anisotropic hydrogel with electrostatic repulsion between cofacially aligned nanosheets

Mingjie Liu[1], Yasuhiro Ishida[1], Yasuo Ebina[2], Takayoshi Sasaki[2], Takaaki Hikima[3], Masaki Takata[3] & Takuzo Aida[1,4]

Machine technology frequently puts magnetic or electrostatic repulsive forces to practical use, as in maglev trains, vehicle suspensions or non-contact bearings[1,2]. In contrast, materials design overwhelmingly focuses on attractive interactions, such as in the many advanced polymer-based composites, where inorganic fillers interact with a polymer matrix to improve mechanical properties. However, articular cartilage strikingly illustrates how electrostatic repulsion can be harnessed to achieve unparalleled functional efficiency: it permits virtually frictionless mechanical motion within joints, even under high compression[3,4]. Here we describe a composite hydrogel with anisotropic mechanical properties dominated by electrostatic repulsion between negatively charged unilamellar titanate nanosheets[5] embedded within it. Crucial to the behaviour of this hydrogel is the serendipitous discovery of cofacial nanosheet alignment in aqueous colloidal dispersions subjected to a strong magnetic field, which maximizes electrostatic repulsion[6] and thereby induces a quasi-crystalline structural ordering[7,8] over macroscopic length scales and with uniformly large face-to-face nanosheet separation. We fix this transiently induced structural order by transforming the dispersion into a hydrogel[9,10] using light-triggered *in situ* vinyl polymerization[11]. The resultant hydrogel, containing charged inorganic structures that align cofacially in a magnetic flux[12–19], deforms easily under shear forces applied parallel to the embedded nanosheets yet resists compressive forces applied orthogonally. We anticipate that the concept of embedding anisotropic repulsive electrostatics within a composite material, inspired by articular cartilage, will open up new possibilities for developing soft materials with unusual functions.

In an extension of our work on water-rich hydrogels supported by a three-dimensional supramolecular network composed of clay nanosheets[20,21], here we replace clays with metal-oxide nanometre-scale sheets. We focused on the unilamellar titanate(IV) nanosheet TiNS (ref. 5, Supplementary Fig. 1a), which combines a number of unusual features (Fig. 1). It consists only of surface atoms adopting a single-crystal-like two-dimensional array and is therefore ultrathin (0.75 nm), with an exceptionally high aspect ratio of about $\sim 10^4$ (Fig. 1b). In aqueous media, it has a high density of negative surface charges that are screened by counterions to give an electric double layer; these counterions ensure efficient dispersion without the need for surfactants. Irradiation with ultraviolet light (wavelength $\lambda \approx 260$ nm) of an aqueous colloidal dispersion of the semiconducting TiNSs produces hydroxyl radicals that trigger *in situ* radical polymerization of added acrylamide derivatives into polymer chains, which are then non-covalently linked by the TiNSs to produce a cross-linked hydrogel network[11] (Fig. 1d). During the course of our present investigation we also discovered that colloidally dispersed TiNSs in a strong magnetic field will align cofacially (Fig. 2a), which gives rise to unusual electrostatics in that it maximizes the electrostatic repulsive force acting between two sheets[6] (Fig. 1a).

Although magnetic orientation is classically used for non-contact and nondestructive orientation of one- and two-dimensional anisotropic objects[22,23], it is rarely applied to metal-oxide nanosheets[12–14]. In the most studied system, that of the diamagnetic niobate(V) nanosheet NbNS (Fig. 1c and Supplementary Fig. 1b)[12,13], the sheets align not cofacially as in TiNS (Fig. 2a), but parallel to the applied magnetic flux (Fig. 2b), as shown using light-scattering measurements. With no applied magnetic field, an aqueous dispersion containing 0.4 wt% NbNS exhibited an optical transmittance of 22% at 450 nm (broken line in Fig. 2d). Upon placing the dispersion in a superconducting 10 T magnet with its magnetic flux directed orthogonal to the incident light ($\perp$) and then parallel (//), the optical transmittance fell to 18% and then increased to 27%, respectively (Fig. 2d and Supplementary Fig. 4b and d). These magnetic-field-induced changes in optical transmittance are as expected, given the reported orientation behaviour of NbNS in a magnetic field (Fig. 2b)[12,13].

In contrast, TiNS, with its orthogonal sheet orientation to an applied magnetic flux (Fig. 2a), exhibits opposite and also more pronounced magneto-responsive changes: the optical transmittance of a 0.4 wt% TiNS dispersion changed from 67% for orthogonal conditions to 13% for parallel conditions (Fig. 2c and Supplementary Fig. 4a and c). We also note that, as sketched in Fig. 2b and d, NbNSs are still able to rotate freely around the orientation vector[12,13] upon application of a magnetic field, whereas TiNSs form a layered structure with a quasi-crystalline order on a macroscopic length scale, giving rise to a larger optical anisotropy (Fig. 2c) than that seen with NbNSs (Fig. 2d). Superconducting quantum interference device (SQUID) measurements confirm that both TiNS and NbNS are diamagnetic (Supplementary Fig. 3), and the orientation behaviour of both species is consistent with that predicted by a theory established for diamagnetic species (Supplementary Fig. 2 and Supplementary Table 2)[24].

When attenuating the applied magnetic field from 10 T to <4 T, the TiNS dispersion began to lose its optical anisotropy owing to thermal structural relaxation (Supplementary Fig. 5). As expected from the results of earlier works that locked in structural features by covalent crosslinking[17,19,25], this relaxation was completely suppressed by converting the dispersion into a hydrogel using our light-triggered *in situ* polymerization method[11] (Fig. 3a) and the anisotropy of the supramolecular gel product was visible to the naked eye (Fig. 3b). We used here a small amount of an organic crosslinker (Fig. 1d) to tune the mechanical properties of the hydrogel (Supplementary Information section 4). As shown in Fig. 3b, the resultant hydrogel looked opaque when viewed along the applied magnetic flux direction (see Fig. 3b, (i)) but exhibited high optical transparency when viewed from orthogonal directions (see Fig. 3b, (ii) and (iii)).

Synchrotron X-ray measurements on the optically anisotropic hydrogel (TiNS; 0.6 wt%) with beams orthogonal to the TiNS plane produced a two-dimensional small-angle X-ray scattering (SAXS) profile with only a single diffuse spot (Fig. 3c, (i)), whereas parallel X-ray beams produced a SAXS profile with a linear array of multiple diffuse spots up to the (500) face (Fig. 3c, (ii)) that indicates that TiNSs align with a uniform plane-to-plane separation of 35.5 nm. This separation expands to 52.4 nm upon twofold dilution of the dispersion (TiNS; 0.3 wt%) before the dispersion was converted to the gel. Upon further dilution to 0.1 wt%, the diffuse

[1]RIKEN Center for Emergent Matter Science, 2-1 Hirosawa, Wako, Saitama 351-0198, Japan. [2]National Institute for Materials Science, International Center for Materials Nanoarchitectonics, 1-1 Namiki, Tsukuba, Ibaraki 305-0044, Japan. [3]RIKEN SPring-8 Center, 1-1-1 Kouto, Sayo, Hyogo 679-5198, Japan. [4]Department of Chemistry and Biotechnology, School of Engineering, The University of Tokyo, 7-3-1 Hongo, Bunkyo-ku, Tokyo 113-8656, Japan.

©2015 Macmillan Publishers Limited. All rights reserved

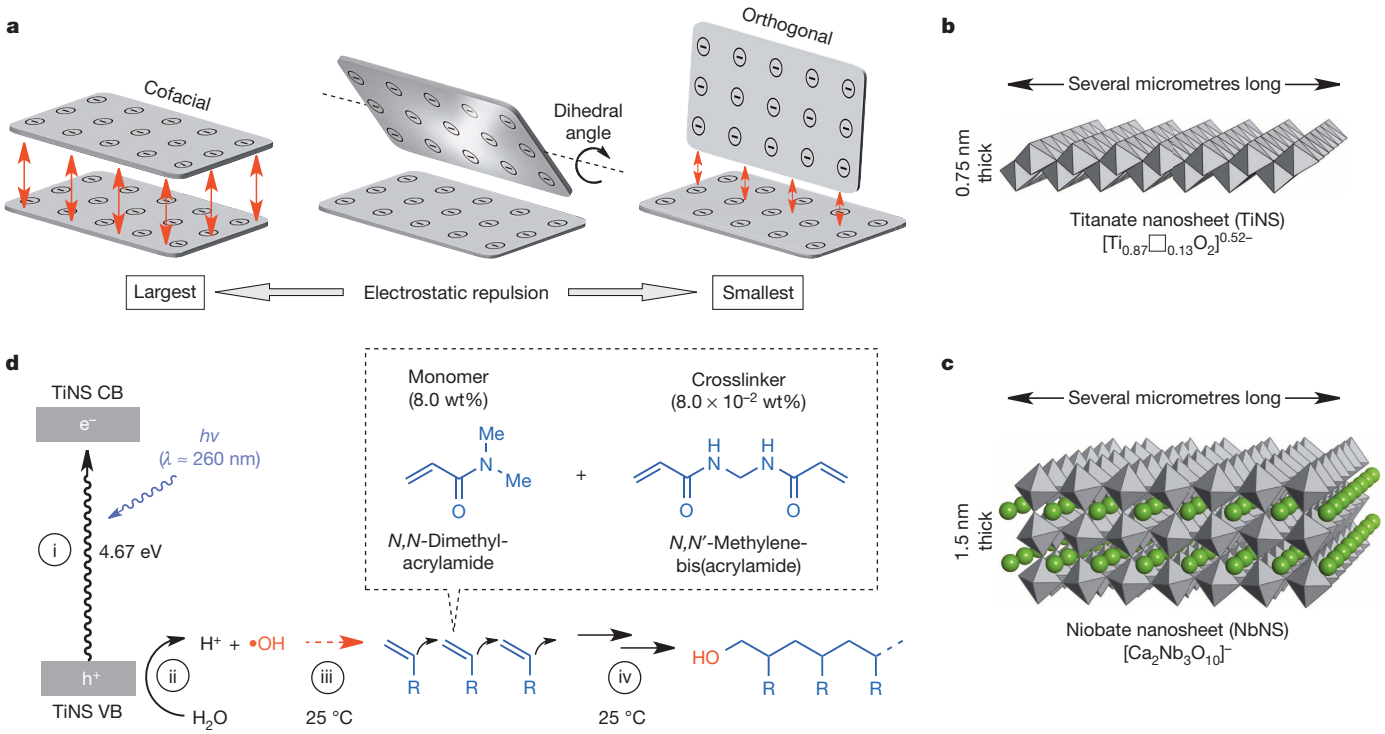


Figure 1 | Negatively charged unilamellar metal-oxide nanosheets of titanate (TiNS) and niobate (NbNS). **a**, Metal-oxide nanosheets in close proximity to one another are electrostatically repulsive. When two nanosheets are positioned at a fixed distance, the repulsive force changes with their dihedral angle, where cofacial (dihedral angle = 0°; left) and orthogonal (dihedral angle = 90°; right) nanosheet orientations provide the maximum and minimum repulsive forces, respectively. The counterions, which form a cationic layer, are omitted for simplicity. **b**, **c**, Schematic structures of TiNS (**b**) and NbNS (**c**) negatively charged, having Me_4N^+ counterions. □ means a vacant site. **d**, Elementary steps for photo-induced hydrogelation at 25 °C by using crosslinking polymerization of a mixture of mono- and difunctional acrylamide derivatives ((iii) and (iv)) initiated by hydroxyl radicals, generated *in situ* upon photoexcitation of TiNS ((i) and (ii)) in aqueous media. VB and CB indicate the valence and conduction bands, respectively, while *hv* is the photon energy. R represents substituents of vinyl monomers.

spots turned obscure (Fig. 3d and Supplementary Fig. 6), indicating that the critical volume fraction of TiNSs for the formation of a uniformly spaced layered structure is approximately 0.03 vol%. As determined from the scattering intensity–azimuthal angle plots (Supplementary Fig. 6), the degree of orientation is remarkably high, with an order parameter of 0.96 (ref. 26). Taking into account that in our dispersion TiNS is negatively charged and attracts tetramethylammonium (Me_4N^+) counterions to furnish an electric double layer, we consider that the most likely explanation for the quasi-crystalline structural order of the system is the electrostatic repulsion among the cofacially oriented TiNSs.

As sketched in Fig. 1a (left), the inter-plane electrostatic repulsion is maximal when the TiNSs are cofacial to one another[6] and the resultant thermodynamic instability can be minimized if the cofacially oriented sheets adopt a uniformly large face-to-face separation that gives rise to a quasi-crystalline structural order[7,8]. This interpretation is supported by the addition of an electrolyte such as Me_4NOH (24 mM) to a 0.8 wt% TiNS dispersion to screen the internal electrostatic repulsion[27], with the plane-to-plane separation in the product hydrogel falling indeed as expected, from 29.7 nm to 9.3 nm (Fig. 3e and Supplementary Fig. 7). We note that when accounting for the large extent of 'contact ion pairing' between TiNS surface charges and Me_4N^+, as indicated by a zeta potential analysis (Supplementary Table 1), the observed distances between nanosheets in Fig. 3d and e appear to obey Debye theory (Supplementary Fig. 8c). We also note that the SAXS pattern became quite ambiguous when producing gels in a lower-dielectric medium composed of a 50:50 mixture of water and ethylene glycol (by volume) (Supplementary Fig. 9), establishing that a highly dielectric medium such as water is essential for forming a TiNS-based hydrogel with long-range structural order.

In view of the anisotropic electrostatic features embedded within our hydrogel, we conjectured that it might resist compressive forces if these are applied orthogonal to the TiNS plane (Fig. 4a), yet readily deform along a shear force applied parallel to the TiNS plane (Fig. 4b). To test this, we prepared three cylindrical pillars (Fig. 4g, 20 mm in diameter and height) from the magnetically structured hydrogel so that cofacially oriented TiNSs (0.8 wt%) are aligned parallel to the cylinder cross-section. The pillars were positioned 40 mm apart on a mechanical oscillator in a triangular geometry to support a glass stage (130 mm in diameter, 5 mm in thickness and 160 g in weight) featuring at its centre a metal sphere (30 mm in diameter and 40 g in weight) on a tee. As shown in Supplementary Video 1, application of a large and continuous oscillatory motion caused restricted and mostly horizontal deformation of the cylindrical pillars. This kept the upper glass stage untilted and moved it only slightly from its initial coordinates, thereby allowing the metal sphere to stay on the tee. In contrast, when we used hydrogel cylinders that had their embedded TiNSs (0.8 wt%) oriented either orthogonal to the cylinder cross-section or randomly, similar experiments caused spatially unrestricted and more severe deformations and generated large irregular displacements for the upper glass stage (Fig. 4h and Supplementary Videos 2 and 3). We emphasize that a mere 0.8 wt% of two-dimensional nanosheets, depending on their orientation within the pillars, gives rise to these strikingly different behaviours.

Further in-depth, quantitative testing of the mechanical properties of a hydrogel containing cofacially oriented TiNSs (0.8 wt%) revealed, upon compression, a stress–strain curve typical of hydrogels but with a stress profile that is clearly dependent on the direction of the compressive force applied to the material (Fig. 4c). Compression orthogonal ($\perp$) to the TiNS plane yielded a tangent elastic modulus $E_\perp$ of 66 kPa at 40% strain, which is 2.6 times greater than the tangent elastic modulus of $E_{//} = 25$ kPa obtained when compressing the hydrogel parallel (//) to the TiNS plane. $E_\perp$ gradually increased with increasing TiNS content ([TiNS]), whereas $E_{//}$ appeared to reach a plateau. Consequently, the gap

©2015 Macmillan Publishers Limited. All rights reserved

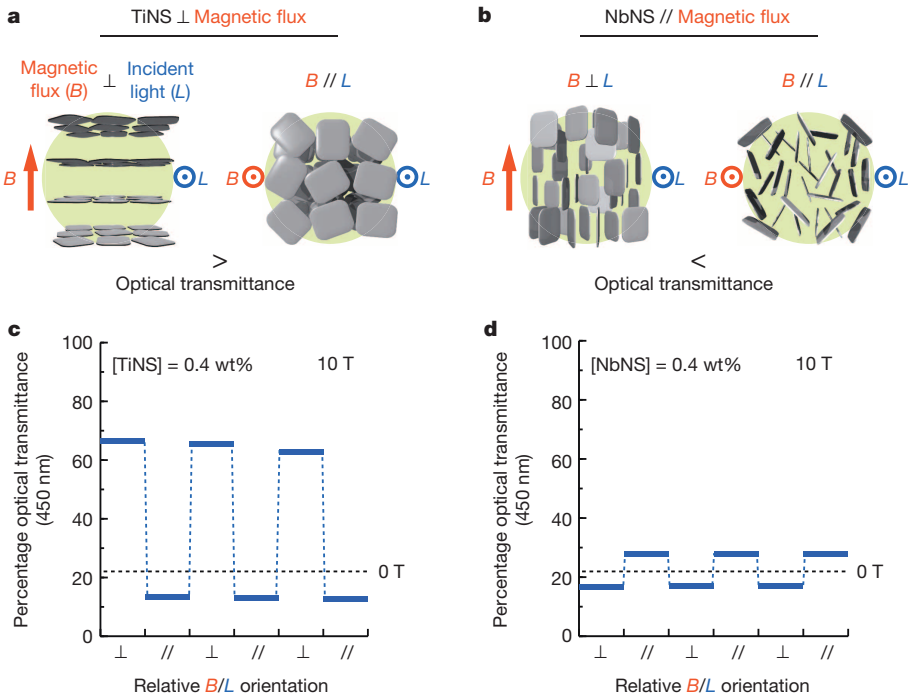


Figure 2 | Magnetic responses of the unilamellar metal-oxide nanosheets TiNS and NbNS. a, TiNSs orient their two-dimensional plane orthogonal to an applied magnetic flux, so that they are cofacial. The optical transmittance along the magnetic flux is smaller than that in its orthogonal direction. **b**, NbNSs direct their orientation vector parallel to an applied magnetic flux, and are freely rotatable around the orientation vector. The optical transmittance along the magnetic flux is larger than that in its orthogonal direction. **c**, **d**, Optical transmittances at 450 nm of aqueous colloidal dispersions of TiNSs (**c**) and NbNSs (**d**) (both 0.4 wt%) upon orthogonal and parallel directions of a 10 T magnetic flux to the incident light. For optical measurements, the dispersions contained 8.0 wt% poly(*N*,*N*-dimethylacrylamide) as a thickener. Dotted lines represent optical transmittances of the dispersions without magnetic flux.

between $E_{\perp}$ and $E_{//}$, as a measure of mechanical anisotropy, became larger as [TiNS] increased (Fig. 4e and Supplementary Fig. 10a and c).

The anisotropic nature of the structured hydrogel is also reflected in its rheological properties (Fig. 4d), in that shearing parallel to the TiNS plane gave a storage modulus $G'_{//}$ of 0.6 kPa, whereas shearing of the same hydrogel sample orthogonal to the TiNS plane gave $G'_{\perp} = 2.2$ kPa. Oscillation experiments vividly illustrate these features: an unweighted hydrogel cylinder with horizontally oriented TiNSs (0.8 wt%) deforms at its free edge much more strongly than a hydrogel cylinder with vertically oriented TiNSs (Supplementary Video 4). Similar to what is seen during compression testing, $G'_{\perp}$ monotonically increased with [TiNS]; however, $G'_{//}$ increased only initially with [TiNS] and then started to fall off after [TiNS] exceeded around 0.2 wt% (Fig. 4f and Supplementary Fig. 10b and d). Because TiNSs provide the crosslinks in the hydrogel[11],

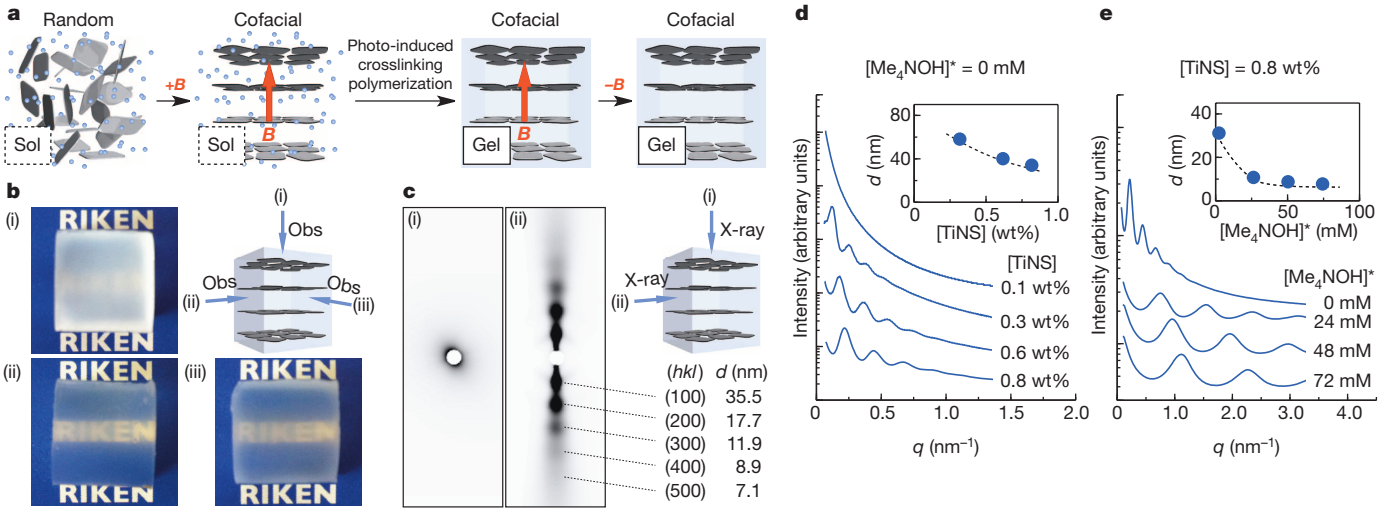


Figure 3 | Structural and optical anisotropic features of hydrogels containing cofacially oriented TiNSs in a quasi-crystalline order. a, Spatial immobilization of cofacially oriented TiNSs by hydrogelation with TiNS-mediated photoinduced crosslinking polymerization (Fig. 1d) in a 10 T magnetic flux. **b**, Optical features of the resultant hydrogel (TiNS; 0.4 wt%) viewed along orthogonal ((i)) and parallel ((ii) and (iii)) directions to the magnetically oriented TiNS plane. **c**, Two-dimensional SAXS images of the resultant hydrogel (TiNS; 0.6 wt%), where the incident X-ray beam was directed orthogonal ((i)) and parallel ((ii)) to the magnetically oriented TiNS plane. **d**, **e**, Effects of [TiNS] at a constant Me_4N^+/TiNS ratio (13 mM/0.1 wt%) (**d**) and of [Me_4NOH]* (the concentration of externally added Me_4NOH) at a constant [TiNS] (0.8 wt%) (**e**) on one-dimensional SAXS (insets show *d*-spacings of TiNSs) profiles of hydrogels prepared with various amounts of TiNS and Me_4NOH. In the insets of **d** and **e**, each point represents a single measurement.

©2015 Macmillan Publishers Limited. All rights reserved

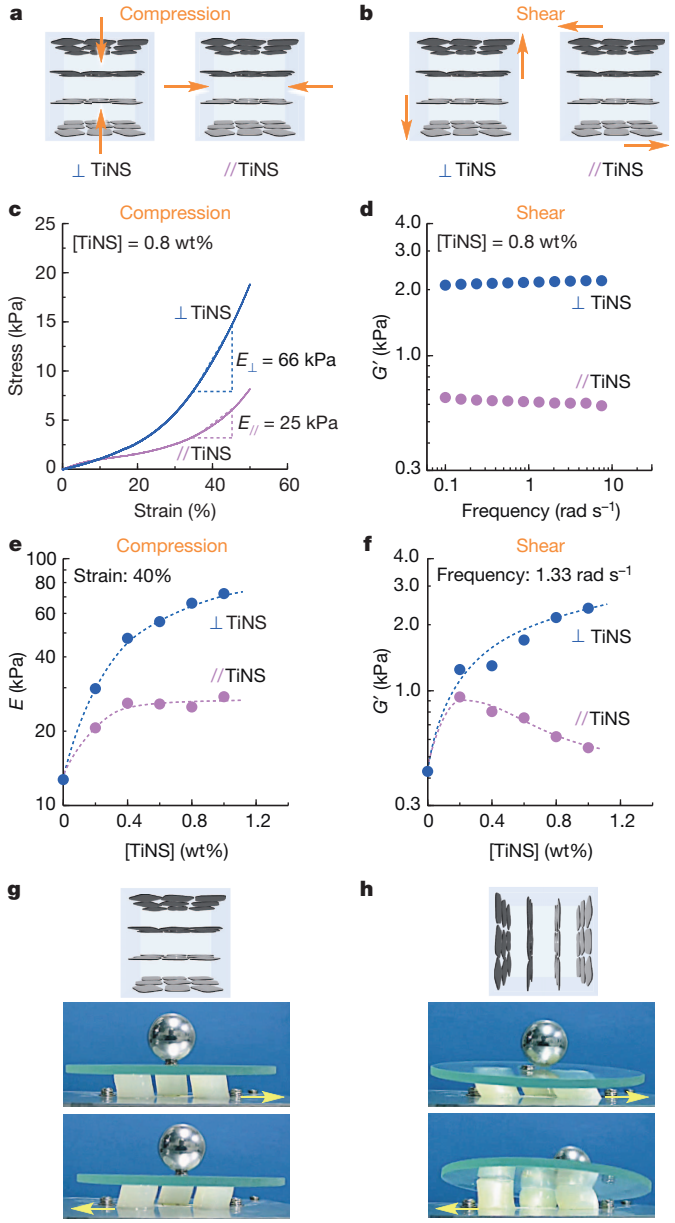


Figure 4 | Mechanical anisotropy of hydrogels containing cofacially oriented TiNSs in a quasi-crystalline order. **a**, **b**, Schematic representations for mechanical deformations of a hydrogel containing cofacially oriented TiNSs (Fig. 1d) sheared (**a**) and compressed (**b**) in orthogonal (left) and parallel (right) directions to the TiNS plane. **c**, Strain–stress curves of a hydrogel (TiNS; 0.8 wt%) with applied compression strain ($\varepsilon = 0$%–50% at a constant compression rate of 20% min^{-1}. **d**, Storage moduli (G') of a hydrogel (TiNS; 0.8 wt%) on frequency ω sweep in a range of 0.1–7.5 rad s^{-1} at a constant shear strain γ of 0.5%. **e**, **f**, Effects of [TiNS] on tangent elastic moduli E at $\varepsilon = 40$% (**e**) and storage moduli G' at $\omega = 1.33$ rad s^{-1} (**f**), where each point represents a single measurement. In **c**–**f**, mechanical properties (in blue and pink) were obtained when the hydrogels were deformed in orthogonal (⊥) and parallel (//) directions to the magnetically oriented TiNS plane, respectively. **g**, **h**, Demonstrations of vibration isolation. On a mechanical oscillator, a glass stage featuring a metal sphere on a tee was supported by three cylindrical pillars of magnetically structured hydrogel containing cofacially oriented TiNSs (0.8 wt%) in parallel (**g**) or orthogonal (**h**) direction to the cylinder cross-section.

the initial increase in $G'_{//}$ with [TiNS] is expected. The reduction in $G'_{//}$ after [TiNS] exceeds around 0.2 wt% might reflect that beyond this critical TiNS concentration, electrostatic repulsion among the cofacially oriented TiNSs dominates $G'_{//}$. The anisotropy of ~7.0 in loss moduli ($G''_{\perp}/G''_{//}$) also supports the conclusion that the unusual electrostatic characteristics of our hydrogel insulates internal mechanical friction in one direction but enhances it orthogonal to that direction (Supplementary Fig. 11), with the large anisotropy in both G' and G'' over a wide range of applied frequency and strain accounting for the excellent performance of our hydrogel in isolating vibrations (Supplementary Video 1). Hydrogels containing randomly oriented TiNSs or magnetically oriented but non-cofacial NbNSs do not exhibit such anisotropic mechanical properties (Supplementary Figs 12 and 13), and such properties are suppressed in hydrogels with cofacially oriented TiNSs prepared in lower-dielectric media such as water/ethylene glycol (50:50 by volume) or in water with 24 mM Me_4NOH added (Supplementary Figs 14 and 15), where electrostatic repulsion is inefficient (Fig. 3d and e).

Although fillers—especially fillers with high aspect ratios—are assumed to enhance the toughness and strength of composite materials[19,28,29], the cofacially oriented charged nanosheets embedded in our hydrogels attenuate friction in one direction while enhancing it orthogonal to that direction, thereby enabling excellent directional isolation of vibrations. Unlike conventional rubber-based anti-vibration materials laminated with multiple metal plates, the amount of energy dissipated in our hydrogels is admittedly minute, owing to its small loss tangent ($G''_{//}/G'_{//}$). However, our hydrogels, whose $G'_{//}$ and $G''_{//}$ are both small, serve as deformable domains with a low internal friction and insulate the effect of a given oscillation. Our materials are readily processable using mainly water, and their G' and G'' values are easily tuned within a given range without loss of the anisotropic mechanical feature by adjusting the amounts of monomer and organic crosslinker used to produce the hydrogel (Supplementary Fig. 16). Of relevance to any potential biomedical applications is that our hydrogel, just like polymer electrolyte hydrogels[30], resists ion penetration (Supplementary Fig. 17), so that upon immersion in physiological saline, its mechanical anisotropy is not appreciably reduced for a week (Supplementary Fig. 18).

Received 15 March; accepted 4 November 2014.

1. Hull, J. R. Superconducting bearings. *Supercond. Sci. Technol.* **13,** R1–R15 (2000).
2. Rhim, W. K. *et al.* An electrostatic levitator for high-temperature containerless materials processing in 1-G. *Rev. Sci. Instrum.* **64,** 2961–2970 (1993).
3. Scott, J. E. Elasticity in extracellular matrix 'shape modules' of tendon, cartilage, etc. A sliding proteoglycan-filament model. *J. Physiol.* **553,** 335–343 (2003).
4. Dean, D., Han, L., Grodzinsky, A. J. & Ortiz, C. Compressive nanomechanics of opposing aggrecan macromolecules. *J. Biomech.* **39,** 2555–2565 (2006).
5. Sasaki, T., Watanabe, M., Hashizume, H., Yamada, H. & Nakazawa, H. Macromolecule-like aspects for a colloidal suspension of an exfoliated titanate. Pairwise association of nanosheets and dynamic reassembling process initiated from it. *J. Am. Chem. Soc.* **118,** 8329–8335 (1996).
6. Anandarajah, A. & Ning, L. Numerical study of the electrical double-layer repulsion between nonparallel clay particles of finite length. *Int. J. Numer. Analyt. Meth. Geomech.* **15,** 683–703 (1991).
7. Cui, H. G. *et al.* Spontaneous and X-ray-triggered crystallization at long range in self-assembling filament networks. *Science* **327,** 555–559 (2010).
8. Palmer, L. C. *et al.* Long-range ordering of highly charged self-assembled nanofilaments. *J. Am. Chem. Soc.* **136,** 14377–14380 (2014).
9. Wu, Z. L. *et al.* Anisotropic hydrogel from complexation-driven reorientation of semirigid polyanion at Ca^{2+} diffusion flux front. *Macromolecules* **44,** 3535–3541 (2011).
10. Wu, J., Zhao, Q., Sun, J. & Zhou, Q. Preparation of poly(ethylene glycol) aligned porous cryogels using a unidirectional freezing technique. *Soft Matter* **8,** 3620–3626 (2012).
11. Liu, M., Ishida, Y., Ebina, Y., Sasaki, T. & Aida, T. Photolatently modulable hydrogels using unilamellar titania nanosheets as photocatalytic crosslinker. *Nature Commun.* **4,** 2029 (2013).
12. Eguchi, M., Angelone, M. S., Yennawar, H. P. & Mallouk, T. E. Anisotropic alignment of lamellar potassium hexaniobate microcrystals and nanoscrolls in a static magnetic field. *J. Phys. Chem. C* **112,** 11280–11285 (2008).
13. Ida, S. *et al.* Photoluminescence of perovskite nanosheets prepared by exfoliation of layered oxides, $K_2Ln_2Ti_3O_{10}$, $KLnNb_2O_7$, and $RbLnTa_2O_7$ (Ln: lanthanide ion). *J. Am. Chem. Soc.* **130,** 7052–7059 (2008).
14. Osada, M. *et al.* Ferromagnetism in two-dimensional $Ti_{0.8}Co_{0.2}O_2$ nanosheets. *Phys. Rev. B* **73,** 153301 (2006).
15. Prosser, S., Hunt, S. A., DiNatale, J. A. & Vold, R. R. Magnetically aligned membrane model systems with positive order parameter: switching the sign of S_{zz} with paramagnetic ions. *J. Am. Chem. Soc.* **118,** 269–270 (1996).
16. Tan, C., Fung, B. M. & Cho, G. Phospholipid bicelles that align with their normals parallel to the magnetic field. *J. Am. Chem. Soc.* **124,** 11827–11832 (2002).
17. Kleinschmidt, F., Hickl, M., Saalwächter, K., Schmidt, C. & Finkelmann, H. Lamellar liquid single crystal hydrogels: synthesis and investigation of anisotropic water diffusion and swelling. *Macromolecules* **38,** 9772–9782 (2005).

©2015 Macmillan Publishers Limited. All rights reserved

18. Haque, M. A., Kamita, G., Kurokawa, T., Tsujii, K. & Gong, J. P. Unidirectional alignment of lamellar bilayer in hydrogel: one-dimensional swelling, anisotropic modulus, and stress/strain tunable structural color. *Adv. Mater.* **22,** 5110–5114 (2010).
19. Erb, R. M., Libanori, R., Rothfuchs, N. & Studart, A. R. Composites reinforced in three dimensions by using low magnetic fields. *Science* **335,** 199–204 (2012).
20. Wang, Q. *et al.* High-water-content mouldable hydrogels by mixing clay and a dendritic molecular binder. *Nature* **463,** 339–343 (2010).
21. Tamesue, S. *et al.* Linear versus dendritic molecular binders for hydrogel network formation with clay nanosheets: studies with ABA triblock copolyethers carrying guanidinium ion pendants. *J. Am. Chem. Soc.* **135,** 15650–15655 (2013).
22. Maret, G. & Dransfeld, K. Biomolecules and polymers in high steady magnetic fields. *Top. Appl. Phys.* **57,** 143–204 (1985).
23. Löwen, H. Colloidal soft matter under external control. *J. Phys. Condens. Matter* **13,** R415–R432 (2001).
24. Uyeda, C. Diamagnetic anisotropies of oxide minerals. *Phys. Chem. Miner.* **20,** 77–81 (1993).
25. Torbet, J., Freyssinet, J. M. & Hudry-Clergeon, G. Oriented fibrin gels formed by polymerization in strong magnetic fields. *Nature* **289,** 91–93 (1981).
26. Feng, S. *et al.* Hierarchical structure in oriented fibers of a dendronized polymer. *Macromolecules* **42,** 281–287 (2009).
27. Verwey, E. J. W. & Overbeek, J. Th. G. *Theory of the Stability of Lyophobic Colloids* (Elsevier, 1948).
28. Podsiadlo, P. *et al.* Ultrastrong and stiff layered polymer nanocomposites. *Science* **318,** 80–83 (2007).
29. Munch, E. *et al.* Tough, bio-inspired hybrid materials. *Science* **322,** 1516–1520 (2008).
30. Budtova, T. & Navard, P. Swelling-induced birefringence of a polyelectrolyte gel strongly interacting with metal ions. *Macromolecules* **30,** 6556–6558 (1997).

Supplementary Information is available in the online version of the paper.

Acknowledgements This work was financially supported by a Grant-in-Aid for Specially Promoted Research (25000005) on ''Physically Perturbed Assembly for Tailoring High-Performance Soft Materials with Controlled Macroscopic Structural Anisotropy''. We also acknowledge the ImPACT Program of Council for Science, Technology and Innovation (Cabinet Office, Government of Japan). The synchrotron X-ray diffraction experiments were performed at BL45XU in SPring-8 with the approval of the RIKEN SPring-8 Center (proposal 20140073).

Author Contributions M.L. designed and performed all experiments. Y.I. and T.A. co-designed the experiments. Y.E. and T.S. prepared colloidally dispersed TiNSs and NbNSs. M.L., Y.I. and T.A. analysed the data and wrote the manuscript. T.H. and M.T. supported the X-ray diffraction measurements at SPring-8.

Author Information Reprints and permissions information is available at www.nature.com/reprints. The authors declare no competing financial interests. Readers are welcome to comment on the online version of the paper. Correspondence and requests for materials should be addressed to Y.I. (y-ishida@riken.jp) or T.A. (aida@macro.t.u-tokyo.ac.jp).

©2015 Macmillan Publishers Limited. All rights reserved

LETTER

doi:10.1038/nature14059

Strong and deep Atlantic meridional overturning circulation during the last glacial cycle

E. Böhm[1], J. Lippold[2], M. Gutjahr[3,4], M. Frank[3], P. Blaser[1], B. Antz[1], J. Fohlmeister[1], N. Frank[1], M. B. Andersen[5] & M. Deininger[1]

Extreme, abrupt Northern Hemisphere climate oscillations during the last glacial cycle (140,000 years ago to present) were modulated by changes in ocean circulation and atmospheric forcing[1]. However, the variability of the Atlantic meridional overturning circulation (AMOC), which has a role in controlling heat transport from low to high latitudes and in ocean CO_2 storage, is still poorly constrained beyond the Last Glacial Maximum[2–4]. Here we show that a deep and vigorous overturning circulation mode has persisted for most of the last glacial cycle, dominating ocean circulation in the Atlantic, whereas a shallower glacial mode with southern-sourced waters filling the deep western North Atlantic prevailed during glacial maxima[3,5]. Our results are based on a reconstruction of both the strength and the direction of the AMOC during the last glacial cycle from a highly resolved marine sedimentary record in the deep western North Atlantic. Parallel measurements of two independent chemical water tracers (the isotope ratios of $^{231}Pa/^{230}Th$ and $^{143}Nd/^{144}Nd$)[6–8], which are not directly affected by changes in the global cycle, reveal consistent responses of the AMOC during the last two glacial terminations. Any significant deviations from this configuration, resulting in slowdowns of the AMOC, were restricted to centennial-scale excursions during catastrophic iceberg discharges of the Heinrich stadials. Severe and multicentennial weakening of North Atlantic Deep Water formation occurred only during Heinrich stadials close to glacial maxima with increased ice coverage, probably as a result of increased freshwater input. In contrast, the AMOC was relatively insensitive to submillennial meltwater pulses during warmer climate states, and an active AMOC prevailed during Dansgaard–Oeschger interstadials (Greenland warm periods).

The question of whether the AMOC has always controlled or at times only responded to climatic oscillations during the last glacial period still awaits full clarification despite its fundamental role in climatology. During the Holocene epoch deep-water formation has been active in the North Atlantic and North Atlantic Deep Water (NADW) has occupied a large fraction of the deep Atlantic basin down to ~5,000 m depth (a circulation mode often referred to as the 'warm', or 'interglacial', circulation mode[1]; Fig. 1). However, the existence of different AMOC modes in the past has been proposed, mostly on the basis of nutrient tracers such as stable carbon isotopes[3,5]. In the 'cold', or 'glacial', mode, the equivalent of NADW has been identified only at shallower depths than today, and is hence termed Glacial North Atlantic Intermediate Water. As a consequence, a large part of the deep North Atlantic was bathed in deep water advected from the Southern Ocean[8,9] (southern-sourced water (SSW)). In addition, there is ample evidence for a third mode that prevailed as a result of transient, catastrophic pulses of meltwater discharges, which essentially led to a collapse of deep-water formation in the North Atlantic during the Heinrich events[1] (the 'off', or 'Heinrich', mode). These shifts highlight the sensitivity of North Atlantic convection to buoyancy forcing, in particular to fresh-water inputs.

Here we reconstruct changes in the AMOC based on combined extraction of seawater radiogenic neodymium (Nd) isotopes and particulate $^{231}Pa_{xs,0}/^{230}Th_{xs,0}$ (the activity ratio of unsupported ^{231}Pa and ^{230}Th in sediments, decay-corrected to the time of deposition; $^{231}Pa/^{230}Th$ hereafter) from sediments recovered in the deep subtropical northwest Atlantic (Bermuda Rise; ODP Site 1063, Leg 172, 33° 41′ N, 57° 37′ W, water depth 4,584 m; Supplementary Information). Owing to its position in the mixing zone between NADW and Antarctic Bottom Water, this site has sensitively recorded past changes in circulation dynamics and water mass mixing[10,11]. The $^{143}Nd/^{144}Nd$ ratio (expressed as ε_{Nd}, the deviation, in parts per 10,000, of the measured $^{143}Nd/^{144}Nd$ ratio from that of the chondritic uniform reservoir) is used as a quasi-conservative proxy for changes in sources and mixing of water masses[7,12]. The key difference in Nd isotope signatures between the major water masses in the Atlantic is the significantly less radiogenic (lower) ε_{Nd} signature of NADW (mostly as a result of the contribution of highly unradiogenic Labrador Sea water (LSW)) relative to that of SSW. Thus, this tracer allows the determination of changes in the relative contributions of waters originating from the North Atlantic and the Southern Ocean at the core site[8]. In contrast, $^{231}Pa/^{230}Th$ is a measure of the overall strength of the AMOC[6]. Unlike their homogeneously distributed dissolved parents ^{234}U and ^{235}U, from which both isotopes are uniformly produced in seawater by radioactive decay, ^{231}Pa and ^{230}Th are particle reactive. However, a difference in the timescale of removal causes a preferential export of ^{231}Pa to the Southern Ocean, and low $^{231}Pa/^{230}Th$ in the deep Atlantic is consequently a sensitive indicator of a strong, large-scale AMOC. In turn, high $^{231}Pa/^{230}Th$ approaching the production ratio (0.093) indicates a weak or collapsed AMOC[13].

The data set presented here extends beyond the Eemian interglacial into the glacial before termination 2 (140 kyr ago). It reveals fundamental changes in the AMOC under variable forcings, including orbital parameters, continental ice-sheet volume and the associated sea-level variability. In addition, high sedimentation rates at the core location (10–150 cm kyr^{-1}) allow the resolution of short-term climatic excursions such as the Dansgaard–Oeschger interstadials[14]. The combination of high-resolution records of Nd isotopes (used to identify deep-water provenance) with $^{231}Pa/^{230}Th$ (tracing AMOC strength) obtained from the same samples excludes any chronological or phasing issues.

Direct comparison of the tracer's time series across glacial terminations 2 and 1 reveal differences and similarities in the timings and amplitudes of changes in both ε_{Nd} and $^{231}Pa/^{230}Th$ (Fig. 2). Glacial maxima were characterized by radiogenic (less negative) ε_{Nd} signatures of about −11 and thus clearly indicate a strongly enhanced presence of SSW in the deep North Atlantic. The deep circulation abruptly switched to a regime dominated by northern-sourced water (NSW) by the time of onset of the following interglacials. Furthermore, both deglaciations were characterized by a drastically weakened export of NADW during Heinrich stadials 1 and 11 (HS1 and HS11, respectively), as indicated by $^{231}Pa/^{230}Th$ values close to the production ratio[13]. Although orbital forcing and the evolution of ice volume were different in each termination[15], the strikingly similar evolution of the AMOC during terminations 1 and 2 (Fig. 2) suggests a coherent response of high-latitude

[1]Institute of Environmental Physics, University of Heidelberg, 69120 Heidelberg, Germany. [2]Oeschger Centre for Climate Change Research, Institute of Geological Sciences, University of Bern, 3012 Bern, Switzerland. [3]GEOMAR Helmholtz Centre for Ocean Research Kiel, 24148 Kiel, Germany. [4]National Oceanography Centre Southampton, Southampton SO14 3ZH, UK. [5]Institute of Geochemistry and Petrology, ETH Zürich, 8092 Zürich, Switzerland.

©2015 Macmillan Publishers Limited. All rights reserved

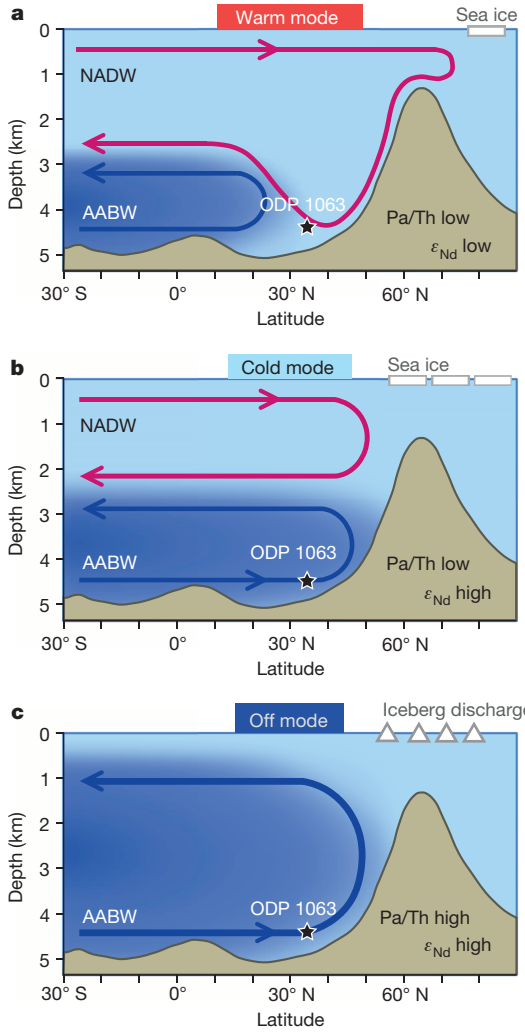


Figure 1 | Conceptual modes of the AMOC. The diagrams depict the interplay of NSW (red) and SSW (blue) masses bathing sediment core ODP 1063 (black star) (following ref. 1). **a**, The warm mode is dominated by deep ventilation of NADW. At the position of ODP 1063 this is reflected by low $^{231}Pa/^{230}Th$ and unradiogenic (more negative) ε_{Nd} signatures (the deviation, in parts per 10,000, of the measured $^{143}Nd/^{144}Nd$ ratio from that of the chondritic uniform reservoir). AABW, Antarctic Bottom Water. **b**, The cold mode was characterized by an active but shoaled northern circulation cell resulting in a significantly more-positive ε_{Nd} signature, and $^{231}Pa/^{230}Th$ increased only slightly. **c**, The off mode represents the near shutdown of NADW formation and the dominance of SSW in the deep and intermediate North Atlantic. In this mode ε_{Nd} did not differ from the cold mode and $^{231}Pa/^{230}Th$ increased significantly.

ocean stratification and deep-water formation to the large-scale melting of continental ice sheets and the subsequent sea-level rise following peak glacial conditions (Fig. 3). In contrast to termination 1, no event like the Younger Dryas occurred during termination 2 (Fig. 2), indicating that a temporary switch back to glacial conditions has not been an inherent feature of deglacial periods during the late-Quaternary period[16]. Another difference between the two glacial–interglacial transitions is the timing of the reorganization of Atlantic deep-water circulation: during termination 1 both circulation strength ($^{231}Pa/^{230}Th$) and prevailing water masses (ε_{Nd}) switched rapidly and synchronously to the interglacial mode of the Bølling–Allerød warm period. In contrast, during termination 2 radiogenic ε_{Nd} signatures imply that SSW was still present at the core location until 127 kyr ago, when Northern Hemisphere summer insolation was already well above modern levels. Very low $^{231}Pa/^{230}Th$ ratios at the end of termination 2 point to an exceptionally vigorous but shallow NSW overturning cell, still underlain by significant volumes of SSW.

Distinct time intervals of different prevailing modes of Atlantic deep circulation are documented in our new records (Fig. 3). A persistent baseline of low $^{231}Pa/^{230}Th$ well below the production ratio indicates an active and deep AMOC mode throughout most of the past 140 kyr. This is supported by generally unradiogenic ε_{Nd} values (of around −14, close to the modern NADW value[17]), providing evidence for continuous NADW formation with a strong contribution of LSW to glacial NADW resulting in ε_{Nd} values below −12 apart from at glacial maxima. This active deep-water circulation regime lasted from ~127 kyr

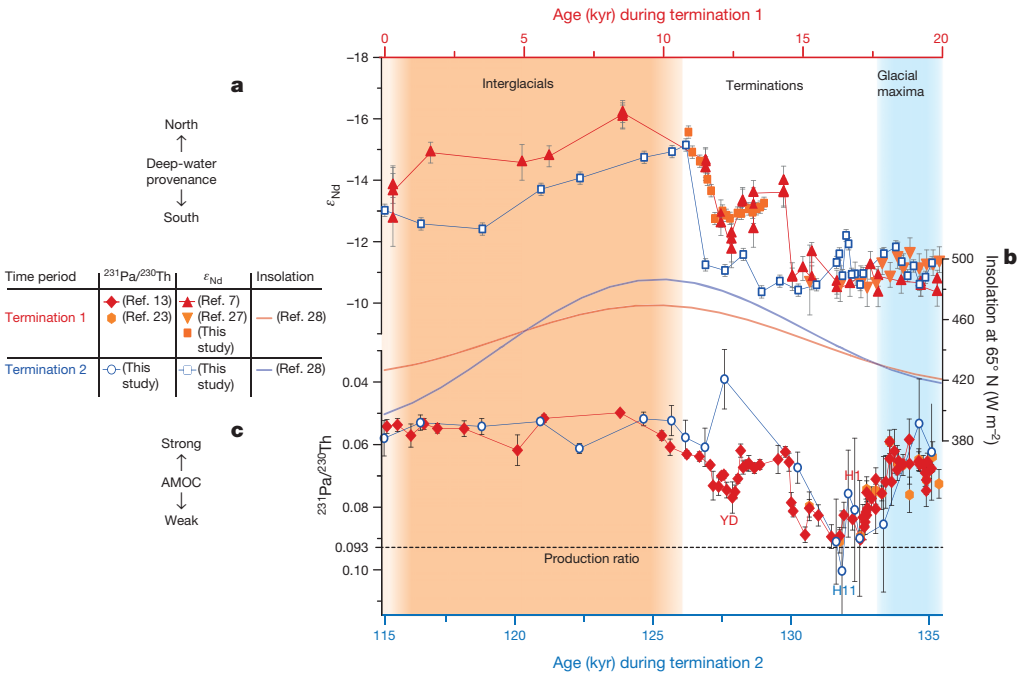


Figure 2 | The evolution of circulation proxies during termination 1 and termination 2. Termination 1 is indicated by the upper *x* axis (red) and termination 2 is represented by the lower *x* axis (blue). **a**, **c**, Bermuda Rise ε_{Nd} (**a**) and $^{231}Pa/^{230}Th$ (**c**) records of termination 1 (refs 8, 13, 23, 27) are compared with those of termination 2 (error bars, 2 s.d.). Major climatic events during termination 1 (YD, Younger Dryas; BA, Bølling–Allerød; H1, Heinrich stadial 1) and termination 2 (H11, Heinrich stadial 11) are indicated. We note that the *y* axes are reversed. The $^{231}Pa/^{230}Th$ production ratio of 0.093 (dotted line) indicates sluggish or absent overturning. The higher uncertainties of the ratios in the oldest part of the record originate from the measurements of the ^{231}Pa activities at very low values as a consequence of radioactive decay (half-life, 32.7 kyr). **b**, The summer insolation curve at 65° N (ref. 28), shown for comparison.

©2015 Macmillan Publishers Limited. All rights reserved

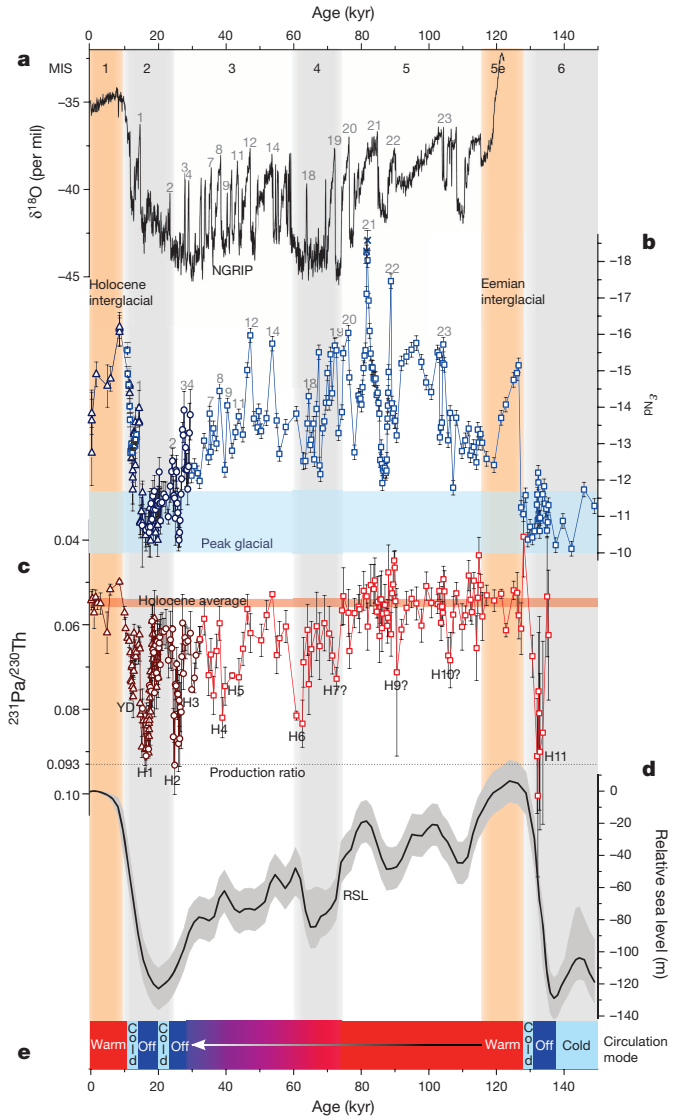


Figure 3 | Proxies of ocean circulation compared with palaeoclimatic conditions over the past 140 kyr. **a**, Oxygen isotope record ($\delta^{18}O = (^{18}O/^{16}O)_{sample}/(^{18}O/^{16}O)_{VSMOW} - 1$) of the NGRIP ice core[29]. (VSMOW, Vienna Standard Mean Ocean Water.) Dansgaard–Oeschger interstadials corresponding to peaks of unradiogenic ε_{Nd} signatures are labelled. **b**, ε_{Nd} (axis reversed; errors, 2 s.d.; blue open squares) from the Bermuda Rise (also including data in dark blue from ref. 8 (open triangles) and ref. 27 (open circles)) constrain the appearances of the cold and off circulation modes and the arrival of SSW in the North Atlantic to relatively short time periods during peak glacials (horizontal blue bar). Extremely unradiogenic leachate compositions around Dansgaard–Oeschger interstadials 21 have been reproduced using foraminiferal ε_{Nd} data (crosses) following the method of ref. 8, confirming the reliability and comparability of both approaches. **c**, Bermuda Rise $^{231}Pa/^{230}Th$ data (axis reversed; error bars, 2 s.d.; open red squares, also including data from ref. 13 (dark red triangles) and ref. 23 (dark red circles)) display a low baseline (distinctly below production ratio) providing evidence for persistent export of ^{231}Pa as a consequence of an active deep AMOC. HS1–HS11 mark the timing of major iceberg surges in the North Atlantic[21] when $^{231}Pa/^{230}Th$ shifts towards the production ratio of 0.093. **d**, The movement of SSW into the North Atlantic has been tightly connected to relative sea level (RSL; the grey range covers minimal and maximal sea-level estimates[30]) suggesting that the available amount of meltwater and the location of Northern deep-water formation were crucial parameters for controlling the AMOC modes. **e**, Predominant AMOC modes (Fig. 1) as derived from the combined $^{231}Pa/^{230}Th$ and ε_{Nd} records. Grey shadings (MISs 2, 4 and 6) mark glacial conditions, and orange shadings indicate interglacials (MISs 1 and 5e).

ago until ~27 kyr ago, when ε_{Nd} signatures reached less negative values owing to the increasing influence of SSW in the deep North Atlantic for the first time after the end of Marine Isotope Stage 6 (MIS 6). Accordingly, active formation and export of NADW during all of MIS 5, MIS 4 and MIS 3, similar to the warm mode during the Eemian (MIS 5.5) or the Holocene (MIS 1) interglacial, prevailed.

The most striking features of this record covering the last glacial cycle are the markedly brief occurrences of the cold mode, which have very positive ε_{Nd} values and are restricted to peak glacial conditions and maximum continental ice-sheet extent (Figs 1b and 3b). Only during these intervals was the key area of deep-water formation sufficiently vulnerable to both extended sea-ice coverage and high fresh-water runoff[18,19].

At the transition between MIS 5 and MIS 4, which has been identified as a key period in the evolution of the AMOC[2], we note a subtle but significant shift to higher $^{231}Pa/^{230}Th$ values, which persisted during the entire MIS 3 (Fig. 3). This slightly weakened export of ^{231}Pa is in good agreement with grain size and isotopic proxy data from the same location[20] and cannot be explained by the concurrent moderate increase of preserved biogenic opal deposition (Methods).

The $^{231}Pa/^{230}Th$-versus-ε_{Nd} cross-plot reveals the gradual transitions between the circulation modes (Fig. 4). A wide spectrum of pairs of values is observable with distinct signatures for each Marine Isotope Stage (see averages for each time period in Fig. 4), and there are very few combinations of low $^{231}Pa/^{230}Th$ and high ε_{Nd}, and vice versa. The different states of the AMOC are identified as transient changes between the endmember situations of the warm mode (low $^{231}Pa/^{230}Th$ and ε_{Nd}) and the off mode (high $^{231}Pa/^{230}Th$ and ε_{Nd}). We observe a gradual shift in the average signatures following the chronological sequence MIS 5–MIS 4–MIS 3–MIS 2. In contrast, the transitions from peak glacials (MIS 2 and MIS 6) to the interglacials (MIS 1 and MIS 5e) are marked by abrupt and large changes similar to the rapid increases in global temperatures and sea level during glacial terminations.

Distinct excursions of $^{231}Pa/^{230}Th$ to values higher than 0.08 and close to the production ratio coincide with the most pronounced Heinrich stadials[21] (HS 1, HS 2 and HS 11). Although enhanced scavenging of ^{231}Pa induced by higher fluxes of biogenic opal during Heinrich stadials has been suspected to contribute to the high $^{231}Pa/^{230}Th$ (refs 22, 23),

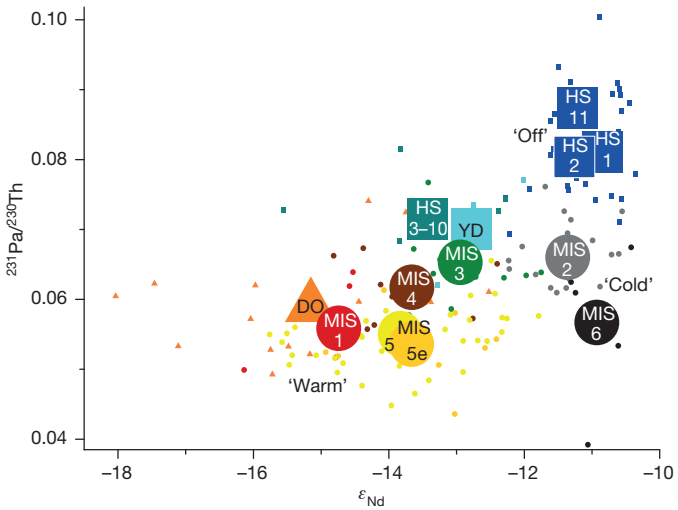


Figure 4 | Circulation modes of the AMOC as indicated by paired $^{231}Pa/^{230}Th$ and ε_{Nd} signatures from identical sediment samples colour-coded for distinct time periods. Large symbols indicate the average values of the scattered points. Data from refs 8, 13 for MISs 1 and 2 have been merged for sample ages separated by less than 500 yr. Low $^{231}Pa/^{230}Th$ during MISs 1, 3, 4 and 5 and Dansgaard–Oeschger interstadials indicates persistently strong export of NADW (^{231}Pa export), with variable contributions of LSW (high ε_{Nd} variability). Highly radiogenic ε_{Nd} signatures are characteristic for stadials (HS1, HS2 and HS11) and peak glacials (MISs 2 and 6), indicating pronounced SSW presence in the deep North Atlantic.

©2015 Macmillan Publishers Limited. All rights reserved

the total preserved opal concentration hardly exceeds 5% (Methods and Extended Data Figs 4 and 5), rendering ^{231}Pa–^{230}Th fractionation driven by opal unlikely. The ^{231}Pa/^{230}Th signatures of HS 3–HS 10 are, in contrast to those of the three Heinrich stadials mentioned above, less elevated or not elevated at all. These results suggest that iceberg discharge events were capable of severely perturbing NADW formation only in a SSW-dominated Atlantic.

The discussion presented so far is based on a simple seesaw alternation between SSW and NADW, presuming these to be the only major constituents of the AMOC. Yet NADW itself is a multicomponent water mass consisting of variable contributions of LSW ($\varepsilon_{Nd} \approx -18$), Denmark Strait Overflow Water ($\varepsilon_{Nd} \approx -8$) and Iceland–Scotland Overflow Water ($\varepsilon_{Nd} \approx -8$) (ref. 24). Several short-term excursions to very negative ε_{Nd} values that coincided with Dansgaard–Oeschger interstadials 21 and 22 of MIS 5 imply active deep-water formation with temporally significantly increased contributions of LSW compared with the modern mixing proportions. Thus, in contrast to previous findings[25] our ε_{Nd} record supports the persistent production of LSW during most of the last glacial cycle (Extended Data Fig. 6). In combination with a deep South Atlantic ε_{Nd} record, tracing the variability of the SSW endmember signature exported to the North Atlantic between 94 and 6 kyr ago[7], the fractions of NADW and SSW at our North Atlantic study site can be estimated. The results of a simple mixing calculation (Methods) provide evidence for an overall dominance of NADW (up to 100%) during the past 94 kyr, with the greatest decrease occurring during MIS 2, but to a NSW fraction no lower than 60% (Methods and Extended Data Fig. 7).

Our results indicate that NADW formation has been remarkably stable. Although significant variations in the AMOC (for example Dansgaard–Oeschger interstadials and Heinrich stadials) were recorded in both the ε_{Nd} and the ^{231}Pa/^{230}Th signatures over the entire record, fully developed continental ice sheets of dimensions close to glacial maxima are required for the AMOC to become prone to destabilization. For instance, meltwater forcing during HS3–HS10 or the Younger Dryas caused some transient weakening of NADW formation, but did not result in its collapse and an invasion of SSW into the deep North Atlantic at the expense of NADW. Only those Heinrich events that occurred close to glacial maxima coinciding with massive expansions of marine- and land-based ice sheets (HS1, HS2 and HS11) were able to trigger the off mode. This points to a critical threshold of expanded continental (and marine) ice volume, with sea level approximately 80–100 m below that of the present day (Fig. 3d); this threshold must be exceeded to generate a collapse of the AMOC in the North Atlantic during elevated Heinrich stadial fresh-water inputs. Accordingly, the likelihood of dramatic changes in the strength of the AMOC as a consequence of man-made global warming is considered low. Furthermore, as an implication of the persistent active NADW formation, significant carbon storage in the deep North Atlantic during MIS 3–MIS 5 is unlikely, supporting hypotheses of large-scale, old marine carbon reservoirs in the deep Pacific Ocean and Southern Ocean[4,26].

Online Content Methods, along with any additional Extended Data display items and Source Data, are available in the online version of the paper; references unique to these sections appear only in the online paper.

Received 28 May; accepted 3 November 2014.
Published online 15 December 2014.

1. Rahmstorf, S. Ocean circulation and climate during the past 120,000 years. *Nature* **419,** 207–214 (2002).
2. Adkins, J. The role of deep ocean circulation in setting glacial climates. *Paleoceanography* **28,** 539–561 (2013).
3. Boyle, E. & Keigwin, L. North Atlantic thermohaline circulation during the past 20,000 years linked to high-latitude surface temperature. *Nature* **330,** 35–40 (1987).
4. Sigman, D., Hain, M. & Haug, G. The polar ocean and glacial cycles in atmospheric CO_2 concentration. *Nature* **466,** 47–55 (2010).
5. Sarnthein, M. *et al.* Changes in east Atlantic deepwater circulation over the last 30,000 years: eight time slice reconstructions. *Paleoceanography* **9,** 209–267 (1994).
6. Yu, E., Francois, R. & Bacon, M. Similar rates of modern and last-glacial ocean thermohaline circulation inferred from radiochemical data. *Nature* **379,** 689–694 (1996).
7. Piotrowski, A., Goldstein, S., Hemming, S. & Fairbanks, R. Temporal relationships of carbon cycling and ocean circulation at glacial boundaries. *Science* **307,** 1933–1938 (2005).
8. Roberts, N., Piotrowski, A., McManus, J. & Keigwin, L. Synchronous deglacial overturning and water mass source changes. *Science* **327,** 75–78 (2010).
9. Lynch-Stieglitz, J. *et al.* Atlantic meridional overturning circulation during the Last Glacial Maximum. *Science* **316,** 66–69 (2007).
10. Keigwin, L. & Jones, G. Western North Atlantic evidence for millennial-scale changes in ocean circulation and climate. *J. Geophys. Res.* **99,** 12397–12410 (1994).
11. Adkins, J., Boyle, E., Keigwin, L. & Cortijo, E. Variability of the North Atlantic thermohaline circulation during the last interglacial period. *Nature* **390,** 154–156 (1997).
12. Frank, M. Radiogenic isotopes: tracers of past Ocean Circulation and erosional input. *Rev. Geophys.* **40,** 1001 (2002).
13. McManus, J., Francois, R., Gherardi, J., Keigwin, L. & Brown-Leger, S. Collapse and rapid resumption of Atlantic meridional circulation linked to deglacial climate change. *Nature* **428,** 834–837 (2004).
14. Sachs, J. & Lehman, S. Subtropical North Atlantic temperatures 60,000 to 30,000 years ago. *Science* **286,** 756–759 (1999).
15. Tzedakis, P. *et al.* Can we predict the duration of an interglacial? *Clim. Past* **8,** 1473–1485 (2012).
16. Carlson, A. Why there was not a Younger Dryas-like event during the penultimate deglaciation. *Quat. Sci. Rev.* **27,** 882–887 (2008).
17. Piepgras, D. & Wasserburg, G. Rare earth element transport in the western North Atlantic inferred from Nd isotopic observations. *Geochim. Cosmochim. Acta* **51,** 1257–1271 (1987).
18. McManus, J., Oppo, D. & Cullen, J. A 0.5-million-year record of millennial-scale climate variability in the North Atlantic. *Science* **283,** 971–975 (1999).
19. Carlson, A. & Clark, P. Ice sheet sources of sea level rise and freshwater discharge during the last deglaciation. *Rev. Geophys.* **50,** RG4007 (2012).
20. Thornalley, D., Barker, S., Becker, J., Hall, I. & Knorr, G. Abrupt changes in deep Atlantic circulation during the transition to full glacial conditions. *Paleoceanography* **28,** 253–262 (2013).
21. Rasmussen, T., Oppo, D., Thomsen, E. & Lehman, S. Deep sea records from the southeast Labrador Sea: ocean circulation changes and ice-rafting events during the last 160,000 years. *Paleoceanography* **18,** 1081 (2003).
22. Keigwin, D. & Boyle, E. Did North Atlantic overturning halt 17,000 years ago? *Paleoceanography* **23,** PA1101 (2008).
23. Lippold, J. *et al.* Does sedimentary ^{231}Pa/^{230}Th from the Bermuda Rise monitor past Atlantic meridional overturning circulation? *Geophys. Res. Lett.* **36,** L12601 (2009).
24. Lacan, F. & Jeandel, C. Acquisition of the neodymium isotopic composition of the North Atlantic Deep Water. *Geochem. Geophys. Geosyst.* **6,** Q12008 (2005).
25. Hillaire-Marcel, C., de Vernal, A., Bilodeau, G. & Weaver, A. Absence of deep-water formation in the Labrador Sea during the last interglacial period. *Nature* **410,** 1073–1077 (2001).
26. Jaccard, S. *et al.* Two modes of change in Southern Ocean productivity over the past million years. *Science* **339,** 1419–1423 (2013).
27. Gutjahr, M. & Lippold, J. Early arrival of Southern Source Water in the deep North Atlantic prior to Heinrich event 2. *Paleoceanography* **26,** PA2101 (2011).
28. Berger, A. & Loutre, M. Insolation values for the climate of the last 10 million years. *Quat. Sci. Rev.* **10,** 297–317 (1991).
29. Andersen, K. *et al.* The Greenland ice core chronology 2005, 15–42 ka. Part 1: constructing the time scale. *Quat. Sci. Rev.* **25,** 3246–3257 (2006).
30. Waelbroeck, C. *et al.* Sea-level and deep water temperature changes derived from benthic foraminifera isotopic records. *Quat. Sci. Rev.* **21,** 295–305 (2002).

Supplementary Information is available in the online version of the paper.

Acknowledgements Sediment material for this study was provided by the ODP/IODP core repository Bremen. The manuscript benefited from input by S. Jaccard and A. Mangini. We thank J. Grützner, H. Dicht, J. Link and S. Rheinberger for advice and analytical assistance. Financial support for this research was provided by the Deutsche Forschungsgemeinschaft through grant Ma821/41 to E.B. J.L. was supported by the FP7-PEOPLE-2013-IEF, Marie Curie proposal 622483.

Author Contributions J.L. developed the concept and designed the study. E.B., J.L., P.B. and B.A. carried out the chemical preparations of the samples. E.B., J.L., M.B.A. and B.A. performed opal, U, Th and Pa measurements. E.B., J.L., M.G. and P.B. performed the Nd isotope measurements. J.F. improved the age model. J.L., E.B., M.G., M.F., M.B.A., J.F., N.F. and M.D. interpreted the results and wrote the manuscript.

Author Information Reprints and permissions information is available at www.nature.com/reprints. The authors declare no competing financial interests. Readers are welcome to comment on the online version of the paper. Correspondence and requests for materials should be addressed to J.L. (joerg.lippold@geo.unibe.ch).

©2015 Macmillan Publishers Limited. All rights reserved

METHODS

ε_{Nd}. The deep-water Nd isotope signal was extracted from the Fe-Mn oxyhydroxide fraction of bulk sediment of ODP 1063 following the leaching procedure described in ref. 31. In total, 177 dried sediment samples (typically 0.2–0.3 g) were homogenized and subsequently treated with an acetic acid/sodium acetate buffer to remove carbonate, followed by removal of adsorbed metals using a 1 M $MgCl_2$ solution. The Fe-Mn oxyhydroxide fraction was extracted using a 0.05 M hydroxylamine hydrochloride/15% acetic acid/0.03 M Na-EDTA solution buffered to pH 4 with NaOH. The REEs were separated from the leachate by cation exchange chromatography using 50W-X8 resin followed by separation of Nd from the other REEs using LN-Spec resin[32,33]. This leaching method was previously successfully applied to sediments from a variety of oceanic settings[7,34,35]. Its application and associated limitations have been well constrained by methodical and geographical studies[36–38]. In addition, the deep-water Nd isotopic composition was extracted from two 'unclean' foraminifera samples (the calcite and Fe-Mn oxyhydroxide fraction of the foraminifera, with only clay and silicates removed), following ref. 39, to confirm the validity of the leaching method. The fraction >63 μm was dried and mixed planktonic foraminiferal species were picked. Individual foraminifera chambers were broken into fragments and rinsed with MilliQ water to remove clays before dissolution in a 0.05 M hydroxylamine hydrochloride/15% acetic acid/0.03 M Na-EDTA solution buffered to pH 4 with NaOH. Our results obtained from the leachates of the Fe-Mn oxyhydroxide fraction are in excellent agreement with the unclean-foraminifera-derived Bermuda Rise ε_{Nd} signatures published in ref. 8 and with the Fe-Mn oxyhydroxide-based Nd isotope record obtained earlier from ODP 1063[27] (Fig. 3). Most importantly, ref. 27 demonstrated that the gentle reductive leaching method applied reproduced the foraminiferal ε_{Nd} compositions remarkably well for time intervals overlapping with those published in ref. 8 from the same location (Extended Data Fig. 8 and Extended Data Table 1). The two new ε_{Nd} signatures extracted from unclean foraminifera in the frame of this study are also fully consistent with the results obtained previously (Fig. 3 and Methods). Our Nd isotope measurements were performed on two Thermo Finnigan Neptune inductively coupled plasma mass spectrometers at the University of Bristol (UK) and the National Oceanography Centre Southampton (UK). Instrumental mass fractionation was corrected by normalizing the measured ratio of $^{143}Nd/^{144}Nd$ to $^{146}Nd/^{144}Nd = 0.7219$ using the mass bias correction procedure in ref. 40. The measured Nd isotope ratios were normalized to the published $^{143}Nd/^{144}Nd$ value of 0.512115 for JNdi-1 (ref. 41). Results given in the Supplementary Table 1 are accompanied by the 2 s.d. external reproducibility of the $^{143}Nd/^{144}Nd$ measurements based on repeated standard measurements, and amounted to 0.20 ε_{Nd} (2 s.d.).

$^{231}Pa/^{230}Th$. Approximately 0.2 g of the dried and ground sediment were spiked with ^{233}Pa (milked from a ^{237}Np solution), ^{229}Th, ^{233}U and ^{236}U, followed by total dissolution in a mixture of concentrated HCl, HNO_3 and HF. The Pa, Th and U aliquots were separated by anion exchange column chromatography using AG1-X8 resin[42]. The ^{233}Pa spike was calibrated against the reference standard material UREM-11[43,44] and an internal pitchblende standard[45]. Total ^{231}Pa and ^{230}Th activities were corrected for detrital input using a lithogenic activity ratio of $^{238}U/^{232}Th = 0.47$ based on the overall minimum of this ratio from a 300 kyr-old record of this core[46]. The ingrowth of ^{231}Pa and ^{230}Th from authigenic uranium was determined by applying the procedure in ref. 47 to calculate corrected excess ^{231}Pa and ^{230}Th activities. Measurements of uranium, thorium and protactinium concentrations were performed on a Thermo Finnigan Element2 and a Neptune inductively coupled plasma mass spectrometer at the University of Heidelberg (Germany) and ETH Zurich (Switzerland), respectively. Uncertainties of the $^{231}Pa/^{230}Th$ ratios are dominated by the uncertainties of the measurements of the ^{231}Pa concentrations and were usually better than 5% (2 s.d.). However, owing to the short half-life of ^{231}Pa the uncertainties increase with the age of the samples. This effect was reduced by using the error-weighted averages from at least three replicates for all data older than 125 kyr. The error in $^{231}Pa/^{230}Th$ for individual samples corresponds to the error propagation of the 2 s.d. errors of four obtained isotope ratios ($^{231}Pa/^{233}Pa$, $^{230}Th/^{229}Th$, $^{232}Th/^{229}Th$, $^{238}U/^{236}U$). For $^{231}Pa/^{230}Th$ samples processed several times (in particular for the age range >125 kyr) the uncertainties were calculated by error propagation from the standard deviations of the average isotopic values. A total of 109 new $^{231}Pa/^{230}Th$ values have been determined.

Biogenic opal. To assess the potential influence of changes in particulate biogenic opal fluxes on $^{231}Pa/^{230}Th$, its preserved concentration was measured on a total of 80 samples. The measurements followed the automated procedure for analysis of dissolved silica by molybdate-blue spectrophotometry[48]. The opal fraction of the sediment samples was dissolved in NaOH and subsequently acidified and mixed with molybdate before the absorption was measured using a photometer. Bulk concentrations ranged from 0.7% to 8.8% with an error range of 2–70% (2 s.d.).

Age model. The age model for the period between 35 and 15 kyr ago is the same as the one used in ref. 23. For the deeper parts of ODP 1063 (16 to 35 metres composite depth), we established the age model by tuning the XRF-derived variability of the Ti/Ca ratios of the core to the $\delta^{18}O$ values of the NGRIP ice core[29,49,50]. The Ti input into the sediments is of terrigenous origin and can essentially be regarded as constant under various climatic conditions at this location[51]. In contrast, the Ca content of the sediment potentially varied mainly with vertical changes of the lysocline and carbonate compensation depths over the last glacial cycle. Lysocline and carbonate compensation depths depend on the carbonate saturation state of the deep water, which is a function of water mass characteristics and organic carbon export from the sea surface and its remineralisation in the deeper water column. For the entire time interval between 130 and 35 kyr ago we assigned 24 tuning points, hence one tuning point per approximately 3,500 yr. We set the tuning points preferentially at the start and end points of Dansgaard–Oeschger interstadials and assumed an uncertainty of ±500 yr for this dating approach. To optimise our choice in setting the tuning points we designed a Monte Carlo algorithm, which varied all tuning points within their given uncertainties to maximise the correlation between the ice core data and the elemental composition of the sediment core. No age uncertainties of the ice core data have been included in our approach. Both data sets were detrended and normalized to their 2 s.d. standard variation before the correlation calculation. The applied age model for ODP core 1063 corresponds to the highest correlation coefficient between both data sets ($r = 0.8$), chosen out of 1,000,000 Monte Carlo realizations (Extended Data Fig. 1). Sections below 35 metres composite depth represent the period before 120 kyr. This date represents the end of the NGRIP ice-core chronology and, hence, the limit of our approach. For the oldest period investigated in our study we thus stuck to the age–depth relationship of ODP 1063 published in ref. 52. Our approach results in homogeneous and relatively low sedimentation rates, with values below 20 cm kyr^{-1} during warm climate conditions. Higher and more variable sedimentation rates occurred during colder stages, with highest values during the LGM yielding sedimentation rates >100 cm kyr^{-1} (Extended Data Fig. 2). A recent study[20] discussed sortable silt mean grain-size distributions from ODP 1063 during MIS 4. The corresponding age model was established by tuning the $\delta^{18}O$ record of planktonic foraminifera to the NGRIP $\delta^{18}O$ record between 91 and 53 kyr ago. Despite the existence of this age model we developed a new one to avoid having to interconnect several age models for the time period from 122 to 35 kyr ago. Both age models are very similar, showing only minor differences (they differ at most by 1.2 kyr, between 75 and 60 kyr ago) during the overlapping time period (Extended Data Fig. 3). Significant deviations occur only in the calculated sedimentation rates. Reference 20 proposed three short periods of time between 76 and 70 kyr ago with sedimentation rates higher than 100 cm kyr^{-1}, which is approximately one order of magnitude higher than in preceding and following time intervals. Such extreme variations cannot be confirmed by our approach. Another advantage of the new age model is the high resolution of the Ti/Ca data, which is crucial for dating the highly resolved ε_{Nd} and $^{231}Pa/^{230}Th$ records. In addition, we obtained ^{14}C dates generated by accelerator mass spectrometry for two samples of the planktonic foraminifera species *Globorotalia inflata* (Extended Data Table 1). Both samples have been chosen to better constrain the age control at the end of termination 1. This is in the age range of the Nd isotope data set in ref. 8, for which leachate Nd isotope measurements also have been performed to better estimate the reproducibility of both methods (Extended Data Fig. 8).

Potential effects of particle fluxes and composition on $^{231}Pa/^{230}Th$. The scavenging efficiency of ^{231}Pa and ^{230}Th is controlled by particle size and composition, and thus influences sedimentary $^{231}Pa/^{230}Th$ ratios[53]. Biogenic opal is believed to have the strongest control on $^{231}Pa/^{230}Th$ given the high affinity of ^{231}Pa to biogenic opal, which reduces the fractionation between the radionuclides in the water column, leading to an increase of sedimentary $^{231}Pa/^{230}Th$ independent of the strength of circulation. In particular, concerns about a biasing effect of ^{231}Pa scavenging by biogenic opal on $^{231}Pa/^{230}Th$ arose from coinciding peaks of both parameters at this location during HS1 and HS2[22,23,54]. To examine a potential control for changes in the effect of biogenic opal flux on the $^{231}Pa/^{230}Th$ we determined biogenic opal contents and compared them with the $^{231}Pa/^{230}Th$ data. Although post-depositional dissolution processes in the North Atlantic possibly mask the initially deposited opal content, the high average sedimentation rate of ODP 1063 supports a high preservation of the biogenic opal content[23]. Of 93 samples, 86 (time period, 135–0 kyr ago; Extended Data Fig. 4) display opal concentrations below 5%, suggesting only a subordinate effect of biogenic opal flux on $^{231}Pa/^{230}Th$ (ref. 55). In addition, the insignificant correlation between opal content and $^{231}Pa/^{230}Th$ ($r^2 = 0.16$, $P = 0.11$; Extended Data Fig. 5), and the absence of systematic opal enrichments coinciding with $^{231}Pa/^{230}Th$ maxima near the production ratio, supports the conclusion that the $^{231}Pa/^{230}Th$ signal has mainly been controlled by the basin-wide AMOC during the investigated period of time at ODP Site 1063.

Extreme ε_{Nd} signatures during Dansgaard–Oeschger interstadials 21 and 22. In the Nd isotope record several short excursions to extremely negative ε_{Nd} signatures (~−18) imply that significantly enhanced LSW production and admixture had a dominant role during these particular two millennial-scale intervals associated with Dansgaard–Oeschger interstadials 21 and 22 at 84 and, respectively,

©2015 Macmillan Publishers Limited. All rights reserved

88 kyr ago. Excursions of almost the same magnitude have also been observed during the early Holocene[8] and were recorded in unclean foraminifera samples, which rules out methodological artefacts (Supplementary Data). To push the Nd isotopic compositions of NADW well below the modern ε_{Nd} signature of −13.5, either the Nd concentration of LSW had to be increased relative to the concentrations of Denmark Strait Overflow Water and Iceland–Scotland Overflow Water[56,57], and/or significantly larger proportions of Central Baffin Bay Water (BBW, $\varepsilon_{Nd} \approx -20$; ref. 58) must have contributed to the Nd isotope signature of LSW and, subsequently, to NADW for a short period of time. There is very little information about past Nd concentrations (c_i) and only a few estimates of endmember ε_{Nd} (ε_i) in NADW[59,60] and SSW, as well as associated water transfer rates ($\dot{W}_{ij}$; Extended Data Fig. 6). In a sensitivity test (steady-state simple three-box model) we constrain these parameters by variation of the modern-day values to produce the unradiogenic Nd isotope compositions of Dansgaard–Oeschger interstadials 21 and 22:

$$\dot{W}_{12}\varepsilon_1 c_1 - \dot{W}_{21}\varepsilon_2 c_2 - \dot{W}_{23}\varepsilon_2 c_2 + \dot{W}_{32}\varepsilon_3 c_3 = 0$$

For this test we assume constant concentrations during the last glacial cycle, because there is very little information about glacial seawater Nd concentrations. The applied parameter set is based on estimates in ref. 58 with $\varepsilon_1 = -20$, $\varepsilon_2 = -18$, $\varepsilon_3 = -9$, $c_1 = 4.7\ \mathrm{pg\,g^{-1}}$, $c_2 = 2.5\ \mathrm{pg\,g^{-1}}$, $c_2 = 2.0\ \mathrm{pg\,g^{-1}}$, $\dot{W}_{23} = \dot{W}_{32} = 18$ Sv and $\dot{W}_{12} = \dot{W}_{21} = 6$ Sv. To obtain the extremely unradiogenic Nd isotope signatures of Dansgaard–Oeschger interstadials 21 and 22 the values for c_1 need to reach $6.5\ \mathrm{pg\,g^{-1}}$. Today such high values have been measured only in central Baffin Bay[58]; values from farther south range between only 2 and $4\ \mathrm{pg\,g^{-1}}$ (ref. 24). Alternatively (with an unchanged $c_1 = 4.7\ \mathrm{pg\,g^{-1}}$) $\dot{W}_{12}$ needs to be increased to up to 10 Sv, which would imply considerable changes in the water mass distribution during these periods. The most likely scenario, though, may comprise the combination of variations in both parameters. The results of this simple sensitivity test imply that the ε_{Nd} signatures observed during Dansgaard–Oeschger interstadials 21 and 22 can be explained by moderate combined changes in both water mass transfer rates and Nd concentrations. For most of the observed time range, however, the variability in the admixture of BBW had a negligible effect on the signature of admixed NADW at the Bermuda Rise given the narrow range of ε_{Nd} values observed during cold and off modes (Fig. 4) and the $^{231}Pa/^{230}Th$ signals clearly below the production ratio over most of the past 140 kyr (Fig. 3).

Comparison to a South Atlantic ε_{Nd} time series. The ε_{Nd} variability in ODP 1063 on the Bermuda Rise is interpreted in terms of mixing of different portions of NADW and SSW. Hence, this record provides information about past changes of the water mass distribution and their mixing proportions in the North Atlantic. The mixing of NADW and SSW at ODP 1063 based on Nd isotopes and concentrations can be described by a linear mixing model:

$$\begin{aligned}\varepsilon_{Nd}(\mathrm{ODP\ 1063}) = {} & \\ & (f_{NADW} c_{Nd}(\mathrm{NADW})\varepsilon_{Nd}(\mathrm{NADW}) \\ & + (1 - f_{NADW}) c_{Nd}(\mathrm{SSW})\varepsilon_{Nd}(\mathrm{SSW})) \\ & \times (f_{NADW} c_{Nd}(\mathrm{NADW}) + (1 - f_{NADW}) c_{Nd}(\mathrm{SSW}))^{-1}\end{aligned} \quad (1)$$

where c_{Nd} is the concentration of Nd in either SSW and NADW, and ε_{Nd} is the endmember ε_{Nd} signature of SSW, NADW or the mixture at ODP 1063.

The fractions of NADW (f_{NADW}) and, consequently, SSW (f_{SSW}) in the mixture are then given by $f_{NADW} = 1 - f_{SSW}$, or

$$f_{NADW} = \left(1 + \frac{\varepsilon_{Nd}(\mathrm{NADW}) - \varepsilon_{Nd}(\mathrm{ODP\ 1063})}{\varepsilon_{Nd}(\mathrm{ODP\ 1063}) - \varepsilon_{Nd}(\mathrm{SSW})} \frac{c_{Nd}(\mathrm{NADW})}{c_{Nd}(\mathrm{SSW})}\right)^{-1} \quad (2)$$

However, not all parameters of equation (1) and (2) are known for the past, and assumptions must be made to constrain their values. Accordingly, given the lack of information on some parameters, the calculations presented here are only a semi-quantitative sensitivity test. What is known, complemented by the ε_{Nd} reconstruction in ref. 8, is our continuous ε_{Nd} record for the last 140 kyr from the deep western North Atlantic, representing ε_{Nd}(ODP1063). Moreover, ref. 7 provided a reconstruction of the ε_{Nd} signature of the SSW endmember ε_{Nd}(SSW) for the time interval from 94 to 6 kyr ago from core RC11-83/TN057 in the South Atlantic. The records are compared with each other by interpolating and incrementing each of them to a time resolution of 100 yr, resulting in two smoothed data sets. Of the unknowns, we first consider the Nd concentrations for NADW (c_{Nd}(NADW)) and SSW (c_{Nd}(SSW)). So far it has not been possible to reconstruct Nd concentrations of past seawater. Given the lack of evidence for variable glacial deep-water c_{Nd}, and because the concentration terms in equation (2) are in fact insensitive to concurrently increasing or decreasing concentrations, the assumption of constant Nd concentrations is a good first-order approach in this sensitivity test. The mean Nd concentration of modern NADW can be quantified as $2.9\ \mathrm{pg\,g^{-1}}$ (refs 58, 61, 62). The Nd concentration of modern SSW found around core RC11-83/TN057 is significantly higher, at about $5\ \mathrm{pg\,g^{-1}}$ (ref. 63). For ε_{Nd}(NADW), we assume a variable endmember composition between −14 and −16, which is close to the least radiogenic data of the ODP 1063 record, neglecting the two pronounced Dansgaard–Oeschger interstadials. Although there is some uncertainty and the choice of ε_{Nd}(NADW) value influences the calculated f_{NADW}, the finding that NADW was the dominant water mass during the past ~100 kyr (Extended Data Fig. 7), not dropping below 60% NSW admixture, is robust.

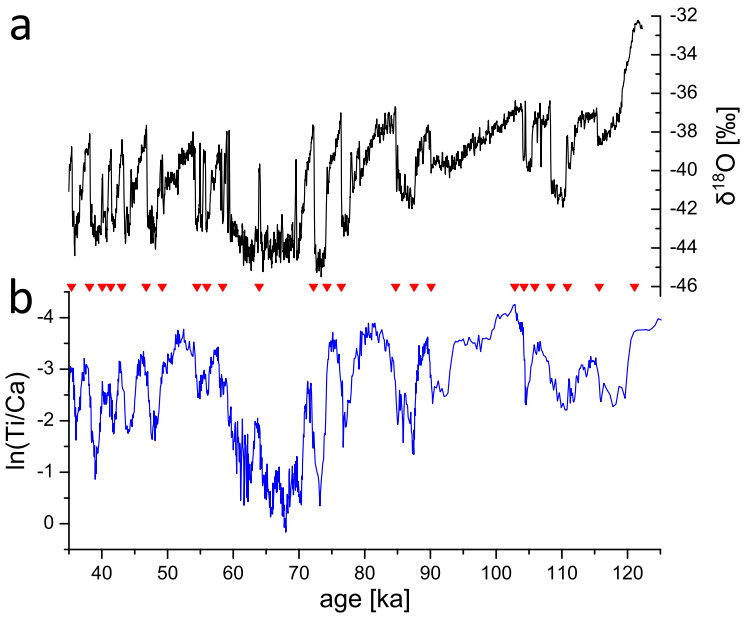
Comparison with a previous $^{231}Pa/^{230}Th$ data set. To exclude the possibility that the $^{231}Pa/^{230}Th$ record of past ocean circulation of ODP 1063 is biased by local variability of particulate fluxes, we compare our record with previously published data in the North Atlantic. Reference 64 provided a down-core $^{231}Pa/^{230}Th$ profile of core SU90-11 (2,000 km to the northeast of the Bermuda Rise, at 3,645 m water depth). Of all North Atlantic $^{231}Pa/^{230}Th$ profiles available at present, SU90-11 is the best for comparison with the ODP 1063 record in terms of oceanic setting, water depth, distance to the margin and, in particular, temporal coverage. The measured values of both records agree very well within the given uncertainties. For the time range of overlap (from 125 kyr to 60 kyr ago), both down-core records consistently indicate an active AMOC and strong NADW export during MISs 4 and 5, and a well-constrained increase across the MIS 5/MIS 4 transition (Extended Data Fig. 9). It is only some short-term excursions to high $^{231}Pa/^{230}Th$ (~105 kyr, ~90 kyr and ~65 kyr ago) that apparently did not occur simultaneously. Small uncertainties in the age models and issues with temporal resolution are most probably responsible for these deviations, given that the generally low opal concentration levels in both cores exclude any local overprinting of the $^{231}Pa/^{230}Th$ circulation signal by changes in opal fluxes.

31. Gutjahr, M. *et al.* Reliable extraction of a deepwater trace metal isotope signal from Fe–Mn oxyhydroxide coatings of marine sediments. *Chem. Geol.* **242,** 351–370 (2007).
32. Cohen, A., Onions, R., Siegenthaler, R. & Griffin, W. Chronology of the pressure-temperature history recorded by a granulite terrain. *Contrib. Mineral. Petrol.* **98,** 303–311 (1988).
33. Pin, C., Briot, D., Bassin, C. & Poitrasson, F. Concomitant separation of strontium and samarium-neodymium for isotopic analysis in silicate samples, based on specific extraction chromatography. *Anal. Chim. Acta* **298,** 209–217 (1994).
34. Gutjahr, M., Frank, M., Stirling, C., Keigwin, L. & Halliday, A. Tracing the Nd isotope evolution of North Atlantic Deep and Intermediate Waters in the western North Atlantic since the LGM from Blake Ridge sediments. *Earth Planet. Sci. Lett.* **266,** 61–77 (2008).
35. Pahnke, K., Goldstein, S. & Hemming, S. Abrupt changes in Antarctic Intermediate Water circulation over the past 25,000 years. *Nature Geosci.* **1,** 870–874 (2008).
36. Wilson, D., Piotrowski, A., Galy, A. & Clegg, J. Reactivity of neodymium carriers in deep sea sediments: implications for boundary exchange and paleoceanography. *Geochim. Cosmochim. Acta* **109,** 197–221 (2013).
37. Elmore, A., Piotrowski, A., Wright, J. & Scrivner, A. Testing the extraction of past seawater Nd isotopic composition from North Atlantic deep sea sediments and foraminifera. *Geochem. Geophys. Geosyst.* **12,** Q09008 (2011).
38. Piotrowski, A. *et al.* Reconstructing deglacial North and South Atlantic deep water sourcing using foraminiferal Nd isotopes. *Earth Planet. Sci. Lett.* **357–358,** 289–297 (2012).
39. Roberts, N., Piotrowski, A., Elderfield, H., Eglinton, T. & Lomas, M. Rare earth element association with foraminifera. *Geochim. Cosmochim. Acta* **94,** 57–71 (2012).
40. Vance, D. & Thirlwall, M. An assessment of mass discrimination in MC-ICPMS using Nd isotopes. *Chem. Geol.* **185,** 227–240 (2002).
41. Tanaka, T. *et al.* JNdi-1: a neodymium isotopic reference in consistency with La Jolla neodymium. *Chem. Geol.* **168,** 279–281 (2000).
42. Pichat, S. *et al.* Lower export production during glacial periods in the equatorial Pacific derived from $^{231}Pa/^{230}Th_{xs,0}$ measurements in deep-sea sediments. *Paleoceanography* **19,** PA4023 (2004).
43. Geibert, W. & Vöge, I. Progress in determination of 227-Ac in sea water. *Mar. Chem.* **109,** 238–249 (2008).
44. Hansen, R. & Ring, E. *The Preparation and Certification of a Uranium Reference Material* Vol. M84 (Randburg, 1983).
45. Fietzke, J., Bollhöfer, A., Frank, N. & Mangini, A. Pa determination in manganese crust VA12/2 by TIMS. *Nucl. Instrum. Methods Phys. Res. B* **149,** 353–360 (1999).
46. Christl, M., Lippold, J., Steinhilber, F., Bernsdorff, F. & Mangini, A. Reconstruction of global ^{10}Be production over the past 250 ka from highly accumulating Atlantic drift sediments. *Quat. Sci. Rev.* **29,** 2663–2672 (2010).
47. Henderson, G. & Anderson, R. The U-series toolbox for paleoceanography. *Rev. Mineral. Geochem.* **52,** 493–531 (2003).
48. Müller, R. & Schneider, R. An automated leaching method for the determination of opal in sediments and particulate matter. *Deep-Sea Res. I* **40,** 425–444 (1993).
49. Wolff, E., Chappellaz, J., Blunier, T., Rasmussen, S. & Svensson, A. Millennial-scale variability during the last glacial: the ice core record. *Quat. Sci. Rev.* **29,** 2828–2838 (2010).
50. Svensson, A. *et al.* The Greenland ice core chronology 2005, 15–42 ka. Part 2: comparison to other records. *Quat. Sci. Rev.* **25,** 3258–3267 (2006).

©2015 Macmillan Publishers Limited. All rights reserved

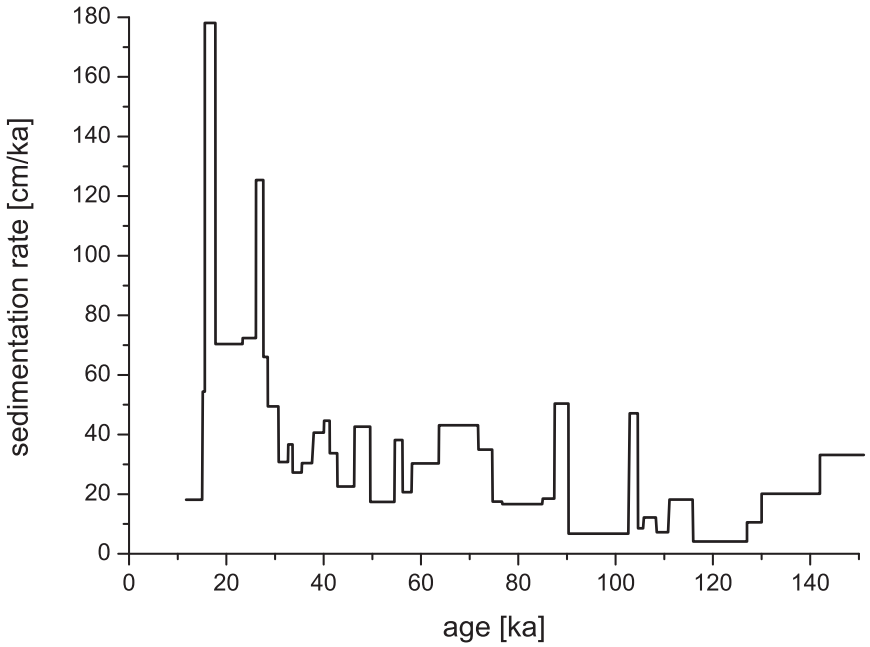
51. Jaeschke, A., Rühlemann, C., Arz, H., Heil, G. & Lohmann, G. Coupling of millennial-scale changes in sea surface temperature and precipitation off northeastern Brazil with high-latitude climate shifts during the last glacial period. *Paleoceanography* **22,** PA4206 (2007).
52. Channell, J., Hodell, D. & Curtis, J. ODP Site 1063 (Bermuda Rise) revisited: oxygen isotopes, excursions and paleointensity in the Brunhes Chron. *Geochem. Geophys. Geosyst.* **13,** Q02001 (2012).
53. Anderson, B., Bacon, M. & Brewer, P. Removal of ^{230}Th and ^{231}Pa at ocean margins. *Earth Planet. Sci. Lett.* **66,** 73–90 (1983).
54. Gil, I., Keigwin, L. & Abrantes, F. Deglacial diatom productivity and surface ocean properties over the Bermuda Rise, northeast Sargasso Sea. *Paleoceanography* **24,** PA4101 (2009).
55. Lippold, J. *et al.* Strength and geometry of the glacial Atlantic meridional overturning circulation. *Nature Geosci.* **5,** 813–816 (2012).
56. Lacan, F. & Jeandel, C. Subpolar Mode Water formation traced by neodymium isotopic composition. *Geophys. Res. Lett.* **31,** L14306 (2004).
57. Piepgras, D. & Wasserburg, G. Neodymium isotopic variations in seawater. *Earth Planet. Sci. Lett.* **50,** 128–138 (1980).
58. Stordal, M. & Wasserburg, G. Neodymium isotopic study of Baffin Bay water: sources of REE from very old terranes. *Earth Planet. Sci. Lett.* **77,** 259–272 (1986).
59. Foster, G., Vance, D. & Prytulak, J. No change in the neodymium isotope composition of deep water exported from the North Atlantic on glacial-interglacial time scales. *Geology* **35,** 37–40 (2007).
60. van de Flierdt, T., Robinson, L., Adkins, J., Hemming, S. & Goldstein, S. Temporal stability of the neodymium isotope signature of the Holocene to glacial North Atlantic. *Paleoceanography* **21,** PA4102 (2006).
61. Swift, J. The circulation of the Denmark Strait and Iceland-Scotland overflow waters in the North Atlantic. *Deep-Sea Res. A* **31,** 1339–1355 (1984).
62. Lacan, F. & Jeandel, C. Neodymium isotopic composition and rare earth element concentrations in the deep and intermediate Nordic Seas: constraints on the Iceland Scotland Overflow Water signature. *Geochem. Geophys. Geosyst.* **5,** Q11006 (2004).
63. Stichel, T., Frank, M., Rickli, J. & Haley, B. The hafnium and neodymium isotope composition of seawater in the Atlantic sector of the Southern Ocean. *Earth Planet. Sci. Lett.* **317–318,** 282–294 (2012).
64. Guihou, A. *et al.* Enhanced Atlantic meridional overturning circulation supports the last glacial inception. *Quat. Sci. Rev.* **30,** 1576–1582 (2011).
65. Bronk Ramsey, C. & Lee, S. Recent and planned developments of the program OxCal. *Radiocarbon* **55,** 720–730 (2013).
66. Reimer, P. J. *et al.* IntCal13 and Marine13 radiocarbon age calibration curves 0-50,000 years cal BP. *Radiocarbon* **55,** 1869–1887 (2013).

©2015 **Macmillan Publishers Limited. All rights reserved**



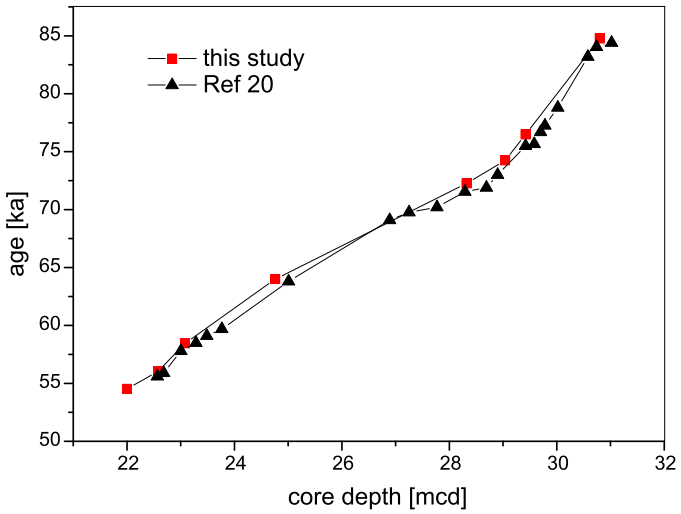
Extended Data Figure 1 | Bermuda Rise sediment Ti/Ca compared with NGRIP ice-core $\delta^{18}O$. Age control points (red) aligning the Ti/Ca profile of ODP 1063 (**b**) with the $\delta^{18}O$ time series of the NGRIP ice core (**a**).

©2015 Macmillan Publishers Limited. All rights reserved



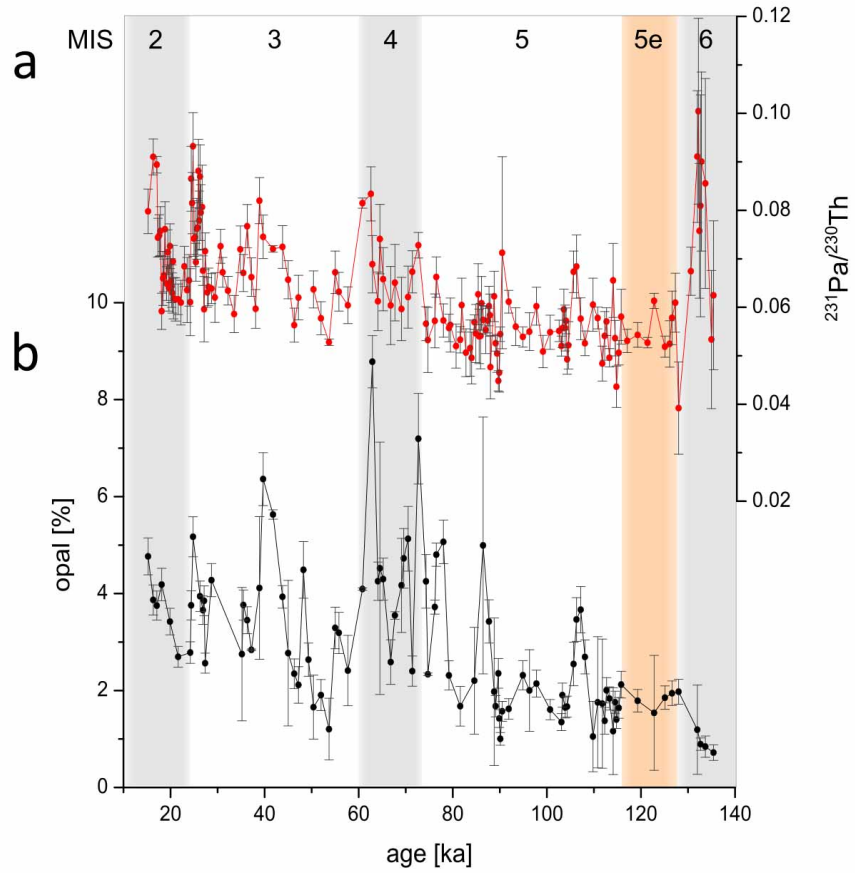
Extended Data Figure 2 | Sedimentation rates of ODP 1063.

©2015 Macmillan Publishers Limited. All rights reserved



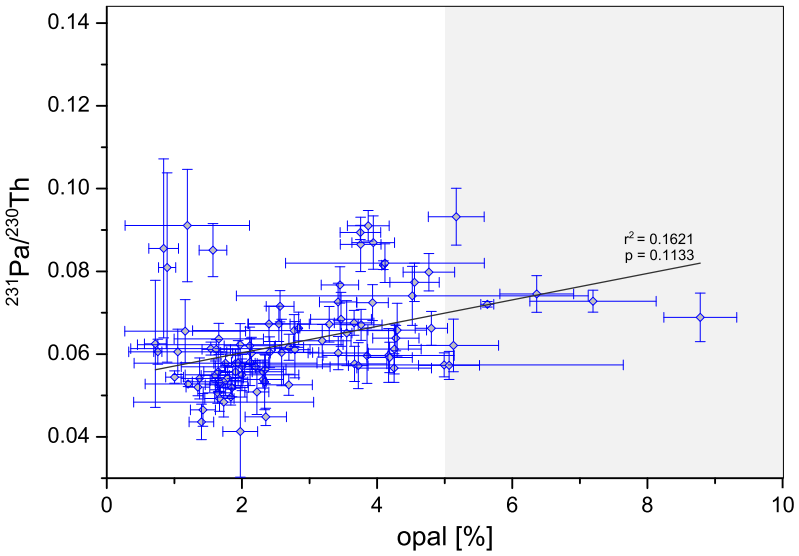
Extended Data Figure 3 | Comparison of age models for ODP 1063. Tuning points used in this study and by ref. 20. The age models agree within few 100 yr.

©2015 Macmillan Publishers Limited. All rights reserved



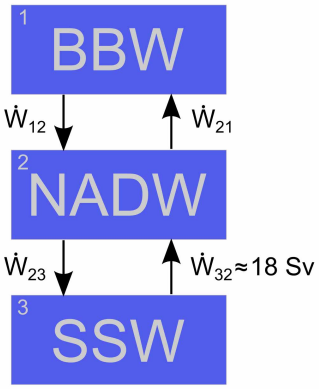
Extended Data Figure 4 | ^{231}Pa/^{230}Th and opal concentration records of ODP 1063. Comparison of the ^{231}Pa/^{230}Th data (**a**; error bars, 2 s.d.) with the variations in the opal concentration (**b**; error bars, 2 s.d.).

©2015 Macmillan Publishers Limited. All rights reserved



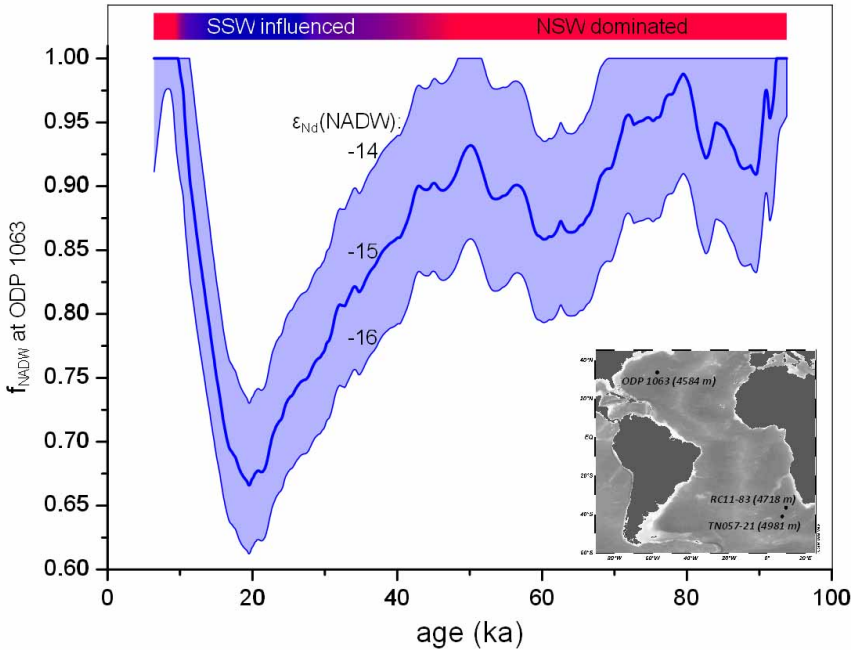
Extended Data Figure 5 | ^{231}Pa/^{230}Th as a function of opal concentration. According to the *P* value the weak positive correlation ($r^2 = 0.16$, $\alpha > 5\%$) of the opal concentration (error bars, 2 s.d.) and the ^{231}Pa/^{230}Th ratio (error bars, 2 s.d.) is not significant. The grey shaded area indicates preserved opal concentrations above 5%, below which no measurable influence on sedimentary ^{231}Pa/^{230}Th has been found in the framework of an Atlantic-wide study[55].

©2015 Macmillan Publishers Limited. All rights reserved



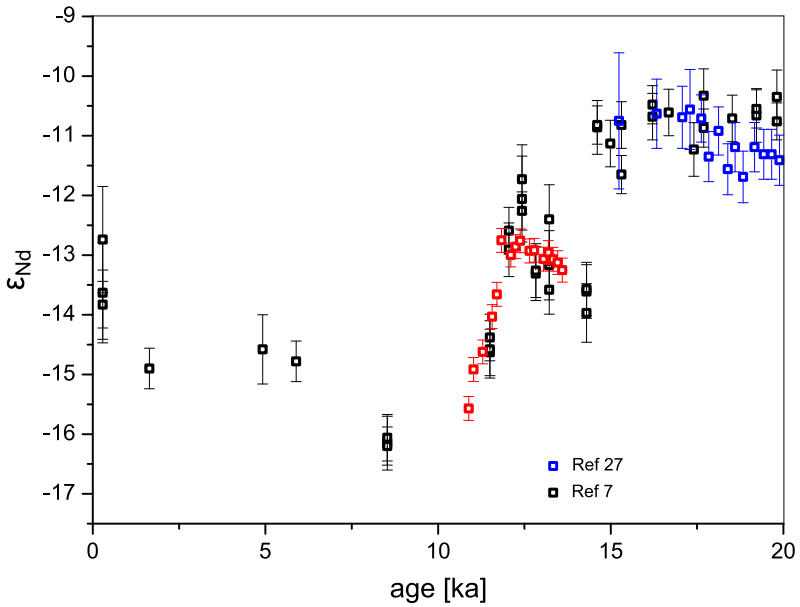
Extended Data Figure 6 | Three-box model including Nd isotope ratios, Nd concentrations and exchange rates. $\dot{W}_{ij}$ is the water exchange between the boxes *i* and *j*, ε_i is the Nd isotope composition, and c_i is the Nd concentration.

©2015 Macmillan Publishers Limited. All rights reserved



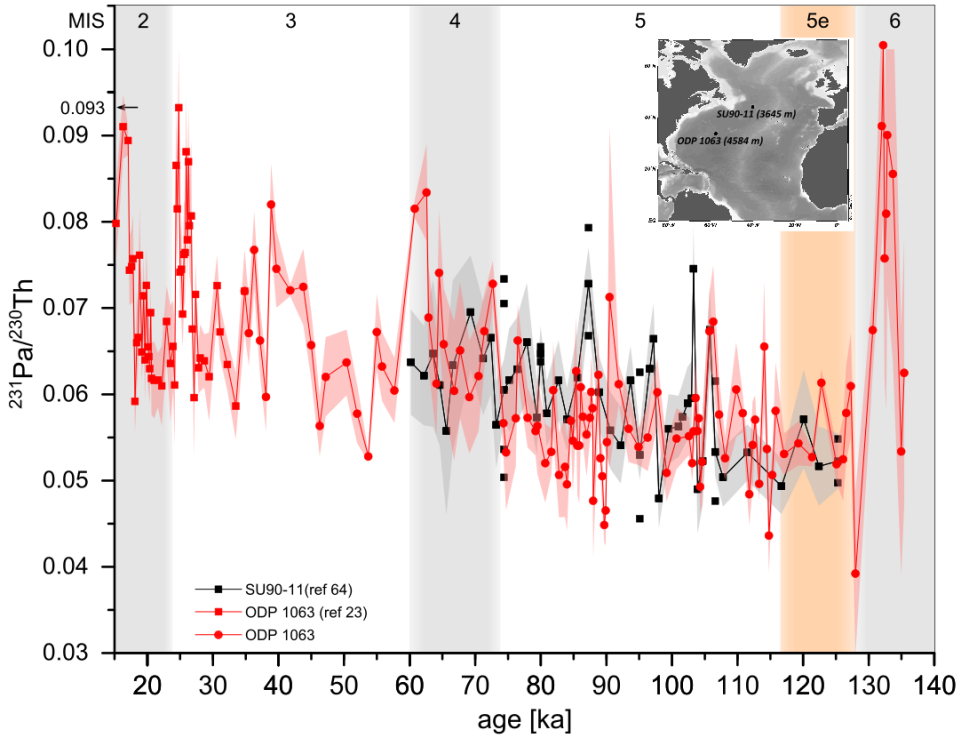
Extended Data Figure 7 | Fraction of NADW at the Bermuda Rise. Water mass mixing is derived from a linear mixing model and ε_{Nd} data sets from ODP 1063 and RC11-83/TN057[7] for three different ε_{Nd}(NADW) values. Given the uncertainties of the boundary conditions, in particular Nd concentrations and endmember variability, we focus on the long-term trend of the AMOC only and use a 10 kyr running mean for ε_{Nd}(ODP 1063) and ε_{Nd}(SSW). For the calculations a range of endmember compositions for ε_{Nd}(NADW) has been assumed (−14 to −16), defining the range of uncertainty (bright blue). The calculations show that there was an increase in the fraction of SSW and a decrease in the fraction of NSW in the water mass mixture at ODP 1063 only during the peak of the last glacial period.

©2015 Macmillan Publishers Limited. All rights reserved



Extended Data Figure 8 | Comparison of ε_{Nd} results from the Bermuda Rise. ε_{Nd} obtained from bulk sediment leachates (blue[27]; red, this study) reproduces foraminifera-derived ε_{Nd} (black[8]) within the standard deviation (error bars, 2 s.d.).

©2015 Macmillan Publishers Limited. All rights reserved



Extended Data Figure 9 | North Atlantic $^{231}Pa/^{230}Th$ profiles. Data from ODP 1063 (red; error bars, 2 s.d.) compared with data from SU90-11[64] (black; error bars, 1 s.d.).

©2015 Macmillan Publishers Limited. All rights reserved

Extended Data Table 1 | Measured radiocarbon ages for *Globorotalia inflata*

Lab#	hole/core/section/sample	depth mcd [m]	^{14}C age [a]	calibrated age [a]
MAMS 21175	D1H1W 94-95 cm	1.20	8,729 ± 26	9,358 ± 45
MAMS 21176	D1H1A 118-119 cm	1.46	11,000 ± 31	12,596 ± 45

Age uncertainties are given as 1 s.d. The calibration of the radiocarbon ages was performed with OxCal v4.2.3 (ref. 65) using the IntCal2013 data set[66] and assuming a 400 yr surface radiocarbon reservoir age.

©2015 Macmillan Publishers Limited. All rights reserved

LETTER

doi:10.1038/nature13805

Origins of major archaeal clades correspond to gene acquisitions from bacteria

Shijulal Nelson-Sathi[1], Filipa L. Sousa[1], Mayo Roettger[1], Nabor Lozada-Chávez[1], Thorsten Thiergart[1], Arnold Janssen[2], David Bryant[3], Giddy Landan[4], Peter Schönheit[5], Bettina Siebers[6], James O. McInerney[7] & William F. Martin[1,8]

The mechanisms that underlie the origin of major prokaryotic groups are poorly understood. In principle, the origin of both species and higher taxa among prokaryotes should entail similar mechanisms—ecological interactions with the environment paired with natural genetic variation involving lineage-specific gene innovations and lineage-specific gene acquisitions[1–4]. To investigate the origin of higher taxa in archaea, we have determined gene distributions and gene phylogenies for the 267,568 protein-coding genes of 134 sequenced archaeal genomes in the context of their homologues from 1,847 reference bacterial genomes. Archaeal-specific gene families define 13 traditionally recognized archaeal higher taxa in our sample. Here we report that the origins of these 13 groups unexpectedly correspond to 2,264 group-specific gene acquisitions from bacteria. Interdomain gene transfer is highly asymmetric, transfers from bacteria to archaea are more than fivefold more frequent than vice versa. Gene transfers identified at major evolutionary transitions among prokaryotes specifically implicate gene acquisitions for metabolic functions from bacteria as key innovations in the origin of higher archaeal taxa.

Genome evolution in prokaryotes entails both tree-like components generated by vertical descent and network-like components generated by lateral gene transfer (LGT)[5,6]. Both processes operate in the formation of prokaryotic species[1–6]. Although it is clear that LGT within prokaryotic groups such as cyanobacteria[7], proteobacteria[8] or halophiles[9] is important in genome evolution, the contribution of LGT to the formation of new prokaryotic groups at higher taxonomic levels is unknown. Prokaryotic higher taxa are recognized and defined by ribosomal RNA phylogenetics[10], their existence is supported by phylogenomic studies of informational genes[11] that are universal to all genomes, or nearly so[12]. Such core genes encode about 30–40 proteins for ribosome biogenesis and information processing functions, but they comprise only about 1% of an average genome. Although core phylogenomics studies provide useful prokaryotic classifications[13], they give little insight into the remaining 99% of the genome, because of LGT[14]. The core does not predict gene content across a given prokaryotic group, especially in groups with large pangenomes or broad ecological diversity[1,4], nor does the core itself reveal which gene innovations underlie the origin of major groups.

To examine the relationship between gene distributions and the origins of higher taxa among archaea, we clustered all 267,568 proteins encoded in 134 archaeal chromosomes using the Markov Cluster algorithm (MCL)[15] at a $\geq 25\%$ global amino acid identity threshold, thereby generating 25,762 archaeal protein families having ≥ 2 members. Clusters below that sequence identity threshold were not considered further. Among the 25,762 archaeal clusters, two-thirds (16,983) are archaeal specific—they detect no homologues among 1,847 bacterial genomes. The presence of these archaeal-specific genes in each of the 134 archaeal genomes is plotted in Fig. 1 against an unrooted reference tree (left panel) constructed from a concatenated alignment of the 70 single copy genes universal to archaea sampled. The gene distributions strongly correspond to the 13 recognized archaeal higher taxa present in our sample, with 14,416 families (85%) occurring in members of only one of the 13 groups indicated and 1,545 (9%) occurring in members of two groups only (Fig. 1). Another 6% of archaeal-specific clusters are present in more than two groups, and 0.3% are present in all genomes sampled (Fig. 1).

The remaining one-third of the archaeal families (8,779 families) have homologues that are present in anywhere from one to 1,495 bacterial genomes. The number of genes that each archaeal genome shares with 1,847 bacterial genomes and which bacterial genomes harbour those homologues is shown in the gene sharing matrix (Extended Data Fig. 1), which reveals major differences in the per-genome frequency of bacterial gene occurrences across archaeal lineages. We generated alignments and maximum likelihood trees for those 8,471 archaeal families having bacterial counterparts and containing ≥ 4 taxa. In 4,397 trees the archaeal sequences were monophyletic (Fig. 2), while in the remaining 4,074 trees the archaea were not monophyletic, interleaving with bacterial sequences. For all trees, we plotted the distribution of gene presence or absence data across archaeal taxa onto the reference tree.

Among the 4,397 cases of archaeal monophyly, 1,082 trees contained sequences from only one bacterial genome or bacterial phylum (Extended Data Fig. 2), a distribution indicating gene export from archaea to bacteria. In the remaining 3,315 trees (Supplementary Table 3), the monophyletic archaea were nested within a broad bacterial gene distribution spanning many phyla. For 2,264 of those trees, the genes occur specifically in only one higher archaeal taxon (left portion of Fig. 2), but at the same time they are very widespread among diverse bacteria (lower panel of Fig. 2), clearly indicating that they are archaeal acquisitions from bacteria, or imports. Among the 2,264 imports, genes involved in metabolism (39%) are the most frequent (Supplementary Table 2).

Like the archaeal-specific genes in Fig. 1, the imports in Fig. 2 correspond to the 13 archaeal groups. We asked whether the origins of these groups coincide with the acquisitions of the imports.If the imports were acquired at the origin of each group, their set of phylogenies should be similar to the set of phylogenies for the archaeal-specific, or recipient, genes (Fig. 1) from the same group. As an alternative to single origin to account for monophyly, the imports might have been acquired in one lineage and then spread through the group, in which case the recipient and import tree sets should differ. Using a Kolmogorov–Smirnov test adapted to non-identical leaf sets, we could not reject the null hypothesis H_0 that the import and recipient tree sets were drawn from the same distribution for six of the 13 higher taxa: Thermoproteales ($P = 0.32$), Desulfurococcales ($P = 0.3$), Methanobacteriales ($P = 0.96$), Methanococcales ($P = 0.19$), Methanosarcinales ($P = 0.16$), and Haloarchaea ($P = 0.22$), while the slightest possible perturbation of the import set, one random prune and graft LGT event per tree, did reject H_0 at $P < 0.002$ in those six cases, very strongly ($P < 10^{-42}$) for the Haloarchaea, where the largest tree sample is available (Extended Data Fig. 3 and Extended Data Table 1). For these six archaeal higher taxa, the origin

[1]Institute of Molecular Evolution, Heinrich-Heine University, 40225 Düsseldorf, Germany. [2]Mathematisches Institut, Heinrich-Heine University, 40225 Düsseldorf, Germany. [3]Department of Mathematics and Statistics, University of Otago, Dunedin 9054, New Zealand. [4]Genomic Microbiology Group, Institute of Microbiology, Christian-Albrechts-Universität Kiel, 24118 Kiel, Germany. [5]Institut für Allgemeine Mikrobiologie, Christian-Albrechts-Universität Kiel, 24118 Kiel, Germany. [6]Faculty of Chemistry, Biofilm Centre, Molecular Enzyme Technology and Biochemistry, University of Duisburg-Essen, 45117 Essen, Germany. [7]Department of Biology, National University of Ireland, Maynooth, County Kildare, Ireland. [8]Instituto de Tecnologia Química e Biológica, Universidade Nova de Lisboa, 2780-157 Oeiras, Portugal.

©2015 Macmillan Publishers Limited. All rights reserved

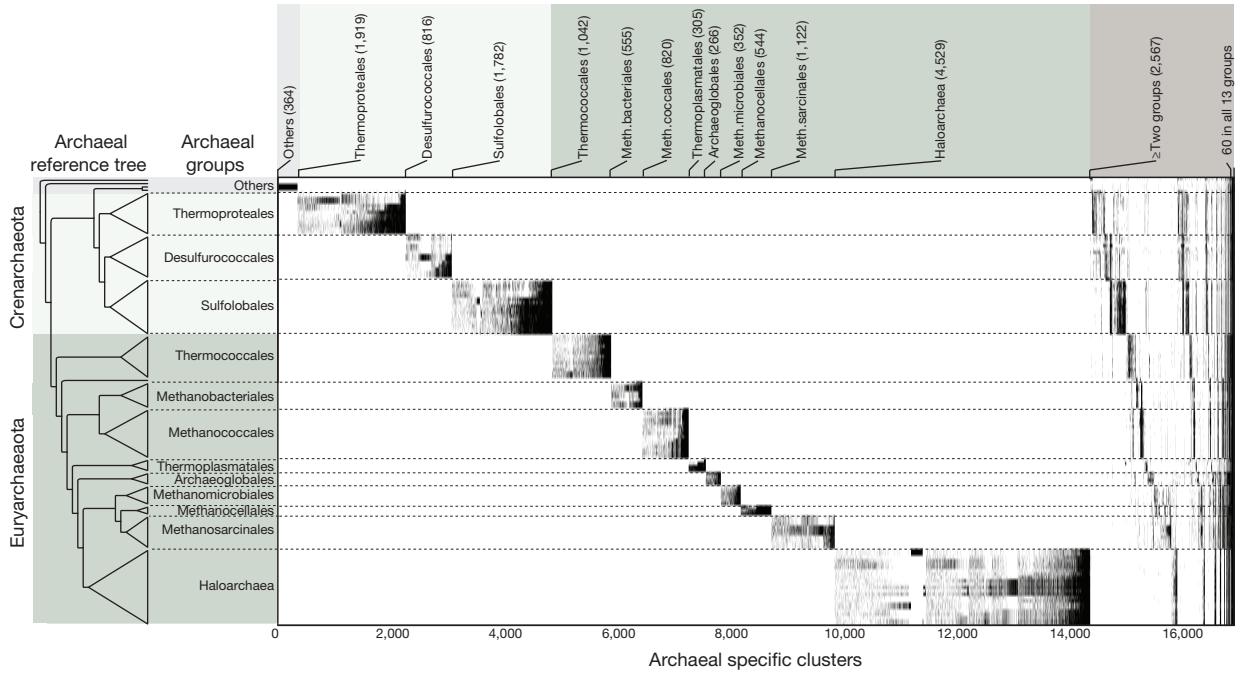


Figure 1 | Distribution of genes in archaeal-specific families. Maximum-likelihood (ML) trees were generated for 16,983 archaeal specific clusters (lower axis). For each cluster, ticks indicate presence (black) or absence (white) of the gene in the corresponding genome (rows, left axis). The number of clusters containing taxa specific to each group is indicated (upper axis). To generate clusters, 134 archaeal and 1,847 bacterial genomes were downloaded from the NCBI website (http://www.ncbi.nlm.nih.gov, version June 2012). An all-against-all BLAST[26] of archaeal proteins yielded 11,372,438 reciprocal best BLAST hits[27] (rBBH) having an *e*-value $< 10^{-10}$ and $\geq 25\%$ local amino acid identity. These protein pairs were globally aligned using the Needleman–Wunsch algorithm[28] resulting in a total of 10,382,314 protein pairs (267,568 proteins, 86.6%). These 267,568 proteins were clustered into 25,762 families using the standard Markov Chain clustering procedure[15]. There were 41,560 archaeal proteins (13.4% of the total) that did not have archaeal homologues, these were classified as singletons and excluded from further analysis. The 23 bacterial groups were defined using phylum names, except for Firmicutes and Proteobacteria. All 25,752 archaeal protein families were aligned using MAFFT[29] (version v6.864b). Archaeal specific gene families were defined as those that lack bacterial homologues at the *e*-value $< 10^{-10}$ and $\geq 25\%$ global amino acid identity threshold. For those archaeal clusters having hits in multiple bacterial strains of a species, only the most similar sequence among the strains was considered for the alignment. Maximum likelihood trees were reconstructed using RAxML[30] program for all cases where the alignment had four or more protein sequences. Archaeal species, named in order, are given in Supplementary Table 1. Clusters, including gene identifiers and corresponding cluster of orthologous groups (COG) functional annotations, are given in Supplementary Table 2. The unrooted reference tree at left was constructed as described in Fig. 2.

of their group-specific bacterial genes and the origin of the group are indistinguishable.

In 4,074 trees, the archaea were not monophyletic (Extended Data Fig. 4; Supplementary Tables 4 and 5). Transfers in these phylogenies are not readily polarized and were scored neither as imports nor exports. Importantly, if we plot the gene distributions sorted for bacterial groups, rather than for archaeal groups, we do not find similar patterns such as those defining the 13 archaeal groups. That is, we do not detect patterns that would correspond to the acquisition of archaeal genes at the origin of bacterial groups (Extended Data Fig. 5), indicating that gene transfers from archaea to bacteria, though they clearly do occur, do not correspond to the origin of major bacterial groups sampled here.

In archaeal systematics, Haloarchaea, Archaeoglobales, and Thermoplasmatales branch within the methanogens[13,16], as in our reference tree (Fig. 2). All three groups hence derive from methanogenic ancestors. Previous studies have identified a large influx of bacterial genes into the halophile common ancestor[17], and gene fluxes between archaea at the origin of these major clades[16]. Figure 2 shows that the acquisition of bacterial genes corresponds to the origin of these three groups from methanogenic ancestors, all of which have relinquished methanogenesis and harbour organotrophic forms[18,19]. Among the 2,264 bacteria-to-archaea transfers, 1,881 (83%) have been acquired by methanogens or ancestrally methanogenic lineages, which comprise 55% of the present archaeal sample.

Neither the archaeal-specific genes nor the bacterial acquisitions showed evidence for any pattern of higher order archaeal relationships or hierarchical clustering[20] among the 13 higher taxa, with the exception of the crenarchaeote–euryarchaeote spilt (Extended Data Fig. 6). While 16,680 gene families (14,416 archaeal-specific and 2,264 acquisitions) recover the groups themselves, only 4% as many genes (491 archaeal-specific and 110 acquisitions) recover any branch in the reference phylogeny linking those groups (Extended Data Fig. 7).

For 7,379 families present in 2–12 groups, we examined all 6,081,075 possible trees that preserve the crenarchaeote–euryarchaeote split by coding each group as an OTU (operational taxonomic unit) and scoring gene presence in one member of a group as present in the group. A random tree can account for 569 (8%) of the families, the best tree can account for 1,180 families (16%), while the reference tree accounts for 849 (11%) of the families (Extended Data Fig. 8). Thus, the gene distributions conflict with all trees and do not support a hierarchical relationship among groups.

Figure 3 shows the phylogenetic structure (grey branches) that is recovered by the individual phylogenies of the 70 genes that were used to make the reference tree. It reveals a tree of tips[21] in that, for deeper branches, no individual gene tree manifests the deeper branches of the concatenation tree. Even the crenarchaeote–euryarchaeote split is not recovered because of the inconsistent position of Thaumarchaea and Nanoarchaea. Projected upon the tree of tips are the bacterial acquisitions that correspond to the origin of the 13 archaeal groups studied here.

The direction of transfers between the two prokaryotic domains is highly asymmetric. The 2,264 imports plotted in Fig. 3 are transfers from bacteria to archaea, occurring only in one archaeal group (Extended Data Table 2, Supplementary Table 6). Yet only 391 converse transfers,

©2015 Macmillan Publishers Limited. All rights reserved

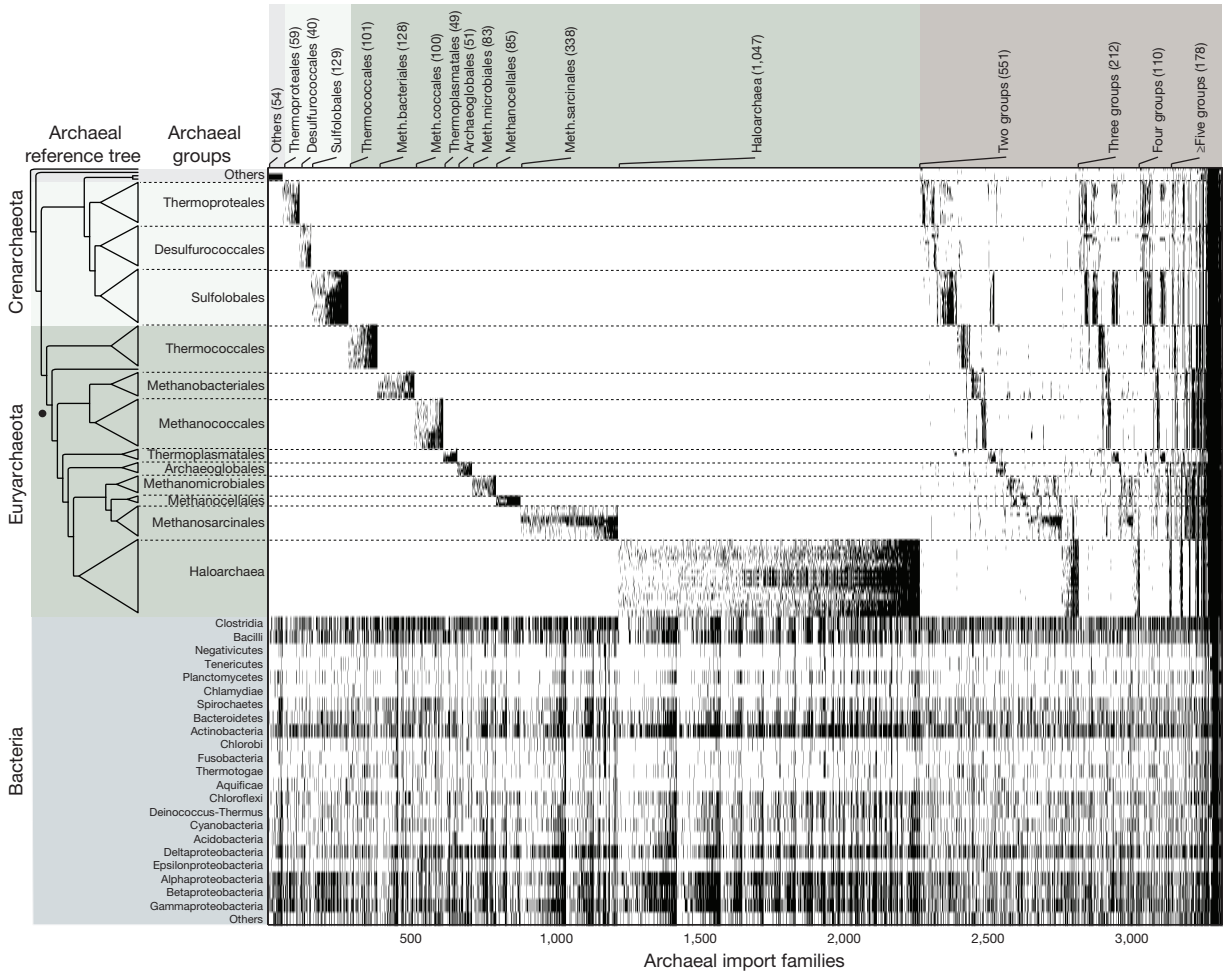


Figure 2 | Bacterial gene acquisitions in archaeal genomes. Upper panel ticks indicate gene presence in the 3,315 ML trees in which archaea are monophyletic. Archaeal genomes listed as in Fig. 1. The lower panel shows the occurrence of homologues among bacterial groups. Gene identifiers including functional annotations are given in Supplementary Table 2. The number of trees containing taxa specific to each archaeal group (or groups) is indicated at the top. The *Methanopyrus kandleri* branch (dot) subtends all methanogens in the tree. There are 56 genes at the far right that occur in all 13 groups (fully black columns) and were probably present in the prokaryote common ancestor. Bacterial homologues of archaeal protein families were identified as described in Fig. 1 (rBBH and ≥ 25% global identity), yielding 8,779 archaeal families having one or more bacterial homologues. An archaeal reference tree was constructed from a weighted concatenation alignment[29] of 70 archaeal single copy genes using RAxML[30] program. The 70 genes used to construct the unrooted reference tree are *rpsJ, rpsK, rps15p, rpsQ, rps19e, rpsB, rps28e, rpsD, rps4e, rpsE, rps7, rpsH, rpl, rpl15, rpsC, rplP, rpl18p, rplR, rplK, rplU, rl22, rpl24, rplW, rpl30P, rplC, rpl4lp, rplE, rpl7ae, rplB, rpsM, rpsH, rplF, rpsS, rpsI, rimM, gsp-3, rli, rpoE, rpoA, rpoB, dnaG, recA, drg, yyaF, gcp, hisS, map, metG, trm, pheS, pheT, rio1, ansA, flpA, gate, glyS, rplA, infB, arf1, pth, SecY, proS, rnhB, rfcL, rnz, cca, eif2A, eif5a, eif2G,* and *valS.*

exports from archaea to bacteria, were observed (Extended Data Table 2), the bacterial genomes most frequently receiving archaeal genes occurring in Thermotogae (Supplementary Table 7). Transfers from bacteria to archaea are thus greater than fivefold more frequent than vice versa, yet sample-scaled for equal number of bacterial and archaeal genomes, transfers from bacteria to archaea are 10.7-fold more frequent (see Supplementary Information). The bacteria-to-archaea transfers comprise predominantly metabolic functions, with amino acid import and metabolism (208 genes), energy production and conversion (175 genes), inorganic ion transport and metabolism (123 genes), and carbohydrate transport and metabolism (139 genes) being the four most frequent functional classifications (Extended Data Table 2).

The extreme asymmetry in interdomain gene transfers probably relates to the specialized lifestyle of methanogens, which served as recipients for 83% of the polarized gene transfers observed (Supplementary Table 8). Hydrogen-dependent methanogens are specialized chemolithoautotrophs, the route to more generalist organotrophic lifestyles that are not H_2 and CO_2 dependent entails either gene invention or gene acquisition. For Haloarchaea, Archaeoglobales and Thermoplasmatales, gene acquisition from bacteria provided the key innovations that transformed methanogenic ancestors into founders of new higher taxa with access to new niches, whereby several methanogen lineages have acquired numerous bacterial genes[22] but have retained the methanogenic lifestyle.

Gene transfers from bacteria to archaea not only underpin the origin of major archaeal groups, they also underpin the origin of eukaryotes, because the host that acquired the mitochondrion was, phylogenetically, an archaeon[23,24]. Our current findings support the theory of rapid expansion and slow reduction currently emerging from studies of genome evolution[25]. Subsequent to genome expansion via acquisition, lineage-specific gene loss predominates, as evident in Figs 1 and 2. In principle, the bacterial genes that correspond to the origin of major archaeal groups could have been acquired by independent LGT events[9,14], via unique combinations in founder lineage pangenomes[3,4], or via mass transfers involving symbiotic associations, similar to the origin of eukaryotes[23,24]. For lineages in which the origin of bacterial genes and the origin of the higher archaeal taxon are indistinguishable, the latter two mechanisms seem more probable.

©2015 Macmillan Publishers Limited. All rights reserved

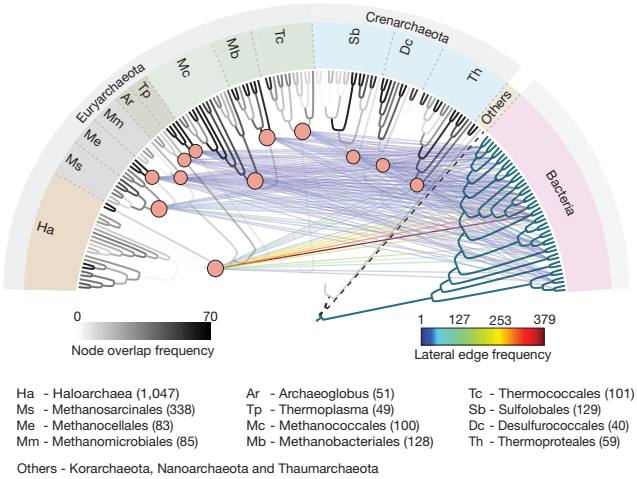


Figure 3 | Archaeal gene acquisition network. Vertical edges represent the archaeal reference phylogeny in Fig. 1 based on 70 concatenated genes, grey shading (from white (0) to dark grey (70)) indicates how often the branch was recovered by the 70 genes analysed individually. The vertical edge weight of each branch in the reference tree (scale bar at left) was calculated as the number of times associated node was present within the single gene trees (see Source Data). Lateral edges indicate 2,264 bacterial acquisitions in archaea. The number of acquisitions per group is indicated in parentheses, the number of times the bacterial taxon appeared within the inferred donor clade is colour coded (scale bar at right). The strongest lateral edge links Haloarchaea with Actinobacteria. Archaea were arbitrarily rooted on the Korarchaeota branch (dotted line). Bacterial taxon labels are (from left to right) Chlorobi, Bacteroidetes, Acidobacteria, Chlamydiae, Planctomycetes, Spirochaetes, ε-Proteobacteria, δ-Proteobacteria, β-Proteobacteria, γ-Proteobacteria, α-Proteobacteria, Actinobacteria, Bacilli, Tenericutes, Negativicutes, Clostridia, Cyanobacteria, Chloroflexi, Deinococcus-Thermococcus, Fusobacteria, Aquificae, Thermotogae. The order of archaeal genomes (from left to right) is as in Fig. 1 (from bottom to top).

Online Content Methods, along with any additional Extended Data display items and Source Data, are available in the online version of the paper; references unique to these sections appear only in the online paper.

Received 4 June; accepted 28 August 2014.
Published online 15 October 2014.

1. Doolittle, W. F. & Papke, R. T. Genomics and the bacterial species problem. *Genome Biol.* **7,** 116 (2006).
2. Retchless, A. C. & Lawrence, J. G. Temporal fragmentation of speciation in bacteria. *Science* **317,** 1093–1096 (2007).
3. Achtman, M. & Wagner, M. Microbial diversity and the genetic nature of microbial species. *Nature Rev. Microbiol.* **6,** 431–440 (2008).
4. Fraser, C., Alm, E. J., Polz, M. F., Spratt, B. G. & Hanage, W. P. The bacterial species challenge: making sense of genetic and ecological diversity. *Science* **323,** 741–746 (2009).
5. Puigbò, P., Wolf, Y. I. & Koonin, E. V. The tree and net components of prokaryote genome evolution. *Genome Biol. Evol.* **2,** 745–756 (2010).
6. Dagan, T. Phylogenomic networks. *Trends Microbiol.* **19,** 483–491 (2011).
7. Hess, W. R. Genome analysis of marine photosynthetic microbes and their global role. *Curr. Opin. Biotechnol.* **15,** 191–198 (2004).
8. Kloesges, T. *et al.* Networks of gene sharing among 329 proteobacterial genomes reveal differences in lateral gene transfer frequency at different phylogenetic depths. *Mol. Biol. Evol.* **28,** 1057–1074 (2011).
9. Williams, D., Gogarten, J. P. & Papke, R. T. Quantifying homologous replacement of loci between haloarchaeal species. *Genome Biol. Evol.* **4,** 1223–1244 (2012).
10. Woese, C. R. Bacterial evolution. *Microbiol. Rev.* **51,** 221–271 (1987).
11. Rivera, M. C., Jain, R., Moore, J. E. & Lake, J. A. Genomic evidence for two functionally distinct gene classes. *Proc. Natl Acad. Sci. USA* **95,** 6239–6244 (1998).
12. Puigbò, P., Wolf, Y. I. & Koonin, E. V. Search for a tree of life in the thicket of the phylogenetic forest. *J. Biol.* **8,** 59 (2009).
13. Brochier-Armanet, C., Forterre, P. & Gribaldo, S. Phylogeny and evolution of the Archaea: one hundred genomes later. *Curr. Opin. Microbiol.* **14,** 274–281 (2011).
14. Lake, J. A. & Rivera, M. C. Deriving the genomic tree of life in the presence of horizontal gene transfer: conditioned reconstruction. *Mol. Biol. Evol.* **21,** 681–690 (2004).
15. Enright, A. J., Van Dongen, S. & Ouzounis, C. A. An efficient algorithm for large-scale detection of protein families. *Nucleic Acids Res.* **30,** 1575–1584 (2002).
16. Wolf, Y. I., Makarova, K. S., Yutin, N. & Koonin, E. V. Updated clusters of orthologous genes for Archaea: a complex ancestor of the Archaea and the byways of horizontal gene transfer. *Biol. Direct* **7,** 46 (2012).
17. Nelson-Sathi, S. *et al.* Acquisitions of 1,000 eubacterial genes physiologically transformed a methanogen at the origin of Haloarchaea. *Proc. Natl Acad. Sci. USA* **109,** 20537–20542 (2012).
18. Bräsen, C., Esser, D., Rauch, B. & Siebers, B. Carbohydrate metabolism in Archaea: current insights into unusual enzymes and pathways and their regulation. *Microbiol. Mol. Biol. Rev.* **78,** 89–175 (2014).
19. Siebers, B. & Schönheit, P. Unusual pathways and enzymes of central carbohydrate metabolism in Archaea. *Curr. Opin. Microbiol.* **8,** 695–705 (2005).
20. Doolittle, W. F. & Bapteste, E. Pattern pluralism and the tree of life hypothesis. *Proc. Natl Acad. Sci. USA* **104,** 2043–2049 (2007).
21. Creevey, C. J. *et al.* Does a tree-like phylogeny only exist at the tips in the tree of prokaryotes? *Proc. R. Soc. Lond. B* **271,** 2551–2558 (2004).
22. Deppenmeier, U. *et al.* The genome of *Methanosarcina mazei*: evidence for lateral gene transfer between bacteria and archaea. *J. Mol. Microbiol. Biotechnol.* **4,** 453–461 (2002).
23. Williams, T. A., Foster, G. F., Cox, C. Y. & Embley, T. M. An archaeal origin of eukaryotes supports only two primary domains of life. *Nature* **504,** 231–236 (2013).
24. McInerney, J. O., O'Connell, M. J. & Pisani, D. The hybrid nature of eukaryota and a consilient view of life on Earth. *Nature Rev. Microbiol.* **12,** 449–455 (2014).
25. Wolf, Y. I. & Koonin, E. V. Genome reduction as the dominant mode of evolution. *Bioessays* **35,** 829–837 (2013).
26. Altschul, S. F. *et al.* Gapped BLAST and PSI-BLAST: a new generation of protein database search programs. *Nucleic Acids Res.* **25,** 3389–3402 (1997).
27. Tatusov, R. L., Koonin, E. V. & Lipman, D. J. A genomic perspective on protein families. *Science* **278,** 631–637 (1997).
28. Rice, P., Longden, I. & Bleasby, A. EMBOSS: the European molecular biology open software suite. *Trends Genet.* **16,** 276–277 (2000).
29. Guindon, S. & Gascuel, O. A simple, fast, and accurate algorithm to estimate large phylogenies by maximum likelihood. *Syst. Biol.* **52,** 696–704 (2003).
30. Stamatakis, A., Ludwig, T. & Meier, H. RAxML-III: a fast program for maximum likelihood-based inference of large phylogenetic trees. *Bioinformatics* **21,** 456–463 (2005).

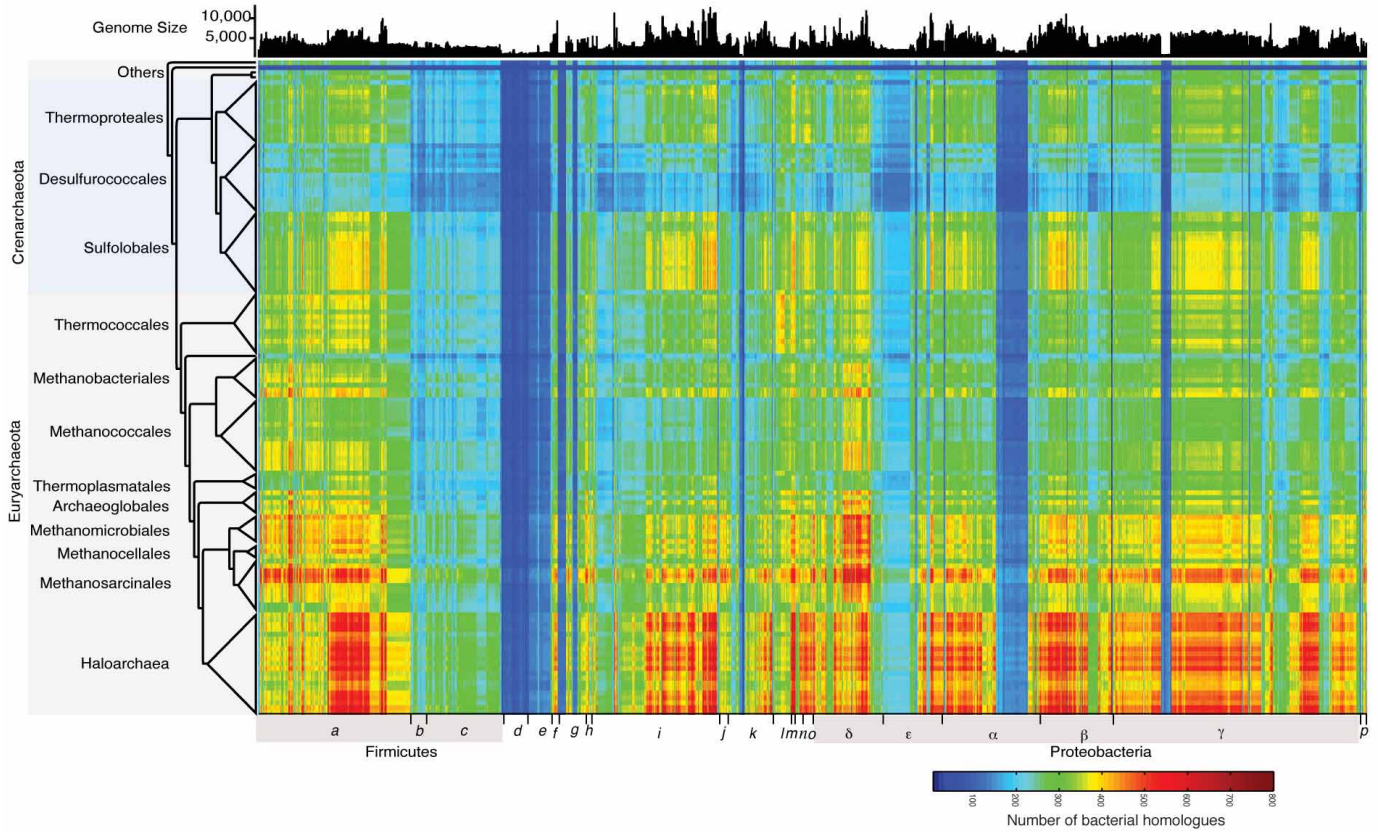
Supplementary Information is available in the online version of the paper.

Acknowledgements We gratefully acknowledge funding from European Research Council (ERC 232975 to W.F.M.), the graduate school E-Norm of the Heinrich-Heine University (W.F.M.), the DFG (Scho 316/11-1 to P.S.; SI 642/10-1 to B.S.), and BMBF (0316188A, B.S.). G.L. is supported by an ERC grant (281357 to Tal Dagan), D.B. thanks the Alexander von Humbold Foundation for a Fellowship. Computational support of the Zentrum für Informations- und Medientechnologie (ZIM) at the Heinrich-Heine University is gratefully acknowledged.

Author Contributions S.N.-S., F.L.S., M.R., N.L.-C. and T.T. performed bioinformatic analyses; A.J., D.B. and G.L. performed statistical analyses; P.S., B.S., J.O.M. and W.F.M. interpreted results; S.N.-S., F.L.S., G.L., J.O.M. and W.F.M. wrote the paper; S.N.-S., G.L. and W.F.M. designed the study. All authors discussed the results and commented on the manuscript.

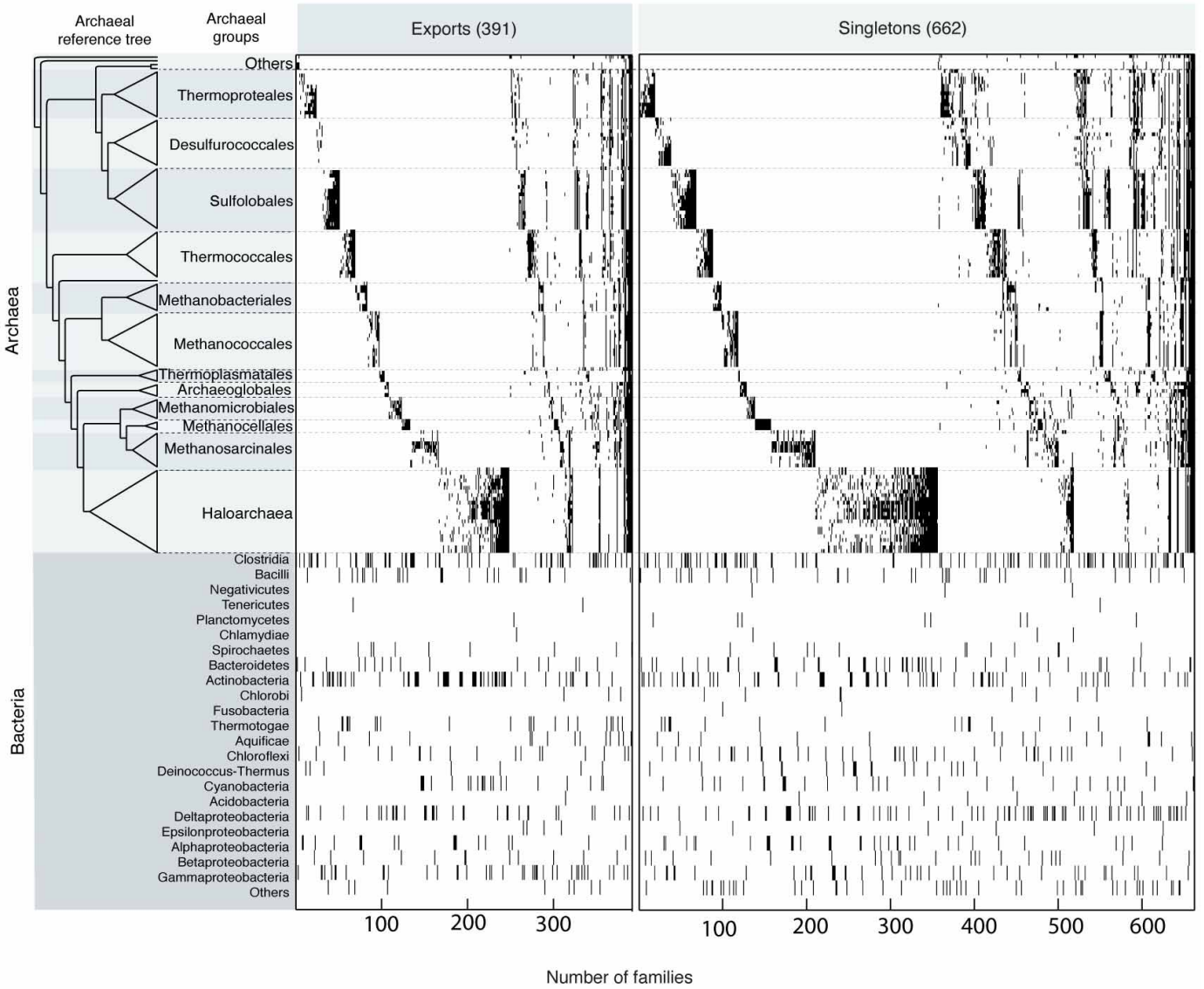
Author Information Reprints and permissions information is available at www.nature.com/reprints. The authors declare no competing financial interests. Readers are welcome to comment on the online version of the paper. Correspondence and requests for materials should be addressed to W.F.M. (bill@hhu.de).

©2015 Macmillan Publishers Limited. All rights reserved



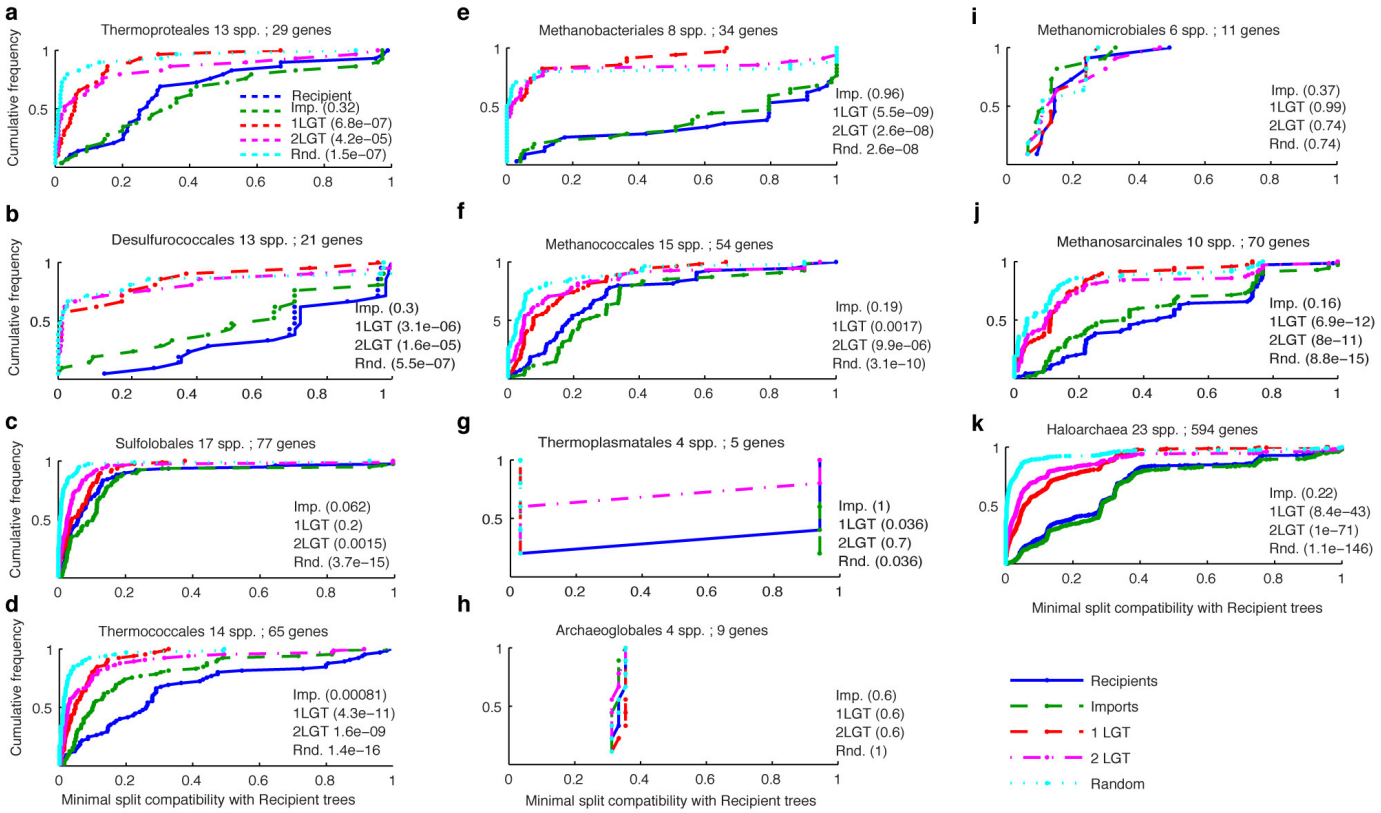
Extended Data Figure 1 | Inter-domain gene sharing network. Each cell in the matrix indicates the number of genes (*e*-value $\leq 10^{-10}$ and $\geq 25\%$ global identity) shared between 134 archaeal and 1,847 bacterial genomes in each pairwise inter-domain comparison (scale bar at lower right). Archaeal genomes are listed as in Fig. 1. Bacterial genomes are presented in 23 groups corresponding to phylum or class in the GenBank nomenclature: *a* = Clostridia; *b* = Erysipelotrichi, Negativicutes; *c* = Bacilli; *d* = Firmicutes; *e* = Chlamydia; *f* = Verrucomicrobia, Planctomycete; *g* = Spirochaete; *h* = Gemmatimonadetes, Synergisteles, Elusimicrobia, Dyctyoglomi, Nitrospirae; *i* = Actinobacteria; *j* = Fibrobacter, Chlorobi; *k* = Bacteroidetes; *l* = Fusobacteria; Thermatogae, Aquificae, Chloroflexi; *m* = Deinococcus-Thermus; *n* = Cyanobacteria; *o* = Acidobacteria; δ, ε, α, β, γ = Delta, Epsilon, Alpha, Beta and Gamma proteobacteria; *P* = Thermosulfurobateria, Caldiserica, Chysiogenete, Ignavibacteria. Bacterial genome size in number of proteins is indicated at the top.

©2015 Macmillan Publishers Limited. All rights reserved



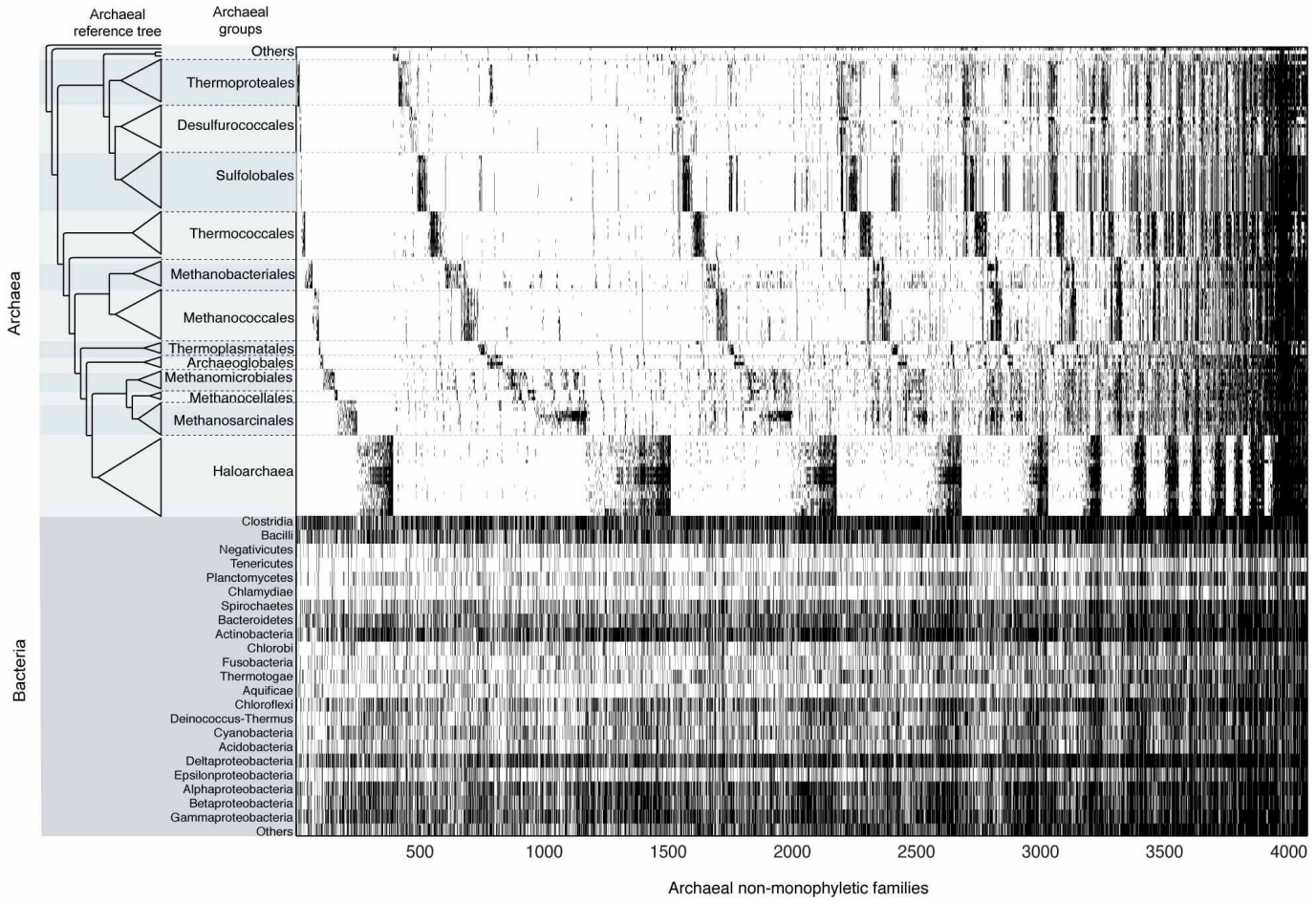
Extended Data Figure 2 | Presence–absence patterns of archaeal genes with sparse distribution among bacteria sampled. Archaeal export families are sorted according to the reference tree on the left. The figure shows the 391 cases of archaea-to-bacteria export (≥ 2 archaea and ≥ 2 bacteria from one phylum only), 662 cases of bacterial singleton trees (≥ 3 archaea, one bacterium). The 25,762 clusters were classified into the following categories (Supplementary Table 2): 16,983 archaeal specific, 3,315 imports, 391 exports, 662 cases of bacterial singletons with ≥ 3 archaea in the tree, 308 cases with three sequences (a bacterial singleton and 2 archaea) in the cluster, 4,074 trees in which archaea were non-monophyletic, and 29 ambiguous cases among trees showing archaeal monophyly. The bacterial taxonomic distribution is shown in the lower panel. Gene identifiers and trees are given in Supplementary Table 3.

©2015 Macmillan Publishers Limited. All rights reserved



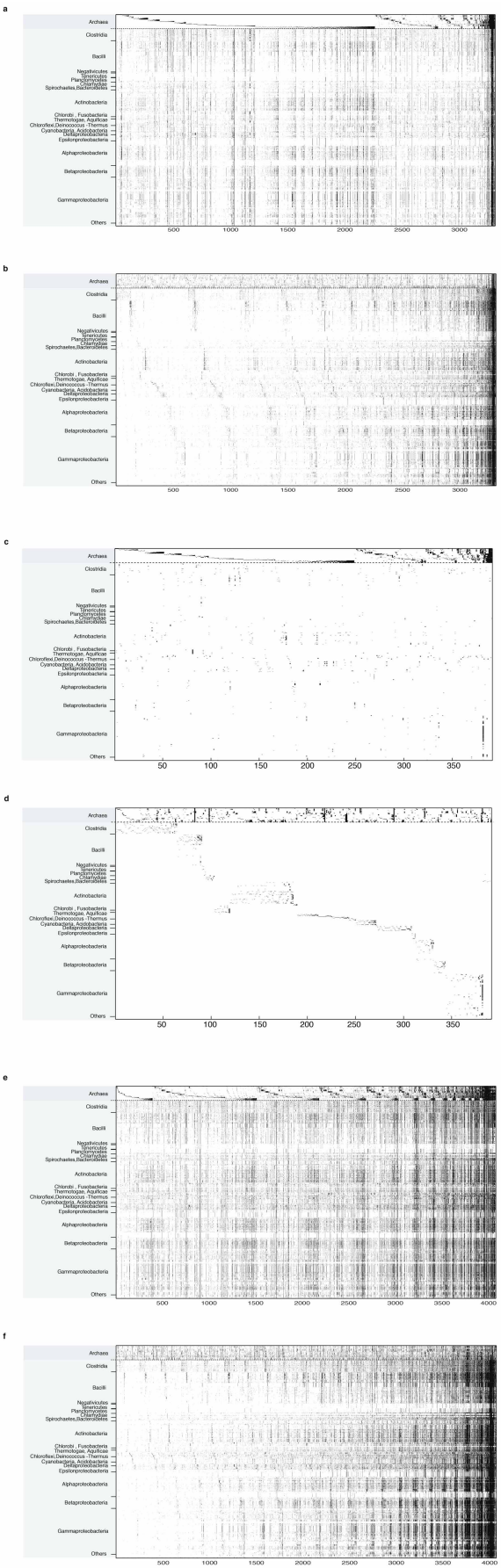
Extended Data Figure 3 | Comparison of sets of trees for single-copy genes in 11 archaeal groups. Cumulative distribution functions for scores of tree compatibility with the recipient data set. Values are *P* values of the two-sided Kolmogorov–Smirnov (KS) two-sample goodness-of-fit test in the comparison of the recipient (blue) data sets against the imports (green) data set and three synthetic data sets, one-LGT (red), two-LGT (pink) and random (cyan). **a**, Thermoproteales. **b**, Desulfurococcales. **c**, Sulfolobales. **d**, Thermococcales. **e**, Methanobacteriales. **f**, Methanococcales. **g**, Thermoplasmatales. **h**, Archaeoglobales. **i**, Methanococcales. **j**, Methanosarcinales. **k**, Haloarchaea.

©2015 Macmillan Publishers Limited. All rights reserved



Extended Data Figure 4 | Presence–absence patterns of all archaeal non-monophyletic genes. Archaeal families that did not generate monophyly for archaeal sequences in ML trees are plotted according the reference tree on the left, the distribution across bacterial genomes groups is shown in the lower panel. These trees include 693 cases in which archaea showed non-monophyly by the misplacement of a single archaeal branch. Gene identifiers and trees are given in Supplementary Tables 4 and 5.

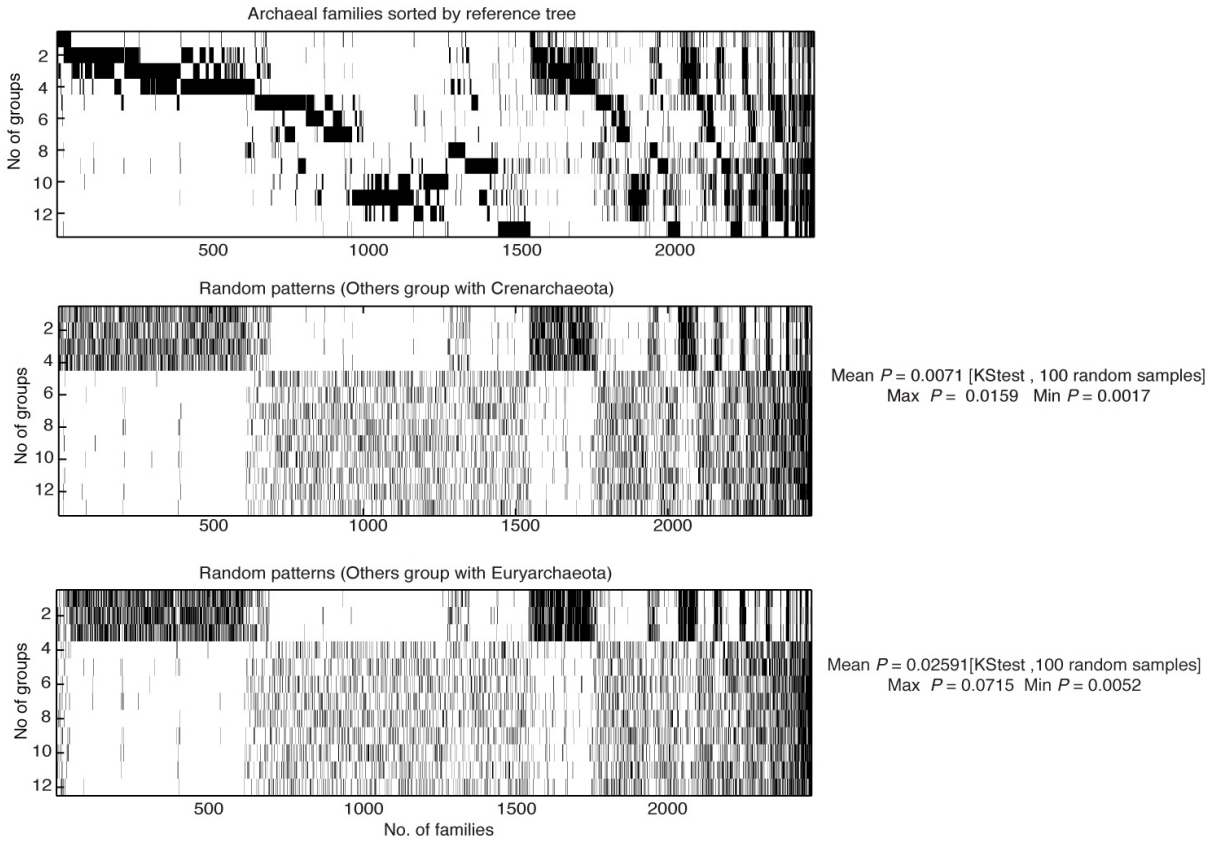
©2015 Macmillan Publishers Limited. All rights reserved



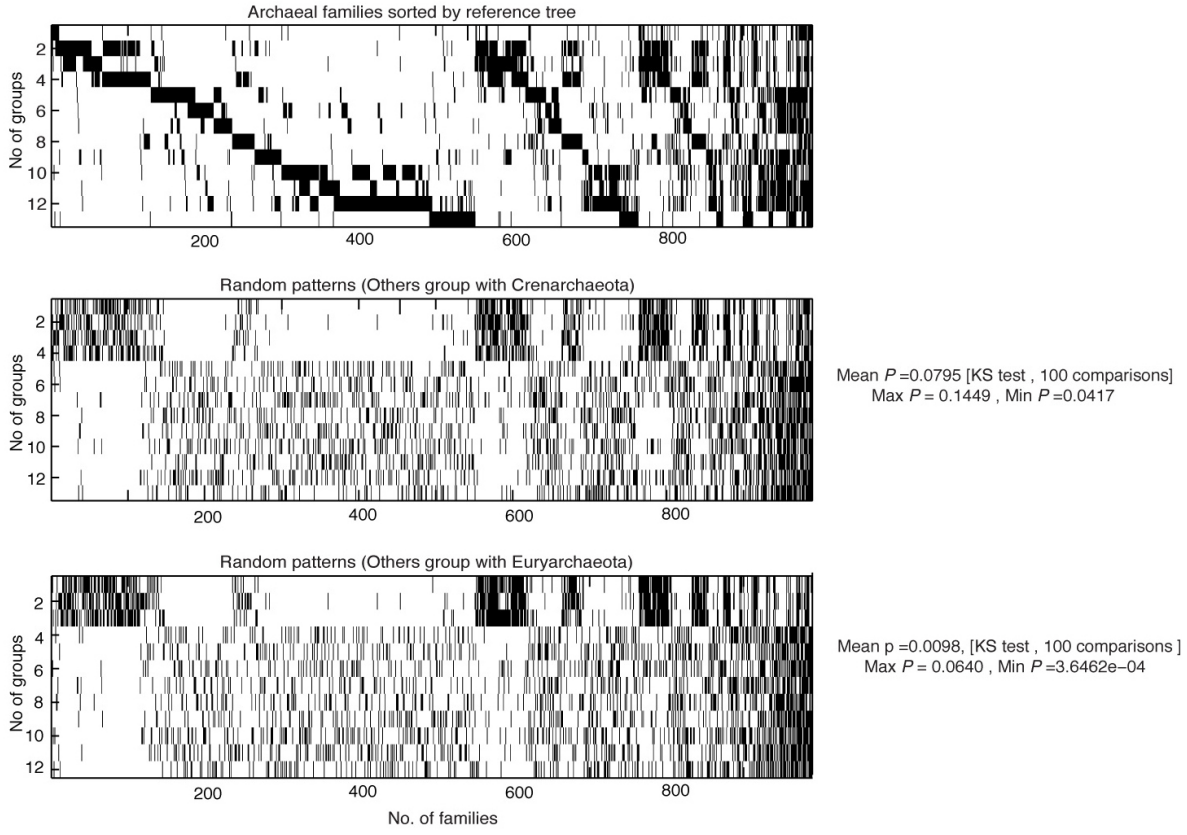
Extended Data Figure 5 | Sorting by bacterial presence absence patterns for archaeal imports, exports and archaeal non-monophyletic families. Archaeal families and their homologue distribution in 1,847 bacterial genomes are sorted by archaeal (top) and bacterial (bottom) gene distributions for direct comparison. **a**–**f**, Distributions of archaeal imports sorted by archaeal groups (**a**) and by bacterial groups (**b**); distributions of archaeal exports sorted by archaeal groups (**c**) and by bacterial groups (**d**); distributions of archaeal non-monophyletic gene families sorted by archaeal groups (**e**) and by bacterial groups (**f**).

©2015 Macmillan Publishers Limited. All rights reserved

a



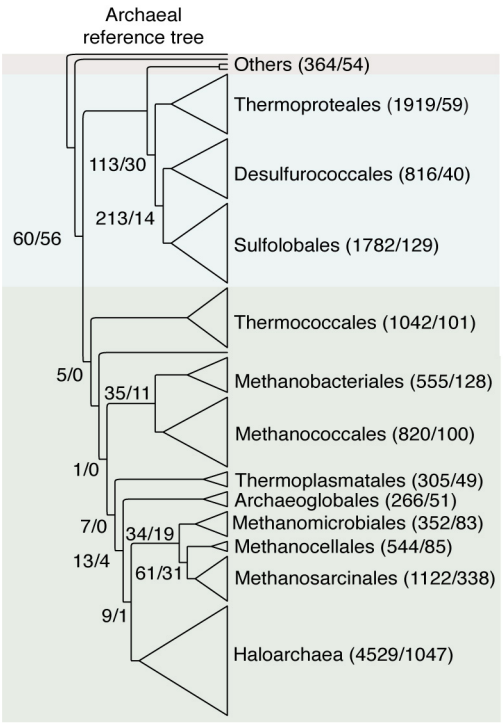
b



©2015 Macmillan Publishers Limited. All rights reserved

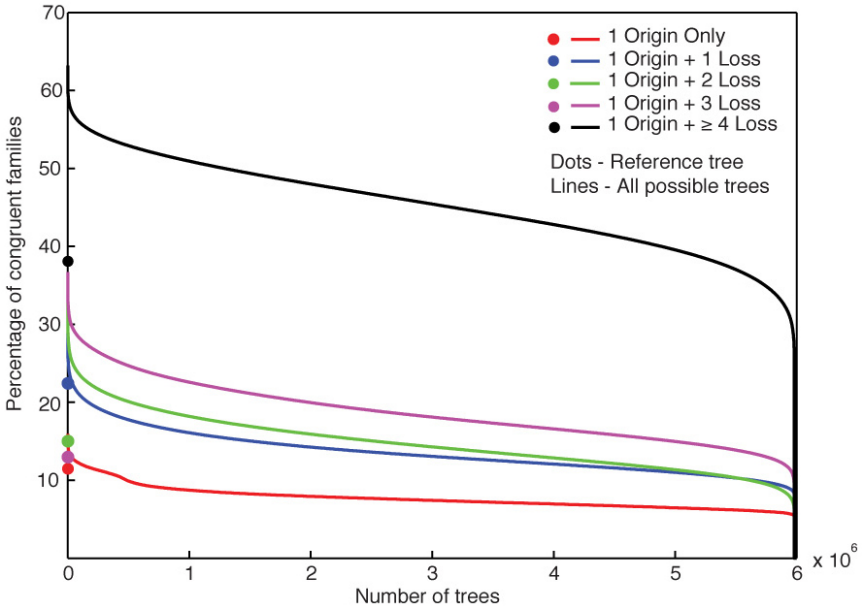
Extended Data Figure 6 | Testing for evidence of higher order archaeal relationships using a permutation tail probability (PTP) test. Comparison of pairwise Euclidian distance distributions between archaeal real and conditional random gene family patterns using the two-sided Kolmogorov-Smirnov (KS) two-sample goodness-of-fit test. **a**, Archaeal specific families: distribution of 2,471 archaeal specific families present in at least 2 and less than 11 groups (top); comparison between real data and 100 conditional random patterns generated by shuffling the entries within Crenarchaeota and Euryarchaeota separately; comparison between real data and conditional random patterns generated by including others (Nanoarchaea, Thaumarchaea and Korarchaeota) into Crenarchaeota (mean $P = 0.0071$, middle) or into Euryarchaeota (mean $P = 0.02591$, bottom). **b**, Archaeal import families: distribution of 989 archaeal import families present in at least 2 and less than 11 groups (top). Comparison between real data and 100 conditional random patterns generated by shuffling the entries within Crenarchaeota and Euryarchaeota separately by including others (Nanoarchaea, Thaumarchaea and Korarchaeota) into Crenarchaeota (mean $P = 0.0795$, middle); comparison between real data and random patterns generated by including others (Nanoarchaea,Thaumarchaea and Korarchaeota) into Euryarchaeota (mean $P = 0.0098$, bottom).

©2015 Macmillan Publishers Limited. All rights reserved



Extended Data Figure 7 | Archaeal specific and import gene counts on a reference tree. Number of archaeal specific and import families corresponding to each node in the reference tree are shown in the order of 'specific/imports'. Numbers at internal nodes indicate the number of archaeal-specific families and families with bacterial homologues that correspond to the reference tree topology. Values at the far left indicate the number of archaeal-specific families and families with bacterial homologues that are present in all archaeal groups.

©2015 Macmillan Publishers Limited. All rights reserved



Extended Data Figure 8 | Non tree-like structure of archaeal protein families. Proportion of archaeal families whose distributions are congruent with the reference tree and with all possible trees. Filled circles indicate the proportion of archaeal families that are congruent to the reference tree allowing no losses (with a single origin) and different increments of losses allowed. Red, blue, green, magenta and black circles represent the proportion of families that can be explained using a single origin (849, 11.5%), single origin plus 1 loss (22.4%), single origin plus 2 losses (15%), single origin plus 3 losses (13%) and single origin plus ≥ 4 losses (38%) respectively. Lines indicate the proportion of families that can be explained by each of the 6,081,075 possible trees that preserve euryarchaeote and crenarchaeote monophyly. Note that on average, any given tree can explain 569 (8%) of the archaeal families using a single origin event in the tree, and the best tree can explain only 1,180 families (16%). In the present data, 208,019 trees explain the gene distributions better than the archaeal reference tree without loss events, underscoring the discordance between core gene phylogeny and gene distributions in the remainder of the genome.

©2015 Macmillan Publishers Limited. All rights reserved

Extended Data Table 1 | Comparison of sets of trees for single-copy genes in 11 archaeal groups

Archaeal groups	Number of taxa	Number of genes	Recipients vs. Imports	Recipients vs. 1 LGT	Recipients vs. 2 LGT	Recipients vs. Random
Thermoproteales	13	29	0.32	6.80E-07	4.20E-05	1.50E-07
Desulfurococcales	13	21	0.3	3.10E-06	1.60E-05	5.50E-07
Sulfolobales	17	77	0.062	0.2	1.50E-03	3.70E-15
Thermococcales	14	65	0.00081	4.30E-11	1.60E-09	1.40E-16
Methanobacteriales	8	34	0.96	5.50E-09	2.60E-08	2.60E-08
Methanococcales	15	54	0.19	0.0017	9.90E-06	3.10E-10
Thermoplasmatales	4	5	1	0.036	0.7	0.036
Archaeoglobales	4	9	0.6	0.6	0.6	1
Methanococcales	15	54	0.19	0.0017	9.90E-06	3.10E-10
Methanosarcinales	10	70	0.16	6.90E-12	8.00E-11	8.80E-15
Haloarchaea	23	594	0.22	8.40E-43	1.00E-71	1.10E-146

Values are *P* values of the Kolmogorov–Smirnov two-sample goodness-of-fit test operating on scores of tree compatibility with the recipient data set.

©2015 Macmillan Publishers Limited. All rights reserved

Extended Data Table 2 | Functional annotations for archaeal genes according to gene family distribution and phylogeny

Function	COG category	Specific	M	NM	Exp	Imp
Information	Chromatin structure and dynamics	14	1	5	1	1
	Translation, ribosome biogenesis	263	84	50	9	27
	Replication, recombination and repair	375	126	185	17	69
	Transcription	524	124	113	10	81
Cellular	Defense mechanisms	48	62	116	4	45
	Cell cycle, division, chromosome partitioning	79	22	15	2	13
	Trafficking, secretion, vesicular transport	97	17	6	3	6
	Cell motility	146	40	29	8	33
	Cell wall/membrane/envelope biogenesis	197	143	203	10	91
	Protein turnover, chaperones	236	85	137	18	61
	Signal transduction mechanisms	308	120	129	16	101
Metabolism	Secondary metabolites	10	46	35	0	30
	Nucleotide transport and metabolism	44	53	105	7	41
	Lipid transport and metabolism	62	113	117	6	72
	Coenzyme transport and metabolism	168	143	219	11	97
	Inorganic ion transport and metabolism	232	176	265	16	123
	Carbohydrate transport and metabolism	118	205	227	14	139
	Energy production and conversion	334	254	403	25	175
	Amino acid transport and metabolism	177	278	440	26	208
No annotation	General function prediction only	949	434	560	49	297
	Function unknown	12602	789	715	139	554
Total		16983	3315	4074	391	2264

Specific: genes that occur in at least two archaea but no bacteria in our clusters. M: archaeal genes that have bacterial homologues and the archaea (≥ 2 genomes) are monophyletic. NM: archaeal genes that have bacterial homologues but the archaea (≥ 2 genomes) are not monophyletic. Exp: exports, the gene occurs in ≥ 2 archaea but with extremely restricted distribution among bacteria (Supplementary Table 6). Imp: imports, archaeal genes with homologues that are widespread among bacterial lineages, while the archaea (≥ 2 genomes) are monophyletic and the archaeal gene distribution is specific to the groups shown in Figs 1 and 2.

©2015 Macmillan Publishers Limited. All rights reserved

LETTER

doi:10.1038/nature13851

Identification of multipotent mammary stem cells by protein C receptor expression

Daisong Wang[1]*, Cheguo Cai[1]*, Xiaobing Dong[1], Qing Cissy Yu[1], Xiao-Ou Zhang[2], Li Yang[2] & Yi Arial Zeng[1]

The mammary gland is composed of multiple types of epithelial cells, which are generated by mammary stem cells (MaSCs) residing at the top of the hierarchy[1,2]. However, the existence of these multipotent MaSCs remains controversial and the nature of such cells is unknown[3,4]. Here we demonstrate that protein C receptor (Procr), a novel Wnt target in the mammary gland, marks a unique population of multipotent mouse MaSCs. Procr-positive cells localize to the basal layer, exhibit epithelial-to-mesenchymal transition characteristics, and express low levels of basal keratins. Procr-expressing cells have a high regenerative capacity in transplantation assays and differentiate into all lineages of the mammary epithelium by lineage tracing. These results define a novel multipotent mammary stem cell population that could be important in the initiation of breast cancer.

The mammary gland is an epithelial organ consisting of myoepithelial (basal) cells and luminal cells. During pregnancy, the luminal cells at side branches undergo terminal differentiation and form alveolar cells. Previous studies using the surface markers Lin^-, $CD24^+$ and $CD29^{hi}$, and transplantation assays, indicate that MaSCs reside in the basal layer of the epithelium[1,2]. This population is heterogeneous, including MaSCs, differentiated basal cells and potential intermediate progenitors. Until now, no marker specific for MaSCs has been identified. On the other hand, the existence of multipotent MaSCs in adults remains in debate as lineage-tracing studies using the pan-basal markers keratin 5 (K5; also known as Krt5) and K14 generate controversial results[3,4]. Multipotent MaSCs may have been missed in other basal subpopulation lineage tracing studies using *Lgr5* or *Axin2*, and the rare occurrence of clones containing both lineages (bi-lineage) could be due to the periodic luminal expression of these genes[3,5,6]. Here we show that Procr, a novel Wnt target in the mammary gland, marks a unique population of multipotent MaSCs.

Wnt signalling is instrumental for MaSC self-renewal[5,7,8]. Our previous work demonstrated that the Wnt3A protein can expand MaSCs in three-dimensional Matrigel culture and maintain their stem cell properties[7]. Taking advantage of this *in vitro* system, we performed microarray analysis of the cultured MaSCs in an attempt to identify Wnt targets specifically expressed in MaSCs (Extended Data Fig. 1a). Among the candidates whose expression was increased in the presence of Wnt3A, we identified *Procr* (Extended Data Fig. 1a). Quantitative polymerase chain reaction (qPCR) confirmed that the gene is upregulated by Wnt3A treatment (Extended Data Fig. 1b).

Procr is a single-pass transmembrane protein originally recognized as protein C receptor through its roles in anticoagulation, inflammation and haematopoiesis[9–14]. We investigated whether Procr is normally expressed in the mammary epithelium. We isolated basal (Lin^- $CD24^+$ $CD29^{hi}$) and luminal (Lin^- $CD24^+$ $CD29^{lo}$) cells from 8-week-old virgin mammary glands (Fig. 1a), and found that *Procr* is expressed at higher levels in basal cells (Fig. 1b). Furthermore, fluorescence-activated cell sorting (FACS) analysis indicated that Procr labels 3–7% of basal cells depending on the genetic background (about $2.9 \pm 0.5\%$ in CD1 and $7 \pm 1.5\%$ in B6), while $Procr^+$ cells were not found among luminal cells (Fig. 1c and Extended Data Fig. 1c–g). $Procr^+$ cells were also detected in the stromal cell compartment (Extended Data Fig. 1c–g). Notably, the Procr expression patterns were similar throughout development (Extended Data Fig. 1c–g). Immunostaining confirmed that a subpopulation of basal cells expresses Procr (Fig. 1d). Intriguingly, $Procr^+$ cells appeared to express less K14 in comparison to their neighbouring $Procr^-$ basal cells (Fig. 1d). Next, we isolated $Procr^+$ and $Procr^-$ cells from the basal cell population and performed RNA-sequencing (RNA-seq) analysis. We found that basal $Procr^+$ cells exhibit features of epithelial-to-mesenchymal transition (EMT), with lower expression of epithelial signatures, for example, Epcam, E-cadherin and claudins, and with increased expression of mesenchymal signature genes, for example, *Vim*, N-cadherin (also known as *Cdh2*), *Foxc2*, *Zeb1* and *Zeb2* (Fig. 1e). Of note, the basal keratins K5 and K14 were expressed at lower levels in $Procr^+$ cells compared with $Procr^-$ basal cells (Fig. 1e). These observations were confirmed by qPCR analysis (Fig. 1f).

We next examined the behaviours of $Procr^+$ basal cells *in vitro* and in transplantation assays. We isolated total basal cells ($CD24^+$ $CD29^{hi}$), $Procr^+$ basal cells ($Procr^+$ $CD24^+$ $CD29^{hi}$) and $Procr^-$ basal cells ($Procr^-$ $CD24^+$ $CD29^{hi}$), and compared their colony-forming ability in three-dimensional Matrigel culture as previously described[7] (Fig. 2a, b). We found that the enrichment of $Procr^+$ cells increased colony-forming efficiency by fivefold when compared to the total basal cell group. One colony formed out of 15 plated total basal cells, while one colony formed out of three plated $Procr^+$ basal cells (Fig. 2b and Extended Data Fig. 2a). Colony sizes were indistinguishable between the two groups (Fig. 2b). In striking contrast, $Procr^-$ basal cells were not able to form colonies in Matrigel culture, suggesting that MaSCs that have colony-forming abilities were absent from this group.

To assess their mammary gland reconstitution capacity, the three groups of isolated cells were transplanted into cleared fat pads. We found that $Procr^+$ basal cells generate the mammary gland more efficiently (repopulating frequency of 1/12) than total basal cells (1/68) (Fig. 2e). The outgrowths displayed normal morphology and marker expression (Fig. 2c). When recipient mice were in late pregnancy, the mammary gland resulting from the transplanted $Procr^+$ basal cells consisted of a dense ductal system ending in clusters of milk-producing alveoli (Fig. 2d). In contrast, $Procr^-$ basal cells showed markedly lower stem cell frequency (1/2,084) (Fig. 2e). These findings demonstrate that the $CD24^+$ $CD29^{hi}$ basal population can be further enriched for MaSCs using the marker Procr.

We found that $Lgr5^+$ cells fell into the $Procr^-$ population that has drastically reduced regenerative capability (Extended Data Fig. 3a, b), raising the question as to whether $Lgr5^+$ cells are enriched for MaSCs. To address this, we isolated the three subpopulations of basal cells, $Procr^+$ $Lgr5^-$, $Procr^-$ $Lgr5^+$ and $Procr^-$ $Lgr5^-$ and examined their regenerative capacities. Consistent with our earlier results, the $Procr^+$ $Lgr5^-$ cells efficiently formed colonies *in vitro* and readily reconstituted mammary gland in transplantation (repopulating frequency of 1/14) (Extended Data Fig. 3c, d). $Procr^-$ $Lgr5^+$ cells were not able to form colonies *in vitro*.

[1]The State Key Laboratory of Cell Biology, Institute of Biochemistry and Cell Biology, Shanghai Institutes for Biological Sciences, Chinese Academy of Sciences, Shanghai 200031, China. [2]Key Laboratory of Computational Biology, CAS-MPG Partner Institute for Computational Biology, Shanghai Institutes for Biological Sciences, Chinese Academy of Sciences, Shanghai 200031, China.
*These authors contributed equally to this work.

©2015 Macmillan Publishers Limited. All rights reserved

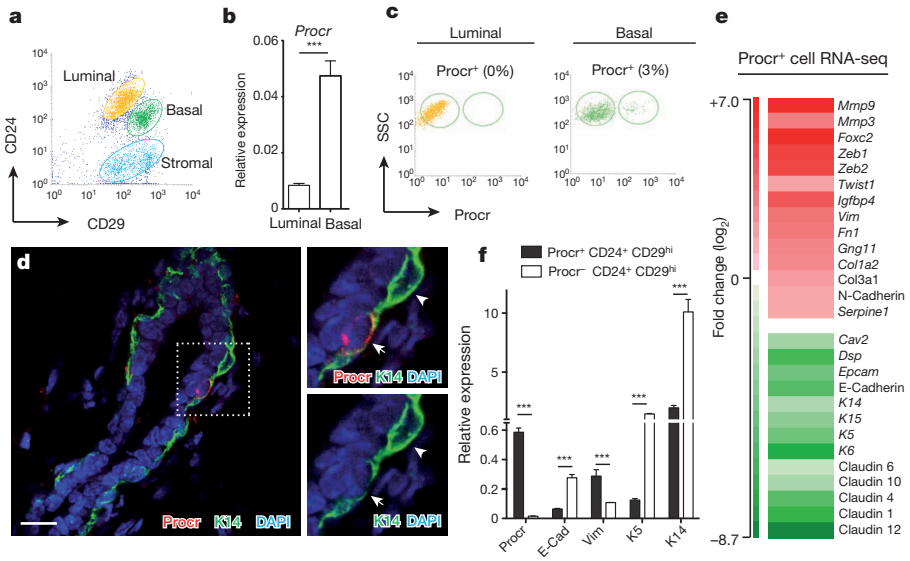


Figure 1 | Procr$^+$ basal cells express lower levels of basal keratin. **a**, **b**, Basal and luminal cells were FACS-isolated and analysed for *Procr* expression by qPCR. **c**, FACS analysis of Procr expression in 8-week-old CD1 mammary epithelial cells. **d**, Immunohistochemistry indicating the expression of Procr in a subpopulation of basal cells (arrows). Ninety-four per cent of Procr$^+$ basal cells ($n = 206$) expressed less K14 compared with the neighbouring basal cells (arrowheads). DAPI, 4′,6-diamidino-2-phenylindole. Scale bar, 20 μm. **e**, Expression of EMT-related genes in Procr$^+$ basal cells. **f**, qPCR analysis of Procr$^+$ basal cells and Procr$^-$ basal cells. Quantification was performed on three independent experiments. E-Cad, E-cadherin. **b**, **f**, Data are presented as mean ± standard deviation (s.d.). ***$P < 0.01$.

Interestingly, they were able to reconstitute *in vivo* by transplantation, although with a significantly lower repopulating frequency (1/165) (Extended Data Fig. 3c, d). Considering a repopulating frequency of 1/68 for total basal cells, our results indicated that Lgr5 expression was not enriched in regenerative MaSCs. This conclusion is different from a previous report[15], yet is consistent with two other studies[4,6]. Finally, the Procr$^-$ Lgr5$^-$ cells were depleted of MaSCs and failed to regenerate *in vitro* or *in vivo* (Extended Data Fig. 3c, d).

We next investigated whether the population of Procr$^+$ cells behave as multipotent MaSCs under physiological conditions. To this end, we generated a knock-in allele of Procr by integrating a *CreERT2-IRES-tdTomato* cassette at the first ATG codon (Fig. 3a and Extended Data Fig. 2b, c). Heterozygous mice were healthy and fertile. Homozygotes died before embryonic day (E)10.5 (Extended Data Fig. 2d, e), resembling the *Procr*-null mutant mice[16]. Confocal imaging of histological sections indicated that tdTomato$^+$ cells resided in the basal layer yet expressed lower levels of K5 and K14 compared with tdTomato$^-$ basal cells (Fig. 3b). FACS analysis indicated that 3% of basal cells were tdTomato$^+$ and no tdTomato$^+$ cells were found in luminal cells. Reminiscent of the expression of Procr itself, some tdTomato$^+$ cells were present in stromal cells (Fig. 3c). We isolated tdTomato$^+$ and tdTomato$^-$ cells from the basal group and assessed their colony formation capability. We found that tdTomato$^+$ cells form colonies efficiently *in vitro*, whereas tdTomato$^-$ cells cannot (Fig. 3d). These results demonstrate that the *Procr$^{CreERT2\text{-}IRES\text{-}tdTomato}$* allele faithfully recapitulates endogenous Procr expression.

The generation of the *Procr$^{CreERT2\text{-}IRES\text{-}tdTomato}$* mouse allowed us to examine the expression of Procr$^+$ cells in detail. Using whole-mount confocal imaging analysis, Procr$^+$ cells were identified as being sparsely located in E18.5 and newborn (postnatal day (P)1.5) mammary gland. At these stages, before the formation of the terminal end buds (TEBs), Procr$^+$ cells could be detected in the middle or at the tip of the mammary ducts (Extended Data Fig. 4a, b). In puberty, dispersed individual Procr$^+$ cells were predominantly present in the mammary ducts, whereas no Procr$^+$ cells were detected in the TEBs (Extended Data Fig. 4c, d). In the mature mammary gland, individual Procr$^+$ cells were also located over the ducts (Extended Data Fig. 4e). As the TEB is the most proliferative structure in the pubertal gland, our observations suggest that Procr$^+$ cells are not the major proliferative force, consistent with the properties of stem cells rather than transient amplifying

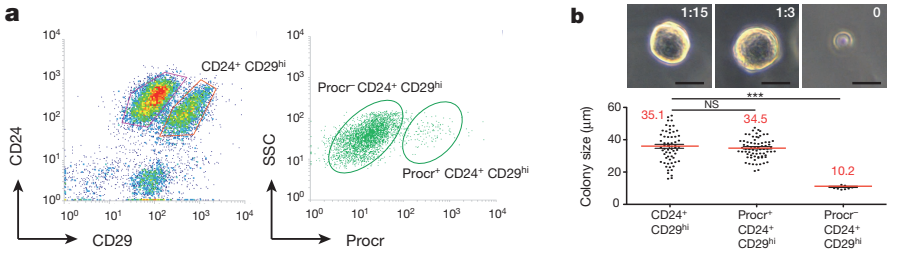


Figure 2 | Procr$^+$ cells are enriched for mammary stem cells with regenerative capabilities. **a**, Isolation of total basal, Procr$^+$ basal and Procr$^-$ basal populations. **b**, Colony-formation efficiency and the colony sizes in Matrigel culture. Scale bars, 20 μm. ***$P < 0.01$. NS, not significant. See also Extended Data Fig. 2a. **c**, **d**, Whole-mount and section images of an outgrowth derived from the transplantation of Procr$^+$ basal cells in nulliparous and late pregnant mammary tissues. Scale bars, 2 mm in whole mount; 20 μm in section. **e**, Transplantation of sorted cells in limiting dilution. Data are pooled from four independent experiments. ***$P < 0.01$.

e

	Number of cells injected per fat pad	Number of outgrowths	Fat pad filled	Repopulating frequency
CD24$^+$ CD29^{hi}	100	7/8	●×6 ◔×1 ○×1	
	50	4/8	●×4 ○×4	
	25	2/12	◔×1 ◑×1 ○×10	1/68.3 (41.3–113.0)
	13	2/12	◔×2 ○×10	
	1	1/22	◑×1 ○×21	
Procr$^+$ CD24$^+$ CD29^{hi}	100	8/8	●×8	
	50	6/6	●×6	
	25	9/12	●×7 ◔×1 ◑×1 ○×3	1/11.9*** (7.3–19.4)
	13	5/8	●×2 ◑×3 ○×3	
	1	5/18	◔×5 ○×13	
Procr$^-$ CD24$^+$ CD29^{hi}	500	2/8	●×2 ○×6	
	250	1/8	◑×1 ○×7	1/2084.2*** (675.3–6,432.1)
	100	0/6	○×6	
	50	0/6	○×6	

©2015 Macmillan Publishers Limited. All rights reserved

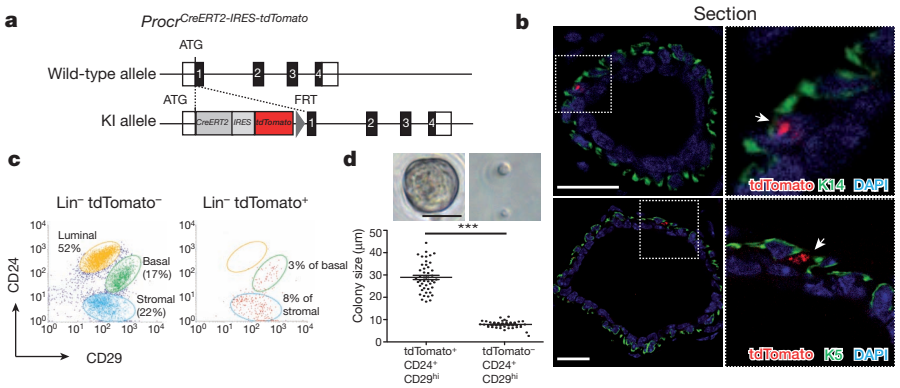


Figure 3 | *Procr*$^{CreERT2\text{-}IRES\text{-}tdTomato}$ knock-in mouse recapitulates the Procr expression pattern and labelled cell behaviour. **a**, Targeting strategy to generate the *Procr*$^{CreERT2\text{-}IRES\text{-}tdTomato}$ knock-in (KI) mouse. See also Extended Data Fig. 2b. **b**, Immunostaining analysis of the knock-in mammary sections. Scale bar, 20 μm. **c**, FACS analysis indicating that tdTomato$^+$ cells are located in 3% of basal and 8% of stromal cells. $n = 4$ mice. One of four similar experiments is shown. **d**, Colony formation of tdTomato$^+$ and tdTomato$^-$ basal cells in Matrigel culture. Scale bars, 20 μm. $^{***}P < 0.01$.

cells. By 5-ethymyl-2′-deoxyuridine (EdU) incorporation assays, we found that in pubertal or mature mammary glands, the majority of Procr$^+$ cells indeed enter the cell cycle (Extended Data Fig. 4f–i). The seemingly higher percentage of EdU$^+$ Procr$^+$ population cells in mature ducts is probably due to a lower number of EdU$^+$ cells at this stage (Extended Data Fig. 4i). Our data suggest that Procr$^+$ cells are proliferative cells residing in the mammary ducts.

To trace the fate of Procr$^+$ cells, we crossed the *Procr*$^{CreERT2\text{-}IRES\text{-}tdTomato/+}$ allele with the *Rosa26*$^{mTmG/+}$ (*R26*$^{mTmG/+}$) reporter strain[17] (Fig. 4a). We first tracked the developmental fate of Procr$^+$ cells in postnatal mammary glands by administering tamoxifen to *Procr*$^{CreERT2/+}$;*R26*$^{mTmG/+}$ pubertal mice (5 weeks old) and analysing the contribution of labelled cells to the mature epithelial network once the mice had reached adulthood. Expression of green fluorescent protein (GFP) was not observed in un-induced mice (data not shown). Short time tracing (48 h) and confocal whole-mount imaging allowed us to visualize single elongated cells initially labelled by GFP (Fig. 4b, e). Immunostaining in tissue sections confirmed that the initially GFP$^+$ cells were basal cells (Fig. 4f). Quantification of the labelling events by FACS analysis indicated that no luminal cells are labelled at the beginning of the analysis (Fig. 4c, d). There were some labelled stromal fibroblasts, which also express Procr (Fig. 4c, d). After 3 weeks of tracing, the GFP$^+$ cells expanded in number (Fig. 4g–i). In addition, their pattern extended to include luminal cells. Clonal expansion of GFP$^+$ cells was visualized by whole-mount imaging, and the clones consisted of both elongated and columnar cells (Fig. 4j). Immunostaining confirmed that GFP$^+$ cells are present in both basal and luminal layers (Fig. 4k). Clonal analysis revealed that the majority of the clones (72%) are bi-lineage, giving rise to basal and luminal cells. Notably, about 13% of the clones were single basal cells that had not entered division since labelling; no luminal clones were found (Extended Data Fig. 5a, b). Importantly, the majority of two-cell clones (65%) comprised one luminal cell and one basal cell (Extended Data Fig. 5c). When the tracing was prolonged to 6 weeks, the average clone sizes increased over time, and the proportion of the bi-lineage clone also increased (from 72% to 93%), indicating that more basal cells had differentiated into luminal cells (Extended Data Fig. 5d, e). The percentage of bi-lineage two-cell clones increased (from 65% to 85%), suggesting that more initially GFP$^+$ labelled cells had asymmetrically divided to become luminal cells (Extended Data Fig. 5f). During pregnancy, GFP$^+$ cells contributed to alveolus formation (Fig. 4l–o). One alveolus could consist solely of GFP$^+$ cells or harbour both GFP$^+$ and mTomato$^+$ cells (Fig. 4p), indicating that alveoli can originate from one or more progenitor(s), which is consistent with previous reports[4,5]. GFP$^+$ cells were maintained at similar percentages across multiple pregnancies, showing that Procr$^+$ cells are capable of long-term self-renewal (Extended Data Fig. 6a–f). Notably, GFP$^+$ stromal cells did not expand over tracing, suggesting a less proliferative nature of Procr$^+$ fibroblasts (Fig. 4c, h, m and Extended Data Fig. 6b, d).

The multipotency of Procr$^+$ basal cells was examined by initiating the labelling in 8-week-old adult mice (Extended Data Fig. 7a). After 3 weeks of tracing, the majority of labelled cells differentiated into bi-lineage clones (74%) (Extended Data Fig. 7b–g), and the percentage increased to 94% by 6 weeks (Extended Data Fig. 7h–j). From 3 weeks to 6 weeks, the percentage of bi-lineage two-cell clones also increased

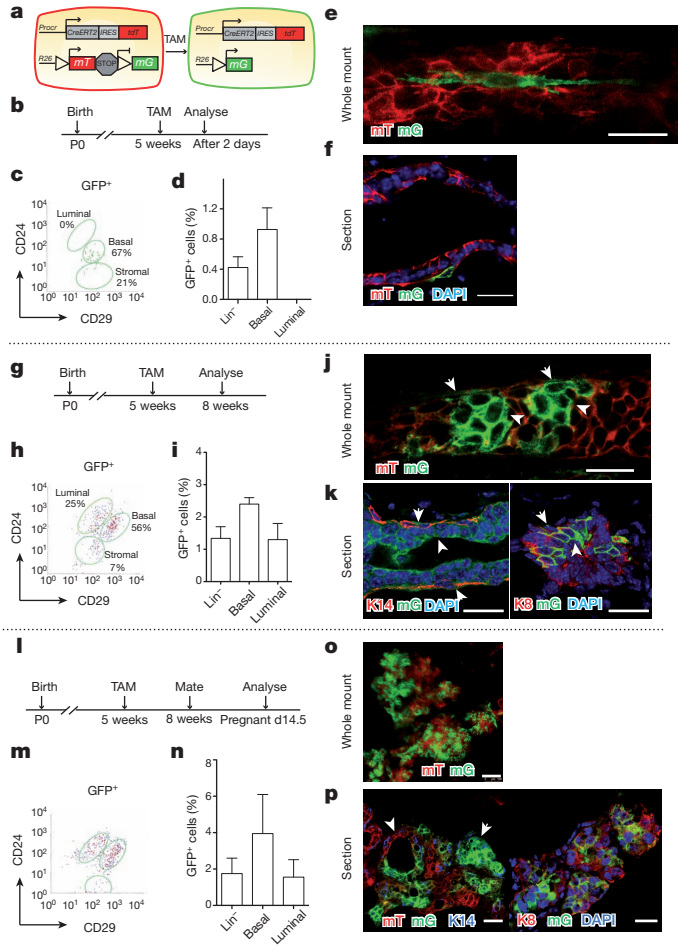


Figure 4 | Procr labels multipotent adult mammary stem cells. **a**, Illustration of lineage tracing strategy. *tdT*, *tdTomato*. **b**, Experimental setup used in short-term tracing. **c**, **d**, FACS analysis indicating that GFP$^+$ cells were restricted to the basal cells at 48 h after tamoxifen (TAM) administration. **e**, Whole-mount confocal microscopy showing an elongated GFP$^+$ basal cell. **f**, Section imaging indicating the basal location of the GFP$^+$ cell. **g**–**k**, FACS and imaging analysis of GFP$^+$ cell distribution after 3 weeks of tracing. **l**–**p**, FACS and imaging analysis of GFP$^+$ cells distribution at pregnant day 14.5 after 5 weeks of tracing. Scale bars, 20 μm. **d**, **i**, **n**, Data are presented as mean ± s.d. $n = 3$ mice.

©2015 Macmillan Publishers Limited. All rights reserved

(from 70% to 90%). Upon pregnancy, GFP^+ cells differentiated to form alveoli (Extended Data Fig. 7k–n).

We next investigated the contribution of $Procr^+$ cells to early mammary development by initiating the labelling in E18.5, P0.5 and prepubescent mice (2 weeks old) (Extended Data Figs 8, 9) and analysing the contribution of GFP^+ cells in mature adults. By FACS analysis and immunostaining, GFP^+ cells were found in both basal and luminal populations. Eight-week tracing from late embryo or at birth predominantly led to bi-lineage clones in adults (98% and 99%) (Extended Data Fig. 8f, m). Consistently, 6-week tracing of $Procr^+$ cells in prepubescent mice (2 weeks old) mostly resulted in bi-lineage clones (90%) (Extended Data Fig. 9f). During pregnancy, GFP^+ cells contributed to alveoli formation (Extended Data Fig. 9h–k). Taken together, these lineage tracing experiments initiated in the embryonic and various postnatal stages show that $Procr^+$ cells contribute to both basal and luminal cell lineages.

To investigate the physiological requirement of $Procr^+$ cells in mammary gland development, we performed targeted ablation of these cells in developing mammary glands. We generated the $Procr^{CreERT2/+}$;$R26^{DTA/+}$ strain to conditionally express diphtheria toxin (DTA) in $Procr^+$ cells (Extended Data Fig. 10a). We administered tamoxifen in $Procr^{CreERT2/+}$;$R26^{DTA/+}$ pubertal mice at P33 every 3 days, and evaluated the effects of targeted ablation of $Procr^+$ cells 9 days later (Extended Data Fig. 10b). At this stage, both the oil-treated control mammary epithelium and the tamoxifen-treated $R26^{DTA/+}$ control mammary epithelium had grown to the distal edge of the fat pad (Extended Data Fig. 10c, d). In striking contrast, tamoxifen administration in $Procr^{CreERT2/+}$;$R26^{DTA/+}$ mice largely prevented the growth of the epithelium (Extended Data Fig. 10e, f). FACS analysis indicated that the basal $Procr^+$ cells were efficiently ablated (Extended Data Fig. 10g, h). Together, these results suggest that the $Procr^+$ cells are important for the development and maintenance of adult mammary gland.

Our study identifies Procr as a novel Wnt target in the mammary epithelium. $Procr^+$ cells express lower levels of K5/K14 compared with other basal cells. They are also unique in that they are multipotent by lineage tracing, and show the highest repopulation efficiency by transplantation. Such a population of cells has not been described before. Much effort has been devoted to delineating the relationships between different epithelial cell populations in the mammary gland. Our work suggests that $Procr^+$ cells are at the top of the hierarchy, supporting the model that multipotent and unipotent stem cells coexist in the adult mammary gland, reconciling the differences found between previous lineage tracing and transplantation studies (Extended Data Fig. 10i).

EMT has been linked to the stemness properties of cancer cells[18]. As $Procr^+$ MaSCs exhibit EMT signatures in the normal mammary gland, it is tempting to speculate that $Procr^+$ MaSCs represent one of the origins of breast cancer stem cells. Indeed, in human breast cancer, Procr is expressed in the $CD44^+$ (cancer-stem-cell-enriched) group[19]. Procr expression in cancer cell lines promotes tumour formation[20,21] and metastasis[22,23]. More similarities may exist between normal stem cells and malignant stem cells.

Online Content Methods, along with any additional Extended Data display items and Source Data, are available in the online version of the paper; references unique to these sections appear only in the online paper.

Received 13 February; accepted 9 September 2014.
Published online 19 October 2014.

1. Shackleton, M. *et al.* Generation of a functional mammary gland from a single stem cell. *Nature* **439,** 84–88 (2006).
2. Stingl, J. *et al.* Purification and unique properties of mammary epithelial stem cells. *Nature* **439,** 993–997 (2006).
3. Van Keymeulen, A. *et al.* Distinct stem cells contribute to mammary gland development and maintenance. *Nature* **479,** 189–193 (2011).
4. Rios, A. C., Fu, N. Y., Lindeman, G. J. & Visvader, J. E. *In situ* identification of bipotent stem cells in the mammary gland. *Nature* **506,** 322–327 (2014).
5. van Amerongen, R., Bowman, A. N. & Nusse, R. Developmental stage and time dictate the fate of Wnt/β-catenin-responsive stem cells in the mammary gland. *Cell Stem Cell* **11,** 387–400 (2012).
6. de Visser, K. E. *et al.* Developmental stage-specific contribution of $LGR5^+$ cells to basal and luminal epithelial lineages in the postnatal mammary gland. *J. Pathol.* **228,** 300–309 (2012).
7. Zeng, Y. A. & Nusse, R. Wnt proteins are self-renewal factors for mammary stem cells and promote their long-term expansion in culture. *Cell Stem Cell* **6,** 568–577 (2010).
8. Badders, N. M. *et al.* The Wnt receptor, Lrp5, is expressed by mouse mammary stem cells and is required to maintain the basal lineage. *PLoS ONE* **4,** e6594 (2009).
9. Fukudome, K. & Esmon, C. T. Identification, cloning, and regulation of a novel endothelial cell protein C/activated protein C receptor. *J. Biol. Chem.* **269,** 26486–26491 (1994).
10. Cheng, T. *et al.* Activated protein C blocks p53-mediated apoptosis in ischemic human brain endothelium and is neuroprotective. *Nature Med.* **9,** 338–342 (2003).
11. Balazs, A. B., Fabian, A. J., Esmon, C. T. & Mulligan, R. C. Endothelial protein C receptor (CD201) explicitly identifies hematopoietic stem cells in murine bone marrow. *Blood* **107,** 2317–2321 (2006).
12. Vetrano, S. *et al.* Unexpected role of anticoagulant protein C in controlling epithelial barrier integrity and intestinal inflammation. *Proc. Natl Acad. Sci. USA* **108,** 19830–19835 (2011).
13. Ivanova, N. B. *et al.* A stem cell molecular signature. *Science* **298,** 601–604 (2002).
14. Bae, J. S., Yang, L., Manithody, C. & Rezaie, A. R. The ligand occupancy of endothelial protein C receptor switches the protease-activated receptor 1-dependent signaling specificity of thrombin from a permeability-enhancing to a barrier-protective response in endothelial cells. *Blood* **110,** 3909–3916 (2007).
15. Plaks, V. *et al.* Lgr5-expressing cells are sufficient and necessary for postnatal mammary gland organogenesis. *Cell Rep.* **3,** 70–78 (2013).
16. Gu, J. M. *et al.* Disruption of the endothelial cell protein C receptor gene in mice causes placental thrombosis and early embryonic lethality. *J. Biol. Chem.* **277,** 43335–43343 (2002).
17. Muzumdar, M. D., Tasic, B., Miyamichi, K., Li, L. & Luo, L. A global double-fluorescent Cre reporter mouse. *Genesis* **45,** 593–605 (2007).
18. Mani, S. A. *et al.* The epithelial-mesenchymal transition generates cells with properties of stem cells. *Cell* **133,** 704–715 (2008).
19. Shipitsin, M. *et al.* Molecular definition of breast tumor heterogeneity. *Cancer Cell* **11,** 259–273 (2007).
20. Schaffner, F. *et al.* Endothelial protein C receptor function in murine and human breast cancer development. *PLoS ONE* **8,** e61071 (2013).
21. Hwang-Verslues, W. W. *et al.* Multiple lineages of human breast cancer stem/progenitor cells identified by profiling with stem cell markers. *PLoS ONE* **4,** e8377 (2009).
22. Beaulieu, L. M. & Church, F. C. Activated protein C promotes breast cancer cell migration through interactions with EPCR and PAR-1. *Exp. Cell Res.* **313,** 677–687 (2007).
23. Spek, C. A. & Arruda, V. R. The protein C pathway in cancer metastasis. *Thromb. Res.* **129** (suppl. 1), S80–S84 (2012).

Acknowledgements The screening was initiated in the laboratory of R. Nusse and we are grateful for his support and generosity. We thank Y. Zhang and Biocytogen for assistance in knock-in mouse generation, and Q. Yin and H. Fang for technical support in RNA-seq analysis. We are grateful to C.-C. Hui and E. Verheyen for critical reading of the manuscript. We thank D. Li for helpful discussion. This work is supported by grants from the Ministry of Science and Technology of China (2014CB964800, 2012CB945000 to Y.A.Z., 2014CB910600 to L.Y.), National Natural Science Foundation of China (31171421, 31371500 to Y.A.Z., 31201098 to C.C.), the Chinese Academy of Sciences (XDA01010307, 20100HTP03 to Y.A.Z., 2012OHTP08 to L.Y.), Shanghai Municipal Science and Technology Commission (12PJ1410100 to Y.A.Z.).

Author Contributions Y.A.Z. conceived the study and designed experiments. D.W. performed transplantation and lineage tracing experiments and carried out data analysis. C.C. and X.D. performed array and screening experiments. D.W., Q.C.Y., X.-O.Z. and L.Y. performed RNA-seq and analysis. Y.A.Z. wrote the manuscript.

Author Information Microarray and RNA-seq data have been deposited in the Gene Expression Omnibus under accession numbers GSE55117 and GSE58088, respectively. Reprints and permissions information is available at www.nature.com/reprints. The authors declare no competing financial interests. Readers are welcome to comment on the online version of the paper. Correspondence and requests for materials should be addressed to Y.A.Z. (yzeng@sibcb.ac.cn).

©2015 Macmillan Publishers Limited. All rights reserved

METHODS

Experimental animals. To generate mice expressing CreERT2-IRES-tdTomato under control of the endogenous *Procr* promoter, we generated the targeting construct depicted in Fig. 3a and Extended Data Fig. 2b. Female mice of *Rosa26*$^{mTmG/+}$, *Rosa26*$^{DTA/+}$ (Jackson Laboratories), *Axin2*$^{lacZ/+}$ (ref. 24), *Lgr5*$^{eGFP\text{-}IRES\text{-}CreERT2/+}$ (*Lgr5-GFP*) (ref. 25), CD1, B6 and Nude strains were used in this study. For lineage tracing experiments induced in prepubescent, pubertal and mature adult mice, animals received a single intraperitoneal injection of 4 mg per 25 g body weight of tamoxifen (TAM; Sigma-Aldrich) diluted in sunflower oil. For lineage tracing experiments induced at birth, each mouse received a single injection of 125 μg tamoxifen. To induce recombination in embryos, pregnant mothers at day 18.5 were injected with a single dose of 0.5 mg per 25 g body weight of tamoxifen. For DTA-mediated cell ablation experiments, pubertal mice were injected with 4 mg per 25 g body weight of tamoxifen in sunflower oil every 3 days a total of three times. Experimental procedures were approved by the Animal Care and Use Committee of Shanghai Institute of Biochemistry and Cell Biology, Chinese Academy of Sciences.

Quantification of lineage-specific cells and the size of clones. A minimum of three different mice were analysed per condition. Dissociated single mammary cells were FACS analysed for the GFP$^+$ cells proportion in basal and luminal compartments. A minimum of 3 mice were analysed by FACS analysis and a minimum of 20 sections were analysed by immunohistochemistry of K14 and K8 to discern the basal and luminal composition of GFP$^+$ cells. Representative clones were documented by confocal imaging. For clonal analysis, a minimum of 200 GFP$^+$ clones were analysed per time point. For each clone, the number of cells and their K14 or K8 expression were scored. The clones were grouped in three classes: one-cell, two-cell, and clones with more than two cells.

Antibodies. Antibodies used were: rat anti-Procr (1:50, eBioscience, catalogue #13-2012, clone 1560), rat anti-K8 (1:250, Developmental Hybridoma Bank, TROMA-I), rabbit anti-K14 (1:1,000, Covance), rabbit anti-K5 (1:1000, Covance), rabbit anti-milk (1:500, Nordic Immunological Laboratories).

Primary cell preparation. Mammary glands from 8- to 12-week-old virgin or an otherwise specified stage of female mice were isolated. The minced tissue was placed in culture medium (RPMI 1640 with 25 mM HEPES, 5% fetal bovine serum, 1% penicillin-streptomycin-glutamine (PSQ), 300 U ml^{-1} collagenase III (Worthington)) and digested for 2 h at 37 °C. After lysis of the red blood cells in NH_4Cl, a single-cell suspension was obtained by sequential incubation with 0.25% trypsin-EDTA at 37 °C for 5 min and 0.1 mg ml^{-1} DNase I (Sigma) for 5 min with gentle pipetting, followed by filtration through 70 μm cell strainers.

Cell labelling and flow cytometry. The following antibodies in 1:200 dilutions were used: biotinylated and FITC-conjugated CD31, CD45, TER119 (BD PharMingen, clone MEC 13.3, 30-F11 and TER-119; catalogue # 553371, #55307, # 553672, # 553372, # 553080 and # 557915), CD24-PE/cy7, CD29-APC (Biolegend, clone M1/69 and HMβ1-1; catalogue #101822 and #102216), Procr-PE (eBioscience, clone 1560, catalogue #12-2012), Streptavidin-V450, and Streptavidin-FITC (BD PharMingen). Antibody incubation was performed on ice for 15 min in HBSS with 10% fetal bovine serum. All sortings were performed using a FCASJazz (Becton Dickinson). The purity of sorted population was routinely checked and ensured to be more than 95%.

***In vitro* colony formation assay.** FACS-sorted cells were resuspended at a density of 4×10^5 cells ml^{-1} in chilled 100% growth-factor-reduced Matrigel (BD Bioscience), and the mixture was allowed to polymerize before covering with culture medium (DMEM/F12, ITS (1:100; Sigma), 50 ng ml^{-1} EGF, plus either vehicle (1% CHAPS in PBS) or 200 ng ml^{-1} Wnt3A[26]). Culture medium was changed every 24 h. Primary colony numbers were scored after 6–7 days in culture. The colonies were mostly spherical. In cases that colonies were oval, the long axis was measured.

RNA extraction, microarray and RNA sequencing. For microarray, total RNA from second-passage MaSC colonies cultured in the presence of vehicle and Wnt3A was extracted with PicoPure (Arcturs) in accordance with the manufacturer's protocol. At the second passage, MaSC colonies in Wnt3A treatment can efficiently reconstitute new mammary glands in transplantation assays, an indication of retaining stemness, while MaSC colonies in vehicle have completely lost the reconstitution capabilities[7]. RNA concentration was determined with NanoDrop ND-1000, and quality was determined using the RNA 6000 Nano assay on the Agilent 2100 Bioanalyzer (Agilent Technologies). Affymetrix microarray analysis, fragmentation of RNA, labelling, hybridization to Mouse Genome 430 2.0 microarrays and scanning were performed in accordance with the manufacturer's protocol (Affymetrix). For RNA-seq, total RNA from freshly isolated Lin$^-$ CD24$^+$ CD29^{hi} Procr$^+$ cells and Lin$^-$ CD24$^+$ CD29^{hi} Procr$^-$ cells were extracted with Trizol. RNA-seq libraries were prepared according to the manufacturer's instructions (Illumina) and then applied to sequencing on Illumina HiSeq 2000 in the CAS-MPG Partner Institute for Computational Biology Omics Core, Shanghai. In total, around 32 million 1×100 single reads for each sample were obtained and uniquely mapped to the mm9 mouse genome with more than 70% mapping rate for both samples using TopHat 1.3.3. Differential gene expression analysis was carried out using Cuffdiff 2.0.2, and genes with significant alteration were extracted for a further analysis.

EdU labelling. *In vivo* EdU labelling was accomplished by intraperitoneal injections of EdU (0.2 mg per 10 g body weight) followed by harvest 3 h after injection. Samples were subjected to Click-it chemistry (Invitrogen).

Immunohistochemistry. Whole-mount staining was performed as described previously[4]. Frozen sections were prepared by air-drying and fixation for 1 h in cold MeOH or PFA. Tissue sections were incubated with primary antibodies at 4 °C overnight, followed by washes, incubation with secondary antibodies for 2 h at 25 °C, and counterstaining with DAPI (Vector Laboratories). For all the immunoflourescence staining at least three independent experiments were conducted. Representative images are shown in the figures.

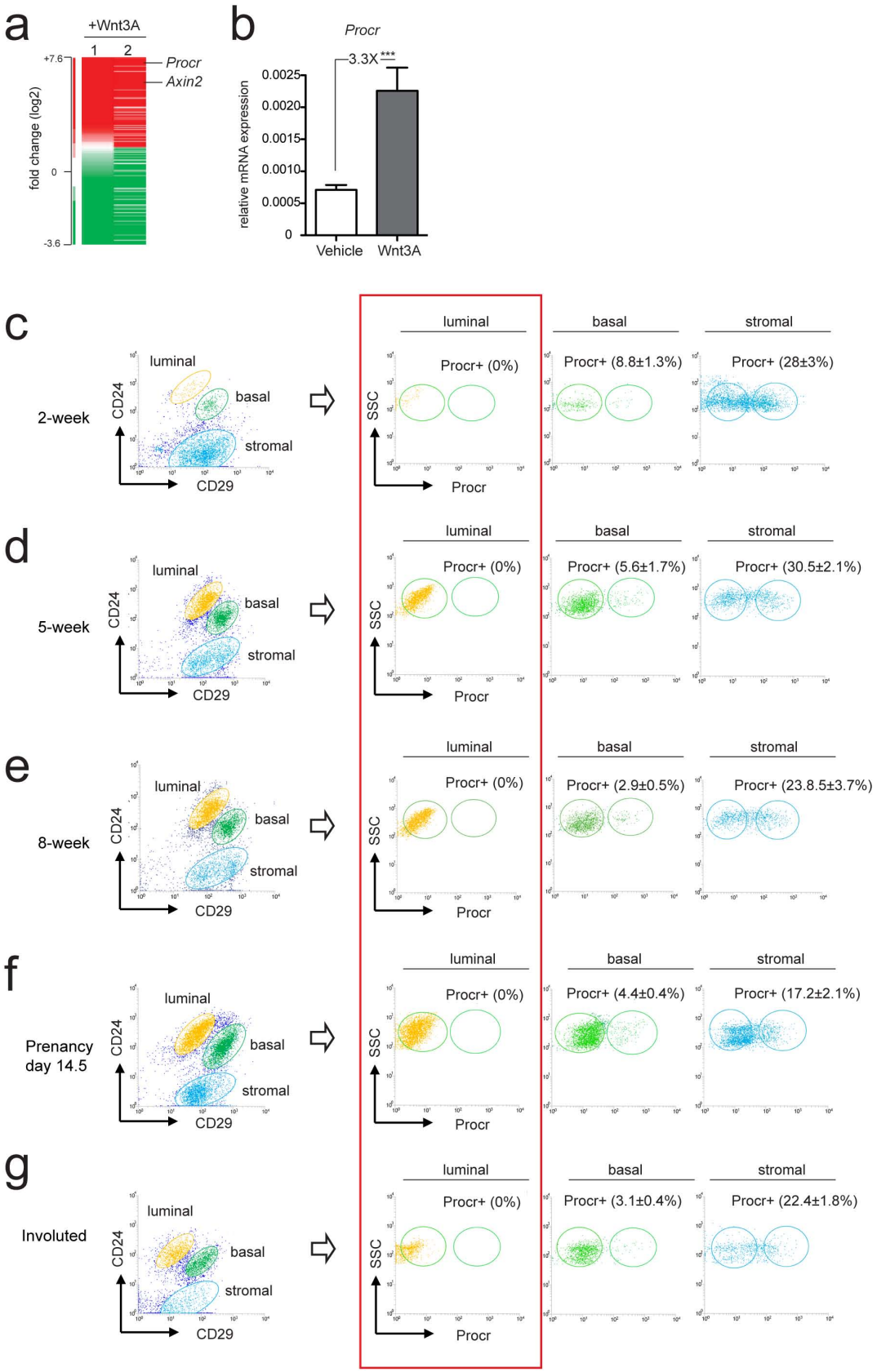
Mammary fat pad transplantation and analysis. Sorted cells were resuspended in 50% Matrigel, PBS with 20% FBS, and 0.04% Trypan Blue (Sigma), and injected in 10 μl volumes into the cleared fat pads of 3-week-old female. Reconstituted mammary glands were harvested after 8–10 weeks post-surgery. Outgrowths were detected by under a dissection microscope (Leica) after Carmine staining. Outgrowths with more than 10% of the host fat pad filled were scored as positive.

Statistical analysis. Student's *t*-test was performed and the *P* value was calculated in Prism on data represented by bar charts, which consisted of results from three independent experiments unless specified otherwise. For all experiments with error bars, the standard deviation (s.d.) was calculated to indicate the variation within each experiment. The experiments were not randomized. The investigators were not blinded to allocation during experiments and outcome assessment.

Primers used in qPCR analysis. Primers used were as follows. Procr forward, CTCTCTGGGAAAACTCCTGACA; Procr reverse, CAGGGAGCAGCTAACAGTGA; K5 forward, TCTGCCATCACCCCATCTGT; K5 reverse, CCTCCGCCAGAACTGTAGGA; K14 forward, TGACCATGCAGAACCTCAATGA; K14 reverse, ATTGGCATTGTCCACGG; E-cadherin forward, CAGGTCTCCTCATGGCTTTGC; E-cadherin reverse, CTTCCGAAAAGAAGGCTGTCC; Vim forward, CGTCCACACGCACCTACAG; Vim reverse, GGGGGATGAGGAATAGAGGCT; Lgr5 forward, CCTACTCGAAGACTTACCCAGT; Lgr5 reverse, GCATTGGGGTGAATGATAGCA; Axin2 forward, AGCCTAAAGGTCTTATGTGGCTA; Axin2 reverse, ACCTACGTGATAAGGATTGACT.

24. Lustig, B. *et al.* Negative feedback loop of Wnt signaling through upregulation of conductin/axin2 in colorectal and liver tumors. *Mol. Cell. Biol.* **22,** 1184–1193 (2002).
25. Barker, N. *et al.* Identification of stem cells in small intestine and colon by marker gene *Lgr5*. *Nature* **449,** 1003–1007 (2007).
26. Willert, K. *et al.* Wnt proteins are lipid-modified and can act as stem cell growth factors. *Nature* **423,** 448–452 (2003).
27. Shehata, M. *et al.* Phenotypic and functional characterization of the luminal cell hierarchy of the mammary gland. *Breast Cancer Res.* **14,** R134 (2012).

©2015 Macmillan Publishers Limited. All rights reserved

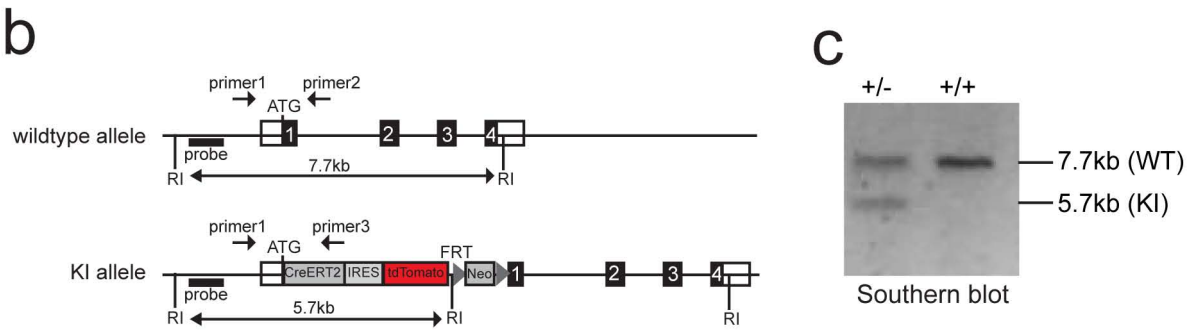


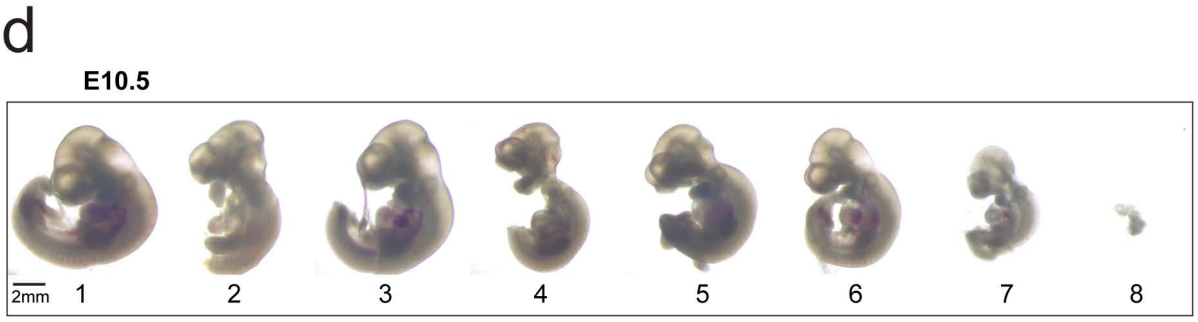
Extended Data Figure 1 | No Procr^{+} cells are found in luminal cells throughout postnatal development. **a**, **b**, Microarray of three-dimensional cultured basal cells in the presence of Wnt3A versus vehicle. 1 and 2 represent two independent experiments. See Methods for details. qPCR indicated that *Procr* is upregulated in basal cells cultured in the presence of Wnt3A compared with cells grown in the absence of Wnt3A. Data are pooled from three independent experiments. Data are presented as mean ± s.d. ***$P < 0.01$. **c**–**g**, The 4th inguinal mammary glands harvested from 2-week-old (**c**), 5-week-old (**d**), 8-week-old (**e**), pregnant day 14.5 (**f**) and 2 weeks post-weaning (**g**) CD1 mice were analysed by FACS. Procr^{+} cells were distributed in basal cells (ranging from 2.9% to 8.8%) and stromal fibroblasts (from 17.2% to 30.5%). No Procr^{+} cells were detected in luminal cells at any postnatal stage.

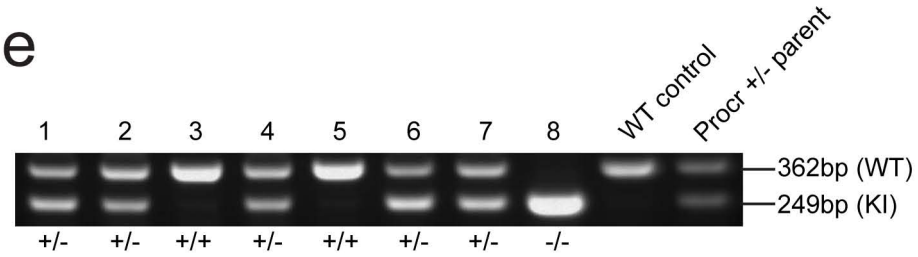
©2015 Macmillan Publishers Limited. All rights reserved

a

	number of cells plated	number of colonies formed	colony-forming efficiency
Lin-, CD24+, CD29hi	30K	2.7K	7.3 ± 0.6%
	20K	1.5K	
	15K	1K	
	10K	620	
Procr+, Lin-, CD24+, CD29hi	20K	7.8K	38.6 ± 4.1%***
	12K	5.2K	
	10K	2.7K	
	8K	3.6K	
Procr- Lin-, CD24+, CD29hi	30K	0	N/A Inf
	30K	0	
	20K	0	
	8K	0	

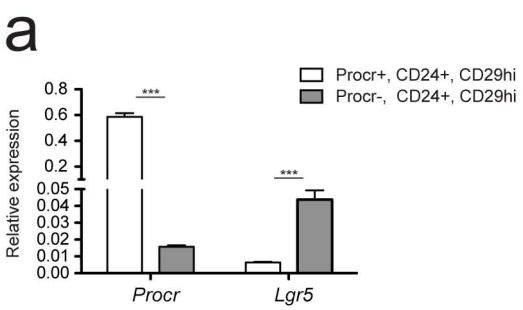


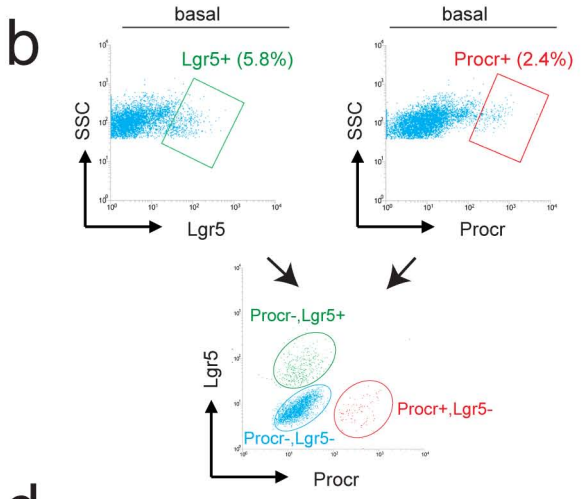


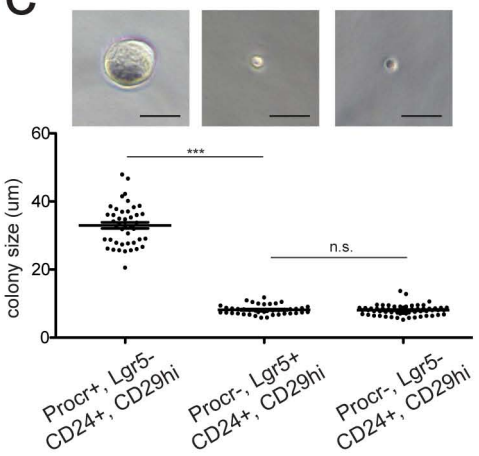


Extended Data Figure 2 | Generation of the *Procr*$^{CreERT2\text{-}IRES\text{-}tdTomato}$ knock-in mouse. **a**, Basal (Lin$^-$ CD24$^+$ CD29^{hi}), Procr$^+$ CD24$^+$ CD29^{hi} and Procr$^-$ CD24$^+$ CD29^{hi} cells were FACS-isolated and placed in Matrigel to assess the colony-formation ability. Data are pooled from four independent experiments. ***$P < 0.01$. **b**, Targeting strategy to generate the *Procr*$^{CreERT2\text{-}IRES\text{-}tdTomato/+}$ knock-in (KI) mouse. Designs of Southern blot probe and genotyping primers are as indicated. **c**, Southern blot analysis with a 5′ external probe of EcoRI-digested DNA from mouse embryonic stem cells, showing a 5.7 kb band in addition to the 7.7 kb wild-type (WT) band in clones that have undergone homologous recombination at the *Procr* locus. **d**, **e**, Embryos resulting from a cross of heterozygous male and female mice were dissected at E10.5 (**d**). Genotyping PCR indicated the proper distribution of wild type and heterozygotes as Mendel's law of segregation, and that homozygotes were lethal before this time point as the embryo had mostly been absorbed (**d**, **e**). One of three similar experiments is shown.

©2015 Macmillan Publishers Limited. All rights reserved

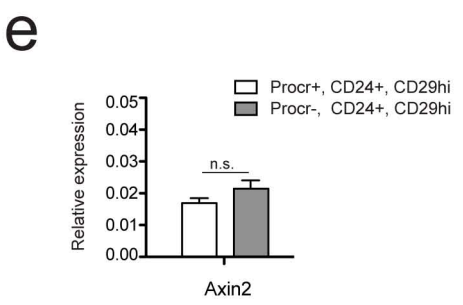


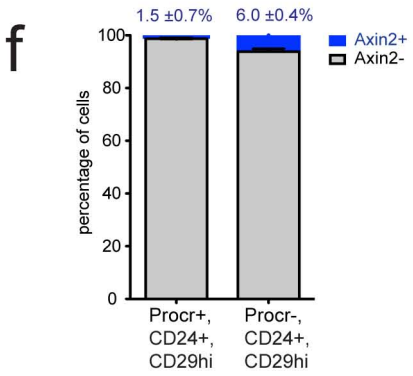




d

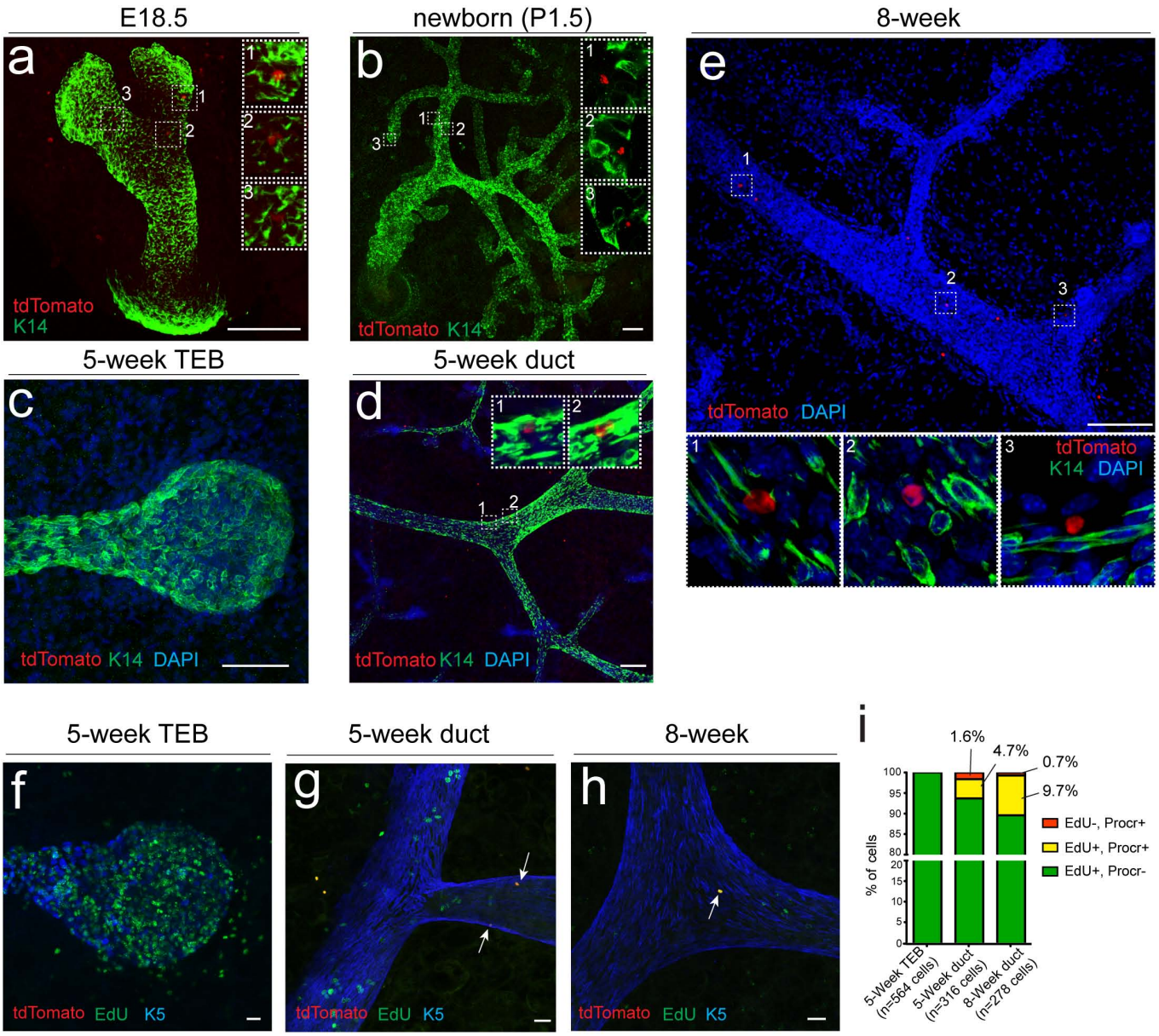
	number of cells injected per fat pad	number of outgrowths	fat pad filled	repopulating frequency
Procr+, Lgr5- CD24+, CD29hi	200	8/8	X8	1/14.4 (43.9-4.7)
	50	8/8	X7 X1	
Procr-, Lgr5+ CD24+, CD29hi	200	5/8	X3 X1 X1 X3	*** 1/165.4 (346.0-79.0)
	50	3/8	X3 X5	
Procr-, Lgr5- CD24+, CD29hi	200	0/8	X8	Inf
	50	0/8	X8	





Extended Data Figure 3 | Procr$^+$ cells and Lgr5$^+$ cells are mutually exclusive populations in the mammary gland, while Procr$^+$ cells and Axin2$^+$ cells are largely non-overlapping in mammary basal cells. **a**, Procr$^+$ CD24$^+$ CD29^{hi} and Procr$^-$ CD24$^+$ CD29^{hi} cells were FACS-isolated and analysed by qPCR. Procr$^+$ cells expressed significantly lower levels of *Lgr5* compared with Procr$^-$ cells. Data are pooled from three independent experiments. ***$P < 0.01$. **b**, Cells isolated from Lgr5–GFP mammary gland were analysed for the expression of GFP and Procr. 5.8% of basal cells (Lin$^-$ CD24$^+$ CD29^{hi}) were Lgr5–GFP$^+$ cells, while 2.4% of basal cells were Procr$^+$ cells. These two populations were not overlapped. **c**, Three basal subpopulations as indicated were FACS-isolated and cultured in Matrigel for colony formation. Only Procr$^+$ Lgr5$^-$ cells formed colonies whereas Procr$^-$ Lgr5$^+$ and Procr$^-$ Lgr5$^-$ cells could not. Data are presented as mean ± s.d. Scale bars, 20 μm. ***$P < 0.01$. **d**, Recipient fat pads were injected with freshly sorted basal subpopulation cells as indicated and harvested at 8 weeks after surgery. Procr$^+$ Lgr5$^-$ cells efficiently formed new mammary glands (frequency 1/14.4). Comparably, Procr$^-$ Lgr5$^+$ cells had significantly lower reconstitution efficiency (1/165.4). Procr$^-$ Lgr5$^-$ cells were not able to reconstitute. **e**, Procr$^+$ CD24$^+$ CD29^{hi} and Procr$^-$ CD24$^+$ CD29^{hi} cells were FACS-isolated and analysed by qPCR. No significant difference in *Axin2* level was detected in the two populations. Data are pooled from three independent experiments. ***$P < 0.01$. **f**, Procr$^+$ CD24$^+$ CD29^{hi} and Procr$^-$ CD24$^+$ CD29^{hi} cells were isolated from *Axin2-lacZ* mammary gland and underwent X-gal staining. About 1.5% of Procr$^+$ CD24$^+$ CD29^{hi} cells were Axin2-lacZ$^+$, while 6.0% of Procr$^-$ CD24$^+$ CD29^{hi} cells were Axin2-lacZ$^+$. Data are pooled from two independent experiments ($n = 1{,}085$ cells and $n = 1{,}103$ cells).

©2015 Macmillan Publishers Limited. All rights reserved



Extended Data Figure 4 | Procr^{+} cells are located in mammary ducts and are proliferative cells. **a**–**e**, The 4th inguinal mammary glands harvested from E18.5 (**a**), P1.5 (**b**), 5-week-old (**c**, **d**) and 8-week-old (**e**) *Procr*$^{CreERT2\text{-}IRES\text{-}tdTomato/+}$ mice were analysed by whole-mount confocal imaging. Individual tdTomato^{+} cells were dispersedly located in all stages of mammary ducts. tdTomato^{+} cells were not found in TEBs of 5-week-old glands (**c**). A minimum of 50 TEBs and 50 ducts were analysed. Scale bars, 100 μm. **f**–**i**, Analysis of proliferative cells in TEBs and ducts of *Procr*$^{CreERT2\text{-}IRES\text{-}tdTomato}$ mice at 3 h after EdU injection. Five-week-old TEBs exhibited abundant EdU^{+} cells (green) but no Procr^{+} cells (red) (**f**). EdU^{+} Procr^{+} cells (yellow) were found in both 5-week-old ducts (**g**) and 8-week-old mammary gland (**h**). Quantification is shown in **i**. Scale bars, 20 μm.

©2015 Macmillan Publishers Limited. All rights reserved

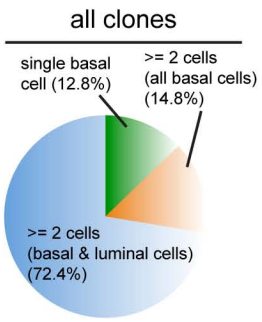
a

Puberty labelled, 3-week tracing

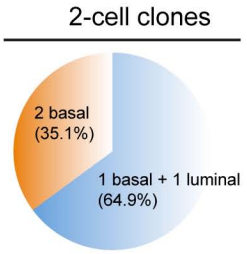
number of luminal cells per clone

number of basal cells per clone	0	1	2	3	4	5	6	7	8	10	12	total
1	38	61	36	15	6	6	1	0	1	0	0	164
2	33	23	12	13	5	4	2	2	0	0	1	95
3	5	8	3	2	2	0	1	1	1	1	0	24
4	6	2	4	0	0	0	0	0	1	0	0	13
5	0	1	1	0	0	0	0	0	0	0	0	2
total	82	95	56	30	13	10	4	3	3	1	1	298

b



c



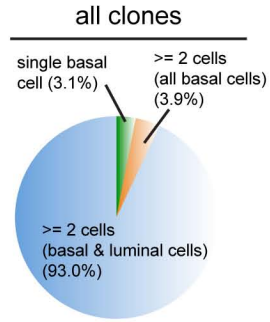
d

Puberty labelled, 6-week tracing

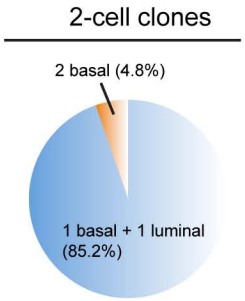
number of luminal cells per clone

number of basal cells per clone	0	1	2	3	4	5	6	7	8	9	>10	total
1	7	40	18	18	6	3	0	2	0	0	1	95
2	2	13	12	12	8	5	0	1	2	1	0	56
3	5	8	12	4	1	3	0	1	3	0	0	37
4	1	6	2	4	2	0	1	3	2	0	1	22
5	1	2	1	0	1	0	1	1	0	0	0	7
6	0	1	1	1	1	0	0	0	0	0	1	5
7	0	0	1	0	1	0	0	0	0	0	0	2
8	0	0	0	0	0	0	0	0	1	0	0	1
10	0	0	0	1	0	0	0	0	0	0	0	1
>10	0	0	0	0	0	0	0	0	0	1	0	1
total	16	70	47	40	20	11	2	8	8	2	3	227

e

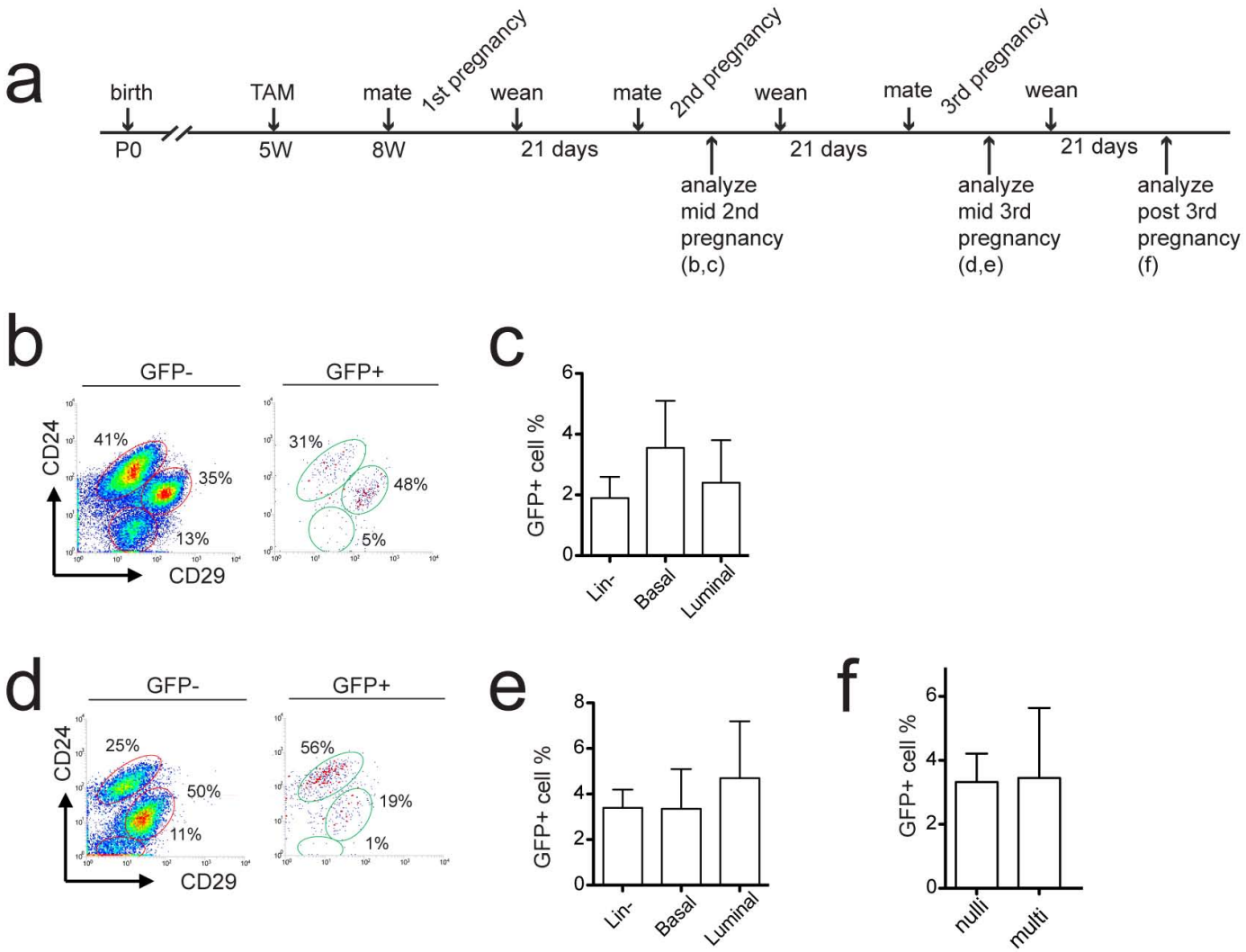


f



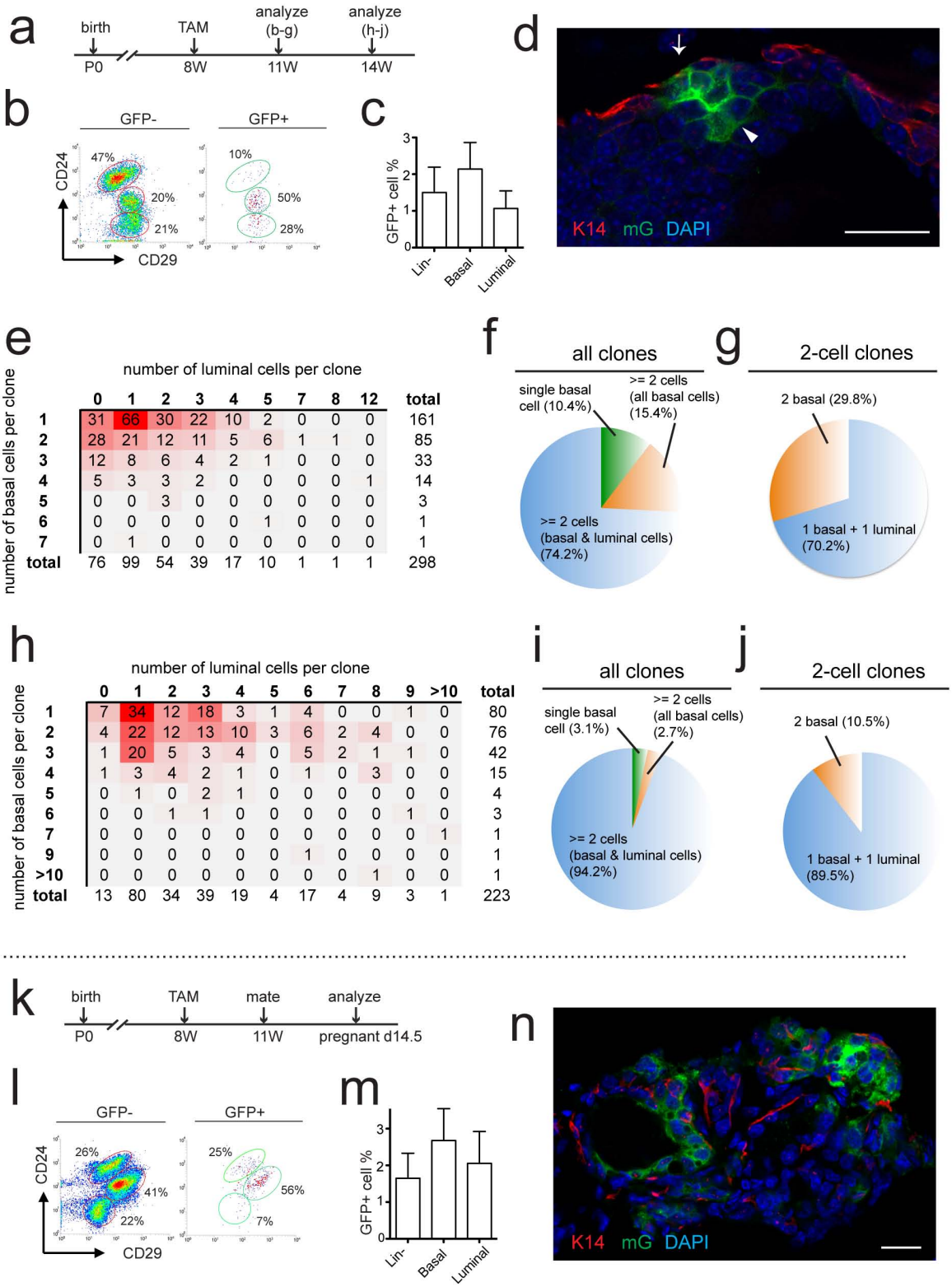
Extended Data Figure 5 | Quantitative clonal analysis of Procr-labelled cells in mammary glands induced in puberty. **a**–**f**, The number of basal and luminal cells in individual GFP$^+$ clones were scored in *Procr*$^{CreERT2/+}$; *R26*$^{mTmG/+}$ mammary glands after 3 weeks (**a**–**c**) or 6 weeks (**d**–**f**) induction. Basal cell numbers are shown along the *y*-axis, and luminal cell numbers are shown along the *x*-axis. Red shading indicates the relative frequency of certain clone composition, with deeper shading indicating higher frequency. **d**, Note that the deeper shading boxes shifted to the right in tracing experiments undertaken for a longer period. **b**, In clones after 3-week tracing, 72.4% were bi-lineage, 14.8% were solely basal cells derived from Procr$^+$ cell division, 12.8% were single basal cells that had not divided. **c**, Among two-cell clones, 64.9% were composed of one basal cell and one luminal cell, while 35.1% consisted of two basal cells. **d**, **e**, In clones after 6-week tracing, the proportion of bi-lineage clone increased to 93%, while the percentage of the other two groups decreased to 3.9% and 3.1%. **f**, In two-cell clones, bi-lineage clones increased to 85.2%, while clones consisting of two basal cells decreased to 4.8%. $n = 4$ mice for 3-week tracing and $n = 3$ mice for 6-week tracing.

©2015 Macmillan Publishers Limited. All rights reserved



Extended Data Figure 6 | Procr^{+} cells are long-lived multipotent MaSCs retained beyond multiple rounds of pregnancy. **a**–**d**, Tamoxifen (TAM) was administered in 5-week-old *Procr*$^{CreERT2/+}$;*R26*$^{mTmG/+}$ mice. Labelled cell contribution was analysed as illustrated in **a**. **b**–**e**, FACS analysis indicating that GFP^{+} cells are distributed in both basal and luminal layer in mid-2nd pregnancy (**b**, **c**) and mid-3rd pregnancy (**d**, **e**). **f**, Quantification of GFP^{+} cells indicating no difference in the percentage of GFP^{+} basal cells between nulliparous mice and multiparous mice that have gone through three complete cycles of pregnancy and involution. $n = 3$ mice. **c**, **e**, **f**, Data are presented as mean ± s.d.

©2015 Macmillan Publishers Limited. All rights reserved

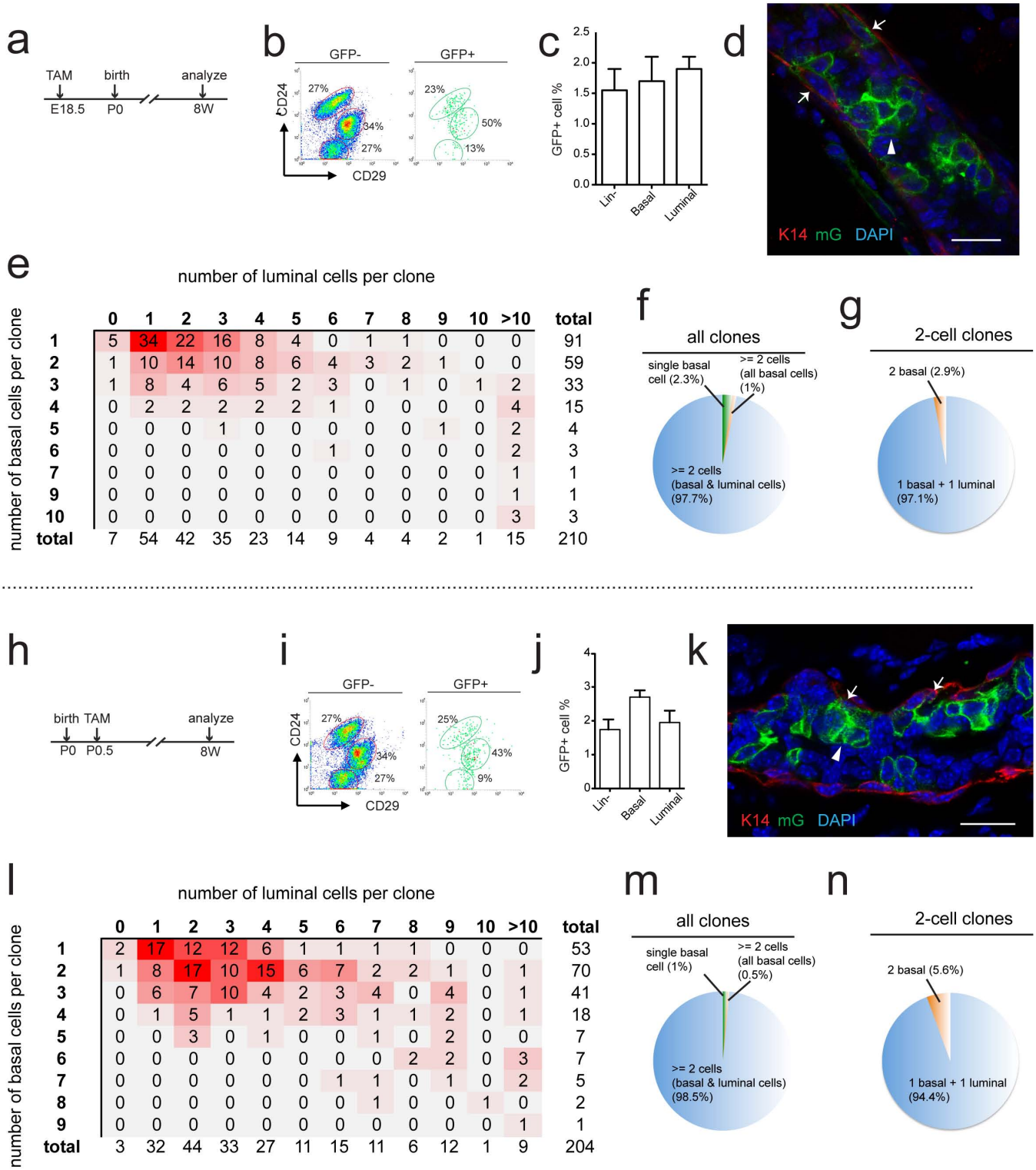


number of basal cells per clone	0	1	2	3	4	5	7	8	12	total
1	31	66	30	22	10	2	0	0	0	161
2	28	21	12	11	5	6	1	1	0	85
3	12	8	6	4	2	1	0	0	0	33
4	5	3	3	2	0	0	0	0	1	14
5	0	0	3	0	0	0	0	0	0	3
6	0	0	0	0	0	1	0	0	0	1
7	0	1	0	0	0	0	0	0	0	1
total	76	99	54	39	17	10	1	1	1	298

number of basal cells per clone	0	1	2	3	4	5	6	7	8	9	>10	total
1	7	34	12	18	3	1	4	0	0	1	0	80
2	4	22	12	13	10	3	6	2	4	0	0	76
3	1	20	5	3	4	0	5	2	1	1	0	42
4	1	3	4	2	1	0	1	0	3	0	0	15
5	0	1	0	2	1	0	0	0	0	0	0	4
6	0	0	1	1	0	0	0	0	0	1	0	3
7	0	0	0	0	0	0	0	0	0	0	1	1
9	0	0	0	0	0	0	1	0	0	0	0	1
>10	0	0	0	0	0	0	0	0	1	0	0	1
total	13	80	34	39	19	4	17	4	9	3	1	223

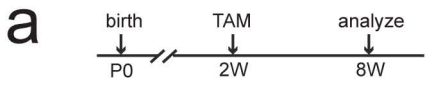
Extended Data Figure 7 | Procr labels multipotent mammary stem cells in mature adult mice. **a**–**g**,Tamoxifen (TAM) was administered in 8-week old *Procr*$^{CreERT2/+}$;*R26*$^{mTmG/+}$ mice. Labelled cell contribution was analysed after 3-week or 6-week induction. After 3 weeks, FACS analysis indicated that GFP$^+$ cells were distributed in both basal and luminal layers (**b**, **c**). Immunostaining in sections showed the clonal expansion of GFP$^+$ cells and confirmed their distribution in both basal and luminal layers. Basal cells were marked by K14, while cells apical to K14$^+$ cells were luminal cells (arrow and arrowhead in **d**). Clonal analysis indicated that bi-lineage clones are the majority in all clones (74.2%) (**e**, **f**), and in two-cell clones (70.2%) (**g**). **h**–**j**, Clonal analysis of 6-week induction indicating that clone sizes are larger (red shaded boxes shifted to the right) (**h**), bi-lineage clone percentage has also increased to 94% in all clones (**i**) and to 89.5% in two-cell clones (**j**). **k**–**n**, Mammary glands were analysed at pregnant day 14.5 after tamoxifen administration at 8 weeks. GFP$^+$ cells were in both basal and luminal layers as indicated by FACS analysis (**l**, **m**). GFP$^+$ cells contributed to alveologenesis by immunohistochemistry analysis in sections (**n**). $n = 3$ mice for 3-week tracing and $n = 3$ mice for 6-week tracing. Scale bars, 20 μm. **c**, **m**, Data are presented as mean ± s.d.

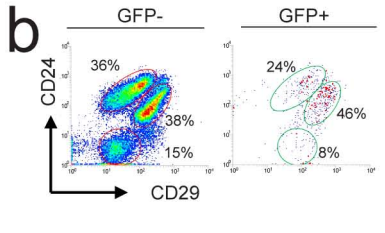
©2015 Macmillan Publishers Limited. All rights reserved

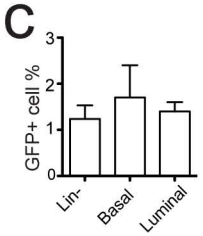


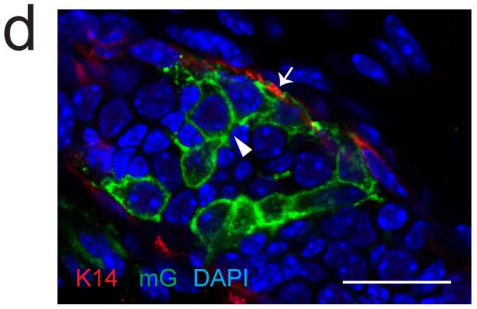
Extended Data Figure 8 | Procr^{+} cells are multipotent MaSCs in embryonic or newborn mammary gland. **a**–**g**, Tamoxifen (TAM) was administered in pregnant day 18.5 mothers bearing *Procr*$^{CreERT2/+}$;*R26*$^{mTmG/+}$ mice. Labelled cell contribution in the pups was analysed after 8-week induction (**a**). FACS analysis indicated that GFP^{+} cells are distributed in both basal and luminal layers (**b**, **c**). Immunostaining in sections showed the clonal expansion of GFP^{+} cells and confirmed their distribution in both basal and luminal layers (arrow and arrowhead in **d**). Scale bar, 20 μm. Clonal analysis indicated that bi-lineage clones are the majority in all clones (97.7%) (**e**, **f**), and in two-cell clones (97.1%) (**g**). $n = 5$ mice. **c**, Data are presented as mean ± s.d. **h**–**n**, Tamoxifen was administered in P0.5 *Procr*$^{CreERT2/+}$;*R26*$^{mTmG/+}$ mice. Labelled cell contribution was analysed after 8-week induction (**h**). FACS analysis indicated that GFP^{+} cells are distributed in both basal and luminal layers (**i**, **j**). Immunostaining in sections showed the clonal expansion of GFP^{+} cells and confirmed their distribution in both basal and luminal layers. Basal cells were marked by K14, while cells apical to K14^{+} cells were luminal cells (arrows and arrowhead in **k**). Scale bar, 20 μm. Clonal analysis indicated that bi-lineage clones are the majority in all clones (98.5%) (**l**, **m**), and in two-cell clones (94.4%) (**n**). $n = 5$ mice. **j**, Data are presented as mean ± s.d.

©2015 Macmillan Publishers Limited. All rights reserved





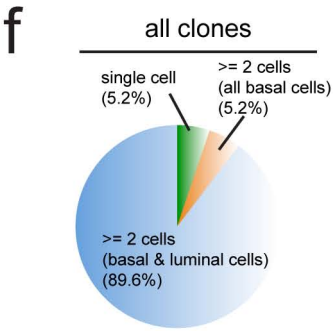


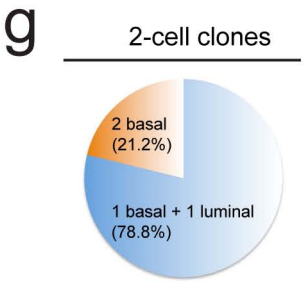


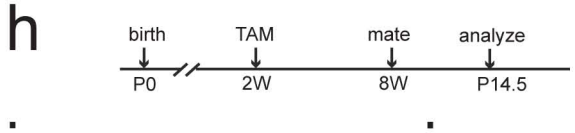
e

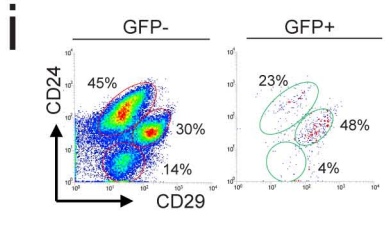
number of luminal cells per clone

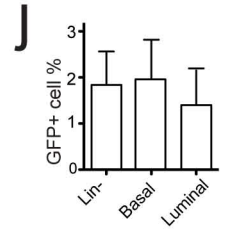
number of basal cells per clone	0	1	2	3	4	5	6	7	8	9	10	total
1	16	41	30	14	6	5	2	0	0	1	0	115
2	11	33	21	7	6	7	3	1	0	2	1	92
3	5	15	9	7	3	2	1	1	0	0	0	43
4	1	3	7	5	1	0	1	0	0	1	2	21
5	0	2	3	0	2	0	0	0	0	0	0	7
6	0	4	0	2	1	0	0	0	0	0	0	7
7	0	2	4	2	1	0	0	0	0	0	0	9
8	0	0	3	2	2	0	0	0	0	0	1	8
9	0	0	0	0	0	0	0	0	0	0	1	1
10	0	0	1	0	0	0	1	0	0	0	0	2
11	0	0	0	0	0	0	1	0	1	0	0	2
total	33	100	78	39	22	14	9	2	1	4	5	307

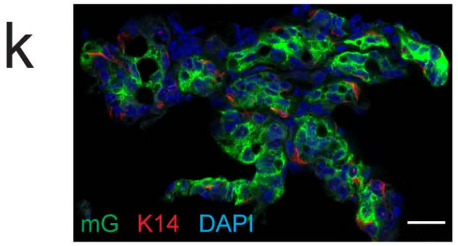






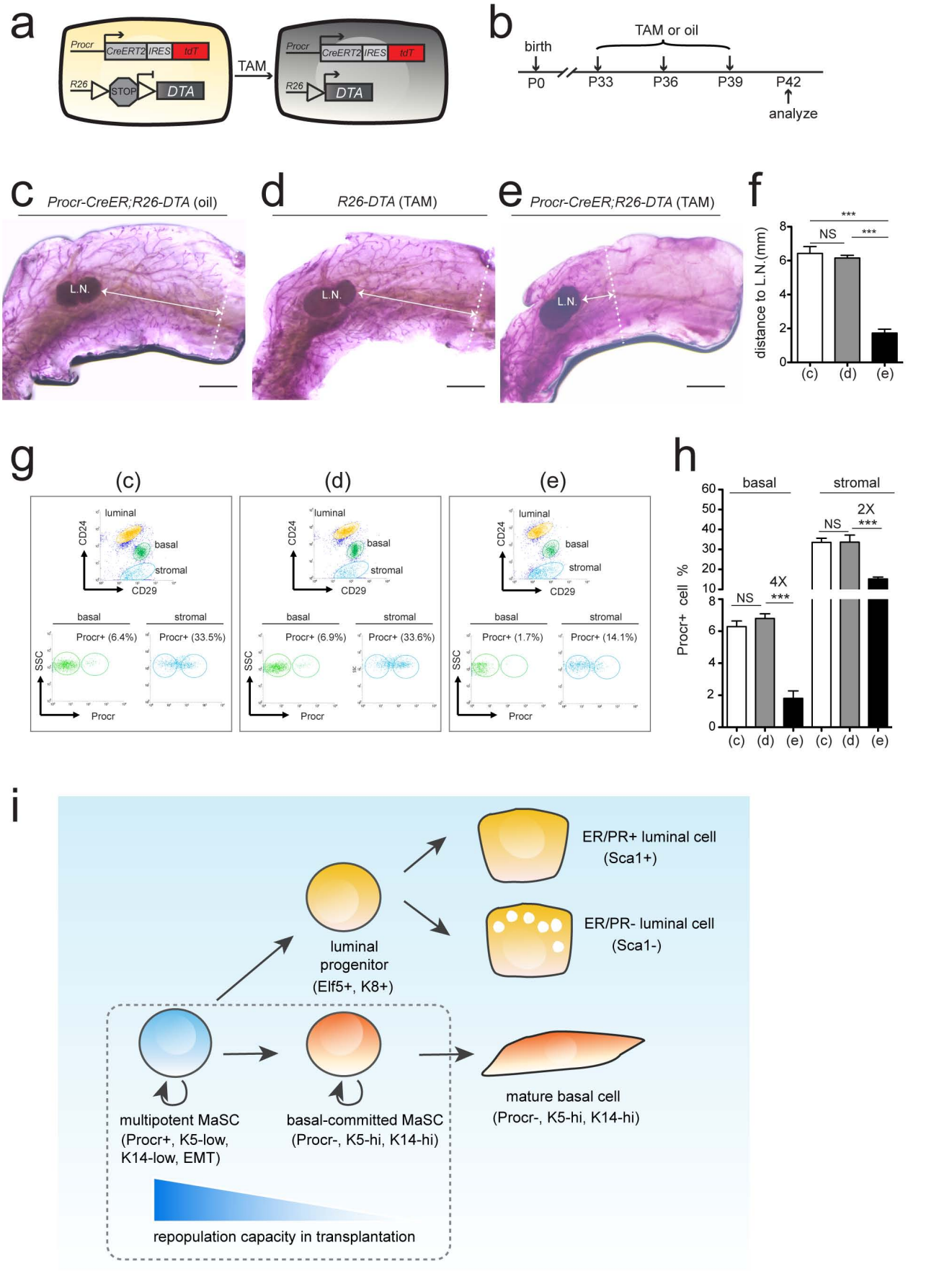






Extended Data Figure 9 | Procr labels multipotent mammary stem cells in prepubescent mice. **a**–**d**, Tamoxifen (TAM) was administered in 2-week old *Procr*$^{CreERT2/+}$;*R26*$^{mTmG/+}$ mice. Labelled cell contribution was analysed at 8 weeks. FACS analysis indicated that GFP$^+$ cells are distributed in both basal and luminal layers (**b**, **c**). Immunostaining in sections showed the clonal expansion of GFP$^+$ cells and confirmed their distribution in both basal and luminal layers. Basal cells were marked by K14, while cells apical to K14$^+$ cells were luminal cells (arrow and arrowhead in **d**). **e**–**g**, Clonal analysis indicated that bi-lineage clones are the majority in all clones (89.6%) (**e**, **f**), and in two-cell clones (78.8%) (**g**). $n = 4$ mice. **h**–**k**, Mammary glands were analysed at day 14.5 gestation after tamoxifen administration at 2 weeks. GFP$^+$ cells were in both basal and luminal layers as indicated by FACS analysis (**i**, **j**). GFP$^+$ cells contributed to alveologenesis by immunohistochemistry analysis in sections (**k**). Scale bars, 20 μm. **c**, **j**, Data are presented as mean ± s.d.

©2015 Macmillan Publishers Limited. All rights reserved



©2015 Macmillan Publishers Limited. All rights reserved

Extended Data Figure 10 | Procr^{+} cells are important for mammary development. **a**, Schematic illustration of targeted ablation of Procr^{+} cells using the Procr-CreERT2 model to drive expression of DTA. **b**, Tamoxifen (TAM) was administered every 3 days a total of three times followed by analysing the 4th mammary gland. **c**–**e**, Whole-mount imaging of the mammary epithelium at P42. The lymph node (L.N.) is indicated. Both the oil-treated control mammary epithelium (**c**) and the tamoxifen-treated *R26*$^{DTA/+}$ control mammary epithelium (**d**) had grown to the distal edge of the fat pad. Tamoxifen administration in *Procr*$^{CreERT2/+;}$*R26*$^{DTA/+}$ mice largely prevented the growth of the epithelium: the forefront of the epithelium halted at a position close to where the forefront was at the initiation of cell ablation (slightly past the lymph node) (**e**). Scale bars, 2 mm. **f**, Quantification of the distance from the epithelium forefront to the lymph node indicated that epithelium extension in the Procr^{+} cell-ablation group is largely compromised (comparing **e** with **d** or **c**). ***$P < 0.01$. NS, not significant. **g**, **h**, FACS analysis indicating that Procr^{+} basal and stromal cells are ablated (fourfold and twofold). $n = 3$ mice. The role of Procr^{+} stromal cells in this study should also be taken into consideration as they were also affected by the ablation. Nonetheless, the reduction of Procr^{+} stromal cells was not as pronounced as Procr^{+} basal cells, probably due to the less proliferative nature of Procr^{+} fibroblasts, thereby fewer progeny cells were affected. Data are presented as mean ± s.d. ***$P < 0.01$. **i**, Multipotent and unipotent MaSCs coexist in the mammary epithelial cell hierarchy. Multipotent MaSCs are characterized by Lin^{-} CD24^{+} CD29^{hi} Procr^{+} K5^{low} K14^{low}, and express EMT features. Multipotent MaSCs generate all differentiated cell types, as determined by lineage tracing, and display the highest repopulation efficiency by transplantation. Basal-committed MaSCs are destined for basal cells in development, yet can repopulate both basal and luminal cells in transplantation, underlining the plasticity of basal-committed MaSCs in response to intervention. Luminal progenitors contribute to only luminal cells in lineage tracing and are not able to repopulate in transplantation. Their markers are as previously reported[3,4,27].

©2015 Macmillan Publishers Limited. All rights reserved

LETTER

doi:10.1038/nature13806

Hepatitis A virus and the origins of picornaviruses

Xiangxi Wang[1]*, Jingshan Ren[2]*, Qiang Gao[1,3]*, Zhongyu Hu[4], Yao Sun[1], Xuemei Li[1], David J. Rowlands[5], Weidong Yin[3], Junzhi Wang[4], David I. Stuart[2,6], Zihe Rao[1,7,8] & Elizabeth E. Fry[2]

Hepatitis A virus (HAV) remains enigmatic, despite 1.4 million cases worldwide annually[1]. It differs radically from other picornaviruses, existing in an enveloped form[2] and being unusually stable, both genetically and physically[3], but has proved difficult to study. Here we report high-resolution X-ray structures for the mature virus and the empty particle. The structures of the two particles are indistinguishable, apart from some disorder on the inside of the empty particle. The full virus contains the small viral protein VP4, whereas the empty particle harbours only the uncleaved precursor, VP0. The smooth particle surface is devoid of depressions that might correspond to receptor-binding sites. Peptide scanning data extend the previously reported VP3 antigenic site[4], while structure-based predictions[5] suggest further epitopes. HAV contains no pocket factor and can withstand remarkably high temperature and low pH, and empty particles are even more robust than full particles. The virus probably uncoats via a novel mechanism, being assembled differently to other picornaviruses. It utilizes a VP2 'domain swap' characteristic of insect picorna-like viruses[6,7], and structure-based phylogenetic analysis places HAV between typical picornaviruses and the insect viruses. The enigmatic properties of HAV may reflect its position as a link between 'modern' picornaviruses and the more 'primitive' precursor insect viruses; for instance, HAV retains the ability to move from cell-to-cell by transcytosis[8,9].

HAV is unique among picornaviruses in targeting the liver and continues to be a source of mortality despite a successful vaccine[10]. HAV isolates belong to a single serotype[11]. Unlike other picornaviruses HAV cannot shut down host protein synthesis, has a highly deoptimized codon usage and grows poorly in tissue culture. Particles are produced with a 67-residue carboxy-terminal extension of VP1, which is implicated in particle assembly (this longer form of VP1 is known as VP1-2A or PX)[12]. Particles containing the extension shroud themselves in host membrane to create enveloped viruses[2]. The extension is cleaved by host proteases to yield mature capsids[12]. While picornavirus VP4 is generally myristoylated this does not happen in HAV[13]; indeed, the putative VP4 is very small (~23 residues[13]) and it has remained unclear if it is present in virus particles[14]. The cell surface molecule T cell immunoglobulin and mucin 1 (TIM-1)[15] acts as a receptor for HAV, and although transcytosis occurs[8,9] it is not clear how the virus gets to the liver, its principal site of replication.

We have analysed formaldehyde-inactivated HAV genotype TZ84 (Methods). Two types of particle were separated, one containing significant amounts of viral RNA (Extended Data Fig. 1). In the RNA-containing full particles VP0 is at least partially cleaved and we detect VP4, as for other picornaviruses, whereas the empty particles harbour only VP0, and are probably similar to the empty particles frequently seen in picornavirus infections (Methods and Extended Data Fig. 1). It remains unclear whether such empty particles can encapsidate RNA and lie on the route to assembly of full particles. Even full particles appear to contain more uncleaved VP0 than is seen in other picornaviruses, in line with observations that VP0 cleavage is 'protracted'[16]. The sedimentation coefficients are approximately 144S and 82S for the full and empty particles, respectively (Extended Data Fig. 1). 144S is a little less than the 155S expected for a full enterovirus particle, while the empty particle has a similar S value to that observed for the more expanded empty enterovirus particles[17].

Very thin crystals (~100 × 100 × 5 μm^3) were obtained for both particles. Diffraction data were collected at Diamond beamlines I03 and I24. Data were collected at 100K to avoid beam-induced crystal movement at room temperature (Supplementary Video 1), and were used to produced reliable atomic models at 3.0 and 3.5 Å resolution for the full and empty particles, respectively (Methods and Extended Data Table 1).

The external surface of HAV is smooth, with no canyon (Fig. 1a)[18]; shortening of the VP1 BC loop lowers the north wall while reductions in the VP2 EF and VP1 GH loops ablate the south wall of the canyon (Fig. 1b). Compared to foot-and-mouth-disease virus, the loops at the five-fold and three-fold axes in HAV are slightly raised, giving the virus the appearance of a facetted triakis icosahedron (Fig. 1a). In line with the low buoyant density in CsCl (ref. 19) there are no apertures in the capsid to permit the entry of Cs^+ ions. The major capsid proteins, VP1–3,

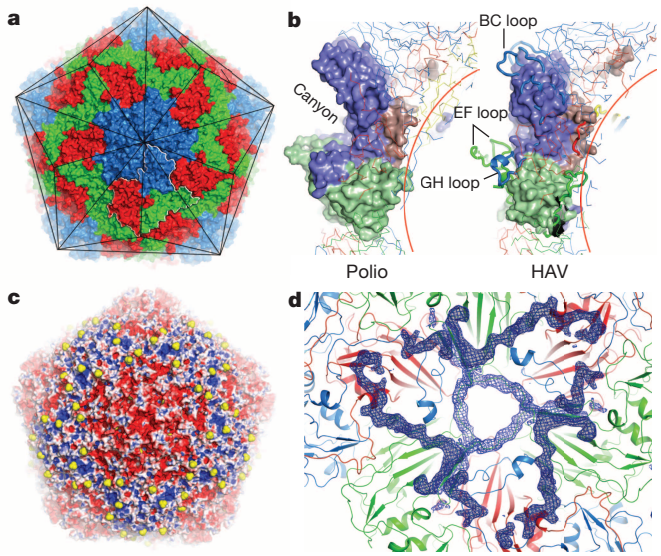


Figure 1 | Overall structure. **a**, HAV accessible surface (VP1, blue; VP2, green; VP3, red for all panels). Black lines, particle facets; white outline, biological protomer. **b**, Surface of the biological protomer of HAV and poliovirus. Loops forming the canyon walls in poliovirus are drawn thicker. **c**, HAV electrostatic surface (calculated using APBS in PyMOL). Red, negative; blue, positive; white, neutral; sulphate ions, yellow. **d**, HAV viewed from inside. Blue, positive $|F_o - F_c|$ electron density calculated taking the correctly positioned empty HAV from the full HAV shows that VP1 2–28 (darker density) and VP2 5–17 are better defined in the full particle.

[1]National Laboratory of Macromolecules, Institute of Biophysics, Chinese Academy of Science, Beijing 100101, China. [2]Division of Structural Biology, University of Oxford, The Henry Wellcome Building for Genomic Medicine, Headington, Oxford OX3 7BN, UK. [3]Sinovac Biotech Co., Ltd, Beijing 100085, China. [4]National Institutes for Food and Drug Control, No. 2, TiantanXili, Beijing 100050, China. [5]Institute of Molecular and Cellular Biology and Astbury Centre for Structural Molecular Biology, Faculty of Biological Sciences, University of Leeds, Leeds LS2 9JT, UK. [6]Diamond Light Sources, Harwell Science and Innovation Campus, Didcot OX11 0DE, UK. [7]Laboratory of Structural Biology, School of Medicine, Tsinghua University, Beijing 100084, China. [8]State Key Laboratory of Medicinal Chemical Biology, Nankai University, Tianjin 300071, China.
*These authors contributed equally to this work.

©2015 Macmillan Publishers Limited. All rights reserved

comprise eight-stranded anti-parallel β-barrels, follow the expected pseudo $T = 3$ arrangement (where T is the triangulation number) and span the thickness of the capsid (Extended Data Fig. 2a–c). The HAV full virus is mostly well ordered (however, VP4, although present, is not visible). As expected there is no evidence for structural modification attributable to formaldehyde inactivation[17].

The empty and full particles are mostly very similar, with the external surface expected to be antigenically indistinguishable (r.m.s.d. for 672 Cα atoms 0.2 Å). Experiments with six antibodies confirmed this (Extended Data Fig. 3). The particle surface is remarkably negatively charged (Fig. 1c) and the fringes of the pentameric assemblies, which show some positive charge, are decorated with a string of sulphate ions derived from the crystallization media. Surface decoration may affect the hydrodynamic properties of the particles. In the empty particle the first 40 residues of VP0 and 47 residues of VP1, which adorn the particle interior near the three-fold axes, are disordered (Fig. 1d). Although neither particle contains the extended form of VP1 we can infer the point on the particle surface from which the extension would continue (Extended Data Fig. 2d).

Perhaps correlated with the lack of a canyon, HAV harbours no contiguous hydrophobic pocket in the VP1 β-barrel. The β-barrel is compressed compared to enteroviruses[20] and the remaining space is largely filled with hydrophobic side chains, as in aphthoviruses and cardioviruses[21] (Fig. 2a–c). In addition, lengthened βC and βH strands essentially cover what would be the entrance to the pocket. We conclude that HAV is unable to bind small molecules in the fashion characteristic of enteroviruses. Unfortunately the particle structure provides no immediate clues as to where the TIM-1 receptor[15] might attach.

The organization of the protein chains broadly mirrors other picornaviruses, except for the amino terminus of VP2. At residue 53 there is a flip in the ψ torsion angle of the peptide, sending the first 53 residues of VP2 across and then along the interpentamer boundary to interact strongly with the neighbouring pentamer (forming an extra strand on the VP2 β-barrel from the adjacent pentamer; Fig. 2d–g). The switch is only ~5 Å from the icosahedral two-fold axis, so that the net effect is to swap the N-terminal structures, in a way reminiscent of domain swaps observed in certain protein structures[22]. As in those cases, it produces a very similar structure overall, but alters the subunit connectivity so that in HAV adjacent protomers of one pentamer are sewn together via the adjacent pentamer (Fig. 2f, g). This arrangement is unprecedented in picornaviruses; however, it occurs in insect picorna-like viruses (for example, cricket paralysis virus (CrPV[6]); Fig. 2d).

We found that both empty and full particles were extraordinarily robust compared to other picornaviruses (remaining stable at up to 80 °C and at pH values down to about 2 (ref. 23); Fig. 3a and Extended Data Fig. 4). It is established for many picornaviruses that the interface between the 12 pentameric assemblies that comprise the icosahedral capsid determine the particle stability[24–26]. In this context we questioned whether the stability of HAV might be a consequence of the VP2 domain swap at the pentamer interface, and so analysed the stability of CrPV (Extended Data Fig. 4d). Although harbouring the same domain swap, CrPV particles showed a stability profile similar to a typical picornavirus. The VP2 switch therefore does not explain the stability; however, the interaction region adjacent to the icosahedral two-fold axes, which separates during the initial stages of enterovirus uncoating[17,27], shows tight packing in HAV (Fig. 3b and Extended Data Fig. 5). The complementarity is similar

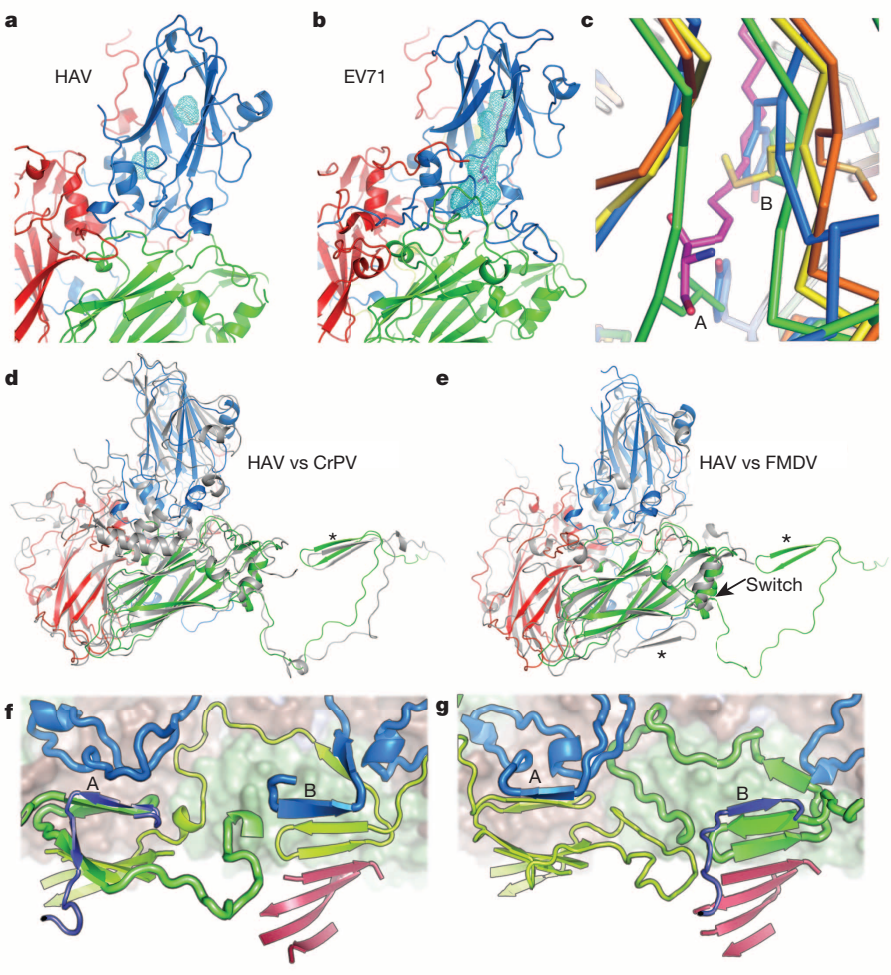


Figure 2 | Structure features. **a**, **b**, HAV (**a**) and EV71 (**b**) are coloured as in Fig. 1a; light-blue mesh: pocket volume calculated with PyMOL. Magenta, EV71 pocket factor. **c**, Pocket close-up of strand C (left) and strand H (right) for HRV14 (yellow), FMDV (blue), EV71 (orange, pocket factor magenta) and HAV (green, note occlusion of pocket entrance). Met 224 occludes part of the empty HRV14 pocket. A and B: bulky side chains occlude the HAV and FMDV pockets (A, Leu-HAV, Tyr-FMDV; B, Phe-HAV and Tyr-FMDV). **d**, **e**, Biological protomers of CrPV (**d**) and FMDV (**e**) superimposed on HAV. The asterisk marks the VP2 N terminus that folds differently in FMDV (switch at residue 53 is indicated). HAV coloured as in **a** (CrPV and FMDV grey). **f**, HAV compared with poliovirus type 1 (1HXS) in **g**. The pentamer interface runs horizontally across the centre with the perpendicular two-fold axis roughly central. Surface drawn for upper pentamer. Two-fold related β-sheets are at A and B. VP1, blue and indigo; VP2, green and lime-green; VP3, red. VP4 is omitted for clarity. Upper pentamer chains are drawn thicker.

©2015 Macmillan Publishers Limited. All rights reserved

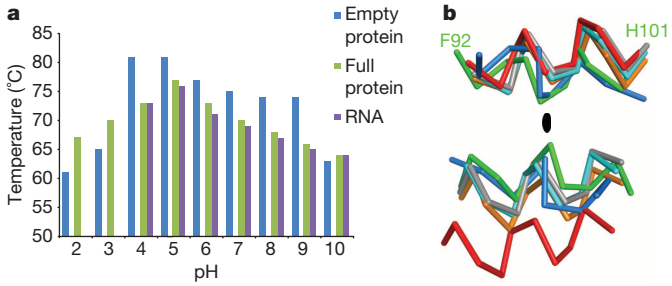


Figure 3 | Stability. **a**, Summary of thermal shift assays for HAV in the pH range from 2 to 10. Purple and green bars represent RNA release and protein-melting temperatures, respectively, for full HAV; blue bars show protein melting for the empty particle. RNA release is not detected at low pH due to quenching of the SYTO9 dye. Extended Data Fig. 4 shows raw fluorescence traces. **b**, The separation of VP2 α-helices at the icosahedral two-fold of HAV (green, 3.8 Å), CrPV (blue, 5.3 Å), EV71 (cyan, 7.3 Å), polio (grey, 7.6 Å), FMDV (orange, 8.2 Å) and 80S-like EV71 (red, 12.2 Å).

to that seen in poliovirus, where instability is probably triggered by pocket factor release. HAV achieves this complementarity by matching small residues and tyrosine side chains nestled around the two-fold axis (Extended Data Fig. 5). This may contribute to the stability of the HAV particle, while the re-wiring of VP2 may reflect a fundamental difference in the mechanism of genome uncoating in HAV compared to enteroviruses. In contrast the other candidate interface for determining stability, which relates protomers within a pentameric assembly, has similar properties to other picornaviruses (Extended Data Fig. 5). We think it unlikely that HAV uses the enterovirus mechanism for genome transfer across the endosomal membrane, via an umbilicus comprising the amphipathic N-terminal helix of VP1, and VP4 membrane pore[28,29], although the extremely short VP4 protein has a sequence consistent with the formation of an amphipathic helix. The process of infection comprises two distinct steps: particle entry and genome release. In the first of these, HAV may be taken intact into the cell since it is well established that the virus can pass from cell to cell via transcytosis[8,9]; whereas the second stage, the release of the RNA genome, remains unclear, and a specific

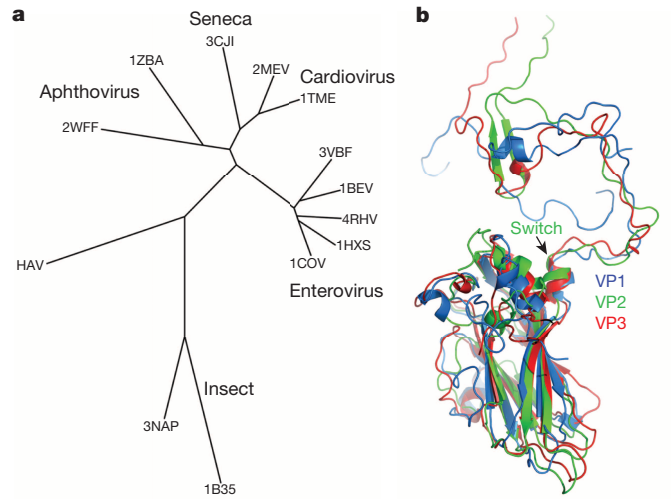


Figure 4 | Phylogeny. **a**, Structure-based phylogenetic tree[30] of representative picornaviruses and cripaviruses: PDB accessions 3VBF (EV71), 1BEV (bovine enterovirus), 4HRV (human rhinovirus14), 1HXS (poliovirus type1), 1COV (coxsackievirus B3), 1TME (Theilers virus), 2MEV (mengo virus), 3CJI (Seneca valley virus), 1ZBA (FMDV A10), 2WFF (equine rhinitis A virus), 3NAP (triatoma virus) and 1B35 (CrPV). Evolutionary distance is derived from the number of unmatched residues and the deviation in matched residues. Residues corresponding to the HAV VP2 switch region (1–53) are excluded (including them does not affect the result). **b**, Superimposition of HAV VP1 (blue), VP2 (green) and VP3 (red); note the similar N-terminal extensions.

host factor (perhaps a protease) may be required for particle disassembly. A recent report suggests that HAV harbours tandem YPX_3L motifs (VP2: Y_{144}PHGLL$_{149}$ and Y_{177}PVWEL$_{182}$), which are suggested to bind the ALIX component of the ESCRT pathway, allowing the virus to engage the ESCRT complex to facilitate release of enveloped particles via exocytosis[2]. Surprisingly, the residues implicated are buried, making their role unclear unless major conformational rearrangements render them accessible, or if they are accessible on a precursor particle.

The antigenicity of HAV is incompletely characterized, with residues S102, V171, A176 and K221 of VP1 and D70, S71, Q74 and 102–121 of VP3 implicated in neutralizing epitopes[4]. All except K221 of VP1 are proposed to form part of a single site; however, they are separated by 40–50 Å on the particle surface (Extended Data Fig. 6). To extend our knowledge, 12 monoclonal antibodies (mAbs) against HAV particles were generated (Extended Data Fig. 7), one of which, mAb 11, combined excellent neutralizing titre with VP3 western blot activity. On the basis of the particle structure a series of peptides covering all exposed virus surface regions were synthesized and tested against mAb 11. VP3 residues 67–77 and 208–219 (Extended Data Fig. 7) reacted mildly. The proximity of these regions on the surface of VP3 (Extended Data Fig. 6) suggests that both may contribute to a conformational epitope, an augmented version of that identified previously[4]. To identify further antigenic sites on HAV we applied structure-based predictive methodology[5], which supports the above findings and suggests that VP2 residues 71 and 198 and VP3 residues 89–96 may comprise additional epitopes (Extended Data Fig. 6).

HAV possesses subtle but profound structural differences compared to previously characterized picornaviruses. A structure-based phylogeny (Fig. 4a) suggests that HAV links classical picornaviruses and the insect picorna-like viruses. Furthermore, the N-terminal domain swap renders VP2 more similar to the homologous VP1 and VP3 proteins (Fig. 4b), supporting the notion that HAV retains structural and functional features characteristic of primordial picornaviruses, which were akin to present-day insect picorna-like viruses, and that the subsequent acquisition of efficient mechanisms of cell entry allowed the explosion in diversity that characterizes present-day mammalian picornaviruses.

Online Content Methods, along with any additional Extended Data display items and Source Data, are available in the online version of the paper; references unique to these sections appear only in the online paper.

Received 12 May; accepted 28 August 2014.
Published online 19 October 2014.

1. WHO. Hepatitis A. *Fact Sheet No. 328* http://www.who.int/mediacentre/factsheets/fs328/en/ (2013).
2. Feng, Z. *et al.* A pathogenic picornavirus acquires an envelope by hijacking cellular membranes. *Nature* **496,** 367–371 (2013).
3. Siegl, G., Weitz, M. & Kronauer, G. Stability of hepatitis A virus. *Intervirology* **22,** 218–226 (1984).
4. Ping, L. H. & Lemon, S. M. Antigenic structure of human hepatitis A virus defined by analysis of escape mutants selected against murine monoclonal antibodies. *J. Virol.* **66,** 2208–2216 (1992).
5. Borley, D. W. *et al.* Evaluation and use of *in-silico* structure-based epitope prediction with foot-and-mouth disease virus. *PLoS ONE* **8,** e61122 (2013).
6. Tate, J. *et al.* The crystal structure of cricket paralysis virus: the first view of a new virus family. *Nature Struct. Biol.* **6,** 765–774 (1999).
7. Squires, G. *et al.* Structure of the Triatoma virus capsid. *Acta Crystallogr. D.* **69,** 1026–1037 (2013).
8. Dotzauer, A., Brenner, M., Gebhardt, U. & Vallbracht, A. IgA-coated particles of Hepatitis A virus are translocalized antivectorially from the apical to the basolateral site of polarized epithelial cells via the polymeric immunoglobulin receptor. *J. Gen. Virol.* **86,** 2747–2751 (2005).
9. Dotzauer, A. *et al.* Hepatitis A virus-specific immunoglobulin A mediates infection of hepatocytes with hepatitis A virus via the asialoglycoprotein receptor. *J. Virol.* **74,** 10950–10957 (2000).
10. Deinhardt, F. Prevention of viral hepatitis A: past, present and future. *Vaccine* **10** (suppl. 1), 10–14 (1992).
11. Lemon, S. M. & Binn, L. N. Antigenic relatedness of two strains of hepatitis A virus determined by cross-neutralization. *Infect. Immun.* **42,** 418–420 (1983).
12. Graff, J. *et al.* Hepatitis A virus capsid protein VP1 has a heterogeneous C terminus. *J. Virol.* **73,** 6015–6023 (1999).
13. Tesar, M., Jia, X. Y., Summers, D. F. & Ehrenfeld, E. Analysis of a potential myristoylation site in hepatitis A virus capsid protein VP4. *Virology* **194,** 616–626 (1993).

©2015 Macmillan Publishers Limited. All rights reserved

14. Martin, A. & Lemon, S. M. Hepatitis A virus: from discovery to vaccines. *Hepatology* **43,** S164–S172 (2006).
15. Kaplan, G. *et al.* Identification of a surface glycoprotein on African green monkey kidney cells as a receptor for hepatitis A virus. *EMBO J.* **15,** 4282–4296 (1996).
16. Bishop, N. E. & Anderson, D. A. RNA-dependent cleavage of VP0 capsid protein in provirions of hepatitis A virus. *Virology* **197,** 616–623 (1993).
17. Wang, X. *et al.* A sensor-adaptor mechanism for enterovirus uncoating from structures of EV71. *Nature Struct. Mol. Biol.* **19,** 424–429 (2012).
18. Rossmann, M. G. *et al.* Structure of a human common cold virus and functional relationship to other picornaviruses. *Nature* **317,** 145–153 (1985).
19. Siegl, G., Frosner, G. G., Gauss-Muller, V., Tratschin, J. D. & Deinhardt, F. The physicochemical properties of infectious hepatitis A virions. *J. Gen. Virol.* **57,** 331–341 (1981).
20. De Colibus, L. *et al.* More-powerful virus inhibitors from structure-based analysis of HEV71 capsid-binding molecules. *Nature Struct. Mol. Biol.* **21,** 282–288 (2014).
21. Acharya, R. *et al.* The three-dimensional structure of foot-and-mouth disease virus at 2.9 Å resolution. *Nature* **337,** 709–716 (1989).
22. Liu, Y. & Eisenberg, D. 3D domain swapping: as domains continue to swap. *Protein Sci.* **11,** 1285–1299 (2002).
23. Walter, T. S. *et al.* A plate-based high-throughput assay for virus stability and vaccine formulation. *J. Virol. Methods* **185,** 166–170 (2012).
24. Porta, C. *et al.* Rational engineering of recombinant picornavirus capsids to produce safe, protective vaccine antigen. *PLoS Pathog.* **9,** e1003255 (2013).
25. Filman, D. J. *et al.* Structural factors that control conformational transitions and serotype specificity in type 3 poliovirus. *EMBO J.* **8,** 1567–1579 (1989).
26. Warwicker, J. Model for the differential stabilities of rhinovirus and poliovirus to mild acidic pH, based on electrostatics calculations. *J. Mol. Biol.* **223,** 247–257 (1992).
27. Garriga, D. *et al.* Insights into minor group rhinovirus uncoating: the X-ray structure of the HRV2 empty capsid. *PLoS Pathog.* **8,** e1002473 (2012).
28. Ren, J. *et al.* Picornavirus uncoating intermediate captured in atomic detail. *Nature Commun.* **4,** 1929 (2013).
29. Butan, C., Filman, D. J. & Hogle, J. M. Cryo-electron microscopy reconstruction shows poliovirus 135S particles poised for membrane interaction and RNA release. *J. Virol.* **88,** 1758–1770 (2014).
30. Riffel, N. *et al.* Atomic resolution structure of Moloney murine leukemia virus matrix protein and its relationship to other retroviral matrix proteins. *Structure* **10,** 1627–1636 (2002).

Supplementary Information is available in the online version of the paper.

Acknowledgements This work was supported by the Strategic Priority Research Program of the Chinese Academy of Sciences, grant no. XDB08020200, the Ministry of Science and Technology 973 Project (grant no. 2014CB542800), the National Major Project of Infectious Disease (2012ZX10004701) and National Science Foundation grant 81330036. D.I.S. and E.E.F. are supported by the UK Medical Research Council (grant G1000099) and J.R. by the Wellcome Trust. This work is a contribution from the Instruct Centre, Oxford. Administrative support was provided by the Wellcome Trust (075491/Z/04). We thank J. Johnson and A. Routh for supplying CrPV, and S. Lemon and K. McKnight for discussions.

Author Contributions Q.G., J.W., Z.H. and W.Y. prepared samples. X.W., J.R., Q.G., X.L., Y.S., E.E.F. and D.I.S. performed research, J.R., X.W., E.E.F. and D.I.S. analysed data and with D.J.R. and Z.R. wrote the manuscript, in discussion with J.W. and Z.H.

Author Information The coordinates and structure factors for the full and empty particles have been deposited with the RCSB Protein Data Bank under accession codes 4QPI and 4QPG, respectively. Reprints and permissions information is available at www.nature.com/reprints. The authors declare no competing financial interests. Readers are welcome to comment on the online version of the paper. Correspondence and requests for materials should be addressed to D.I.S. (dave@strubi.ox.ac.uk), Z.R. (raozh@xtal.tsinghua.edu.cn) or J.W. (wangjz@nicpbp.org.cn).

©2015 Macmillan Publishers Limited. All rights reserved

METHODS

Particle production and purification. HAV virus genotype TZ84 was used to infect 2BS cells at a multiplicity of infection (MOI) of 0.2 at 33–34 °C. Cells were harvested 4 weeks after infection, lysed by treatment with ice-cold 1% sodium deoxycholate in PBS buffer (pH 7.2) and centrifuged to remove cell debris. The supernatant was passed through a 0.22 μm filter, concentrated with a 100 kDa cutoff concentrator and washed with PBS buffer repeatedly. Virus was inactivated by incubation with formaldehyde (1:2,000 dilution) at 4 °C for 7 days, followed by polyethylene glycol 6000 precipitation, chloroform extraction, differential ultracentrifugation and gel filtration. Crude HAV concentrate (1 mg in PBS buffer pH 7.4) was loaded onto a 15–45% (W/V) sucrose density gradient and centrifuged at 29,000 r.p.m. for 3.5 h in an SW41 rotor at 4 °C. Two sets of fractions were collected and dialysed against PBS buffer (Extended Data Fig. 1a): one contained empty particles (containing no RNA) and the other virions. The two types of viral particle were further purified by 10–40% (W/V) sucrose density gradient ultracentrifugation at 29,000 r.p.m. for 3 h in an SW41 rotor at 4 °C. The main bands were collected and dialysed against PBS buffer.

Biochemical, biophysical and EM analysis. SDS–PAGE for protein analysis used a NuPAGE 4–12% Bis-Tris Gel (Invitrogen) according to the manufacturer's protocol (Extended Data Fig. 1b). The sedimentation coefficients for the two types of particle were determined using a Beckman XL-I analytical ultracentrifuge at 4 °C (Extended Data Fig. 1c, d). These results confirmed the two types of HAV particle as full virions containing proteins VP1–4 and RNA and possessing a sedimentation coefficient of 144S and empty particles containing VP0, 1 and 3 with no RNA and a sedimentation coefficient of 82S.

Transmission electron microscope. Inactivated purified HAV viral particles were deposited onto a carbon-coated grid for 1 min. Excess sample was removed with filter paper, the grid washed twice with double distilled water and the sample immediately negatively stained for 30 s with 2% phosphotungstic acid (adjusted to pH 7.0 with 1 M KOH). Excess stain was removed, and the sample air-dried and transferred to an FEI Tecnai 20 transmission electron microscope for visualization (Extended Data Fig. 1e, f).

Thermofluor assay. Thermofluor experiments were performed with an MX3005p RT–PCR instrument (Agilent/Stratagene). SYTO9 and SYPRO red (both Invitrogen) were used as fluorescent probes to detect the presence of single-stranded RNA and exposed hydrophobic regions of proteins, respectively[23]. 50-μl reactions were set up in a thin-walled PCR plate (Agilent), containing 0.5–1.0 μg of either virus or empty particles, 5 μM SYTO9 and 3X SYPRO red in pH ranging from 2 to 10 buffer solutions and ramped from 25–99 °C with fluorescence recorded in triplicate at 1 °C intervals. The RNA release (T_r) and melting temperature (T_m) were taken as the minima of the negative first derivative of the RNA exposure and protein denaturation curves, respectively (Extended Data Fig. 4).

Crystallization and data collection. Full and empty particles were concentrated to 1.5 and 3 mg ml^{-1} respectively before crystallization in Greiner CrystalQuickX plates using a version of the previously described nanolitre vapour diffusion procedure[31] with 30% MPD and 0.5 M ammonium sulphate as precipitants and 0.1 M HEPES-Na buffer at pH 7.5. Crystals (rectangular plates of dimensions ~100 × 100 × 5 μM) were cryo-protected using solutions containing up to 50% MPD and 20% glycerol depending on the crystal age. Data were collected from frozen crystals (100 K) on beamlines I03 and I24 at Diamond Light Source UK. Diffraction images of 0.1° rotation were recorded on a Pilatus6M detector using beam size from 0.02 × 0.02 mm^2 to 0.08 × 0.06 mm^2, commensurate with crystal size. Using 1.0-s exposure time and 100% beam transmission, typically 50 useful images could be collected from one position of a crystal. For some larger crystals, data could be collected from two positions. A total of some 200 crystals of both full and empty particles were frozen and tested. 17 empty particle crystals diffracted and gave a data set to 3.5 Å resolution with 68.0% completeness; 32 full virus crystals resulted in a data set to 3.0 Å resolution with 44.4% completeness. Although the data suffered from the large mosaic spread of the crystals, the minimal divergence of the X-ray beam on I03 ameliorated the problem.

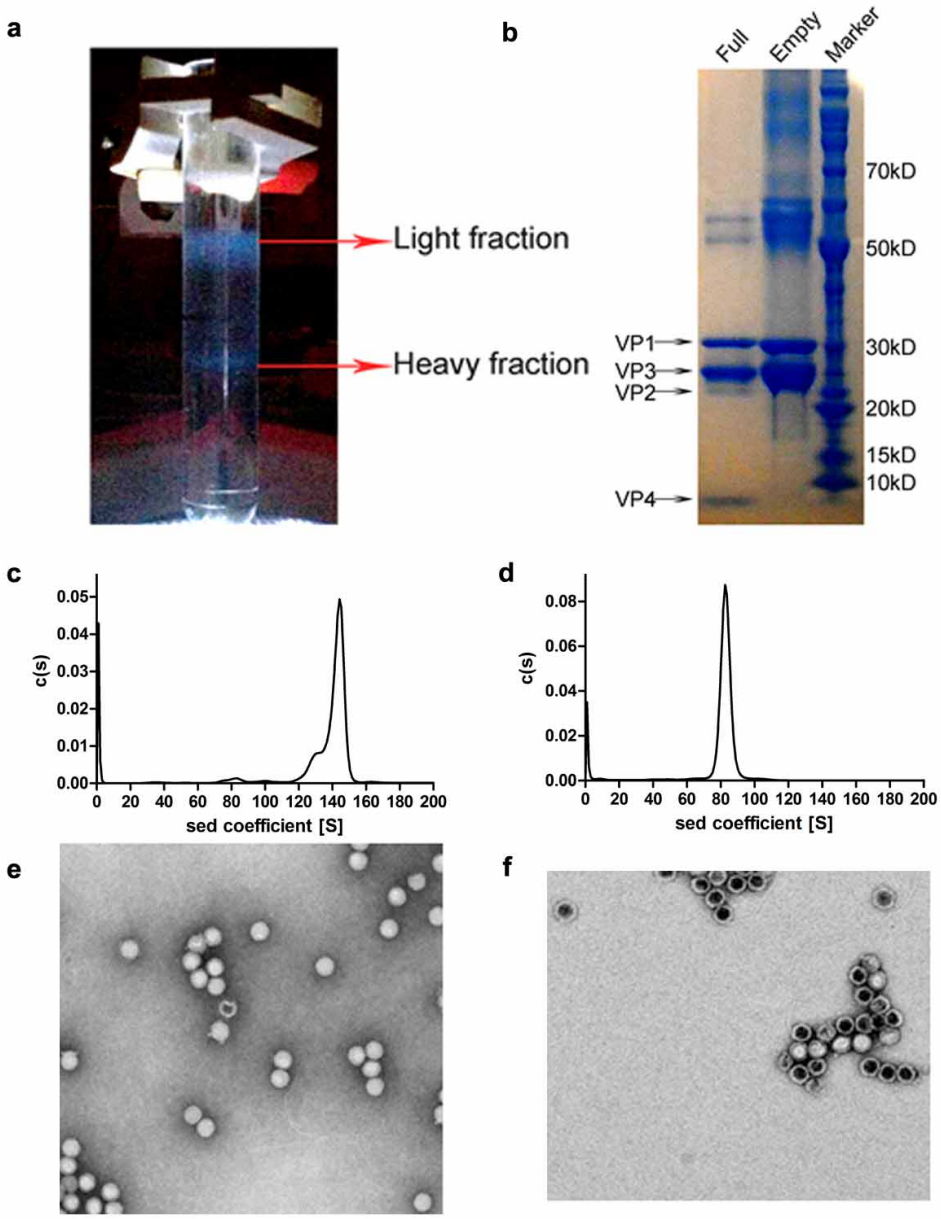
Structure determination. Data were analysed using HKL2000[32]. The mosaicity differed for the full and empty particle crystals ranging from 0.35° to 0.85°. The data were inevitably very weak with average $I/\sigma I$ of 1.4 for the full particle data set and 3.0 for the empty particle data sets. The structures of both particles were determined by molecular replacement. The space group for the empty particle was $P2_12_12$ with unit cell dimensions $a = 366.1$ Å, $b = 442.9$ Å and $c = 289.0$ Å (30 protomers in a crystallographic asymmetric unit). For the full virus, the unit cell dimensions are $a = 291.5$ Å, $b = 423.3$ Å, $c = 314.8$ Å and $\beta = 100.2°$, space group $P2_1$ with a full particle in asymmetric unit. Phasing used molecular replacement with an FMDV model (Cαs of a pentamer, Protein Data Bank accession 1FMD) followed by non-crystallographic symmetry (NCS) averaging and refinement using strict NCS constraints[33]. The full virus was centred at (194.1, 106.1, 85.6) and the empty particle at (0, 221.5, 6.0). For each space group the content of the crystallographic asymmetric unit was subjected to rigid-body refinement, followed by cyclic positional, simulated annealing and B-factor refinement using strict NCS constraints with CNS[33]. Maps were averaged used GAP (D.I.S., J. Grimes and J. Diprose, unpublished) and models were rebuilt with COOT[34]. Refinement of the full particle structure stuck at an *R*-factor of 31.8%, probably attributable to imperfect isomorphism of the constituent crystals and to the extreme weakness of the data. For statistics, see Extended Data Table 1. Structural comparisons used SHP[35]. Unless otherwise noted structural figures were prepared with PyMOL[36].

Production of monoclonal antibody and neutralization assay. Groups of 15 adult (4 weeks old) female BALB/c mice were immunized intraperitoneally with 10 μg inactivated HAV virus. All animal procedures were carried out in accordance with the guideline for the Use of Animals in Research issued by the Institute of Biophysics, Chinese Academy of Sciences. Two booster doses were given at 2 weekly intervals. Two weeks after the last immunization, blood samples were obtained from the tail and tested by enzyme-linked immunosorbent assay (ELISA) using purified HAV virus as antigen. Classical protocols for production of monoclonal antibody were followed (continuous cultures of fused cells secreting antibody of predefined specificity). For the neutralization assay, purified monoclonal antibodies at a concentration of 0.2 mg ml^{-1} were initially diluted eightfold as stocks, and then serially diluted twofold with DMEM containing 2% FBS. 100 μl of twofold antibody dilutions were mixed with 100 μl of HAV virus containing 100 $TCID_{50}$ for 1 h at 37 °C, and then added to monolayers of 2BS cells in cell culture flasks (T25 CM^2), meanwhile, maintaining medium was provided as well. Each dilution was replicated three times along with one control that contained no serum dilution. After 21 days of growth at 33 °C, the medium was removed and the cells washed three times using PBS buffer, 1 ml of trypsin/EDTA was added and the flask left for 3 min at 37 °C. The suspended cells were freeze-thawed five times to collect the virus. Enzyme-linked immunosorbent assay (ELISA) was used to determine neutralizing titre. The titres were read as the highest dilution that gave complete protection.

Peptide-ELISA assay. Synthetic peptides spanning the entire exposed region of HAV VP1, VP2 and VP3 capsid proteins were synthesized by Scilight-Peptide Company (Beijing, China). The reactivity of synthetic peptides with purified HAV neutralizing monoclonal antibody was measured by ELISA. Briefly, 96-well plates were coated with 100 μl well^{-1} of individual peptide (10 μg ml^{-1} in PBS buffer) at 4 °C overnight. An unrelated EV71 peptide was used as a negative control and inactivated HAV as a positive control. The wells were then incubated sequentially with 100 μl well^{-1} of PBST plus 5% skimmed milk powder at 37 °C for 1 h, and 100 μl well^{-1} of HAV neutralizing monoclonal antibodies at the indicated dilutions were incubated at 37 °C for 1 h. Horseradish peroxidase (HRP) conjugated goat anti-mouse IgG diluted (1:5,000) in PBST plus 1% milk powder was used as secondary antibody at 37 °C for 1 h. Five washes with PBST were carried out between incubation steps. For colour development, 100 μl well^{-1} of TMB mixture was added and incubated for 10 min, followed by addition of 50 μl well^{-1} of 1M H_3PO_4 to stop the reaction. Absorbance was measured at 450 nm in a 96-well plate reader.

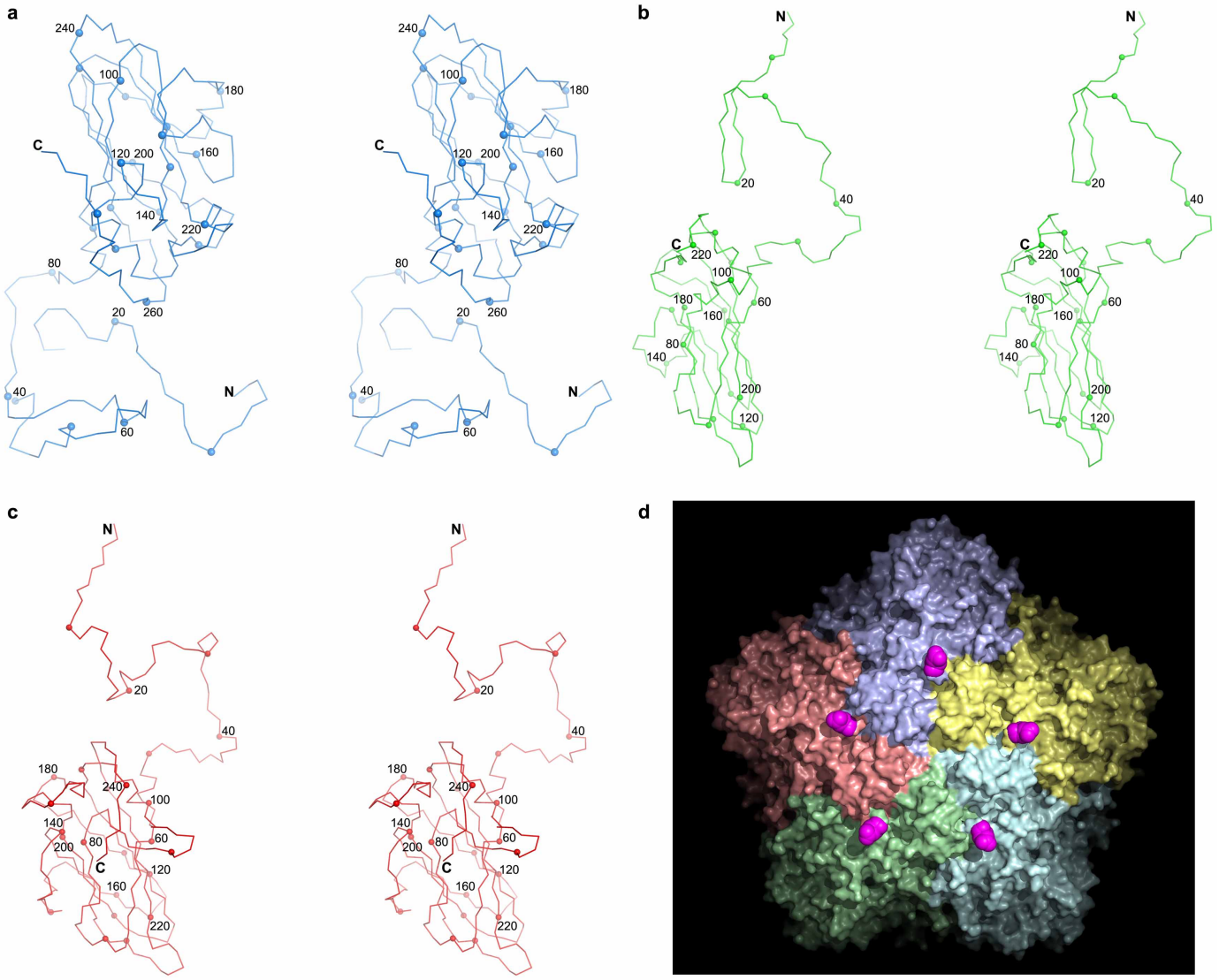
31. Walter, T. S. *et al.* A procedure for setting up high-throughput nanolitre crystallization experiments. Crystallization workflow for initial screening, automated storage, imaging and optimization. *Acta Crystallogr. D* **61,** 651–657 (2005).
32. Minor, W., Cymborowski, M., Otwinowski, Z. & Chruszcz, M. HKL-3000: the integration of data reduction and structure solution—from diffraction images to an initial model in minutes. *Acta Crystallogr. D* **62,** 859–866 (2006).
33. Brünger, A. T. *et al.* Crystallography & NMR system: A new software suite for macromolecular structure determination. *Acta Crystallogr. D* **54,** 905–921 (1998).
34. Emsley, P., Lohkamp, B., Scott, W. G. & Cowtan, K. Features and development of Coot. *Acta Crystallogr. D* **66,** 486–501 (2010).
35. Stuart, D. I., Levine, M., Muirhead, H. & Stammers, D. K. Crystal structure of cat muscle pyruvate kinase at a resolution of 2.6 A. *J. Mol. Biol.* **134,** 109–142 (1979).
36. PyMOL. The PyMOL Molecular Graphics System, Version 1.5.0.4 Schrödinger, LLC. (2002).
37. Schuck, P. Size-distribution analysis of macromolecules by sedimentation velocity ultracentrifugation and lamm equation modeling. *Biophys. J.* **78,** 1606–1619 (2000).
38. Lawrence, M. C. & Colman, P. M. Shape complementarity at protein/protein interfaces. *J. Mol. Biol.* **234,** 946–950 (1993).
39. Chapman, M. S. & Rossmann, M. G. Comparison of surface properties of picornaviruses: strategies for hiding the receptor site from immune surveillance. *Virology* **195,** 745–756 (1993).

©2015 Macmillan Publishers Limited. All rights reserved



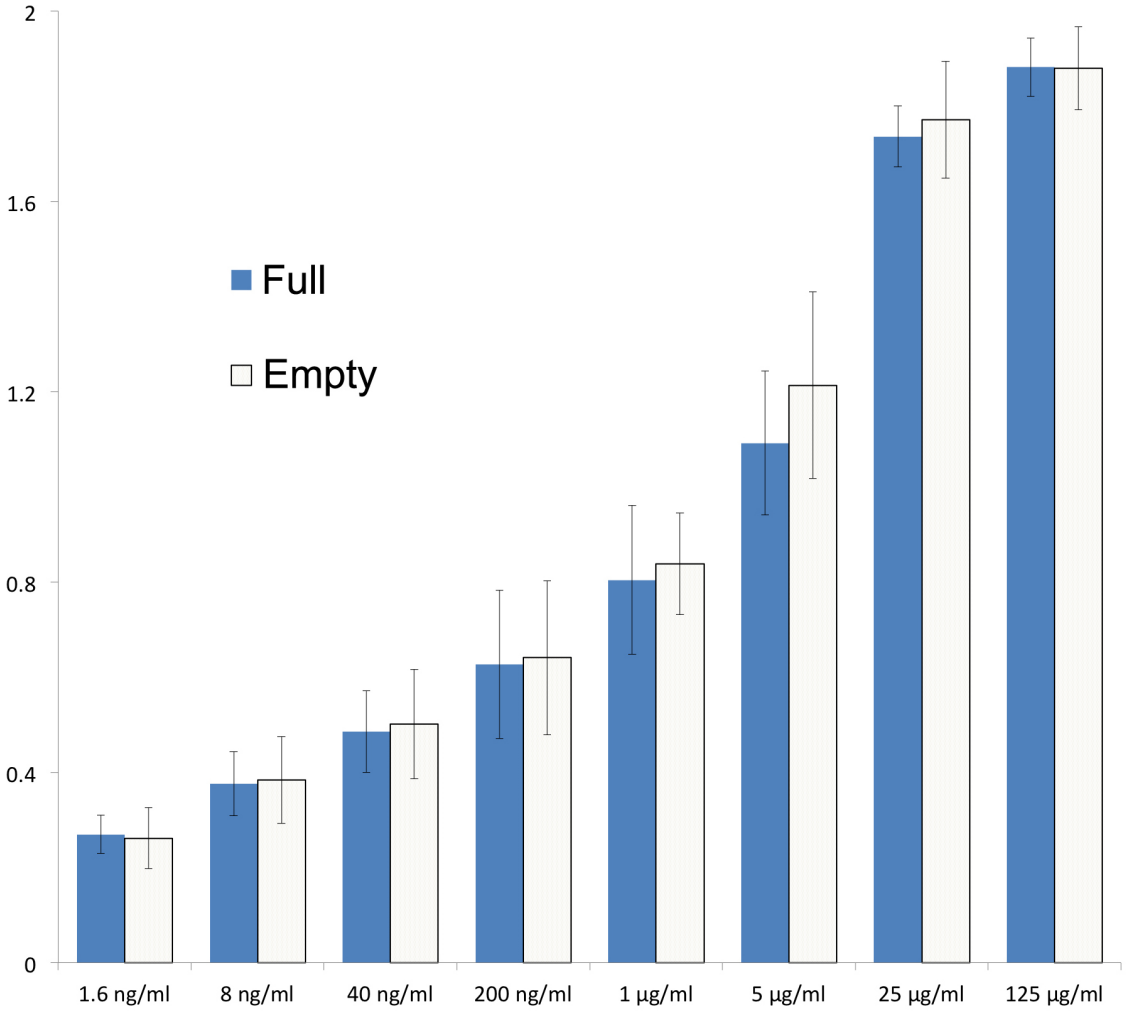
Extended Data Figure 1 | HAV purification and characterization. **a**, Zonal ultracentrifugation of a 15% to 45% (w/v) sucrose density gradient at 103,614 g for 3.5 h was used to purify HAV, as described in Methods. Two predominant particle types were separated; one was located at ~27% sucrose, the other at ~32% sucrose. The absorbance ratios (λ260/λ280) were 0.76 for the top band and 1.66 for the bottom band, indicating that the former contained mainly empty particles without the RNA genome and the latter mainly full particles with the RNA genome. The top band was much broader than the bottom one. Three and two fractions were collected around the top and the bottom bands, respectively, for further purification. **b**, SDS–PAGE for protein composition analysis using A NuPAGE 4–12% Bis-Tris Gel (Invitrogen). Each lane was loaded with 5–10 μg sample (lane 1, full particles; lane 2, empty particles; lane 3, markers). The calculated molecular masses of VP0, VP1, VP2, VP3 and VP4 were 27.26 kDa, 30.73 kDa, 24.80 kDa, 27.86 kDa and 2.50 kDa, respectively. The results appear to show incomplete cleavage of VP0 in the full particles and no VP0 cleavage in the empty particles. **c**, **d**, Sedimentation velocity experiments were performed on a Beckman XL-I analytical ultracentrifuge at 20 °C. Samples were loaded into a conventional double-sector quartz cell and mounted in a Beckman four-hole An-60 Ti rotor. Data were collected at 15,000 r.p.m. at a wavelength of 287 nm. Interference sedimentation coefficient distributions were calculated from the sedimentation velocity data using SEDFIT[37]. The full particle has a sedimentation coefficient of 144S and the empty particle 82S. **e**, **f**, Negative stain electron microscopy of HAV particles. Particles from the top band in panel **a**, shown in panel **f**, suggest that light sedimentation fractions were mainly composed of empty particles. Note that some particles appear to have external features. Panel **e** shows the heavy particles, which appear to contain viral RNA.

©2015 Macmillan Publishers Limited. All rights reserved



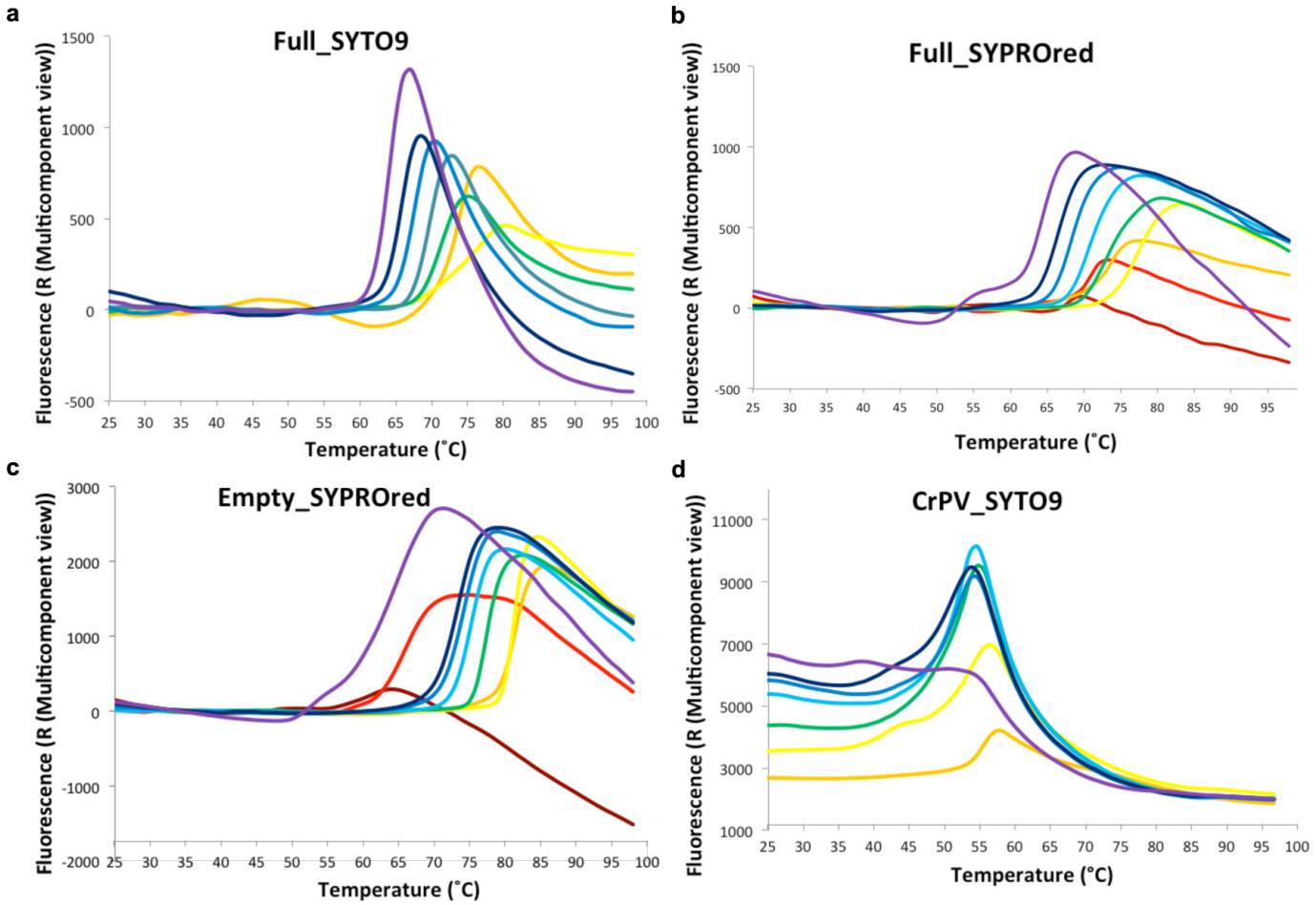
Extended Data Figure 2 | HAV capsid protein structure. **a**–**c**, Stereo diagrams showing the structures of the capsid proteins VP1, VP2 and VP3, respectively. The Cα backbone is shown as a thin line, the N and C termini are labelled, every 10th residue is marked with a small sphere and every 20th is numbered. **d**, VP1 is initially produced with an 8-kDa C-terminal extension (known as PX) unique to HAV among picornaviruses. PX is cleaved from the full particle by an unknown host protease. According to the data shown in Extended Data Fig. 1 and the electron density maps, the particles we have analysed do not contain PX, but if it were present we would expect its course to start at the purple positions (C termini of VP1) on the surface of the virus.

©2015 Macmillan Publishers Limited. All rights reserved



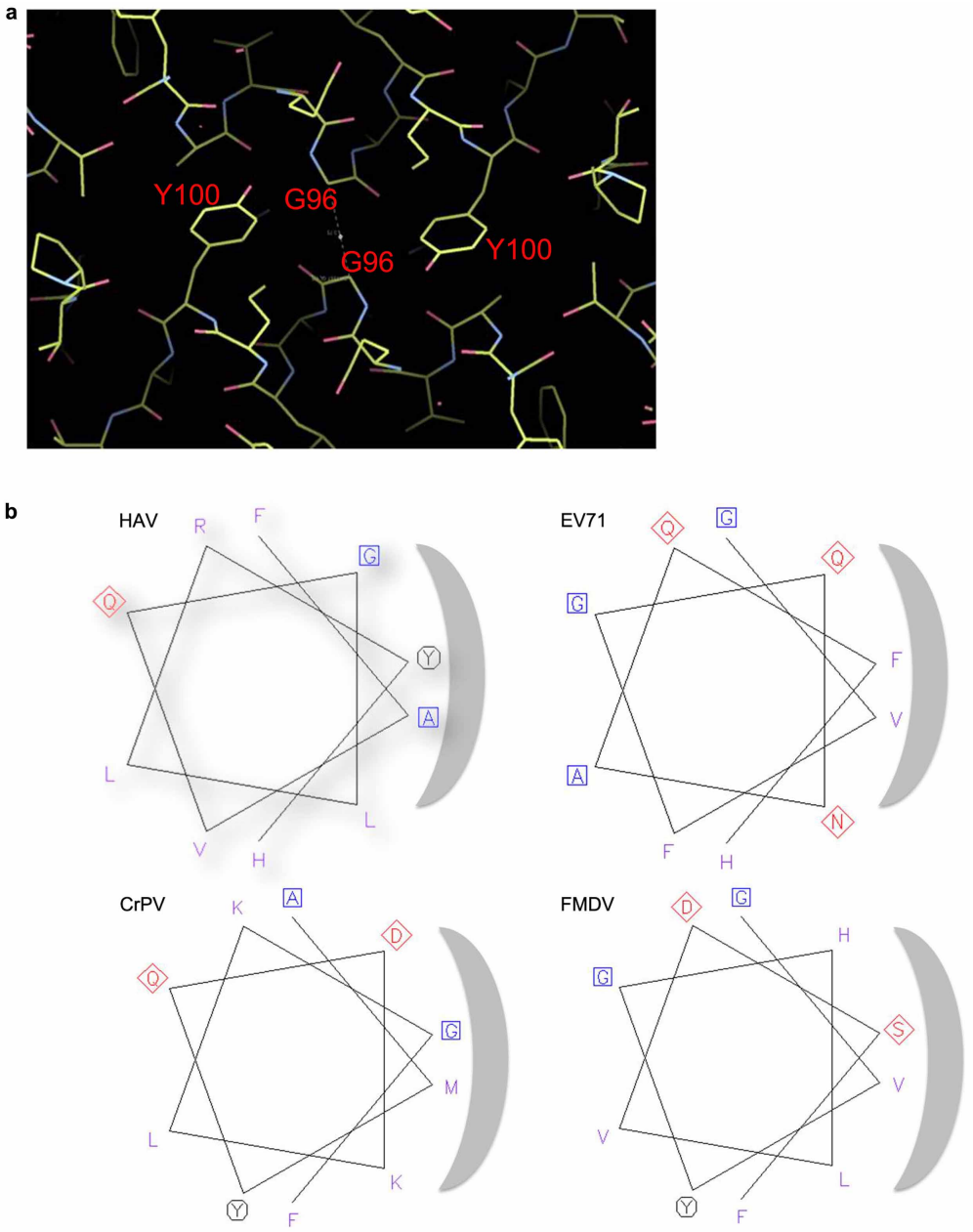
Extended Data Figure 3 | Antigenicity of full and empty particles. The reactivity of HAV full and empty particles against a panel of six purified HAV neutralizing monoclonal antibodies was measured by ELISA. The bar charts represent the average OD_{450} reading for the six monoclonal antibodies at each dilution with the standard deviation shown as an error bar.

©2015 Macmillan Publishers Limited. All rights reserved



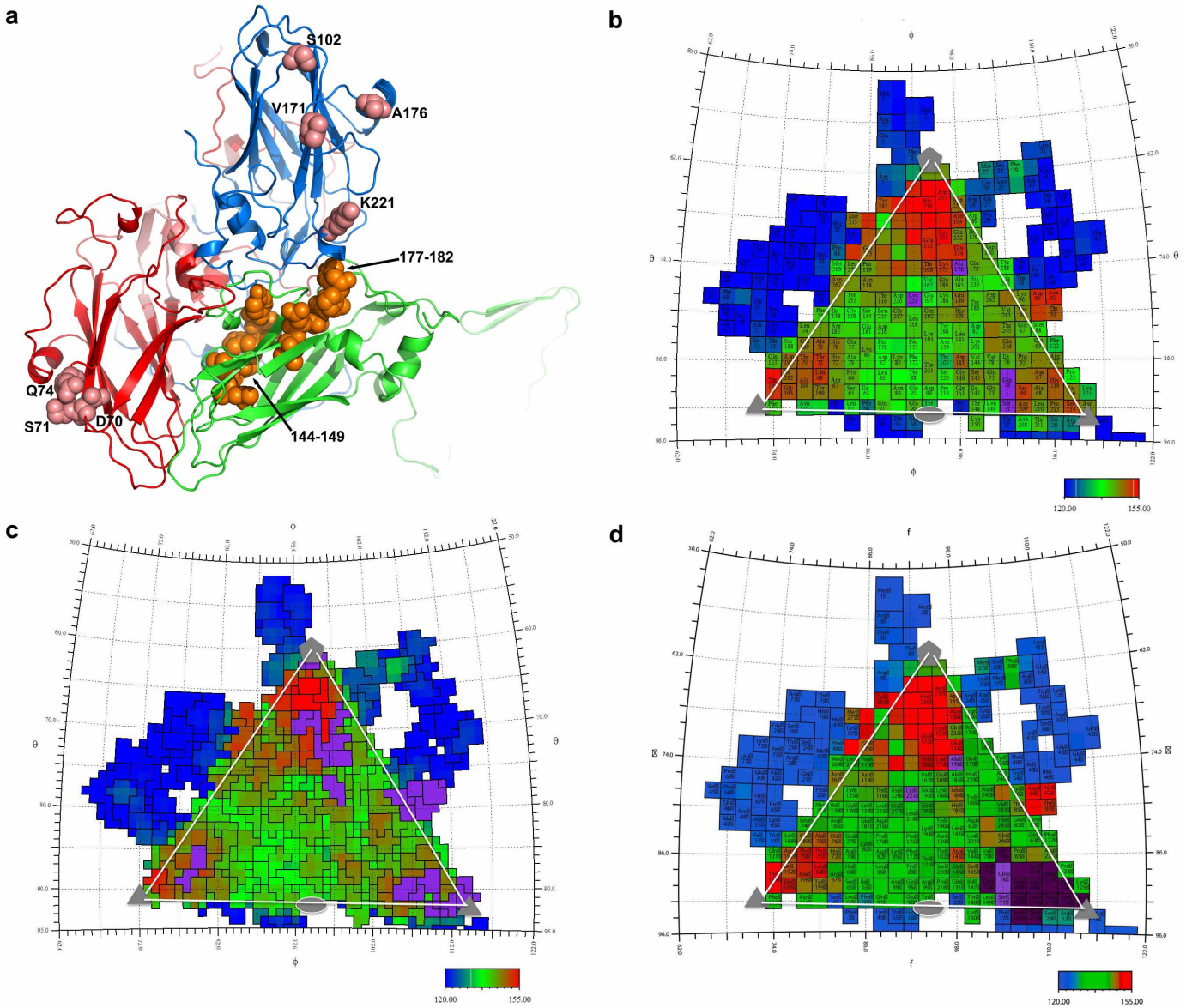
Extended Data Figure 4 | PaSTRy assays. To characterize the stability of HAV full and empty particles compared to CrPv across the pH range from 2.0 to 10.0, differential scanning fluorimetry assays were performed with dyes SYTO9 (to detect RNA exposure) and SYPRO red (to detect protein melting)[23]. **a**, The raw fluorescence traces of HAV full particles incubated with SYTO9. **b**, The raw fluorescence traces of HAV full particles incubated with SYPRO red. **c**, The raw fluorescence traces of HAV empty particles incubated with SYPRO red. **d**, The raw fluorescence traces of CrPV full particles incubated with SYTO9 across the same pH range. The colour scheme is dark red (pH 2.0), red (pH 3.0), orange (pH 4.0), yellow (pH 5.0), green (pH 6.0), sky blue (pH 7.0), blue (pH 8.0), dark blue (pH 9.0) and purple (pH 10.0). Since the SYTO9 dye didn't function well below pH 4.0 the fluorescence traces for pH 2.0 and pH 3.0 are omitted. These results indicate that HAV full virions are most stable at pH 5.0 and RNA genome release occurs at about 76 °C and protein melting at 77 °C; that is, there is no notable transition between RNA release and particle loss. HAV empty particles show a similar trend but appear to withstand temperatures up to 81 °C in low pH buffer. In contrast CrPV is most stable at pH 4.0 and RNA genome release occurs at about 54 °C.

©2015 Macmillan Publishers Limited. All rights reserved



Extended Data Figure 5 | Interactions between α1 helices of VP2 at the icosahedral two-fold. **a**, The close-packing of the two helices is shown, in particular the packing of Tyr 100 against the adjacent helix. The contact area between these helices and the surface complementarity[38] suggests a well-fitting interface for HAV (contact area 83 Å^2, surface complimentarity 0.755; EV71, 111/0.550; Polio-1, 124/0.785; CrPV, 72/0.707; FMDV, 50/0.593). The interface between protomers forming the pentameric units is similar for all of these viruses (HAV, 4,267 Å^2; Polio-1, 4369 Å^2; CrPV, 4,647 Å^2; EV71, 4,131 Å^2; FMDV-A22, 3,432 Å^2). **b**, Helical wheel diagrams for helix α1 of several picornaviruses showing the unusually small side chains at the helix interface in HAV.

©2015 Macmillan Publishers Limited. All rights reserved



Extended Data Figure 6 | Antigenicity and YPX_3L ALIX-interacting motifs. **a**, Previously indicated antigenic sites of HAV are mapped onto the structure (pink spheres). Late domain YPX_3L motifs are shown as orange spheres. **b**–**d**, Surface maps of HAV generated using RIVEM[39] such that area for each residue as drawn corresponds to its accessible area and the coloration is according to the radius from the virus centre (blue, deepest; red, most exposed). On these the antigenic sites of HAV are depicted in purple. **b**, Previously reported antigenic sites; **c**, predicted sites[5]; **d**, new sites determined by peptide mapping (indigo) together with previously identified sites (purple).

©2015 Macmillan Publishers Limited. All rights reserved

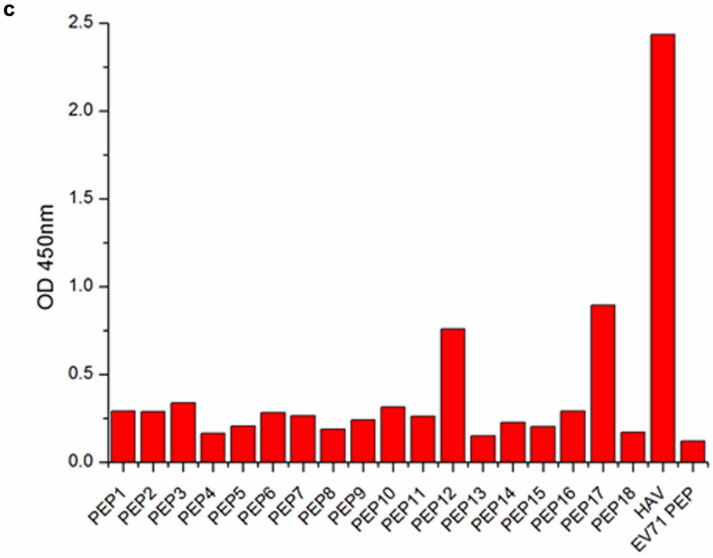
a

Antibodies	Neutralization tilters
# 1	<1:8
# 2	<1:8
# 3	1:64
# 4	<1:8
# 5	1:1024
# 6	1:1024
# 7	1:4096
# 8	<1:8
# 9	1:1024
# 10	1:512
# 11	1:1024
# 12	<1:8
A9(EV71 mAb)	<1:8

b

Peptide name	Residues	Sequence
PEP1	VP1: 260-272	APLNSNAMLSTES
PEP2	VP1: 111-125	TLSSTSNPPHGLPST
PEP3	VP1: 159-178	TPVGLAVDTPWVEKESALSI
PEP4	VP1: 232-245	QIANYNHSDEYLSF
PEP5	VP1: 146-155	IITGATDVDG
PEP6	VP1: 97-108	TFTFNSNNKEYT
PEP7	VP1: 206-225	SYLYAVSGALDGLGDKTDST
PEP8	VP2: 130-146	PGDQSYGSIASLTVYPH
PEP9	VP2: 162-179	PFIYTRGAYHFKDPQYPV
PEP10	VP2: 188-200	SELNIGTGTSAYT
PEP11	VP2: 69-78	LTTHALFHEV
PEP12	VP3: 67-77	NASDSVGQQIK
PEP13	VP3: 81-99	VDPYFFQMTNTNPDQKCIT
PEP14	VP3: 137-153	PGNELIDVSGITLKQAT
PEP15	VP3: 177-198	SDTPYRVNRYTKEAHQKGEYTA
PEP16	VP3: 233-246	CFAPLYHAMDVTTQ
PEP17	VP3: 208-219	NRLTSPSNVAHH
PEP18	VP3: 110-121	FWRGDLVFDFQV
EV71_P	VP1: 211-225	FGEHKQEKDLEYGAC

c



Extended Data Figure 7 | Monoclonal antibody neutralization assays and peptide epitope mapping. **a**, *In vitro* neutralization assays of monoclonal antibodies against HAV (TZ84). **b**, Peptides used for epitope mapping. **c**, Reactivity of the neutralizing mAb 11 against synthetic peptides measured by peptide-ELISA.

©2015 Macmillan Publishers Limited. All rights reserved

Extended Data Table 1 | Data collection, phasing and refinement statistics

	Empty particle	Full particle
Data collection		
Beam line	Diamond I03 and I24	
particle	empty	full
Temperature (K)	100	100
Space group	$P2_12_12$	$P2_1$
No. of crystals (positions)	17(29)	32(36)
Cell dimensions		
a, b, c (Å)	*a*=366.1, *b*=442.9, c=289.0	*a*=291.5, *b*=423.3, *c*=314.8, *β*=100.2°
Resolution (Å)	50.0–3.50 (3.56–3.50)	50.0–3.00 (3.05–3.00)
Unique reflections	404893(2925)	654559(6711)
R_{merge}	0.363(---)	0.410(0.933)
I / σI	3.0(0.3)	1.4(0.5)
Completeness (%)	68.0(9.9)	44.4(9.1)
Redundancy	2.5(1.1)	1.9(1.1)
Refinement		
Resolution (Å)	50.0 – 3.50	50.0 – 3.00
No. reflections	392844/3880	643384/6633
R_{work} /R_{free}*	0.264/0.263	0.318/0.321
No. atoms	5358	5742
Mean B-factors (Å^2)	179	37
r.m.s. deviations		
Bond lengths (Å)	0.004	0.008
Bond angles (°)	1.0	1.4

Note that the R_{free} is of limited significance owing to the considerable non-crystallographic symmetry, 30-fold and 60-fold for the empty and full particles, respectively.

©2015 Macmillan Publishers Limited. All rights reserved

LETTER

doi:10.1038/nature13801

Human intracellular ISG15 prevents interferon-α/β over-amplification and auto-inflammation

Xianqin Zhang[1]*, Dusan Bogunovic[2,3]*, Béatrice Payelle-Brogard[4]*, Véronique Francois-Newton[4]*, Scott D. Speer[3,5,6], Chao Yuan[1], Stefano Volpi[7,8], Zhi Li[4], Ozden Sanal[9], Davood Mansouri[10], Ilhan Tezcan[9], Gillian I. Rice[11], Chunyuan Chen[12], Nahal Mansouri[10], Seyed Alireza Mahdaviani[10], Yuval Itan[2], Bertrand Boisson[2], Satoshi Okada[2], Lu Zeng[1], Xing Wang[1], Hui Jiang[13], Wenqiang Liu[1], Tiantian Han[1], Delin Liu[14], Tao Ma[1], Bo Wang[15], Mugen Liu[1], Jing-Yu Liu[1], Qing K. Wang[1,16], Dilek Yalnizoglu[9], Lilliana Radoshevich[17], Gilles Uzé[18], Philippe Gros[19], Flore Rozenberg[20], Shen-Ying Zhang[2], Emmanuelle Jouanguy[21,22], Jacinta Bustamante[21,22,23], Adolfo García-Sastre[3,5,24], Laurent Abel[2,21,22], Pierre Lebon[20], Luigi D. Notarangelo[7], Yanick J. Crow[11,22,25], Stéphanie Boisson-Dupuis[2,21,22], Jean-Laurent Casanova[21,22,26,27]§ & Sandra Pellegrini[4]§

Intracellular ISG15 is an interferon (IFN)-α/β-inducible ubiquitin-like modifier which can covalently bind other proteins in a process called ISGylation; it is an effector of IFN-α/β-dependent antiviral immunity in mice[1–4]. We previously published a study describing humans with inherited ISG15 deficiency but without unusually severe viral diseases[5]. We showed that these patients were prone to mycobacterial disease and that human ISG15 was non-redundant as an extracellular IFN-γ-inducing molecule. We show here that ISG15-deficient patients also display unanticipated cellular, immunological and clinical signs of enhanced IFN-α/β immunity, reminiscent of the Mendelian autoinflammatory interferonopathies Aicardi–Goutières syndrome and spondyloenchondrodysplasia[6–9]. We further show that an absence of intracellular ISG15 in the patients' cells prevents the accumulation of USP18[10,11], a potent negative regulator of IFN-α/β signalling, resulting in the enhancement and amplification of IFN-α/β responses. Human ISG15, therefore, is not only redundant for antiviral immunity, but is a key negative regulator of IFN-α/β immunity. In humans, intracellular ISG15 is IFN-α/β-inducible not to serve as a substrate for ISGylation-dependent antiviral immunity, but to ensure USP18-dependent regulation of IFN-α/β and prevention of IFN-α/β-dependent autoinflammation.

Calcification of the cerebral basal ganglia during childhood is an important radiological sign associated with a range of genetic and non-genetic states[12,13]. In Fahr's disease, also known as idiopathic basal ganglia calcification (IBGC)[14–17], the genetic causes identified are germline mutations of the *SLC20A2*, *PDGFB* and *PDGFRB* genes[15,16]. Intracranial calcification is also a well recognized feature of a group of Mendelian autoinflammatory diseases associated with upregulation of IFN-α/β signalling[8,18], including Aicardi–Goutières syndrome (AGS) and spondyloenchondromatosis (SPENCD), in particular. We investigated three siblings from China with IBGC. The eldest child (P4) died during an episode of epileptic seizures at the age of 13 years (Supplementary Information, case report). The other two siblings, currently aged 11 (P6) and 13 (P5) years, have suffered only occasional seizures. Despite having been exposed to common childhood viruses (Extended Data Table 1), these children have experienced no severe infectious disease. Whole-exome sequencing (WES) of P5 and P6 and their healthy mother identified only one common nonsense homozygous mutation, which had not been reported in public databases or in in-house WES data for 1,500 other individuals (Extended Data Table 2). This variant was in exon 2 of *ISG15*: c.163C>T/163C>T (p.Gln 55*/Gln 55*; asterisks denote stop codons). Familial segregation was consistent with an autosomal recessive mode of inheritance (Fig. 1a, b and Extended Data Fig. 1a).

This observation was surprising, as we recently described three unrelated children from two families from Turkey and Iran who were homozygous for loss-of-function mutations of *ISG15*[5]. These patients (P1, P2 and P3, now aged 17, 14 and 17 years, respectively) displayed clinical disease caused by the BCG vaccine, which, in otherwise healthy individuals, defines Mendelian susceptibility to mycobacterial disease (MSMD), a rare disorder characterized by severe clinical disease following infection with weakly virulent mycobacteria[19,20]. In these patients, MSMD resulted from insufficient ISG15-dependent IFN-γ production[21]. These patients displayed no severe viral disease[2]. Following the identification of *ISG15* mutations in Chinese children with a putative diagnosis of IBGC, we performed computed tomography (CT) scans on the Iranian and Turkish ISG15-deficient MSMD patients. We found that P1 and P2 displayed calcification of the basal ganglia, with CT imaging in P3 also showing calcification along the cerebral falx (Fig. 1c). The ISG15-deficient patients from China were not vaccinated with BCG at birth, consistent with their current lack of an MSMD phenotype. The c.163C>T/163C>T mutant allele showed no ISG15 protein on western blots (Extended Data Fig. 1b). In total, six patients (P4 with inferred genotype) with IBGC

[1]Key Laboratory of Molecular Biophysics of the Ministry of Education, College of Life Science and Technology, Huazhong University of Science and Technology, Wuhan 430074, China. [2]St. Giles Laboratory of Human Genetics of Infectious Diseases, Rockefeller Branch, The Rockefeller University, New York, New York 10065, USA. [3]Department of Microbiology, Icahn School of Medicine at Mount Sinai, New York, New York 10029, USA. [4]Institut Pasteur, Cytokine Signaling Unit, CNRS URA 1961, 75724 Paris, France. [5]Global Health and Emerging Pathogens Institute, Icahn School of Medicine at Mount Sinai, New York, New York 10029, USA. [6]Microbiology Training Area, Graduate School of Biomedical Sciences of Icahn School of Medicine at Mount Sinai, New York, New York 10029, USA. [7]Division of Immunology, Children's Hospital Boston, Boston, Massachusetts 02115, USA. [8]Department of Neuroscience, Rehabilitation, Ophthalmology, Genetics, Maternal and Child Health, University of Genoa, 16132 Genoa, Italy. [9]Immunology Division and Pediatric Neurology Department, Hacettepe University Children's Hospital, 06100 Ankara, Turkey. [10]Division of Infectious Diseases and Clinical Immunology, Pediatric Respiratory Diseases Research Center, National Research Institute of Tuberculosis and Lung Diseases, Shahid Beheshti University of Medical Sciences, 4739 Teheran, Iran. [11]Manchester Academic Health Science Centre, University of Manchester, Genetic Medicine, Manchester, M13 9NT, UK. [12]Department of Pediatrics, Third Xiangya Hospital, Central South University, Changsha 410013, China. [13]BGI-Shenzhen, Shenzhen 518083, China. [14]Sangzhi County People's Hospital, Sangzhi 427100, China. [15]Genetics Laboratory, Hubei Maternal and Child Health Hospital, Wuhan, Hubei 430070, China. [16]Center for Cardiovascular Genetics, Department of Molecular Cardiology, Lerner Research Institute, Cleveland Clinic, Cleveland, Ohio 44195, USA. [17]Institut Pasteur, Bacteria-Cell Interactions Unit, 75724 Paris, France. [18]CNRS UMR5235, Montpellier II University, Place Eugène Bataillon, 34095 Montpellier, France. [19]Department of Biochemistry, McGill University, Montreal, QC H3A 0G4, Canada. [20]Paris Descartes University, 75006 Paris, France. [21]Laboratory of Human Genetics of Infectious Diseases, Necker Branch, INSERM U1163, Necker Hospital for Sick Children, 75015 Paris, France. [22]Paris Descartes University, Imagine Institute, 75015 Paris, France. [23]Center for the Study of Primary Immunodeficiencies, Necker Hospital for Sick Children, 75015 Paris, France. [24]Department of Medicine, Division of Infectious Diseases, Icahn School of Medicine at Mount Sinai, New York, New York 10029, USA. [25]INSERM UMR 1163, Laboratory of Neurogenetics and Neuroinflammation, Imagine Institute, 75006 Paris, France. [26]Howard Hughes Medical Institute, New York, New York 10065, USA. [27]Pediatric Hematology–Immunology Unit, Necker Hospital for Sick Children, 75015 Paris, France.
*These authors contributed equally to this work.
§These authors jointly supervised this work.

©2015 Macmillan Publishers Limited. All rights reserved

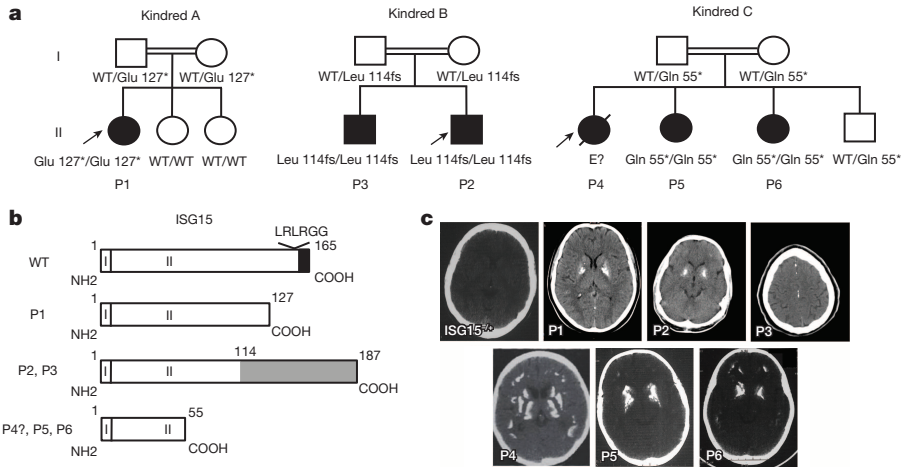


Figure 1 | Familial segregation of the *ISG15* allele and CT scans for the affected families. a, Familial segregation in a family from Turkey (Kindred A), a family from Iran (Kindred B) (previously reported) and a family from China (Kindred C). Asterisks denote stop codons; E denotes unknown genotype; fs, frameshift; WT, wild type. **b**, Graphical representation of the proISG15 protein, with the LRLRGG motif required for substrate ISGylation and the eight-amino-acid sequence (black) cleaved to yield ISG15, and the putative proteins synthesized in the patients. **c**, Axial view cerebral CT scans of P1, P2, P3, P4, P5, P6 and the healthy mother of P4, P5 and P6 ($ISG15^{-/+}$).

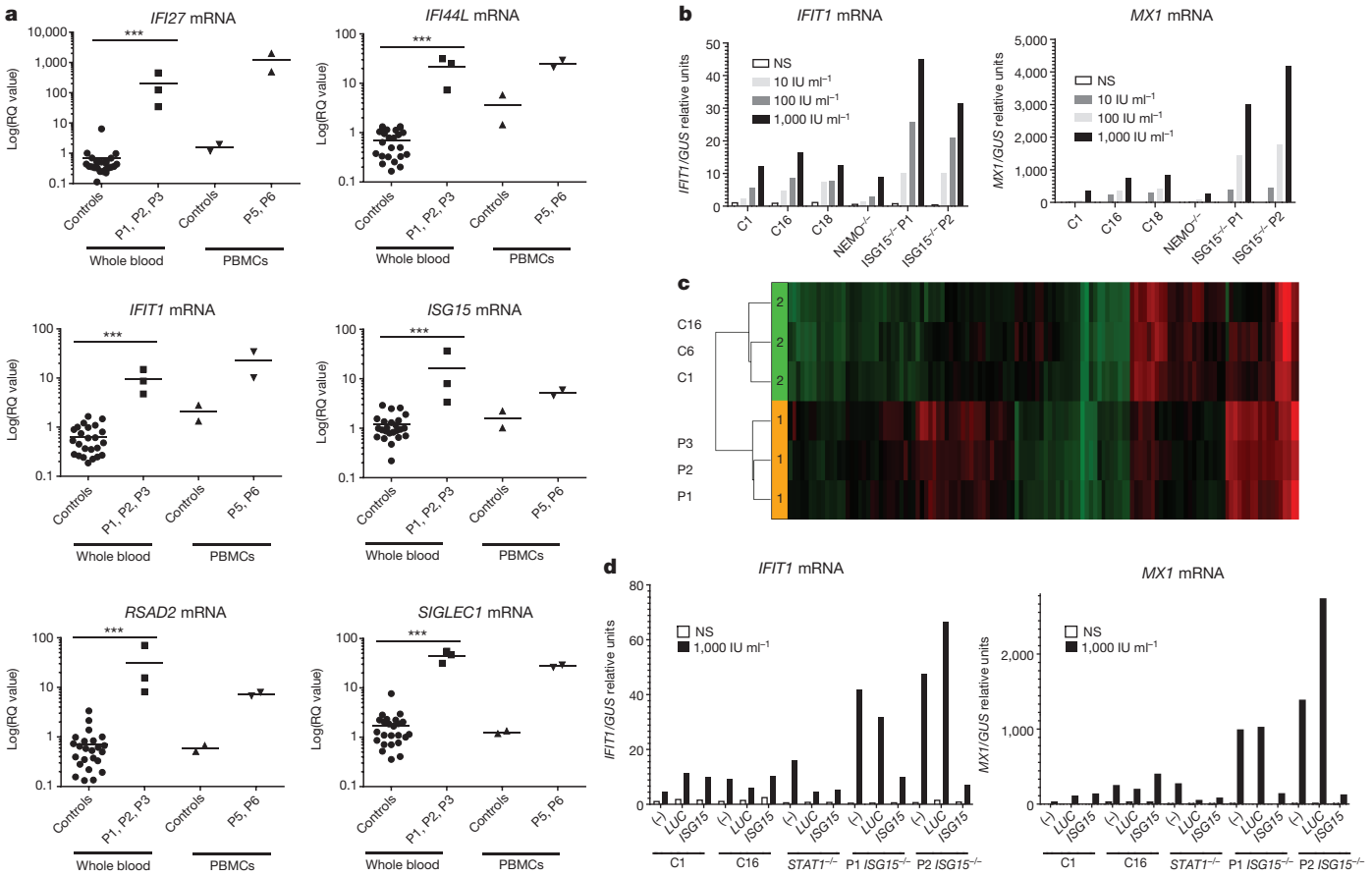


Figure 2 | High levels of interferon-stimulated gene expression in ISG15-deficient individuals. a, Relative mRNA levels for *IFI27*, *IFI44L*, *IFIT1*, *ISG15*, *RSAD2* and *SIGLEC1* in peripheral blood from patients ($n = 3$) or controls (C) ($n = 24$) or in peripheral blood mononuclear cells (PBMCs) from family members (wild type and heterozygous for ISG15 deficiency) ($n = 2$) and patients ($n = 2$), as assessed by RT–qPCR, comparison done with unpaired *t*-tests. ***$P < 0.0001$; horizontal bars represent means; RQ defined in reference to C1 unstimulated condition. **b**, hTert-immortalized fibroblasts from C1, C16, C18, a $NEMO^{-/-}$ subject (as a negative control due to known hyporesponsiveness), P1 and P2 were treated with the indicated doses of IFN-α2b for 12 h, washed with PBS and left to rest for 36 h, after which relative mRNA levels were assessed. **b** shows a representative experiment of three performed. *GUS* is used as a housekeeping control gene. NS, not stimulated. **c**, The same experimental procedure as in **b** was followed, but the mRNA was used for a microarray experiment, for C1, C6, C16, P1, P2 and P3 cells, with green indicating relative upregulation and red indicating downregulation of the probe concerned. **d**, In the same experimental setup, we used lentiviral particles containing luciferase–RFP (red fluorescent protein) or wild-type ISG15–RFP genes to transduce hTert-immortalized fibroblasts and then assessed mRNA levels for *IFIT1* and *MX1* by RT–qPCR. Panel **d** shows one representative experiment of three performed, where (−) denotes not transduced conditions.

©2015 Macmillan Publishers Limited. All rights reserved

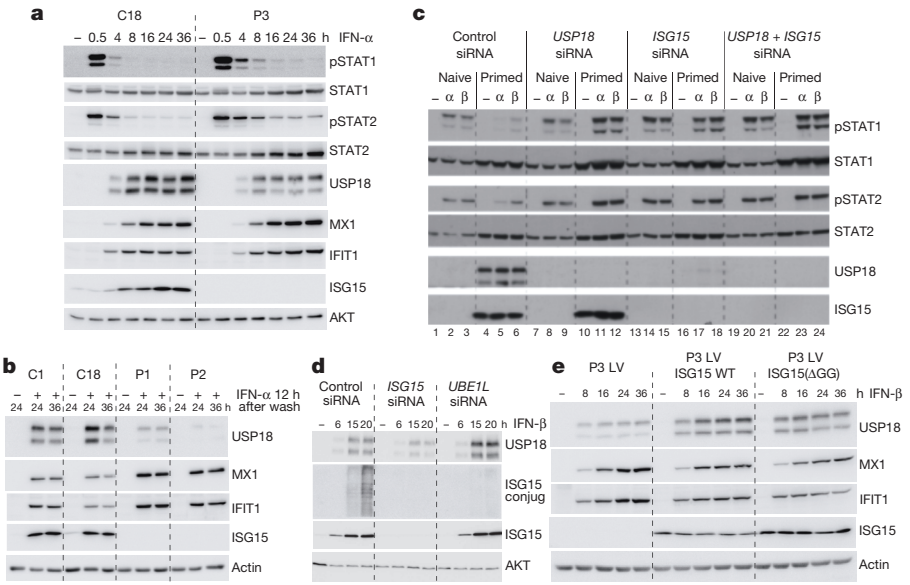


Figure 3 | ISG15 deficiency leads to an enhanced response to type I IFN due to the presence of low levels of USP18. **a**, hTert-immortalized fibroblasts from a control (C18) and patient P3 were treated with 100 pM IFN-α2 for 0.5 to 36 h. Cell lysates were analysed by western blot for levels of phosphorylated STAT (pSTAT) proteins and proteins encoded by interferon-stimulated genes. **b**, hTert-immortalized fibroblasts from controls (C1, C18) and patients P1 and P2 were treated with 100 pM IFN-α2 for 12 h, washed and left to rest for 24 or 36 h. Protein levels were assessed by western blot. **c**, HLLR1-1.4 cells were transfected with control short interfering RNA (siRNA) or with siRNA targeting *USP18*, *ISG15* or both. One day later, cells were left untreated (naive) or were primed for 8 h with 500 pM IFN-β, washed and left to rest for 16 h, and then restimulated for 30 min with 100 pM IFN-α2 or IFN-β. Lysates were analysed with the indicated antibodies. **d**, HLLR1-1.4 cells were transfected with control siRNA, *ISG15* siRNA or *UBE1L* siRNA. One day later, IFN-β (500 pM) was added for various periods of time. Lysates were analysed as indicated. **e**, hTert-immortalized fibroblasts from P3 transduced with lentiviral particles expressing RFP and luciferase (LV), wild-type ISG15 (LV ISG15 WT) or the IS15(ΔGG) mutant (LV ISG15(ΔGG)) were stimulated with IFN-β (500 pM) for 8 to 36 h and protein levels assessed by western blot.

from three kindreds from China, Iran and Turkey were found to have only homozygous rare and null *ISG15* mutant alleles in common (Extended Data Table 3). These findings strongly suggest that the three *ISG15* alleles identified are disease-causing, not only for MSMD, but also for IBGC, an intracranial calcification phenotype unrelated to any obvious cerebral infection.

We next investigated whether enhanced IFN-α/β immunity might account for both the lack of antiviral immunodeficiency[5] and the intracranial calcification, as in patients with autoinflammatory AGS and SPENCD[18]. AGS- and SPENCD-causing mutations can lead to high levels of IFN-α/β in the blood and cerebrospinal fluid, and an upregulation of interferon-stimulated genes[9]. Such an IFN-α/β signature is also observed in patients with the autoimmune disorder systemic lupus erythematosus (SLE), which is sometimes associated with basal ganglia calcification and may be allelic with AGS in rare cases[6,22,23]. We determined the expression levels of six interferon-stimulated genes reported to be upregulated in patients with AGS[7]. *IFI27*, *IFI44L*, *IFIT1*, *ISG15*, *RSAD2* and *SIGLEC1* transcripts were measured in peripheral blood or peripheral blood mononuclear cells from ISG15-deficient patients and controls. Notably, all ISG15-deficient patients, like patients with AGS, had significantly higher levels of interferon-stimulated gene messenger RNA than unaffected relatives or healthy controls (Fig. 2a). The two Chinese patients who displayed seizures (P5 and P6) also had detectable IFN-α antiviral activity in their plasma (Extended Data Fig. 1c, d). These findings indicate that the constitutive enhancement of IFN-α/β activity characterizes ISG15 deficiency, in addition to AGS and SPENCD. All three of these conditions have the same prominent radiological sign, intracranial calcification.

ISG15 is an IFN-α/β-inducible ubiquitin-like protein that can be conjugated to many intracellular substrates via ISGylation[1,3,4,24–26]; we wondered how and why ISG15 deficiency would be associated with enhanced IFN-α/β immunity. We investigated the relationship between ISG15 deficiency and enhanced IFN-α/β immunity by monitoring the IFN-α response of hTert-immortalized fibroblasts from P1, P2, P3 and controls by reverse transcription with quantitative PCR (RT–qPCR) and genome-wide microarray analyses (Fig. 2b, c and Extended Data Table 4). The relative levels of 78 transcripts, including 20 canonical interferon-stimulated genes (including *RSAD2*, *IFI27*, *OAS3*, *IFI44*, *USP18*, *IFIT1* and *MX1*; Extended Data Table 4) were significantly higher in patients than in controls. This *in vitro* phenotype was rescued by transduction with wild-type *ISG15* (Fig. 2d) or with *ISG15(ΔGG)*, a mutant incapable of conjugation (Extended Data Fig. 2a)[5]. We excluded the involvement of secreted ISG15 (Extended Data Fig. 2b). Consistent with mRNA levels, cells from patients expressed more MX1 and IFIT1 proteins than control cells (Fig. 3a, b). Remarkably, however, levels of USP18 were low in patients' cells (Fig. 3a, b), despite their higher levels of *USP18* mRNA (Fig. 2c and Extended Data Table 4). Similar data were obtained for patient-derived Epstein–Barr virus (EBV)-transformed B cells and Simian virus 40 (SV40)-transformed cell lines, as well as for fibrosarcoma cells (HLLR1-1.4) and a human epithelial cell line, WISH, in which *ISG15* was silenced (Extended Data Fig. 3a, b, c). These results demonstrate a positive impact of ISG15 deficiency on the IFN-α/β response and suggest the possible involvement of USP18.

USP18 is an interferon-stimulated gene, an isopeptidase and a potent negative regulator of IFN-α signalling[10,27,28]. We therefore hypothesized that, in the absence of ISG15, IFN-α/β signalling would be inadequately attenuated due to insufficient USP18. Indeed, in patients' cells, STAT1 and STAT2 were more persistently phosphorylated and IFIT1 and MX1 levels were higher than in controls, whereas USP18 levels were low (Fig. 3a, b and Extended Data Fig. 3a). The same was observed following the knockdown of *USP18* and/or *ISG15* expression in HLLR1-1.4 cells primed with IFN-β (Fig. 3c). ISG15 appeared to act in its unconjugated free form, since silencing of *UBE1L* or of other ISGylation enzymes failed to reduce USP18 levels (Fig. 3d and Extended Data Fig. 3d) and patients' cells transduced with wild-type *ISG15* or *ISG15(ΔGG)* exhibited attenuated levels of interferon-stimulated-gene transcripts and proteins (Extended Data Fig. 2a and Fig. 3e). These data indicate that intracellular free ISG15 downregulates the IFN-α/β response by maintaining levels of the negative-feedback regulator USP18.

We then investigated the mechanism by which ISG15 regulates USP18. We measured the translation-independent decay of USP18 in hTert fibroblasts. In cells lacking ISG15, unlike control cells, USP18 levels began to decline after as little as one hour of cycloheximide (CHX) treatment (Fig. 4a and Extended Data Fig. 4a, b). This phenotype was reversed by transduction of patients' cells with wild-type *ISG15* or *ISG15(ΔGG)* constructs (Fig. 4b and Extended Data Fig. 4c). In HEK293T cells,

©2015 Macmillan Publishers Limited. All rights reserved

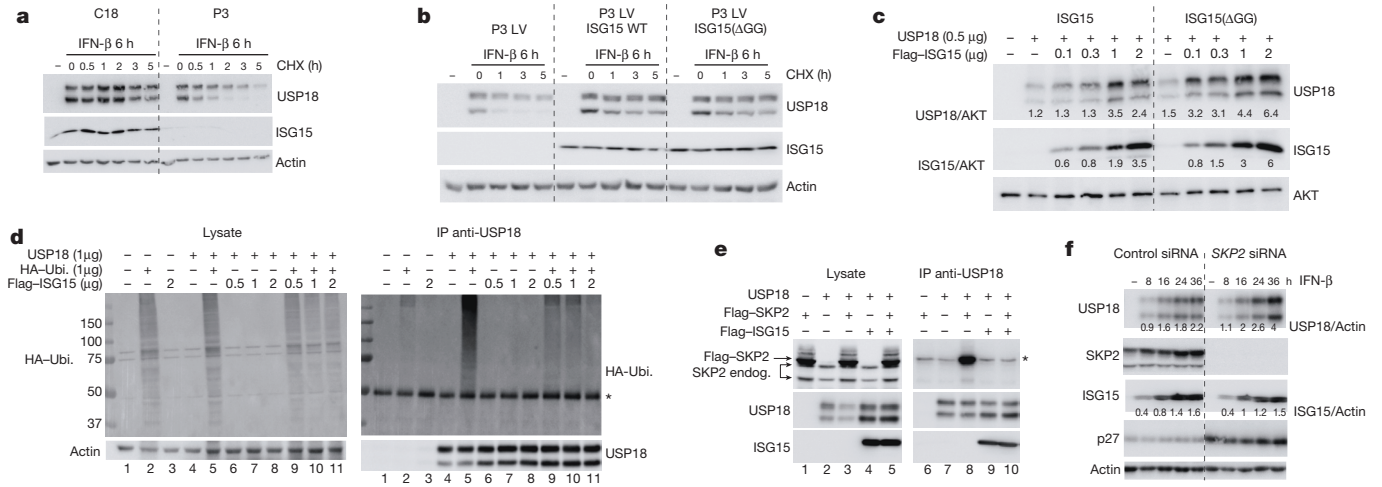


Figure 4 | Free ISG15 stabilizes USP18 by preventing SKP2-dependent ubiquitination. **a**, hTert-immortalized fibroblasts from control (C18) and patient P3 were left untreated (−) or treated for 6 h with IFN-β (500 pM). Cycloheximide (CHX) was added for an additional 0.5 to 5 h. Lysates were analysed as indicated. **b**, hTert fibroblasts from P3 transduced with lentiviral particles expressing RFP and luciferase (LV) conjugated to wild-type ISG15 (LV ISG15 WT) or the non-conjugatable ISG15(ΔGG) mutant (LV ISG15(ΔGG)) were processed as in **a**. **c**, HEK293T cells were transfected with USP18 expression vector alone or in combination with various amounts of ISG15 (Flag–ISG15), either wild-type or ΔGG. Two days later, lysates were analysed as indicated. Ratios of USP18 or ISG15 to AKT are shown below gels. **d**, HEK293T cells were cotransfected with USP18 and haemagglutinin (HA)–ubiquitin in the presence of wild-type ISG15 (Flag–ISG15). Two days later, lysates were subjected to immunoprecipitation (IP) with anti-USP18 antibodies. Lysates (left panels) were analysed with antibodies against HA and actin. Immunoprecipitates (right panels) were analysed with antibodies against HA and USP18. Asterisk indicates IgG heavy chain. **e**, HEK293T cells were transfected with USP18, Flag–SKP2 and Flag–ISG15 expression vectors, as indicated. Two days later, USP18 was immunoprecipitated. Lysates (left panels) and immunoprecipitates (right panels) were analysed with antibodies against SKP2, USP18 and ISG15. Arrowheads indicate two endogenous SKP2 isoforms; arrow indicates ectopic Flag–SKP2; asterisk, background band (lanes 6, 7 and 9, 10). **f**, HLLR1-1.4 cells were transfected with control siRNA or *SKP2* siRNA and 24 h later IFN-β (500 pM) was added and cells were incubated for various times. Lysates were analysed as indicated. USP18 and ISG15 levels were quantified relative to actin levels.

co-transfection of *USP18* with either wild-type *ISG15* or *ISG15(ΔGG)* resulted in augmented USP18 protein levels (Fig. 4c). Co-transfection of *USP18* with ubiquitin led to strong ubiquitination of USP18 (Fig. 4d, lane 5 and Extended Data Fig. 4d), as previously reported[11]. The co-expression of either wild-type *ISG15* or *ISG15(ΔGG)* with *USP18* and ubiquitin resulted in markedly lower levels of USP18 ubiquitination (Fig. 4d, lanes 9–11 and Extended Data Fig. 4e) and larger total amounts of USP18. Overall, these data indicate that free intracellular ISG15 antagonizes USP18 ubiquitination and degradation, thereby promoting the stability and function of this protein.

USP18 is subject to S-phase kinase-associated protein 2 (SKP2)-mediated proteolysis[11,29]. We therefore analysed the impact of ISG15 on SKP2-mediated USP18 degradation. The formation of the USP18–SKP2 complex (Fig. 4e, lane 8), was prevented by co-expression of ISG15 (lane 10 versus lane 8) and ISG15 co-immunoprecipitated with USP18 independently of SKP2 expression (lanes 9 and 10). Finally, we assessed IFN-induced USP18 accumulation in cells silenced for SKP2. At 24 h and beyond, USP18 levels were higher in SKP2-silenced than in unsilenced cells (Fig. 4f and Extended Data Fig. 4f). These results suggest that ISG15 can antagonize SKP2-mediated proteolysis of USP18, although the involvement of other E3 ligases cannot be excluded. In the absence of ISG15, USP18 proteolysis is more rapid, driving the dysregulated IFN-α/β response and resulting in both the blood IFN-α/β signature and brain calcifications seen in the patients.

In conclusion, we have shown that all six ISG15-deficient children identified to date display abnormally strong IFN-α/β immunity, as demonstrated by their high levels of circulating IFN-α and/or leukocyte interferon-stimulated genes. As in patients with AGS and SPENCD[30], ISG15-deficient individuals display marked intracranial calcification. Three of the six ISG15-deficient individuals experienced epileptic seizures, which were lethal in one case. These patients also had autoantibody levels higher than those in age-matched controls (Extended Data Fig. 5). We found that ISG15 deficiency led to reduced levels of the negative regulator USP18 because of increased proteolysis due, at least in part, to SKP2-mediated ubiquitination, resulting in stronger responses to IFN-α/β and an ensuing amplification of IFN-α/β-induced responses. The observed enhancement of cellular responses to IFN-α/β provides an explanation for the lack of overt viral infection phenotypes in patients with ISG15 deficiency[5]. More importantly, human ISG15 is not only redundant for antiviral immunity in these patients, it is a key negative regulator of IFN-α/β. The role of ISG15 in stabilizing USP18 is essential and independent of conjugation. We have not tested whether ISGylated proteins might also stabilize USP18. The broad susceptibility to viral infections of ISG15-deficient mice[2] but not humans[21] may be due to different biochemical properties of murine versus human ISG15 and/or USP18, affecting their interaction potential. Simultaneously, the lack of free extracellular ISG15 resulted in lower IFN-γ production by lymphocytes, thereby underlying MSMD in these patients[5]. The phenotypic dichotomy of this monogenic disease, with both autoimmunity and MSMD, probably reflects the functional dichotomy of intracellular versus extracellular ISG15, respectively. There is currently no evidence that IFN-α/β-inducible human intracellular ISG15 exerts antiviral effects on documented viral infections via ISGylation. On the contrary, we show that IFN-α/β-inducible ISG15 is essential to negatively regulate IFN-α/β responses via USP18 stabilization, thereby preventing autoinflammatory consequences of uncontrolled IFN-α/β amplification.

Online Content Methods, along with any additional Extended Data display items and Source Data, are available in the online version of the paper; references unique to these sections appear only in the online paper.

Received 1 December 2013; accepted 27 August 2014.
Published online 12 October 2014.

1. Jeon, Y. J., Yoo, H. M. & Chung, C. H. ISG15 and immune diseases. *Biochim. Biophys. Acta* **1802,** 485–496 (2010).
2. Morales, D. J. & Lenschow, D. J. The antiviral activities of ISG15. *J. Mol. Biol.* **425,** 4995–5008 (2013).
3. Skaug, B. & Chen, Z. J. Emerging role of ISG15 in antiviral immunity. *Cell* **143,** 187–190 (2010).
4. Zhang, D. & Zhang, D. E. Interferon-stimulated gene 15 and the protein ISGylation system. *J. Interferon Cytokine Res.* **31,** 119–130 (2011).
5. Bogunovic, D. *et al.* Mycobacterial disease and impaired IFN-γ immunity in humans with inherited ISG15 deficiency. *Science* **337,** 1684–1688 (2012).

©2015 Macmillan Publishers Limited. All rights reserved

6. Baechler, E. C. *et al.* Interferon-inducible gene expression signature in peripheral blood cells of patients with severe lupus. *Proc. Natl Acad. Sci. USA* **100,** 2610–2615 (2003).
7. Crow, Y. J. Aicardi–Goutières syndrome. *Handb. Clin. Neurol.* **113,** 1629–1635 (2013).
8. Crow, Y. J. & Rehwinkel, J. Aicardi–Goutières syndrome and related phenotypes: linking nucleic acid metabolism with autoimmunity. *Hum. Mol. Genet.* **18,** R130–R136 (2009).
9. Rice, G. I. *et al.* Assessment of interferon-related biomarkers in Aicardi–Goutières syndrome associated with mutations in *TREX1*, *RNASEH2A*, *RNASEH2B*, *RNASEH2C*, *SAMHD1*, and *ADAR*: a case–control study. *Lancet Neurol.* **12,** 1159–1169 (2013).
10. Malakhova, O. A. *et al.* UBP43 is a novel regulator of interferon signaling independent of its ISG15 isopeptidase activity. *EMBO J.* **25,** 2358–2367 (2006).
11. Tokarz, S. *et al.* The ISG15 isopeptidase UBP43 is regulated by proteolysis via the SCFSkp2 ubiquitin ligase. *J. Biol. Chem.* **279,** 46424–46430 (2004).
12. Kendall, B. & Cavanagh, N. Intracranial calcification in paediatric computed tomography. *Neuroradiology* **28,** 324–330 (1986).
13. Livingston, J. H., Stivaros, S., van der Knaap, M. S. & Crow, Y. J. Recognizable phenotypes associated with intracranial calcification. *Dev. Med. Child Neurol.* **55,** 46–57 (2013).
14. Manyam, B. V. What is and what is not 'Fahr's disease'. *Parkinsonism Relat. Disord.* **11,** 73–80 (2005).
15. Wang, C. *et al.* Mutations in *SLC20A2* link familial idiopathic basal ganglia calcification with phosphate homeostasis. *Nature Genet.* **44,** 254–256 (2012).
16. Keller, A. *et al.* Mutations in the gene encoding PDGF-B cause brain calcifications in humans and mice. *Nature Genet.* **45,** 1077–1082 (2013).
17. Nicolas, G. *et al.* Mutation of the PDGFRB gene as a cause of idiopathic basal ganglia calcification. *Neurology* **80,** 181–187 (2013).
18. Briggs, T. A. *et al.* Tartrate-resistant acid phosphatase deficiency causes a bone dysplasia with autoimmunity and a type I interferon expression signature. *Nature Genet.* **43,** 127–131 (2011).
19. Casanova, J. L. & Abel, L. Genetic dissection of immunity to mycobacteria: the human model. *Annu. Rev. Immunol.* **20,** 581–620 (2002).
20. Casanova, J. L. & Abel, L. The genetic theory of infectious diseases: a brief history and selected illustrations. *Annu. Rev. Genomics Hum. Genet.* **14,** 215–243 (2013).
21. Bogunovic, D., Boisson-Dupuis, S. & Casanova, J. L. ISG15: leading a double life as a secreted molecule. *Exp. Mol. Med.* **45,** e18 (2013).
22. Bennett, L. *et al.* Interferon and granulopoiesis signatures in systemic lupus erythematosus blood. *J. Exp. Med.* **197,** 711–723 (2003).
23. Raymond, A. A., Zariah, A. A., Samad, S. A., Chin, C. N. & Kong, N. C. Brain calcification in patients with cerebral lupus. *Lupus* **5,** 123–128 (1996).
24. Durfee, L. A., Lyon, N., Seo, K. & Huibregtse, J. M. The ISG15 conjugation system broadly targets newly synthesized proteins: implications for the antiviral function of ISG15. *Mol. Cell* **38,** 722–732 (2010).
25. Broering, R. *et al.* The interferon stimulated gene 15 functions as a proviral factor for the hepatitis C virus and as a regulator of the IFN response. *Gut* **59,** 1111–1119 (2010).
26. Chua, P. K. *et al.* Modulation of alpha interferon anti-hepatitis C virus activity by ISG15. *J. Gen. Virol.* **90,** 2929–2939 (2009).
27. François-Newton, V. *et al.* USP18-based negative feedback control is induced by type I and type III interferons and specifically inactivates interferon α response. *PLoS ONE* **6,** e22200 (2011).
28. Francois-Newton, V., Livingstone, M., Payelle-Brogard, B., Uze, G. & Pellegrini, S. USP18 establishes the transcriptional and anti-proliferative interferon α/β differential. *Biochem. J.* **446,** 509–516 (2012).
29. Frescas, D. & Pagano, M. Deregulated proteolysis by the F-box proteins SKP2 and β-TrCP: tipping the scales of cancer. *Nature Rev. Cancer* **8,** 438–449 (2008).
30. Hertzog, P. J. & Williams, B. R. Fine tuning type I interferon responses. *Cytokine Growth Factor Rev.* **24,** 217–225 (2013).

Supplementary Information is available in the online version of the paper.

Acknowledgements The Laboratory of Human Genetics of Infectious Diseases is supported by grants from the French National Agency for Research (ANR), the EU grant HOMITB (HEALTH-F32008-200732), the St Giles Foundation, the National Center for Research Resources and the National Center for Advancing Sciences (NCATS), National Institutes of Health grant number 8UL1TR000043, the Rockefeller University, the National Institute of Allergy and Infectious Diseases grant number R37AI095983, Institut Merieux research grant and the Empire State Stem Cell fund through NYSDOH Contract #C023046 to Flow Cytometry Research Core at the Rockefeller University. The Cytokine Signaling Unit is supported by the Institut Pasteur, CNRS and INSERM. S.P. and G.U. received funding from the EU Seventh Framework Programme under grant agreement 223608. V.F.-N. was supported by the Ligue contre le Cancer. L.R. is a Human Frontier Science Program long-term fellow. L.D.N. was supported by the National Institute of Allergy and Infectious Diseases grant number 1PO1AI076210-01A1. Y.J.C. thanks the Manchester Biomedical Research Centre and the Greater Manchester Comprehensive Local Research Network, the European Union's Seventh Framework Programme (FP7/2007-2013) under grant agreement 241779, and the European Research Council (GA 309449). A.G.-S. acknowledges NIAID grants U19AI083025 and P01AI090935 for support. We thank C. Daussy for technical assistance, E. Bianchi and F. Michel for discussions. We thank D. Zhang and the members of the Zhang laboratory for assistance, advice and discussions. This work was supported by Chinese National Natural Science Foundation grants (81000079, 81170165) to X.Z. D.B. is supported by the National Institute of Allergy and Infectious Diseases grant number R00AI106942-02.

Author Contributions D.B., X.Z., B.P.-B., V.F.-N., O.S., D.M., P.G., A.G.-S., L.A., P.L., L.D.N., S.B.-D., Y.J.C., J.-L.C. and S.P. wrote the manuscript. D.B., X.Z., B.P.-B., V.F.-N., S.D.S., C.Y., S.V., Z.L., I.T., G.I.R., C.C., N.M., S.A.M., Y.I., B.B., S.O., L.Z., X.W., H.J., W.L., T.H., D.L., T.M., B.W., D.Y., L.R., G.U., P.G., F.R., S.-Y.Z., E.J., J.B., A.G.-S., L.A., P.L., L.D.N., S.B.-D., Y.J.C., J.-L.C. and S.P. designed and/or performed experiments. M.L., J.-Y.L., Q.K.W., O.S., D.M., N.M., I.T. and S.A.M. took clinical care of the patients and provided advice.

Author Information Microarray data have been deposited in the Gene Expression Omnibus under accession number GSE60359; WES data have been deposited in the BioProject database under accession number PRJNA167660. Reprints and permissions information is available at www.nature.com/reprints. The authors declare no competing financial interests. Readers are welcome to comment on the online version of the paper. Correspondence and requests for materials should be addressed to D.B. (Dusan.Bogunovic@mssm.edu).

©2015 Macmillan Publishers Limited. All rights reserved

METHODS

Exome capture, sequencing, alignments and variant calling. Exome sequencing was performed on two affected sisters and their unaffected mother. Libraries were prepared following the kit manufacturer's protocol. In brief, we randomly fragmented 3 μg of purified genomic DNA with an ultrasonoscope (Covaris, Massachusetts, USA) to produce fragments of 150~200 base pairs (bp) in length. The shotgun library was then subjected to hybridization with the Agilent SureSelect Human All Exon 50Mb kit (Agilent Technologies, California, USA) for exome capture, followed by several cycles of amplification before quality control with a 2100 Bioanalyzer (Agilent Technologies) and quantification by RT–qPCR with the StepOnePlus Real-Time PCR System (Life Technologies, California, USA). The final library was sequenced on an Illumina Hiseq2000 (Illumina, California, USA) with 90-bp paired-end reads, following the Hiseq2000 protocol. We used BWA Aligner to align the sequences with the human genome reference sequence (hg18 build). Downstream processing was carried out with the Genome analysis toolkit (GATK) SAMtools and Picard Tools (http://picard.sourceforge.net). Substitution calls were made with a GATK Unified Genotyper, whereas insertion/deletion (indel) calls were made with a GATK Indel GenotyperV2. All calls with a read coverage ≤2× and a Phred-scaled SNP quality ≤20 were filtered out. All the variants were annotated with the GATK Genomic Annotator. For filtering purposes, we used the 1000 Genomes and EVS databases, and an in-house exome database containing data for over 1,000 individuals. For the comparative analysis of P1, P2, P5 and P6, we removed variants with less than six reads and a mapping quality of less than 40 (per GATK), and we used the dbSNP database in addition to the 1000 Genomes and EVS databases.

qPCR and microarray analysis. We assessed the expression of six known interferon-stimulated genes in whole blood. Total RNA was extracted from whole blood with the PAXgene (PreAnalytix) RNA isolation kit. RNA concentration was assessed with a spectrophotometer (FLUOstar Omega, Labtech). Quantitative reverse transcription PCR analysis was performed with the *Taq*Man Universal PCR Master Mix (Applied Biosystems) and cDNA derived from 40 ng of total RNA. The relative abundance of target transcripts, measured with *Taq*Man probes for *IFI27* (Hs01086370_m1), *IFI44L* (Hs00199115_m1), *IFIT1* (Hs00356631_g1), *ISG15* (Hs00192713_m1), *RSAD2* (Hs01057264_m1), and *SIGLEC1* (Hs00988063_m1), was normalized with respect to the expression of *HPRT1* (Hs03929096_g1) and *18S* (Hs999999001_s1) and assessed with Applied Biosystems StepOne Software v2.1 and Applied Biosystems Data Assist Software v3.01. Data for the patients are expressed relative to mean values for 23 normal controls. For PBMCs, total RNA was extracted with the RNeasy Mini kit (Qiagen). It was not possible to standardize the amount of RNA added to the cDNA synthesis reaction, but expression was nonetheless normalized with respect to the level of expression of *HPRT1* (Hs03929096_g1) and *18S* (Hs999999001_s1). For PBMCs and hTert fibroblasts, total RNA was extracted with the RNeasy Mini kit (Qiagen) and the standard protocol for hybridization to Affymetrix HTA 2.0 chips was performed. In microarray experiments, we used 1,000 IU ml^{-1} IFN-α2b as a stimulus. Affymetrix Expression Console and Transcriptome Analysis Console were used for analysis. Upregulation or downregulation was defined as significant if expression was twofold higher or lower for P1, P2 and P3 IFN-α2b-stimulated cells than for C1, C6 and C18 IFN-α2b-stimulated cells.

Cell lines and reagents. Human fibrosarcoma HLLR1-1.4 cells, which have been described elsewhere[25], were cultured in Dulbecco's modified Eagle's medium (DMEM) (Gibco) supplemented with 10% fetal calf serum, hypoxanthine, thymidine and aminopterin (HAT) and 400 μg ml^{-1} G418 (Gibco). WISH amnion-derived epithelial cells, HEK293T cells, SV40-transformed and hTert-immortalized fibroblasts from controls and patients were cultured in DMEM supplemented with 10% fetal calf serum. EBV-transformed B cells from patient P1 and controls were cultured in RPMI medium supplemented with 10% fetal calf serum. Recombinant IFN-α2b was a gift from D. Gewert (Wellcome Foundation, Beckenham, Kent, UK; now at BioLauncher Ltd, Cambridge, UK) or was purchased from Schering; IFN-β was obtained from Biogen Idec, Cambridge, MA, USA. IFNs were purified to specific activities of $>10^8$ units per mg of protein. Cycloheximide (CHX) (Sigma) was used at a concentration of 20 μg ml^{-1}.

Plasmids and transfection. HEK293T cells were transiently transfected with the FuGENE6 system (Roche Applied Science). The pMET7-USP18 expression vector has been described elsewhere[27]; pcDNA3+His_6-3xFlagISG15 (Fig. 4d, e and Extended Data Fig. 4d) was provided by J. M. Huibregtse (University of Texas at Austin, TX, USA), pBabe-3xFlag6His-ISG15 (BUG3354) and pBabe-3xFlag6His-ISG15(ΔGG) (BUG3355) (Fig.4c and Extended Data Fig. 4e) were derived from this plasmid; pcDNA3 Flag–SKP2 and HA–ubiquitin constructs were obtained from E. Bianchi (Institut Pasteur, Paris, France). In co-transfection experiments, empty vector was added to keep the total amount of DNA constant.

siRNA-mediated silencing. *USP18, UBE1L, UbcH8, HERC5, SKP2* ON-TARGETplus SMART pools and a control siRNA (ON-TARGETplus non-targeting pool) were obtained from Dharmacon. Three individual *ISG15*-targeting siRNAs from Sigma were tested: *ISG15#9*, GGACAAAUGCGACGAACCU; *ISG15#11*, GCAGAUCA CCCAGAAGAUU; *ISG15#12*, GCAACGAAUUCCAGGUGUC. All efficiently targeted *ISG15* transcripts. In all the experiments shown, *ISG15#12* was used. Cells were transfected with 25 nM siRNA for 24 h in the presence of the Lipofectamine RNAi max reagent (Invitrogen), according to the manufacturer's instructions. Cells were then stimulated with IFN.

Protein analyses. Cells were lysed in modified RIPA buffer (50 mM Tris/HCl pH 8, 200 mM NaCl, 1% Nonidet P40, 0.5% deoxycholate, 0.05% SDS, 2 mM EDTA), 1 mM orthovanadate and a protease inhibitor cocktail and subjected to western blotting. For co-immunoprecipitation, cells were lysed in 50 mM Tris, pH 6.8, 0.5% Nonidet P40, 200 mM NaCl, 10% glycerol, 1 mM EDTA and a protease inhibitor cocktail. For the analysis of USP18 ubiquitination (Fig. 4d and Extended Data Fig. 4d and 4e), cells were lysed in modified RIPA buffer and a protease inhibitor cocktail, and USP18 was immunoprecipitated from post-nuclear lysates for 2 h at 4 °C. It was then subjected to protein A capture and western blotting. The antibodies used were directed against STAT1 and STAT2 (Millipore), phospho-Tyr 701 STAT1 (Cell Signaling Technology), phospho-Tyr 689 STAT2 (Millipore), USP18 and AKT (Cell Signaling Technology), actin (Sigma), p27 (Santa Cruz Biotechnology), SKP2 (Invitrogen), HA (Santa Cruz Biotechnology), ISG15 (a gift from E. C. Borden, Cleveland Clinic, Cleveland, OH, USA or purchased from ABGENT, no. AP1150a), IFIT1 (a gift from G. Sen, Cleveland Clinic, Cleveland, OH, USA), OAS2 p69 (a gift from A. Hovanessian, Université Paris-Descartes, Paris, France), MxA (a gift from O. Haller, University of Freiburg, Freiburg, Germany) and ubiquitin (clone FK2 recognizing mono- and poly-ubiquitinated proteins, Enzo Life Sciences). An enhanced chemiluminescence detection reagent was used for detection (Western Lightning, Perkin Elmer). Relative band intensities were measured with a Fuji ImageQuant LAS-4000.

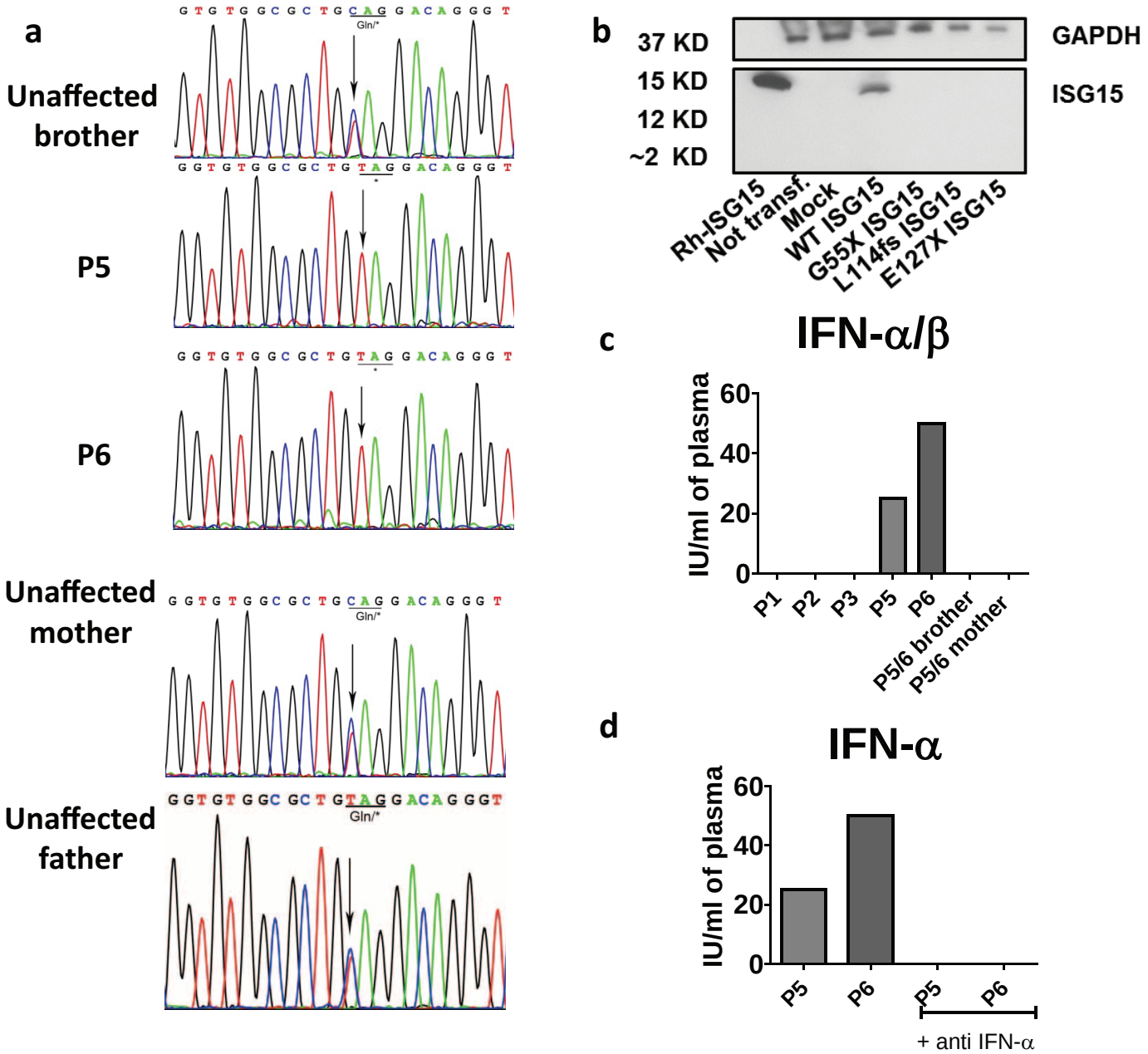
Statistics. For larger samples there is a normal distribution, while for smaller samples (for example, $n = 2$) a distribution cannot be established. For larger samples there is a normal variance, while for smaller samples (for example, $n = 2$) variance cannot be established. Statistical methods used were defined in the legends of the figures where appropriate.

Autoantibody detection. Screening for a broad panel of IgG and IgA autoantibodies was performed with autoantibody arrays (University of Texas Southwestern Medical Center, Genomic and Microarray Core Facility), as previously described[31]. In brief, diluted serum samples were incubated in duplicate with the autoantigen array and the autoantibodies binding to the antigens were detected with Cy3 and Cy5 fluorescent labelled anti-Ig antibodies (IgG and IgA), by the generation of TIFF images. Genepix Pro 6.0 software was used to analyse the images. Net fluorescence intensities (defined as fluorescence intensity for the spot minus background fluorescence intensity) for duplicate spots were averaged. The signal-to-noise ratio (SNR) was used as a quantitative measurement of the ability to resolve true signal from background noise and SNR values of at least 3 were considered to differentiate a true signal from background noise.

Data were normalized as follows: immunoglobulin positive control (IgG or IgA) values across all samples were averaged and the positive control value for each sample was divided by the mean positive control value to generate a normalization factor for each sample. Each signal was then multiplied by the normalization factor for each block (sample).

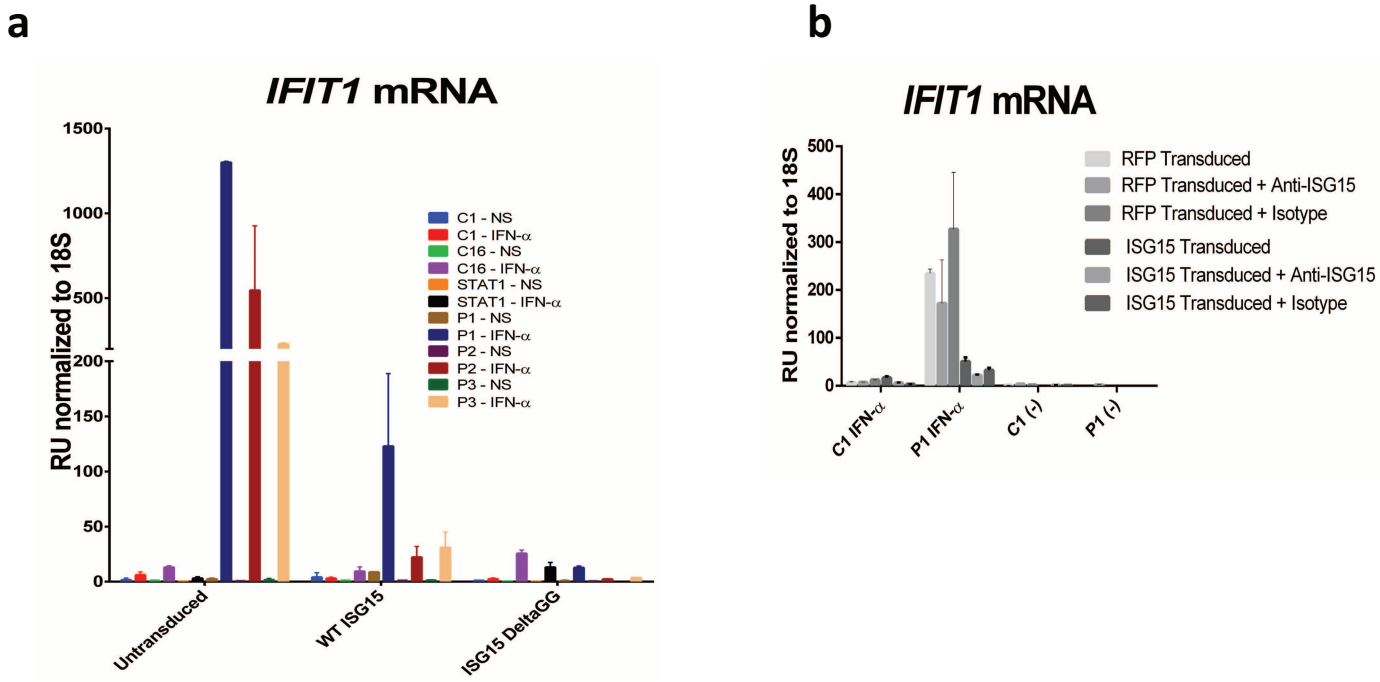
31. Li, Q. Z. *et al.* Protein array autoantibody profiles for insights into systemic lupus erythematosus and incomplete lupus syndromes. *Clin. Exp. Immunol.* **147,** 60–70 (2007).

©2015 Macmillan Publishers Limited. All rights reserved



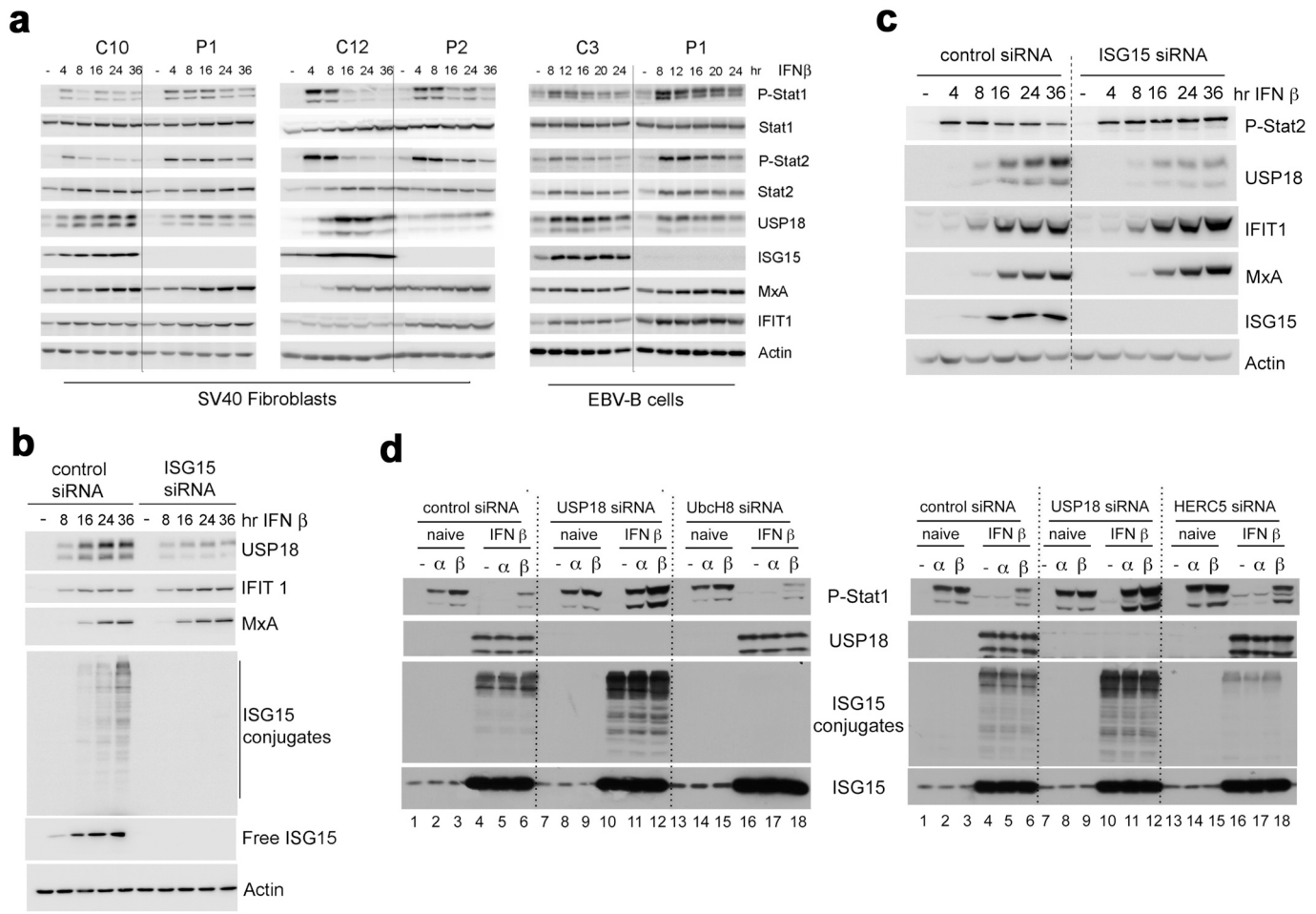
Extended Data Figure 1 | Mutations in ISG15-deficient individuals, allele characterization and serum IFN-α concentrations. a, Sanger sequencing of *ISG15* exon 2 from genomic DNA in kindred C, with the variants highlighted. **b**, The wild type (WT) and three mutant alleles (G55X, L114fs, E127X- ISG15) were inserted into an expression vector and used to transfect HEK293T cells. Other HEK293T cells were mock-transfected (mock) or left untransfected (not transf.). The cell lysates isolated were subjected to western blotting, with recombinant human (Rh)-ISG15 used as a control. **c**, **d**, Plasma samples from P1, P2, P3, P5, P6 and the mother and brother of P5/6 were used in cytopathic protection assays, to measure antiviral activity (**c**) and blocking antibodies against IFN-α were used to assess specificity (**d**) (experiment was performed one time).

©2015 Macmillan Publishers Limited. All rights reserved



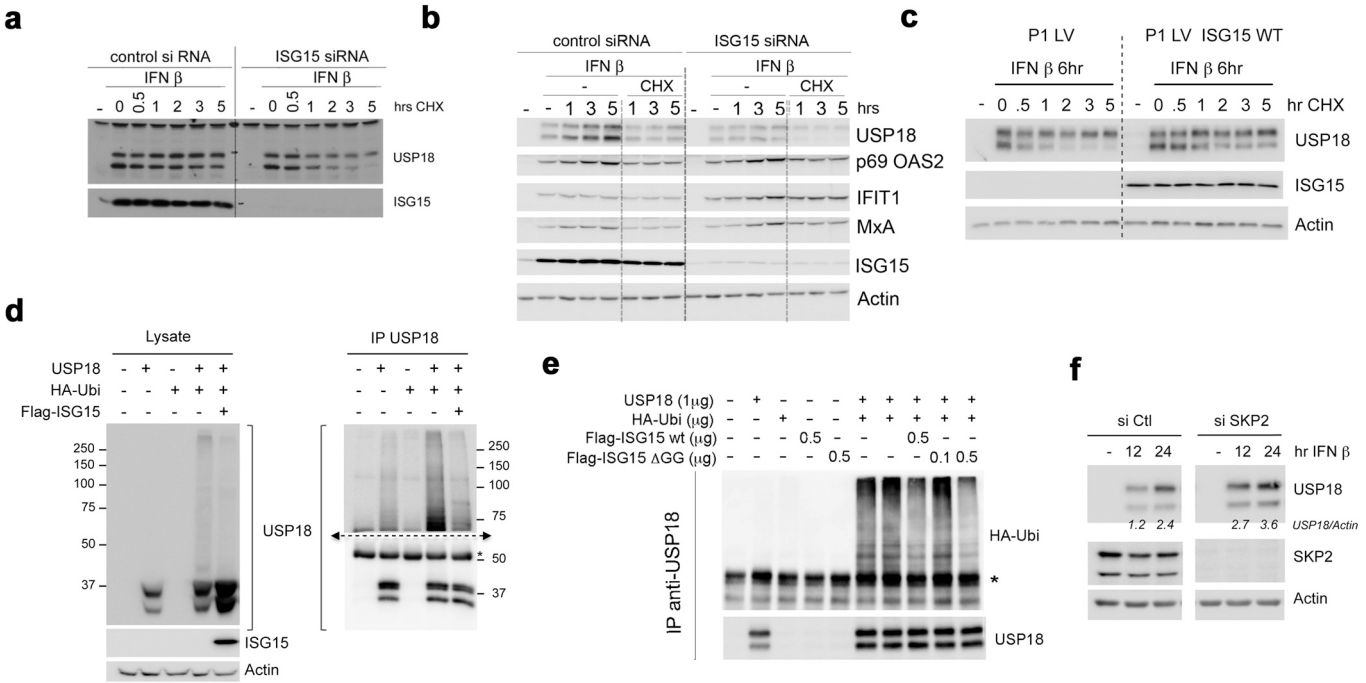
Extended Data Figure 2 | A form of ISG15 that cannot be conjugated rescues the phenotype of ISG15-deficient cells. **a**, Lentiviral particles containing luciferase, wild-type (WT) *ISG15-RFP* or *ISG15(ΔGG)-RFP* genes were used to transduce hTert-immortalized fibroblasts from C1, a STAT1$^{-/-}$ subject, P1, P2 and P3. RFP-positive cells were obtained by sorting and were cultured for a few weeks. The cells were then treated with 1,000 IU of IFN-α2b for 12 h, washed with PBS and left to rest for 36 h, after which relative mRNA levels for *IFIT1* were determined. **b**, The experimental setting described in **a** was used in the presence or absence of vehicle control, anti-ISG15 antibodies or control IgG for luciferase and wild-type ISG15–RFP-transduced C1 and P1 hTert-immortalized fibroblasts (showing representative experiments with technical replicates and s.e.m., out of 3 performed).

©2015 Macmillan Publishers Limited. All rights reserved



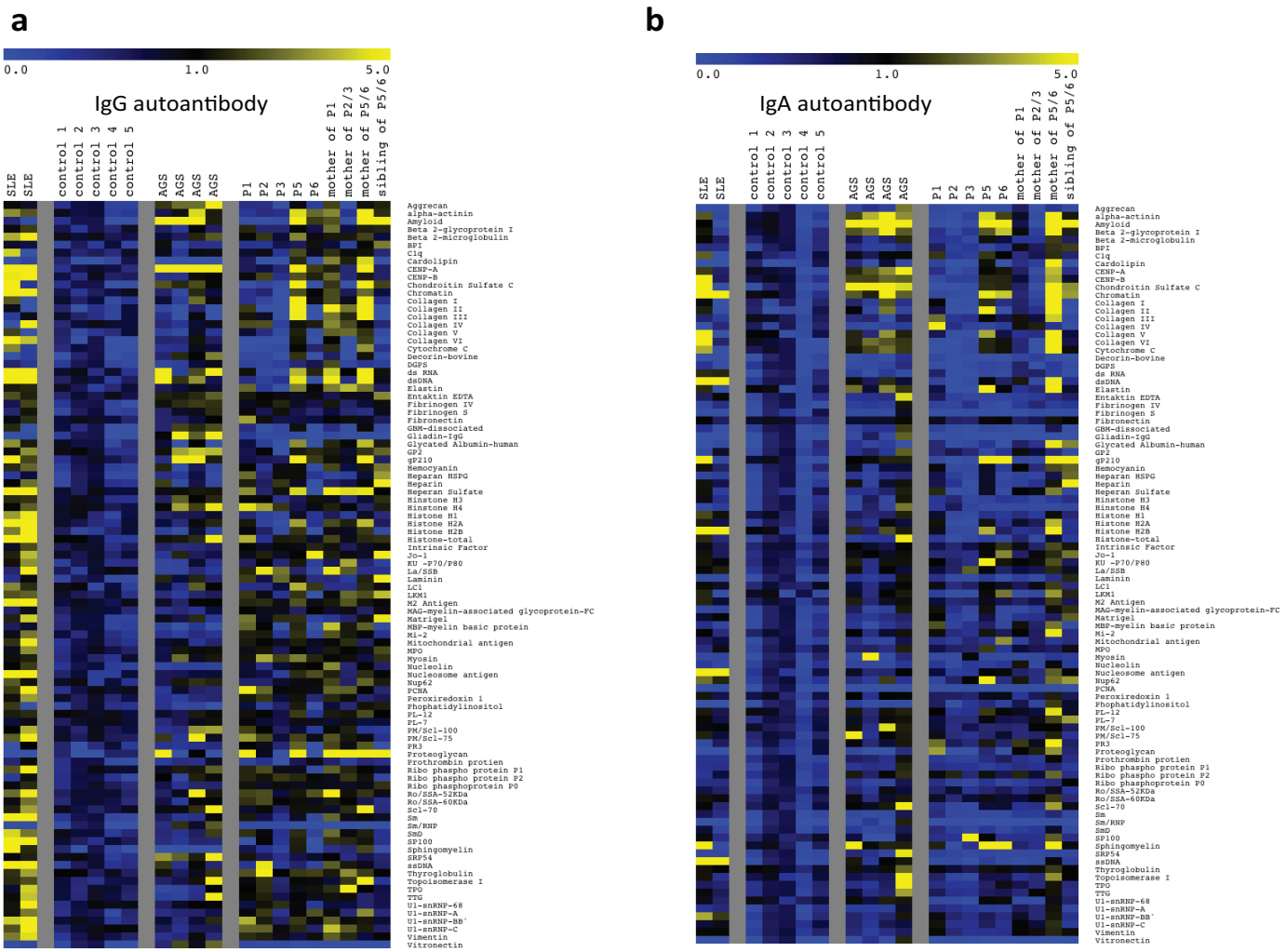
Extended Data Figure 3 | Prolonged IFN signalling, low USP18, and high interferon-stimulated-gene-encoded protein levels in patient-derived cells and in ISG15-silenced human fibrosarcoma HLLR1-1.4 cells. **a**, Left panels, SV40-immortalized fibroblasts from two controls (C10 and C12) and two ISG15-deficient patients (P1 and P2) were stimulated with IFN-β (500 pM) for 4 to 36 h. Cell lysates (30 μg) were analysed with the indicated antibodies. Right, EBV-transformed B cells from control (C3) and patient P1 were stimulated with IFN-β for 8 to 24 h. Cell lysates (30 μg) were analysed with the indicated antibodies. **b**, HLLR1-1.4 cells were transfected with control siRNA or *ISG15* siRNA. One day post-transfection, IFN-β (500 pM) was added for various amounts of time. Cell lysates (30 μg) were analysed with the indicated antibodies (MxA and MX1 are used synonymously). **c**, WISH cells were stimulated and lysates analysed as described in **b**. **d**, HLLR1-1.4 cells were transfected with control siRNA, *USP18* siRNA and *UbcH8* (also known as *UBE2E2*) siRNA (left) or control siRNA, *USP18* siRNA and *HERC5* siRNA (right). One day post-transfection, cells were left untreated (naive) or were primed for 8 h with IFN-β (500 pM). Cells were washed and left to rest for 16 h before being pulsed for 30 min with 100 pM IFN-α2 or IFN-β. Cell lysates (30 μg) were analysed with the indicated antibodies.

©2015 Macmillan Publishers Limited. All rights reserved



Extended Data Figure 4 | ISG15 controls the stability of the USP18 protein, but not of other interferon-stimulated-gene products. **a**, HLLR1-1.4 cells were transfected with either control siRNA or *ISG15* siRNA. One day post-transfection, cells were stimulated with IFN-β (500 pM) for 6 h. Cycloheximide (CHX, 20 μg ml^{-1}) was then added for various time periods, from 30 min to 5 h. Cell lysates (30 μg) were analysed with the indicated antibodies. **b**, As in **a**, with additional controls, cells treated with IFN only. Several interferon-stimulated genes were analysed. **c**, hTert-immortalized fibroblasts from patient P1 transduced with lentiviral particles expressing RFP and luciferase and wild-type ISG15 (LV ISG15 WT) were stimulated with IFN-β (500 pM) for 6 h. CHX was then added for the indicated times. Cell lysates (15 μg) were analysed by western blotting. **d**, HEK293T cells were transfected with USP18, HA–ubiquitin and Flag–ISG15 as indicated. Two days later, cells were lysed in modified RIPA buffer, USP18 was immunoprecipitated (IP) and analysed with anti-USP18 antibodies. Left panels, cell lysates (30 μg) were analysed by western blot with the indicated antibodies. Right panels, the immunoprecipitates were gel separated and transferred onto a membrane. The membrane was cut into two parts above the 50 kDa marker, both of which were blotted with anti-USP18 antibodies. The top part was exposed for 2 min, the bottom part for 20 s. Asterisk indicates IgG heavy chain. **e**, HEK293T cells were transfected with 1 μg of the USP18 construct alone or with 1 μg of HA–ubiquitin, in the presence or absence of Flag-tagged ISG15, either wild type or a mutant form of ISG15 that cannot be conjugated as it lacks the two carboxy-terminal glycine residues (Flag–ISG15(ΔGG)). Two days later, cells were lysed in modified RIPA buffer, USP18 was immunoprecipitated and analysed with anti-HA or anti-USP18 antibodies. Asterisk indicates IgG heavy chain. **f**, hTert-immortalized fibroblasts from patient P3 were transfected with control siRNA or *SKP2* siRNA. We added IFN-β (500 pM) 24 h later and the cells were incubated for the indicated times. Cell lysates were analysed with the indicated antibodies and USP18 levels were determined as a function of actin levels.

©2015 Macmillan Publishers Limited. All rights reserved



Extended Data Figure 5 | Autoantibody development in ISG15-deficient individuals. a, b, Serum samples from ISG15-deficient, SLE and AGS patients were evaluated for the presence of IgG and IgA autoantibodies in a blinded experiment. Values for the negative control samples for each antigen were averaged and ratios of each sample to the mean for the negative controls plus 2 standard deviations were calculated, with values greater than 1 considered positive. A heat map of the ratio values was generated with MultiExperiment Viewer software (MeV, DFCI Boston, MA), with values coded as follows: 0, blue; 1, black; 5, yellow.

©2015 Macmillan Publishers Limited. All rights reserved

Extended Data Table 1 | Patients have normal titres of antibodies against many viral antigens

Antibody responses

	HAV	EBV	Measles	VZV	CMV	HSV-1, HSV-2	Mumps	Influenza A
Reference value	(<49%)	α-VCA IgG	(<70)	(mUI/ml <150)	(<0.6) IgG	(<1.1)	(<50)	(<30)
P1	NO	YES	NO	YES	YES	YES	N/A	YES
P2	N/A	YES	NO	NO	YES	NO	NO	YES
P3	YES	YES	NO	YES	YES	YES	YES	YES
P5	NO	NO	NO	NO	YES	NO	NO	NO
P6	NO	NO	YES	NO	YES	YES	NO	YES

YES= antibodies present
NO= antibodies not present
N/A= not done

Serum samples from patients and, when available, immediate family members, were tested for the presence of antibodies against hepatitis A virus (HAV), EBV, measles, varicella zoster virus (VZV), cytomegalovirus (CMV), herpes simplex viruses 1 and 2 (HSV-1 and HSV-2), mumps and influenza A viruses. NA, not available; YES, antibodies present; NO, antibodies not present. α-VCA IgG denotes anti EBV capsid antibodies.

©2015 Macmillan Publishers Limited. All rights reserved

Extended Data Table 2 | Whole-exome sequencing results for patients with putative IBGC

		Whole Exome		
		P5	P6	P5/6 Mother
Nonsense (stop-gained)	Total	177	168	174
	Novel homozygous	1*	2*	0
	Novel heterozygous	7	5	5
Readthrough (stop-lost)	Total	78	77	74
	Novel homozygous	0	0	0
	Novel heterozygous	1	1	1
Missense	Total	11104	10967	11352
	Novel homozygous	8	17	9
	Novel heterozygous	210	204	234
Silent	Total	9848	9721	10065
	Novel homozygous	6	9	1
	Novel heterozygous	97	92	99
Frameshift	Total	178	168	178
	Novel homozygous	0	0	0
	Novel heterozygous	4	3	4
Inframe	Total	163	156	153
	Novel homozygous	2	2	0
	Novel heterozygous	3	1	2
UTR	Total	8508	8331	10131
	Novel homozygous	15	22	29
	Novel heterozygous	117	127	137
Splice	Total	3071	3067	3181
	Novel homozygous	6	5	1
	Novel heterozygous	41	42	39
ncRNA	Total	345	319	356
	Novel homozygous	1	1	0
	Novel heterozygous	3	4	3

Genomic DNA from the patients was used for massively parallel sequencing and the analysis (described in Methods) yielded the variants reported above. Asterisks denotes coding mutations reported in the main text. ncRNA, non-coding RNA; UTR, untranslated region.

©2015 Macmillan Publishers Limited. All rights reserved

Extended Data Table 3 | Homozygous variants of genes other than *ISG15* present in P1, P2, P5 and P6

P1	P2	P5	P6
SRP19	C1orf101	AIF1	APOBEC4
	GAB4	ALS2CR11	C19orf55
	MLL3	C19orf55	DEFB136
	PIK3CB	HLA-DRB5	KAZN
	THUMPD2	LILRA3	KDM4B
	ZC4H2	LST1	LRRFIP2
		MUC16	MGAM
		PRDX2	MUC16
		ZC3H12B	PADI4
			PLEKHN1
			PLXNB3
			PRDX2
			SMCR7
			TAS1R2
			TAS2R60
			TIAM2

Homozygous nonsense and missense variations from the four patients that were not present in the 1000 Genomes, EVS or dbSNP databases.

©2015 Macmillan Publishers Limited. All rights reserved

Extended Data Table 4 | ISG15-deficient hTert fibroblasts have enhanced responses to IFN-α

No.	Fold Change	ANOVA p-value	FDR p-value	Gene Symbol	Description	Group
1	25.05	0.04796	0.788081	COLEC12	collectin sub-family member 12	Coding
2	11.72	0.000829	0.570142	---	ensembl_havana_lincrna:lincRNA c	Coding
3	8.97	0.025411	0.765877	---	accn=AK093732 class=mRNAlike lnc	NonCoding
4	7.73	0.025123	0.765877	---	accn=AK057151 class=mRNAlike lnc	NonCoding
5	6.95	0.044472	0.781343	HTRA3	HtrA serine peptidase 3	Coding
6	6.88	0.005831	0.665451	---	accn=DQ470079 class=mRNAlike lnc	NonCoding
7	6.66	0.000225	0.523843	SNORD114-	small nucleolar RNA, C/D box 114-2	Coding
8	6.59	0.020343	0.758127	RSAD2	radical S-adenosyl methionine dom	Coding
9	6.42	0.015871	0.757325	---	accn=AF026942 class=mRNAlike lnc	NonCoding
10	6.16	0.047461	0.786588	---	linc-WDR7-7 chr18:+:52559874-5256	NonCoding
11	6.13	0.008562	0.68638	IFI27	interferon, alpha-inducible protein	Coding
12	5.78	0.00754	0.682518	---	accn=AJ294851 class=mRNAlike lncf	NonCoding
13	5.52	0.000091	0.435886	---	accn=NR_030672 class=lncRNA nam	NonCoding
14	5.08	0.016151	0.757325	---	Positive Housekeeping Controls - P	Other
15	5.06	0.021768	0.758383	---	accn=NULL class=lncRNA name= ref	NonCoding
16	4.9	0.017117	0.758127	OAS3	2'-5'-oligoadenylate synthetase 3, 1	Coding
17	4.71	0.004252	0.650281	IFI44	interferon-induced protein 44	Coding
18	4.66	0.00854	0.68638	---	accn=AJ303364 class=mRNAlike lncf	NonCoding
19	4.58	0.018461	0.758127	OAS1	2'-5'-oligoadenylate synthetase 1, 4	Coding
20	4.52	0.005169	0.650281	TLR3	toll-like receptor 3	Coding
21	4.52	0.002347	0.641309	OASL	2'-5'-oligoadenylate synthetase-lik	Coding
22	4.38	0.033644	0.775063	ZNF608	zinc finger protein 608	Coding
23	4.23	0.018847	0.758127	---	linc-CBR1-1 chr21:+:37377635-37379	NonCoding
24	4.16	0.007073	0.67996	---	accn=NR_037687 class=lncRNA nam	NonCoding
25	4.01	0.000633	0.570142	---	accn=NULL class=lincRNA name=Hu	NonCoding
26	3.95	0.041228	0.775063	NDNF	neuron-derived neurotrophic facto	Coding
27	3.82	0.018711	0.758127	SLCO2A1	solute carrier organic anion transpc	Coding
28	3.82	0.010603	0.72494	NOVA1	neuro-oncological ventral antigen 1	Coding
29	3.7	0.035475	0.775063	HERC6	HECT and RLD domain containing E3	Coding
30	3.51	0.029036	0.772054	NRN1	neuritin 1	Coding
31	3.46	0.015614	0.757325	---	havana:lincRNA chromosome:GRCh	Coding
32	3.46	0.022994	0.759536	MX1	myxovirus (influenza virus) resistar	Coding
33	3.41	0.022783	0.758383	EPB41L3	erythrocyte membrane protein bar	Coding
34	3.4	0.014995	0.754201	DHX58	DEXH (Asp-Glu-X-His) box polypept	Coding
35	3.39	0.01101	0.729998	PLXNC1	plexin C1	Coding
36	3.39	0.014229	0.743786	GDF5	growth differentiation factor 5	Coding
37	3.37	0.008001	0.684489	DCLK1	doublecortin-like kinase 1	Coding
38	3.16	0.012124	0.738151	MX2	myxovirus (influenza virus) resistar	Coding
39	3.14	0.027568	0.765877	---	accn=DQ914956 class=mRNAlike lnc	NonCoding
40	3.12	0.012473	0.739668	USP18	ubiquitin specific peptidase 18	Coding
41	3.08	0.018572	0.758127	DDX58	DEAD (Asp-Glu-Ala-Asp) box polype	Coding
42	3.06	0.03665	0.775063	IFI35	interferon-induced protein 35	Coding
43	3.04	0.045433	0.783121	IL1R1	interleukin 1 receptor, type I	Coding
44	2.99	0.016966	0.758127	USP41	ubiquitin specific peptidase 41	Coding
45	2.98	0.03053	0.775063	LRRC32	leucine rich repeat containing 32	Coding
46	2.77	0.015518	0.756307	DDX60L	DEAD (Asp-Glu-Ala-Asp) box polype	Coding
47	2.7	0.027738	0.765877	---	linc-COL1A2-2 chr7:+:93652144-9369	NonCoding
48	2.67	0.018424	0.758127	---	accn=AL049990 class=mRNAlike lncl	NonCoding
49	2.67	0.000091	0.435886	KIAA1324L	KIAA1324-like	Coding
50	2.66	0.011206	0.731959	KCNA4	potassium voltage-gated channel, s	Coding
51	2.59	0.0137	0.741338	IFIT1	interferon-induced protein with te	Coding
52	2.56	0.007034	0.67996	SAMHD1	SAM domain and HD domain 1	Coding
53	2.53	0.045909	0.783121	SNED1	sushi, nidogen and EGF-like domair	Coding
54	2.5	0.0122	0.738151	---	accn=AK311114 class=mRNAlike lnc	NonCoding
55	2.43	0.033812	0.775063	---	havana:lincRNA chromosome:GRCh	Coding
56	2.43	0.020752	0.758127	SECTM1	secreted and transmembrane 1	Coding
57	2.39	0.042614	0.7768	PARP12	poly (ADP-ribose) polymerase fami	Coding
58	2.36	0.006938	0.67996	---	accn=NULL class=lncRNA name= ref	NonCoding
59	2.34	0.031174	0.775063	---	M35980,uc011gjx.2	Coding
60	2.33	0.001283	0.613989	---	DQ593902,uc021tyq.1	Coding
61	2.32	0.022003	0.758383	KCNJ15	potassium inwardly-rectifying chan	Coding
62	2.26	0.006149	0.674842	---	Negative Housekeeping Controls - I	Other
63	2.25	0.022299	0.758383	PPL	periplakin	Coding
64	2.23	0.030911	0.775063	SELENBP1	selenium binding protein 1	Coding
65	2.23	0.045121	0.783042	KIT	v-kit Hardy-Zuckerman 4 feline sarc	Coding
66	2.23	0.033234	0.775063	CPE	carboxypeptidase E	Coding
67	2.22	0.016735	0.758127	SP110	SP110 nuclear body protein	Coding
68	2.2	0.004368	0.650281	RFX8	regulatory factor X, 8	Coding
69	2.14	0.045843	0.783121	HLA-DRB1	major histocompatibility complex,	Coding
70	2.13	0.042907	0.7768	---	ncrna:snoRNA chromosome:GRCh3	Coding
71	2.08	0.027865	0.765877	PITPNC1	phosphatidylinositol transfer prote	Coding
72	2.06	0.011247	0.731959	RXFP1	relaxin/insulin-like family peptide	Coding
73	2.06	0.024753	0.765425	---	accn=AY665470 class=mRNAlike lncl	NonCoding
74	2.05	0.03305	0.775063	CYYR1	cysteine/tyrosine-rich 1	Coding
75	2.03	0.030124	0.775063	ARHGEF3	Rho guanine nucleotide exchange f	Coding
76	2.02	0.023303	0.759536	---	linc-CNTNAP3B-1 chr9:+:43313920-4	NonCoding
77	2.01	0.005787	0.665451	NMI	N-myc (and STAT) interactor	Coding
78	2.01	0.003072	0.644953	---	accn=NULL class=lincRNA name=Hu	NonCoding
79	-2.01	0.048814	0.791563	---	BC022047,uc003pyw.1	Coding
80	-2.01	0.003758	0.647229	ACO1	aconitase 1, soluble	Coding
81	-2.03	0.048774	0.791314	ATP10D	ATPase, class V, type 10D	Coding
82	-2.05	0.01095	0.729998	---	accn=AF086045 class=mRNAlike lncl	NonCoding
83	-2.07	0.02484	0.765425	---	accn=DQ004397 class=mRNAlike lnc	NonCoding
84	-2.08	0.000915	0.570142	---	DQ586227,uc001zzt.2	Coding
85	-2.1	0.040285	0.775063	---	accn=NULL class=lincRNA name=Hu	NonCoding
86	-2.1	0.021565	0.758383	---	Negative Housekeeping Controls - I	Other
87	-2.14	0.036392	0.775063	NTN4	netrin 4	Coding
88	-2.15	0.00482	0.650281	HOXC9	homeobox C9	Coding
89	-2.16	0.000139	0.435886	---	accn=NULL class=lincRNA name=Hu	NonCoding
90	-2.19	0.001455	0.625179	CDR1	cerebellar degeneration-related pr	Coding
91	-2.25	0.016418	0.758127	---	Negative Housekeeping Controls - I	Other
92	-2.26	0.027323	0.765877	LTBP2	latent transforming growth factor b	Coding
93	-2.27	0.019149	0.758127	---	linc-PIK3CG-3 chr7:+:106264517-106	NonCoding
94	-2.27	0.043332	0.778351	SLC38A1	solute carrier family 38, member 1	Coding
95	-2.29	0.008635	0.68638	LOC90784	uncharacterized LOC90784	Coding
96	-2.31	0.031712	0.775063	HSBP1L1	heat shock factor binding protein 1	Coding
97	-2.32	0.019638	0.758127	BAIAP2L1	BAI1-associated protein 2-like 1	Coding
98	-2.36	0.02371	0.759536	TMEM130	transmembrane protein 130	Coding
99	-2.37	0.013599	0.741338	---	accn=S77359 class=mRNAlike lncRN	NonCoding
100	-2.38	0.000814	0.570142	---	ncrna:lincRNA chromosome:GRCh3	Coding
101	-2.47	0.000151	0.435886	---	linc-EPHA6-1 chr3:+:96336028-9633	NonCoding
102	-2.5	0.024874	0.765425	SH3BGRL2	SH3 domain binding glutamic acid-r	Coding
103	-2.52	0.001499	0.625613	---	accn=NR_028343 class=lncRNA nam	NonCoding
104	-2.57	0.005854	0.665451	PPP1R3C	protein phosphatase 1, regulatory s	Coding
105	-2.61	0.041643	0.775063	---	accn=NR_024179 class=lncRNA nam	NonCoding
106	-2.67	0.003801	0.647229	ZNF415	zinc finger protein 415	Coding
107	-2.82	0.028784	0.770664	---	AK124511,uc003jyj.1	Coding
108	-2.89	0.001615	0.636575	---	accn=AK001007 class=mRNAlike lnc	NonCoding
109	-2.89	0.026776	0.765877	SLC30A4	solute carrier family 30 (zinc transp	Coding
110	-2.91	0.010608	0.72494	DCLK2	doublecortin-like kinase 2	Coding
111	-3.04	0.042969	0.7768	TGFB2	transforming growth factor, beta 2	Coding
112	-3.15	0.046017	0.783121	IGFBP7	insulin-like growth factor binding p	Coding
113	-3.2	0.020952	0.758127	PLCB4	phospholipase C, beta 4	Coding
114	-3.53	0.011009	0.729998	---	accn=NR_036614 class=lncRNA nam	NonCoding
115	-3.64	0.001799	0.641309	---	DQ583712,uc022bav.1	Coding
116	-3.74	0.040415	0.775063	---	Positive Housekeeping Controls - P	Other
117	-4.09	0.039055	0.775063	---	accn=AF540057 class=mRNAlike lncl	NonCoding
118	-4.31	0.008198	0.684489	COL4A2	collagen, type IV, alpha 2	Coding
119	-4.42	0.039009	0.775063	HOXC11	homeobox C11	Coding
120	-5.29	0.009866	0.710704	---	accn=X05562 class=mRNAlike lncRN	NonCoding
121	-5.62	0.034432	0.775063	SERPINB7	serpin peptidase inhibitor, clade B	Coding
122	-6.57	0.000376	0.551172	HOXC10	homeobox C10	Coding
123	-6.82	0.009785	0.710704	COL4A1	collagen, type IV, alpha 1	Coding
124	-14.31	0.000866	0.570142	TRHDE	thyrotropin-releasing hormone deg	Coding

We treated hTert-immortalized fibroblasts from three controls and three patients with 1,000 IU IFN-α2b for 12 h. The cells were then washed three times with PBS and left to rest for an additional 36 h, after which we isolated mRNA for microarray analysis. We found that 124 transcripts were significantly different in patients, by a factor of more than two with respect to control cell lines, in statistical analyses based on ANOVA and false discovery rates.

©2015 Macmillan Publishers Limited. All rights reserved

LETTER

doi:10.1038/nature14019

A PP1–PP2A phosphatase relay controls mitotic progression

Agnes Grallert[1]*, Elvan Boke[1]*†, Anja Hagting[2], Ben Hodgson[1], Yvonne Connolly[3], John R. Griffiths[3], Duncan L. Smith[3], Jonathon Pines[2] & Iain M. Hagan[1]

The widespread reorganization of cellular architecture in mitosis is achieved through extensive protein phosphorylation, driven by the coordinated activation of a mitotic kinase network and repression of counteracting phosphatases. Phosphatase activity must subsequently be restored to promote mitotic exit. Although Cdc14 phosphatase drives this reversal in budding yeast, protein phosphatase 1 (PP1) and protein phosphatase 2A (PP2A) activities have each been independently linked to mitotic exit control in other eukaryotes[1–6]. Here we describe a mitotic phosphatase relay in which PP1 reactivation is required for the reactivation of both PP2A-B55 and PP2A-B56 to coordinate mitotic progression and exit in fission yeast. The staged recruitment of PP1 (the Dis2 isoform) to the regulatory subunits of the PP2A-B55 and PP2A-B56 (B55 also known as Pab1; B56 also known as Par1) holoenzymes sequentially activates each phosphatase. The pathway is blocked in early mitosis because the Cdk1–cyclin B kinase (Cdk1 also known as Cdc2) inhibits PP1 activity, but declining cyclin B levels later in mitosis permit PP1 to auto-reactivate[1,7–10]. PP1 first reactivates PP2A-B55; this enables PP2A-B55 in turn to promote the reactivation of PP2A-B56 by dephosphorylating a PP1-docking site in PP2A-B56, thereby promoting the recruitment of PP1. PP1 recruitment to human, mitotic PP2A-B56 holoenzymes and the sequences of these conserved PP1-docking motifs[11,12] suggest that PP1 regulates PP2A-B55 and PP2A-B56 activities in a variety of signalling contexts throughout eukaryotes.

Cdk1–cyclin B phosphorylation of a conserved site in the carboxy terminus of PP1 depresses PP1 activity at mitotic commitment[1,7–10]. Declining Cdk1–cyclin B levels then allow the compromised PP1 to dephosphorylate itself to promote a return to full activity[1,7]. Of the two fission yeast PP1 enzymes, $PP1^{Sds21}$ and $PP1^{Dis2}$, only $PP1^{Dis2}$ harbours the conserved inhibitory phosphorylation site[2,9] (Extended Data Fig. 1a). *In vitro* $PP1^{Dis2}$ activity assays recapitulated previous observations that T316 phosphorylation by Cdk1–cyclin B depressed activity (Fig. 1a and Extended Data Fig. 1b, c)[1,7,9]. Mutating T316 to aspartic acid to mimic phosphorylation reduced the activity to a similar degree to phosphorylation by Cdk1–cyclin B (Fig. 1a and Extended Data Fig. 1c). Replacement of $PP1^{dis2+}$ with a $PP1^{dis2}.T316A$ allele increased $PP1^{Dis2}$ levels, whereas they were reduced in $PP1^{dis2}.T316D$ (Fig. 1b), indicating that phosphorylated T316 might act as a phospho-degron. Since this interpretation conflicted with reports of stable $PP1^{Dis2}$ levels throughout mitosis[10,13], we monitored $PP1^{Dis2}$ levels with both low and high antibody dilutions as size-selected cells synchronously transited the cell cycle. A transient reduction in $PP1^{Dis2}$ levels as T316 phosphorylation peaked (Fig. 1c) was blocked when proteosome function was inhibited (Extended Data Fig. 1e). Consistently, $PP1^{Dis2}$ levels were persistently low in $PP1^{dis2}.T316D$ and persistently high in $PP1^{dis2}.T316A$ (Fig. 1c and Extended Data Fig. 1f, g), indicating that phosphorylation of T316 by Cdk1–cyclin B both reduces $PP1^{Dis2}$ levels and inhibits its phosphatase activity.

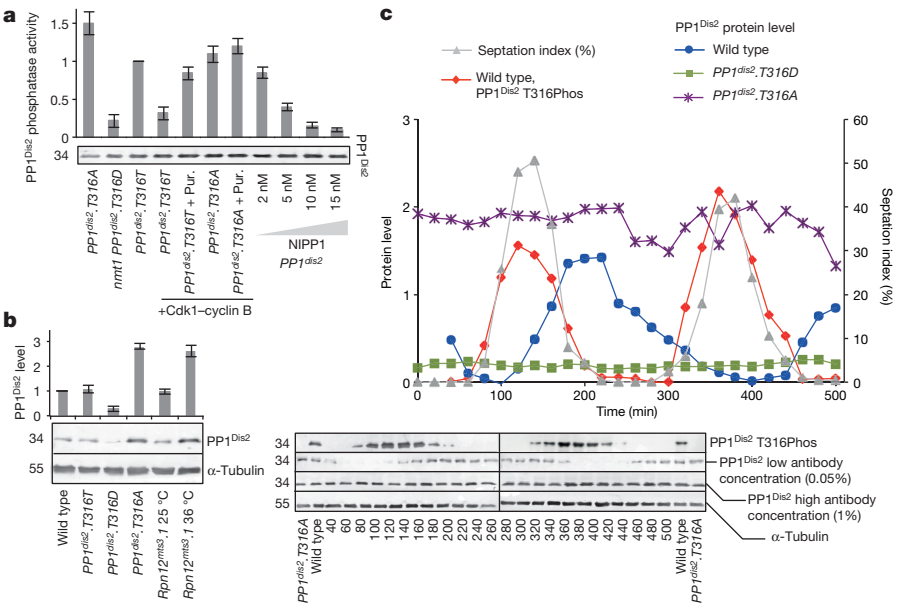


Figure 1 | $PP1^{Dis2}$ T316 phosphorylation and stability. **a**, EnzChek phosphatase assays (Extended Data Fig. 1b) of $PP1^{Dis2}$ isolated from the indicated strains by antibody precipitation. '+Cdk1–cyclin B' indicates the addition of sepharose beads to which covalently linked $p13^{Suc1}$ protein had recruited Cdk1–cyclin B from *S. pombe* cell extracts. NIPP1 is a highly specific PP1 inhibitor. Purvalanol (Pur.) is a Cdk1 inhibitor. **b**, **c**, $PP1^{Dis2}$ and T316 phosphorylation (T316Phos) levels ($Rpn12^{mts3}.1$ is a temperature-sensitive proteasome mutation). For **b**, $n = 5$ biological replicates; error bars show standard deviation (s.d.). **c**, Size-selected cells transit the cell division cycle. The septation profile is for the wild-type culture. $n = 2$ biological with two technical replicates each. $PP1^{Dis2}$.T316D and $PP1^{Dis2}$.T316A levels from the experiments in Extended Data Fig.1f, g are superimposed on this wild-type data set.

[1]Cell Division Group, CRUK Manchester Institute, University of Manchester, Wilmslow Road, Manchester M20 4BX, UK. [2]The Gurdon Institute, Tennis Court Road, University of Cambridge, Cambridge CB2 1QN, UK. [3]Biological Mass Spectrometry, CRUK Manchester Institute, University of Manchester, Wilmslow Road, Manchester M20 4BX, UK. †Present address: Department of Systems Biology, Harvard Medical School, Boston, Massachusetts 02115, USA.
*These authors contributed equally to this work.

©2015 Macmillan Publishers Limited. All rights reserved

PP2A holoenzymes combine a catalytic and scaffolding subunit with one of four regulatory B subunits[14], of which PP2A-B55 and PP2A-B56 have been linked to mitotic control[3–5,15,16]. We noticed that the B55 and B56 regulatory subunits had highly conserved PP1-docking-site consensus motifs (RVxF/RxVxF)[12] (Fig. 2a). The *Schizosaccharomyces pombe* genome encodes one B55 ($B55^{Pab1}$) and two B56 subunits ($B56^{Par1}$ and $B56^{Par2}$)[17,18], and we found that both $B55^{Pab1}$ and $B56^{Par1}$ associated with $PP1^{Dis2}$ in immunoprecipitation assays (Fig. 2b and Extended Data Fig. 2a–d). $B56^{Par1}$ also bound $PP1^{Dis2}$ in a yeast two-hybrid assay (Extended Data Fig. 3), and the functional replacement of the PP1-docking site of the morphogenesis regulator Wsh3 (also known as Tea4)[19] by the SKEVLF motif of $B56^{Par1}$ confirmed its ability to recruit PP1 (Extended Data Fig. 4a–d). The interaction between $PP1^{Dis2}$ and $B55^{Pab1}$ was abolished by mutating the PP1-docking consensus motif (Fig. 2b and Extended Data Fig. 2a). No association was found between $PP1^{Sds21}$ and any regulatory subunit (Extended Data Fig. 2b, c), nor between $B56^{Par2}$ and $PP1^{Dis2}$ (Extended Data Figs 2d and 3). L482 of $B56^{Par2}$ occupies a position occupied by only valine or isoleucine in validated PP1-docking sites[12]. Changing this leucine to valine allowed $PP1^{Dis2}$ to bind $B56^{Par2}$ (Extended Data Fig. 2e).

Core K/RxVxF PP1-docking motifs can be accompanied by secondary motifs[12]. Although the $B55^{Pab1}$ docking site is an isolated K/RxVxF motif, the GLLR sequence of $B56^{Par1}$ bears a striking resemblance to the secondary element G/SILK/R[11,12] (Fig. 2a, green box). Mutating the GLLR motif (*$B56^{par1}$.G367V*) mimicked mutating the R/KxVxF motif (*$B56^{par1}$.K379AV381AF383A*) in abolishing interactions between $PP1^{Dis2}$ and $B56^{Par1}$ in two-hybrid assays (Extended Data Fig. 3), and in compromising their ability to co-immunoprecipitate (Fig. 2b and Extended Data Fig. 2a). Mutating both motifs had an additive effect, severely compromising the affinity of $B56^{Par1}$ for $PP1^{Dis2}$ in co-immunoprecipitation assays (Fig. 2b and Extended Data Fig. 2a). Finally, the GLLR motif efficiently substituted for the characterized PP1-binding GILK motif of Cut12 (Extended Data Fig. 4e–g)[20]. We conclude that GLLR is a 'G/SILK/R' motif.

To confirm that the motifs we identified represent genuine $PP1^{Dis2}$-docking sites, we generated PP1-docking-site-null mutants (PDSN) of *$B55^{pab1}$* (*R52A/V54A/F56A*) and *$B56^{par1}$* (*G367V/K379A/V381A/F383A*), and purified the respective holoenzymes and wild-type controls from yeast cultures. The purified proteins were mixed with purified $PP1^{Dis2}$ and the $PP1^{Dis2}$ re-isolated to identify interacting partners. In each case, wild-type but not PDSN holoenzymes were captured by $PP1^{Dis2}$ (Extended Data Fig. 5a–d). Moreover, $PP1^{Dis2}$ co-migrated with the largest form of each of the wild-type PP2A holoenzyme complexes in size-exclusion chromatography (Extended Data Fig. 5e). We conclude that both $B56^{Par1}$ and $B55^{Pab1}$ contain genuine $PP1^{Dis2}$-docking motifs.

To assess the mitotic defects of the *$B55^{pab1}$.PDSN* and *$B56^{par1}$.PDSN* PP1-docking site mutants (Fig. 2c, d), we exploited transient arrest at the G2/M boundary with the temperature-sensitive *$Cdk1^{cdc2}$.33* mutation to synchronize mitotic progression[21] (Fig. 2e). Blocking $PP1^{Dis2}$ recruitment to either $B55^{Pab1}$ or $B56^{Par1}$ in synchronized divisions generated major errors in chromosome segregation and delayed the metaphase/anaphase transition (Fig. 2e and Extended Data Fig. 6a). To assay

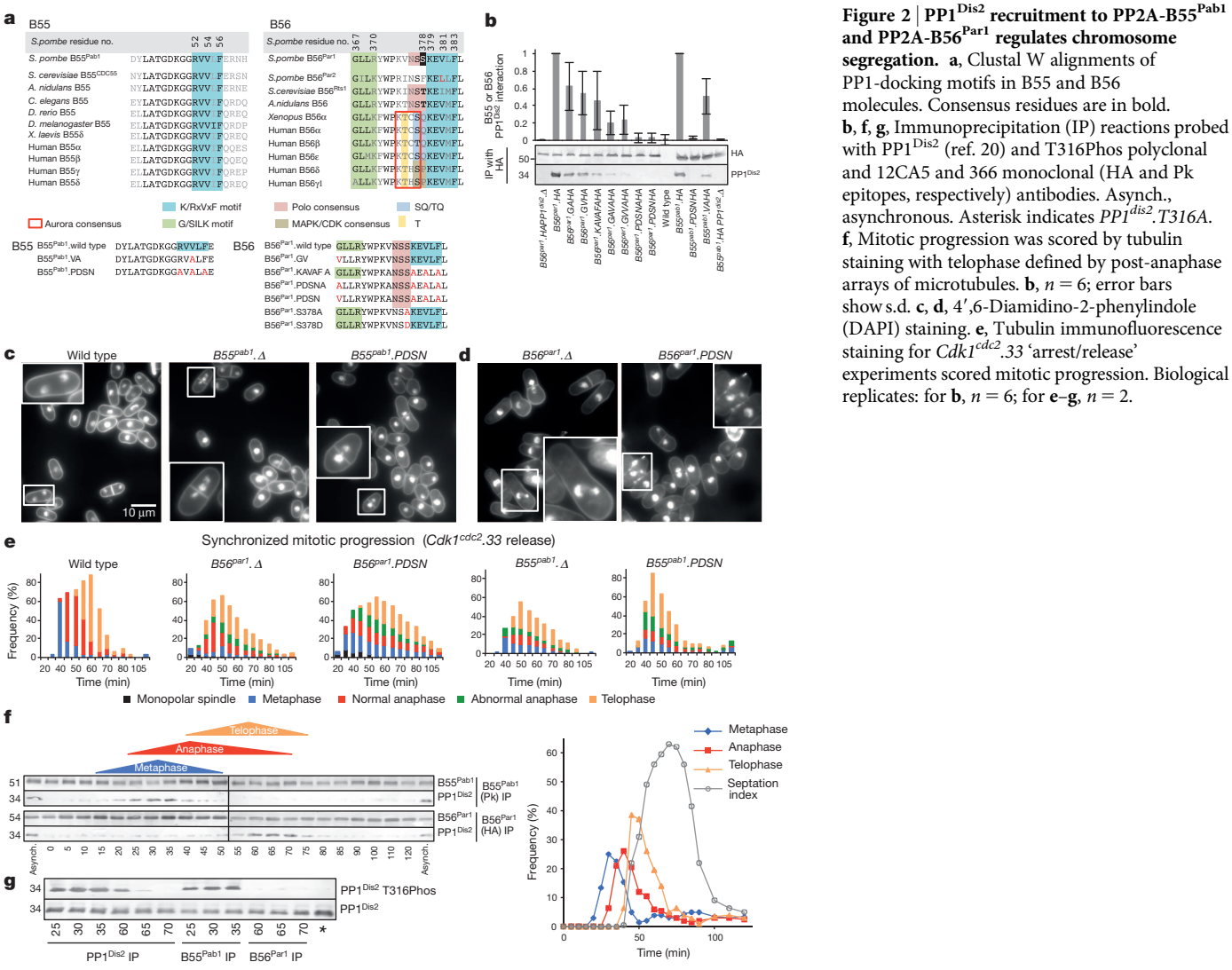


Figure 2 | $PP1^{Dis2}$ recruitment to PP2A-$B55^{Pab1}$ and PP2A-$B56^{Par1}$ regulates chromosome segregation. **a**, Clustal W alignments of PP1-docking motifs in B55 and B56 molecules. Consensus residues are in bold. **b**, **f**, **g**, Immunoprecipitation (IP) reactions probed with $PP1^{Dis2}$ (ref. 20) and T316Phos polyclonal and 12CA5 and 366 monoclonal (HA and Pk epitopes, respectively) antibodies. Asynch., asynchronous. Asterisk indicates *$PP1^{dis2}$.T316A*. **f**, Mitotic progression was scored by tubulin staining with telophase defined by post-anaphase arrays of microtubules. **b**, $n = 6$; error bars show s.d. **c**, **d**, 4′,6-Diamidino-2-phenylindole (DAPI) staining. **e**, Tubulin immunofluorescence staining for *$Cdk1^{cdc2}$.33* 'arrest/release' experiments scored mitotic progression. Biological replicates: for **b**, $n = 6$; for **e**–**g**, $n = 2$.

©2015 Macmillan Publishers Limited. All rights reserved

the timing of PP1^{Dis2} association with each PP2A holoenzyme, we used a *Cdk1^{cdc2}.33* strain in which B55^{Pab1} and B56^{Par1} were fused to different epitope tags, SV5 P protein (Pk) and haemagglutinin (HA) (*Cdk1^{cdc2}.33*, *B55^{pab1}.Pk* and *B56^{par1}.HA*). PP1^{Dis2} levels in B55^{Pab1}.Pk precipitates peaked at metaphase (25–35 min) whereas PP1^{Dis2} levels in B56^{Par1}.HA immunoprecipitates peaked later as spindles disassembled in telophase (60–70 min) (Fig. 2f).

An established assay for PP2A-B56^{Par1} (ref. 22), in which PP1^{Dis2} displayed no activity (Extended Data Fig. 6b–d), revealed a mitotic decline in bulk PP2A-B56^{Par1} activity before recovery at the start of the next cycle (Fig. 3a). PP2A-B56^{Par1} activity was severely compromised when either the GLLR (GILK) or KEVLF (RxVxF) motifs were individually mutated (Extended Data Fig. 6e, f), and abolished when both were simultaneously mutated to disrupt PP1^{Dis2} recruitment (Fig. 3b and Extended Data Fig. 6g). This indicated that PP1^{Dis2} could activate PP2A-B56^{Par1}; we confirmed this by adding immunopurified PP1^{Dis2} to PP2A-B56^{Par1} that had been isolated by immunoprecipitation from synchronized cells that lacked PP1^{Dis2} (*PP1^{dis2}.Δ*) (Fig. 3c). Moreover, PP1^{Dis2} activated wild-type PP2A-B56^{Par1} but not the PP1-docking-site mutant (Fig. 3c, d and Extended Data Fig. 6g, h), and genetically inhibited PP1^{Dis2}.T316D was unable to activate PP2A-B56^{Par1} (Fig. 3c and Extended Data Fig. 6h). Similar docking-site-dependent activity enhancement of purified PP2A-B56^{Par1} enzymes by purified PP1^{Dis2} (Extended Data Fig. 5f) further confirmed that recruitment of active PP1^{Dis2} to the PP2A-B56^{Par1} docking site reactivated PP2A-B56^{Par1}.

Phosphorylation between the G/SILK/R and RxVxF motifs of a bipartite docking site can block PP1 recruitment[20]. Mass spectrometry analysis of B56^{Par1} from mitotic cells appeared to indicate phosphorylation on S378 between the GLLR and KEVLF motifs (boxed residue in Fig. 2a; data not shown). Attempts to generate antibodies to recognize B56^{Par1} when phosphorylated on S378 failed, prompting us to generate a polyclonal antibody that would recognize B56^{Par1} when phosphorylated on both S377 and S378 (Extended Data Fig. 7a). This antibody (B56-Phos) revealed increasing phosphorylation in mitosis that declined as PP1^{Dis2}

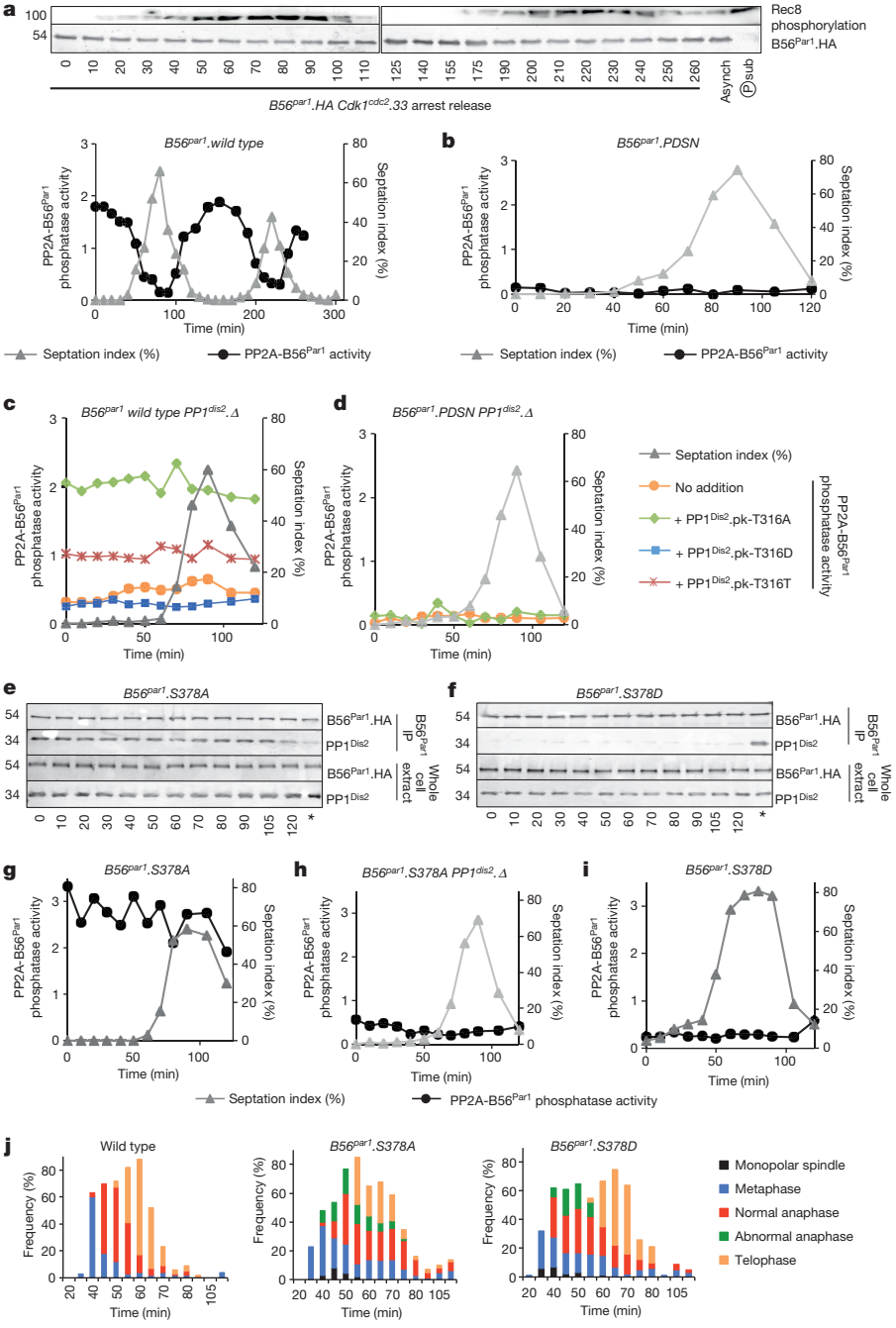


Figure 3 | Phosphorylation status of S378 determines competence to recruit active PP1^{Dis2} to PP2A-B56^{Par1} to promote PP2A-B56^{Par1} activity. **a**, **b**, **g**–**i**, Assays of PP2A-B56^{Par1} activity after B56^{Par1}.HA immunoprecipitation (with 12CA5 antibodies) of *Cdk1^{cdc2}.33* arrest/release synchronized cultures followed for one (**b**, **g**–**i**) or two (**a**) cycles. Activity changes (loss of GST–Rec8$^{391–561}$ ^{32}P radioactivity[22]) at each point were normalized to the activity of B56^{Par1}.HA from an asynchronous (Asynch.) culture processed in parallel on the same gel (penultimate lane). sub, phosphorylated substrate. **c**, **d**, Aliquots of PP1^{Dis2} protein immunoprecipitates (isolated under high salt (1.2 M NaCl) extraction conditions to disassociate partners) from *Cdk1^{cdc2}.33* arrested (interphase) cultures were added to PP2A-B56^{Par1} assays from *Cdk1^{cdc2}.33 dis2.Δ* cultures (Extended Data Fig. 6). **e**, **f**, Co-immunoprecipitation assays as for Fig. 2b. Asterisks indicate extracts from asynchronous *B56^{par1}.HA* cultures. **j**, Phenotype analysis of *Cdk1^{cdc2}.33* synchronized mitoses as for Fig. 2e. Biological replicates: for **a**, $n = 3$; for all other panels, $n = 2$.

©2015 Macmillan Publishers Limited. All rights reserved

was recruited to PP2A-B56^{Par1} (Fig. 4a). Mutating S378 to alanine to block phosphorylation (*B56^{par1}.S378A*) promoted persistent PP1^{Dis2} recruitment to PP2A-B56^{Par1} and persistently high levels of PP2A-B56^{Par1} activity throughout mitosis that depended upon the presence of PP1^{Dis2} (Fig. 3e, g, h and Extended Data Fig. 6i, j). Conversely, when S378 was mutated to aspartic acid to mimic phosphorylation (*B56^{par1}.S378D*), this severely compromised PP1^{Dis2} recruitment and B56^{Par1}.S378D activity remained low throughout division (Fig. 3f, i and Extended Data Fig. 6k). Anaphase was delayed and frequently abnormal in *B56^{par1}.S378D* cells (Fig. 3j), and it was striking that the persistent mitotic association of PP1^{Dis2} with PP2A-B56^{Par1} in *B56^{par1}.S378A* cells generated similar mitotic errors (Fig. 3j). Thus, dynamic phosphate turnover on S378 appears to be crucial for orderly mitotic progression. As anticipated from the match to the consensus phosphorylation site for the human polo-like kinase PLK1 (N/D/ExS/T)[23], Polo^{Plo1} was solely responsible for S378 phosphorylation (Fig. 4b, c).

PP1^{Dis2} recruitment to B56^{Par1} at telophase (Fig. 2f) indicated that S378 should be removed at this time, and the inability of *B55^{pab1}.Δ* cells to recruit PP1^{Dis2} to B56^{Par1} (Fig. 4d) indicated that PP2A-B55^{Pab1} could be responsible for this dephosphorylation. In support of this, PP2A-B55^{Pab1} removed B56-Phos reactivity from B56^{Par1} in an *in vitro* assay (Extended Data Fig. 7b). This phosphatase activity peaked during mitosis and was abolished when PP1^{Dis2} recruitment to B55^{Pab1} was blocked by removal of PP1^{Dis2}, when the PP1-docking site in B55^{Pab1} was ablated, and when genetically inhibited *PP1^{dis2}.T316D* was recruited (Fig. 4f–i and Extended Data Fig. 7c–f). Consistently, the failure of PP1^{Dis2} to associate with PP2A-B56^{Par1} in *B55^{pab1}.Δ* cells correlated with persistent phosphorylation on S378 throughout mitosis (*B55^{pab1}.Δ*; Fig. 4e). Finally, purified PP1^{Dis2} enhanced the B56-Phos activity of purified PP2A-B55^{Pab1} in a docking-site-dependent manner (Extended Data Fig. 5f).

In summary, PP1^{Dis2}, PP2A-B55^{Pab1} and PP2A-B56^{Par1} are linked in a phosphatase relay (Fig. 4j and Extended Data Fig. 8). At mitotic commitment all three activities are repressed[4] (Extended Data Fig. 9a); subsequently PP1^{Dis2} activity recovers auto-catalytically as cyclin B is degraded. The binding of repressed, T316-phosphorylated PP1^{Dis2} to PP2A-B55^{Pab1} (Fig. 2g) promotes rapid restoration of PP2A -B55^{Pab1} activity upon reduction of Cdk1–cyclin B activity. Reactivated PP2A-B55^{Pab1} can then begin to dephosphorylate S378 of B56^{Par1} but is antagonized by Polo^{Plo1} activity towards this site. Consequently, PP1^{Dis2} can only be recruited to PP2A-B56^{Par1} at telophase when Polo^{Plo1} activity declines (Fig. 4j and Extended Data Fig. 8). Thus, Cdk1–cyclin B phosphorylation of PP1 at mitotic commitment[1,7–10] locks all three phosphatases in the 'off' state. This lock is bolted through a Cdk1–cyclin B phosphorylation-mediated

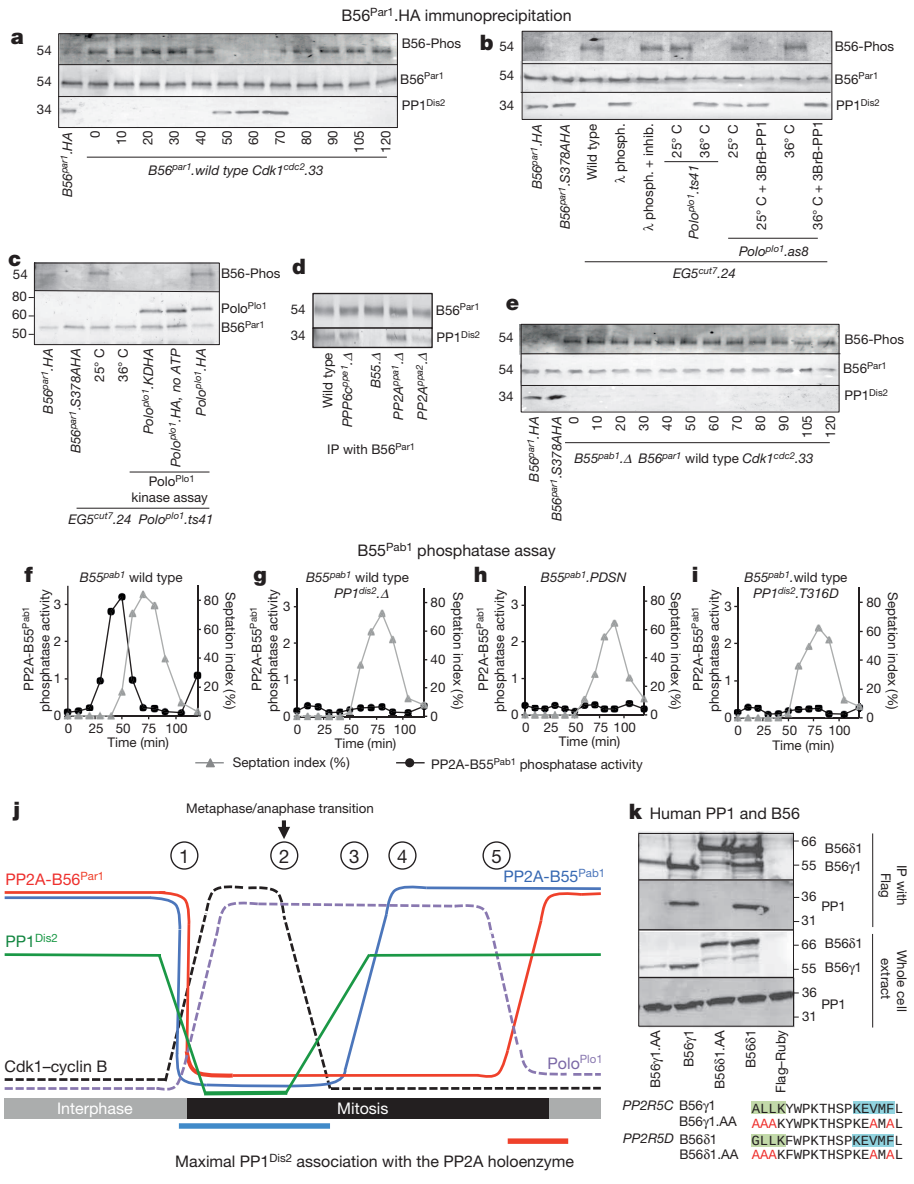


Figure 4 | PP2A-B55^{Pab1} dephosphorylation of B56^{Par1} promotes PP1^{Dis2} recruitment to activate PP2A-B56^{Par1} phosphatase in a mitotic phosphatase relay. a, **e–i**, *Cdk1^{cdc2}.33* synchronized mitoses. **a–c**, **e**, B56-Phos antibodies (Extended Data Fig. 7a) detected phosphorylation on B56^{Par1} after immunoprecipitation from the indicated strains and the indicated treatments. PP1^{Dis2} levels were monitored where indicated. λ phosph., λ phosphatase; 3BrB-PP1, 3-[(3-bromophenyl)methyl]-1-tert-butylpyrazolo[3,4-d]pyrimidin-4-amine; *Polo^{Plo1}.KDHA*, HA-tagged catalytically inactive; inhib., inhibitor. **d**, B56^{Par1} precipitates probed for PP1^{Dis2}. **f–i**, PP2A-B55^{Pab1} phosphatase assays (Extended Data Fig. 7c–f). **j**, Bulk activities are illustrated: local activities at any given time will depend on the specific balance of each activity at a particular site. (1) Cdk1–cyclin B activation represses all three phosphatase activities (Extended Data Fig. 9a). Direct phosphorylation of PP1^{Dis2} TPRR motif inhibits catalytic activity[1,7–10] and promotes destruction. PP1^{Dis2} binds B55^{Pab1} but cannot reactivate PP2A-B55^{Pab1} while TPRR phosphorylation persists. Polo^{Plo1} phosphorylation of B56^{Par1} prevents PP1^{Dis2} recruitment to PP2A-B56^{Par1}. (2) Declining Cdk1–cyclin B activity facilitates PP1 auto-reactivation. (3) Re-activated PP1^{Dis2} promotes PP2A-B55^{Pab1} reactivation. (4) PP2A-B55^{Pab1} dephosphorylates the PP1-docking site in B56^{Par1} less efficiently than Polo^{Plo1} phosphorylates it, keeping PP2A-B56^{Par1} activity low. (5) Declining Polo^{Plo1} activity enables PP2A-B55^{Pab1} to dephosphorylate B56^{Par1} and promote reactivating recruitment of PP1^{Dis2} (Extended Data Fig. 8). **k**, Flag-tagged B56γ and B56δ isoforms were stably expressed in HeLa-FRT cell lines, immunoprecipitated from mitotic cells isolated by shake-off from nocodazole-treated cells, and the immunoprecipitates probed with an antibody that recognizes all forms of PP1. Biological replicates: for **k**, $n = 3$; for all other panels, $n = 2$.

©2015 Macmillan Publishers Limited. All rights reserved

reduction of PP1^{Dis2} levels. These controls join a range of other modes of PP1 and PP2A regulation, including Greatwall/ENSA control of PP2A-B55δ, and PP2A-B56 regulation by Bod1, to provide the accurate control of phosphorylation status that is critical for faithful cell division[1,6,11,24,25].

The conservation of the PP1-docking-site motifs in PP2A regulatory subunits (Fig. 2a) prompted us to investigate the association between human PP1 and PP2A enzymes. PP1α, β and γ bound B56γ in yeast two-hybrid assays, and PP1 co-immunoprecipitated with Flag epitope-tagged B56γ and B56δ expressed in mitotic human cells. Each of these interactions was abolished by mutation of the PP1-docking-site motif (Fig. 4k and Extended Data Fig. 9b–d). Thus, the principle of a phosphatase relay, whereby PP1 recruitment activates PP2A to control mitosis, is conserved in human cells. It is notable that the NXS Polo kinase consensus sequences in fungal B56 subunits are replaced by SP and SQ motifs in metazoa (Fig. 2a), suggesting that CDK/MAP kinases modulate PP1 docking to B56δ and B56γ, whereas ATM/ATR/DNA-PK may coordinate docking to B56 α, β, ε. Furthermore, these serine/threonine residues also conform to consensus motifs for AGC kinases, including aurora B (KXXS/T), while the threonine highlighted in yellow in Fig. 2a could facilitate control by further kinases. We believe, therefore, that PP1 regulation of PP2A-B56 activity will emerge as a ubiquitous feature in diverse signalling contexts. Although bulk biochemical assays reveal core principles of phosphatase control, local controls sit at the heart of many transitions[26]. Thus, we propose that competition between kinases and PP1 and PP2A holoenzymes at specific locations will generate locally active, dephosphorylated phosphatases at times when assays show the activity of the bulk population is depressed.

The direct recruitment of PP1 to B55 and B56 subunits that we observed is unanticipated. Although the majority of predicted PP1-docking sites reside within regions that are predicted to be intrinsically disordered[11], PP1 recruitment to the docking sites of B55^{Pab1}, B56^{Par1} and CENP-E[11,27] suggest that this requirement is not axiomotic. A second conundrum is that the PP1-docking motifs are inaccessible in structures of the PP2A holoenzyme complexes that have been solved so far[28–30]. PP1-docking site residues, and the equivalent residue to S378, form bonds that are crucial to the integrity of these structures, yet, contrary to predictions arising from these structures, mutation of these residues to alanine has no impact on the integrity of either PP2A-B55 or PP2A-B56 holoenzymes (Extended Data Fig. 10). Moreover, S378 is phosphorylated in purified PP2A-B56^{Par1} complexes and holoenzymes isolated by one-step immunoprecipitation (Extended Data Figs 5g and 10c). Our data therefore add to established discrepancies between *in vivo* and *in vitro* PP2A holoenzyme assembly[24] to suggest that alternative structures will emerge from structural studies of active enzymes that have undergone the extensive array of modifications required for activity that impact upon PP2A conformation *in vivo*[24].

Online Content Methods, along with any additional Extended Data display items and Source Data, are available in the online version of the paper; references unique to these sections appear only in the online paper.

Received 4 June 2013; accepted 27 October 2014.
Published online 10 December 2014.

1. Wu, J. Q. *et al.* PP1-mediated dephosphorylation of phosphoproteins at mitotic exit is controlled by inhibitor-1 and PP1 phosphorylation. *Nature Cell Biol.* **11,** 644–651 (2009).
2. Ohkura, H., Kinoshita, N., Miyatani, S., Toda, T. & Yanagida, M. The fission yeast *dis2*$^{+}$ gene required for chromosome disjoining encodes one of 2 putative type-1 protein phosphatases. *Cell* **57,** 997–1007 (1989).
3. Mochida, S. & Hunt, T. Calcineurin is required to release *Xenopus* egg extracts from meiotic M phase. *Nature* **449,** 336–340 (2007).
4. Mochida, S., Ikeo, S., Gannon, J. & Hunt, T. Regulated activity of PP2A–B55δ is crucial for controlling entry into and exit from mitosis in *Xenopus* egg extracts. *EMBO J.* **28,** 2777–2785 (2009).
5. Schmitz, M. H. *et al.* Live-cell imaging RNAi screen identifies PP2A–B55α and importin-β1 as key mitotic exit regulators in human cells. *Nature Cell Biol.* **12,** 886–893 (2010).
6. Qian, J., Winkler, C. & Bollen, M. 4D-networking by mitotic phosphatases. *Curr. Opin. Cell Biol.* **25,** 697–703 (2013).
7. Dohadwala, M. *et al.* Phosphorylation and inactivation of protein phosphatase 1 by cyclin-dependent kinases. *Proc. Natl Acad. Sci. USA* **91,** 6408–6412 (1994).
8. Kwon, Y. G., Lee, S. Y., Choi, Y., Greengard, P. & Nairn, A. C. Cell cycle-dependent phosphorylation of mammalian protein phosphatase 1 by cdc2 kinase. *Proc. Natl Acad. Sci. USA* **94,** 2168–2173 (1997).
9. Yamano, H., Ishii, K. & Yanagida, M. Phosphorylation of Dis2 protein phosphatase at the C-terminal Cdc2 consensus and its potential role in cell-cycle regulation. *EMBO J.* **13,** 5310–5318 (1994).
10. Ishii, K., Kumada, K., Toda, T. & Yanagida, M. Requirement for PP1 phosphatase and 20S cyclosome/APC for the onset of anaphase is lessened by the dosage increase of a novel gene *sds23*$^{+}$. *EMBO J.* **15,** 6629–6640 (1996).
11. Bollen, M., Peti, W., Ragusa, M. J. & Beullens, M. The extended PP1 toolkit: designed to create specificity. *Trends Biochem. Sci.* **35,** 450–458 (2010).
12. Heroes, E. *et al.* The PP1 binding code: a molecular-lego strategy that governs specificity. *FEBS J.* **280,** 584–595 (2013).
13. Kinoshita, N., Ohkura, H. & Yanagida, M. Distinct, essential roles of type-1 and type-2a protein phosphatases in the control of the fission yeast-cell division cycle. *Cell* **63,** 405–415 (1990).
14. Sents, W., Ivanova, E., Lambrecht, C., Haesen, D. & Janssens, V. The biogenesis of active protein phosphatase 2A holoenzymes: a tightly regulated process creating phosphatase specificity. *FEBS J.* **280,** 644–661 (2013).
15. Kitajima, T. S. *et al.* Shugoshin collaborates with protein phosphatase 2A to protect cohesin. *Nature* **441,** 46–52 (2006).
16. Suijkerbuijk, S. J., Vleugel, M., Teixeira, A. & Kops, G. J. Integration of kinase and phosphatase activities by BUBR1 ensures formation of stable kinetochore-microtubule attachments. *Dev. Cell* **23,** 745–755 (2012).
17. Kinoshita, K. *et al.* The regulatory subunits of fission yeast protein phosphatase 2A (PP2A) affect cell morphogenesis, cell-wall synthesis and cytokinesis. *Genes Cells* **1,** 29–45 (1996).
18. Jiang, W. & Hallberg, R. L. Isolation and characterization of *par1*$^{+}$ and *par2*$^{+}$: two *Schizosaccharomyces pombe* genes encoding B′ subunits of protein phosphatase 2A. *Genetics* **154,** 1025–1038 (2000).
19. Alvarez-Tabarés, I., Grallert, A., Ortiz, J. M. & Hagan, I. M. *Schizosaccharomyces pombe* protein phosphatase 1 in mitosis, endocytosis and a partnership with Wsh3/Tea4 to control polarised growth. *J. Cell Sci.* **120,** 3589–3601 (2007).
20. Grallert, A. *et al.* Removal of centrosomal PP1 by NIMA kinase unlocks the MPF feedback loop to promote mitotic commitment in *S. pombe*. *Curr. Biol.* **23,** 213–222 (2013).
21. King, S. M. & Hyams, J. S. Synchronization of mitosis in a cell-division cycle mutant of *Schizosaccharomyces pombe* released from temperature arrest. *Can. J. Microbiol.* **28,** 261–264 (1982).
22. Ishiguro, T., Tanaka, K., Sakuno, T. & Watanabe, Y. Shugoshin–PP2A counteracts casein-kinase-1-dependent cleavage of Rec8 by separase. *Nature Cell Biol.* **12,** 500–506 (2010).
23. Johnson, L. N. Substrates of mitotic kinases. *Sci. Signal.* **4,** pe31 (2011).
24. Janssens, V., Longin, S. & Goris, J. PP2A holoenzyme assembly: *in cauda venenum* (the sting is in the tail). *Trends Biochem. Sci.* **33,** 113–121 (2008).
25. Porter, I. M., Schleicher, K., Porter, M. & Swedlow, J. R. Bod1 regulates protein phosphatase 2A at mitotic kinetochores. *Nat. Commun.* **4,** 2677 (2013).
26. Pines, J. & Hagan, I. The renaissance or the cuckoo clock. *Phil. Trans. R. Soc. Lond. B* **366,** 3625–3634 (2011).
27. Kim, Y., Holland, A. J., Lan, W. & Cleveland, D. W. Aurora kinases and protein phosphatase 1 mediate chromosome congression through regulation of CENP-E. *Cell* **142,** 444–455 (2010).
28. Xu, Y. *et al.* Structure of the protein phosphatase 2A holoenzyme. *Cell* **127,** 1239–1251 (2006).
29. Cho, U. S. & Xu, W. Crystal structure of a protein phosphatase 2A heterotrimeric holoenzyme. *Nature* **445,** 53–57 (2007).
30. Xu, Y., Chen, Y., Zhang, P., Jeffrey, P. D. & Shi, Y. Structure of a protein phosphatase 2A holoenzyme: insights into B55-mediated Tau dephosphorylation. *Mol. Cell* **31,** 873–885 (2008).

Supplementary Information is available in the online version of the paper.

Acknowledgements This work was supported by Cancer Research UK (CRUK) grant numbers C147/A16406 and C29/A13678. We thank I. Alvarez-Tabares, K. Labib, K. Gull, M. Yanagida, V. Simanis, J. Bähler and K. Gould for reagents.

Author Contributions E.B. carried out the initial identification, validation and timing of PP1^{Dis2}–B55^{Pab1}/B56^{Par1} association, initial two-hybrid and co-immunoprecipitation assays, initial determination of specificity and timing of PP1^{Dis2}.T316 phospho-recognition, and phospho-mapping of B56^{Par1} (with D.L.S. and Y.C.) and generated some mutant alleles. E.B. generated Fig. 4d; all other data, except for Fig. 4k and Extended Data Figs 5c, 9b–d, were generated and largely devised by A.G. Data for Extended Data Fig. 5c were generated by A.G., Y.C., D.L.S. and J.R.G. Molecular biology and background work for human two-hybrid assays and generation of human vectors was carried out by B.H. I.M.H. devised the work presented in Figs 1c, 2a, c, f and 4d with E.B., and devised the remainder of the work with A.G. A.H. and J.P. designed and executed the human work and gel filtration.

Author Information Reprints and permissions information is available at www.nature.com/reprints. The authors declare no competing financial interests. Readers are welcome to comment on the online version of the paper. Correspondence and requests for materials should be addressed to I.M.H. (lain.Hagan@cruk.manchester.ac.uk).

©2015 Macmillan Publishers Limited. All rights reserved

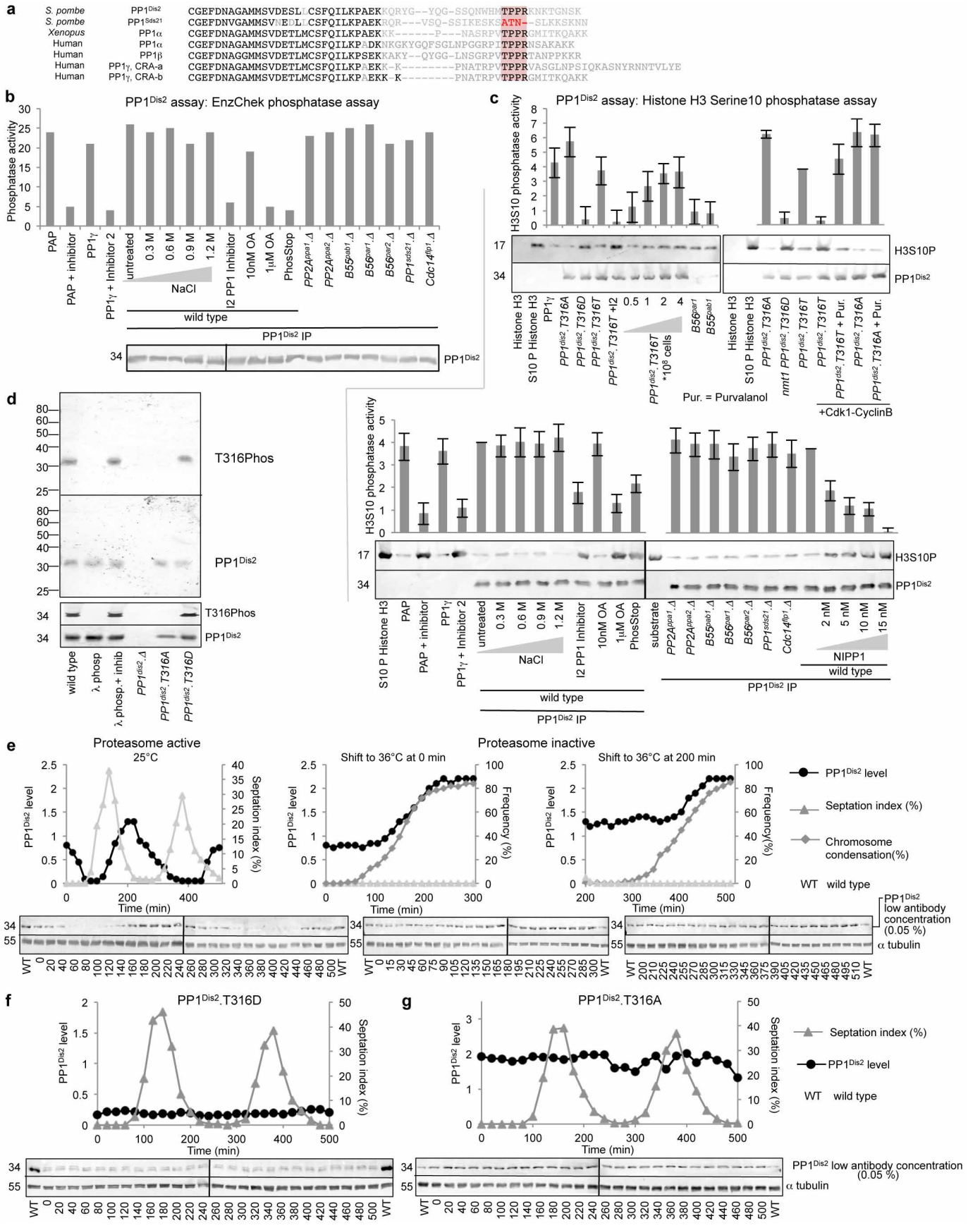
METHODS

Standard procedures[31,32] were used to grow and maintain yeast strains (Supplementary Table 1). Appropriately supplemented EMM2 synthetic medium was used throughout with the exception of TAP tag purification, for which we used 10× YES. The generation of size-selected synchronous cultures was as described previously[33]. Two-hybrid assays used the matchmaker gold system (Clontech 630489). 'Phospho-specific' rabbit polyclonal antibodies were generated by Eurogentec. Commercial antibodies detected C^{Ppa1} and C^{Ppa2} (Cell Signaling, 2038), A^{Paa1} (Abcam, ab28350) and human B56ε (Santa Cruz sc-135223). In house polyclonal antibodies detected $PP1^{Dis2}$ (ref. 20) and green fluorescent protein (GFP). To detect associations between $PP1^{Dis2}$ and $B55^{Pab1}$ and $PP1^{Dis2}$ and $B56^{Par1}$ the complexes were isolated from 2×10^8 cells in the buffer (50 mM HEPES (pH 7.5), 50 mM NaF, 0.4 mM Na_3VO_4, 40 mM Na–β-glycerol phosphate, 1 mM EDTA, 50 mM NaCl, 0.1% NP40, 1 mM PMSF). The EnzChek (Molecular Probes E12020) or histone H3 serine 10 dephosphorylation assays[34] monitored $PP1^{Dis2}$ activity (Extended Data Fig. 1) with the use of recombinant rabbit PP1γ (NEB P0754S), full-length NIPP1 (Abcam, ab131705), Phos-Stop (Roche 04906845001) and potato acid phosphatase (Molecular Probes E12020). Manufacturer's instructions were followed for EnzChek assays (Molecular Probes E12020). For Histone H3 serine 10 assays, histone H3 (Millipore 14-4-11) that had been phosphorylated by established $aurora^{Ark1}$ kinase assays[35] was used as a substrate. The dephosphorylation reaction was conducted in 20 mM HEPES, 100 mM NaCl, 1 mM EDTA, 0.1% NP40 at 30 °C for 1 h. An established $PP2A\text{-}B56^{Par1}$ activity assay used $GST\text{–}Rec8^{391–561}$ phosphorylated by recombinant GST–Hhp2 (*S. pombe* casein kinase I) as a substrate[22]: $PP2A\text{-}B56^{Par1}$.HA was isolated from 2×10^8 cells with 12CA5 antibody (Roche) under non-denaturing conditions. The dephosphorylation reaction was maintained at 30 °C for 1 h, in 50 mM HEPES (pH 7.5), 100 mM NaCl, 0.1% NP40, 2 mM $MnCl_2$, 2 mM dithiothreitol (DTT). ^{32}P levels in the substrate were determined with a Phosphoimager (BioRad). Phosphatase activity was calculated as the reduction of ^{32}P incorporation per unit $B56^{Par1}$ normalized to the activity of a standard sample from an asynchronous culture. $PP2A\text{-}B55^{Pab1}$ activity was monitored by detecting phosphorylation on S377 and S378 of $B56^{Par1}$ with the phospho-specific antibody B56-Phos (Extended Data Fig. 7a). $B56^{Par1}$.HA substrate from 6×10^8 mitotically arrested cells[36] was independently isolated for three individual assays (scaling up substrate production failed owing to substrate dephosphorylation and degradation during preparation). To isolate this $B56^{Par1}$.HA devoid of other subunits for $PP2A\text{-}B55^{Pab1}$ assays (Extended Data Fig. 7b, right), a TCA precipitation of total protein was resuspended in a denaturing IP buffer (50 mM HEPES (pH 7.5), 50 mM NaF, 0.4 mM Na_3VO_4, 40 mM Na–β-glycerol phosphate, 1 mM EDTA, 200 mM NaCl, 0.2% NP40, 1 mM PMSF). The dephosphorylation assay was performed at 30 °C for 1 h (100 mM Tris (pH 7.5), 150 mM NaCl, 10 mM DTT). PP2A and PP1 enzymes were purified by established sequential TAP and immuno-affinity/peptide elution methods[37]. For TAP tagging, Econo-Pac Chromatography Columns (Biorad 9704652) were packed with IgG Sepharose 6 FastFlow (GE Healthcare 170969-01) or Calmodulin Affinity Resin (Agilent Technologies 214303-52). The following were used for subsequent affinity isolation: anti-HA Affinity Matrix (Roche 101677100), HA peptide (Sigma, I2149), Dynabeads A (Life Technologies) pre-loaded with $PP1^{Dis2}$ antibodies[20] according to manufacturer's instructions, and the SQNWHMTPPRKNK peptide for elution of $PP1^{Dis2}$ from the $PP1^{Dis2}$ polyclonal antibody. Coomassie (Brilliant Blue, Sigma, B2025-1EA) stained 4–12% SDS–NUPAGE gradient gels (Life Technologies, NP20327). Size-exclusion chromatography was performed on a Superdex 200 PC 3.2/30 column (VWR) using buffer B (50 mM HEPES (pH 7.5), 100 mM NaCl, 0.1% NP-40) collecting 50 µl fractions at a flow rate of 50 µl ml^{-1} (ref. 38). All other *S. pombe* techniques were performed as described previously[20].

For immunoprecipitation of human complexes, tetracycline-inducible HeLa cell lines were generated using a pcDNA5/FRT/TO vector (Invitrogen). Cells were grown in advanced DMEM (Invitrogen) supplemented with 2% fetal bovine serum and penicillin/streptavidin. Cells were blocked with thymidine (Sigma-Aldrich) for 24 h and released into fresh medium with 300 nM nocodazole (Sigma-Aldrich) and 1 µg ml^{-1} tetracycline (EMD). Prometaphase cells were collected by mitotic shake-off after 12 h. Cells were lysed for 20 min on ice in extraction buffer A (50 mM Tris-HCl (pH 8.0), 150 mM NaCl, 0.2% NP-40, 1 mM EDTA, complete inhibitor cocktail tablet (Roche), 0.2 µM microcystin (LGC-Promotech)) and lysates were cleared by centrifugation for 15 min at 12,000*g* and 4 °C. Protein complexes were precipitated for 1.5 h at 4 °C with anti-Flag (M2; Sigma-Aldrich) covalently coupled to Dynabeads (Invitrogen), washed in extraction buffer, and bound proteins were eluted with LDS-sample buffer (Invitrogen) before analysis by immunoblotting[38]. Antibodies against the Flag epitope and PP1 (E-9; Santa Cruz sc-7482) were used at 1;1,000.

31. Moreno, S., Klar, A. & Nurse, P. Molecular genetic analysis of fission yeast *Schizosaccharomyces pombe*. *Methods Enzymol.* **194,** 795–823 (1991).
32. Fennessy, D. *et al.* Extending the *Schizosaccharomyces pombe* molecular genetic toolbox. *PLoS ONE* **9,** e97683 (2014).
33. Creanor, J. & Mitchison, J. M. Reduction of perturbations in leucine incorporation in synchronous cultures of *Schizosaccharomyces pombe* made by elutriation. *J. Gen. Microbiol.* **112,** 385–388 (1979).
34. Qian, J., Lesage, B., Beullens, M., Van Eynde, A. & Bollen, M. PP1/Repo-man dephosphorylates mitotic histone H3 at T3 and regulates chromosomal aurora B targeting. *Curr. Biol.* **21,** 766–773 (2011).
35. Petersen, J., Paris, J., Willer, M., Philippe, M. & Hagan, I. M. The *S. pombe* aurora related kinase Ark1 associates with mitotic structures in a stage dependent manner and is required for chromosome segregation. *J. Cell Sci.* **114,** 4371–4384 (2001).
36. Hagan, I. & Yanagida, M. Novel potential mitotic motor protein encoded by the fission yeast *cut7*$^+$ gene. *Nature* **347,** 563–566 (1990).
37. Gould, K. L., Ren, L., Feoktistova, A. S., Jennings, J. L. & Link, A. J. Tandem affinity purification and identification of protein complex components. *Methods* **33,** 239–244 (2004).
38. Mansfeld, J., Collin, P., Collins, M. O., Choudhary, J. S. & Pines, J. APC15 drives the turnover of MCC-CDC20 to make the spindle assembly checkpoint responsive to kinetochore attachment. *Nature Cell Biol.* **13,** 1234–1243 (2011).
39. Beullens, M. *et al.* Molecular determinants of nuclear protein phosphatase-1 regulation by NIPP-1. *J. Biol. Chem.* **274,** 14053–14061 (1999).
40. Gordon, C., McGurk, G., Wallace, M. & Hastie, N. D. A. Conditional-lethal mutant in the fission yeast 26-S protease subunit $Mts3^+$ is defective in metaphase to anaphase transition. *J. Biol. Chem.* **271,** 5704–5711 (1996).
41. Gambus, A. *et al.* GINS maintains association of Cdc45 with MCM in replisome progression complexes at eukaryotic DNA replication forks. *Nature Cell Biol.* **8,** 358–366 (2006).
42. Hachet, O. *et al.* A phosphorylation cycle shapes gradients of the DYRK family kinase Pom1 at the plasma membrane. *Cell* **145,** 1116–1128 (2011).
43. Nurse, P. Universal control mechanism regulating onset of M-phase. *Nature* **344,** 503–508 (1990).
44. Hudson, J. D., Feilotter, H. & Young, P. G. *stf1*: non-wee mutations epistatic to *cdc25* in the fission yeast *Schizosaccharomyces pombe*. *Genetics* **126,** 309–315 (1990).
45. Ishihama, Y. *et al.* Exponentially modified protein abundance index (emPAI) for estimation of absolute protein amount in proteomics by the number of sequenced peptides per protein. *Mol. Cell Proteomics* **4,** 1265–1272 (2005).
46. Ohkura, H. & Yanagida, M. S. *pombe* gene $sds22^+$ essential for a midmitotic transition encodes a leucine-rich repeat protein that positively modulates protein phosphatase-1. *Cell* **64,** 149–157 (1991).
47. Stone, E. M., Yamano, H., Kinoshita, N. & Yanagida, M. Mitotic regulation of protein phosphatases by the fission yeast Sds22 protein. *Curr. Biol.* **3,** 13–26 (1993).

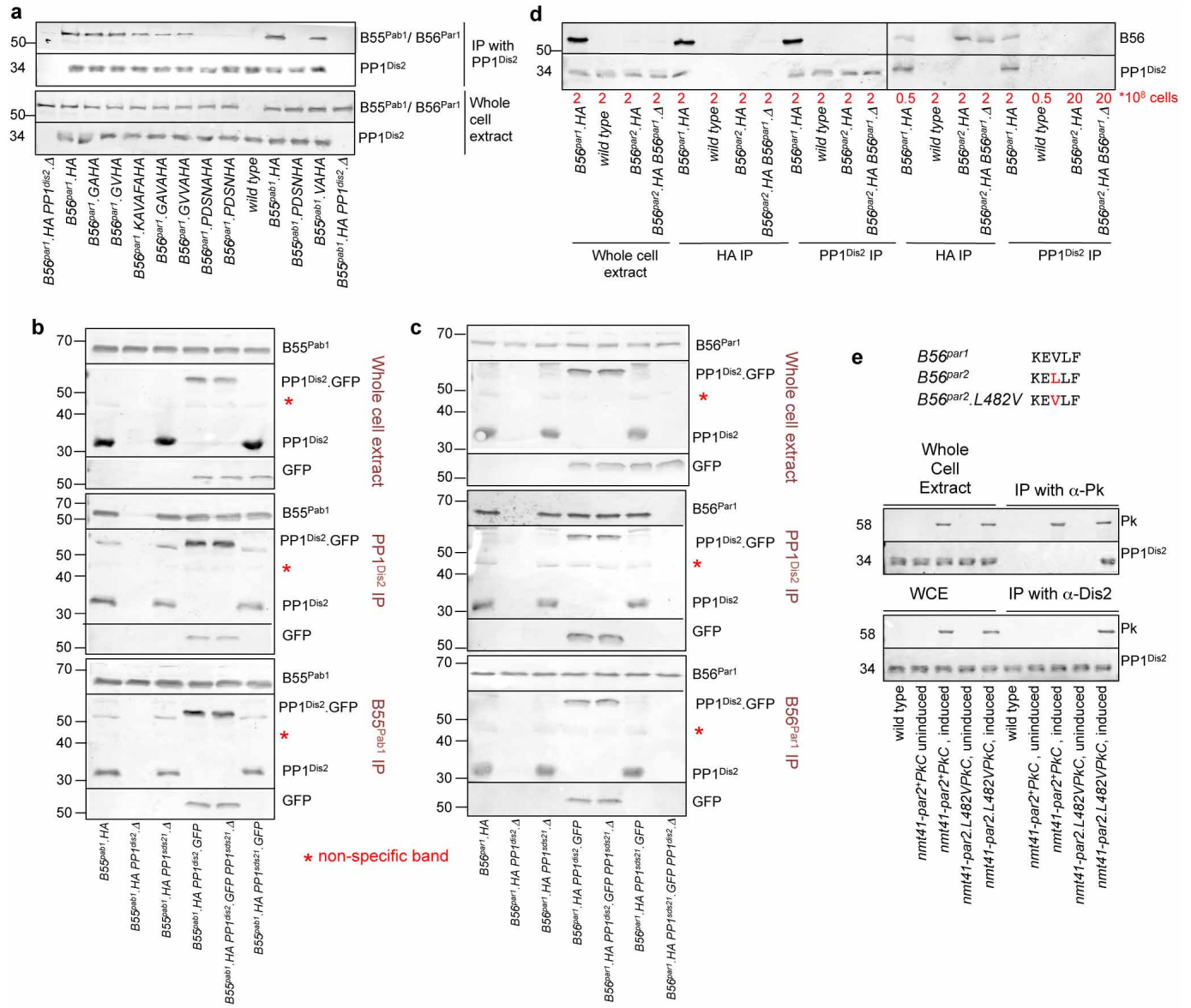
©2015 Macmillan Publishers Limited. All rights reserved



©2015 Macmillan Publishers Limited. All rights reserved

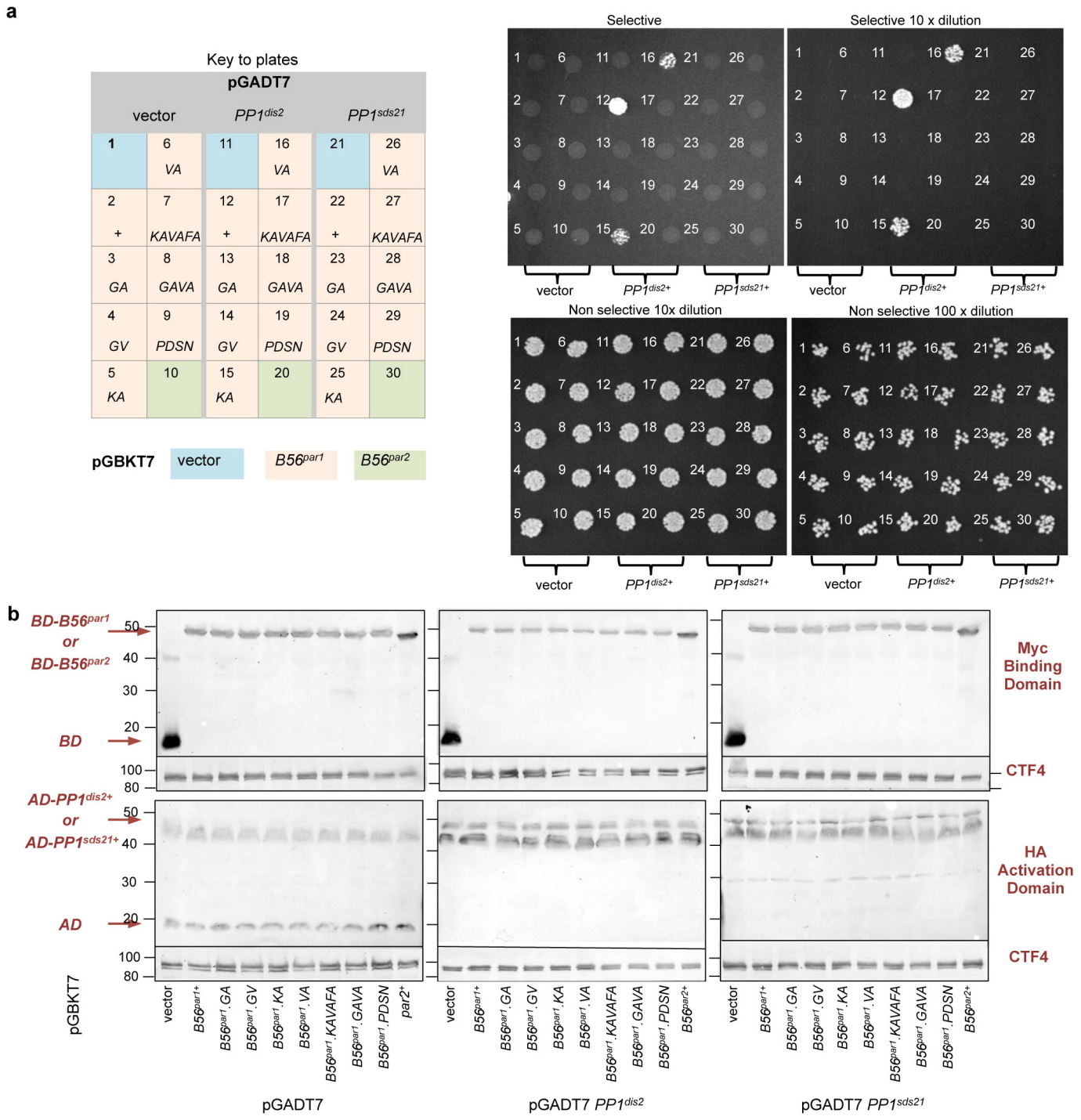
Extended Data Figure 1 | PP1 phosphorylation by Cdk1–cyclin B on T316 represses activity and reduces abundance in a manner that is mimicked by mutation of the target site to an acidic residue in $PP1^{Dis2}$.T316D. **a**, Clustal W alignments of the C-terminal residues of the indicated PP1 isoforms. The Cdk1–cyclin B phosphorylation site is highlighted by red shading. Red letters within this region of shading highlight the clear deviation from this consensus in the *S. pombe* $PP1^{Sds21}$ isoform. $PP1^{Sds21}$ is unable to bind to either $B55^{Pab1}$ or $B56^{Par1}$. The molecular basis for this inability of $PP1^{Sds21}$ to bind the regulatory subunits of PP2A remains to be established. The initial threonine in the *S. pombe* $PP1^{Dis2}$ shaded consensus sequence region is T316. **b**, **c**, Phosphatase assays of the indicated samples with activity detection by either EnzChek (**b**) or a second established PP1 activity assay[34] histone H3 serine 10 dephosphorylation (**c**) . For each assay the graphs show arbitrary units. Error bars show s.d. Identical results were obtained with each assay. The similarity between the recombinant rabbit PP1γ and potato acid phosphatase (PAP) activities indicate that both reactions measure PP1 activity. The inhibition of the activity of $PP1^{Dis2}$ precipitates by 1 μM, but not 10 nM okadaic acid (OA), suggests that it is the $PP1^{Dis2}$ activity rather than any co-precipitating PP2A activity that is being monitored in these assays. This view is consolidated by the inhibition of activity in both assays by the PP1-specific inhibitor NIPP1 (2, 5, 10 and 15 nM; **c** and Fig. 1a). 5 nM is routinely used to inhibit mammalian PP1 (refs 34, 39). Manufacturer's instructions were followed for EnzChek assays. For histone H3 serine 10 assays, histone H3 that had been phosphorylated by $aurora^{Ark1}$ kinase[35] was used as a substrate. The dephosphorylation reaction was conducted in 20 mM HEPES, 100 mM NaCl, 1 mM EDTA, 0.1% NP40 at 30 °C for 1 h. The molarity of NaCl indicates the salt concentration of the buffer used for the immunoprecipitation, not the molarity within the phosphatase reaction. All phosphatase reactions for each substrate were conducted under identical conditions. A 1.2 M NaCl, buffer was used to isolate $PP1^{Dis2}$ for the experiments in Fig. 3c, d and Extended Data Fig. 6d, g, h. The level of PP1 activity detected in either assay shown in **b** and **c** was the same irrespective of the NaCl concentration in the buffer used to isolate $PP1^{Dis2}$. Phos-Stop is a universal phosphatase inhibitor. The key conclusion from all these assays is that the $PP1^{Dis2}$.T316D protein has a similar level of activity as the Cdk1–cyclin B phosphorylated enzyme and so behaves as a 'genetically inhibited' phosphatase in the subsequent experiments described in the manuscript. **d**, Validation of the T316Phos antibody. $PP1^{Dis2}$ immunoprecipitates from the indicated strains were treated as indicated and probed with either $PP1^{Dis2}$ or T316Phos polyclonal antibodies. **e**–**g**, Cultures synchronized with respect to cell cycle progression by size selection through elutrient centrifugation were probed with the $PP1^{Dis2}$ antibodies at the high dilution that revealed the fluctuations in $PP1^{Dis2}$ levels in Fig. 1c. Graphs show the septation index alongside the $PP1^{Dis2}$ levels in each sample normalized to the level of the α-tubulin loading control and a sample from an asynchronous culture that was run on each gel. **e**, Samples from this $Rpn12^{mts3}$*.1* culture were split into three immediately after elution and one-third was maintained at the permissive temperature of 25 °C for the remainder of the experiment, another third was immediately shifted to 36 °C to inactivate this essential component of the proteasome 26S subunit[40], while the inactivating temperature shift of the remaining third was done 200 min later, after cells had completed one round of division at 25 °C. Note that the mitotic decline in $PP1^{Dis2}$ levels at the permissive temperature as cells progress from mitotic commitment to the metaphase anaphase transition is not seen at 36 °C when the proteasome function is inactivated, despite the fact that the chromosome condensation index indicates that over 60% of cells have arrested cell cycle progression with a metaphase spindle. **f**, **g**, $PP1^{Dis2}$ levels fail to oscillate when the Cdk1–cyclin B phosphorylation site at position T316 is mutated. A switch to the phospho-mimetic glutamic acid results in persistently low protein levels (**f**) while levels are persistently high upon mutation to alanine to block phosphorylation (**g**). Because these levels remain constant throughout the cell cycle these normalized levels have been superimposed upon the data from a wild-type culture in Fig. 1c to show each level relative to the oscillating wild-type protein levels. The septation profile in Fig. 1c is the profile for that wild-type culture. The septation profile in Fig. 1c does not contain any data from either of the cultures shown here in Extended Data Fig. 1f, g. The septation profiles for each mutant culture are shown in **f** and **g**. Biological replicates: for **b** and **c**, $n = 3$; for **d**, $n = 2$; for **e**–**g**, $n = 1$.

©2015 Macmillan Publishers Limited. All rights reserved



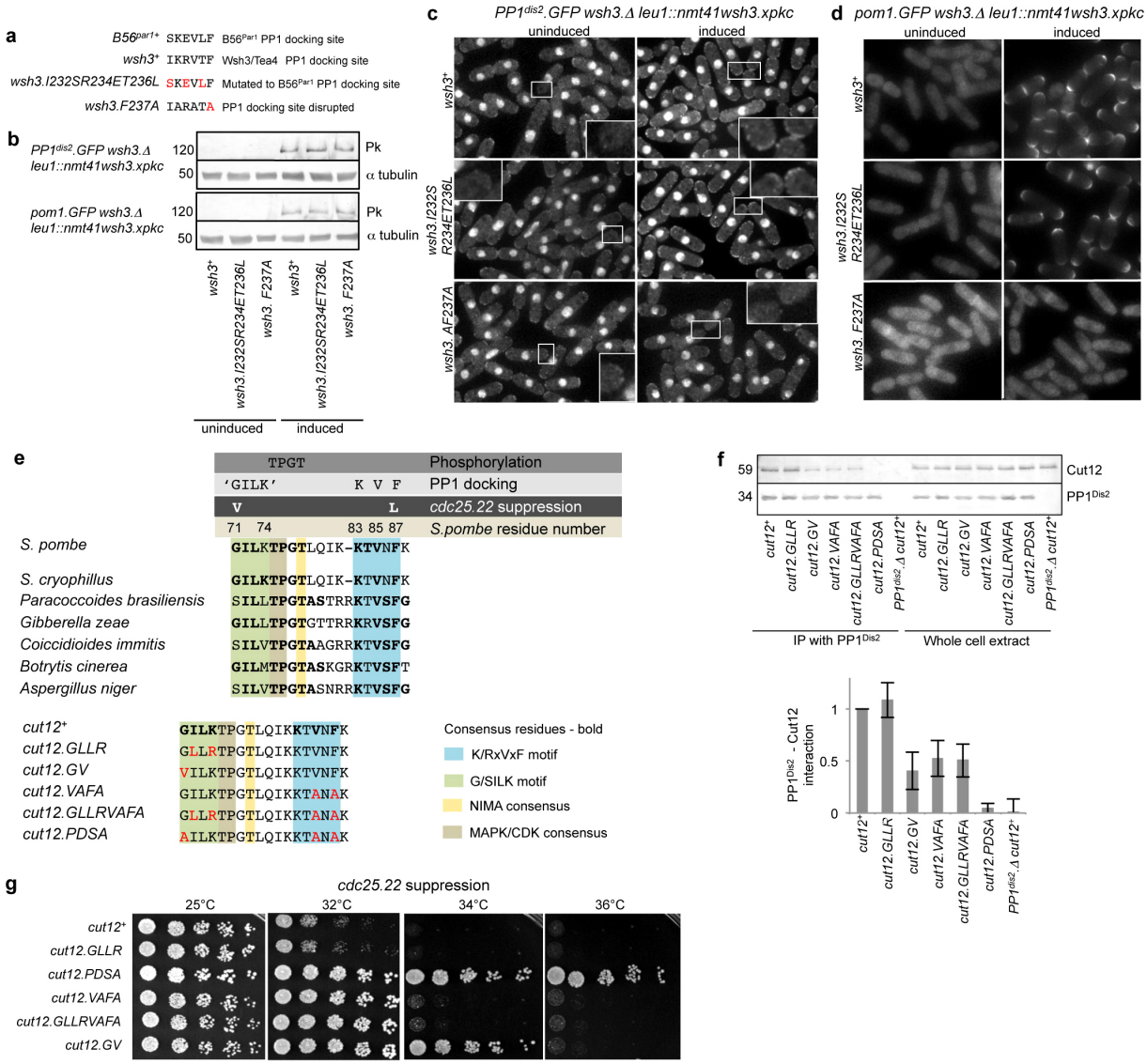
Extended Data Figure 2 | Association of PP1^{Dis2} with the PP2A regulatory subunits B56^{Par1} and B55^{Pab1}. **a**–**d**, Immunoprecipitation reactions in which PP1^{Dis2} polyclonal antibodies precipitated and detected PP1^{Dis2}, green fluorescent protein (GFP) antibodies precipitated and detected either PP1^{Dis2} or PP1^{Sds21} functional fusion proteins[19] or 12CA5 monoclonal antibodies precipitated HA-tagged B55^{Pab1} and B56^{Par1} regulatory subunits of the PP2A phosphatase, as indicated. These blots establish that the association between PP1^{Dis2} and both B56^{Par1} and B55^{Pab1} was independent of PP1^{Sds21} function. No association was detected between PP1^{Sds21} and any PP2A regulatory subunit (including B56^{Par2} (data not shown)). **b**, **c**, Red asterisks indicate a non-specific band that was detected by the anti-GFP antibodies. **d**, No association was detected between B56^{Par2} and PP1^{Dis2}, even when cell numbers in the precipitates were increased tenfold (numbers shown in red under the panel are $x \times 10^8$ cells per ml) to enhance the sensitivity of detection and the *B56^{par1+}* gene encoding the B56^{Par1} subunit was deleted in an attempt to remove any competition from this primary B56 isoform. **e**, Expression of *B56^{par2}.PkC* and *B56^{par2}. L482VPkC* genes from the pINT41PkC integration vector[32] was de-repressed by removal of thiamine. B56^{Par2} proteins (top) or PP1^{Dis2} (bottom) were precipitated with antibodies against the Pk epitope (top) or PP1^{Dis2} peptide (bottom), respectively, and these immunoprecipitation reactions were run alongside aliquots of the equivalent whole-cell extracts (WCE), before western blotting detected PP1^{Dis2} and B56^{Par2} fusion proteins. In both assays, the PP1-docking-site mutant in which the leucine of B56^{Par2} was replaced with the valine of B56^{Par1} (B56^{Par2}.L482V) associated with PP1 whereas the wild-type B56^{Par2} protein did not. Biological replicates: for **a**, $n = 6$; for other panels, $n = 2$.

©2015 Macmillan Publishers Limited. All rights reserved



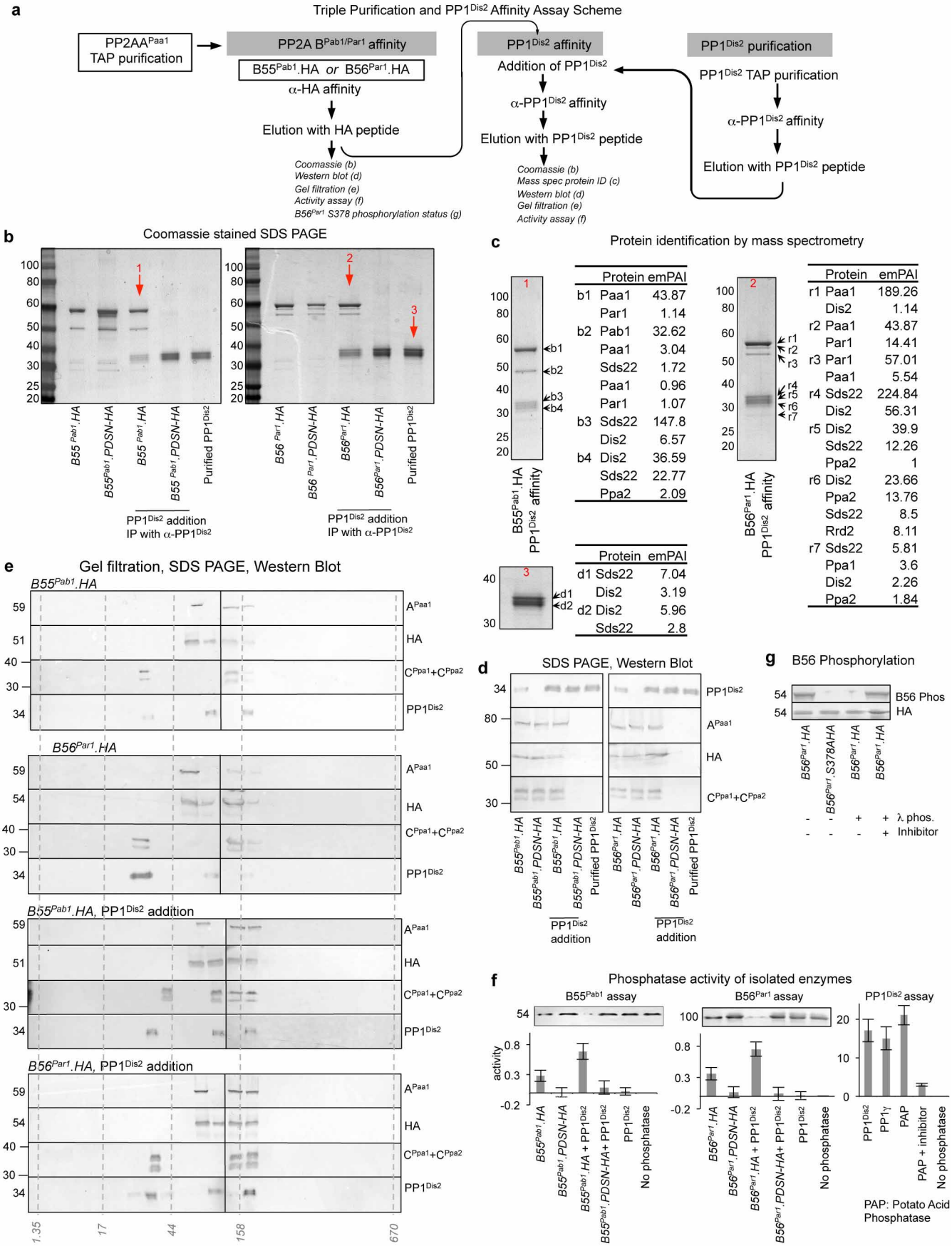
Extended Data Figure 3 | Yeast two-hybrid assays reveal docking-site-dependent association between B56^{Par1} and PP1^{Dis2}. **a**, Yeast two-hybrid assays in which *PP1*$^{dis2+}$ and *PP1*$^{sds21+}$ sequences were fused to the activating domain of Gal4 and the indicated version of the core homology domains of the PP2A regulatory subunits *B56*$^{par1+}$ (encoding amino acids 112–424) and *B56*$^{par2+}$ (encoding amino acids 213–525) were fused to the Gal4 DNA-binding domain according to the procedures of the matchmaker gold yeast two-hybrid system. **b**, Blotting the cell extracts with 12CA5 and 9E10 monoclonal antibodies that recognized HA and Myc epitopes within the cassettes harbouring the activation (HA) and DNA-binding domains (Myc) indicated that equivalent protein expression levels were achieved for each version of the protein. Probing for the DNA replication factor Ctf4 was used as a loading control[41]. Thus, the failure of the PP1-docking-site mutants to interact with *PP1*$^{dis2+}$ suggests that the change in the PP1-docking site abolished the affinity between the two molecules. Biological replicates: for **a**, $n = 3$; for **b**, $n = 1$.

©2015 Macmillan Publishers Limited. All rights reserved



Extended Data Figure 4 | Validation of the SKEVLF and GLLR motifs of the PP1-docking consensus site of B56^{Par1} in the polarity protein Wsh3 and the mitotic regulator Cut12. **a**–**d**, The morphology protein Wsh3 is required to recruit PP1^{Dis2} to cell tips[19]. Wsh3-recruited PP1 promotes the dephosphorylation of the DYRK family kinase Pom1 (ref. 42). Dephosphorylation of Pom1 promotes its association with the cell cortex. Subsequent auto-phosphorylation diminishes this newfound affinity for the cortex until the kinase loses its affinity for the cortex. Because Wsh3 is only found at cell tips, Pom1 only associates with the cortex at the tips[42]. We exploited this relationship to test the ability of the SKEVLF sequence in the PP1-docking consensus site of B56^{Par1} to function as a PP1^{Dis2}-docking site *in vivo*. **a**, The indicated *wsh3* alleles were cloned into the pINTL41PkN vector[32] and integrated at the *leu1* locus before introduction into *wsh3.Δ* background in which the endogenous *wsh3*$^{+}$ gene had been deleted. **b**, Expression of the transgenes was repressed by the addition of thiamine to culture medium (uninduced) before filtration into thiamine-free medium induced expression of each allele 24 h later (induced). **c**, PP1^{Dis2}.GFP was not enriched at cell tips in the absence of *wsh3* induction. Induction of the wild-type or *wsh3.I232SR234ET236L* allele in which the SKEVLF motif of the B56^{Par1} PP1^{Dis2}-docking site was substituted for the native IFRVTF motif of Wsh3 led to the recruitment of PP1^{Dis2}.GFP to cell tips whereas expression of the PP1-docking-site mutant *wsh3.F237A* failed to do so. **d**, Pom1 recruitment to cell tips upon expression of both the wild-type and SKEVLF alleles, but not the PP1-docking-site alleles, indicated that the PP1^{Dis2} recruited to Wsh3 by the SKEVLF allele was functionally indistinguishable from that recruited by the wild-type molecule. **e**–**g**, Commitment to mitosis is promoted by the activation of Cdk–cyclin B. Cdk1–cyclin B activity is regulated by the level of phosphorylation on threonine 14 and tyrosine 15 within its ATP-binding site. Wee1 kinase phosphorylates these residues while Cdc25 removes the phosphate to trigger mitotic commitment[43]. The lack of Cdc25 phosphatase activity achieved by incubating cells harbouring the temperature-sensitive *cdc25.22* mutation at temperatures above 34 °C kills cells because they are unable to remove the inhibitory phosphate from Cdk1. The *cut12.s11* and *cut12.s14* mutations enable *cdc25.22* cells to divide at 34 °C (refs 20, 44). *cut12.s11* is a G71V mutation at the start of a highly conserved bipartite PP1-docking site **GILK**TPGTLQIK**K**T**V**N**F** (the letters in bold indicate the residues that constitute the PP1-docking site). *cut12.s14* is a F87L mutation at the end of the same docking motif[20]. **e**, Alignment of the conserved PP1-docking site of Cut12 homologues from the indicated fungi and the mutations generated in each of the indicated *cut12* alleles. **f**, **g**, Mutation of the PP1-docking site of *S. pombe* Cut12 to abolish the function of either the GILK or the KxVxF motifs of Cut12 reduces PP1^{Dis2} association in immunoprecipitation assays (**f**) and suppresses the lethal mitotic commitment defect of *cdc25.22* (**g**). Simultaneous mutation of both motifs abolishes PP1 association in immunoprecipitation assays and confers a higher level of suppression of *cdc25.22* (**g**) that can enable cells to survive complete removal of *cdc25*$^{+}$ coding sequences[20]. We asked whether the GLLR sequence found upstream of the B56^{Par1} KxVxF motif (Fig. 2a) would substitute for the GILK sequence of Cut12 in both the co-immunoprecipitation and *cdc25.22* suppression assays; in both cases we found that it could. The association between PP1^{Dis2} and Cut12 in the *cut12.I72LK74R* mutant that converts the GILK motif to a GLLR was indistinguishable from wild type. Also, the G71V mutation of *cut12.s11* suppressed *cdc25.22* whereas *cut12.I72LK74R* did not (**g**). Thus, the function bestowed on Cut12 by the GILK sequence is fully maintained upon substitution with GLLR, indicating that GLLR is a functional variant of GILK. Error bars show s.d. Biological replicates: for **b**–**d**, $n = 1$; for **f**, $n = 5$; for **g**, $n = 3$.

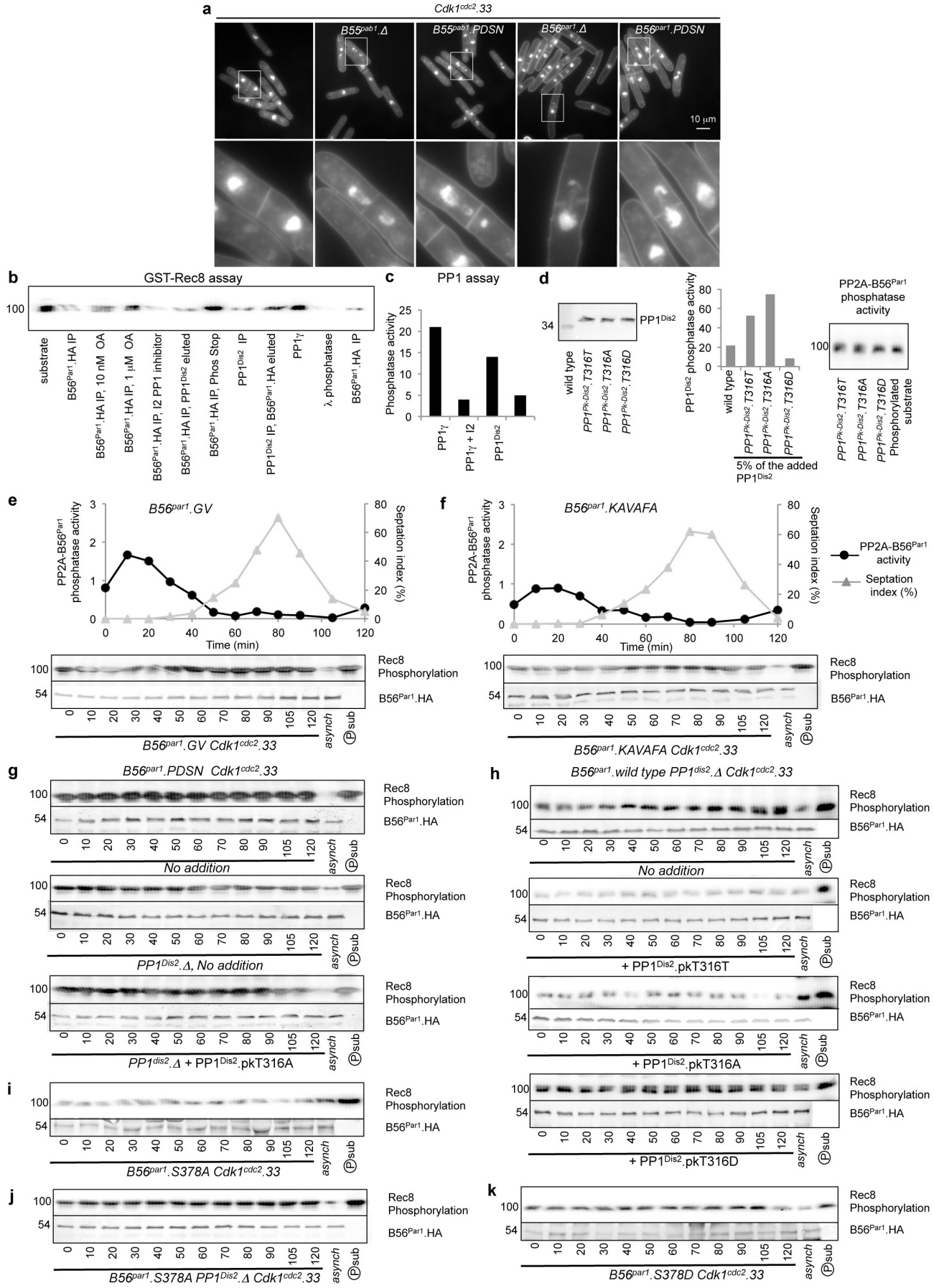
©2015 Macmillan Publishers Limited. All rights reserved



©2015 Macmillan Publishers Limited. All rights reserved

Extended Data Figure 5 | *In vitro* association of purified $PP1^{Dis2}$ with $PP2A\text{-}B55^{Pab1}$ and $PP2A\text{-}B56^{Par1}$ complexes in a docking-site-dependent manner. **a**–**g**, The tandem affinity purification steps used in Extended Data Fig. 10e were followed by immuno-affinity with antibodies directed against the HA epitope on $B55^{Pab1}$.HA, $B56^{Par1}$.HA fusion proteins or the unique sequence SQNWHMTPPRKNK in the C terminus of $PP1^{Dis2}$ (ref. 20) using anti-HA Affinity Matrix followed by elution with HA peptide, or Dynabeads A pre-loaded with $PP1^{Dis2}$ antibodies[20] followed by elution with the SQNWHMTPPRKNK peptide, respectively. **b**, Coomassie-stained 4–12% SDS–NUPAGE gradient gels. In each case the first two sample lanes show the purified wild-type and PDSN PP2A holoenzymes and the fifth lane shows the purified $PP1^{Dis2}$ enzyme. The quantity of $PP1^{Dis2}$ in the fifth lane was mixed with the quantity of each PP2A complex shown in lanes 1 and 2 before the $PP1^{Dis2}$ was re-isolated from the mixture with beads that bore $PP1^{Dis2}$ antibodies. This re-isolated $PP1^{Dis2}$ (and any associated partner molecules) was then eluted from these beads with the SQNWHMTPPRKNK peptide and the eluted proteins run in lanes 3 and 4 of each gel. For both the $B55^{Pab1}$ (left) and $B56^{Par1}$ (right) PP2A holoenzymes, the wild type but not the PDSN complex bound to $PP1^{Dis2}$. The numbered arrows indicate the lanes from which bands were excised for protein identification by mass spectrometry in **c**. **c**, Protein identification by mass spectrometry of the indicated bands from the lanes on the SDS–PAGE gels highlighted by the numbered arrows in **b**. emPAI scores[45] show that the purified $PP1^{Dis2}$ preparations used for the *in vitro* reconstitution reaction and run in lane 5 of the two gels in **b** also contained the conserved and well-characterized PP1 partner Sds22 (refs 46, 47). emPAI scores for the bands found in the reconstituted PP2A holoenzyme–PP1 complexes show that the predominant molecule identified in each complex corresponds with a known subunit of the PP2A complex, $PP1^{Dis2}$ or Sds22. **d**, Western blotting to detect the indicated components in the complexes used for **b** and **c**. The epitope-tagged regulatory $B55^{Pab1}$ and $B56^{Par1}$ molecules were detected with antibodies against the HA tag, while the catalytic C^{Ppa1} and C^{Ppa2} and scaffolding A^{Paa1} subunits of PP2A were detected with commercial antibodies. **e**, Western blots of gel filtration chromatography fractions of either the isolated PP2A holoenzyme complexes (top two blots) or the eluted PP2A holoenzyme/PP1 quaternary complexes (bottom two blots) corresponding to lanes 1 and 3 of the two SDS–NUPAGE gels of **b**. Note the very low level of $PP2A\text{-}B55^{Pab1}/PP1^{Dis2}$ and $PP2A\text{-}B56^{Par1}/PP1^{Dis2}$ quaternary complexes in the isolated PP2A holoenzyme preparations in the top two blots. Migration of the different complexes at the appropriate size suggests that the procedures used isolated correctly folded proteins. **f**, Phosphatase assays of the isolated enzymes used in **b**–**e** show that these molecules are active phosphatases and so the procedures used isolated functional, correctly folded complexes rather than denatured, inappropriately folded, proteins. Error bars show s.d. **g**, B56-Phos blots of the TAP- and HA-purified holoenzyme complex preparations used in **c** alongside a similarly purified $PP2A\text{-}B56^{Par1}$.S378A holoenzyme complex. Biological replicates: for **b**, $n = 3$; for **c** and **e**, $n = 1$; **d** and **g**, $n = 2$; for **f**, $n = 5$.

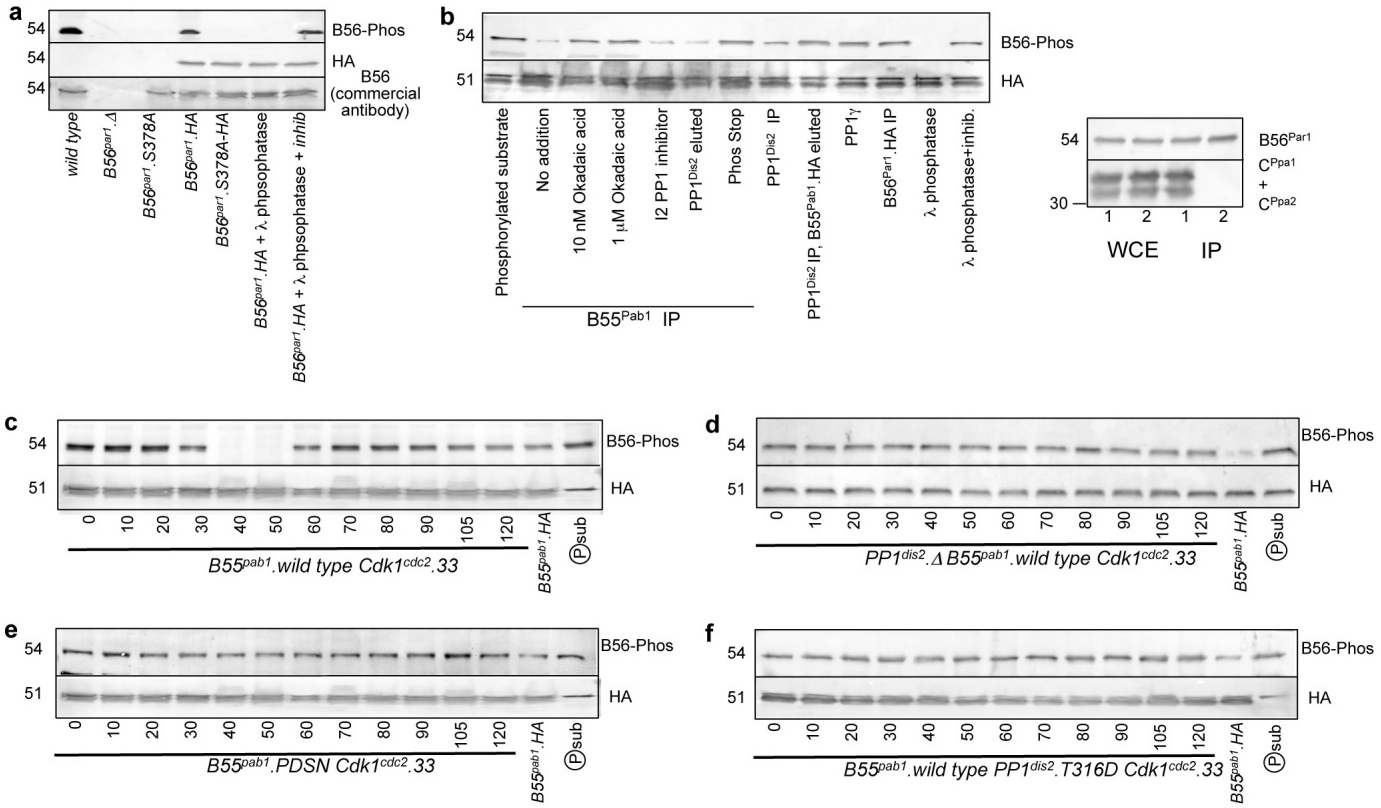
©2015 Macmillan Publishers Limited. All rights reserved



©2015 Macmillan Publishers Limited. All rights reserved

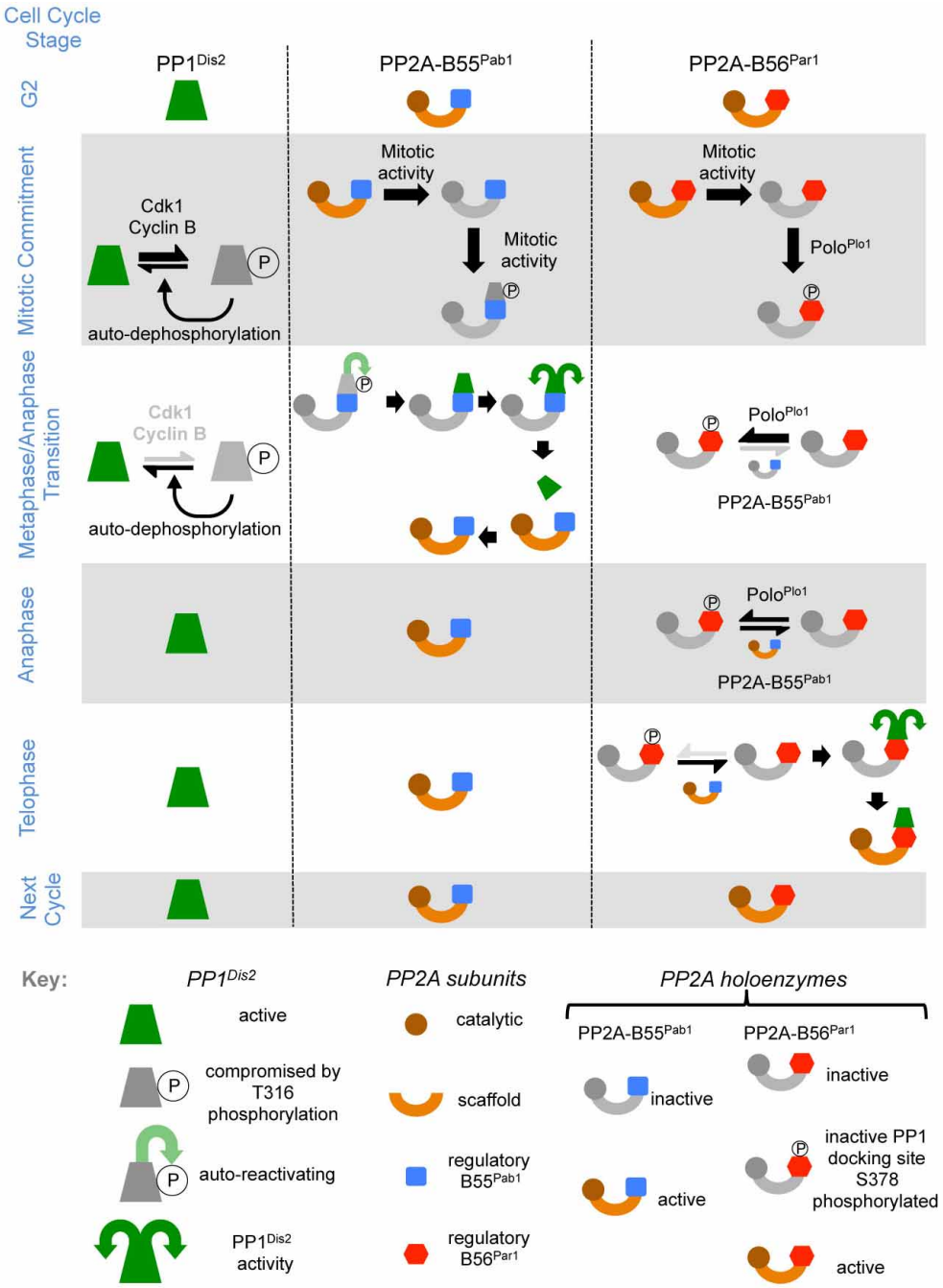
Extended Data Figure 6 | Mitotic enhancement of PP2A-B56 activity relies upon recruitment of active $PP1^{Dis2}$ and is required for accurate chromosome segregation. **a**, DAPI staining of the *Cdk1^{cdc2}.33* strains in which mitotic progression has been synchronized by transient arrest at the restrictive temperature of 36 °C. While two evenly sized chromatin masses are generated by the anaphase in wild-type cells, chromosome segregation is uneven in the mutant lines and lagging chromosomes are frequently observed. The frequency of phenotypes is presented in Fig. 2e. **b**, The PP2A-$B56^{Par1}$ phosphatase assay was carried out as previously described, in which recombinant GST–$Rec8^{391–561}$ was phosphorylated by a fusion between glutathione and *S. pombe* casein kinase I (Hhp2) that had also been produced in *Escherichia coli*[22]. PP2A-$B56^{Par1}$.HA was isolated from 2×10^8 cells with 12CA5 antibody under non-denaturing conditions. Phosphatase activity was calculated from the reduction of ^{32}P incorporation in the GST–$Rec8^{391–561}$ substrate per unit $B56^{Par1}$.HA. The level obtained in this assay (and every assay presented in this study) was normalized to the reduction in substrate phosphorylation displayed by a $B56^{Par1}$ precipitate from 2×10^8 cells of an asynchronous *B56^{par1}.HA* culture run on the same gel (the second lane in **b**). OA, okadaic acid. **c**, $PP1^{Dis2}$ activity assays conducted in parallel with the same samples used in **b**. These assays established that both the recombinant rabbit PP1γ and the $PP1^{Dis2}$ samples that were added to the PP2A-$B56^{Par1}$ assay in **a** contained PP1 phosphatase activity. We conclude that we have successfully re-established the phosphatase assays described previously[22] and that the addition of PP1 to this assay did not alter the phosphorylation status of the phosphorylated GST–Rec8 substrate, indicating that $PP1^{Dis2}$ displays no activity towards phosphorylated GST–Rec8 used in this PP2A-$B56^{Par1}$ enzyme assay. **d**, This panel presents blots of protein levels (left), $PP1^{Dis2}$ activity assays (centre) and PP2A-$B56^{Par1}$ phosphatase assays (right) of the $PP1^{Dis2}$ samples used in the add back experiments in **g** (bottom blot) and **h** (bottom three blots). The blot of $PP1^{Dis2}$ levels on the left shows that similar levels of the different $PP1^{Dis2}$ proteins were added in each case, while the central panel shows that these samples possessed $PP1^{Dis2}$ activity. The panel on the right shows that none of the $PP1^{Dis2}$ samples exhibited any activity in the PP2A-$B56^{Par1}$ phosphatase assay. In other words, there was no PP2A-$B56^{Par1}$ in these pull downs despite the fact that $PP1^{Dis2}$ is able to bind to PP2A-$B56^{Par1}$. The absence of PP2A-$B56^{Par1}$ from these samples is either due to the fact that only a minor fraction of the $PP1^{Dis2}$ complex formed a complex with PP2A-$B56^{Par1}$, or, as we anticipate, that the high salt (1.2 M NaCl) conditions we used in the immunopreciptation reactions that isolated these $PP1^{Dis2}$ molecules for the add back experiments (**g**, **h** and Fig. 3c, d) had disassociated any PP2A-$B56^{Par1}$ molecules that partnered these $PP1^{Dis2}$ molecules *in vivo*. **e**–**k**, PP2A-$B56^{Par1}$ assays as for **b**. A quantitative plot of the data in **g** (top blot) is shown in Fig. 3b while the data from **g** (bottom blot) and **h** are represented in the plots in Fig. 3c, d and data from **i**–**k** are shown in Fig. 3g–i. For the experiments in **g** (middle and bottom blots) and **h** we exploit the redundancy between $PP1^{Dis2}$ and $PP1^{Sds21}$ to use $PP1^{Sds21}$ to provide essential PP1 function and support the viability of *PP1^{dis2}.Δ* cells[2]. The PP2A-$B56^{Par1}$ complexes isolated from these cells have therefore never been exposed to $PP1^{Dis2}$ regulation and so will be fully phosphorylated on $PP1^{Dis2}$-target sites. The addition of $PP1^{Dis2}$ *in vitro* enables us to assess the impact of dephosphorylation of these sites. To ensure that there could be no cell cycle dependency to any outcome in these assays we assessed the impact of $PP1^{Dis2}$ addition on PP2A-$B56^{Par1}$ samples from all stages of a *Cdk1^{cdc2}.33* synchronized mitosis. The data from these experiments that are presented in Fig. 3 and in **d**, **g** and **h** clearly demonstrate that the addition of active $PP1^{Dis2}$ to naive PP2A-$B56^{Par1}$ complexes that have never been exposed to $PP1^{Dis2}$ *in vivo* was able to reactivate the PP2A activity as long as the $PP1^{Dis2}$-docking site within $B56^{Par1}$ was intact. In contrast, $PP1^{Dis2}$ addition failed to reactivate these naive PP2A-$B56^{Par1}$ complexes when the $PP1^{Dis2}$-docking site in $B56^{Par1}$ had been mutated to block $PP1^{Dis2}$ recruitment, or the Cdk1–cyclin B inhibition site at T316 of $PP1^{Dis2}$ had been mutated to aspartic acid to mimic the phosphorylated state. Biological replicates: for **b**, $n = 3$; for **c** and **d**, $n = 1$; for all other panels, $n = 2$.

©2015 Macmillan Publishers Limited. All rights reserved



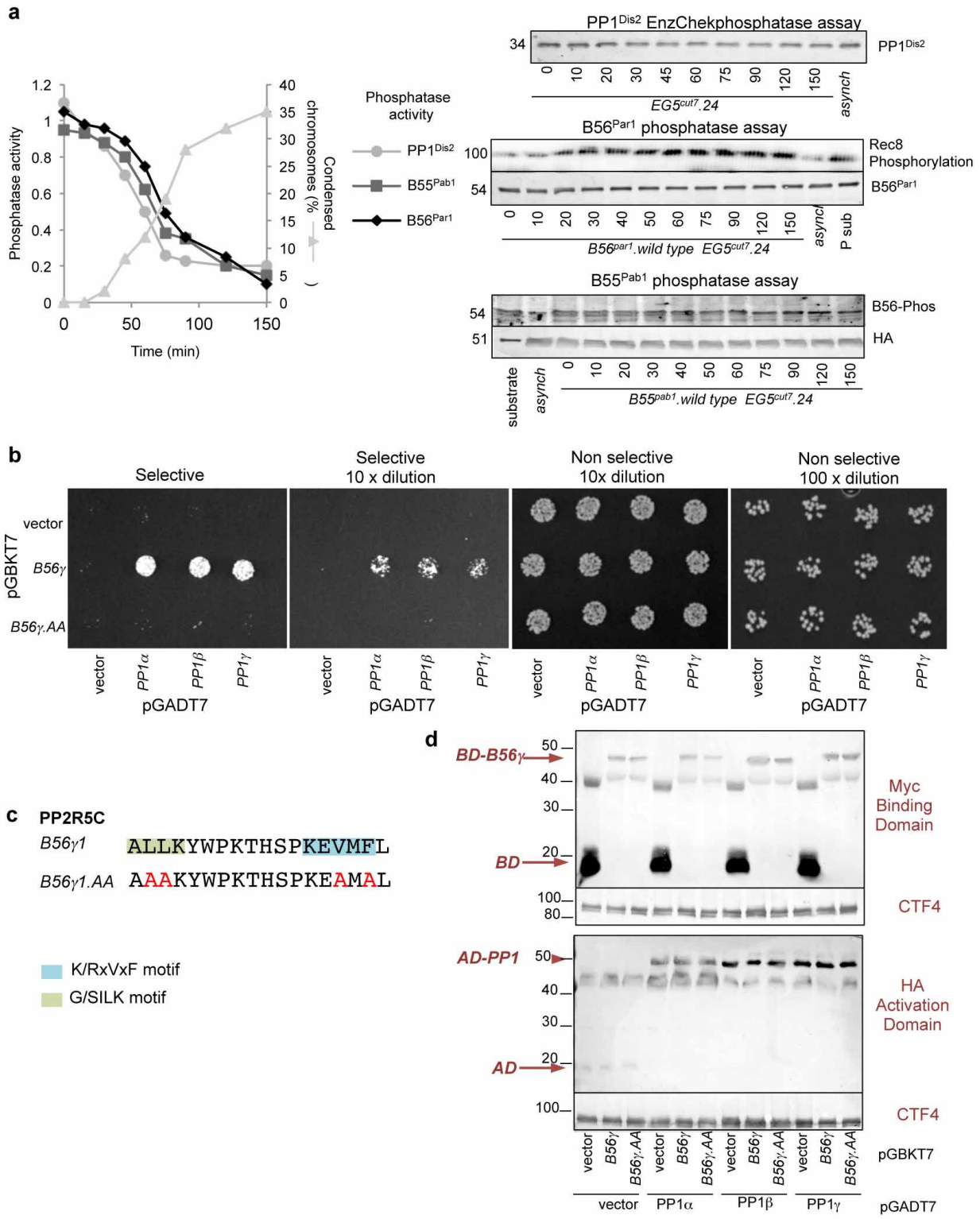
Extended Data Figure 7 | Residue 378 within the PP1-docking site of B56^{Par1} was dephosphorylated by PP2A-B55^{Pab1} that had been activated by PP1^{Dis2} recruitment to its own PP1-docking site. **a**, Validation of the B56-Phos antibody that was raised against and affinity purified with a peptide in which residues corresponding to S377 and S378 were each phosphorylated. Immunoprecipitates in which the 12CA5 monoclonal antibody was used to recognize the HA epitope on a B56^{Par1}.HA fusion protein or commercial rabbit antibodies raised against human B56ε were used to precipitate B56^{Par1} and probed as indicated. **b**, Validation of the PP2A-B55^{Pab1} activity assay. This assay exploits the fact that PP2A-B55^{Pab1} removes B56-Phos reactivity from B56^{Par1}.HA. The phosphorylated B56^{Par1}.HA substrate was precipitated from cells in which mitotic progression had been arrested by incubation of *Eg5^{cut7}.24* cells at the restrictive temperature for 3 h. *Eg5^{cut7}.24* is a temperature-sensitive mutation in the kinesin 5 motor protein that is required for interdigitation of the two halves of the bipolar spindle[36]. To ensure that these B56^{Par1} precipitates were free of any B56^{Par1} partners, the total protein content of intact cells was precipitated by trichloroacetic acid (TCA) treatment before cells were homogenized and resuspended in 2% SDS. After a centrifugation clearing step, the addition of 1% Triton X-100 to the resultant supernatant sequestered the SDS into micelles thereby generating conditions for immunoprecipitation (IP) of phosphorylated B56^{Par1}.HA substrate. Lane 2 on the right shows that that this procedure disassociated the B56^{Par1} subunit from the other subunits of the tripartite PP2A-B56 complex whereas non-denaturing immunoprecipitation conditions (lane 1) do not. The C^{Ppa1} and C^{Ppa2} catalytic subunits are detected with a commercial antibody. The B56^{Par1} samples generated in this way were incubated with the indicated components. 'Eluted' indicates reactions in which the B55^{Pab1} immunoprecipitate was incubated with a peptide corresponding to the PP1^{Dis2}-docking site on B56^{Par1} (CWPKVNSSKEVLF) to disassociate the PP1^{Dis2} enzyme from the PP2A-B55^{Pab1} complex before a re-purification isolated the PP1^{Dis2} complex once more. It was this re-isolated PP1^{Dis2} that was used for the assay in lane 9 while the residual PP2A-B55^{Pab1} was used in the assay in lane 6. The impact of this disassociation can be seen by comparing lanes 8 and 9. The PP1^{Dis2} immunoprecipitate exhibited a low level of B56-Phos phosphatase activity when the elution step was not performed. Displacement of partner molecules through peptide incubation removed the activity that reduced B56-Phos reactivity in the uneluted PP1^{Dis2} precipitates. The inhibitor profiles all support the conclusion that this assay specifically detected PP2A-B55^{Pab1} activity. Phos-Stop is a commercial pan-phosphatase inhibitor. **c**–**f**, PP2A-B55^{Pab1} activity assays of cultures in which mitotic progression had been synchronized by the *Cdk1^{cdc2}.33* arrest/release protocol. The quantification of these assays is presented in Fig. 4f–i. Biological replicates: $n = 2$ for all panels except the right panel of **b**, where $n = 1$.

©2015 Macmillan Publishers Limited. All rights reserved



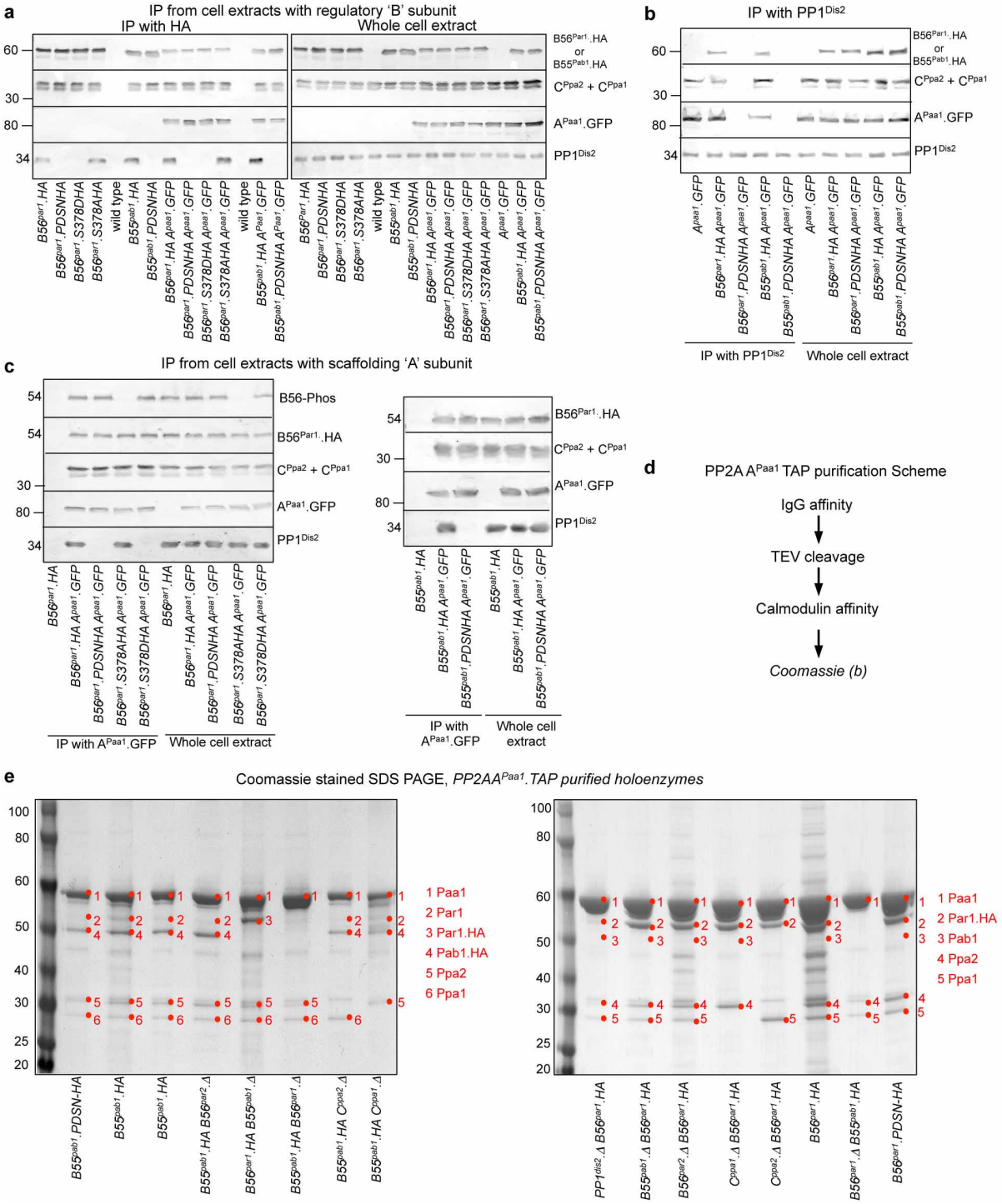
Extended Data Figure 8 | Mitotic control of phosphatase activities. A schematic representation of the control and activity levels of the three phosphatase activities. This view is derived from bulk activity assays. We believe that localized reactions at particular times at discrete locations will differ; however the basic relationships between the three phosphatases outlined here will apply. Left, as previously established in a number of studies[1,7–10], $PP1^{Dis2}$ activity is repressed by Cdk1–cyclin B phosphorylation upon mitotic commitment through phosphorylation on T316 at a rate that exceeds the rate at which auto-dephosphorylation reactivates inhibited PP1. $PP1^{Dis2}$ T316 phosphorylation also targets $PP1^{Dis2}$ for destruction to further reduce $PP1^{Dis2}$ activity, although the majority of the protein persists. It is currently unclear whether this reflects a highly localized destruction of a particular pool of $PP1^{Dis2}$ in its entirety or a rate of destruction across the population that is simply too slow to outcompete synthesis. Cyclin B destruction curtails the inhibitory phosphorylation on T316, enabling $PP1^{Dis2}$ to auto-reactivate and persist in an active state for the remainder of mitosis. Middle, $PP2A\text{-}B55^{Pab1}$ activity is inhibited upon mitotic commitment (Extended Data Fig. 9a). The mechanism by which this inhibition is achieved is currently unclear. The inactivated $PP2A\text{-}B55^{Pab1}$ recruits T316-phosphorylated (and therefore catalytically compromised) $PP1^{Dis2}$ upon mitotic commitment. Cyclin B destruction upon the metaphase/anaphase transition promotes $PP1^{Dis2}$ reactivation (left). The reactivation of the $PP2A\text{-}B55^{Pab1}$-associated $PP1^{Dis2}$ enables this $PP1^{Dis2}$ to reactivate $PP2A\text{-}B55^{Pab1}$. $PP1^{Dis2}$ then disassociates from $B55^{Pab1}$. The molecular basis for the staged association between $PP1^{Dis2}$ and $B55^{Pab1}$ upon mitotic commitment and dissociation at the metaphase/anaphase transition remains to be established. $PP2A\text{-}B55^{Pab1}$ persists in an active state for the remainder of mitosis. Right, $PP2A\text{-}B56^{Par1}$ activity is inhibited upon mitotic commitment (Extended Data Fig. 9a). The mechanism by which this inhibition is achieved is currently unclear. $Polo^{Plo1}$ activation upon mitotic commitment enables it to phosphorylate S378 within the PP1-docking site on $B56^{Par1}$ to block $PP1^{Dis2}$ recruitment to this B′ regulatory subunit of the PP2A-B56 holoenzyme. This phosphorylation persists to block $PP1^{Dis2}$ recruitment until telophase when the balance between $Polo^{Plo1}$ kinase and $PP2A\text{-}B55^{Pab1}$ phosphatase activities tips in favour of $PP2A\text{-}B55^{Pab1}$ to remove phosphate from S378, thereby promoting the recruitment of active, T316-dephosphorylated $PP1^{Dis2}$. $PP1^{Dis2}$ recruitment enables this phosphatase to reactivate the $PP2A\text{-}B56^{Par1}$ holoenzyme.

©2015 Macmillan Publishers Limited. All rights reserved



Extended Data Figure 9 | PP1^{Dis2}, PP2A-B55^{Pab1} and PP2A-B56^{Par1} activities decline as cells arrest cell cycle progression in mitosis, and the association between human PP1 and PP2A-B56 isoforms. **a**, The temperature of *Eg5^{cut7}.24 B55^{pab1}.HA*, *Eg5^{cut7}.24 B56^{par1}.HA* and *Eg5^{cut7}.24* cultures that had been grown overnight to early log phase in supplemented EMM2 medium at 25 °C was increased to 36 °C at $t = 0$ to inactivate this kinesin 5 and so arrest cell cycle progression in mitosis[36]. Samples were taken for the phosphatase assays and to monitor the degree of mitotic arrest by scoring the frequency of cells with condensed chromosomes[36]. Protein phosphatase assays were conducted as described for Extended Data Figs 1b, 6b and 7b. Each activity declined as there was an increase in the frequency of cells in which the inability to form a bipolar spindle has triggered a mitotic arrest due to activation of the spindle assembly checkpoint. **b**, Two-hybrid assays with the indicated human PP1 isoforms with wild-type and mutant isoforms of the conserved core domain (sequences encoding amino acids 84–400) of human B56γ. **c**, The mutations introduced in each case. **d**, Blotting the cell extracts from the two-hybrid clones shown in **b** with 12CA5 and 9E10 monoclonal antibodies that recognized HA and Myc epitopes within the cassettes harbouring the Gal4 activation and DNA-binding domains, respectively, indicated that equivalent protein expression levels were achieved for each version of the protein. Thus, the failure of the PP1-docking site mutants indicates that the change in the PP1-docking site abolished the affinity between the two molecules. Biological replicates: for **a** and **d**, $n = 1$; for **b**, $n = 3$.

©2015 Macmillan Publishers Limited. All rights reserved



Extended Data Figure 10 | PP1-docking-site mutations do not alter the stoichiometry of PP2A subunits in immunoprecipitation assays or of holoenzymes isolated by TAP-tag purification. **a**–**c**, Immunoprecipitation reactions from cell extracts of the indicated strains in which the 12CA5 antibodies were used to precipitate epitope-tagged versions of the $B55^{Pab1}$ or $B56^{Par1}$ PP2A regulatory subunits or in which polyclonal antibodies against GFP were used to precipitate a GFP-tagged version of the A^{Paa1} PP2A scaffolding subunit. Although mutation of either the PP1-docking site motif sequences or the *B56^{par1}.S378D* mutation abolished PP1 precipitation with each PP2A holoenzyme, they had no impact upon the stoichiometry of PP2A subunits precipitating with either the regulatory or the scaffolding subunits. We conclude that the PP1-docking site mutations do not alter the integrity of the PP2A-B55 or PP2A-B56 holoenzyme complexes. The ability to detect S377/S378 phosphorylation in A^{Paa1} precipitates consolidates the data in Extended Data Fig. 5g to demonstrate that this site between the two elements of the PP1-docking site of $B56^{Par1}$ can be phosphorylated in the PP2A-$B56^{Par1}$ holoenzyme complexes. Catalytic C^{Ppa1} and C^{Ppa2} and the scaffolding A^{Paa1} subunits of PP2A were detected with commercial antibodies. **d**, The tandem affinity purification scheme used to isolate PP2A phosphatases from yeast cultures via the TAP tag fused to the scaffolding A^{Paa1} subunit. **e**, Coomassie-stained 4–12% SDS–NUPAGE gradient gels of A^{Paa1}.TAP purifications of the indicated strains. The disappearance of bands upon gene deletion combined with mass spectrometric analysis of isolated bands after a further round of purification (Extended Data Fig. 5b, c) confirms that this procedure isolates PP2A enzymes. The persistence of the wild-type pattern in *B55^{pab1}.PDSN*, *B56^{par1}.PDSN* and *B56^{par1}.S378A* strains indicates that these mutations do not alter the composition of either PP2A holoenzyme, that is, they do not alter the structural bonds that maintain the integrity of the PP2A holoenzyme complexes, as predicted from existing current crystal structures of PP2A holoenzyme complexes[28–30]. Biological replicates: for all panels, $n = 2$.

©2015 Macmillan Publishers Limited. All rights reserved

LETTER

doi:10.1038/nature13991

Native structure of photosystem II at 1.95 Å resolution viewed by femtosecond X-ray pulses

Michihiro Suga[1]*, Fusamichi Akita[1]*, Kunio Hirata[2,3], Go Ueno[2], Hironori Murakami[2], Yoshiki Nakajima[1], Tetsuya Shimizu[1], Keitaro Yamashita[2], Masaki Yamamoto[2], Hideo Ago[2] & Jian-Ren Shen[1]

Photosynthesis converts light energy into biologically useful chemical energy vital to life on Earth. The initial reaction of photosynthesis takes place in photosystem II (PSII), a 700-kilodalton homodimeric membrane protein complex that catalyses photo-oxidation of water into dioxygen through an S-state cycle of the oxygen evolving complex (OEC). The structure of PSII has been solved by X-ray diffraction (XRD) at 1.9 ångström resolution, which revealed that the OEC is a Mn_4CaO_5-cluster coordinated by a well defined protein environment[1]. However, extended X-ray absorption fine structure (EXAFS) studies showed that the manganese cations in the OEC are easily reduced by X-ray irradiation[2], and slight differences were found in the Mn–Mn distances determined by XRD[1], EXAFS[3–7] and theoretical studies[8–14]. Here we report a 'radiation-damage-free' structure of PSII from *Thermosynechococcus vulcanus* in the S_1 state at a resolution of 1.95 ångströms using femtosecond X-ray pulses of the SPring-8 ångström compact free-electron laser (SACLA) and hundreds of large, highly isomorphous PSII crystals. Compared with the structure from XRD, the OEC in the X-ray free electron laser structure has Mn–Mn distances that are shorter by 0.1–0.2 ångströms. The valences of each manganese atom were tentatively assigned as Mn1D(III), Mn2C(IV), Mn3B(IV) and Mn4A(III), based on the average Mn–ligand distances and analysis of the Jahn–Teller axis on Mn(III). One of the oxo-bridged oxygens, O5, has significantly longer distances to Mn than do the other oxo-oxygen atoms, suggesting that O5 is a hydroxide ion instead of a normal oxygen dianion and therefore may serve as one of the substrate oxygen atoms. These findings provide a structural basis for the mechanism of oxygen evolution, and we expect that this structure will provide a blueprint for the design of artificial catalysts for water oxidation.

PSII is a multi-subunit pigment-protein complex embedded in the thylakoid membranes of higher plants, green algae and cyanobacteria, and is the only molecular machine capable of oxidizing water by use of visible light. Water molecules are split into electrons, hydrogen atoms and oxygen molecules at the catalytic centre of PSII, namely, the OEC, through four electron and/or proton removing steps as described in the S_i-state cycle (with $i = 0$–4, where i indicates the number of oxidative equivalents accumulated). Because of its ability to split water, the OEC is considered a promising template for the synthesis of artificial catalysts for water-splitting aimed at obtaining clean and renewable energy from sunlight, which is considered a promising way to supplement the consumption of limited and environmentally unfriendly fossil fuels.

In order to elucidate the mechanism of the water-splitting reaction, the structure of PSII has been studied extensively by XRD, with a resolution that has gradually increased from 3.8 to 1.9 Å using synchrotron radiation (SR) X-ray sources[1,15–18]. In particular, the SR structure of PSII at atomic resolution revealed that the OEC is a Mn_4CaO_5 cluster organized into a distorted-chair shape, in which the cuboidal part is composed of Mn_3CaO_4 and the outer manganese is attached via two μ-oxo-bridges[1]. The high-resolution structure also revealed that four water molecules are coordinated to the Mn_4CaO_5 cluster, among which, two are coordinated to the Ca^{2+} ion and two are attached to the outer manganese[1] (designated Mn4A; the naming of the Mn ions employed in this study combines the nomenclatures of those used in the EXAFS[4] and XRD[1] studies). Although these provided an important structural basis for the mechanism of water-splitting, the average Mn–ligand and Mn–Mn distances were found to be slightly longer than those deduced from EXAFS[3–7] and from computational analysis based on the SR structure[8–14]. This has been suggested to result from radiation damage, as hydrated electrons generated by X-ray irradiation[19] are able to reduce metal catalytic centres (such as the OEC in PSII) rapidly, although the SR PSII structure at 1.9 Å resolution was obtained with an X-ray dose much reduced compared to those used previously[15–18]. Based on the EXAFS analysis, the dose used for collecting the SR structure at 1.9 Å resolution may cause 25% of the Mn ions in the OEC to be reduced to 2+ ions[2]. Such radiation damage to biological samples is inevitable with SR X-ray sources, since the shortest time to collect a diffraction image is of the order of one second, which is long enough for structural changes to occur upon breakage of covalent bonds by the radicals generated by the strong X-ray irradiation.

In order to eliminate the radiation damage, a new approach employing a femtosecond X-ray free electron laser (XFEL) has been developed which demonstrated that a radiation-damage-free structure may be obtained by using the ultra-short and high-brilliance XFEL pulses to collect diffraction images before the onset of radiation damage (a 'diffraction before destruction' approach)[20]. So far XFEL has been mainly used to collect diffraction data from nanocrystals using the method of serial femtosecond crystallography (SFX), in which a stream of nanometre-to-micrometre sized crystals flows across the XFEL beam and a large number of single-crystal diffraction data are collected in random orientations at room temperature, and the data obtained are processed by a Monte Carlo approach[21–23]. However, as diffraction intensities are proportional to the diffraction volume and inversely proportional to the unit cell volume[24], the resolution obtainable with this method is limited, especially for large membrane protein complexes such as PSII and cytochrome *c* oxidase (C*c*O), whose unit cell volumes exceed 6 MÅ^3. In addition, the nanometre–micrometre sized crystals used for SFX are often obtained under sub-optimal conditions, and their properties are easily affected by post-crystallization handling procedures; all of these will limit the resolution of large membrane protein crystals. Very recently, it was demonstrated that a radiation-damage-free structure can be obtained from large crystals using the XFEL beam by collecting still diffraction images at a cryogenic temperature from well separated positions in a crystal and by using a number of large, highly isomorphous crystals. This method has been used successfully to obtain a radiation-damage-free structure of C*c*O at 1.9 Å resolution[25]. Here we determined the radiation-damage-free structure of PSII in the dark-stable S_1 state by use of this method and hundreds of large PSII crystals with high isomorphism.

[1]Photosynthesis Research Center, Graduate School of Natural Science and Technology, Okayama University, 3-1-1 Tsushima Naka, Okayama 700-8530, Japan. [2]RIKEN SPring-8 Center, 1-1-1 Kouto Sayo, Hyogo 679-5148, Japan. [3]Japan Science and Technology Agency (JST), Core Research for Evolutional Science and Technology (CREST), Kawaguchi, Saitama 332-0012, Japan.
*These authors contributed equally to this work.

©2015 Macmillan Publishers Limited. All rights reserved

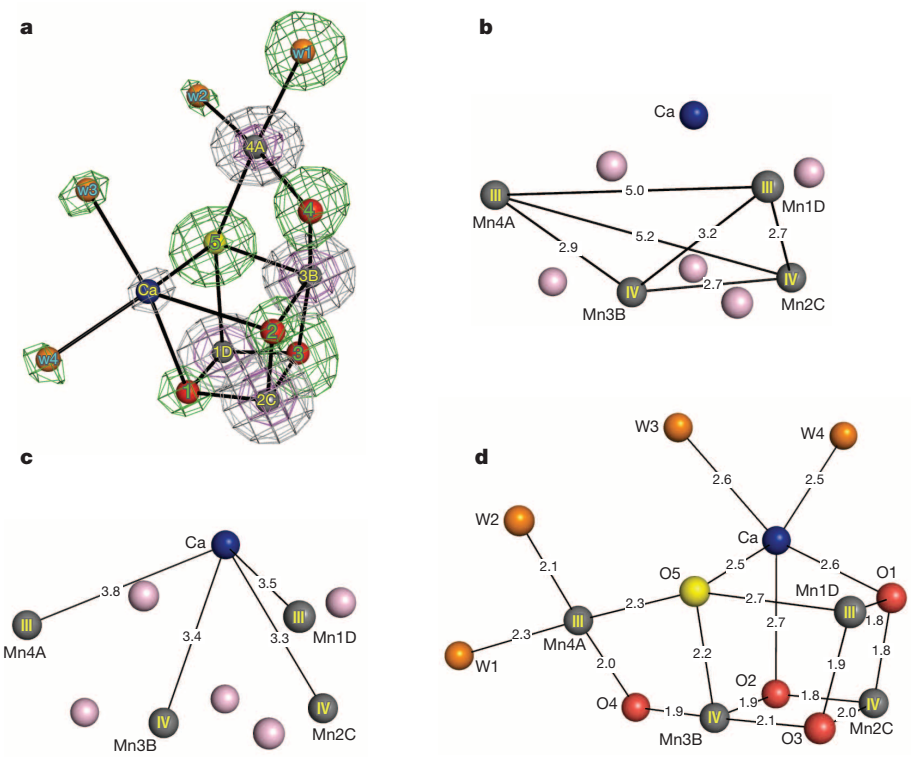


Figure 1 | Atomic structure of the OEC by XFEL. **a**, Electron density maps of the OEC. Grey, $2mF_o - DF_c$ map contoured at 7σ; magenta, $2mF_o - DF_c$ map contoured at 15σ; green, $mF_o - DF_c$ map contoured at 6σ. The $2mF_o - DF_c$ map was calculated before placing any atoms in the OEC, and the $mF_o - DF_c$ map was calculated after introducing the manganese and calcium atoms but without the oxygen atoms and water molecules. Colour codes for atoms: grey, manganese; blue, calcium; red, oxo-oxygen; yellow, O5; orange, water. Numbers 1–4 in the red spheres indicate O1–O4 atoms, and 1D, 2C, 3B and 4A indicate the four manganese ions named by a combination of crystal structure and previous EXAFS numbering. **b**, Mn–Mn distances in the OEC (in Å). Roman numerals in the spheres indicate the valence of manganese atoms assigned in this work. Oxygen atoms in the OEC are shown pink. **c**, Mn–Ca distances in the OEC (in Å). **d**, Mn–O, Ca–O, Mn–water and Ca–water distances in the OEC (in Å).

Still diffraction images were collected with XFEL provided by SACLA and large PSII crystals ($1.2 \times 0.5 \times 0.2$ mm). Each irradiation point on a crystal was separated by 50 μm (Extended Data Fig. 1a, b), which has been shown to be enough to avoid the effect of radiation damage from the previous irradiation point[25] (see Methods). The crystals were rotated in steps of 0.2° following the previous irradiation, which was smaller than one-third of the typical mosaic spread of the PSII crystals; this ensured data quality high enough for the subsequent structural refinement[25]. Diffraction spots up to 1.85 Å resolution were observed (Extended Data Fig. 2); we collected two independent data sets, data set 1 with 5,592 still images from 254 crystals, and data set 2 with 2,058 images from 82 crystals, from which two complete data sets were processed, both to 1.95 Å resolution. The total absorbed dose and photon density of each irradiation point for both data sets were 1.4 MGy and 0.26×10^{10} photons per μm^2, respectively, which were approximately equal to that each irradiation point received in the SR data set used for the analysis of the 1.9 Å structure[1]. Structure analysis was performed as described in Methods, and the statistics for the diffraction experiments and structural refinement

Table 1 | OEC interatomic distances obtained using XFEL and SR techniques

	XFEL	SR		XFEL	SR		XFEL	SR
Mn–Mn			**Ca–O**			**B-factor**		
Mn1D–Mn2C	2.68 (0.05)*	2.8	Ca–O1	2.61 (0.03)*	2.4	Mn1D	23.4 (3.3)*	24.3
Mn1D–Mn3B	3.20 (0.08)*	3.3	Ca–O2	2.67 (0.06)*	2.5	Mn2C	23.4 (1.4)*	24.8
Mn1D–Mn4A	4.95 (0.04)*	5.0	Ca–O5	2.54 (0.08)*	2.7	Mn3B	22.0 (2.2)*	24.5
Mn2C–Mn3B	2.70 (0.03)*	2.9				Mn4A	23.4 (1.6)*	27.5
Mn2C–Mn4A	5.21 (0.04)*	5.4	**Water**			Ca	33.0 (3.8)*	26.0
Mn3B–Mn4A	2.87 (0.03)*	3.0	Mn4A–W1	2.25 (0.08)*	2.2	O1	23.3 (3.6)*	23.8
			Mn4A–W2	2.10 (0.09)*	2.2	O2	22.6 (2.1)*	26.3
Mn–Ca			Ca–W3	2.60 (0.01)*	2.4	O3	26.3 (6.5)*	25.2
Mn1D–Ca	3.47 (0.03)*	3.5	Ca–W4	2.47 (0.04)*	2.5	O4	20.7 (2.1)*	27.2
Mn2C–Ca	3.32 (0.03)*	3.4	O5–W2	3.00 (0.09)*	3.1	O5	17.7 (2.3)*	26.1
Mn3B–Ca	3.40 (0.06)*	3.4	O5–W3	3.12 (0.13)*	3.1	Overall OEC	23.6 (2.0)*	25.6
Mn4A–Ca	3.77 (0.06)*	3.8	W2–W3	3.26 (0.09)*	3.3	All atoms	35.1	35.2
Mn–O			**Ligand**					
Mn1D–O1	1.80 (0.05)*	1.9	Mn1D–E189	1.79 (0.02)*	1.9			
Mn1D–O3	1.87 (0.08)*	1.8	Mn1D–H332	2.12 (0.03)*	2.2			
Mn1D–O5	2.70 (0.01)*	2.6	Mn1D–D342	2.22 (0.05)*	2.3			
Mn2C–O1	1.82 (0.07)*	2.1	Mn2C–D342	2.13 (0.04)*	2.2			
Mn2C–O2	1.83 (0.07)*	2.1	Mn2C–A344	1.90 (0.06)*	2.0			
Mn2C–O3	2.02 (0.06)*	2.1	Mn2C–E354†	2.13 (0.05)*	2.2			
Mn3B–O2	1.90 (0.12)*	1.9	Mn3B–E333	2.06 (0.03)*	2.1			
Mn3B–O3	2.06 (0.07)*	2.1	Mn3B–E354†	2.13 (0.02)*	2.2			
Mn3B–O4	1.90 (0.02)*	2.1	Mn4A–D170	2.03 (0.04)*	2.1			
Mn3B–O5	2.20 (0.14)*	2.4	Mn4A–E333	2.08 (0.02)*	2.2			
Mn4A–O4	2.02 (0.05)*	2.1	Ca–D170	2.36 (0.08)*	2.4			
Mn4A–O5	2.33 (0.03)*	2.5	Ca–A344	2.43 (0.01)*	2.5			

The Mn–Mn, Mn–Ca, Mn–O, Ca–O, water and ligand distances are given in Å. Values for the XFEL structure are the average of four monomers, whereas values for the SR structure are the average of two monomers.
* Numbers in parentheses represent standard derivations calculated from four PSII monomers. For the individual values in each monomer, see Extended Data Table 2.
† Residue from the CP43 protein.

©2015 Macmillan Publishers Limited. All rights reserved

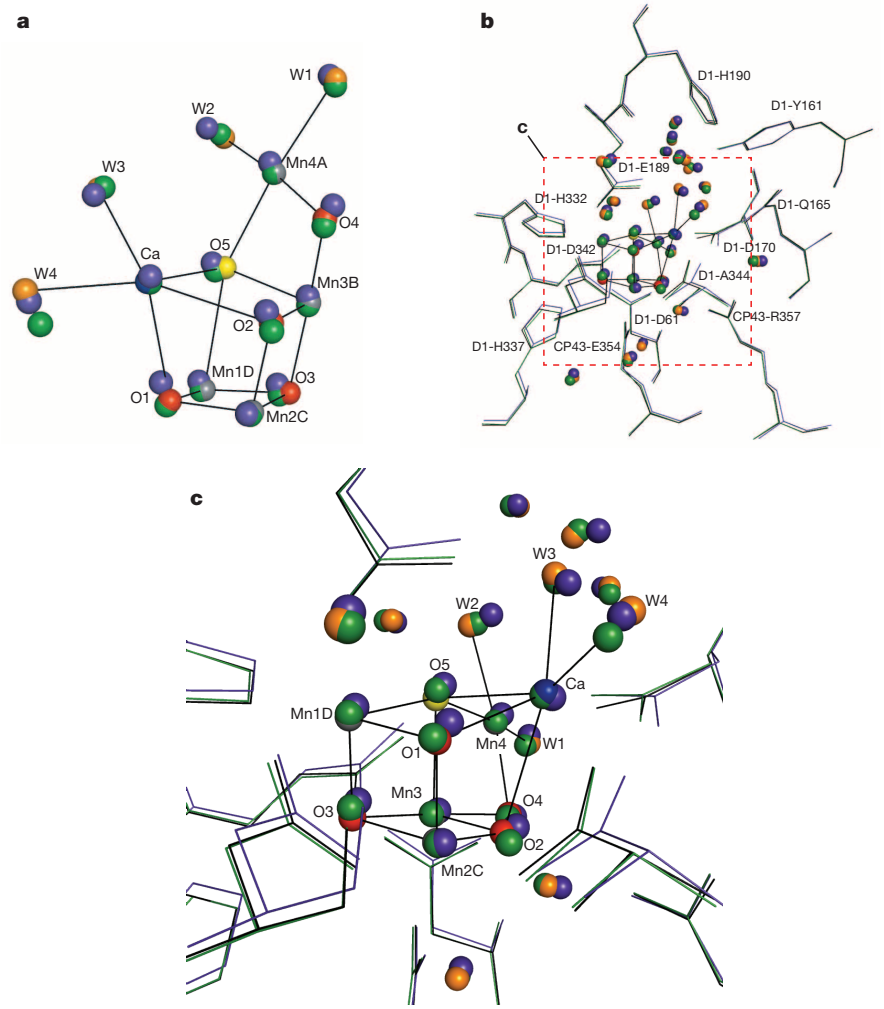


Figure 2 | Comparison of the OEC structures obtained by XFEL and SR. **a**, Superposition of three OEC structures, two from XFEL and one from SR. The OEC is depicted as in Fig. 1a. **b**, Superposition of the OEC and its ligand environment from the three structures. For clarity, the structures are rotated relative to that shown in **a**. Additional water molecules close to the OEC are also shown as spheres. **c**, An enlarged view of the region boxed by red dashed lines in **b**. In all three panels, the structure from XFEL data set 1 is coloured by atomic element as in Fig. 1a. Structures from XFEL data set 2 and SR are coloured in green and purple, respectively.

are given in Extended Data Table 1. The R_{free} values were 0.238 (data set 1) and 0.225 (data set 2), which, together with the 1.95 Å resolution, allowed us to build the structure of the OEC unambiguously. In this structure, the positions of heavy metals were confirmed clearly, even in the anomalous difference Fourier map (Fig. 1a, Extended Data Fig. 3a, b). In fact, the *B*-factors for the OEC atoms (23.6 Å^2) were found to be lower than those observed in the overall protein atoms of both XFEL (35.1 Å^2) and SR (35.2 Å^2) structures (Table 1, Extended Data Tables 1 and 2), showing the reliability of the OEC structure. Nevertheless, we repeated the same experiments using the crystals from different preparations in the two data sets to verify the reproducibility of the bond distances within the OEC, which showed a very good agreement among the four PSII monomers in the two independent dimer structures.

The overall architecture of the OEC in the XFEL structure is very similar to that of the SR structure (PDB ID 3ARC), but distinct differences were observed in Mn–Mn and Mn–O distances (Figs 1b–d and 2a, Extended Data Table 3). For comparison, we take the average distances from four monomers of the two independent dimers, and the average Mn–Mn distances were 2.7 Å for Mn1D–Mn2C, 3.2 Å for Mn1D–Mn3B, 5.0 Å for Mn1D–Mn4A, 2.7 Å for Mn2C–Mn3B, 5.2 Å for Mn2C–Mn4A and 2.9 Å for Mn3B–Mn4A (Fig. 1b, Table 1, Extended Data Table 2). All of these distances were 0.1–0.2 Å shorter than those in the SR structure, in good accordance with the results of EXAFS[3–7] and theoretical calculations[8–14]. This clearly indicated that the X-ray damage possibly included in the previous SR structure has been eliminated. In particular, we assigned two 2.7 Å Mn–Mn vectors to Mn1D–Mn2C and Mn2C–Mn3B and one 2.8-2.9 Å vector to Mn3B–Mn4A; the presence of these three vectors has been suggested by precision EXAFS measurements, although their exact geometry may not be the same as that revealed from the crystal structure[3–7]. In contrast to the slightly shorter Mn–Mn distances, no clear differences were observed in the Mn–Ca distances compared with those in the SR structure (there were three proximal Mn–Ca distances with 3.5 Å for Mn1D–Ca, 3.3 Å for Mn2C–Ca, 3.4 Å for Mn3B–Ca, and one distal distance of 3.8 Å for Mn4A–Ca, see Fig. 1c, Table 1, Extended Data Table 3). The OEC model proposed from the EXAFS studies has possibly one to two interactions of Mn–Ca distance around 3.9 Å, which is different from the present XFEL structure[4].

A distinct feature of the SR OEC structure is the unusual position of O5, which binds weakly to Mn1D, Mn3B, Mn4A and Ca with distances ranging from 2.4 to 2.7 Å[1]. In the XFEL structure, the average bond distances were 2.2 Å for Mn3B–O5, 2.3 Å for Mn4A–O5, 2.7 Å for Mn1D–O5, and 2.5 Å for Ca–O5 (Fig. 1d, Table 1, Extended Data Table 3). Compared with the SR structure, three bond distances from O5 to Mn3B, Mn4A and Ca were shortened by 0.2 Å; in contrast, the distance to Mn1D was elongated by 0.1 Å. The longer Mn4A–O5 distance in the SR structure may imply that Mn4A has received some reduction by the attack of hydrated electrons generated by the radiation damage, leading to a longer distance to O5 in the SR structure; this in turn implies that Mn4A is more prone to radiation damage than Mn1D because of its dangling position which leads to a larger exposure to the solvent (and hence easier access by the free radicals), whereas Mn1D exists in the solid cuboidal part of the structure with less exposure to the solvent. Recent computational studies failed to reproduce the long bond distances from O5 to the Mn ions, and instead resulted in strong binding to either Mn1D or Mn4A (with bond lengths shorter than 1.9 Å), giving rise to either R-type (right-side open) or L-type (left-side open) structures, when O5 is

©2015 Macmillan Publishers Limited. All rights reserved

assumed to be in a deprotonated state[11,13]. Our XFEL structure showed that O5 indeed exists in a position closer to Mn4A than to Mn1D, however, such preference for Mn4A was much less than that shown by typical theoretical analyses, and the unusual nature of the bonds involving O5 is largely preserved. Therefore, we confirmed that the longer distances of μ-oxo bridges from O5 were an intrinsic and remarkable feature of the OEC structure, not an artefact of X-ray reduction. Based on this, we propose that O5 is a hydroxide ion rather than an oxygen dianion (deprotonated oxygen) in the S_1 state. Indeed, theoretical calculations based on the assumption that O5 is a hydroxide ion have yielded long bond distances between O5 and nearby Mn ions that are largely comparable with the present XFEL structure[11,26].

Another feature of the Mn–O bond distances in the XFEL structure was that all of the oxo-bridges connected with Mn2C were 0.1–0.3 Å shorter than the corresponding distances in the previous SR structure[1], which may indicate that Mn2C was also partially photo-reduced in the SR structure. Furthermore, structural differences were also found in the ligand environment around the OEC between the XFEL and SR structures. All of the ligand groups coordinated to the OEC had slightly shorter distances, some of them faced in slightly different directions and some water molecules existed in different positions (Table 1, Fig. 2b and 2c, Extended Data Table 3). In contrast, no apparent differences were observed in the acceptor side (the bound plastoquinone acceptors Q_A and Q_B, and the non-haem iron) or the region surrounding Y_D (D2-Y160) in the D2 subunit.

Based on the current XFEL structure, all of the four Mn ions are six-coordinated (Extended Data Fig. 4a–d). The averaged ligand distances, including those to amino acids, oxo-bridges and terminal water ligands, are 2.1 Å for Mn1D, 2.0 Å for Mn2C, 2.0 Å for Mn3B and 2.1 Å for Mn4A (Extended Data Table 4). Because of the longer pair of Mn1D–O5/OD2 (D1-Asp342) and Mn4A–O5/W1 (one of the two water ligands to Mn4A) distances, the average ligand distances of Mn1D and Mn4A are slightly longer than those of Mn2C and Mn3B. These longer pairs also contributed to the non-uniform distribution of the ligand distances, which is a typical characteristic of Mn ions in the 3+ oxidation state having a Jahn–Teller axis (Extended Data Fig. 5a, b, Extended Data Table 4). Based on the high oxidation scenario—that the oxidation states of the four Mn ions are (III, III, IV, IV) in the S_1 state—we propose that the valences of Mn1D, Mn2C, Mn3B and Mn4A can be assigned as III, IV, IV and III, respectively. This assignment is supported by the near-centre localization of the O5 atom, as the III valence of the two Mn ions (Mn1D and Mn4A) connected to the two sides of the O5 atom would lead to a longer and almost equal distance for the two Mn–O bonds as observed in the XFEL structure (Fig. 3). The assignment of Mn1D as in a 3+ valence state is consistent with the proposal from the combined study of multi-frequency electron paramagnetic resonance, ^{55}Mn-electron nuclear double-resonance and theoretical calculations showing that Mn1D is a 3+ ion in the S_2 state[27].

The present XFEL structure provides important clues to the mechanism of water oxidation. The unusual properties of O5 and the proposal that it is an OH^- ion in the S_1 state suggests that it is a water molecule in the S_0 state; upon transition from S_0 to S_1, a proton is released from the O5 site, leading to the OH^- species in the S_1 state. These inferences strongly suggest that O5 provides one of the substrate water molecules for the O=O bond formation, which is in agreement with recent ^{17}O electron-electron double resonance-detected NMR experiments[28]. Based on the involvement of O5, formation of the O=O bond in the water oxidation reaction can proceed between O5 and another nearby oxygen atom, which could be a newly inserted water molecule, as proposed in ref. 29 and supported by a recent advanced EPR study[30] (Fig. 3). It should be pointed out, however, that the second oxygen atom might instead be provided by one of the already present terminal water ligands, W2 or W3, without imposing the insertion of a new water molecule (Fig. 3), as both W2 and W3 are within hydrogen-bond distances to O5 and therefore may be able to move towards to O5 to form the O=O bond during the S-state transition. Determination of which mechanism is correct will require further XFEL experiments to analyse the intermediate structures at atomic resolution, using the approach established in this study.

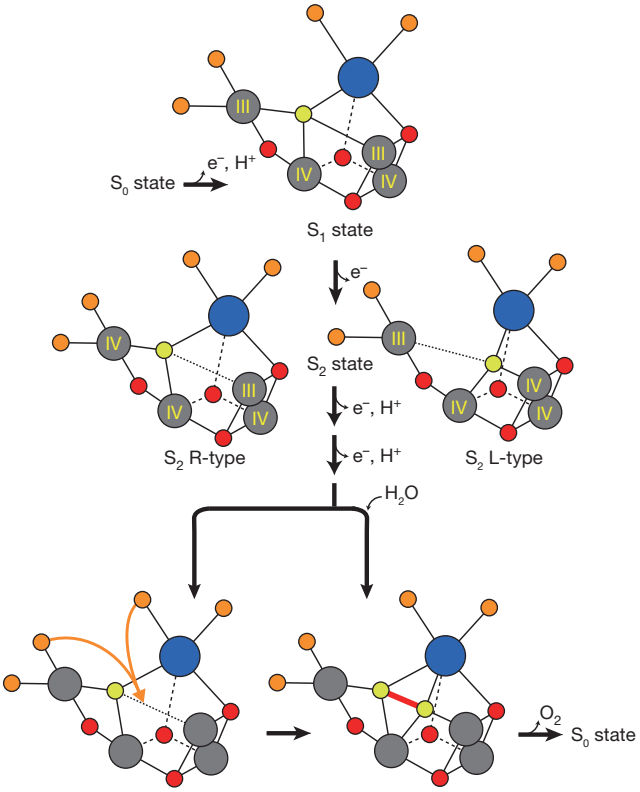


Figure 3 | Possible mechanisms for the oxygen-evolving reaction. O5 in the S_1 state is connected to both Mn1D(III) and Mn4A(III). Upon transition from S_1 to S_2, an electron may be removed from Mn4A, leading to a right-side open structure ('R-type'), or from Mn1D, leading to a left-side open structure ('L-type'). Both structures will allow insertion of a new water molecule during the subsequent S-state transition, preparing for the transition state immediately before O=O bond (indicated by a red bond in the right-hand structure in the bottom row) formation. Alternatively, the transition state ready for O=O bond formation may be formed by moving either W2 or W3 towards O5 (indicated by orange arrows in the left-hand structure in the bottom row). See text for more details. Colour code is the same as Fig. 1a.

Online Content Methods, along with any additional Extended Data display items and Source Data, are available in the online version of the paper; references unique to these sections appear only in the online paper.

Received 30 August; accepted 21 October 2014.
Published online 26 November 2014.

1. Umena, Y., Kawakami, K., Shen, J.-R. & Kamiya, N. Crystal structure of oxygen-evolving photosystem II at a resolution of 1.9 Å. *Nature* **473,** 55–60 (2011).
2. Yano, J. *et al.* X-ray damage to the Mn_4Ca complex in single crystals of photosystem II: a case study for metalloprotein crystallography. *Proc. Natl Acad. Sci. USA* **102,** 12047–12052 (2005).
3. Yano, J. *et al.* High-resolution Mn EXAFS of the oxygen-evolving complex in photosystem II: structural implications for the Mn_4Ca cluster. *J. Am. Chem. Soc.* **127,** 14974–14975 (2005).
4. Yano, J. *et al.* Where water is oxidized to dioxygen: structure of the photosynthetic Mn_4Ca cluster. *Science* **314,** 821–825 (2006).
5. Dau, H. & Haumann, M. The manganese complex of photosystem II in its reaction cycle — basic framework and possible realization at the atomic level. *Coord. Chem. Rev.* **252,** 273–295 (2008).
6. Dau, H., Grundmeier, A., Loja, P. & Haumann, M. On the structure of the manganese complex of photosystem II: extended-range EXAFS data and specific atomic-resolution models for four S-states. *Phil. Trans. R. Soc. Lond. B* **363,** 1237–1243 (2008).
7. Glöckner, C. *et al.* Structural changes of the oxygen-evolving complex in photosystem II during the catalytic cycle. *J. Biol. Chem.* **288,** 22607–22620 (2013).

©2015 Macmillan Publishers Limited. All rights reserved

8. Ames, W. *et al.* Theoretical evaluation of structural models of the S_2 state in the oxygen evolving complex of Photosystem II: protonation states and magnetic interactions. *J. Am. Chem. Soc.* **133,** 19743–19757 (2011).
9. Galstyan, A., Robertazzi, A. & Knapp, E. W. Oxygen-evolving Mn cluster in photosystem II: the protonation pattern and oxidation state in the high-resolution crystal structure. *J. Am. Chem. Soc.* **134,** 7442–7449 (2012).
10. Grundmeier, A. & Dau, H. Structural models of the manganese complex of photosystem II and mechanistic implications. *Biochim. Biophys. Acta* **1817,** 88–105 (2012).
11. Isobe, H. *et al.* Theoretical illumination of water-inserted structures of the $CaMn_4O_5$ cluster in the S_2 and S_3 states of oxygen-evolving complex of photosystem II: full geometry optimizations by B3LYP hybrid density functional. *Dalton Trans.* **41,** 13727–13740 (2012).
12. Luber, S. *et al.* S_1-state model of the O_2-evolving complex of photosystem II. *Biochemistry* **50,** 6308–6311 (2011).
13. Pantazis, D. A., Ames, W., Cox, N., Lubitz, W. & Neese, F. Two interconvertible structures that explain the spectroscopic properties of the oxygen-evolving complex of photosystem II in the S_2 state. *Angew. Chem. Int. Edn Engl.* **51,** 9935–9940 (2012).
14. Blomberg, M. R. A., Borowski, T., Himo, F., Liao, R. Z. & Siegbahn, P. E. M. Quantum chemical studies of mechanisms for metalloenzymes. *Chem. Rev.* **114,** 3601–3658 (2014).
15. Zouni, A. *et al.* Crystal structure of photosystem II from *Synechococcus elongatus* at 3.8 Å resolution. *Nature* **409,** 739–743 (2001).
16. Kamiya, N. & Shen, J.-R. Crystal structure of oxygen-evolving photosystem II from *Thermosynechococcus vulcanus* at 3.7-Å resolution. *Proc. Natl Acad. Sci. USA* **100,** 98–103 (2003).
17. Ferreira, K. N., Iverson, T. M., Maghlaoui, K., Barber, J. & Iwata, S. Architecture of the photosynthetic oxygen-evolving center. *Science* **303,** 1831–1838 (2004).
18. Guskov, A. *et al.* Cyanobacterial photosystem II at 2.9-Å resolution and the role of quinones, lipids, channels and chloride. *Nature Struct. Mol. Biol.* **16,** 334–342 (2009).
19. Southworth-Davies, R. J., Medina, M. A., Carmichael, I. & Garman, E. F. Observation of decreased radiation damage at higher dose rates in room temperature protein crystallography. *Structure* **15,** 1531–1541 (2007).
20. Neutze, R., Wouts, R., van der Spoel, D., Weckert, E. & Hajdu, J. Potential for biomolecular imaging with femtosecond X-ray pulses. *Nature* **406,** 752–757 (2000).
21. Kern, J. *et al.* Simultaneous femtosecond X-ray spectroscopy and diffraction of photosystem II at room temperature. *Science* **340,** 491–495 (2013).
22. Kupitz, C. *et al.* Serial time-resolved crystallography of photosystem II using a femtosecond X-ray laser. *Nature* **513,** 261–265 (2014).
23. Kern, J. *et al.* Taking snapshots of photosynthetic water oxidation using femtosecond X-ray diffraction and spectroscopy. *Nature Commun.* **5,** 4371 (2014).
24. Holton, J. M. & Frankel, K. A. The minimum crystal size needed for a complete diffraction data set. *Acta Crystallogr. D* **66,** 393–408 (2010).
25. Hirata, K. *et al.* Determination of damage-free crystal structure of an X-ray-sensitive protein using an XFEL. *Nature Methods* **11,** 734–736 (2014).
26. Shoji, M. *et al.* Theoretical modeling of biomolecular systems I. Large scale QM/MM calculations of hydrogen bonding networks of oxygen evolving complex of photosystem II. *Mol. Phys.* http://dx.doi.org/10.1080/00268976.2014.960021 (published online 29 September 2014).
27. Cox, N. *et al.* Effect of Ca^{2+}/Sr^{2+} substitution on the electronic structure of the oxygen-evolving complex of photosystem II: a combined multifrequency EPR, ^{55}Mn-ENDOR, and DFT study of the S_2 state. *J. Am. Chem. Soc.* **133,** 3635–3648 (2011).
28. Rapatskiy, L. *et al.* Detection of the water-binding sites of the oxygen-evolving complex of Photosystem II using W-band ^{17}O electron-electron double resonance-detected NMR spectroscopy. *J. Am. Chem. Soc.* **134,** 16619–16634 (2012).
29. Siegbahn, P. E. Water oxidation mechanism in photosystem II, including oxidations, proton release pathways, O-O bond formation and O_2 release. *Biochim. Biophys. Acta* **1827,** 1003–1019 (2013).
30. Cox, N. *et al.* Electronic structure of the oxygen-evolving complex in photosystem II prior to O-O bond formation. *Science* **345,** 804–808 (2014).

Acknowledgements We thank T. Ishikawa, M. Yabashi, K. Tono and Y. Inubushi for help in using the SACLA beamline, T. Tsukihara and S. Yoshikawa for suggestions and comments on the experiments, F. Seno for assistance with sample preparation, and K. Kawakami and Y. Umena for suggestions in the initial stage of the project. F. H. M. Koua participated in the initial stage of this work. This work was supported by an X-ray Free Electron Laser Priority Strategy Program (The Ministry of Education, Culture, Sports, Science and Technology of Japan, MEXT) (H.A. and J.-R.S.), a JST/CREST grant (K.H.), a grant-in-aid for Specially Promoted Research no. 24000018 (J.-R.S.) and KAKENHI grant no. 26840023 (M.S.) from JSPS, MEXT, Japan. The XFEL experiments were performed at beamline 3 of SACLA with the approval of the Japan Synchrotron Radiation Research Institute (JASRI) (proposal nos 2012A8011, 2012B8040, 2013A8047, 2013B8052 and 2014A8036), and we thank staff at SACLA for their help.

Author Contributions H.A. and J.-R.S. planned and organized the experiments, F.A. and Y.N. prepared the samples, F.A. made the crystals, G.U., H.M., K.H., H.A. and M.Y. designed and established the experimental set-up, M.S., F.A., T.S., Y.N., G.U., H.M., K.H., H.A., M.Y. and J.-R.S. conducted the diffraction experiments, K.Y. performed scaling of raw diffraction images, M.S. performed the structural analysis, M.S. and J.-R.S. wrote the manuscript, and all authors discussed and commented on the results and the manuscript.

Author Information Coordinates and structure factors for the structure determination have been deposited in the Protein Data Bank with accession codes 4UB6 and 4UB8 for data sets 1 and 2, respectively. Reprints and permissions information is available at www.nature.com/reprints. The authors declare no competing financial interests. Readers are welcome to comment on the online version of the paper. Correspondence and requests for materials should be addressed to H.A. (ago@spring8.or.jp), M.Y. (yamamoto@riken.jp) or J.-R.S. (shen@cc.okayama-u.ac.jp).

©2015 Macmillan Publishers Limited. All rights reserved

METHODS

Pulse parameters of SACLA. The pulse parameters of SACLA were as follows: pulse duration, 10 fs or shorter; pulse flux, 2.6×10^{10} photons; photon energy, 10.0 keV; beam size, 4.0 (H) × 2.5 (V) μm^2 (FWHM) at a position 20 mm downstream from the focal position of the X-ray beam; pulse frequency, 30 Hz.

Preparation of crystals of *T. vulcanus* PSII in the S_1 state. Highly active dimeric PSII core complexes were purified from the thermophilic cyanobacterium *T. vulcanus* and crystallized as described previously[1,31]. The crystals appeared in a few days and reached their maximum size of $1.2 \times 0.5 \times 0.2$ mm within one week. The crystals were stored at 12 °C in the crystallization buffer[1] to which glycerol, PEG 1,450 and PEG 5,000 MME were added gradually with an increment of 1% for each of the reagents every 30 min. When the cryoprotectant reagents reached the final concentrations of 25% glycerol, 10% PEG 1,450 and 10% PEG 5,000 MME, the crystals were quickly frozen in a nitrogen stream at 100 K. Purification, crystallization and freezing of the crystals were performed in the dark or under dim green light. Therefore, the crystals were fixed into the dark-stable S_1 state.

Evaluation of radiation damage propagation induced by XFEL irradiation. Before image data collection, the distance that radiation damage induced by each XFEL pulse may propagate was evaluated by following the protocol developed by our group using PSII crystals[25]. In brief, a point on a large PSII crystal was exposed to an XFEL pulse with full intensity, followed by irradiation by weak XFEL pulses with an intensity attenuated by two orders of magnitude applied to various points separated by 1 μm to 50 μm with a step of 1 μm in both vertical and horizontal directions from the originally irradiated point. The numbers of diffraction spots of each still image obtained with the weak XFEL pulses were counted at various distances from the originally irradiated point, and the radiation damage was defined to occur when the number of diffraction spots was lower than that expected from a crystal without prior exposure to the full intensity XFEL pulse. The distance of propagation of radiation damage determined in this way for PSII crystals was very similar to those determined for other protein crystals such as lysozyme and C*c*O, which is around 10 μm[25]. No perceptible radiation damage was detected beyond 11 μm from the irradiation point with a full intensity XFEL pulse. Thus we estimated that as long as each irradiation point was spatially separated by 15 μm, they would not be affected by other XFEL pulses and the diffraction images would be essentially identical to the ones from intact PSII crystals. In order to ensure a complete avoidance of radiation damage from adjacent XFEL pulses, we adopted a distance of 50 μm (an additional 35 μm 'safety margin' was used) between each irradiation point to collect consecutive still images from the large PSII crystals.

Diffraction experiments. All images were collected at beamline 3 of SACLA using a Rayonix MX225-HE detector. The very strong X-ray pulse of SACLA at its focused position produced physical damage in crystals placed at that focus; some cracked or burst, making data collection difficult. To avoid such damage, the samples were set at a position 20 mm downstream from the focal position of the X-ray beam to reduce the flux density of XFEL pulses irradiated onto the crystals. This basically eliminated physical damage, thereby enabling more efficient data collection.

Still diffraction images were recorded from the large PSII crystals sequentially. Before the irradiation by an XFEL pulse, the crystal was moved by at least 50 μm and rotated by 0.2° (Extended Data Fig. 1a, b). This stepwise rotation was aimed to record consecutive still diffraction images so that they could be processed in the same manner as the conventional oscillation diffraction method. Here, the size of the rotation step should be smaller than one-third of the crystal mosaicity to ensure the consecutiveness of the images based on the studies using crystals of lysozyme and C*c*O[25]. As the typical mosaicity of the PSII crystals was 0.60° to 0.80°[1], a 0.2° step was adequate.

Processing of the diffraction images. Some of the images recorded had significantly lower or higher intensities than typical images, probably due to fluctuations in the XFEL pulses. This situation was more severe for the first half of the images of data set 1 than for the rest of data set 1 and data set 2 because of a larger variation in the pulse intensities during collection of the first half of the images of data set 1. The intensities of the first half images of data set 1 were therefore scaled for each crystal on the basis of the I_0 values from an X-ray beam monitor placed in the optics hutch. The standard deviations of the averaged pixel values in the groups derived from the same crystal decreased by 30% after the scaling process (Extended Data Fig. 6a, b). Among these images, (1) the images that showed characteristics of 'not single' or 'cracked' crystals, or (2) a block of images that had a significant discontinuity in the course of the crystal rotation that made the data processing as continuous rotational images impossible, were not processed. In these cases, we restarted the diffraction experiments with a new crystal to cover all the unique reflections in the asymmetric unit of the reciprocal space. The images selected based on these criteria were processed with the programs ipmosflm and scala in CCP4[32]. The final images used for structural refinement were selected as follows: we discarded the 'block' of processed images whose diffraction limit was lower than 2.5 Å resolution, or the ones that made the statistics worse significantly. Those images were selected one-by-one by eye. Since we collected multiple images at similar rotational angles with multiple crystals, the selection of images with resolution higher than 2.5 Å did not affect the completeness of our data as shown in Extended Data Table 1.

The total dose was calculated with the program RADDOSE[33], which showed that the total dose absorbed and photon density were 1.4 MGy and 0.26×10^{10} photons per μm^2, respectively, for each irradiation point in a crystal. This total dose and photon density was approximately equal to that each point received for the data set collected previously at the SR source[1]. The conditions and statistics for diffraction experiments are provided in Extended Data Table 1, which showed that the unit cell constants were slightly different between the XFEL and SR data. This is because, as we have shown previously[1,31], post-crystallization treatment is very important to obtain better and isomorphous diffracting PSII crystals. Our crystals are very sensitive to cryo-conditions, and the conditions (that is, the composition of the final cryo-protectant buffer) we used in this work were slightly different from those used in the previous work. We used 25% glycerol, 10% PEG 1,450 and 10% PEG 5,000 MME for the final cryo-protectant solution, whereas 25% glycerol and 20% PEG 3000 were used in the previous cases for the SR data collection. This may be the reason for the unit cell change between the XFEL and SR data.

The *R*-factor between data set 1 and data set 2 is 0.177. This is larger than the *R*-factors among sub-data sets obtained from the same data sets, which is typically less than 0.05 based on our studies at synchrotron sources. This is largely due to an insufficient isomorphism among the crystals grown from different batches of samples between data sets 1 and 2, although we cultured, purified and crystallized the sample using the same protocols.

Structural determination. The initial phase information up to 3.0 Å resolution was obtained by the molecular replacement method with the Phaser program in CCP4[32] using the 1.9 Å resolution structure (PDB ID 3ARC) as a search model, in which all of the cofactors including OEC, amino acid residues coordinating OEC and water molecules were omitted. The phases obtained were then extended and improved using the program DM in CCP4[32]. Because the XFEL structure and the SR structure were essentially equivalent at 3.0 Å resolution, the phases obtained after density modification should not be biased by the SR structure. The model was built manually using COOT[34] in the resulting electron density map ($F_o \times \exp(i\alpha_{DM})$). The structural refinement was carried out with Phenix[35]. OEC was not included in the structural model until the final stage of the structural refinement which is described in the next section.

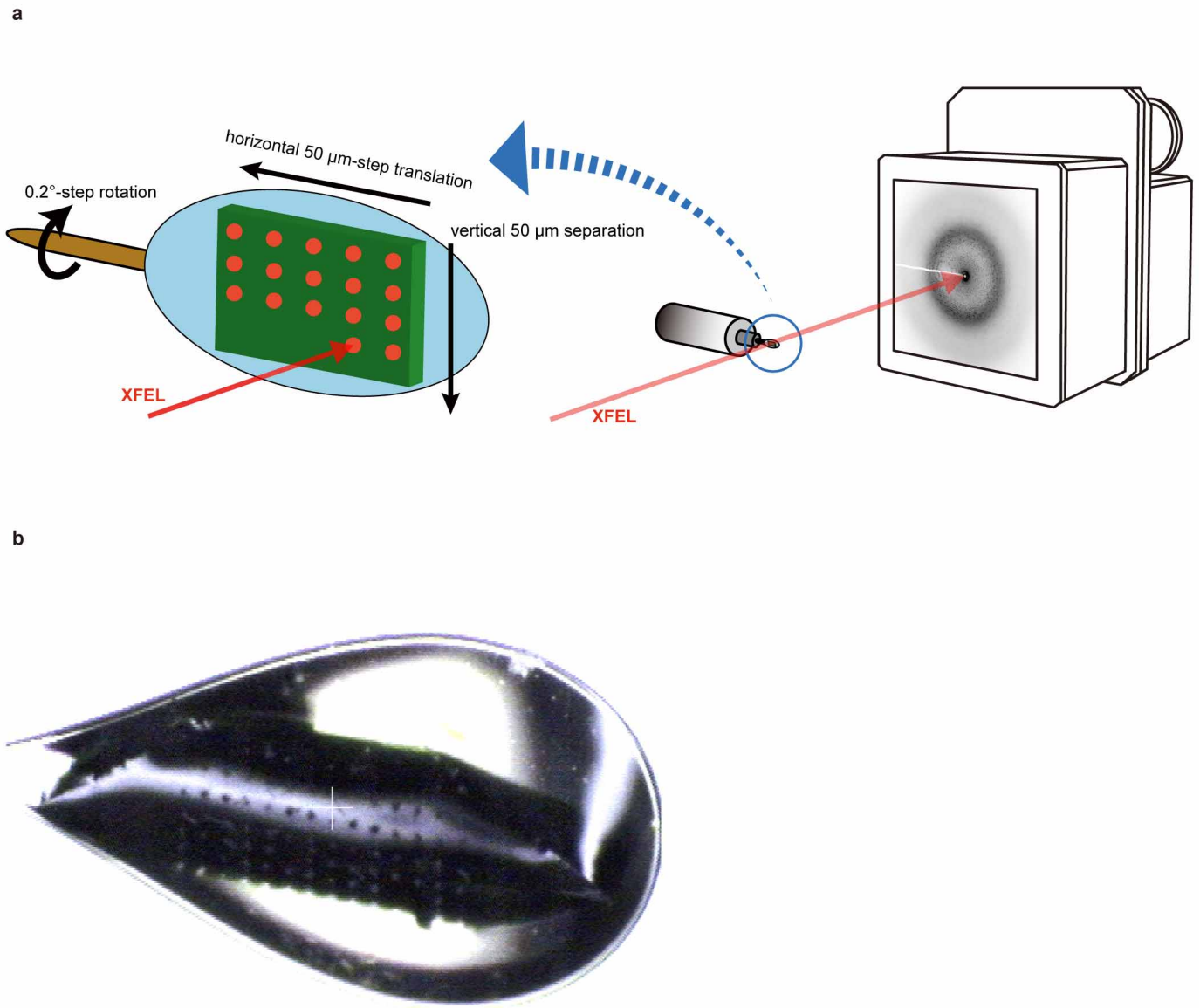
Refinement of the OEC structure. The positions of four manganese atoms, one calcium atom and ligand residues were clearly visible in the $2mF_o - DF_c$ map before placement of any of these atoms (Fig. 1a), whereas the positions of the five oxo-oxygen atoms were clearly identified in the $mF_o - DF_c$ map after placement of the manganese and calcium atoms as shown in Fig. 1a. When we started to build the OEC model, we placed the Mn_4CaO_5 cluster manually, and performed the structural refinement with strict restraints for bond distances (Mn–O and Ca–O) that were taken exactly from the SR structure (PDB ID 3ARC). This refinement resulted in a shortening of all Mn–Mn distances compared to the SR structure, and some of the positions of the refined oxo-oxygen atoms using 'the strict SR structure restraints' for Mn–O and Ca–O distances did not agree well with the positions identified from the $mF_o - DF_c$ map calculated before placing any oxo-oxygen atoms. Moreover, the refinement with 'the strict SR structure restraints' for Mn–Mn distances but loose restraints for Mn–O and Ca–O led to a significant increase in the residual density in the $mF_o - DF_c$ map. Therefore, although the overall shape was very similar, the OEC in the XFEL structure was apparently different from that in the SR structure in terms of the positions of the individual atoms. Therefore, the refinements were accomplished with rounds of geometry optimizations in which the optimal geometry for the Mn_4CaO_5 cluster was determined from the previous refined structure under loose constraints for bond distances of Mn–O and Ca–O. Then the restrained refinement was performed successively using the modified 'new' library for the bond distances. This geometry optimization procedure was repeated several times until no further changes in the bond distances were observed, and the correctness of the structural refinements was confirmed by checking the decrease in the residual density of the $mF_o - DF_c$ maps. In the final refined structure obtained, all of the oxo-oxygen atoms existed in the central position of the density in the $mF_o - DF_c$ map calculated before placing them, and the residual electron density in the $mF_o - DF_c$ map was minimized. The average and standard deviation of the distances of Mn–Mn, Mn–Ca, Mn–O and Mn–ligand were calculated from four independent PSII monomers (two dimers in each data set) and are listed in Extended Data Table 3, which shows that they had very small deviations, therefore enabling comparisons of the inter-atomic distances between the XFEL and SR structures.

31. Shen, J.-R. & Kamiya, N. Crystallization and the crystal properties of the oxygen-evolving photosystem II from *Synechococcus vulcanus*. *Biochemistry* **39,** 14739–14744 (2000).
32. Collaborative Computational Project, Number 4. The CCP4 suite: programs for protein crystallography. *Acta Crystallogr. D* **50,** 760–763 (1994).

©2015 Macmillan Publishers Limited. All rights reserved

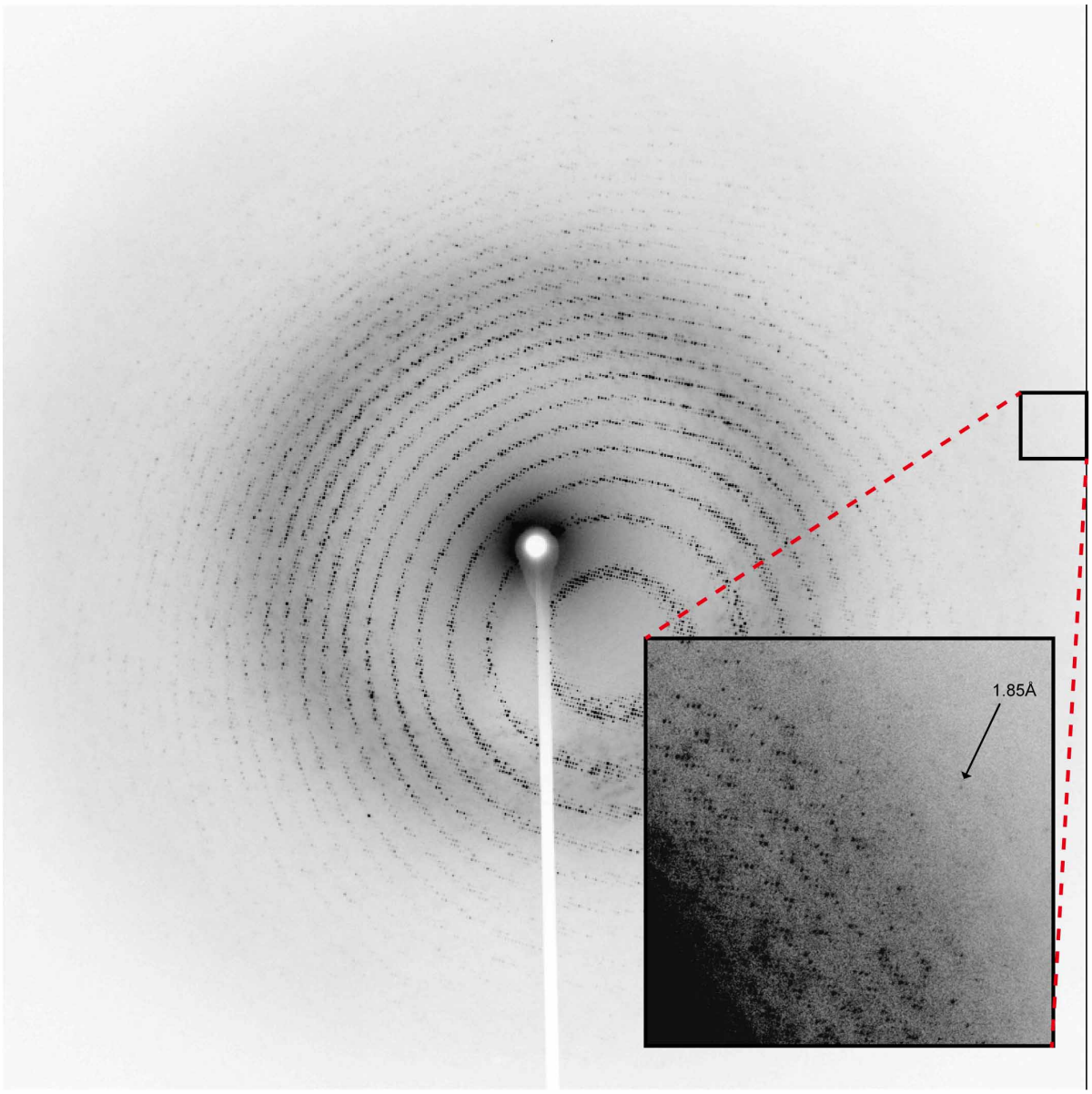
33. Murray, J., Garman, E. & Ravelli, R. X-ray absorption by macromolecular crystals: the effect of wavelength and crystal composition on absorbed dose. *J. Appl. Crystallogr.* **37,** 513–522 (2004).
34. Emsley, P. & Cowtan, K. Coot: model-building tools for molecular graphics. *Acta Crystallogr. D* **60,** 2126–2132 (2004).
35. Adams, P. D. *et al.* PHENIX: a comprehensive Python-based system for macromolecular structure solution. *Acta Crystallogr. D* **66,** 213–221 (2010).

©2015 **Macmillan Publishers Limited. All rights reserved**



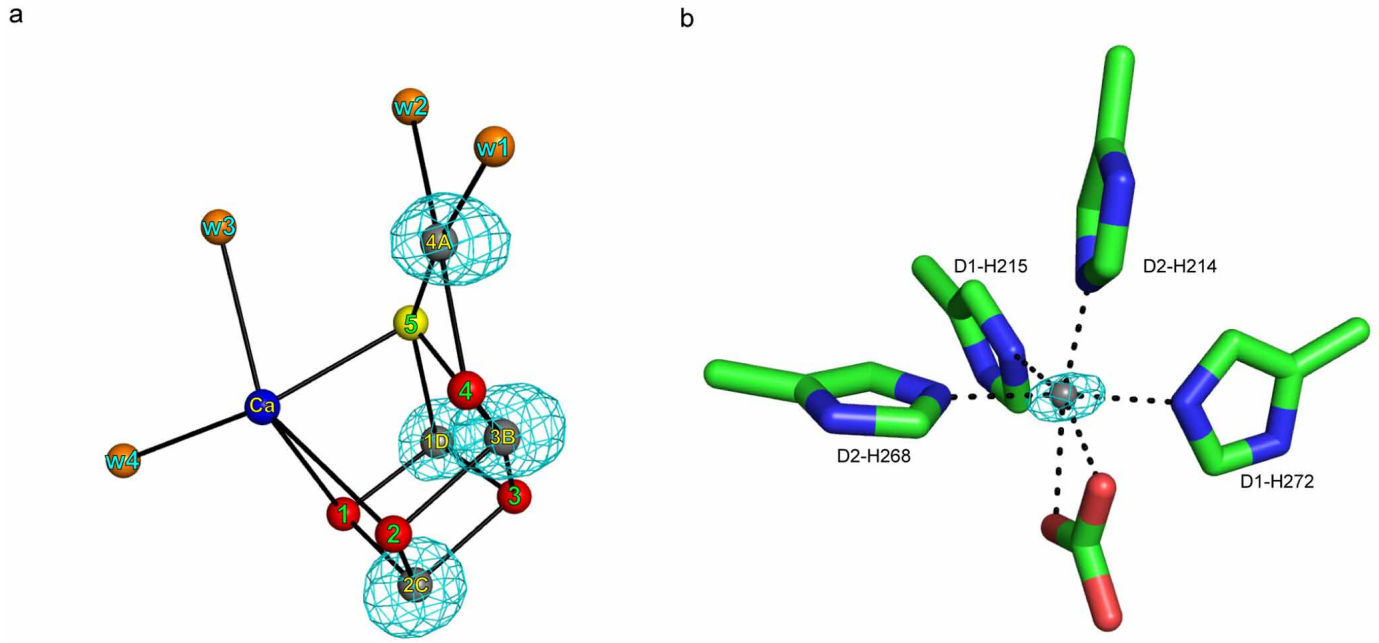
Extended Data Figure 1 | Diffraction experiment using the XFEL beam at SACLA. **a**, Schematic drawing of the diffraction experiment. Still diffraction images were recorded from different points on large PSII crystals. The crystals were rotated by 0.2° between each image over a range of 180°. Adjacent irradiation points were separated by 50 μm in the horizontal direction for any rotational angle. Translation in the vertical direction was varied depending on the rotational angle, so that the irradiation points were also separated by 50 μm in the vertical direction. **b**, A picture of the PSII crystal in a cryo-loop after the XFEL diffraction experiment. Note that the path where the XFEL beam passed through became hollowed out, and resulted in footprints of the irradiation points, which were well separated.

©2015 Macmillan Publishers Limited. All rights reserved



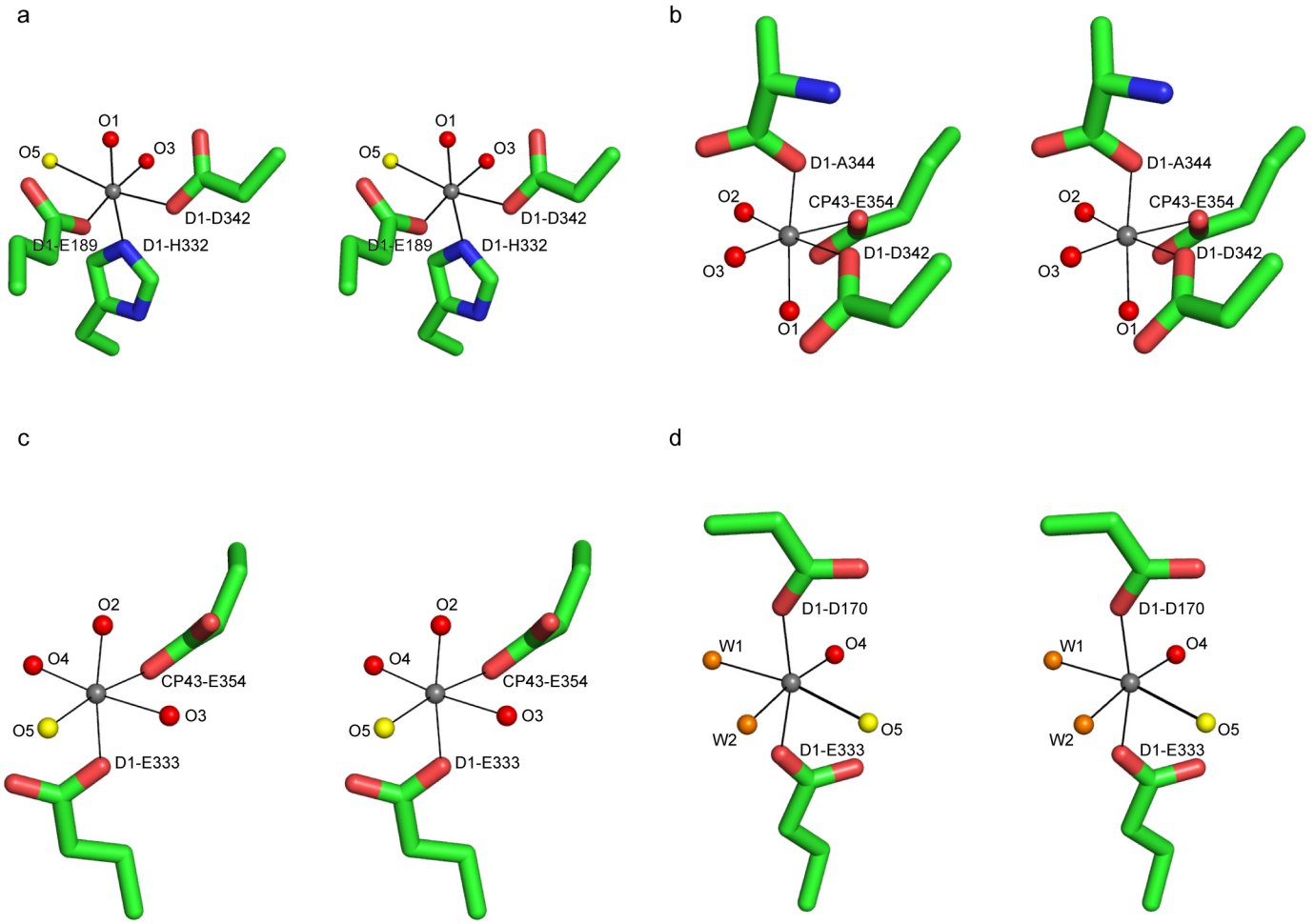
Extended Data Figure 2 | A diffraction image from a PSII crystal obtained with the XFEL beam. A typical diffraction image is shown; the boxed area at the right is shown enlarged in the inset, where diffraction spots at the maximum resolution are visible.

©2015 Macmillan Publishers Limited. All rights reserved



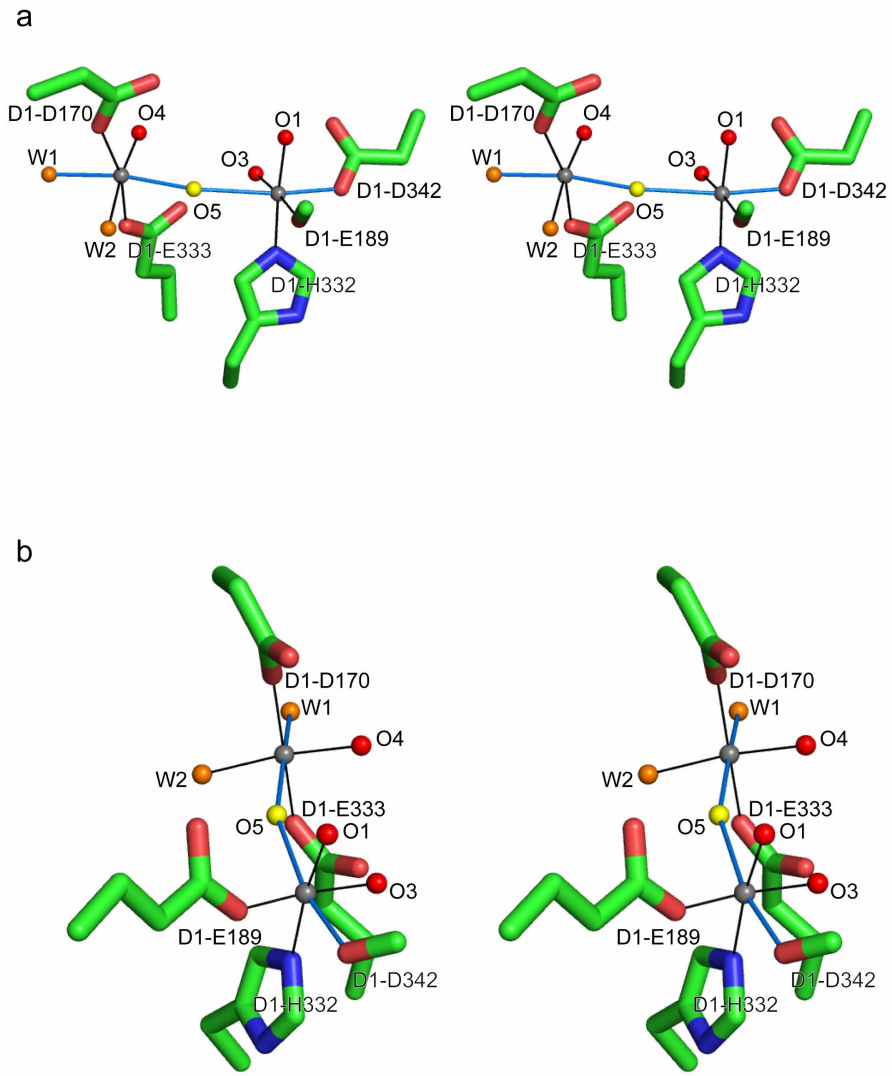
Extended Data Figure 3 | Anomalous signals of the metal ions obtained with the XFEL beam. Shown are anomalous difference Fourier maps contoured at 5σ distributions. **a**, Manganese atoms of the OEC. **b**, The non-haem iron in the acceptor side between Q_A and Q_B.

©2015 Macmillan Publishers Limited. All rights reserved



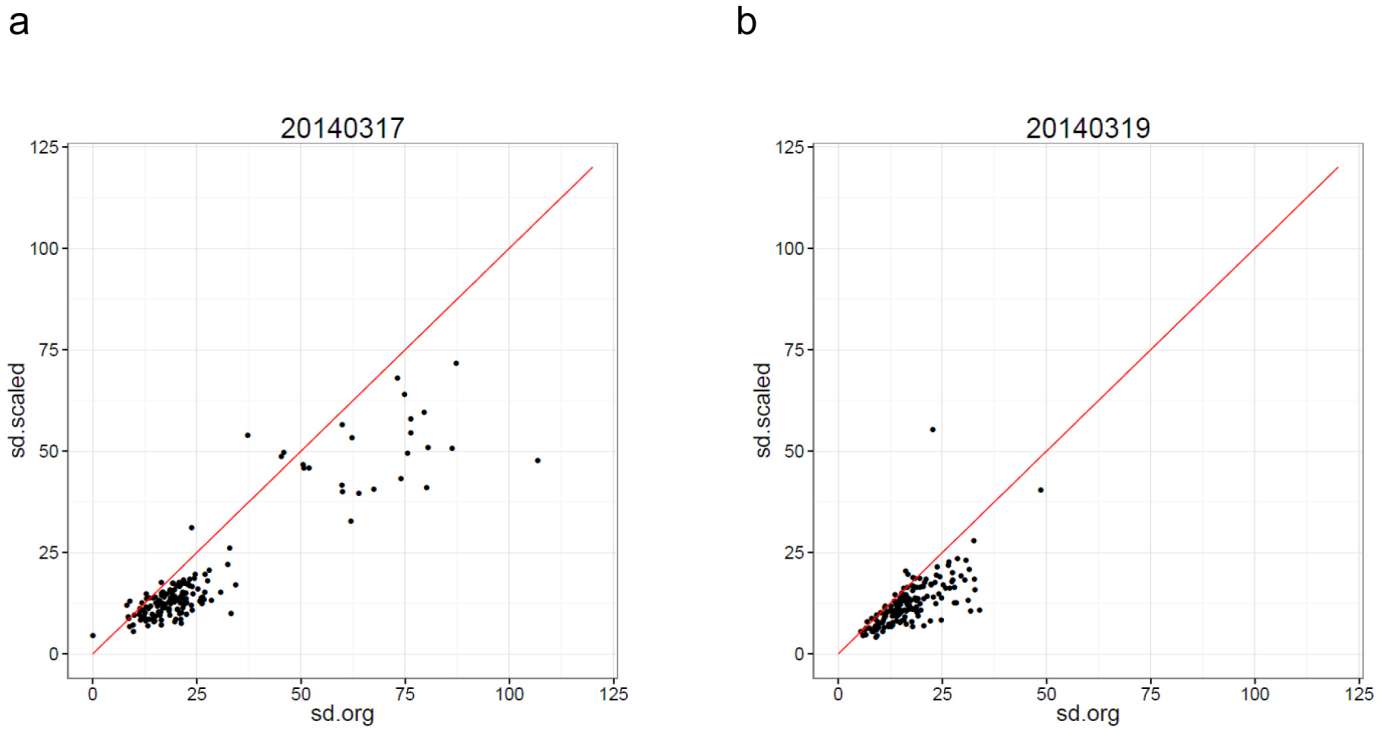
Extended Data Figure 4 | Coordination environment of Mn1D, Mn2C, Mn3B and Mn4A. The ligand environment of **a**, Mn1D, **b**, Mn2C, **c**, Mn3B and **d**, Mn4A are drawn in stereo view. The ligand bonds involving O5 coordination are slightly longer than the others in both Mn1D and Mn4A. Note that Mn1D is in a pseudo-five-coordinated, trigonal bipyramidal geometry with additional weak interaction to O5. Colour code: grey, manganese; green, carbon; blue, nitrogen; red, oxo-oxygen; yellow, O5; orange, water.

©2015 Macmillan Publishers Limited. All rights reserved



Extended Data Figure 5 | Jahn-Teller axes on Mn1D and Mn4A. The ligand environments of Mn1D and Mn4A are drawn in a stereo view. Based on the longer ligand bonds involving the O5 coordination as shown in Extended Data Fig. 4a, d, two possible Jahn–Teller axes were assigned which are approximately parallel. Colour codes are the same as those in Extended Data Fig. 4. Light blue lines indicate two Jahn–Teller axes found in the OEC in the S_1 state. **a**, View direction almost orthogonally oriented relative to the two Jahn–Teller axes. **b**, View direction rotated by 90° from **a**.

©2015 Macmillan Publishers Limited. All rights reserved



Extended Data Figure 6 | Scaling of the raw images. Standard deviations of the average pixel values calculated in the group belonging to the same crystal before and after scaling are plotted. *X* and *Y* axes indicate standard deviations obtained before and after scaling, respectively. Red line in the plot represents the relationship $Y = X$. **a**, Plot of the images collected during the first half of the beam time (including the first half of the images for data set 1). **b**, Plot of the images collected during the last half of the beam time (including the rest of the images for data set 1 and all of the images for data set 2).

©2015 Macmillan Publishers Limited. All rights reserved

Extended Data Table 1 | Data collection and refinement statistics with the XFEL beam (data set 1 and data set 2) in comparison with the SR data

	XFEL (data set 1)	XFEL (data set 2)	SR
Experimental conditions			
Wavelength / Å	1.24357	1.24357	0.90000
Osillation width / deg.	0	0	0.2
Step width / deg.	0.2	0.2	
Total dose / Gy	1.4E+06	1.4E+06	7.4E+05
Photon density per μm^2	2.6E+09	2.6E+09	2.8E+09
No. of screened crystals	254	82	1
No. of total collected images	5,592	2,058	900
No. of processed images	1,643	1,167	900
No. of images used for refinement	658	680	900
Data collection statistics			
Space group	$P2_12_12_1$	$P2_12_12_1$	$P2_12_12_1$
Unit cell / Å	a=123.8, b=230.0, c=288.3	a=123.8, b=230.0, c=288.5	a=122.2, b=228.5, c=286.4
Resolution / Å	62.7 - 1.95 (2.06 - 1.95)*	62.3 - 1.95 (2.06 - 1.95)*	50 - 1.90 (1.97 - 1.90)*
No. of reflections	585,462 (83,527)*	586,125 (82,791)*	622,012
Completeness / %	98.7 (97.0)*	98.4 (95.9)*	99.6 (99.7)*
Redundancy	4.9 (4.6)*	5.1 (4.7)*	7.4 (6.7)*
R sym / R mrg †	0.330 (1.184)*	0.294 (1.579)*	0.060 (0.773)*
R pim ‡	0.172 (0.634)*	0.192 (1.070)*	
CC1/2§	0.919 (0.166)*	0.929 (0.362)*	
I/σ (I)	3.5 (0.9)*	3.1 (0.6)*	21.6 (2.6)*
Refinement statistics			
R factor	0.198	0.188	0.174
R free	0.238	0.225	0.201
Average B (overall) / $Å^2$	34.3	35.9	35.2
Average B (OEC) / $Å^2$	22.2	25.0	25.6
RMSD bond length / Å	0.009	0.009	0.010
RMSD bond angle / deg.	1.44	1.44	3.05
Ramachandran plot‖			
Favored / %	97.7	97.9	98.4
Allowed / %	2.1	2.0	1.5
Outliers / %	0.2	0.1	0.1

* Values in parentheses indicate those for the highest resolution shells.
† R_{sym} was calculated with scala in CCP4[32] for data set 1 and data set 2, R_{mrg} was calculated with scalepack in HKL2000 for the SR data[1].
‡ $R_{pim} = \sum_{hkl}[1/(N-1)]^{1/2}\sum_i|I_i(hkl)-I(hkl)| / \sum_{hkl}\sum_i I_i(hkl)$
§ CC1/2 is the correlation coefficient between two random half data sets.
‖ Calculated with MolProbility.

©2015 Macmillan Publishers Limited. All rights reserved

Extended Data Table 2 | *B*-factor values of the individual atoms in the OEC of the XFEL structures

	data set 1		data set 2		XFEL		SR		
	A	B	A	B	Average	std	A	B	Average
Mn1D	20.2	24.7	21.4	27.4	**23.4**	**3.3**	22.6	26.0	**24.3**
Mn2C	22.1	22.9	23.2	25.3	**23.4**	**1.4**	22.9	26.7	**24.8**
Mn3B	19.6	21.5	22.1	25.0	**22.0**	**2.2**	23.5	25.5	**24.5**
Mn4A	21.5	22.8	24.2	25.2	**23.4**	**1.6**	26.3	28.7	**27.5**
Ca	28.3	34.0	32.5	37.4	**33.0**	**3.8**	24.6	27.5	**26.0**
O1	21.0	20.3	28.1	24.0	**23.3**	**3.6**	22.5	25.1	**23.8**
O2	24.2	19.6	23.6	22.9	**22.6**	**2.1**	25.2	27.3	**26.3**
O3	24.6	24.0	21.0	35.8	**26.3**	**6.5**	23.3	27.1	**25.2**
O4	20.0	18.9	23.8	20.3	**20.7**	**2.1**	26.6	27.7	**27.2**
O5	15.1	18.8	16.7	20.2	**17.7**	**2.3**	24.1	28.1	**26.1**
overall (OEC)	21.6	22.7	23.7	26.4	**23.6**	**2.0**	24.2	27.0	**25.6**

The individual absolute *B*-factor values of Mn, Ca and O atoms in the Mn_4CaO_5 cluster of both A and B monomers in the two XFEL structures (data set 1 and data set 2) are shown, together with the average *B*-factors calculated from four PSII monomers. For comparison, the *B*-factors in the SR structure are also shown.

©2015 **Macmillan Publishers Limited. All rights reserved**

Extended Data Table 3 | Mn–Mn, Mn–Ca, Mn–O, Mn–water, Ca–O, Ca–water, O5–water and ligand distances of the OEC in each PSII monomer of the two XFEL structures

	data set 1		data set 2		XFEL		SR
	A	B	A	B	Average	std	Average
Mn1D-Mn2C	2.67	2.61	2.74	2.68	**2.68**	**0.05**	2.8
Mn1D-Mn3B	3.24	3.18	3.27	3.10	**3.20**	**0.08**	3.3
Mn1D-Mn4A	4.95	4.97	4.97	4.89	**4.95**	**0.04**	5.0
Mn2C-Mn3B	2.70	2.67	2.73	2.71	**2.70**	**0.03**	2.9
Mn2C-Mn4A	5.17	5.18	5.21	5.27	**5.21**	**0.04**	5.4
Mn3B-Mn4A	2.86	2.83	2.88	2.91	**2.87**	**0.03**	3.0
Mn1D-Ca	3.51	3.45	3.49	3.43	**3.47**	**0.04**	3.5
Mn2C-Ca	3.35	3.29	3.33	3.32	**3.32**	**0.03**	3.4
Mn3B-Ca	3.47	3.39	3.41	3.33	**3.40**	**0.06**	3.4
Mn4A-Ca	3.76	3.86	3.71	3.76	**3.77**	**0.06**	3.8
Mn1D-O1	1.85	1.80	1.81	1.73	**1.80**	**0.05**	1.9
Mn1D-O3	1.94	1.93	1.80	1.80	**1.87**	**0.08**	1.8
Mn1D-O5	2.70	2.72	2.70	2.69	**2.70**	**0.01**	2.6
Mn2C-O1	1.83	1.72	1.88	1.83	**1.82**	**0.07**	2.1
Mn2C-O2	1.90	1.74	1.83	1.83	**1.83**	**0.07**	2.1
Mn2C-O3	1.95	2.06	2.01	2.07	**2.02**	**0.06**	2.1
Mn3B-O2	1.78	1.81	2.00	2.00	**1.90**	**0.12**	1.9
Mn3B-O3	2.08	1.99	2.14	2.02	**2.06**	**0.07**	2.1
Mn3B-O4	1.91	1.92	1.89	1.88	**1.90**	**0.02**	2.1
Mn3B-O5	2.17	2.01	2.32	2.30	**2.20**	**0.14**	2.4
Mn4A-O4	1.94	2.04	2.05	2.03	**2.02**	**0.05**	2.1
Mn4A-O5	2.32	2.30	2.38	2.33	**2.33**	**0.03**	2.5
Mn4A-W1	2.34	2.15	2.26	2.24	**2.25**	**0.08**	2.2
Mn4A-W2	2.15	1.97	2.14	2.14	**2.10**	**0.09**	2.2
Ca-O1	2.57	2.61	2.64	2.61	**2.61**	**0.03**	2.4
Ca-O2	2.67	2.58	2.73	2.69	**2.67**	**0.06**	2.5
Ca-O5	2.59	2.60	2.43	2.52	**2.54**	**0.08**	2.7
Ca-W3	2.61	2.60	2.59	2.59	**2.60**	**0.01**	2.4
Ca-W4	2.51	2.49	2.44	2.42	**2.47**	**0.04**	2.5
O5-W2	3.07	2.91	3.08	2.95	**3.00**	**0.09**	3.1
O5-W3	3.21	3.25	2.98	3.05	**3.12**	**0.13**	3.1
W2-W3	3.38	3.17	3.23	3.27	**3.26**	**0.09**	3.3
Mn1D-OE2 (Glu189)	1.78	1.76	1.81	1.81	**1.79**	**0.02**	1.9
Mn1D-NE2 (His332)	2.08	2.11	2.13	2.16	**2.12**	**0.03**	2.2
Mn1D-OD2 (Asp342)	2.16	2.19	2.26	2.25	**2.22**	**0.05**	2.3
Mn2C-OD1 (Asp342)	2.14	2.07	2.16	2.15	**2.13**	**0.04**	2.2
Mn2C-OXT (Ala344)	1.92	1.85	1.97	1.86	**1.90**	**0.06**	2.0
Mn2C-OE1 (Glu354*)	2.12	2.19	2.10	2.09	**2.13**	**0.05**	2.2
Mn3B-OE1 (Glu333)	2.03	2.08	2.04	2.08	**2.06**	**0.03**	2.1
Mn3B-OE2 (Glu354*)	2.12	2.12	2.16	2.12	**2.13**	**0.02**	2.2
Mn4A-OD2 (Asp170)	2.05	2.08	2.00	2.00	**2.03**	**0.04**	2.1
Mn4A-OE2 (Glu333)	2.07	2.10	2.06	2.10	**2.08**	**0.02**	2.2
Ca-OD1 (Asp170)	2.28	2.46	2.34	2.34	**2.36**	**0.08**	2.4
Ca-O (Ala344)	2.41	2.43	2.43	2.43	**2.43**	**0.01**	2.5

A and B represent distances in two monomers of two independent dimer structures (data set 1 and data set 2) obtained by XFEL crystallography, and the average distances and standard deviations are calculated from the four monomers. For comparison, the average distances from the SR structure are also shown.
* Residue from CP43.

©2015 **Macmillan Publishers Limited. All rights reserved**

Extended Data Table 4 | Assignment of valences of individual manganese atoms in the OEC in the S_1 state based on average ligand distance and distribution of Jahn–Teller axes

Axis pair of the ligands	Average distance (Å)	Deviation from the average (%)	Assigned valance
Mn1D			
O1/NE2 (His332)	1.96	-5.9	
O3/OE2 (Glu189)	1.83	-12.2	
O5/OD2* (Asp342)	2.46	18.1	
Average	**2.08**		**III**
Mn2C			
O1/OE1 (Glu354‡)	1.97	0.0	
O2/OD1 (Asp342)	1.98	0.4	
O3/OXT (Ala344)	1.96	-0.4	
Average	**1.97**		**IV**
Mn3B			
O2/OE1 (Glu333)	1.98	-3.1	
O3/O4	1.98	-3.0	
O5/OE2† (Glu354‡)	2.17	6.1	
Average	**2.04**		**IV**
Mn4A			
O4/W2	2.06	-3.6	
O5/W1†	2.29	7.3	
OD2 (Asp170)/OE2 (Glu333)	2.06	-3.6	
Average	**2.14**		**III**

Shown are the average distances for the pair of ligands in the same axis line in the six-coordination geometry (Extended Data Figs 4, 5), together with their deviations from the average distance. The valence of each Mn atom was assigned based on the average ligand distance and the existence of the possible Jahn–Teller axis.
* Plausible Jahn-Teller axis
† Possible Jahn–Teller axis
‡ Residue from CP43.

©2015 Macmillan Publishers Limited. All rights reserved

LETTER

doi:10.1038/nature13797

Structure of an integral membrane sterol reductase from *Methylomicrobium alcaliphilum*

Xiaochun Li[1], Rita Roberti[2] & Günter Blobel[1]

Sterols are essential biological molecules in the majority of life forms. Sterol reductases[1] including Δ^{14}-sterol reductase (C14SR, also known as TM7SF2), 7-dehydrocholesterol reductase (DHCR7) and 24-dehydrocholesterol reductase (DHCR24) reduce specific carbon–carbon double bonds of the sterol moiety using a reducing cofactor during sterol biosynthesis. Lamin B receptor[2] (LBR), an integral inner nuclear membrane protein, also contains a functional C14SR domain. Here we report the crystal structure of a Δ^{14}-sterol reductase (MaSR1) from the methanotrophic bacterium *Methylomicrobium alcaliphilum* 20Z (a homologue of human C14SR, LBR and DHCR7) with the cofactor NADPH. The enzyme contains ten transmembrane segments (TM1–10). Its catalytic domain comprises the carboxy-terminal half (containing TM6–10) and envelops two interconnected pockets, one of which faces the cytoplasm and houses NADPH, while the other one is accessible from the lipid bilayer. Comparison with a soluble steroid 5β-reductase structure[3] suggests that the reducing end of NADPH meets the sterol substrate at the juncture of the two pockets. A sterol reductase activity assay proves that MaSR1 can reduce the double bond of a cholesterol biosynthetic intermediate, demonstrating functional conservation to human C14SR. Therefore, our structure as a prototype of integral membrane sterol reductases provides molecular insight into mutations in DHCR7 and LBR for inborn human diseases.

Sterols, amphipathic molecules, are widespread in animals, plants, fungi and some prokaryotes and a large variety exist[4], including ergosterol, hopanoids, phytosterol and cholesterol. The most abundant sterol in animals is cholesterol, which not only has a vital role in the maintenance of membrane strength and permeability, but also serves as a precursor for the biosynthesis of steroid hormones[5,6]. Endogenous biosynthesis is the major source of sterols, and the biosynthetic pathway from water-soluble small metabolites via intermediates of increasing complexity up to water-insoluble sterols encompasses numerous distinct enzymes[1,7], many of which contain multiple transmembrane segments. To date, no structure of the integral membrane enzymes involving sterol biosynthesis has been determined. Sterol reductases[1], integral membrane enzymes including C14SR, DHCR7 and DHCR24, can reduce specific carbon–carbon double bonds of the sterol moiety using a reducing cofactor at distinct steps in sterol and cholesterol biosynthesis (Extended Data Fig. 1).

Curiously, the multifunctional lamin B receptor[2] (LBR), located in the inner nuclear envelope membrane, also contains a domain in its C-terminal portion that is highly homologous to human sterol reductase[8] (Extended Data Fig. 2). Indeed, complementary DNA of human LBR complements reductase gene (*ERG24*) deletion in yeast, supporting the idea that LBR can substitute for sterol reductase activity[9]. Mutations in LBR and DHCR7 lead to various human genetic diseases[1] (Pelger–Huët anomaly[10] (PHA) and Greenberg skeletal dysplasia[11] (also known as hydrops-ectopic calcification-moth-eaten skeletal dysplasia, HEM) related to LBR; and Smith–Lemli–Opitz syndrome[12,13] (SLOS) related to DHCR7). However, structural knowledge of these important membrane-embedded enzymes is lacking, and therefore a mechanistic understanding cannot be developed.

To gain more insight into sterol reductases, we set out to determine the crystal structure of one of its family members. In screening for crystal-forming representatives of integral membrane sterol reductases, we found a homologue from the methanotrophic bacterium *Methylomicrobium alcaliphilum* 20Z, MaSR1, which shares 38–45% sequence identity and 51–62% similarity to human C14SR, DHCR7 and the C-terminal portion of LBR (Extended Data Fig. 2). *Methylomicrobium alcaliphilum* 20Z is an aerobic methanotroph, the cell membrane of which contains significant levels of sterols and hopanoids[14].

Expression of MaSR1 complements the deletion of the Δ^{14}-sterol reductase gene (*ERG24*) in yeast, indicating that MaSR1 is a bona fide sterol reductase (Extended Data Fig. 3, lanes 1–3). To test whether MaSR1 can function in human cholesterol biosynthesis, we performed the sterol reductase activity assay of MaSR1 after expression in human HEK293 cells and employed 5α-cholesta-8,14-dien-3β-ol ($C27\Delta^{8,14}$), a human cholesterol biosynthetic intermediate analogue[15–17] of 4,4-dimethylcholesta-8,14-dien-3β-ol ($C29\Delta^{8,14}$, Extended Data Fig. 1), as the substrate (Fig. 1a). This assay has been used for initial identification[15] and further investigation[16,17] of mammalian sterol reductases. The catalytic efficiency of MaSR1 is about 75% of that of human C14SR (Fig. 1b, c). We conclude that MaSR1 can function like human C14SR and specifically reduce the double bond of the approximate cholesterol biosynthetic intermediate.

We crystallized MaSR1 in space group *P*1 with NADPH. The diffraction of the crystal is anisotropic (Methods and Extended Data Fig. 4). The structure was determined by selenium-based single-wavelength anomalous dispersion and refined at 2.74 Å resolution (Extended Data Tables 1 and 2). Introduction of additional selenium anomalous scatterers by selective mutation and preparation of platinum derivatives confirmed that the atomic model was correct (Extended Data Fig. 5 and Extended Data Table 3).

Two MaSR1 molecules (rotated by 180°) pack into a crystallographic dimer that forms the asymmetric unit. The dimensions of the MaSR1 monomer are $50 \times 45 \times 58$ Å. The enzyme contains ten transmembrane helices (TM1–10). On the basis of the 'positive inside rule' for membrane proteins[18], we assigned the amino and carboxy termini to face the cytoplasm, consistent with the biochemically determined topology of the yeast homologue Erg24 (ref. 19). There are two short antiparallel β-sheet regions (β1–4) interspersed in the cytoplasm-exposed loops as well as two short α-helices, designated α1 and α2 (Fig. 2a and Extended Data Fig. 2). Residues 1–23 and 162–176 (part of the loop between TM4 and TM5) are not visible in the electron density map and therefore presumed to be disordered. The binding pocket for NADPH was localized to the C-terminal domain (TM6–10) and a cavity with an unidentified ligand density facing the lipid bilayer is surrounded by TM7 and TM10 (Fig. 2b, c).

Except for the nicotinamide-ribose moiety, the remainder of the NADPH molecule could be clearly identified (Extended Data Fig. 6a, b). The nicotinamide ring is the hydrogen donor in the transient interaction

[1]Laboratory of Cell Biology, Howard Hughes Medical Institute, The Rockefeller University, New York, New York 10065, USA. [2]Department of Experimental Medicine, University of Perugia, Perugia 06132, Italy.

©2015 Macmillan Publishers Limited. All rights reserved

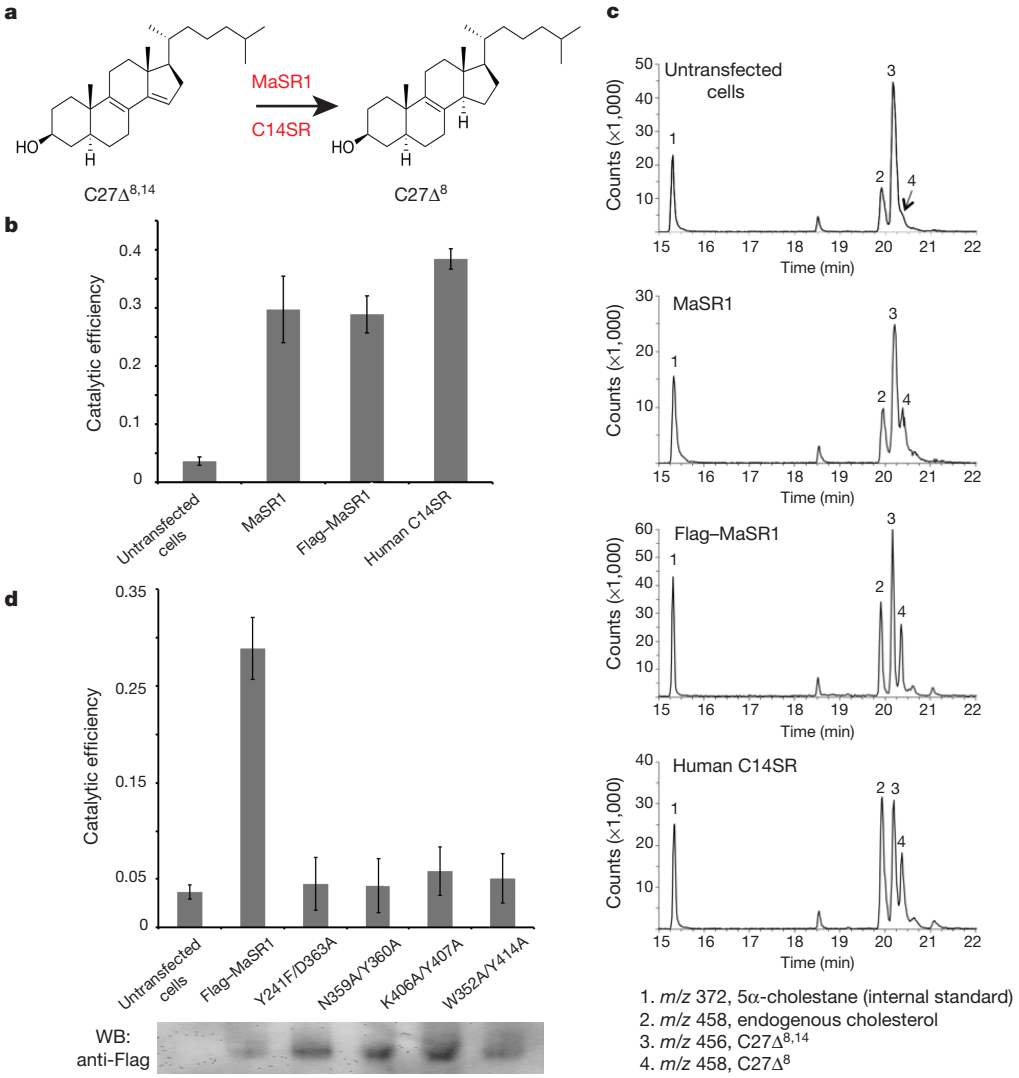


Figure 1 | Δ^{14}-reductase activity of MaSR1. **a**, Reaction catalysed by transfected human C14SR or MaSR1 in which 5α-cholesta-8,14-dien-3β-ol ($C27\Delta^{8,14}$) is converted to 5α-cholesta-8-en-3β-ol ($C27\Delta^{8}$). **b**, The average catalytic efficiency in two different experiments (calculated as the integrated gas chromatography–mass spectrometry (GC–MS) chromatogram peak area ratio $C27\Delta^{8}/(C27\Delta^{8,14} + C27\Delta^{8})$) of untransfected HEK293 cells and cells transfected with MaSR1, Flag–MaSR1 and human C14SR is 3.6%, 29.7%, 28.9% and 38.4%, respectively. The thin black lines show the spread between the two individual measurements **c**, GC–MS chromatograms of Δ^{14}-sterol reductase assay. Peak 1, mass to charge ratio (*m*/*z*) 372, 5α-cholestane (an internal standard); peak 2, *m*/*z* 458, endogenous cholesterol; peak 3, *m*/*z* 456, $C27\Delta^{8,14}$; peak 4, *m*/*z* 458, $C27\Delta^{8}$. The reduced products (peak 4) were detected in MaSR1, Flag–MaSR1 and C14SR but little in untransfected cells. **d**, The catalytic efficiency of Flag–MaSR1 mutants. All mutants expressed by anti-Flag western blot (WB) detection. The plotted values in the grey bars are the average of two different experiments. The thin black lines show the spread between the measurements.

with the substrate. In our structure, the absence of a sterol substrate probably fails to coordinate the nicotinamide ring and hence causes it to be disordered. By contrast, the other half of the NADPH molecule is well defined in the electron density and stabilized by a hydrogen bond from the centrally located Tyr 414 of α2 (Fig. 3a). The remainder of the NADPH pocket is lined with residues from TM9 and TM10 as well as two residues from TM8 (Fig. 3a). The NADPH pocket extends further around TM10 providing enough space to house the nicotinamide-ribose moiety of NADPH (Extended Data Fig. 6c). We mutated several residues in the NADPH binding pocket of MaSR1 (Extended Data Fig. 2). These mutations led to the loss of catalytic activity, as judged by the human Δ^{14}-sterol reductase activity assay (Fig. 1d) and by the Erg24 complementation assay in yeast (Extended Data Fig. 3, lanes 4, 6 and 7).

The working principle of reductases is to bring the nicotinamide of NADPH into close proximity to the substrate, leading to carbon–carbon double bond reduction. Analogous to the catalytic pocket of soluble steroid 5β-reductase[3] (AKR1D1, Protein Data Bank (PDB) accession number 3COT), bound to progesterone (Fig. 3b), the lipid-bilayer-facing cavity of MaSR1 is the likely candidate for the sterol binding pocket (Fig. 3c). Notably, the sterol binding pockets of both enzymes contain a 'signature' motif forming triangular hydrogen bonds that coordinate the β3 hydroxyl of either sterol or steroid; for MaSR1, this signature motif includes Tyr 241 bonded to Asp 363 (Fig. 3c) and for steroid 5β-reductase, Tyr 58 bonded to Glu 120 (Fig. 3b). The distance between Tyr 58 and Glu 120 (4.1 Å) in steroid 5β-reductase is similar to that of Tyr 241 and Asp 363 (3.9 Å) in MaSR1. The MaSR1 double mutant Y241F/D363A loses sterol reductase function in the human Δ^{14}-sterol reductase activity assay (Fig. 1d) and the yeast Erg24 complementation assay (Extended Data Fig. 3, lane 5). For the putative sterol binding pocket, extensive hydrophobic contacts between the highly conserved Trp 274

©2015 Macmillan Publishers Limited. All rights reserved

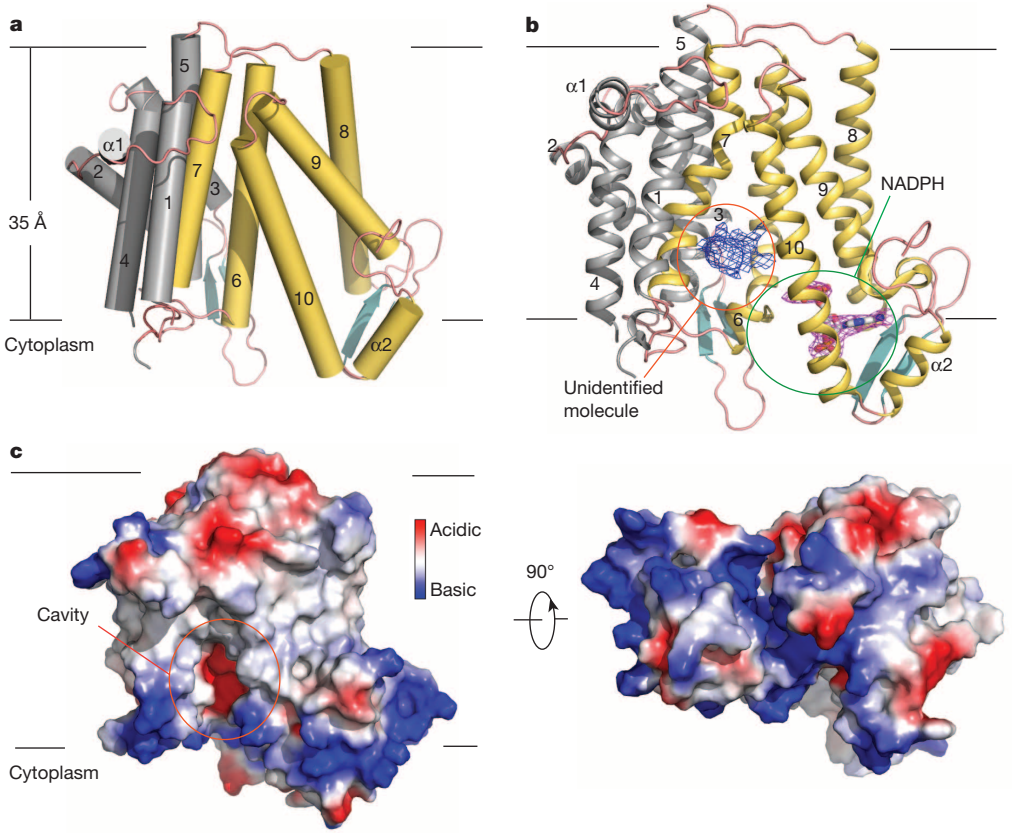


Figure 2 | The molecular architecture of MaSR1. **a**, Overall structure of MaSR1 viewed parallel to the membrane. The ten transmembrane segments are divided into an N-terminal half (TM1–5 and α1, grey) and a C-terminal half (TM6–10 and α2, yellow). The two black lines show the approximate location of the lipid bilayer. **b**, MaSR1 structure cartoon with NADPH shown by stick representation. $2F_o - F_c$ map for an unidentified molecule (blue mesh) and simulated annealing (SA)-omit map ($F_o - F_c$ densities) for NADPH (magenta mesh) both contoured at 2σ. **c**, The cavity is indicated by an orange circle in an electrostatic surface representation. The right and left panels represent two perpendicular views.

and Tyr 387 residues enforce the interaction of TM7 and TM10 (Extended Data Fig. 6d). Notably, in each monomer of the crystallographic dimer there is the extra electron density of an unidentified molecule in front of the cavity (Figs 2b and 3c). Although the molecular identity of this density could not be unambiguously determined (maybe an endogenous molecule from *Escherichia coli* or the detergent used for purification), it may represent a substrate for the putative sterol binding pocket. We modelled that two binding pockets bring the reducing end of NADPH into close proximity to the sterol (steroid) carbon–carbon double bond to be reduced (Fig. 3d), similar to the aldo-keto reductase (AKR) family of enzymes involved in human steroidgenesis[20] (for example, AKR1C3 and AKR1C2).

Owing to the high sequence homology with human LBR and human DHCR7, we generated structural models based on MaSR1 to highlight disease-related mutations (Fig. 4). The PHA/HEM-related mutations of LBR and the SLOS-related mutations of DHCR7 could be almost entirely mapped to the sterol reductase catalytic domain affecting the cofactor binding or sterol entry/binding sites. The similarities in pathogenesis between PHA/HEM and SLOS could therefore arise from a defect in sterol reduction.

Intriguingly, substrate recognition for sterol reductases is not very specific. MaSR1 could reduce the double bond of both C27$\Delta^{8,14}$ (Fig. 1b) and of the yeast sterol substrate ergosta-8,14-dien-ol (Extended Data Fig. 3). This is consistent with previous observations for LBR: it can reduce C27$\Delta^{8,14}$ (ref. 16); complement C14SR function in *C14SR*$^{-/-}$ (also known as *Tm7sf2*$^{-/-}$) mice[21]; and also reduce different yeast sterol substrates[9]. Finally, our structure also provides insight into the function of LBR. A DALI search for structural homologues of MaSR1 shows

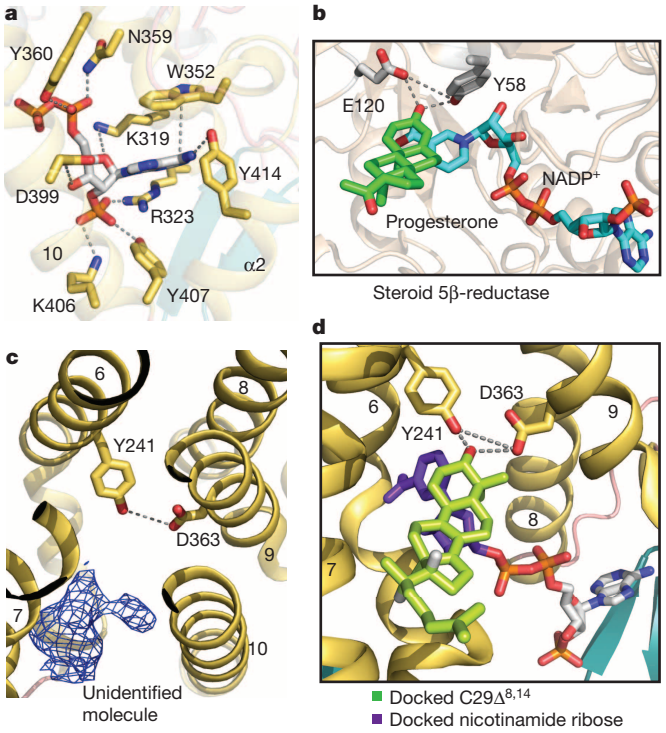


Figure 3 | NADPH, putative sterol binding pockets and homology modelling with steroid 5β-reductase. **a**, Close-up view of the NADPH binding pocket. NADPH is shown in stick representation with the phosphates in red. The interactions between NADPH and MaSR1 are indicated by dashed lines. **b**, Close-up view of the active pockets of steroid 5β-reductase (PDB accession number 3COT). Tyr 58 and Glu 120 clamp the β3 carbonyl oxygen of progesterone. **c**, The putative sterol binding site is accessible from the lipid bilayer. An unidentified ligand density is shown with $2F_o - F_c$ map (blue mesh) at a 2.5σ. **d**, Modelling of MaSR1 putative sterol binding pocket. On the basis of the active sites of steroid 5β-reductase, the missing nicotinamide-ribose moiety (purple) of NADPH was docked into the NADPH pocket and C29$\Delta^{8,14}$ (light green) modelled into the pocket of the MaSR1 structure.

©2015 Macmillan Publishers Limited. All rights reserved

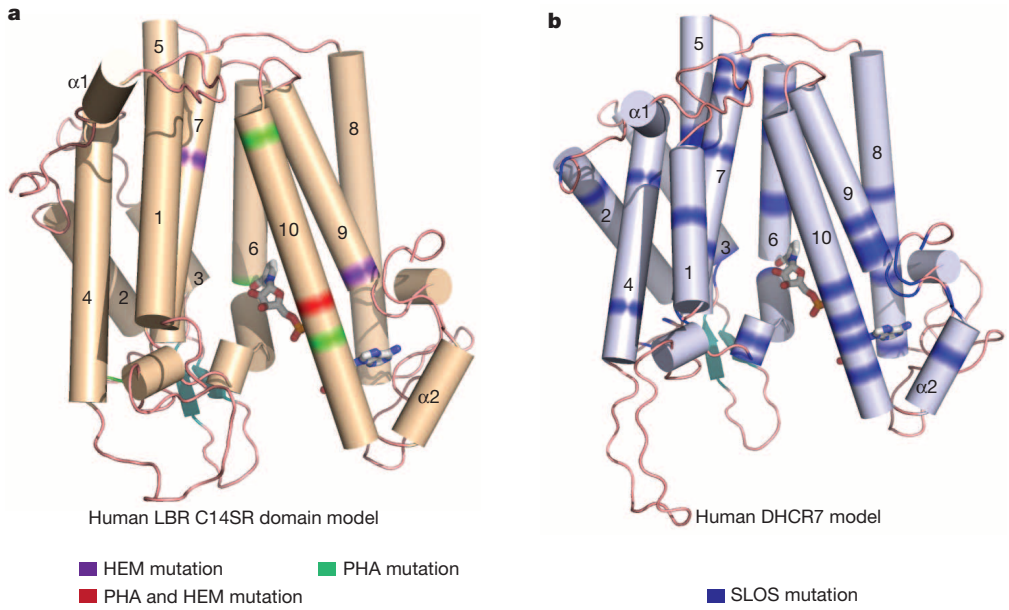


Figure 4 | Models of human LBR and human DHCR7. a, Human LBR model and the distribution of PHA and HEM mutations in green and purple, respectively. **b**, Human DHCR7 model and the distribution of SLOS mutations in blue. The cofactor NADPH (grey) is shown in stick representation.

no similar entry for the entire MaSR1 structure. However, it identified the membrane-embedded isoprenylcysteine carboxyl methyltransferase[22] (ICMT, PDB accession number 4A2N) as the closest entry for the TM6–10 segments of MaSR1 (Extended Data Fig. 7). The function of ICMT, which recognizes and then carboxymethylates the farnesylated cysteine of its substrate, points towards a similar role of the C14SR domain of LBR, which may recognize the farnesylated cysteine of either prelamin A or lamin B as the ligand[23].

Online Content Methods, along with any additional Extended Data display items and Source Data, are available in the online version of the paper; references unique to these sections appear only in the online paper.

Received 15 June; accepted 26 August 2014.
Published online 12 October 2014.

1. Porter, F. D. & Herman, G. E. Malformation syndromes caused by disorders of cholesterol synthesis. *J. Lipid Res.* **52,** 6–34 (2011).
2. Worman, H. J., Yuan, J., Blobel, G. & Georgatos, S. D. A lamin B receptor in the nuclear envelope. *Proc. Natl Acad. Sci. USA* **85,** 8531–8534 (1988).
3. Di Costanzo, L., Drury, J. E., Penning, T. M. & Christianson, D. W. Crystal structure of human liver Δ^4-3-ketosteroid 5β-reductase (AKR1D1) and implications for substrate binding and catalysis. *J. Biol. Chem.* **283,** 16830–16839 (2008).
4. Fahy, E. *et al.* A comprehensive classification system for lipids. *J. Lipid Res.* **46,** 839–862 (2005).
5. Miller, W. L. & Bose, H. S. Early steps in steroidogenesis: intracellular cholesterol trafficking. *J. Lipid Res.* **52,** 2111–2135 (2011).
6. Miller, W. L. Steroid hormone synthesis in mitochondria. *Mol. Cell. Endocrinol.* **379,** 62–73 (2013).
7. Goldstein, J. L., DeBose-Boyd, R. A. & Brown, M. S. Protein sensors for membrane sterols. *Cell* **124,** 35–46 (2006).
8. Olins, A. L., Rhodes, G., Welch, D. B., Zwerger, M. & Olins, D. E. Lamin B receptor: multi-tasking at the nuclear envelope. *Nucleus* **1,** 53–70 (2010).
9. Silve, S., Dupuy, P. H., Ferrara, P. & Loison, G. Human lamin B receptor exhibits sterol C14-reductase activity in *Saccharomyces cerevisiae*. *Biochim. Biophys. Acta* **1392,** 233–244 (1998).
10. Hoffmann, K. *et al.* Mutations in the gene encoding the lamin B receptor produce an altered nuclear morphology in granulocytes (Pelger–Huët anomaly). *Nature Genet.* **31,** 410–414 (2002).
11. Waterham, H. R. *et al.* Autosomal recessive HEM/Greenberg skeletal dysplasia is caused by 3β-hydroxysterol Δ^{14}-reductase deficiency due to mutations in the lamin B receptor gene. *Am. J. Hum. Genet.* **72,** 1013–1017 (2003).
12. Porter, F. D. Smith–Lemli–Opitz syndrome: pathogenesis, diagnosis and management. *Eur. J. Hum. Genet.* **16,** 535–541 (2008).
13. Herman, G. E. & Kratz, L. Disorders of sterol synthesis: beyond Smith–Lemli–Opitz syndrome. *Am. J. Med. Genet. C* **160,** 301–321 (2012).
14. Shchukin, V. N., Khmelenina, V. N., Eshinimaev, B., Suzina, N. E. & Trotsenko, Yu. A. Primary characterization of dominant cell surface proteins of halotolerant methanotroph *Methylomicrobium alcaliphilum* 20Z. *Microbiology* **80,** 595–605 (2011).
15. Paik, Y. K., Trzaskos, J. M., Shafiee, A. & Gaylor, J. L. Microsomal enzymes of cholesterol biosynthesis from lanosterol. Characterization, solubilization, and partial purification of NADPH-dependent $\Delta^{8,14}$-steroid 14-reductase. *J. Biol. Chem.* **259,** 13413–13423 (1984).
16. Roberti, R. *et al.* Cloning and expression of sterol Δ14-reductase from bovine liver. *Eur. J. Biochem.* **269,** 283–290 (2002).
17. Bennati, A. M. *et al.* Sterol dependent regulation of human *TM7SF2* gene expression: role of the encoded 3β-hydroxysterol Δ^{14}-reductase in human cholesterol biosynthesis. *Biochim. Biophys. Acta* **1761,** 677–685 (2006).
18. von Heijne, G. Control of topology and mode of assembly of a polytopic membrane protein by positively charged residues. *Nature* **341,** 456–458 (1989).
19. Kim, H., Melen, K., Osterberg, M. & von Heijne, G. A global topology map of the *Saccharomyces cerevisiae* membrane proteome. *Proc. Natl Acad. Sci. USA* **103,** 11142–11147 (2006).
20. Miller, W. L. & Auchus, R. J. The molecular biology, biochemistry, and physiology of human steroidogenesis and its disorders. *Endocr. Rev.* **32,** 81–151 (2011).
21. Bennati, A. M. *et al.* Disruption of the gene encoding 3β-hydroxysterol Δ^{14}-reductase (*Tm7sf2*) in mice does not impair cholesterol biosynthesis. *FEBS J.* **275,** 5034–5047 (2008).
22. Yang, J. *et al.* Mechanism of isoprenylcysteine carboxyl methylation from the crystal structure of the integral membrane methyltransferase ICMT. *Mol. Cell* **44,** 997–1004 (2011).
23. Hennekes, H. & Nigg, E. A. The role of isoprenylation in membrane attachment of nuclear lamins. A single point mutation prevents proteolytic cleavage of the lamin A precursor and confers membrane binding properties. *J. Cell Sci.* **107,** 1019–1029 (1994).

Acknowledgements We thank W. Shi and H. Robinson at National Synchrotron Light Source (NSLS) beamline X29 and N. Sukumar at Advanced Photon Source (APS) beamline 24-ID-E for on-site assistance and J. Wang for support with the structure determination. We also thank L. Gatticchi and B. Sebastiani for assistance with the sterol reductase assays, and E. Coutavas, E. Debler and H. Shi for constructive comments in manuscript preparation. The C27$\Delta^{8,14}$ substrate was a gift to R.R. by G. Galli, University of Milano, Italy. This work was supported by funds from the Rockefeller University and the Howard Hughes Medical Institute. X.L. is supported by C.H. Li Memorial Scholar Fund fellowship of the Rockefeller University.

Author Contributions X.L. designed the research and performed structural biological studies; X.L. and R.R. performed sterol reductase activity assays; X.L., R.R. and G.B. contributed to data analysis and manuscript preparation; X.L. and G.B. wrote the manuscript.

Author Information Coordinates and structure factors for MaSR1 are deposited in the Protein Data Bank under accession code 4QUV. Reprints and permissions information is available at www.nature.com/reprints. The authors declare no competing financial interests. Readers are welcome to comment on the online version of the paper. Correspondence and requests for materials should be addressed to X.L. (xli05@rockefeller.edu) or G.B. (blobel@rockefeller.edu).

©2015 Macmillan Publishers Limited. All rights reserved

METHODS

Protein expression and purification. We expressed a homologue of eukaryotic sterol reductases from the methanotrophic bacterium *Methylomicrobium alcaliphilum* 20Z (MaSR1, NCBI GI number: 503913803). Its cDNA was cloned into pET-21b (Novagen) with an N-terminal 8-His tag and expressed in *E. coli* C43(DE3) (Lucigen). The transformed cells were grown to an optical density of 1.0 at OD_{600} and induced with 0.2 mM isopropyl-β-D-thiogalactopyranoside (IPTG). Cells were disrupted using a French press with two passes at 15,000 p.s.i., in a buffer containing 25 mM Tris-Cl, pH 8.0, and 150 mM NaCl (buffer A). After low-speed centrifugation, the resulting supernatant was centrifuged at high speed to sediment a membrane fraction, which then was incubated in buffer A with 2% (w/v) *N*-dodecyl-β-D-maltopyranoside (DDM, Anatrace) for 1 h at 4 °C. The lysate was centrifuged again and the supernatant was loaded onto Ni^{2+}-NTA affinity column (Qiagen). After washing twice, the protein was eluted with 25 mM Tris-Cl, pH 8.0, 150 mM NaCl, 300 mM imidazole, and 0.1% DDM, and concentrated by centricon for subsequent gel filtration (Superdex-200, GE Healthcare) in buffer A with 0.4% (w/v) *N*-nonyl-β-D-glucopyranoside (β-NG, Anatrace). The peak fraction was collected for crystallization. All mutations were generated using two-step PCR. Selenomethionine (SeMet)-labelled protein was purified similarly with the exception that 1 mM Tris [2-carboxyethyl] phosphine (TCEP) was included during the purification process.

Crystallization. Before crystallization, the protein solution was incubated with 2 mM NADPH (Sigma-Aldrich). Crystals were grown at 20 °C by the hanging-drop vapour-diffusion method. The crystals appeared after 5 days in the well buffer containing 0.1 M Tris-Cl pH 7.0, 0.2 M NH_4Ac, 30% (v/v) pentaerythritol ethoxylate (15/4 EO/OH). DDM was added into crystallization buffer at 1% (v/v) final concentration to improve diffraction. SeMet-labelled protein was crystallized in the same buffer supplemented with 6 mM dithiothreitol (DTT). Platinum derivatives were obtained by soaking native crystals for 12 h in mother liquor plus 10 mg ml^{-1} $K_2Pt(NO2)_4$. All crystals were directly flash-frozen in a cold nitrogen stream at 100 K.

Data collection and structure determination. The data were collected at National Synchrotron Light Source (NSLS) beamline X29. All data sets were processed using HKL2000 (ref. 24). Owing to the anisotropic diffraction properties, the outlier reflections were rejected based on extreme-value Wilson statistics using the program XTRIAGE[25] in the PHENIX package[26]. The anomalous signal in the SeMet-derivative data was further magnified with the local-scaling algorithm using the program SOLVE[27]. Then, the selenium sites were determined using the program SHELXD[28]. The identified sites were refined and the initial phases were generated in the program PHASER[29] with the single-wavelength anomalous dispersion experimental phasing module. Twofold NCS averaging along with solvent flattening and histogram matching was performed using DM[30]. The initial model was built in COOT[31] manually. The structure was refined with phenix.refine[26]. Model validation was performed with MolProbity[32]. Introduction of additional selenium anomalous scatterers by selective mutation and preparation of platinum derivatives confirmed the correctness of the atomic model.

The homology models of human LBR and human DHCR7 were generated by the program MODELLER[33] on the basis of the structure of MaSR1 in which the N-terminal regions (1–200 of LBR and 1–58 of DHCR7) were excluded because of low sequence conservation (Extended Data Fig. 2). All figures were generated using the program PyMOL (http://www.pymol.org/).

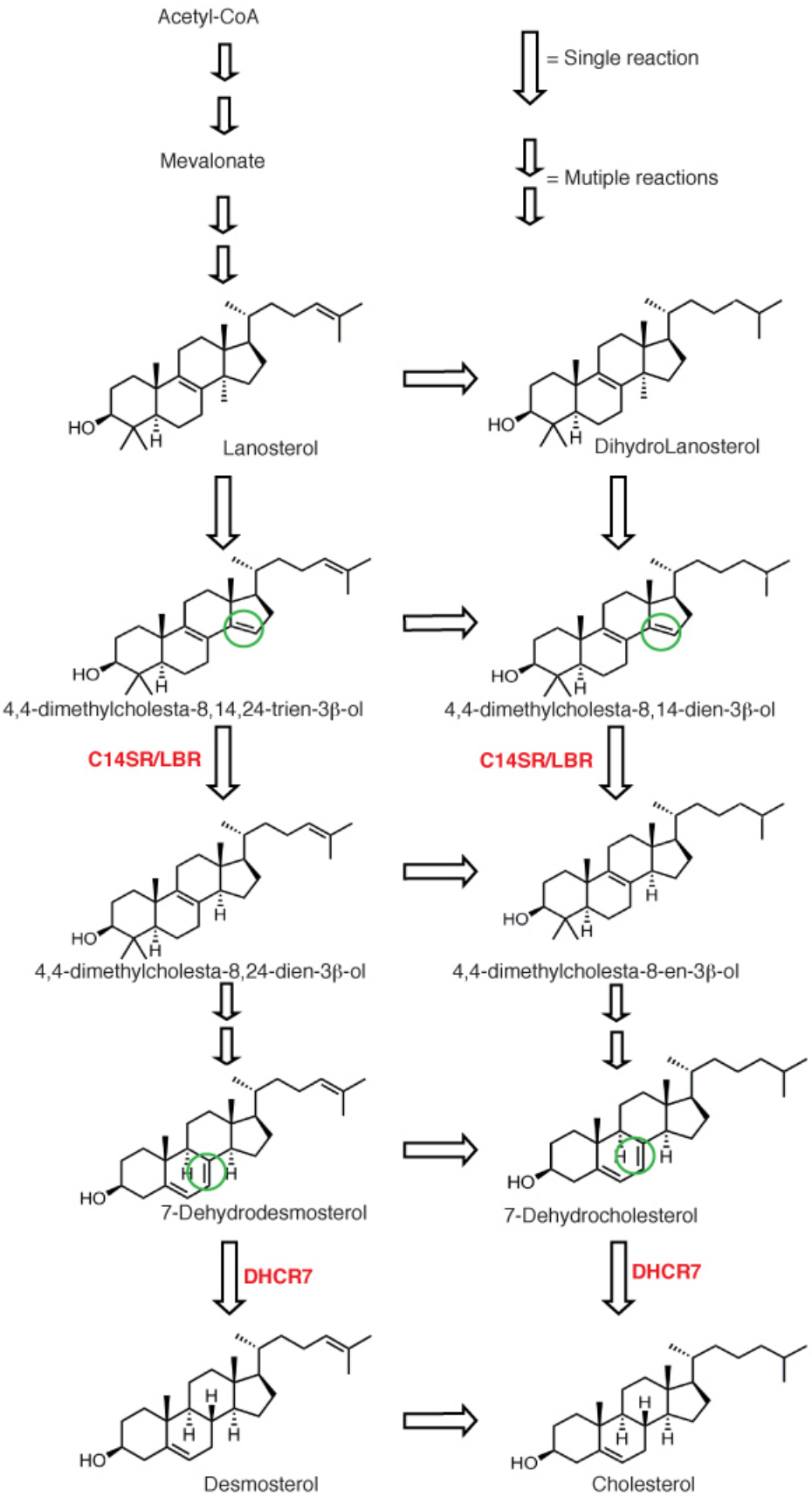
Yeast reductase complementation assay. Wild-type and mutant MaSR1 and ScErg24 were subcloned into the URA3 shuttle vector pCM190 (Euroscarf, Germany). The plasmids were introduced in Erg24-deficient *Saccharomyces cerevisiae* strain Y11164 (Euroscarf) by electroporation. A single colony was picked from a URA^- selective plate. For the yeast rescue assay, the yeast was grown on URA^- plates either in the absence or the presence of sub-inhibitory concentrations of cycloheximide (20 ng ml^{-1}) at 30 °C for 24 to 48 h. The results were confirmed by three independent experiments with different colonies.

Δ^{14}-reductase assay. The cDNA encoding human Δ^{14}-sterol reductase (C14SR) was subcloned into pCMV-SPORT6 (Open Biosystems). Wild-type and mutant MaSR1 were subcloned into pEGFP-N1 (Clontech) without the EGFP tag. HEK293 cells were grown in a 5% CO_2 incubator at 37 °C in DMEM supplemented with 10% fetal bovine serum, 2 mM L-glutamine, 100 U ml^{-1} penicillin and 0.1 mg ml^{-1} streptomycin. Cells were cultured in 10-cm Petri dishes to 80% confluence and transfected with the plasmids, using Lipofectamine 2000 (Life Technologies). After 48 h, transfected cells were recovered and the washed cell pellet was resuspended in PBS containing complete protease inhibitor cocktail (Sigma-Aldrich). Cells were lysed by sonication three times for 10 s on ice. After low-speed centrifugation, the resulting supernatant was ultracentrifuged to sediment a membrane fraction. The isolated membrane fraction was resuspended in 10 mM KPO_4/0.5 mM EDTA (pH 7.4) and frozen in aliquots for further analyses. Protein concentration was determined by Bradford method, using bovine serum albumin as a standard. Proteins of the membrane fraction were separated by SDS–PAGE, blotted on PVDF and probed with mouse monoclonal anti-Flag M2 (Sigma-Aldrich) and peroxidase-conjugated goat anti-mouse (Santa Cruz). The protein was detected using Super Signal West Pico Chemiluminescent Substrate (Pierce).

Δ^{14}-reductase activity was assayed in the membrane fractions obtained from transfected cells (0.25 mg protein per assay) using 5α-cholesta-8,14-dien-3β-ol ($C27\Delta^{8,14}$) as a substrate[15–17]. After the addition of 5α-cholestane (5 μg) as an internal standard, sterols were extracted with petroleum ether, desiccated under nitrogen stream and converted to trimethylsilyl derivatives using N,O-Bis (trimethylsilyl) trifluoroacetamide (BSTFA) and pyridine (1:1, v/v). Gas chromatography–mass spectrometry (GC–MS) analysis was performed in multiple ion detection mode using a Varian GC-MS 2000 apparatus with a Varian CP-Sil8 CB low bleed capillary column. The trimethylsilylation of sterol products yields a molecular mass increase of 72 Da. Sterol retention times were: 15.31 min, 5α-cholestane (*m/z* 372); 19.90 min, cholesterol (*m/z* 458); 20.16 min, 5α-cholesta-8,14-dien-3β-ol ($C27\Delta^{8,14}$, *m/z* 456); 20.34 min, 5α-cholesta-8-en-3β-ol ($C27\Delta^{8}$, *m/z* 458). Δ^{14}-reductase catalytic efficiency is calculated as the peak area ratio $C27\Delta^{8}/(C27\Delta^{8,14} + C27\Delta^{8})$. The $C27\Delta^{8}$ sterol was undetectable at zero incubation time.

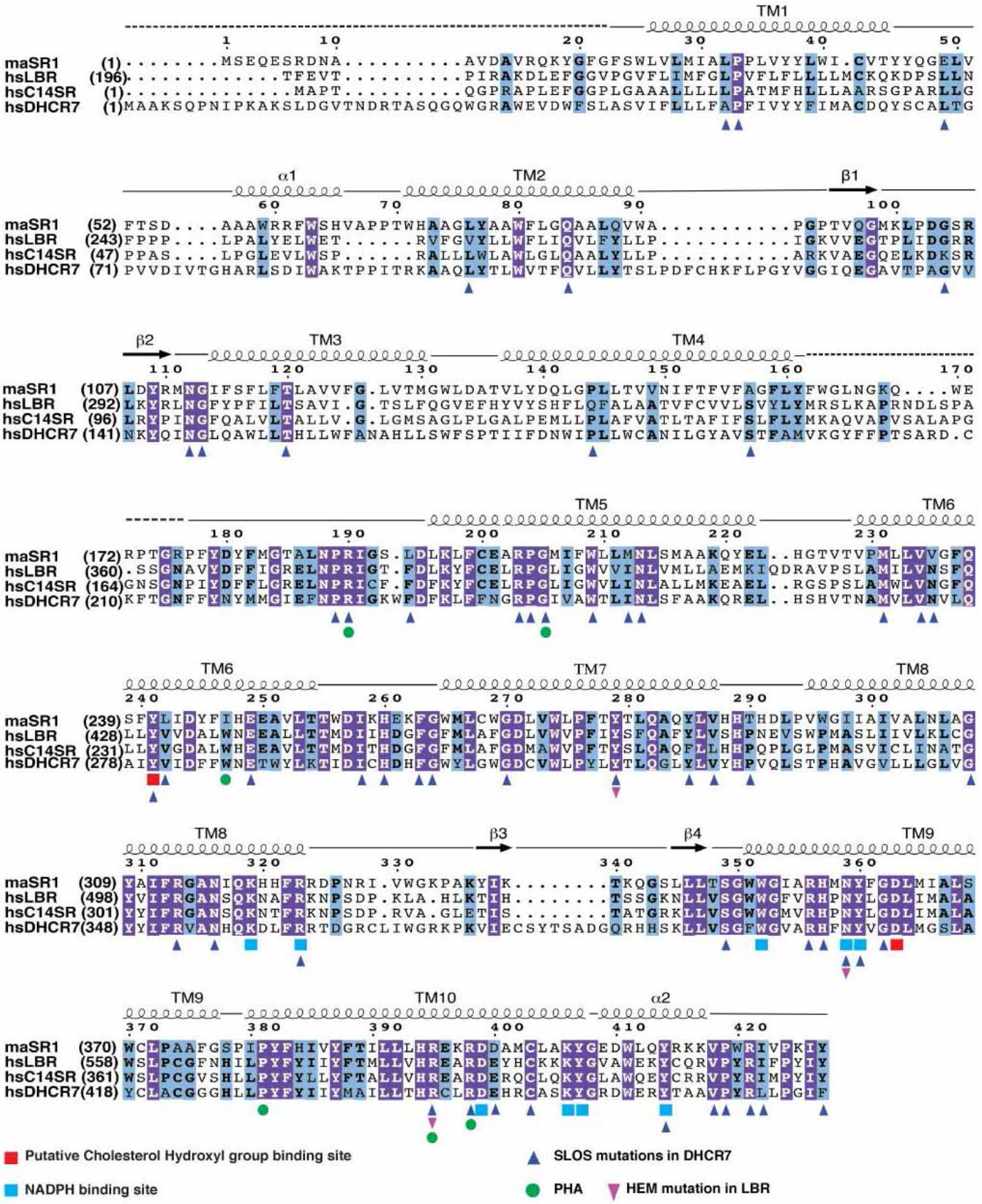
24. Otwinowski, Z. & Minor, W. Processing of X-ray diffraction data collected in oscillation mode. *Methods Enzymol.* **276,** 307–326 (1997).
25. Zwart, P. H., Grosse-Kunstleve, R. W. & Adams, P. D. Xtriage and Fest: automatic assessment of X-ray data and substructure structure factor estimation. *CCP4 Newsletter* **43,** 27 (2005).
26. Adams, P. D. *et al.* PHENIX: a comprehensive Python-based system for macromolecular structure solution. *Acta Crystallogr. D* **66,** 213–221 (2010).
27. Terwilliger, T. C. & Berendzen, J. Automated MAD and MIR structure solution. *Acta Crystallogr. D* **55,** 849–861 (1999).
28. Schneider, T. R. & Sheldrick, G. M. Substructure solution with SHELXD. *Acta Crystallogr. D* **58,** 1772–1779 (2002).
29. McCoy, A. J. *et al.* Phaser crystallographic software. *J. Appl. Crystallogr.* **40,** 658–674 (2007).
30. Cowtan, K. dm: An automated procedure for phase improvement by density modification. *Joint CCP4 and ESF-EACBM Newsletter on Protein Crystallogr.* **31,** 34–38 (1994).
31. Emsley, P. & Cowtan, K. Coot: model-building tools for molecular graphics. *Acta Crystallogr. D* **60,** 2126–2132 (2004).
32. Chen, V. B. *et al.* MolProbity: all-atom structure validation for macromolecular crystallography. *Acta Crystallogr. D* **66,** 12–21 (2010).
33. Fiser, A. & Sali, A. Modeller: generation and refinement of homology-based protein structure models. *Methods Enzymol.* **374,** 461–491 (2003).
34. Thompson, J. D., Higgins, D. G. & Gibson, T. J. CLUSTAL W: improving the sensitivity of progressive multiple sequence alignment through sequence weighting, position-specific gap penalties and weight matrix choice. *Nucleic Acids Res.* **22,** 4673–4680 (1994).
35. Clayton, P. *et al.* Mutations causing Greenberg dysplasia but not Pelger anomaly uncouple enzymatic from structural functions of a nuclear membrane protein. *Nucleus* **1,** 354–366 (2010).
36. Holm, L. & Rosenstrom, P. Dali server: conservation mapping in 3D. *Nucleic Acids Res.* **38,** W545–W549 (2010).

©2015 Macmillan Publishers Limited. All rights reserved



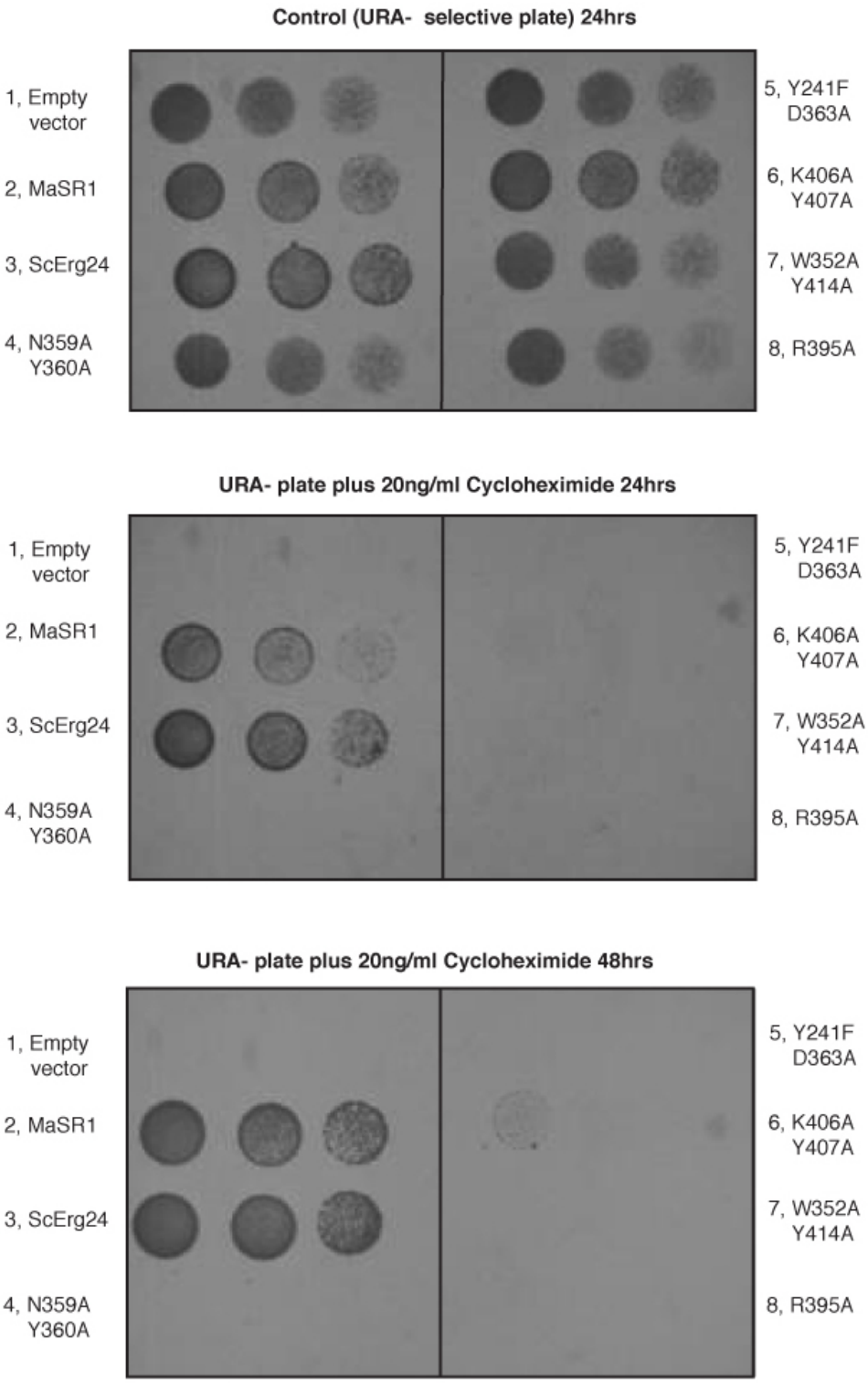
Extended Data Figure 1 | Cholesterol biosynthesis pathway[1] and sterol reductase family. Acetyl-CoA is the precursor for cholesterol biosynthesis. After several reactions, the intermediate lanosterol is synthesized. Conversion of lanosterol to cholesterol (Bloch pathway) involves many reactions, some of which are catalysed by C14SR, LBR and DHCR7 (MaSR1 homologues, in red). C14SR, LBR and DHCR7 are homologues of NADPH-dependent reductases that catalyse the reduction of the sterol double bonds indicated in the green circles.

©2015 Macmillan Publishers Limited. All rights reserved



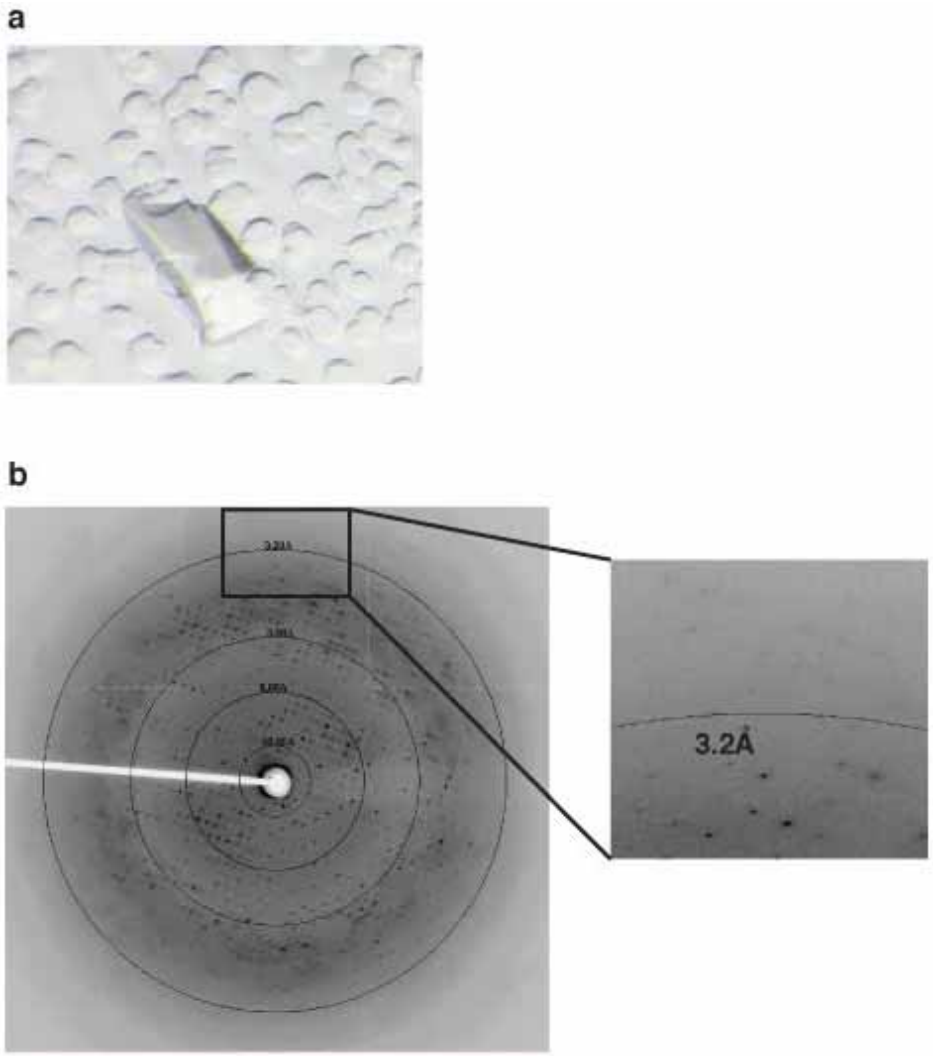
Extended Data Figure 2 | Sequence alignment of MaSR1 with human C14SR, DHCR7 and C-terminal domain of LBR. Secondary structural elements of MaSR1 are indicated above the sequences. Disordered regions in the MaSR1 structure are shown by a dashed line. Invariant amino acids are highlighted in blue (invariant in 3 of 4 proteins) and purple (invariant in all proteins). Putative cholesterol hydroxyl group binding sites are highlighted in red, NADPH binding sites are highlighted in cyan. Human disease mutations are also highlighted by different symbols. Sequence alignment was carried out using ClustalW[34].

©2015 Macmillan Publishers Limited. All rights reserved



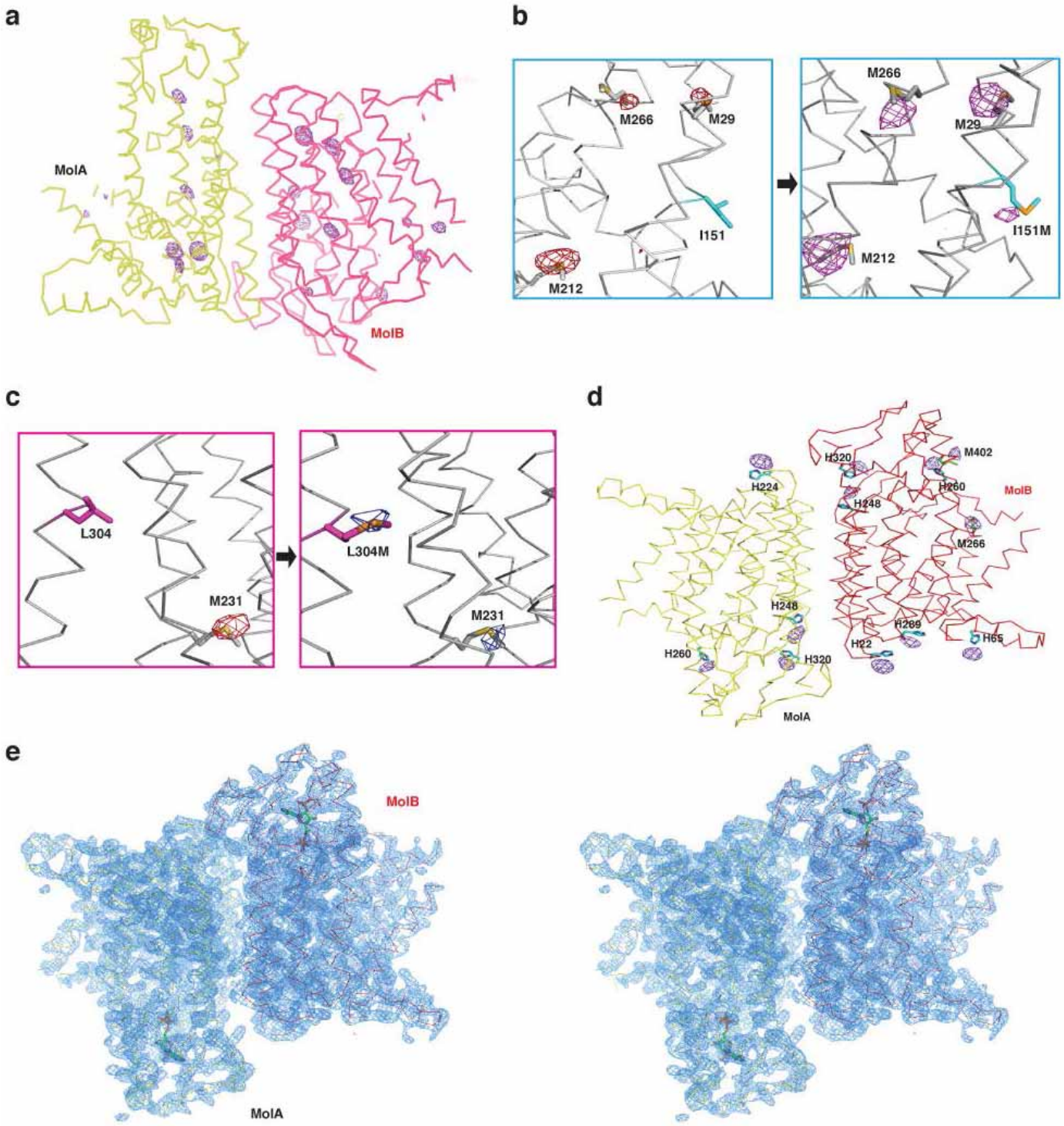
Extended Data Figure 3 | Yeast complementation assay. MaSR1 can rescue the growth of a *Saccharomyces cerevisiae* Δ^{14}-sterol reductase Erg24 (yeast MaSR1 homologue) deletion strain (ΔErg24). ΔErg24 yeast expressing wild-type MaSR1, ScErg24 and mutated MaSR1 from a URA3 shuttle vector can grow under URA^- selection (upper panel). Growth of yeast expressing MaSR1, ScErg24 and various mutated MaSR1 versions in the presence of sub-inhibitory concentrations of cycloheximide (20 ng ml^{-1}) for 24 to 48 h (lower panel). The yeast expressing MaSR1 or ScErg24 is able to grow in the presence of cycloheximide. R395A (lane 8) corresponds to R583Q in LBR which has been reported to lead to loss of activity in yeast[35]. Results are representative of three independent experiments.

©2015 Macmillan Publishers Limited. All rights reserved



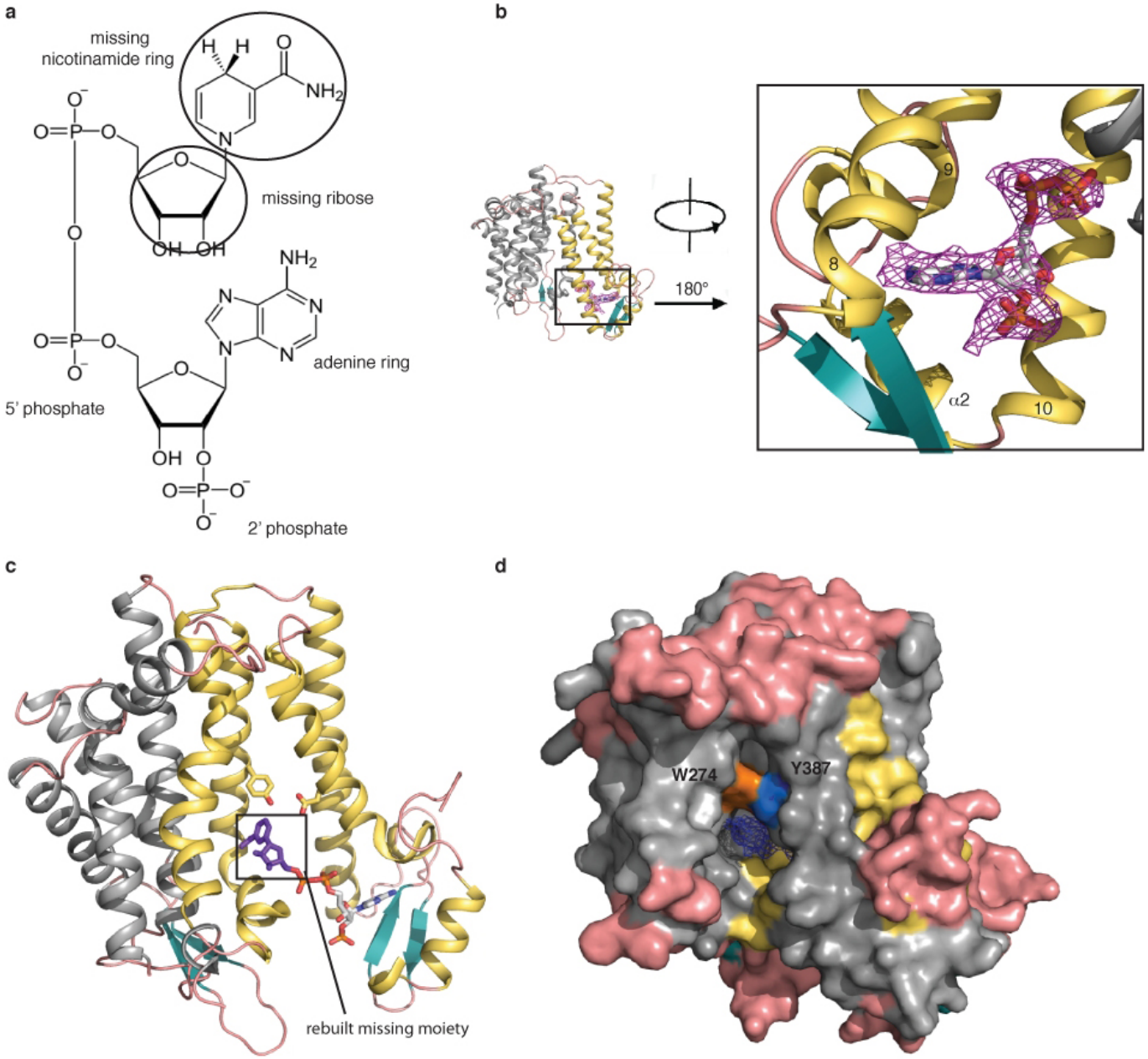
Extended Data Figure 4 | MaSR1 crystal and X-ray diffraction image. **a**, Photograph of MaSR1 crystal. **b**, A representative X-ray diffraction image of MaSR1 crystals with various resolution rings indicated by the circles.

©2015 Macmillan Publishers Limited. All rights reserved



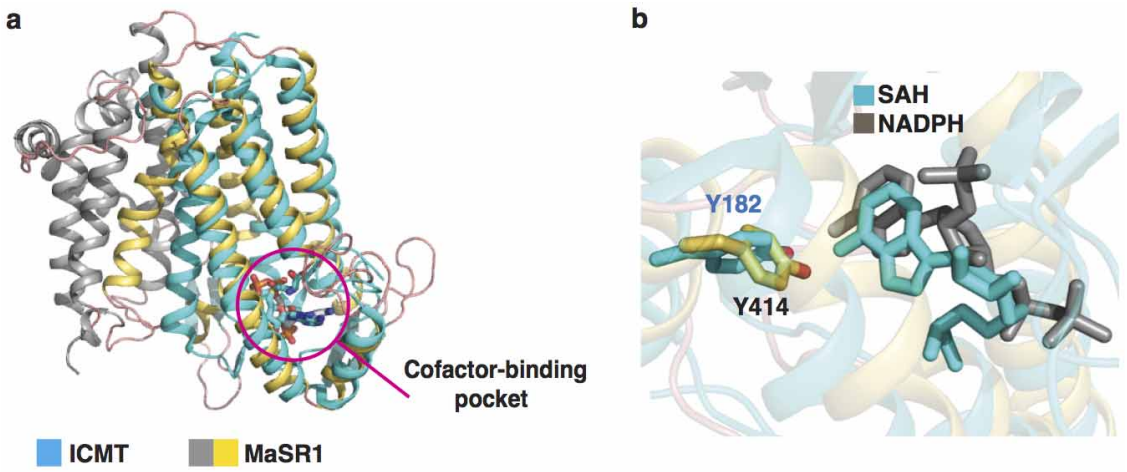
Extended Data Figure 5 | Anomalous difference Fourier electron density. **a**, Overview of the anomalous difference Fourier map for selenium atoms in an asymmetric unit. The electron density is contoured at 4.5σ (purple mesh). Two molecules (MolA, molecule A; MolB, molecule B) were observed in each asymmetric unit. **b**, Examination of the atomic model in TM4 by selenium anomalous difference signals. Left panel shows wild-type SeMet anomalous difference signals; right panel shows mutated SeMet anomalous difference signals at 3σ (purple mesh). **c**, Examination of the atomic model in TM8 by selenium anomalous difference signals. Left panel shows wild-type SeMet anomalous difference signals, right panel shows mutated SeMet anomalous difference signals at 3σ (blue mesh). **d**, A view of the anomalous difference Fourier map for platinum atoms in an asymmetric unit. The electron density is contoured at 3σ (purple mesh). There are four platinum atoms binding to histidine residues in molecule A (yellow), but there are eight platinum atoms binding to six histidine and two methionine residues in molecule B (red). **e**, An overall view of the $2F_o - F_c$ electron density, contoured at 2σ, in one asymmetric unit.

©2015 Macmillan Publishers Limited. All rights reserved



Extended Data Figure 6 | NADPH binding pocket and interaction between Trp 274 and Tyr 387 of MaSR1. **a**, The structure of NADPH with the missing moiety in the MaSR1 structure indicated in the black circles. **b**, Overview of the NADPH-bound MaSR1. SA-omit map ($F_o - F_c$ densities, magenta mesh) for NADPH contoured at 2σ. The right panel is an enlargement of the left panel (same orientation as Fig. 2a), rotated by 180°. **c**, The rebuilt missing moiety (purple) of NADPH in MaSR1. **d**, The surface representation shows Trp 274 (orange) and Tyr 387 (blue) located in the back of the sterol binding pocket. $2F_o - F_c$ map for an unidentified ligand (blue mesh) contoured at 2σ.

©2015 Macmillan Publishers Limited. All rights reserved



Extended Data Figure 7 | Comparison of MaSR1 structure with ICMT structure. **a**, A comparison of MaSR1 (grey and yellow) and ICMT[22] (cyan) structure with *S*-adenosyl-L-homocysteine (SAH) bound (PDB accession number 4A2N). DALI search[36] shows the closest entry (*Z*-score of 7.5) to MaSR1 is the structure of ICMT, consisting of 5 transmembrane helices, which had 193 Cα atoms aligned to MaSR1 (TM6–10 and α2) with r.m.s.d. of 2.8 Å. Both proteins have a similar cofactor binding pocket (magenta circle), although the sequence conservation is low. **b**, Comparison of NADPH and SAH binding pockets of MaSR1 (grey) and ICMT (cyan). The orientation of adenine–ribose moiety of SAH and NAPDH is similar with respect to the coordinating tyrosine residues in the cofactor pockets of these two enzymes.

©2015 Macmillan Publishers Limited. All rights reserved

Extended Data Table 1 | Data collection and refinement statistics

	Native	Se-SAD
Wavelength (Å)	1.0750	0.9791
Space group	P1	P1
Unit cell (Å) (a,b,c; α,β,γ)	74.66, 74.62, 79.55; 66.00, 90.37, 86.86	74.81, 75.88, 80.27; 64.96, 89.95, 86.30
Resolution (Å)	50~2.74 (2.84~2.74)	50~3.3 (3.42~3.3)
R_{merge} (%)	4.1 (41.5)	12.0 (64.6)
I/σ_I	21.1 (1.4)	20.4 (1.7)
Completeness* (%)	74.8 (28.5)	83.0 (53.0)
Number of measured reflections	63,092	136,260
Number of unique reflections	30,595	19,876
Redundancy	2.1 (1.9)	6.9 (5.4)
Wilson B factor ($Å^2$)	76.7	85.1
R_{work} / R_{free} (%)	23.29 / 28.37	
Molecules in ASU	2	
Number of atoms / B-factor:		
All atoms	6487 / 89.89	
Main chain	3128 / 89.13	
Side chain	3297 / 90.60	
Other entities	62 / 90.56	
Ramachandran plot (%):		
Favored/Allowed/Disallowed	90.8/9.2/0	
RMS-deviation in:		
Bond distances (Å)	0.013	
Bond angles (°)	1.646	

Values in parentheses are for the highest resolution shell. R_{free} was calculated with 5% of the reflections selected in the thin shell. ASU, asymmetric unit.
* See Extended Data Table 2 of the native data completeness of each shell.

©2015 Macmillan Publishers Limited. All rights reserved

Extended Data Table 2 | Native data completeness of each shell

Resolution (Å)	Completeness (%)
50.00 – 6.09	95
6.09 – 4.83	98
4.83 – 4.23	97
4.23 – 3.84	98
3.84 – 3.56	97
3.56 – 3.35	89
3.35 – 3.19	73
3.19 – 3.05	60
3.05 – 2.93	49
2.93 – 2.83	37
2.83 – 2.74	28
Overall	74.8

©2015 Macmillan Publishers Limited. All rights reserved

Extended Data Table 3 | Data collection statistics for the MaSR1 mutants I151M, L304M and Pt-derivatives

Data Set	I151M	L304M	Pt-derivatives
Wavelength (Å)	0.9791	0.9791	1.0717
Space group	P1	P1	P1
Unit cell (Å) (a,b,c; α,β,γ)	74.77, 75.38, 79.75; 65.39,89.86,86.19	74.80, 76.81, 81.37; 63.69, 90.171, 86.67	78.63, 75.00, 74.48; 94.20, 65.88, 90.80
Resolution (Å) (outer shell)	50~3.2 (3.31~3.2)	50~4.3 (4.45~4.3)	50~3.51 (3.64~3.51)
R_{merge} (%)	8.4 (53.8)	17.3 (81.5)	13.1 (79.3)
I/σ (outer shell)	24.0 (2.2)	7.3 (1.2)	12.8 (1.1)
Completeness (%)	86.9 (59.0)	81.2 (68.1)	82.2 (49.7)
Number of measured reflections	197,021	56,642	102,898
Number of unique reflections	22,484	8,813	15,845
Redundancy	8.9 (7.5)	6.4 (5.1)	6.5 (4.7)

Values in parentheses are for the highest resolution shell.

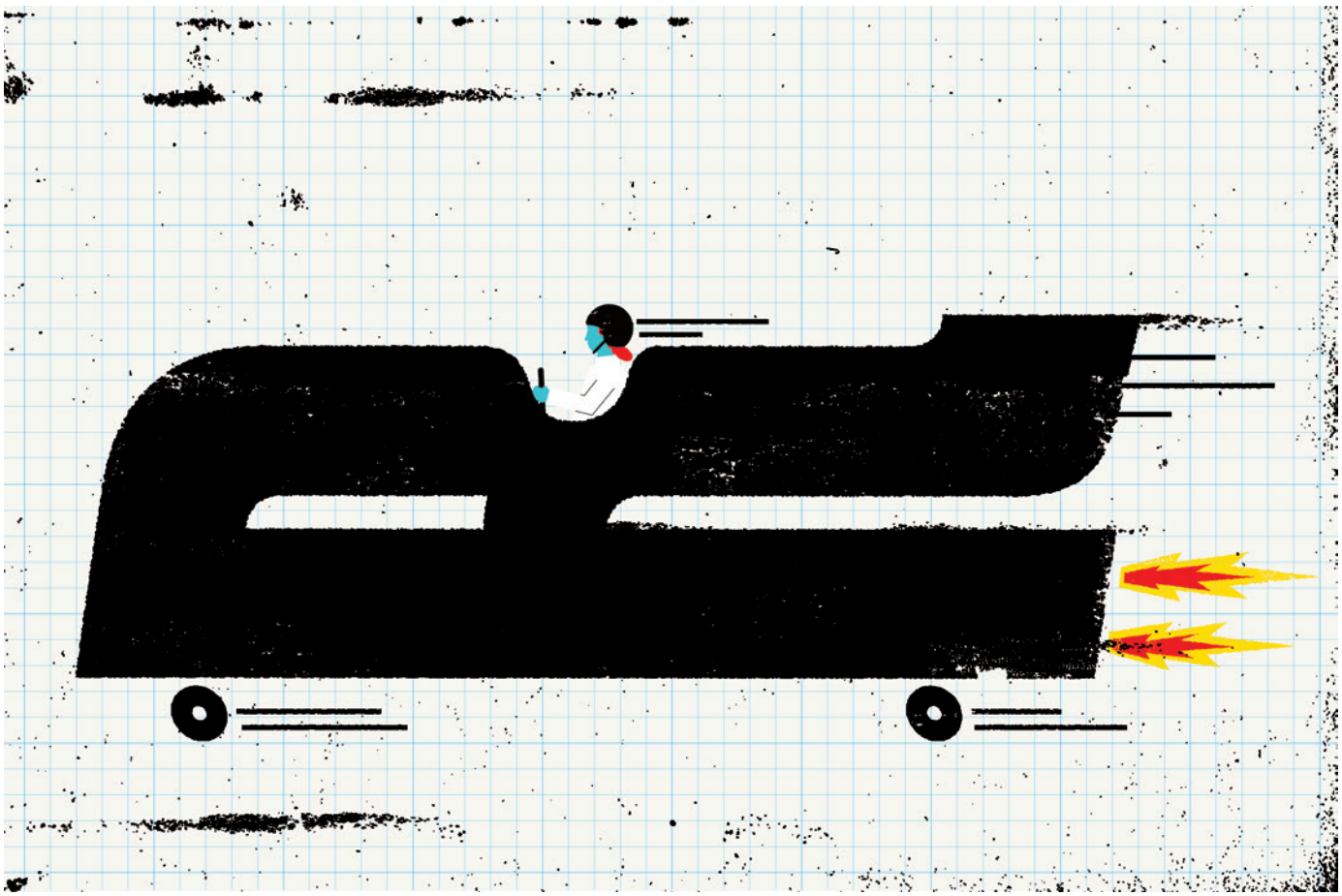
©2015 Macmillan Publishers Limited. All rights reserved

TOOLBOX

PROGRAMMING TOOLS: ADVENTURES WITH R

A guide to the popular, free statistics and visualization software that gives scientists control of their own data analysis.

ILLUSTRATION BY THE PROJECT TWINS



BY SYLVIA TIPPMANN

For years, geneticist Helene Royo used commercial software to analyse her work. She would extract DNA from the developing sperm cells of mice, send it for analysis and then fire up a package called GeneSpring to study the results. "As a scientist, I wanted to understand everything I was doing," she says. "But this kind of analysis didn't allow that: I just pressed buttons and got answers." And as Royo's studies comparing genetic activity on different chromosomes became more involved, she realized that the commercial tool could not keep up with her data-processing demands.

With the results of her first genomic sequencing experiments in hand at the start of a new postdoc, Royo had a choice: pass the sequences over to the experts or learn to analyse the data herself. She took the plunge, and began learning how to parse data in the free, open-source software package R. It helped that the centre she had joined — the Friedrich Miescher Institute for Biomedical Research in Basel, Switzerland — ran regular courses on the software. But she was also following a wider trend: for many academics seeking to wean themselves off commercial software, R is the data-analysis tool of choice.

Besides being free, R is popular partly because it presents different faces to different users. It is, first and foremost, a programming language — requiring input through a command line, which may seem forbidding to non-coders. But beginners can surf over the complexities and call up preset software packages, which come ready-made with commands for statistical analysis and data visualization. These packages create a welcoming middle ground between the comfort of commercial 'black-box' solutions and the expert world of code. "R made it very easy," says Rojo. "It did everything for me."

That, indeed, is what R's developers ▶

© 2015 Macmillan Publishers Limited. All rights reserved

intended when they designed it in the 1990s. Ross Ihaka and Robert Gentleman, statisticians at the University of Auckland in New Zealand, had an interest in computing but lacked practical software for their needs. So they developed a programming language with which they could perform data analysis themselves. R got its name in part from its developers' initials, although it was also a reference to the most widely used coding language at the time, S.

In the early days of the World Wide Web, R quickly attracted interest from scientists around the globe who needed statistical software and were willing to contribute ideas. Gentleman and Ihaka decided to make their source code accessible to everybody, and coding-literate scientists quickly developed packages of pre-programmed routines and commands for particular fields. "I can write software that would be good for somebody doing astronomy," says Gentleman, "but it's a lot better if someone doing astronomy writes software for other people doing astronomy."

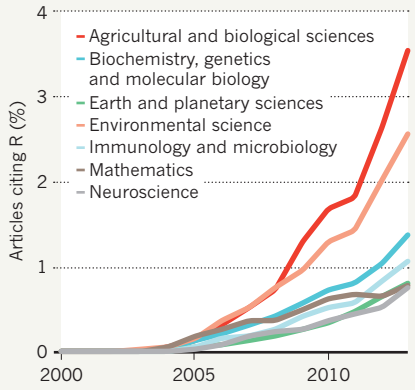
MATHEMATICAL SOLUTIONS

Karline Soetaert, an oceanographer at the Royal Netherlands Institute for Sea Research in Yerseke, took up that idea when, in 2008, she wanted to check the health of zooplankton in the estuary of the river Scheldt. Soetaert wanted to calculate how fast zooplankton were dying, using measurements along the river, but R was not equipped for that. To tackle the problem, she worked with two ecologists to develop deSolve — the first package written in R to solve differential equations. "Other software can do that, but it is expensive and closed source," she notes. Now deSolve is used by epidemiologists modelling infectious diseases, geneticists working on gene-regulatory networks and drug developers working on pharmacokinetics (how compounds behave in living organisms).

By 2003, 10 years after R's first release, scientists had developed more than 200 packages, and the first citations of the 'R Project' appeared. Today, nearly 6,000 packages exist for all kinds of specialized purposes. They allow scientists to compare a human and a Neanderthal genome (using Bioconductor: go.nature.com/s7mq39); to model population growth (IPMpack: go.nature.com/cyhons); predict equity prices (quantmod: go.nature.com/jxqasm); and visualize the results in polished graphics (ggplot2: ggplot2.org) in a few lines of code. Experts can use R to write up manuscripts, embedding raw code in them to be run by the reader (knitr: http://yihui.name/knitr). Nearly 1 in 100 scholarly articles indexed in Elsevier's Scopus database last year cites R or one of its packages — and in agricultural and environmental sciences, the share is even higher (see 'A rising tide of R').

A RISING TIDE OF R

An increasing proportion of research articles explicitly reference R or an R package.



SYLVIA TIPPMANN/SOURCE: ELSEVIER SCOPUS DATABASE

STATISTICAL SUCCESS

For many users, R's quality as statistics software stands out. The tool is on a par with commercial packages such as SPSS and SAS, says Robert Muenchen, a statistician at the University of Tennessee in Knoxville who analyses the popularity of software used in statistical computing. In the past decade, R has caught up with and overtaken the market leaders. "Most likely, R became the top statistics package used during the summer of this year," he says.

In genomics and molecular biology, a software project called Bioconductor was developed on the back of R. It helps scientists to process and compare huge numbers of genetic sequences, to query results against databases such as Gene Expression Omnibus and to upload data to the databases . It includes almost 1,000 packages, some of which help to link the millions of DNA snippets from next-generation sequencing experiments to annotated genes.

For her dive into R, Royo had intensive training: under the supervision of Michael Stadler, head of the Friedrich Miescher Institute's bioinformatics group, she took about half a year to work on R and Bioconductor. But there are plentiful chances to learn, says Karthik Ram, an ecologist at the Berkeley Institute for Data Science in California who founded rOpenSci, an initiative that helps scientists to adopt and develop R (see 'An R starter kit'). He and his colleagues teach free courses that do not require existing programming skills and are targeted towards scientists' specific problems.

One researcher who took that training is Megan Jennings, an ecologist at San Diego State University in California. She tracks bobcats, mountain lions and other wild animals, to understand their movements. Armed with more than 400,000 time-stamped photos to which she had appended species names — taken from 36 cameras running for almost a year — Jennings wanted to follow particular species at particular times of year. At first, she manually selected the photos she wanted and fed them into a black-box program called PRESENCE. But with Ram's help, she is creating an R package that reads in the tagged photos, cleans them up and then sends customized subsets of the data to a pre-existing modelling package in R. "What took me one hour to do manually, I will now be able to do in five minutes," Jennings says.

One of the greatest perks of R is its online support. Discussion forums about R-related topics outstrip online questions about any commercial statistics software says Muenchen.

"It's common to see someone post a question and the person who developed the package answer within half an hour," he says. This rapid response is key for scientists in basic research. "I can find an answer to almost any question online," says Royo. She can confidently do most of her day-to-day data analysis herself, and she helps out less proficient colleagues. Still, "I google things every day", she adds. Learning R, says Royo, has not only taught her coding skills, but has also made her more critical about other scientists' analyses.

Not every scientist is enthusiastic about learning the necessary programming — even though, says Ram, R is less intimidating than languages such as Python (let alone Perl or C). "There are going to be far more scientists that will be comfortable with click-and-drop interfaces than will ever learn to program at any time," Muenchen says. Geneticist Rabih Murr, for example, took the same R course as Royo when he was a postdoc, but he did not invest as much time in practising. To get started and develop research-specific skills in R definitely requires a commitment: "It's a matter of priorities," he says. But after becoming a lab head at the University of Geneva in Switzerland this year, he is planning to hire someone with R experience.

Like any other skill, learning R cannot be done overnight. But Jennings says that it is worth it. "Make that time. Set it aside as an investment: for saving time later, and for building skills that can be used across multiple problems we face as scientists." ■

TUTORIALS

An R starter kit

- Install R at the Comprehensive R Archive Network: http://cran.r-project.org. This also provides an introduction to the system: go.nature.com/jh9jb8.
- Many researchers recommend using a (free) powerful interface called RStudio: www.rstudio.com
- Among many online tutorials are those provided by DataCamp (go.nature.com/qndp6w), rOpenSci (ropensci.org), Software Carpentry (go.nature.com/wg3s9u) and R-bloggers (www.r-bloggers.com).
- For a sample list of R packages in different sciences, see the online version of this article at go.nature.com/zrhdkj.

NATURE.COM
For more on scientific software, apps and online tools, visit:
nature.com/toolbox

© 2015 Macmillan Publishers Limited. All rights reserved

CAREERS

@NATUREJOBS Follow us on Twitter for the latest on science jobs **go.nature.com/e492gf**

NATUREJOBS BLOG Hot science-careers news and tips **go.nature.com/lelkkf**

NATUREJOBS For the latest career listings and advice **www.naturejobs.com**

ILLUSTRATION BY DAVID PARKINS



Hopes for the year ahead

To kick off 2015, Nature*'s Careers section asked several young scientists — all 40 or under — about their plans for the year ahead and their wishes for the future of science.*

FIND THE FRONTIER

Óscar Fernández-Capetillo, 40, wants to find what causes a type of DNA damage that is linked to cancer and ageing. A group leader at the Spanish National Cancer Research Center in Madrid, he survived a serious motorbike accident last year. He also developed an easy way to find genes that help cancers to resist chemotherapies.

My New Year's resolution is to travel less. Enough of one-night stays in beautiful cities that I only get to see through the window on the taxi ride! I want time to study organic chemistry — my future life seems to be linked to drug development, and I want to understand the language of my chemist colleagues. I have bought plenty of books from Amazon and they are sitting on my desk, looking at me. But first I have to travel less.

Normal mammalian cells have two copies of each gene, so even if you mutate one copy you still have the other, and the efficiency of screening for gene function is severely reduced. Now we can screen mammalian cell lines that stay haploid, and contain just one copy of each gene. This has been like a quantum leap for us. We are looking for routes of resistance to cancer drugs and trying to understand how DNA repair genes work. Now that we have these screening platforms, I am happy to test anything that comes to mind.



NATURE.COM
Tweet your own plans and hopes at #scihopes15
For more responses: go.nature.com/6jgyce

My personal hope is that something amazing will happen that I cannot predict today and that will keep my mind busy for another 5 or 6 years. If I can tell you what I'll be doing in 5 years then it's pretty boring.

My hopes for science are that we evolve a little bit and identify scientists not from their papers but as individuals. In Europe, the system is very bureaucratic — they want you to tell them every step that you will be taking in the next five years: 'I'm going to construct a bridge, and by 2016 I'll have the first wall'. If you know where you're going, it's not science. Frontier science means that you are lost, that you are exploring, that you don't know what you'll get at the other end. ▶

© 2015 Macmillan Publishers Limited. All rights reserved

Lab-wise, I want to surround myself with colleagues who, when talking science, come up with questions that start with "Why don't you…", rather than "Why did you…" Destructive egos are OK to add control to your experiment. Constructive people move the world forward.

LOVE KNOWLEDGE

Last year, structural biologist Nieng Yan, 37, at Tsinghua University in Beijing, China, used crystallography to solve the structure of a protein that brings essential fuel into cells and that scientists have been studying for more than 40 years.

I want to go to more places. I like to travel with my parents, so I would like to bring them to see the world. They are in their 60s, and it is the right time for them: they don't need to worry about finances and they are strong enough to walk long distances. Next year, I will see New Zealand and Australia. I'm a big fan of *Lord of the Rings* and *the Hobbit*.

We're at the best and worst time for structural biology. We crystallize molecules and use x-rays to get diffraction patterns that reveal their structure, but an approach called cryo-electron microscopy (cryo-EM) has undergone a revolution because of technological advances. Challenging projects that might have taken 10 years using crystallography take just half a year with cryo-EM. You have to wonder what you will do for the other nine years. I have this anxiety about what is next. I might need to restructure my lab to expand the lab's expertise or maybe go on sabbatical.

Everyone is always talking about translational research, but if you look back, it's always the basic research that is revolutionary. I don't want people to ask me, 'Can your research save our lives?' One of our aims is to benefit human beings, but basic research is really about revealing the facets of nature. Knowing something is very cool.



"It's always the basic research that is revolutionary."
Nieng Yan

For science in general, I hope that people will no longer need to worry about funding so much. From principal investigators to graduate students, everyone is complaining about funding. I feel very sad about that. In China it's a little better; I am glad that people have begun to realize that economic growth will depend on science and technology.



DANIEL GAINES PHOTOGRAPHY 2014

Suchitra Sebastian sometimes refers to herself as a "quantum alchemist".

REACH FOR HIGH-HANGING FRUIT

Materials scientist Jen Dionne, 33, at Stanford University in California has developed a technique to visualize how light interacts with materials at the nanometre scale. Last year she gave birth to her first child and won a Presidential Early Career Award for Scientists and Engineers.

Having a baby changes your perspective — you want to work on advances that can truly make the world better for the next generation.

As a new mom, I've needed to devise alternate strategies for striking a work–life balance. I'm hoping that the schedule structure imposed by a newborn will make me more productive in lab when I'm on campus, and better able to execute writing tasks when my baby is sleeping. When given just a few hours to work on a paper or proposal, focusing quickly is key.

As a child, I remember seeing the iridescent wings of the blue morpho butterfly, and learning how their colour emerges not from pigments but from how light interacts with the microscopic structure of transparent materials. These beautiful natural examples probably drove my interest in engineering materials that interact with light in precise ways. Next year, I'm eager to experimentally demonstrate nanostructured materials in which photons travel in just one direction. Devices today — from mobile phones to supercomputers — rely on electronic components, partly because it's easy to use these to make electrons go one way. Replacing electronic components with optical ones could make technology smarter, smaller and more energy efficient.

My hope for the scientific community is that budding scientists aren't afraid to pursue research that they are genuinely interested in and enthusiastic about.

There's a quote by author Jack Kerouac: "The only people for me are the mad ones, the ones who are mad to live, mad to talk, mad to be saved, desirous of everything at the same time." I hope that scientists can find what makes them "mad to live" and to plan their careers accordingly. I would advise them not to be afraid to reach for the high-hanging fruit, and to maintain their passion for discovery amid the daily challenges that come with being a scientist.

SOLVE PROBLEMS IN NETWORKS

Bioengineer Danielle Bassett, 33, at the University of Pennsylvania in Philadelphia, last year won a MacArthur 'Genius' grant. She uses network science to understand the human brain.

KENZABURO FUKUHARA

Ahead for 2015 is to get more sleep. With a newborn and a 3-year-old, sleep is hard to come by. Also, I want to have a bowl of chocolate on my office table that is consistently filled up, because creative scientific thought is always better with chocolate!

I also want to explore applying tools from systems engineering to medicine, asking how drugs or electromagnetic stimulation could help those with mental-health problems or brain injuries. The big questions lie at the intersection between systems engineering and neuroscience. How do brains work as networks, and how does that shape understanding?

To enable more discoveries, more scientists need to spend time together. Instead of organizing single-discipline conferences, we need more interdisciplinary calls to work on a problem area, to increase the conversations about problems. How should we quantify the neurobiological effects of the learning

© 2015 Macmillan Publishers Limited. All rights reserved

AMPARO GARRIDO





RANGA RAM CHARY

Óscar Fernández-Capetillo wants to surround himself with constructive thinkers, and Hilke Schlichting wants to encourage small-group discovery.

environment — for instance, a classroom — if we want to have a translational or societal impact? If we all got together and thought about that, we could come up with new directions.

PLAN FOR DISCOVERY

Physicist Suchitra Sebastian, 38, searches for materials that could revolutionize energy transport and storage at the University of Cambridge, UK. Last year, she was listed as one of thirty exceptional young scientists by the World Economic Forum. She sometimes refers to herself as a 'quantum alchemist'.

I do live theatre, mostly comedies, and I want to make that more frequent this year. Physics can be isolating; you are constantly thinking. I do theatre because that takes you out of your head — you have to connect with people, the actors, the audience.

In my lab this year, we want to find superconductors that can work without being chilled to impractically low temperatures. We grow high-purity crystals from materials that we think are on the brink of superconductivity, then subject them to very high pressures with diamond anvils — the tips of the diamonds apply pressure in a similar way to a stiletto heel. If we push them a little bit, the electron organization in the material will tip over and become a superconductor, a material that can carry electricity with no loss of energy. It's like taking dust and making it into gold.

For the science community, I think we should focus more on the process of discovery. To make a discovery, you have to be willing to take risks and to be wrong some of the time. But the current culture of science rewards you more for being incremental, for not being wrong. Although the incremental work is crucial, the field is skewed towards it. Creativity and discovery should be equal goals.

CROSS DISCIPLINES

Trained in biomedical and electrical engineering, Christine Hendon, 31, at Columbia University in New York is working out ways to monitor beating hearts at the scale of cells or even smaller. Last year she won a New Innovator Award from the US National Institutes of Health.

I've just had my first child. It will be hard to manage conferences and travel, so my goal is to find conferences on the East Coast.

A specific goal for us is to use a device that we developed this year in explanted hearts and to demonstrate it in hearts functioning within the body. Most imaging techniques give you an idea of how the tissue looks, but when you are making a medical decision, you want to know how it functions. We want to fill in gaps in medical imaging by correlating structure with function. Then we can address clinical problems — monitoring arrhythmia or electrical abnormalities in the heart — for which ultrasound is ineffective.

If I had a hope for the scientific community, it would be to break down disciplines, to encourage students to take classes outside of their departments. For a lot of applied work, you need to work in groups. And you need a good understanding of both your own discipline and those of your collaborators. So it's good not to associate yourself only with electrical engineers or only with biologists.

Not everyone views cross-training as valuable — it means longer training times — but when you are working in these large groups on big problems, you're really effective only if you can communicate with your collaborators.

MAKE SPACE FOR SMALL GROUPS

Astrophysicist Hilke Schlichting, 32, at the Massachusetts Institute of Technology in Cambridge believes that learning how planets form is the first step in learning where we come from and how likely life is to happen.

I want to work a bit less and to spend more time with my husband and Alaskan malamute, Makalu, named after the fifth-highest mountain in the world. We have already made plans to go to Indonesia, Namibia and Tanzania together.

The big question for my lab right now is trying to understand how a newly discovered class of planets formed. The Kepler space observatory, which NASA launched in 2009, has found more than 4,000 candidate planets around other stars. It has found planets with orbits that are smaller than Mercury's and that circle their suns in 10–30 days or even fewer. Nothing like them is found in our Solar System. I want to know if these planets formed close to where we see them today or in larger orbits that moved inwards.

In terms of the future, it is getting harder and harder for people to do work in small groups that are not tied to consortia. We need to keep the diversity and independence of small research groups, particularly for junior faculty members.

There is funding for missions; people make small contributions to big missions, and that's important, but we still need to make sure that we have independent lines of inquiry. Theoretical research is generally done in small groups. I hope that we will be able to maintain that. ■ SEE COMMENT P.15

From interviews conducted and edited by **Monya Baker**.

© 2015 Macmillan Publishers Limited. All rights reserved

INFRACTION

Rapid progress.

BY JOHN GILBEY

I've read the *Daily Bulletin* religiously every work day since I started at the Accelerator Division. It gives me a picture of what is happening on the site, who is joining or leaving, when the research seminars are and even what is on the café menu. A few years ago, just after I'd taken over as project manager, I noticed a crabbily terse message in the *Bulletin* from Tony, the security chief: "All staff are reminded that access to areas within the radiation perimeter is strictly controlled. No unauthorized access is permitted or permissible. Offenders are subject to disciplinary action under Section 14 of the Code."

As most of my project is in that area, I wandered down to the Main Gate and found Tony lodged in the back office, surrounded by video monitors, binders of reports and the other paraphernalia of his trade. He slid his boots off the console as I knocked on the door frame, and stood to greet me — offering coffee. The coffee was dark and bitter, like his mood. A career in the Marines has left Tony with a distrust of non-military government employees and what he views as the slack way we do business. When I asked about the note in the *Bulletin* he sighed and waved me to a seat.

"Some joker has been using the road next to the beam line as a running track after hours," Tony reported. "And it isn't the first time. My guys tell me they've seen something before, only this time we've got a picture." He slid a print across to me. The image was murky and blurred — the output from a low-resolution surveillance camera. It showed a figure, perhaps male, jogging east along the off-limits access road, beyond that it gave little away.

"Is this the best image you've got? Is there any more footage?" Tony shook his head slowly. "Nope, this is the only one. The cameras on the gantries are hard-wired to grab a frame when an object goes past — they don't record anything else. They've promised us an upgrade to HD streaming but, hey, they've been doing that for years. I take it you can't ID the guy?"

I couldn't, and it remained a mystery. No one confessed to being inside the perimeter at night, and there were plenty of nicer places on campus to take a run if you wanted to — like across the range-land to the ridge, for example. We agreed that Tony would keep me posted if he got any more sightings and left it at that. Time passed, and occasionally an internal envelope would arrive with a printed report from Tony and a screen-shot paper-clipped to it. Always indistinct and blurry, sometimes little more than an oval blob, the runner remained enigmatic. I filed the reports under "Weird" and got on with life — until Emma, the programme director, saw the folder on my desk and asked about it.

When I explained, she flipped through the reports, then stopped — frowning. "I'm sure you've checked, but doesn't there seem to be a pattern to this?" I shrugged, it hadn't occurred to me to look. Slightly chastened, I plotted the dates of the sightings and, after a struggle with the site geolocation database, the positions of the figure. Emma was right, the events were broadly correlated — but when I swapped the time axis to a log scale the fit became almost perfect. As time passed, the sightings were getting more frequent — and all were moving west along the beam line track. When I extrapolated from the data, the events looked set to become almost continuous ten years hence — at a location about 500 metres from the first encounter.

I realized that my hands were slick with sweat. Wiping them on my shirt, I dropped an overlay onto the plot — adding the physical site layout. The end-point of the image trail would be close to the centre of the new Experiment Hall, the huge unfinished concrete bunker where we were building the new-generation detectors. Emma was oddly pleased, but sceptical — suggesting that we think hard before risking two promising careers on a wildly improbable speculation. I pondered this for a good long while, looking out of my office window at the distant hills — now burning red in the evening sun — then headed off to see Tony.

He was already on his way to find me, with a look that urged me to talk. As I told him about our analysis he kept passing an envelope to and fro between his hands, as though it might be alive. Tony perched on the low concrete wall at the side of the walkway and pulled a sheet of photo paper from the envelope, handing it to me. "The new HD cameras finally got commissioned last week, so I thought you'd like to see what they make of our friend …"

I slumped down beside him, shock building like a breaking wave as I studied the image. A lean, dishevelled figure in an unfamiliar style of labcoat was captured in mid stride, coat tails flared by his rapid movement. The face showed unmistakable fear, distress, horror.

Tony leaned across. "Now that, my friend, is what I call full haul-ass!" He rubbed his chin in a contemplative manner for a moment or two, then looked into my eyes.

"When did you say the lines cross on this graph of yours? Ten years? Hmm …" He held the photo up in front of me and pointed at the frozen figure. "Well heck, John. I don't know what you're running away from, but I'd say you're making pretty good time for a man in his late sixties. Good to see you'll be losing some weight though …" ■



ILLUSTRATION BY JACEY

John Gilbey *writes from the academic seclusion of the University of Rural England.*

NATURE.COM
Follow Futures:
@NatureFutures
go.nature.com/mtoodm

© 2015 Macmillan Publishers Limited. All rights reserved